Three-dimensional features of chondritic meteorites : applying micro-computed tomography to extraterrestrial material

Three-dimensional features of chondritic meteorites: applying micro-computed tomography to extraterrestrial material

Natasha Vasilki Almeida
(MSci. Hons Planetary Science & MA Museum Studies, UCL)

Supervisors: Professor Sara Russell (NHM), Dr Caroline Smith (NHM), & Professor Hilary Downes (Birkbeck College London)

July 2017

A thesis submitted to Birkbeck College, University of London, for the degree of Doctor of Philosophy

I, Natasha Vasiliki Almeida, confirm that the work submitted in this thesis is my own. Where information has been derived from other sources, this is clearly indicated in the text.

Abstract

This work examines the application of X-ray computed tomography (XCT) in meteoritics. This powerful technique uses the attenuation of X-rays passing through a sample to map it in three dimensions, allowing for the imaging and quantification of phases and features without the need for destructive sampling. XCT is a novel method with its applications to planetary science only recently recognised and not extensively explored. As such, this study presents two examples of using XCT to both elucidate its potential, and better understand the constituents of chondritic meteorites and the processes experienced on their parent bodies. To test the reliability of XCT, the data are conjoined with standard analytical techniques.

Firstly, the 3D fabric and textural properties of 17 L chondrites of varying petrological type and shock stage are described. Specifically, porosity is imaged, quantified and compared with pycnometry data. For each chondrite, the size distribution and orientations of metal grains are reconstructed and correlated with the degree and direction of anisotropy of magnetic susceptibility in the sample. Both porosity and metal grain fabrics reveal trends with progressive thermal and shock metamorphism. The mechanisms accounting for such correlation are explored.

Secondly, XCT is used to survey fragments of the Barwell L6 meteorite to identify and locate igneous inclusions. From this data, several inclusions were then subsampled and further geochemically investigated, including oxygen isotopic compositions, hafnium-tungsten systematics, and trace element analysis. Studied inclusions are found to be similar in composition and age to chondrules, but depleted in metal. A possible formation scenario is proposed and the potential link to chondrule formation is discussed.

Using these examples, the factors influencing the accuracy of XCT data acquisition and processing are described. The benefits and limitations of the technique, with respect to the analysis of extraterrestrial material and implications for future use, are also considered.

Humans may crave absolute certainty; they may aspire to it; they may pretend, as partisans of certain religions do, to have attained it. But the history of science - by far the most successful claim to knowledge accessible to humans - teaches that the most we can hope for is successive improvement in our understanding, learning from our mistakes, an asymptotic approach to the Universe, but with the proviso that absolute certainty will always elude us.

- Carl Sagan, The Demon-Haunted World (1995).

Acknowledgements

Firstly, many thanks to my supervisors for the life-changing opportunity, the helpful discussions, the patience, and the ‘open door policy’. Caroline, your encouragement has been a driving force behind my development as a curator – thank you for always pushing me forward, and for the laughs along the way. Sara, you always found time to listen to my thoughts and to support me in every way, whilst being an inspiration for women in our field. Hilary, your seeming disdain for my use of the Oxford comma is only surpassed by your never-failing belief in my success and ability. Immense thanks to you all and I look forward to working together in the years to come.

Many thanks to my collaborators during the past four years – Ryan Zeigler, Jérôme Gattacceca, Jan Hellmann, Thorsten Kleine and Richard Greenwood. The opportunity to work with you, and in your laboratories, has been both a pleasure and a privilege. Similarly, I am grateful to Martin Lee and Matt Genge - their advice and challenges during the examination process have been much appreciated.

This work would not have been possible without studentship funding from the Science and Technology Facilities Council, and funding for a Transnational Access visit to the University of Münster, awarded by the EU Europlanet 2020 Research Infrastructure.

Thanks to the lovely folk in the labs for their great advice, teaching, patience and good company – John, Tony (the Meteorite Slayer), Alex, Emma, Farah, Will, Anton, Tomasz, Brett, Amin, Stas, and Callum. I would also like to thank Andy Fleet and Richard Herrington – and with them, the whole Earth Sciences department at the Natural History Museum – for a multitude of reasons, not least access to specimens, funding to attend conferences, support with everyday work and for providing a home for the past four years. I would like to honour all my friends at the NHM, but particularly Bex, Julie, Mr Brown, Claire, Mike S., Zoë, Mike R., and all my fellow curators (especially the Lyme Regis crew!).

I am hugely indebted to those in the Meteorites team at the NHM that have kept me sane and shared many a Gin Friday. Much love for Epi, Penny, Jenny (hello to Jason Isaacs), Ashley, Enrica, Jay, Matthias, Paul, Nachiketa, and Helena.

Special mentions must go to those who have enriched my life immeasurably during this Ph.D. training. Debs – without whom I would never have walked through the door to Mineralley and who convinced me I was good enough (whilst also sharing a rendition of Black Sabbath on the kazoo). Dan – whose humour, kindness, music taste, and XCT smarts saw me through many a late night in the lab. Agata – whose willingness to share ideas, teach me to classify shock, and build my confidence, has shown me the great pleasure of working with true friends.

As in all aspects of life, my family are key to my success in this endeavour - feeling loved is such a privilege. Thanks to Debbie and Phil for treating me as one of their own, and to my brother, Antonio, whose pride in me has been a constant source of strength. And of course my nieces, Sophie and Rebecca, who have provided much-needed joy and fun!

I would like to dedicate this work to my mother, Elli Constantatou, and partner, Chris Le Monde. Both have held my hands throughout and I cannot express how much they mean to me. To my Pappou, Gerasimos Constantatos (1921-2015), and Yaya, Vasiliki Constantatou (1935-1995), who are always in my mind and drive me to be the best I can be. Σ'αγαπώ πάρα πολύ.

Lastly, to those we lost along the way – Gerasimos, Ismini, Teresa, Tony and Nigel – thank you.

Table of Contents

List of figures

List of tables

1 Introduction

1.1 Meteorites

Meteorites are stones of extraterrestrial origin. After ejection from their parent body, their orbit through the Solar System crossed paths with that of the Earth and they were captured by the planet's gravitational field. There are currently 56530 approved meteorites (as of 31st May 2017, Meteoritical Bulletin). As fragments of planetary or asteroidal bodies, they are a key source of evidence for scientific understanding of the formation and evolution of our Solar System. Meteorites derive from a variety of parent bodies in the asteroid belt, as well as from the Moon and Mars. The link between meteorites and asteroids has developed from the first suggestion of geological diversity in the asteroid belt, based on colour differences (Bobronikoff, 1929) to the prediction of composition of asteroid 25143 Itokawa by ground-based telescopes (Binzel et al., 2001) and confirmation via sample return by the JAXA Hayabusa mission (Tsuchiyama, 2014). In fact, the recent NASA mission, *Dawn,* provided new evidence supporting the long-proposed link between howardite, eucrite and diogenite (HED) meteorites, and the second-largest body in the asteroid belt, 4 Vesta (McCord et al., 1970; McSween et al., 2013). Although we lack context regarding the provenance of most meteorites, the nature of asteroids speaks to one of the most crucial aspects of these messengers. The vast majority are chondrites, which derive from parent bodies that did not experience widespread melting, thus preserve a record of material and processes that occurred at the very beginning of our Solar System. In contrast, the Earth's rocks have been processed continuously for over 4.5 Ga, thus much of the planet's history and starting material has been lost. Similarly, meteorites from more evolved bodies, including the Moon (297 lunar meteorites as of 31st May 2017, Meteoritical Bulletin), Mars (189 martian meteorites as of 31st May 2017, Meteoritical Bulletin), and the asteroid 4 Vesta (1871 HED meteorites as of 31st May 2017, Meteoritical Bulletin), are invaluable for our understanding of the processes that have occurred on larger planetary bodies.

The aims of the science of meteoritics are broad, including developing our knowledge of: the starting material from which our Solar System originated, the process of accretion of asteroids and planets, the process of melting and differentiation leading to

core formation, the starting material from which the Earth formed, the contribution of meteorites to the Earth's (and Moon's) volatile inventory, the geological evolution of the Moon and Mars, the potential for life elsewhere in the Solar System, and many other 'big questions' inherent in our exploration of our place in the Universe.

1.2 Formation and timescales of the Solar System

To contextualise the work in this thesis, we must consider the wider history of our Solar System. Thorough reviews can be found in Russell (2007), Lauretta and McSween (2006) and many others. The canonical theory for Solar System formation begins with the Big Bang (circa 13.7 Ga) and subsequent enrichment of the interstellar medium by generations of stars that, through nucleosynthesis, produced the elements that make up all the matter we know of. Our Solar System is defined by the birth of the Sun, following the collapse of a dense molecular cloud – a part of the interstellar medium that contained heavy elements. The reason for this collapse is not known, though theories include triggering by a nearby supernova (Hester et al., 2005). Surrounding the proto-Sun, was a disc of dust and gas, known as the protoplanetary, or accretionary, disc. It is here that meteorites are our key source of information. The innermost part of the disc was hottest, thus the terrestrial, or rocky, planets formed here. Temperatures were much lower, below that of the condensation temperature of water further out, past the orbit of the asteroid belt. This is commonly referred to as the 'snow line', beyond which planetary bodies are predominantly composed of volatile compounds. Although first suggested in the works of Kant (1755) and Laplace (1796), modern technologies have been crucial in our understanding of the protoplanetary disc, including direct observation by both ground- and space-based telescopes such as Hubble and the Atacama Large Millimetre Array, providing insight into the distribution of dust in discs around other stars, and the duration for which they remain around young stars (Figure 1.1).

The first Solar System solids formed in this protoplanetary disc. These are refractory inclusions, so-called for the refractory nature of the minerals that form them, condensing from the hot solar gas. They are preserved in unaltered calcium-aluminium-rich inclusions (CAIs) which have been isotopically dated at 4.567 Ga (Amelin et al., 2002). CAIs are predominantly found within carbonaceous chondrite meteorites and explored in more depth later in this chapter. The next major step was the formation of chondrules. From the Greek, χόνδρος, meaning clump or grain,

chondrules are small (~ mm-sized), usually spherical objects, composed of silicate minerals (predominantly olivine, pyroxene, plagioclase), iron-nickel (FeNi) metal, sulphides and glass. They exhibit igneous textures, which suggests formation from a melt, or partial melt. Their formation is a source of much debate in meteoritical research, and, with direct application to this thesis, is explored further below.

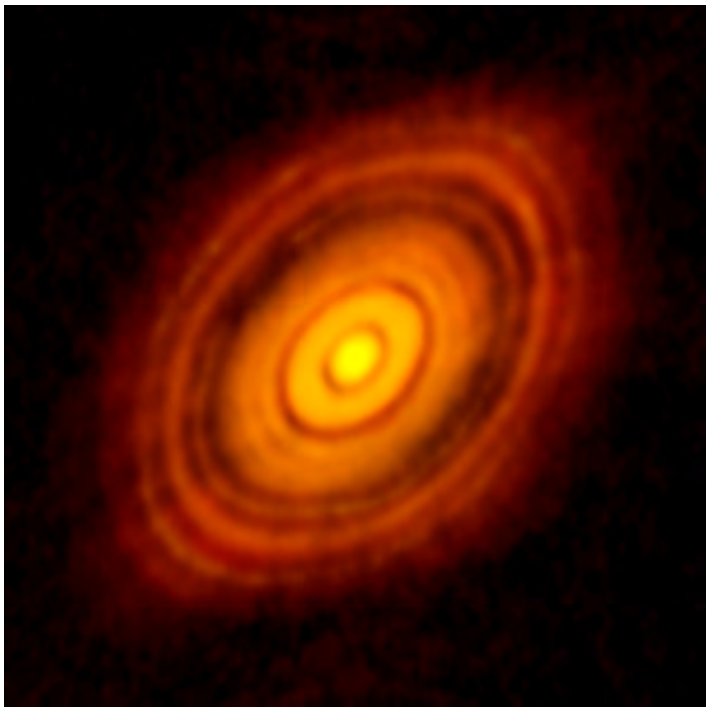

Figure 1.1. A protoplanetary disk around the HL Tauri star, thought to be ~ 1 Ma old. The gaps are hypothesised to show the location of planetesimal accretion. The disk is ~ 1500 light-minutes across, and ~ 450 light years from Earth. Image taken by the Atacama Large Millimetre Array (ALMA). Credit: European Southern Observatory/National Astronomical Observatory of Japan/National Radio Astronomy Observatory/National Science Foundation.

It is thought that refractory inclusions, chondrules, metal grains, and dust all coexisted in the accretionary disc. There is evidence of high temperature events that melted and/or remelted these components to various degrees. Isotopic evidence using the ^{206}Pb-^{204}Pb system, indicates that CAIs are the oldest materials, however there is evidence of igneous textures in some CAIs, which is thought to be a result of late-stage reprocessing (Russell et al., 2005). Evidence from ^{26}Al-^{26}Mg suggests that chondrules formed, potentially contemporaneously with CAIs, over a period of ~3 Ma (Connelly et al., 2012; Kita et al., 2000; Rudraswami and Goswami 2007).

The following step in the evolution of our Solar System was the accretion of planetesimals, which are > kilometre-size bodies. As yet, there is no consensus on the mechanism of formation, however suggestions include sedimentation of dust to the midplane of the disc. Theories must consider several lines of evidence from meteorites, observations of long-lived accretionary discs around other stars, the effect

of a turbulent protoplanetary disc, combined with constraints on accretion times e.g. due to the gas-drag effect that pulled material into the early Sun. Subsequent to their formation, planetesimals experienced some degree of post-accretionary processing: thermal metamorphism, impact, melting and differentiation. This post-processing is further explored below.

1.3 Meteorite classification

Meteorites can be classified in a number of ways. Firstly, if they have been seen to fall and retrieved soon after, they are considered 'falls'. Conversely, if not associated with a witnessed event, they are 'finds'. The distinction has important research implications, since any time spent on Earth implies terrestrial contamination, such as weathering or other chemical interactions with the environment. In this study, falls are predominantly used to mitigate against this effect.

Broadly, meteorite compositions can be resolved into two groups: those that experienced significant melting (achondrites) and those that remained relatively unscathed by differentiation (chondrites). Meteorites are frequently classified using their whole-rock chemical and oxygen isotopic compositions, as well as petrological characteristics, and are thought to represent over 120 parent bodies (Hutchison et al., 2004). Oxygen isotope systematics point to the accretion of the meteorite parent bodies from reservoirs with distinct O isotope compositions, i.e. different parts of the solar nebula, and are used to fingerprint the origin of extraterrestrial material. This is explored further in *Section 2.6*. There are several taxonomic studies that outline different arguments for the hierarchy of meteorite relationships (Wasson, 1985; Kallemeyn et al., 1996; Krot et al., 2004). Figure 1.2 is a schematic diagram of meteorite taxonomy outlining the groupings. Figure 1.3 shows the diversity of textures in different groups of meteorite – iron, pallasite, primitive chondrite, and achondrite.

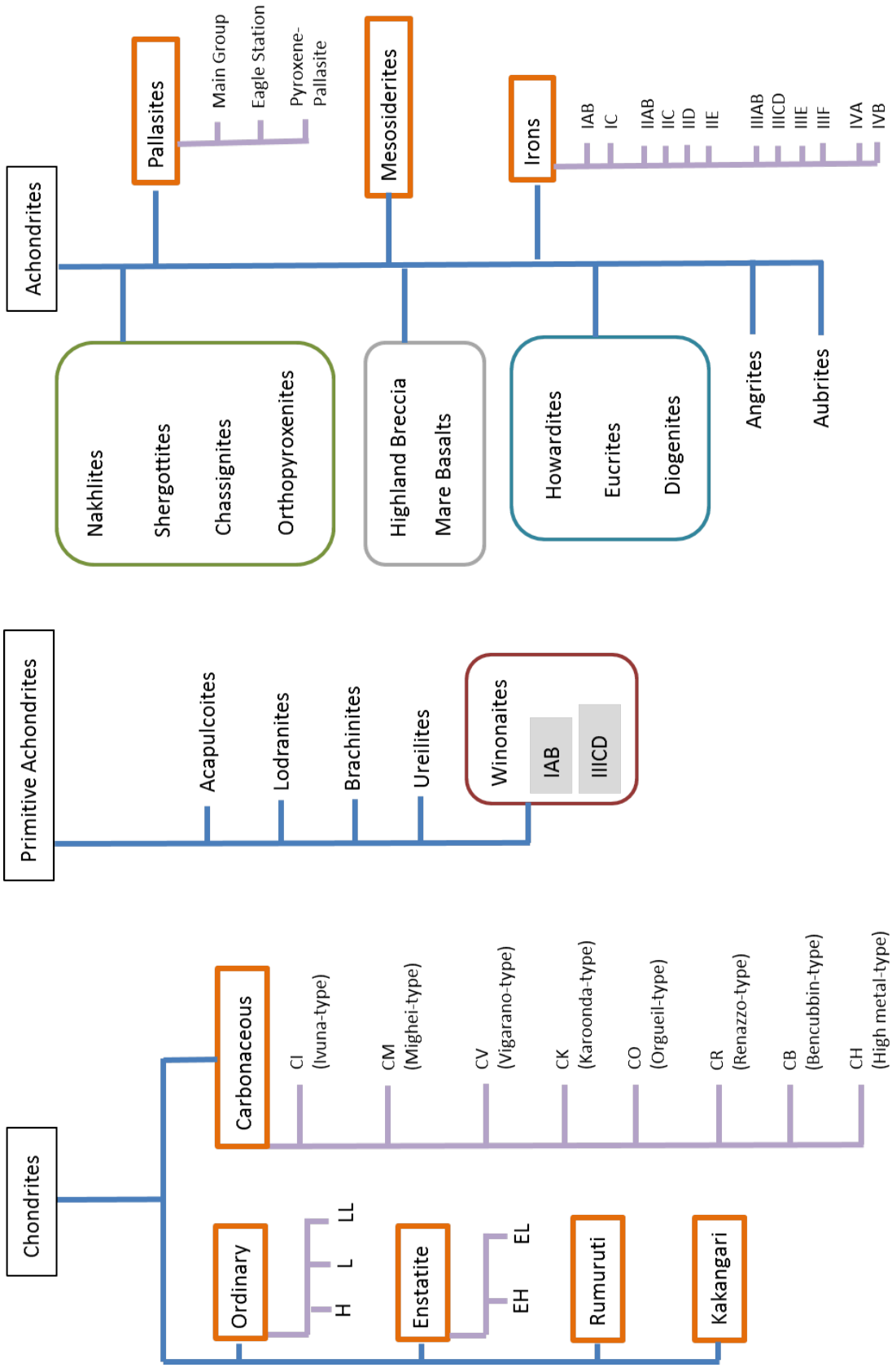

Figure 1.2. A schematic of meteorite classification showing the division between chondritic (unmelted) material and achondrites, which have experience varying degrees of parent body processing and metal-silicate segregation.

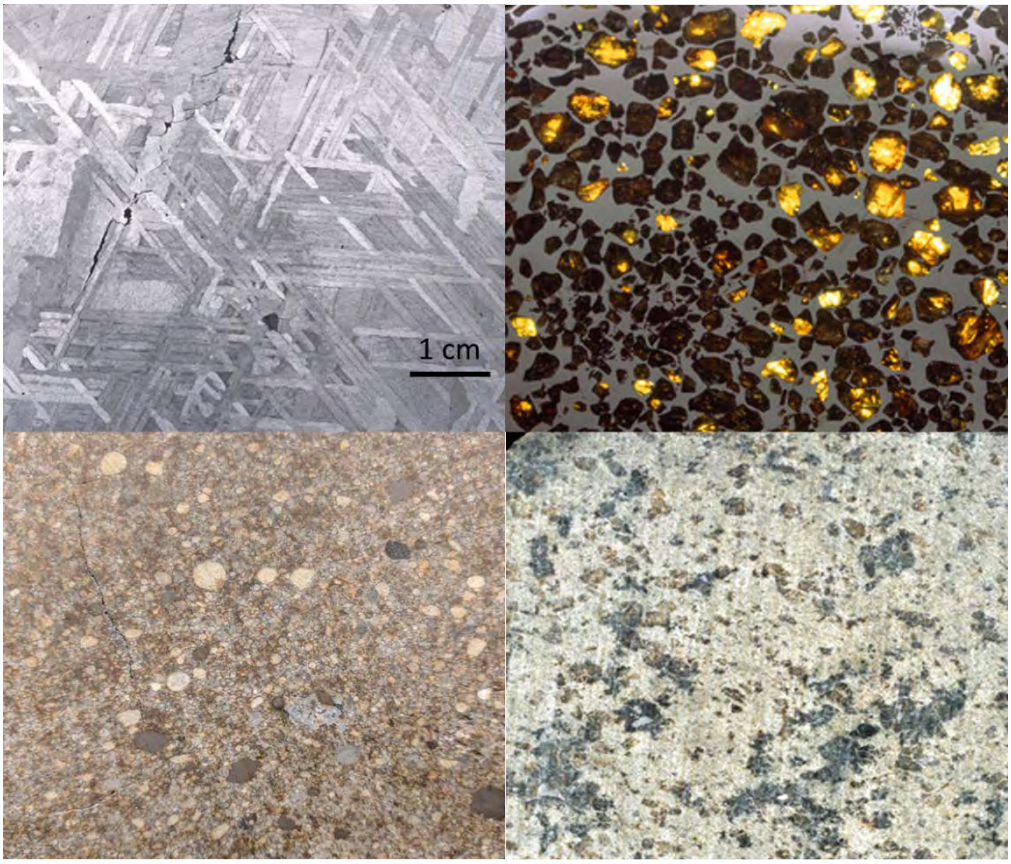

Figure 1.3. Images from different groups of meteorites illustrating the diversity in composition and texture. Top: Canyon Diablo IAB iron meteorite (left) and Esquel main group pallasite (right). Bottom: Parnallee LL3.6 ordinary chondrite (left) and Sayh al Uhaymir 008 martian shergottite (right). Images copyright of the Trustees of the Natural History Museum.

Achondrites are the result of varying degrees of physical and chemical separation of metal and silicate on their parent bodies. They are essentially igneous rocks i.e. melts, partial melts and residues. Evidence from achondritic meteorites is combined with modelling and experimental petrology to further understand the process of differentiation, which is thought to have been driven by heating from radioactive decay of short-lived radionuclides such as ^{26}Al (e.g. Huss et al., 2006). Recent work on tungsten isotopes has indicated that accretion and differentiation occurred very soon (~ 0.2-0.7 Ma) after CAI formation (Kleine et al., 2005; Kruijer et al., 2014).

The achondrites include the iron meteorite group, whose modern classification is based on chemical composition where four groups are ordered based on their Ga and Ge contents (e.g. Wasson and Kimberlin, 1967). Some groups are thought to represent the cores of differentiated bodies (Scott and Wasson, 1975), whereas others may result from local differentiation in impact melt pools (Wasson and Kallemeyn, 2002). The

stony-iron pallasites, which consist of olivine (~ 35 - 85 vol%) and metal, may originate from the core-mantle boundary of differentiated asteroids (Wasson and Choi, 2003). Mesosiderites, also stony-iron meteorites, are breccias of FeNi metal, troilite and silicates that range from lithic clasts to mineral grains and fine-grained matrix. Although there is no clear consensus, they are though to originate from turbulent metal-crust mixing during core formation, and/or as a result of the disruption and reassembly of colliding asteroids (Hewins, 1983). Crustal achondrites include the aforementioned lunar and martian meteorites, as well as aubrites (with close affinity to the enstatite chondrites) angrites and the HED clan. Most are volcanic, plutonic, cumulates, or breccias, and provide insight into activity on large differentiated bodies whose planetary heat engines were active for longer than most asteroids in the belt. Primitive achondrites show chemical similarities with chondrite groups, i.e. their precursors, but also evidence of considerable processing on the parent body. They include ureilites, the acapulcoite-lodranite clan, the winonaites-IAB-IICD clan, and brachinites (Weisberg et al., 2006).

Chondrites, the most plentiful group of meteorites, originate from unmelted, undifferentiated parent bodies. Thus, these asteroids have not experienced prolonged geological activity, and retain the characteristics of some of the earliest processes occurring in the Solar System. There are five groups of chondrites: ordinary chondrites (O; n = 48792), carbonaceous chondrites (C; n = 2146), enstatite chondrites (E; n = 599), Rumuruti chondrites (R; n = 182), and Kakangari chondrites (K; n = 4) (as of 31st May 2017, Meteoritical Bulletin). This study is concerned with ordinary chondrites, which are explained in more detail later. Enstatite chondrites are divided according to their iron content – into high Fe (EH) and low Fe (EL) groups. Their mineralogy and chemistry, including Fe-poor silicate, Si-bearing metal, and unusual sulphide and nitride phases, indicate that enstatite chondrites formed in highly reduced nebular environment (Kallemeyn and Wasson, 1986). They are notable as their O isotope compositions fall on the TFL, suggesting a possible relationship with the Earth (Clayton et al., 1984). Rumuruti chondrites are mostly regolith breccias with rare CAIs, rich in noble gases and exhibiting some similarity to ordinary chondrites in bulk composition (Bischoff et al., 2011). The Kakangari group share some characteristics with each other class of chondrite, e.g. metal abundances similar to H chondrites, or oxygen isotopes similar to CR chondrites, but are not affiliated with any of the main groups – O, E, or C (Weisberg et al., 1996).

Carbonaceous chondrites (CCs) are further divided into eight groups, named for the meteorite that typifies the characteristics of the group, such as similar refractory lithophile element abundances, chondrule size, oxygen isotopic composition and mineral compositions. They are: CI (Ivuna-like), CM (Mighei-like), CO (Ornans-like), CV (Vigarano-like), CK (Karoonda-like), CR (Renazzo-like), CB (Bencubbin-like), and CH (high Fe; ALH 85085-like). They represent the most primitive material that has remained unmodified since the beginning of the Solar System, for example sub-micron sized grains in CC matrix. Calcium-aluminium-rich inclusions (CAIs), which were the first solids to form and thus provide the age of formation of the Solar System at 4567 Ma (Amelin et al, 2002; Bouvier and Wadhwa, 2010; Connelly et al. 2012), are also more commonly found in CCs. They are broadly grouped into clans based on similarities in their chemistry or petrology, for example, indication of formation in the same region of the solar nebula based on isotopic compositions. CI chondrites, named for the type specimen, Ivuna, are notable for their elemental abundances being near identical to the solar photosphere, minus highly volatile elements like hydrogen and helium (McSween, 1987; Anders and Grevesse, 1989).

1.4 Chondrules

Chondrules are broadly spherical objects consisting of ferromagnesian silicates, metal, and feldspathic mesostasis, but showing considerably diversity including completely or incompletely melted (thus possibly lacking 'droplet form'), and fragmented particles (Jones et al., 2005). Chondrules are a primary component (50-80 vol%) of chondrites, and therefore asteroids. There are many reviews of chondrule characteristics and formation processes (e.g. Lauretta et al. 2006; Rubin, 1997; Brearley and Jones, 1998; Jones and Scott, 1996; Jones et al., 2005; Connelly and Jones, 2016) but a brief overview is included here, since all specimens included in this study are chondrites.

1.4.1 Types of chondrules

Data on chondrules include petrological, physical, bulk and mineral chemical, trace element and isotopic investigations. Chondrule textures are not correlated with size or shape. They are primarily composed of olivine [$(Mg,Fe)_2SiO_4$], low-Ca pyroxene [$(Mg,Fe)SiO_3$], and high-Ca pyroxene [$Ca(Mg,Fe)Si_2O_6$]. Chondrules may also contain a glassy silicate mesostasis which is often rich in Na, Al, Si, Ca and K relative to the

bulk composition of the chondrite (Hewins, 1997). Iron-nickel alloys, sulphides and oxides are also found. Chondrules in unequilibrated chondrites often have rims of fine-grained material, which are compositionally distinct from the chondrules, but also comprised of silicate, metal and sulphide minerals (Brearley and Jones, 1998). Unequilibrated chondrites show wide variations in their chemistry, implying that the components were not in 'chemical communication' for a sufficient length of time to homogenise. Thus, they contain a more primitive chemical and mineralogical signature from the protoplanetary disk (Lauretta et al., 2006). McSween (1977) developed a scheme dividing chondrules in to two main groups based on iron content: type I are FeO-poor (Fo and En > 90) and type II are FeO-rich (Fo and En < 90). Gooding and Keil (1980) further developed a chondrule classification system based on texture and dominant mineral:

- Porphyritic chondrules exhibit abundant large (up to half the chondrule diameter) crystals in a fine-grained or glassy mesostasis.
- Porphyritic olivine (PO) and pyroxene (PP) chondrules contain a dominant mineral (olivine or pyroxene respectively) at >10:1 volume ratio.
- If the mineral abundances are intermediate, they are defined as porphyritic olivine-pyroxene (POP) chondrules.
- Granular chondrules contain many very small grains of uniform size, typically < 10μm with poorly defined outlines. They are further subdivided into granular olivine (GO), olivine-pyroxene (GOP) and pyroxene (GP) groups as with porphyritic chondrules.
- Barred olivine (BO) chondrules are defined by olivine crystals with one dimension significantly greater than the other two. These grains all share the same crystallographic orientation, or may have several sets of grains with shared orientations.
- The texture of radiating pyroxene (RP) chondrules appears as a fan-like array of low-Ca pyroxene radiating from a point near the chondrule boundary. They may contain more than one such fan.
- Cryptocrystalline chondrules are defined by a lack of crystal structure in optical microscopy, due to a large abundance of glassy material. Submicron dendritic textures have been observed in some chondrules.
- Metallic chondrules, consisting primarily of FeNi metal with some troilite and minor schreibersite and metallic Cu are also found.

Subsequent classification work has employed a combination of these criteria (Lauretta et al., 2006). Examples of different types and textures of chondrules are given in Figure

1.4 and Figure 1.5. For unequilibrated chondrites, chondrules with porphyritic texture are classified as Type I (FeO-poor) or Type II (FeO-rich) and are further subdivided as A (SiO_2-poor, i.e. olivine-rich) or B (SiO_2-rich, i.e. pyroxene-rich). Type IA PO chondrules contain abundant small euhedral olivine crystals (15-40μm) along with rounded grains of metallic FeNi in a glassy or microcrystalline mesostasis. Type IAB and IB are poikilitic in texture where olivine grains are enclosed by larger pyroxene crystals. These low-Ca pyroxene crystals are frequently rimmed by Ca-rich pyroxene. Type IB porphyritic chondrules are distinguishable from Type IAB by their high proportion of pyroxene and low olivine, which often occurs as relict grains. Type IIA PO chondrules often host larger olivine crystals (up to 150 μm) than type IA PO. Low-Ca pyroxene crystals in these chondrules in Semarkona, one of the most primitive ordinary chondrites, have been described as twinned, generally tabular and exhibiting lamellar compositional zoning. These chondrules also contain metal grains, and glassy mesostasis. Type III chondrules are radial pyroxene are very Si-rich and similar composition to Type IB chondrules. Chondrules described as granular, with very-fine grained textures in optical observations, are found to be porphyritic in SEM observation.

An additional system to describe chondrules has been proposed by Sears et al. (1992), which classifies the particles based on their catholuminescence and mineral composition rather than modal mineralogy and texture. Catholuminescence, a measure of visible light emission from the sample when excited by electron beam interaction, is dependent on trace element abundances and lattice defects. Group A chondrules show brightly luminescence, whereas Group B exhibit little or no luminescence. The FeO and CaO concentrations in olivine, along with the mesostasis composition, further subdivide the groups. Sears et al. (1992) used this classification to suggest that chondrule groupings represent alteration of primitive chondrules on parent bodies.

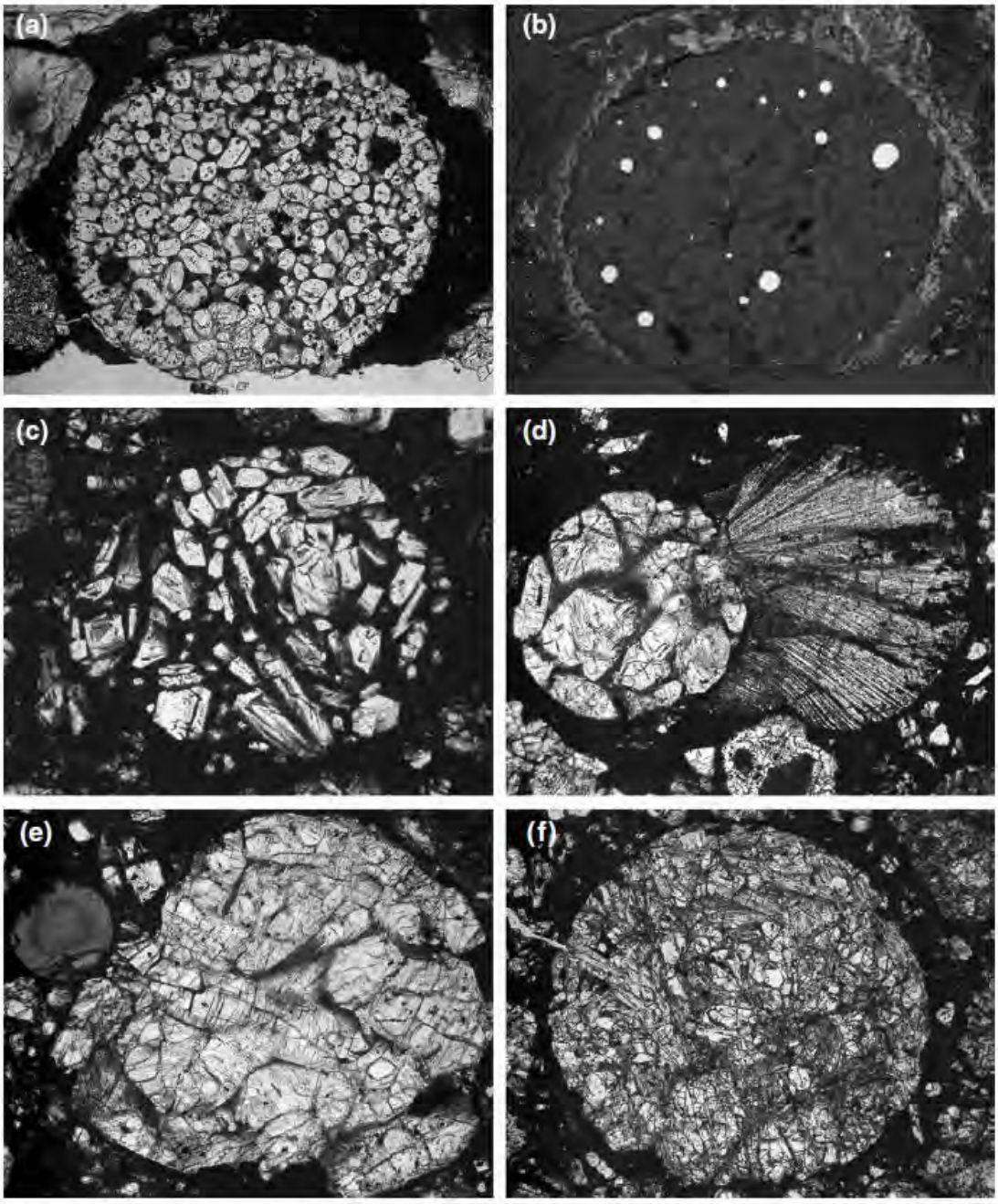

Figure 1.4. From Lauretta et al. (2006): Optical microscopy images of a selection of porphyritic chondrule textures. The field-of-view is 1.35mm. (a) PO chondrule from L chondrite QUE 97008. (b) reflected light image of the same chondrule as (a) showing rounded droplets of metal near the chondrule boundary. (c) PO chondrule from Clovis (H chondrite) with larger grains than (a). (d) a PO-RP chondrule pair from the L chondrite EET 90066. (e) a PP chondrule from ALHA 78119 (L chondrite) with small cryptocrystalline chondrule in upper left of image. (f) POP chondrule from LL chondrite Bishunpur, dominated by olivine crystals in the centre and pyroxene towards the outer edges.

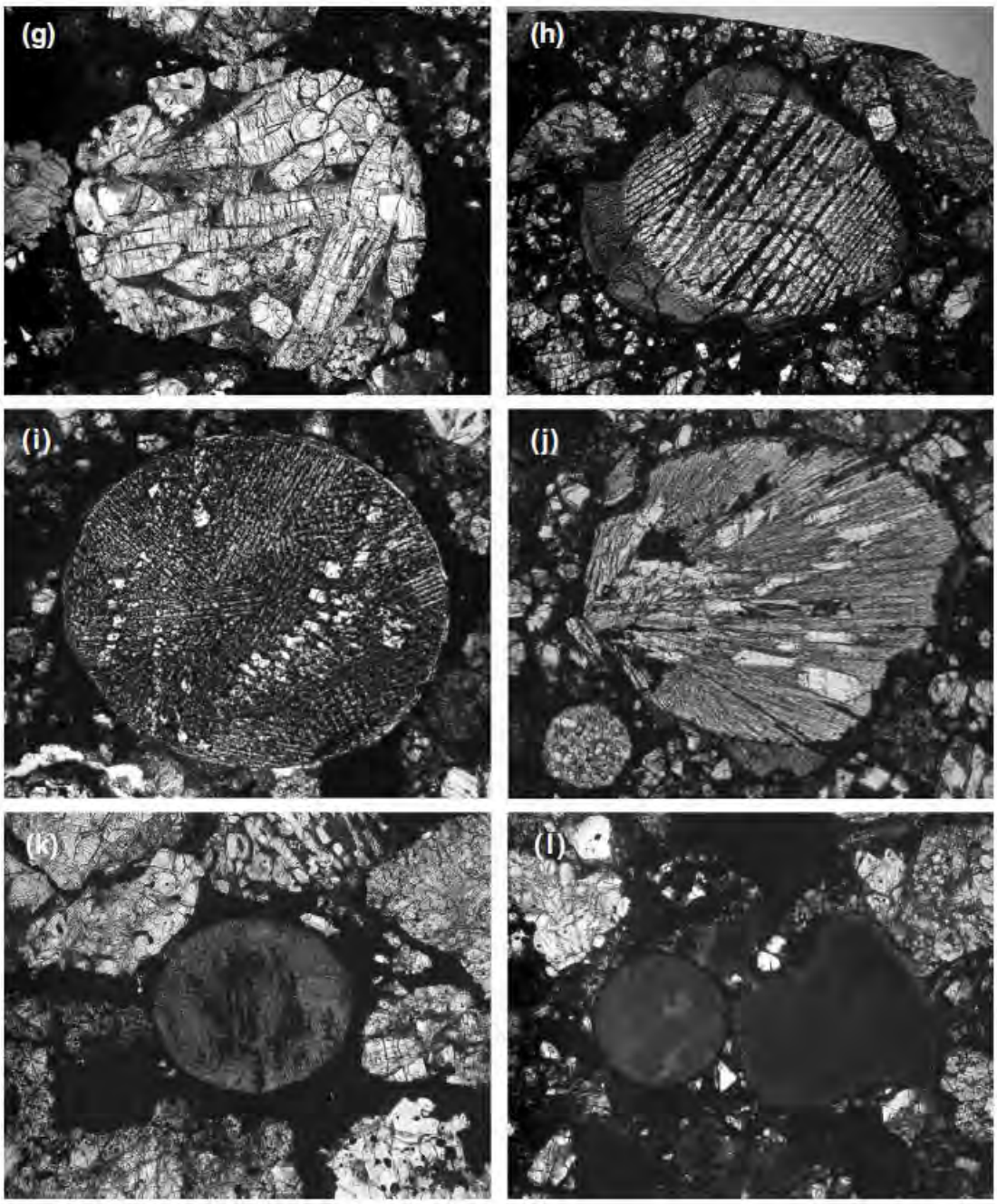

Figure 1.5. From Lauretta et al. (2006): Optical microscopy images of a selection of non-porphyritic chondrule textures in L chondrites. The field-of-view is 1.35mm, apart from (h) where FOV is 2.7mm. (g) a coarse-grained PP chondrule from EETA 90066. (h) a BO chondrule in Bishunpur. (i) BO chondrule in Saratov showing multiple barred groups (j) an RP chondrule from ALH 78119. (k) a GO chondrule from QUE 97008. (l) a cryptocrystalline chondrule pair from ALH 78119.

1.4.2 Chondrule formation

A common theory holds that chondrules formed from pre-existing aggregations of dust in the early protoplanetary nebula (Hewins, 1997), however there is still no consensus in the community. In a recent review of formation processes, Connelly and Jones (2017) asserted that ‘chondrules would not be predicted to exist if they did not exist’,

i.e. that no observations or models of young planetary systems suggest the formation of chondrules. Yet, the abundance of chondrules in extraterrestrial samples indicates not only that chondrules are important, but also that melting of small particles was common early in the Solar System. They are mostly spherical with igneous textures and crystal size is often zoned from coarse-grained in the interior to finer-grained near the edges – all implying that chondrules experienced melting and crystallisation as free-floating droplets. Chondrule formation has been dated using several isotopic systems, including Al-Mg (e.g. Kita et al., 2000; Rudraswami and Goswami, 2007), Hf-W (Budde et al. 2016), Pb-Pb (e.g. Amelin et al., 2002). Some studies have indicated an extended period of chondrule formation, possibly in several generations, from contemporaneous with CAI and extending for 3 Ma (Connelly et al., 2012). Therefore, any hypothesis of formation process should consider protracted formation, as well as the conditions of the early solar nebula.

The question of the formation process(es) of chondrules is still controversial, with several competing theories, including:

- An 'Early Active Sun', whereby proximity to the Sun induced heating and transfer of the products (i.e. CAIs and chondrules) further out in the nebula (e.g. Sorby, 1877; Shu et al., 1997, 2001; Ireland et al., 2016). However, this theory does not explain rapid heating and relatively slow cooling.
- Flash heating of dust in the nebula, with varying mechanisms for heating, including lightning discharges, shock waves generated by the Sun, or motion of planetesimals. Modelling by Morris et al. (2012) suggested that a fast-moving planetary embryo (~3000 km radius) would create bow shocks, compressing the gas-dust cloud and creating chondrules which would then flow through volatiles outgassed by the planet's magma ocean and accrete onto smaller bodies.
- Impact disruption of molten planetesimals, where collisions between objects ~30-100 km in diameter (Asphaug et al. 2011) occur too slowly to disrupt the bodies but melt is released in 'massive sheets' and forms chondrules. This idea of 'splashing' is further explored by Sanders and Scott (2012). However, this model has yet to constrain the thermal histories of the chondrules produced (Connelly and Jones, 2017).
- Impact jetting –a variant on the planetesimal impact model, whereby molten material 'jets' out from the point of impact between two planetesimals. i.e. chondrules as 'by-products of planet formation' (Johnson et al., 2015). Although

modelled thermal histories match chondrule observations, this model has yet to account for the range in chemical and isotopic composition in chondrules (Connelly and Jones, 2017).

Connelly and Jones (2017) outlined the primary characteristics that must be satisfied for an adequate theory of chondrule formation. A first-order requirement is to address the compositions, mineralogy and sizes to determine the thermal histories of chondrules, the timing of formation, and in what kind of environment they formed. Chondrules are compositionally diverse, and yet almost all types of chondrules are found in almost all different chondrite groups. However, it is not yet understood why the sizes of chondrules vary between groups, or whether their sizes reflect their formation process or a sorting mechanism occurring in the nebula.

Chondrule textures are key to understanding their thermal histories. Experimental melting of chondrule analogues has been conducted to recreate the observed textures (e.g. Maharaj and Hewins, 1998). For example, it is likely that non-porphyritic chondrules cooled faster; however, such textures could also indicate higher peak temperatures (~1750-2200 °C) which led to the loss of all crystallisation nuclei (Connelly and Jones, 2017). Conversely, porphyritic chondrules are thought to result from incompletely melted precursors. Additionally, some chondrules are surrounded by igneous rims, and/or contain relic fragments of either refractory inclusions or earlier generations of chondrules, which suggests that chondrule formation was repetitive (Russell et al. 2005; Jones, 2012). The survival of such grains supports a short duration (on the order of minutes to hours) at peak temperature, otherwise grains would be resorbed into melts (Jones, 2012). Cooling rates for chondrules have been estimated using textural indicators such as silicate crystal morphology, as well as diffusion profiles of Cu and Ga in FeNi metal grains (Connelly and Jones, 2017 and references therein). Experimental evidence indicates cooling rates of 0.5 -100 °C/ hour for porphyritic textures (e.g. Jones and Lofgren, 1993; Desch and Connelly, 2002). Non-porphyritic chondrules would likely require faster cooling times, ~1000 -3000 °C/hour (Connelly and Jones, 2017). Similarly, experimental heating has indicated that chondrule precursors must have been anhydrous, otherwise chondrules would show vesicular textures (Maharaj and Hewins, 1998).

Another consideration is that the OC parent bodies are formed of chondrules (as well as metal grains and matrix), thus they accreted after chondrule formation. They did not experience widespread melting and differentiation, i.e. they preserve signatures of

nebula processes (at least in unequilibrated OCs). If accretion of OC parent bodies occurred ~ 2 Mya after CAI (Huss et al., 2006), then it is likely the chondrules that formed them have similar ages, since it is thought that chondrules cannot survive in free space for long periods, as they are susceptible to destruction by turbulence or dragged towards the Sun (Weidenschilling, 1977; Weidenschilling and Cuzzi, 2006).

1.5 Ordinary chondrites

The OC meteorites, accounting for ~ 85% of all known meteorites, are classified into three groups: H (high metal), L (low metal), and LL (low metal, low iron). This classification is based on the abundance of FeNi metal and the ratio of metallic Fe (Fe^0) to oxidised Fe (FeO) (Weisberg et al., 2006).

Oxidation causes iron metal to be converted to iron oxide or iron-bearing silicates. Increased oxidation is reflected in a change in the relative proportions of olivine and pyroxene. Both minerals are magnesium iron silicates, differing primarily in the ratio of silicon to magnesium + iron. Oxidation of iron metal forms FeO that must be accommodated in silicates. Since the total amount of silicon is fixed, oxidation causes pyroxene to be converted to olivine, which contains proportionally less silicon. Thus, the least oxidised enstatite chondrites are predominantly composed of pyroxene with abundant iron metal, whereas moderately oxidised ordinary chondrites have twice as much olivine as pyroxene and less metal.

Oxidation state is manifest in several chemical measures: mean Fa of olivine and Fs in low-Ca pyroxene, modal abundance of FeNi metal, ratio of olivine to pyroxene, and the concentration of Co and Ni in kamacite (Rubin, 2005). In H chondrites, the Fe^0/FeO ratio is 0.58, reducing to 0.29 in L chondrites, and 0.11 in LL chondrites. Olivine has a range of 16-20 mol% Fa in H, 23-26 mol% Fa in L, and 27-32 mol% Fa in LL, and low-Ca pyroxene has compositions 14-18 mol% Fs, 19-22 mol% Fs, 22-26 mol% Fs in H, L, and LL chondrites respectively (Hutchison, 2004; Jones, 1998).

During thermal metamorphism, any phyllosilicates accreted into the OC parent bodies were dehydrated, thus leading to oxidation of FeNi metal by the liberated water (Rubin, 2005). The various trends, such as the decrease in amount of native metal, or the increases in Fa in olivine and Fs of low-Ca pyroxene, from H to L to LL chondrites can

be explained by the H parent body acquiring the least amount (and LLs the greatest) of phyllosilicates. Rubin (2005) further attributes the difference in oxygen isotopes to this phyllosilicate abundance, which had a high ^{17}O.

The OC meteorites are thought to represent three parent bodies (Burbine et al., 2002). Using spectral reflectance, L chondrites have been linked to S-group asteroids, which are the second most common of the minor bodies in the asteroid belt (Bus and Binzel, 2002). Gaffey and Gilbert (1998) have further suggested that the main-belt asteroid 6 Hebe is likely the parent body of the H chondrites. It is thought that the material making up the three OC bodies originated in the same reservoir, based on the oxygen isotopic composition of chondrules in unequilibrated OCs, which span a wide range across all groups and show no correlation with host meteorite type (H/L/LL) (Clayton et al., 1991). Bulk rock oxygen isotopes do, however, show group-specific oxygen isotopic compositions, with H chondrites showing the lowest $\delta^{17}O$ and $\delta^{18}O$ compositions, and LL chondrites have the highest (Taylor et al., 1965; Clayton et al., 1976; Clayton et al., 1991).

Hellmann et al. (2017) showed that the OC parent bodies have distinct Hf and W isotopic evolutions, which they interpret to mean that they originated in different reservoirs and formed under different accretion conditions, i.e. are from distinct parent bodies. They suggest that the OC parent bodies must have accreted very soon after metal-silicate fractionation at 2 Ma, otherwise the reservoirs would have been mixed and acquired a similar Hf-W ratio again. It is not clear what process created the separate reservoirs in which the parent bodies formed, i.e. the high metal-silicate ratio in Hs vs the very low metal-silicate ratio in LLs. Furthermore, mean chondrule sizes increase in the order of H < L < LL due to size-sorting (Rubin, 1989). This size-sorting of chondrules may be responsible for the difference in whole-rock oxygen isotopic composition.

1.6 Metamorphism

1.6.1 Thermal metamorphism

Chondritic meteorites represent the oldest and most primitive material in the Solar System. One major challenge in research of these specimens is to deconvolute the signatures of primary (nebula) and secondary (parent body) processes, in order to

better understand both the primary material and the processes themselves. There is some challenge in assessing degree of thermal metamorphism in chondrites, since heating from shock can affect material similarly to heating due from radiogenic sources, or gravitational compression/overburden. However, the latter is unlikely to contribute in chondritic parent bodies, where metamorphism likely occurred at pressures ≤ 1 kb (Dodd, 1981).

Van Schmus and Wood (1967) first devised a scheme for the classification of degree of metamorphism for chondritic meteorites that have experienced thermal and aqueous alteration, but not widespread melting. Petrological types 1 and 2 describe un-metamorphosed but aqueously altered specimens (e.g. McSween, 1987), whereas types 3 to 7 describe thermally metamorphosed material. Sears et al. (1980) and Sears and Dodd (1988) made the addition of subtypes 3.0 to 3.9 to describe the least processed material. The scheme is regularly refined with new indicators of pristinity with increasing technical capabilities (e.g. Grossman and Brearley, 2005). Whilst OCs exhibit a wide range of metamorphic grades, many CC groups (i.e. CI, CO, CM, CR, CV) show no evidence of metamorphism above type 4.

Thermal metamorphism, of varying degrees, is evident in the textural properties of many OCs, such as mineral recrystallisation and chemical homogenisation. There are many well-defined physical effects of metamorphism (Table 1.1). With increasing petrological type: chondrules lose distinct shapes and definition, including loss of rims (such that by type 6, very few chondrules are visible); chondrule glass devitrifies and plagioclase is found in high petrological type chondrites; originally opaque matrix material becomes more crystalline and coarser-grained; metal and sulphide grains are mobilised and coalesce (Huss et al., 2006). Additionally, low-Ca clinopyroxene is absent from types 5 and 6 OCs as it transforms to orthopyroxene at ~ 630 °C (Huss et al. 2006). Kimura et al. (2008) found that the number density of Ni-rich metal grains decreases with increasing metamorphism from type 3 to 3.9. The effect of metamorphism on metal is further explored in *Section 3.3*. Chemically, increasing metamorphism is seen in bulk volatile loss and the equilibration of silicate minerals, meaning that the chemical composition of minerals is homogenised and converges on a small range. Olivine is equilibrated by type 4, whereas pyroxene equilibration is not complete until type 5 (Van Schmus and Wood, 1967).

Thermal metamorphism in chondrites also contributes to variations in the oxygen isotopic composition. Clayton et al. (1991) reported a 0.5‰ variation in $\delta^{18}O$ for

different petrological grades within the OCs, and inferred a closed oxygen system during metamorphism, supported by the anhydrous OC parent body or bodies. During metamorphism, O isotopes experienced redistribution amongst the mineral phases, following the mass-dependent equilibrium fractionations that corresponded to the peak temperature experienced. Olsen et al. (1981) showed that, even in Type 6 OCs, the transport of O atoms only reached distances of a few millimetres. Clayton et al. (1991) used mineral-pair fractionations to estimate the temperature of metamorphism.

Metamorphic temperatures, both peak (i.e. highest temperature experienced) and equilibration (i.e. the lowest temperature at which minerals remained in diffusive equilibrium when cooling), have been estimated by various methods (Huss et al., 2006). For example, in unequilibrated OCs: an upper limit of 260°C was suggested for Semarkona (LL3.00) based on matrix clay mineralogy (Alexander et al. 1989); temperatures of 500–600°C were inferred for type 3.5 chondrites based on the order/disorder transition of feldspar (Sears et al., 1991). In petrological types 4-6, the upper limit is set by the onset of melting at ~950°C (Dodd, 1981). The closure temperature for high-Ca pyroxene is used to provide the peak metamorphic temperature in type 6 chondrites, at 800-950°C for H6, 850-950°C for L6, and 900-960°C for LL6 (McSween and Patchen, 1989; Harvey et al., 1993). Huss et al. (2006) noted that it is more complicated to estimate the temperatures associated with types 4 and 5 chondrites since mineral thermometers are not equilibrated, however they suggested that these meteorites may have experienced peak temperatures close to that of type 6 OCs, but cooled more quickly, thus do not show the same degree of metamorphism (Harvey et al., 1993; Kessel et al., 2002).

The timing of thermal metamorphism is estimated by isotopic age dating. Huss et al. (2006) compiled data from various short-lived nuclide studies, suggesting that, relative to CAI formation, accretion of OCs took place ~2 Ma, metamorphism of types 3.0-3.2 occurred at 2-4 Ma, from type 3.7-4 continued until ~6 Ma, and >7 Ma in type 6. Recent work on closure temperatures of the Hf-W system during metamorphism indicate ages of ~ 3-4 Ma after CAI for type 4 OCs, and ~ 9-11 Ma after CAI for type 6 OCs (Hellman et al., 2017).

Criterion	1	2	3	4	5	6	7
Homogeneity of olivine compositions	—	>5% mean deviations		≤5%	Homogeneous		
Structural state of low-Ca pyroxene	—	Predominantly monoclinic		>20% monoclinic	≤20% monoclinic	Orthorhombic	
Feldspar	—	Minor primary grains		Secondary <2-μm grains	Secondary 2–50-μm grains	Secondary >50-μm grains	
Chondrule glass	Altered or absent	Mostly altered, some preserved	Clear, isotropic	Devitrified	Absent		
Metal: Maximum Ni (wt%)	—	<20 taenite minor or absent	>20 kamacite and taenite in exsolution relationship				
Sulfides: Mean Ni (wt%)	—	>0.5	<0.5				
Matrix	Fine grained opaque	Mostly fine-grained opaque	Opaque to transparent	Transparent, recrystallized			
Chondrule-matrix integration	No chondrules	Sharp chondrule boundaries		Some chondrules can be discerned, fewer sharp edges	Chondrules poorly delineated	Primary textures destroyed	
Carbon (wt%)	3–5	0.8–2.6	0.2–1	<0.2			
Water (wt%)	18–22	2–16	0.3–3	<1.5			

Table 1.1. Criteria for the classification of petrological type showing the compositional and textural changes observed in chondritic meteorites. From Weisberg et al. (2006), after Van Schmus and Wood (1967), Sears and Dodd (1988) and Brearley and Jones (1998).

A common explanation of the range in petrological type OCs is the 'onion-shell' model (Figure 1.6). This suggests that type 3 and 4 meteorites are closer to the surface of asteroids whereas type 6 meteorites represent material buried at greater depth, thus experiencing higher peak temperatures and/or heating for longer periods/slower cooling rates, owing to internal heating from the decay of ^{26}Al and ^{60}Fe (Fish et al., 1960; Ghosh and McSween, 1998; Huss et al., 2006). This is supported by evidence from Hf-W systematics, which show ages of 3-4 Ma after CAI for type 4 OCs, and 9-11 Ma for type 6 OCs (Kleine et al., 2008; Hellmann et al., 2017). Trieloff et al. (2003) used ^{207}Pb-^{206}Pb dating and ^{244}Pu fission track ages – two methods with different closure temperatures – to add support to the onion-shell model. Using the Pb system, they found that metamorphism of type 4 H chondrites ended 4-6 Ma after CAI, 10-16 Ma for H5, and 45-63 Ma for H6 chondrites. Alternatively, using Pu, these ages are ~10 Ma, 50-65 Ma and 55-65 Ma after CAI for H4, H5 and H6 respectively (Trieloff et al. 2003).

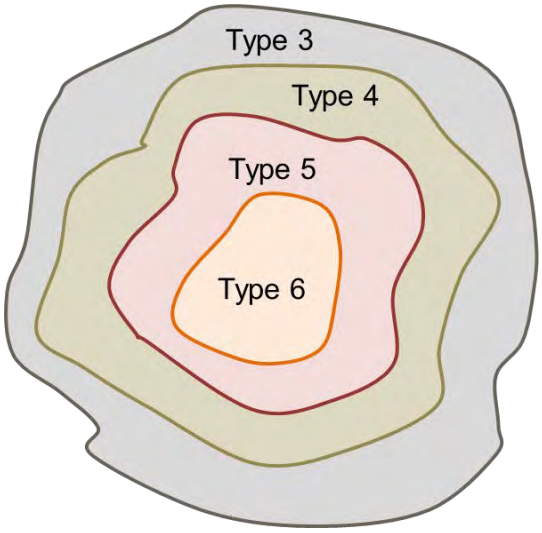

Figure 1.6. A schematic of the onion-shell model, whereby lower petrological type meteorites originate from closer to the surface of undifferentiated asteroids, thus experience less heating and faster cooling rates, whereas high petrological type chondrites are subject to higher temperatures for longer (e.g. Miyamoto et al. 1981; Trieloff et al. 2003; Herndon and Herndon, 1977).

There is some conflicting evidence, including high petrological type meteorites that show fast cooling rates, or vice versa, which indicate a more complicated evolution of the H chondrite parent body. It has thus been suggested that very large impacts occurred before the parent body cooled below ~ 800 K. These impacts led to the excavation of deep material (i.e. hotter material that was instantly transported to colder

regions) and the deposition of hot debris on colder material (thus slowing their cooling rates) (e.g. Miyamoto et al., 1981; Trieloff et al., 2003; Herndon and Herndon, 1977).

1.6.2. Shock metamorphism

It is clear from the plentiful impact craters on planetary bodies and the shocked nature of many meteorites that collision has been a key process in the evolution of the Solar System. Impacts between bodies have had an important role in the history of asteroids, for example in the induration of material (e.g. Bischoff et al., 1983; Scott and Wilson, 2005), or providing a heat source for metal-silicate separation on the parent body (e.g. Kring et al., 1991; Ruzicka et al. 2005). As they are airless bodies, there is no atmosphere on asteroids to decelerate the bolide, thus the effects are more significant. Figure 1.7 shows three scenarios in which shocked meteorites may form, showing that the effect on the parent body is a function of the relative size of the impactor and target.

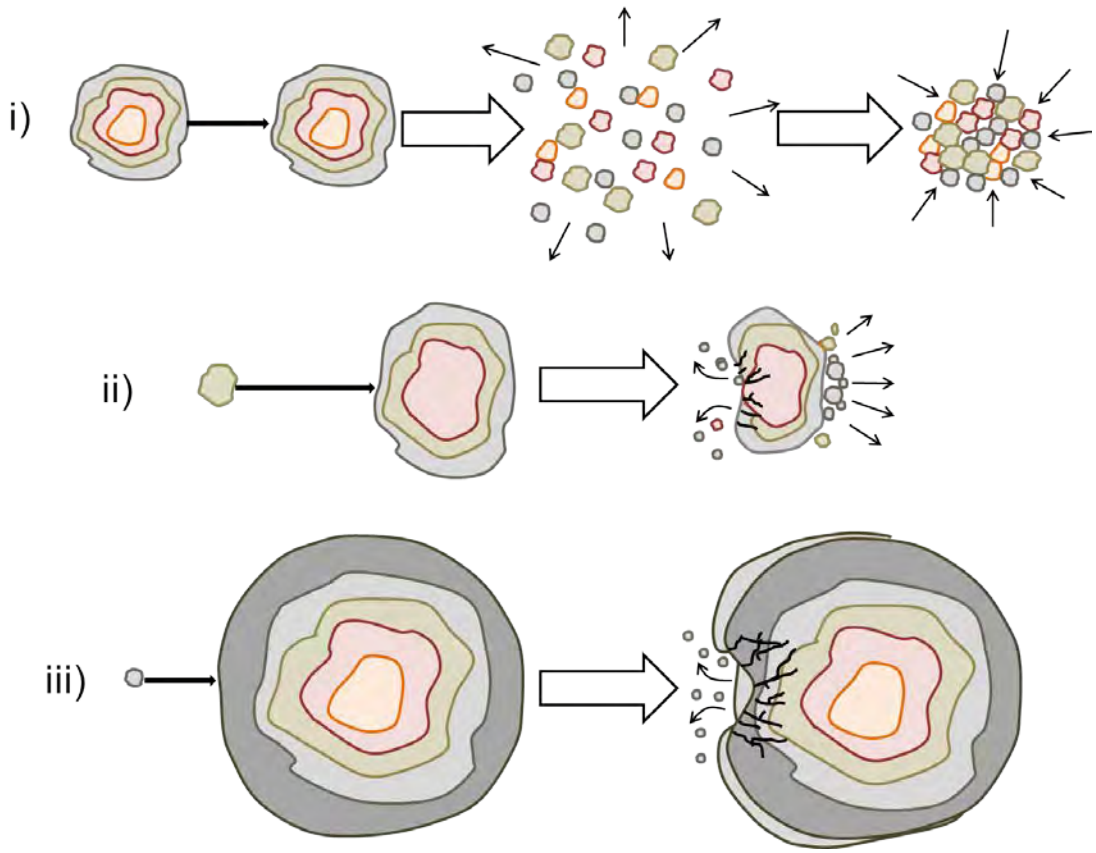

Figure 1.7. Schematic of the different scenarios leading to the formation of shocked chondrites, showing the effect of differences in the relative sizes of the colliding bodies, after Bischoff and Stöffler (1992). i) catastrophic disruption of both impactor and target, plus possible subsequent re-accretion as a 'rubble-pile asteroid'; ii) cratering, escape and spallation; iii) cratering, ejecta deposition and regolith formation on a large asteroid/planet.

Collision at hypervelocity leads to a shock wave that near instantly raises pressure to tens of GPa and temperatures on the order of thousands of degrees (Melosh, 1989).

Rock can be vaporised, melted, or shocked. The propagation of the shock wave and its effect depends on many factors, for example, the impactor size, the distance from the impact, as well as pre-impact conditions such as ambient temperature and nature of materials (Sharp and DeCarli, 2006). Shock wave propagation is complex, especially in heterogeneous materials, with initial peak pressures varying by an order of magnitude between, or even within, grains (Sharp and DeCarli, 2006). This initial "spike" is followed by equilibration to lower pressure, via a complex series of shock interactions, where waves are reflected or refracted at the interfaces between grains and cracks or pores. This pressure equilibration takes around a microsecond, whereas temperature equilibration is complete in seconds in a typical chondrite, with mm-sized grains (Sharp and DeCarli, 2006).

The effects observed in meteorites can broadly be divided into deformation, and transformation. Deformation includes fracturing, undulatory extinction and mosaicism in silicates, whereas transformation is manifest in solid-state transformation (i.e. to high pressure/temperature polymorphs) or melting and recrystallisation (Stöffler et al., 1991). These indicators of shock stage and their observation via optical microscopy are described in *Section 2.9* and used in *Section 3.3.*

Shock-induced fabrics can be observed in metal grains owing to their specific properties. Shock waves act most strongly at boundaries with a high density contrast, e.g. metal and silicate (Sharp and DeCarli, 2006). For this reason, metal, being the densest phase in chondrites, is preferentially affected by shock. For example, melt veins are predominantly composed of metal, and or plagioclase, which is also susceptible. Additionally, FeNi metal has a lower melting temperature than silicate minerals and is ductile, meaning that it will deform, rather than fracture (Friedrich et al. 2008). The effects of shock on porosity and metal grains are relevant to this study. Most previous work has examined and described the heterogeneous effects in 2D. These studies, and the growing body of literature investigating fabrics in 3D, are separately reviewed in *Section 3.1*.

In OC groups, shock effects, the sequence of increasing degrees of shock metamorphism and the frequency distribution of shock stages are all similar, indicating that the H, L and LL parent bodies shared similar collisional histories (Stöffler et al., 1991). S3 is the most common shock stage across most petrological types. Typically, type 3 chondrites do not show shock stages S4 to S6, but the frequency of these higher shock stages increases with increasing petrological type (Stöffler et al., 1991).

Stoffler et al. (1991) suggested that the more porous, volatile-rich type 3 chondrites are likely to melt at lower shock pressures than non-porous chondrites of higher petrological type. Where volatiles are trapped in pores, this causes dispersal of the shocked material into small particles which are not expected to survive as meteorites.

Noble gas losses are not recorded for shock pressures below ~10 GPa (or S1 and S2) whereas shock pressures exceeding ~35 GPa (or S5 and S6) cause the complete loss of ^{4}He and ^{40}Ar (Stöffler et al., 1991). Gas retention ages (^{40}Ar-^{39}Ar) for shock-darkened H chondrite impact melt breccias indicate significant impacts very early on (in the first ~100 Ma after CAI formation), again during the epoch of heavy bombardent (circa 3.9-4.0 Ga) and more recently around 300 Ma (Swindle et al., 2009). Petrological observations and ^{39}Ar-^{40}Ar measurements of impact melted L chondrites suggest a catastrophic impact on the L chondrite parent body at ~500 Ma (Heymann, 1967; Bogard et al., 1995; Haack et al. 1996). This event has since been linked to the discovery of mid-Ordovician fossil meteorites from Sweden (Greenwood et al. 2007) and may have accelerated the 'Great Ordovician Biodiversification Event' (Schmitz et al., 2007).

With the swift advancement of computing capabilities, both microscale (at atomic/molecular scale) and mesoscale (~ on the order of micrometres) modelling has been used to calculate shock wave propagation and, where validated with observation of effects in natural specimens, can provide insight into the impact conditions. Davison et al. (2010) showed that impacts that do not result in the catastrophic fragmentation of the parent body are inefficient at producing large-scale partial melting. Bland et al. (2014) showed that velocities of only 1.5 km/s are capable of causing temperature increases of > 1000 K in the porous matrix of primitive chondrites, which compresses and takes much of the strain leaving non-porous chondrules relatively unscathed.

Shock experiments have also been conducted to attempt to duplicate metamorphic effects in meteorites, and thus better constrain the shock parameters (e.g. Schmitt, 2000). For example, Hörz et al. (2005) created a 'regolith' by crushing an L6 chondrite before carrying out shock experiments that indicated that initial pore space of 40-50% was closed at ~15 GPa leaving a dense aggregate of interlocking grains, with grain-boundary melting occurring at pressures > 27 GPa. However, there are limitations to the experimental conditions; for example, peak pressures, peak pressure durations, and ambient temperatures of impacts occurring in the asteroid belt cannot feasibly be simulated in laboratory conditions (Sharp and DeCarli, 2006).

1.7 X-ray Computed Tomography (XCT)

1.7.1 3D vs 2D

Petrography, the study of the size, form, distribution and modal abundance of minerals forming rocks, is frequently carried out on thin sections or polished blocks. Thin sections are used for a whole gamut of techniques such as scanning electron microscopy, optical microscopy, ion microprobe, electron backscatter diffraction, and electron microprobe analyses. These allow only a single two-dimensional surface to be explored, and thus do not truly represent the three-dimensional structure of the meteorite. Hence, some analyses are only approximations of the rock, e.g. size distributions of chondrules or igneous textures. Furthermore, thin sections are limited by size – a relatively small part of the sample is studied compared to CT, which can accommodate large samples depending on the resolution required.

The production of thin sections requires the destruction of part of the sample. Thus a certain amount of the material is no longer available for study and it is prudent to conserve as much material as possible in perpetuity for potential future techniques and applications. In some circumstances, the act of creating a thin section can affect the accuracy of results – by 'mineral plucking' or by introducing scratches and cracks (Consolmagno et al., 2008). For example, Russell and Howard (2013) attribute the lack of wollastonite in thin section to its destruction during section making – breaking from their surfaces and being washed away, despite the presence of voids similar to those in which wollastonite was observed. Furthermore, Russell & Howard (2013) acknowledged the impact that thin-sectioning may have on the bulk composition of CAIs through point counting.

To elucidate the true nature of features, inclusions, and networks in these samples, it is necessary to understand how these characteristics are arranged in three dimensions. Various methods have been employed to expand the two dimensional constraints, from model-based assumptions to direct three dimensional techniques such as serial sectioning, confocal microscopy, magnetic resonance imaging, synchrotron-based computed tomography and, as is the focus of this work, X-ray computed tomography. Goldman et al. (2014) manually segmented chondrules and CAIs from two carbonaceous chondrites, Moss (CO3.6) and Colony (CO3.0), to measure their volumes and calculate their diameters, which were then compared to 2D diameters calculated from areas of objects measured from element maps from microprobe

analyses. These measurements were then also compared to the conversion methods of Hughes (1978) and Eisenhour (1996). They found that as the true size of the object increases, the 2D (cross-sectional) measured diameter underestimates the actual object size. In contrast, Eisenhour (1996) found that larger chondrules are overrepresented in thin section. A well-constrained relationship, and correction factor between 2D and 3D measurements of these inclusions is crucial when correlating their 3D sizes to their chemistry, which currently can only be performed in 2D.

Micro-computed tomography can offer solutions to many of the limitations of two-dimensional analysis, providing data on the true three-dimensional petrography of a sample and non-destructively analysing a wide range of volumes of rare or precious meteorites, as well as potentially identifying new features for further study. As a relatively new technique, there are limitations in experience of dealing with the data and understanding its full potential.

1.7.2 Applications in planetary science

X-ray CT was first applied in medical sciences in the 1970s, led by Hounsfield, however the applications to geosciences were noted soon after. Early instances of CT analyses of rocks include studying meteorite inclusions (Arnold et al., 1983), slabs of the Allende meteorite (Heymann et al. 1985), petroleum cores (Wellington and Vinegar, 1987), and soil bulk density (Petrovic et al., 1982). There were relatively few examples of high-resolution XCT in geosciences until the late 1990s, (see Rowe, 1996, Cifelli et al. 1996), with improvements in detector design making significant leaps in the resolution achievable.

In the last decade, XCT has expanded rapidly, with scanners widely available and relatively inexpensive (Abel et al., 2012). The technique is constantly being refined, improving resolution, with sub-micron voxel lengths possible with lab-based systems, and increasing penetration depths of dense specimens such as metal-rich nodules (Garwood et al., 2009). This study is limited to lab-based XCT and its uses in thresholding and quantifying phases, or for identification of particular features, but the technique has been used in a variety of studies within meteoritics, some of which are briefly explored here.

1.7.3 Mineralogy

Characterising the mineralogy of meteorites allows for discussion and exploration of the magmatic history of the source region. This could aid in spectral unmixing or 'deconvolution' of spacecraft data by providing a more accurately characterised spectra for mineral phases (Cloutis et al., 2014). Phase distribution is an important area where CT can reduce the bias of 2D polished sections, such as probe mounts or thin sections, which may not provide an accurate representation of phase proportions in a sample. However, the data resulting from CT investigations of a sample are greyscale tomograms, where the greyscale value is a function of X-ray attenuation and therefore directly correlated to the density of the sample material. The mineralogy of a rock is determined by both the atomic composition and the atomic arrangement; essentially, these are the same factors in constraining the density of a sample, however, they are not directly correlated due to the complexity in mineral forms. Many minerals show solid solution, with the degree of substitution between elements (e.g. Mg and Fe in olivine) significantly affecting the density. There is thus overlapping of the attenuation peaks of different components in the CT data. As Consolmagno et al. (2008) observe, this is less of an issue when dealing with meteorites with simpler mineralogies where their chemistry is bound by elements in near solar abundances. Obtaining chemical data using CT is increasingly being explored, with new technological aspects of the technique are being developed to tackle this issue, for example, the use of dual-energy CT for mapping minerals in Hayabusa samples (Tsuchiyama et al., 2013), or the combination of X-ray diffraction with CT.

Thresholding greyscale tomograms into the constituent minerals is thus complicated because the distribution of the different attenuation coefficients is not discrete, but rather consists of many overlapping modes. This is especially problematic when the materials are of similar attenuation coefficient (i.e. if they have similar density and atomic number). Furthermore, the issue of partial volume averaging can complicate interpretation. This occurs at the boundaries between materials or phases, when a single voxel represents more than one component.

Although not in the field of meteoritics, a relevant study is that of Long et al. (2009). The authors performed 3D quantification of mineral components and porosity distribution in Westphalian sandstone and compared their CT data with point counting results of stained thin sections to understand the sensitivity of the μCT data. To identify the rock constituents, Long et al. (2009) calculated greyscale values for the expected

minerals (based on their thin section analysis) by first determining the greyscale ranges for two characteristic minerals (ankerite and quartz) in order to calculate constants in the attenuation coefficient equation, which could then be applied to other minerals, based on a theoretical density and effective atomic number. They were then able to identify three groups of constituents: i) pyrite, iron oxides and hydroxides, ii) quartz, and unaltered feldspar grains, iii) clay minerals, kaolinite, dickite, and illite.

Hunt et al. (2011) studied the winonaite meteorite, Pontlyfni. The metal and sulphide distribution was mapped using XCT and compared to mineral modes from combined elemental maps from SEM thin sections. They found that Pontlyfni bears a greater resemblance to IAB irons, with silicate-rich clasts in sulphide-rich matrix, than to typical winonaite specimens. Similarly, Ross et al (2011) compared mapping of mineral phases using SEM data to phases thresholded in XCT data of ureilites, to illustrate the wide variation in appearance and percentages of the metal in different samples. Russell & Howard (2013) used CT to divide a single CAI into three components of low, medium and high density. Minerals typically found in CAIs all share very similar densities but were distinguished by narrow gaps between layers. Tomography showed that the CAI was a complex intergrowth of rounded nodules. In 2D, these appear unconnected however 3D visualisation allowed a more accurate understanding of their relationship. This network of nodules was inferred to suggest a condensation origin for the CAI.

Tait et al. (2014a) used XCT to map the 3D distribution of plagioclase in the H7 chondrite, Watson 012, showing that although plagioclase crystals appeared isolated in thin-section, they were in fact, an interconnected network. Skeletonising the network allowed calculation that > 60% of nodes have coordinations or 3 or 4, which suggests a grain-supported melt network.

Hezel et al. (2013) devised ‘PhaseQuant’ – a program for the automated analysis of CT data, which is optimized for CV chondrites. However, they report that the program is not capable of automatically distinguishing between type I and II chondrules. Type II chondrules have very similar attenuation to matrix, as do dark inclusions in CV chondrites. Similarly, CAIs are also confused with chondrules in PhaseQuant. Hezel et al. (2013) also mentioned the similarity in density between troilite and magnetite which tend to be grouped together when separating metals and opaques. Hezel et al. (2013) reported their modal abundances of the chondrite components, including whether sulphides or metals are in chondrules or the matrix. This is compared to Ebel et al.

(2009) who reported modal abundances from a 120 cm^2 slab of Allende, and found to be in agreement, thus validating the accuracy of PhaseQuant. The chondrule/matrix modal abundance is interpreted to indicate chondrule-matrix complementarity, i.e. that both formed from the same nebular reservoir (Hezel et al., 2013).

The high density contrasts between metal and other chondrite phases, or porosity and other phases, means that XCT is ideally suited to their analysis in 3D. Several studies have approached this, for example, in the 3D study of metal grains in shocked L chondrites which show increased orientation with greater degrees of impact compaction and shock loading (Friedrich, 2008). This study and others on porosity and/or petrofabrics from metal analyses are explored in *Section 3.1*.

1.7.4 Features of chondrites in 3D

X-ray computed tomography also enables the determination of three-dimensional modal abundances of components for understanding the relationship between chondrite groups. Quantitative measurements of the size distributions and abundances of chondrite components provide limits for modelling the accretion of parent bodies, and elucidating the causes behind chondrule size sorting (e.g. Kuebler et al., 1999). There are significant variations in these properties across chondrite groups, the cause of which is still debated. Chondrule sorting may have arisen from a sorting process, either by mass (e.g. Teitler et al., 2010), by X-winds (e.g. Shu et al., 1996), by turbulent concentration, or by photopheresis – the non-uniform interaction of a particle with the surrounding gaseous environment caused by a temperature gradient on the surface which results from absorption of radiation, i.e. sunlight (Wurm and Krauss, 2006). Furthermore, finding the abundance of opaques in both chondrules and matrix offers a way to constrain their formation (e.g. Schrader et al., 2008). Additionally, the frequency of compound chondrules can be used as a marker for density in chondrule-forming regions, in that the higher the density of chondrules in the forming region, the more likely that chondrules could collide whilst still molten (Akaki and Nakamura, 2005).

Insight into these questions may be gleaned by better-constrained chondrule size distributions, or indeed size distributions for any chondrite component, systematically across the different meteorite groups. More traditionally, this was carried out by slicing a sample and using 2D mapping to segment chondrules before applying a correction model. For example, Srinivasan et al. (2013) imaged a large slab of Allende at 5.4

μm/pixel with a camera attached to a petrological microscope. 513 chondrules and CAIs were outlined, and the image binarised for analysis of particle area, location and axes with ImageJ. The chondrules size populations measured by Srinivasan et al. (2013) agree with reported values but with a higher frequency of smaller CAIs than larger, which they suggest may indicate a similar sorting process for CAIs as for chondrules.

Kuebler et al. (1999) used tomography to measure volumes of metal-troilite grains in low petrological type OCs. They combined this data with sizes and masses of chondrules derived from thin-section measurements, to suggest that chondrules were more efficiently sorted than the metal-troilite grains, potentially due to their irregular shapes. At the time, the quality of CT data was such that metal could not be distinguished from troilite, and chondrules were indistinct.

Outlining chondrules in XCT data (e.g. Sherman et al., 2010) involves manually drawing around the features in 2D and stacking. Thus, there is no error associated from using a correction model. However, this method is considerably time consuming. Other techniques include: physical separation and either CT or laser scanning, however, this method means individual chondrules could be susceptible to disaggregation. There has been less work on the sorting of CAIs, potentially because they are less common and because very large CAIs are rarely present in chondrite thin sections due to their size. The visualisation and quantification of CV chondrite petrography has been approached using XCT (Hezel et al., 2013). They described the petrography of Allende (CV3.7) and Mokoia (CV3.6), and found that modal abundances of the components fit previous literature from 2D analyses. They were able to identify two types of chondrules (one encapsulated with sulphide and one almost devoid of sulphide). They described the opaque-layered chondrules as having multiple layers of opaques and silicates of rims “peppered with opaques”. The rims are said to be patchy, enclosing a normal inner chondrule. Hezel et al. (2013) proposed that these irregular layers were aggregated during a lower-temperature second stage of formation that only affected a fraction of the chondrules. They also noted that opaques in chondrules tend to be up to hundreds of microns, as opposed to the matrix, where grains up to 1.5mm in size are found. This size disparity is believed to rule out the possibility that opaques formed inside the chondrules and were later separated (as suggested by Connolly et al. 2001). The large size of opaques, a minor component in the matrix, implies they could not have formed from condensation. Wasson et al. (1995) and Rubin (2010) described “enveloping chondrules”, which are likely the Type I and II chondrules

described as opaque-layered by Hezel et al. (2013). The authors noted the presence of large pore spaces within chondrules, potentially forming as a result of volume reduction when the chondrule crystallised. They propose that these pores could also be remnants of the precursor aggregates of chondrules.

Sherman et al. (2010) used synchrotron CT data to manually outline ~330 chondrules in 95 alternating slices of Semarkona (17 micron/voxel resolution). Data sets were eroded by resetting outline stroke widths to 5 pixels, to determine the centre of mass coordinated of each chondrule. Using a code written in IDL, the centres of mass were overlaid on the 0 pixel outline stack and then individually built upon until they reach either matrix material or another chondrule. They found that Semarkona chondrules were significantly smaller (finding an average radius of 0.2216 mm (σ = 0.0940) than previously reported (1 mm in diameter). This radius was calculated from the volume measured, assuming that the chondrules are perfect spheres. The accuracy of these values is dependent on the resolution of the data as well as the manual outlining, suggesting this would be more accurate if completed for every slice.

Similarly, Lobo et al. (2014) reported using the manual outlining technique on a composite map made from elemental electron microprobe data of a polished thin section of Semarkona, using Adobe Illustrator and a drawing tablet. They further divided the chondrules into types, using the Mg and Si intensities in the images as visual cues to estimate pyroxene and olivine ratios. Small sulphide, iron and olivine grains, along with any object too small to be resolved or contoured, were included with the matrix. Areas were measured using ImageJ and custom IDL code. They reported chondrule type abundances as a percentage area, and fraction of total X-ray intensity for major elements in both inclusions and matrix.

Almeida et al. (2015) compared measurements of chondrule aspect ratio in 2D with manually segmented chondrules in XCT data, demonstrating that the 2D analyses consistently underestimate the strain experienced by the Leoville (CV3) meteorite (Figure 1.8). Furthermore, the study showed aspect ratios in 3D were comparable to those observed after experimental shocking with pressures > 20 GPa (from Nakamura et al., 2000).

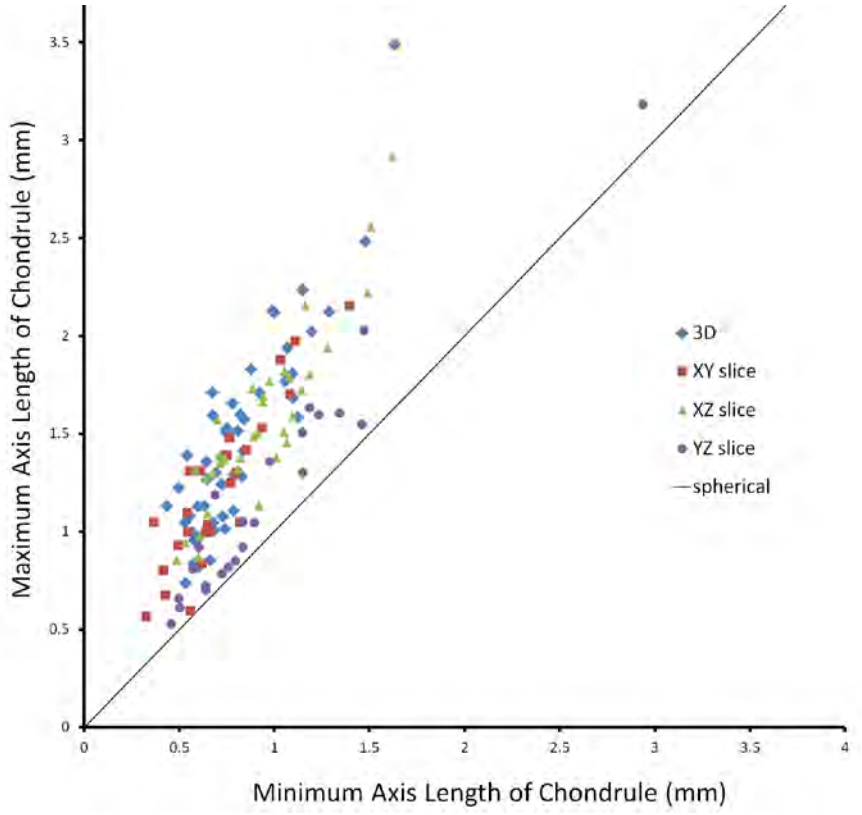

Figure 1.8. Major vs minor axis length of chondrules in randomly selected 2D slices, in each orthogonal plane (XY, XZ, YZ) compared with 3D analyses of chondrules in Leoville (CV3) (Almeida et al., 2015).

Tait et al. (2014b) used XCT to image 19 CAIs in Allende (CV3) using BoneJ (Doube et al., 2010) to fit ellipsoids to a 3D mesh. Flinn's method was used to show the oblate strain ellipsoid and provide a uniaxial shortening estimation of 49%. This was then compared with 2D strain analyses of chondrules and matrix. They found the strain partitioning to be greatest in chondrules, followed by matrix, then rims, and finally CAIs.

Hanna and Ketcham (2013) linked measurements of deformation of chondrules in Murchison (CM) to the pre-deformation bulk microporosity of the sample, assuming that chondrules are "squeezed" into surrounding pore space. Using Avizo and Blob 3D to segment the data, they used a best-fit ellipsoid to calculate size and orientation of each of the 165 chondrules. Segmentation of the chondrules in three orthogonal planes and fitting of ellipse to these extents allowed for more rapid segmentation however this feature is not accessible in current open-access release of the program. Orientations were analysed with Stereo 32 and shape analysed using Sneed and Folk ternary diagrams. They found the mean aspect ratio to be 1.52, (ranging from 1.22 to 2.38) with a standard deviation of 0.21, which indicated uniaxial shortening of 0.24, and a pre-deformation porosity of 40.8% (~ 6%). There are necessary assumptions to be made to validate this method. For example, that the chondrules were spherical before

deformation, that chondrules are incompressible and that the strain is completely accounted by loss of porosity. Lindgren et al. (2012) inferred the deformation history of Murchison based on calcite twin stress analysis (crystallographic orientiations determined by EBSD) and combined this with Hanna's XCT observations of chondrules segmented with Avizo and orientations analysed in Blob 3D. The CT data show a flattening and preferred orientation of the chondrules, which coincides with the measurement of greatest stress from the calcite twins, indicating that the same deformation event caused both phenomena. Hanna et al. (2015) continued the study with electron backscatter diffraction (EBSD) showing that plastic deformation within the chondrules was minimal and that the dominant mechanism for strain accommodation was brittle, in the form of cataclasis, fracturing and grain boundary sliding.

Hanna and Ketcham (2015, 2016) used XCT to analyse the fine-grained rims (FGRs) around chondrules in Murchison (CM2), by segmenting the object twice – once with and once without the FGR. They designed a program to measure the thickness of the rim is each direction from the chondrule centre, allowing for comparison with the foliation defined by the long axes of the chondrules. They showed that the FGRs are consistently thicker in the plane of foliation and that FGR volume is related to the chondrule equivalent spherical diameter, supporting the FGR formation proposed by Cuzzi et al. (2004).

1.8 Curation

Increasingly, CT is recognised as a crucial tool for the characterisation of extraterrestrial samples. Thus, the applications of the technique to curation are key, both to identify features, to inform subsampling for other techniques and to curate virtual representations of samples. Examples include Chaumard et al (2014) who used CT to locate type 1 chondrules that were surrounded by large metal grains to inform slicing of the fragment to ensure the sectioning was taken close to the equatorial plane, thus avoiding any under-estimations of the cooling rates from Cu and Ga diffusion profiles by random sectioning. Additionally, observations were made from CT scanning of the Sutter's Mill CM breccia by Ebel et al. (2012) and Wallace et al. (2013). Volume, bulk density, number of lithologies present, clast abundance, zonation of individual objects and fracturing of the sample were all measured or observed.

Allen (2013) discussed curation of extraterrestrial samples as the critical interface between sample return missions and research carried out internationally. Increasingly, sample return missions are being invested in, e.g. OSIRIS-REx, Hayabusa 1 and 2. As such, it is crucial to advance curatorial practices and employ novel techniques to increase the value of rare collections where sample preservation is key (e.g. Zeigler et al., 2014; Blumenfeld et al., 2015). XCT was successfully used to determine the soundness of the sample capsule returned by the JAXA Hayabusa mission (Fujimura et al., 2011). Further CT investigations have been carried out, such as Tsuchiyama et al. (2013) and Uesugi et al. (2012), who are developing a novel method of using analytical dual-energy synchrotron micro-tomography to map mineral phases in three-dimensions. This is conducted by scanning a sample, in this case Hayabusa mission samples of Itokawa, at two energies, above and below the absorption edge of an abundant element and using the linear attenuation coefficient of the mineral at the two energies to map its distribution.

Part of the curatorial responsibility when employing novel techniques is consideration of the impact of that technique. This is especially crucial for planetary materials with low sample availability, and thus the need to perform multiple analyses on the same sample. XCT is frequently described as non-destructive and non-contaminating. That may not be true. X-rays interact with material at the atomic level, causing ionisation and potentially heating. Sears et al. (2015, 2016) measured a significant increase in the thermoluminescence (TL) of several OCs subsequent to XCT analysis, at levels comparable to the natural TL measured in Antarctic meteorites. Changes in TL provide a measurement of terrestrial residence time, thus specimens exposed to CT could provide artificially young terrestrial ages (Sears et al., 2016). Ongoing work by Hanna and Fu (referenced in Hanna et al. 2017) has tested the effects of XCT on the ferromagnetic properties of basaltic cores, thus far indicating no change in the magnetic moment of samples after CT. Friedrich et al. (2016) investigated the effect of synchrotron X-ray CT on amino acids in two samples of Murchison (CM). They found no effect and estimated the dose experienced by the samples at ~ 1.1 kilograys, with < 1 °C heating. However, previous work has indicated that interstellar grains collected by the Stardust mission exhibit evidence of radiation damage as a result of synchrotron X-ray fluorescence and diffraction (Bechtel et al., 2014), though this may be related to the medium in which the particles were embedded.

It is only possible to test current technology. Responsible curation must ensure that all samples undergoing CT-scanning are documented as such, as it is impossible

to predict the effect that such analysis may have on techniques that are not yet developed.

1.9 Research Justification

Chondrites are essentially conglomerates of particles, hosting interstellar grains, chondrules, refractory inclusions (CAIs and AOAs), varying amounts of iron-nickel metal and iron sulphides, held together with fine-grained matrix material. Each of these components can represent and record diverse nebular histories. The story of this material is further complicated as processing can occur either on individual components within the nebula or on whole rock after accretion of the parent body. Secondary processes include aqueous alteration, thermal metamorphism and shock metamorphism. This project will provide three-dimensional analysis of chondrite components, at varying degrees of metamorphism. Accurate characterisation of the porosity of meteorites is crucial for constraining models of parent body formation and evolution, revealing details such as permeability and hence providing insights into asteroidal processes, such as aqueous alteration. Porosity is a key characteristic for models of asteroids and adds to our understanding of how this material lithified from the accumulation of solar nebula dust to chondritic rock.

There are many questions outstanding relating to the three-dimensional properties of extraterrestrial material, for example: what is the density, porosity and permeability of meteorites and what can this tell us about the physical properties of their parent asteroids? What is the three-dimensional structure of chondrules and what constraints do these place on chondrule formation mechanisms? How are shock features, such as shock veins and sheets, arranged in three-dimensional space? How common is the presence of exotic clasts in meteorites and what does this tell us about mixing processes in the Solar System? The two streams of research in this thesis were selected from the numerous potential applications of 3D analysis for several reasons. Each project assesses a different use of XCT data. The first, an investigation of porosity and metal grain distributions in OCs, relies on accurate thresholding of a single component of the XCT data. The second, investigating inclusions in Barwell, relies on manual segmentation of shapes in the data and uses XCT as a tool for accurately subsampling meteorites for other techniques.

As a relatively new technique in meteoritics, there is much scope to illustrate the use of XCT through original research. In particular, widening experience of the technique adds to our understanding the errors and limitations of the technique, especially when applied to complex materials. Furthermore, there is a multitude of both commercial and open source software available for XCT analysis. This project will also test several programs to develop workflows for accurately interrogating the data.

One key motivation for this study is the non-destructive nature of the technique. Meteorites are inherently rare and each meteorite is itself a type specimen. There is limited material available, and retrieving more material through meteorite collection is dependent on chance, and through sample return missions, is costly and technologically challenging. For this reason, there is a delicate balance for curators to develop the scientific value of a collection, whilst at the same time preserving material in perpetuity. The NHM Collection is one of the world's most important and wide-ranging. With almost five thousand meteorite specimens, careful curation of this collection is crucial. This project will also assess XCT as a tool for curation, by adding to knowledge of specimens, by informing subsampling to improve accuracy and minimise loss of material, and potentially by providing a non-destructive method for classifying extraterrestrial material.

Additionally, this research technique has applications to sample return missions. From a materials perspective, XCT can be used for testing the integrity of collection vessels to ensure adherence to planetary protection protocol. From a scientific perspective, characterisation can be carried out prior to opening and potential contamination. This can then be used to informing sampling, as well as providing 3D data on porosity, density, phase distributions and other features of the sample.

Traditionally, meteorites have been studied in 2D, via thin-section optical microscopy, SEM, or other techniques requiring polished surface preparation. Additionally, bulk analyses require invasive and destructive sampling. Increasingly, there is demand to illustrate the information that can be gleaned without destroying material. With XCT, it is possible to create 3D representations of the interior of a sample, based on the X-ray attenuation of the material. This not only allows for repeatable analyses, but accounts for future developments in technology and instrumentation. As it is non-destructive, any visible porosity can be considered inherent and not due to preparation. Similarly, 2D sections through a given metal grain will vary widely based on grain shape and

orientation, and fail to provide an accurate measurement of the grain volume. A key advantage is that this data is digital, and therefore open to quantitative methods of analysis, including grain number, size, and orientation. Importantly, unlike other techniques, CT data allows for the visualisation of pore space as well as quantification, which could provide a new method for investigating the origin of porosity. This study will explore the benefits of three-dimensional data and to elucidate the place of XCT within the greater suite of techniques used in the study of extraterrestrial material.

1.10 Research Aim and Objectives

This project aims to use micro-computed tomography instrumentation at the Natural History Museum to elucidate the three-dimensional properties of OCs and provide insight into early Solar System processes including mixing of OC constituents, accretion and both thermal and shock metamorphism, and to evaluate the strengths and limitations of the technique. There are two scientific questions:

i) How abundant are igneous inclusions in the Barwell (L6) meteorite and what is their relationship to the host meteorite?
ii) Can XCT provide quantitative measures of porosity and metal grains in OCs, and how are they affected by parent body metamorphism (thermal and shock)?

Objectives

1. Conduct XCT imaging of a selection of meteorites to develop analytical routines for working with different types of extraterrestrial material.
2. Use XCT to determine the frequency of large igneous inclusions in Barwell and to inform sampling to expose material.
3. Use scanning electron microscopy to create X-ray maps, image textures and determine modal mineralogies of igneous inclusions in Barwell, and electron microprobe analysis to measure their chemical compositions.
4. Use accessory techniques – O isotopic analysis, trace element analysis and Hf-W isotopic analysis – to provide insight into origin and evolution of Barwell inclusions.
5. Investigate commercial and open-source software packages to develop workflows for interrogation of XCT data.

6. Measure and visualise porosity using XCT and correlate to gas pycnometry to assess accuracy of technique.
7. Measure metal grain size distributions and orientations of individual grains and compare with magnetic susceptibility measurements to find if correlated.

1.11 Samples

The samples used in this study fall into two categories. For *Section 4*, on igneous inclusions in the Barwell meteorite, the following specimens of Barwell were investigated (Table 1.2). These include, the original 'Pebble' specimen described by Hutchison et al. (1988), two large stones selected for their size, which was deemed the largest possible (in terms of maximum dimension) to achieve a reasonable resolution and sufficient penetration of X-rays for the XCT analysis.

Meteorite	Accession Number	Petrological Type	Shock stage	Mass of sample (g)
Barwell	BM1966,59	6	3	232.7
Barwell	BM1966,59	6	3	441
Barwell	BM1966,58b	6	3	203
Barwell	BM1985, M68	6	3	19.359
Barwell	BM1985, M68	6	3	9.961
Barwell	BM1985, M68	6	3	2.286

Table 1.2. NHM specimens of the Barwell L6 meteorite used in this study. Petrological type from Meteoritical Bulletin, shock stage from Macke (2010). Masses vary in precision due to measurement limitations.

Table 1.3 shows the L chondrites selected for the study of the effects of metamorphism on ordinary chondrites (*Section 3*). They were chosen as they are all falls (to mitigate against the effects of weathering), most with descriptions of porosity and shock stage in the literature (for comparison), and suitably sized and shaped fragments (~ 1 g, fairly equant in three dimensions) were available in the collection, to adhere to the non-destructive ethos of the study.

Meteorite	Accession Number	Petrological Type	Shock stage	Mass of sample (g)
Aumale	BM.1985,M63	6	4	1.336
Aumieres	BM.1985,M64	6		1.390
Ausson	BM.1985,M65	5	3	1.144
Barwell	BM.1966,59	6	3	0.999
Bjurbole	BM.1927,11	4	1	1.765
Chervettaz	BM.86761	5	3	0.556
Crumlin	BM.86115	5	4	1.078
Elenovka	BM.1956,166	6	2	0.453
Farmington	BM.66200	5	4	1.163
Hallingeberg	BM.1974,M24	3	1	1.840
Holbrook	BM.1912,677	6	2	1.792
Jackalsfontein	BM.1908,431	6		1.164
Jhung	BM.51190	5	2	0.960
Kyushu	BM.1905,67	6	5	1.913
Little Piney	BM.1985,M107	5		1.613
Monze	BM.1951,103	6		1.927
Nikolskoe	BM.1956,326	4	2	1.970

Table 1.3. NHM specimens of 17 L chondrites used in this study. Petrological types from Meteoritical Bulletin, shock stages from Macke (2010) and Gattacceca et al. (2005).

2 Methods

2.1 Micro-Computed Tomography

X-ray computed tomography, first developed in the medical industry in the 1970s, is based on mapping the X-ray attenuation (the loss of intensity of radiation as it passes through the sample) of a rotating sample in three dimensions, i.e. volume scanning. The technique is thus based on the interaction between matter and electromagnetic radiation and is non-destructive, therefore of particular importance when investigating rare extra-terrestrial material. XCT produces radiographs, or projections, of the rotating sample on a two-dimensional detector panel array, from which tomograms are constructed. Recent advances in technology for lab-based scanners have produced increased resolution, shorter acquisition times, better reconstruction algorithms, the addition of multi-row detector arrays and so on, all of which have contributed to improved quality in data. This is the primary technique used in this study therefore the instrumentation, parameters and methods of analysis are more fully described below.

2.1.1 Physics of XCT

It is necessary to understand the interaction between X-rays and matter when selecting scanning parameters. Full accounts of the physics of X-rays can be found in Als-Neilsen and McMorrow (2011) and Sutton et al. (2013). X-rays have wavelengths between 0.01 and 10nm. The energy of a photon is inversely proportional to its wavelength:

$$\boldsymbol{E = \frac{hc}{\lambda} = hf}$$

where E = energy, h = Planck's constant (6.626 x 10^{34} J·s), c = speed of light, λ = wavelength, and f = frequency. Therefore, a longer wavelength corresponds to lower energy X-ray photons. The X-ray energy determines the degree of attenuation in a material, the mechanism by which it occurs, and the penetrative ability of the X-ray itself. Higher energy X-rays are less sensitive to changes in composition, i.e. will provide less contrast between phases, but are more effective at penetrating samples. X-rays are often referred to as 'soft' (λ = 0.1 nm – 10 nm; E = 12.4 keV – 124 eV) or 'hard' (λ = 0.01 nm – 0.1nm; E = 124 keV – 12.4 keV).

The intensity of the X-ray, i.e. the number of X-ray photons per unit time, is also a determining factor. Higher beam intensities result in better signal-to-noise ratios; however, higher intensity beams require a source with a larger focal spot, which results in a lower resolution.

Attenuation is a function of various properties of the material being investigated, primarily its density and elemental composition and concentration. In XCT, there are two primary mechanisms of X-ray attenuation: absorption and scattering (Figure 2.1).

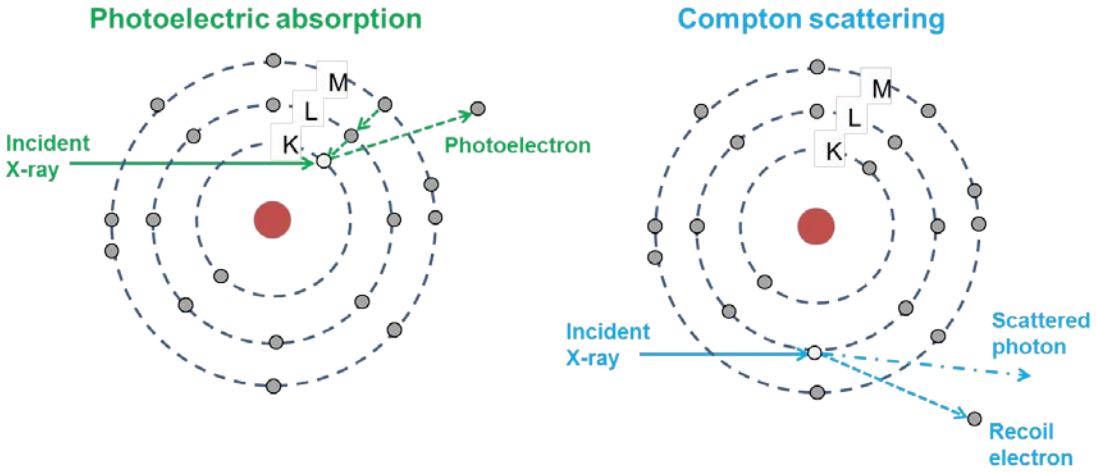

Figure 2.1. Diagram of attenuation mechanisms, adapted from Sutton et al. (2013).

The two mechanisms illustrated in Figure 2.1 – the photoelectric effect and Compton scattering – are dependent on the scanning energy. Other mechanisms can occur, however these are correlated to very high energies or cause very small attenuations, therefore they are often deemed irrelevant in XCT. The photoelectric effect is more common at lower energies and the probability of this mechanism occurring decreases as excess photon energy increases. At lower energies, the chemical composition of the sample significantly affects the attenuation (represented in the tomograms), whereas when dealing with higher X-ray energies, the density of the sample is a more important factor.

The photoelectric effect occurs when an X-ray collides with an electron with a lower binding energy than that of the incident ray. This transfer of energy results in the liberation of an electron and the destruction of the incident X-ray. If this occurs in an inner shell, i.e. if the X-ray energy is high enough, the ejection of the photoelectron results in a vacancy, which causes a cascade of electrons from outer shells (the final vacancy is then filled by an environmental electron). The “absorption

edge" describes the jump in attenuation coefficient of an element when the X-ray energy approaches the electron binding energy of a given shell.

Compton scattering takes over when the photon energy is considerably in excess of the binding energy of electrons. Therefore, Compton scattering is dominant at higher X-ray energies. As photons lose energy through the collision with electrons, they are scattered, or deflected, resulting in the attenuation of X-rays (i.e. a reduction in the intensity), corresponding linearly to the mass density of the sample. This then frees a secondary electron.

It is possible to calculate the attenuation coefficient of a given material and thus estimate the relative brightness in greyscales of different phases, should the mineralogy of the sample be well-characterised. This can only provide a guide for several reasons mentioned in the literature review such as effect of porosity. The MuCalc Tool, developed by the High Resolution X-Ray CT Facility at the University of Austin at Texas, allows the user to plot the attenuation of several mineral phases, in order to determine if the phases will be distinct in a tomogram, and to find the optimum scanning energy to maximise their differences. Figure 2.2 shows a graph of the attenuation of various minerals common in meteorites against source energy. This illustrates that at lower energies, there is a greater difference between the olivine and pyroxene silicates. At an energy of approximately 140keV, the contrast between the two is decreased beyond distinction.

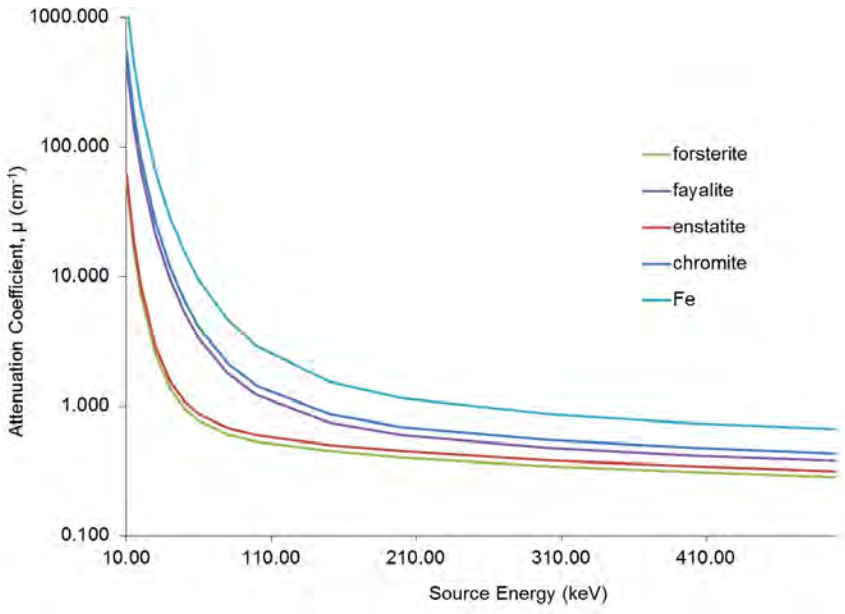

Figure 2.2. A graph of attenuation coefficient against source energy for various minerals (forsterite, fayalite, enstatite, chromite and iron metal). Based on MuCalc Tool (UTCT, http://www.ctlab.geo.utexas.edu/software/index.php)

2.1.2 Instrumentation

The Nikon HMXST 225 system was used throughout this study. This system can utilise two different targets, transmission and reflection. In the case of the extra-terrestrial samples studied in this project, the reflection target, using a tungsten filament, was optimal. X-rays are generated from a source and directed at the sample, which is rotated through 360° during one scan. Varying this angle of incidence creates a sequence of evenly spaced, parallel tomograms, mapping the X-ray attenuation.

During a scan, the projections are collected by a detector, generally a solid-state scintillator, located behind the rotating stage holding the sample. The Nikon HMXST 225 system uses a Perkin-Elmer detector. The size of the panel affects the quality of the scan data, as does the efficiency with which the detector collects the resultant energy spectrum. Individual lines of pixels on a detector array are constructed as single tomograms. For example, the panel in the NHM scanner, with 2000 x 2000 pixels will produce 2000 tomograms and hence the resultant data set will be 2000 x 2000 x 2000 voxels. The systems combine the detectors with photodetectors that convert the light into electrical signals for processing. As both the source and detector are built into the scanner, they are fixed and cannot be changed by the user.

Figure 2.3 shows a schematic of the instrument set-up. Sample preparation is minimal; each specimen is wrapped in plastic and then embedded in oasis (florist's foam) for stability. This should prevent movement during the scan which would cause blurring in the data. Prior to the collection of projections, a shading correction is carried out, including a dark reference image (with the detector shuttered) and a light reference image (without the sample in the beam) to correct for background contributions and variations in the brightness of the source across the detector panel.

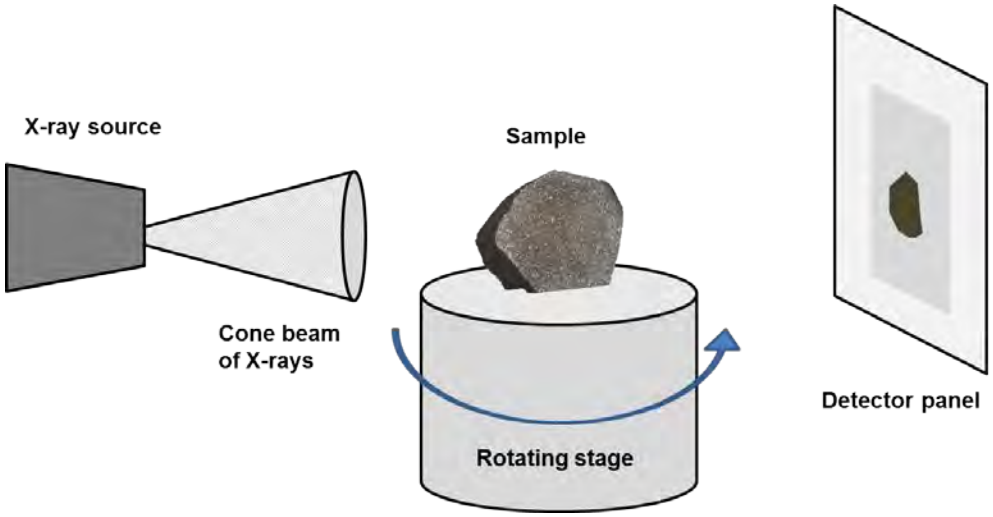

Figure 2.3. Schematic representation of instrumentation set up for XCT scanning.

2.1.3 Scanning parameters

To achieve the full potential of the technique, it is crucial to understand how to obtain the best scans for a given sample, i.e. what parameters are required for the best contrast of phases and resolution of the scan. Typically, the scanning parameters are optimised by the user to ensure that the data are spread across as wide a range of greyscale values as possible. Each scan is independent and greyscale values cannot be directly compared between data sets, without the use of standards. The following parameters can be varied by the user:

- Source voltage:

The kV chosen for a scan sets the maximum energy. X-rays of lower energy are still produced, i.e. this parameter denotes a range rather than a single energy. The keV is numerically about half the kV when using the tungsten source and will vary with source. Essentially, the voltage determines the penetration achieved by the X-rays and must be higher for more attenuating materials.

- Current:

The current, measured in μA, is the energy of the X-ray. This determines the energy of the beam and the range of voltages of resultant X-rays. For example, increasing the current for a given scan will increase the range of kV represented and increase the counts at the highest kV. Simplistically, the current is correlated to the number of X-rays created.

- Resolution:

The resolution of the scan is reported by voxel size, which is a measure of the distance between two adjacent voxel centres. It is constrained by the size of sample, the dimensions of the detector, and the spot size of the X-ray source. The spatial resolution refers to the resolvability of close phases or objects as separate entities and depends on the same parameters as well as the reconstruction algorithms employed, and the physical properties of the materials in the sample.

- Gain:

This is a digital boost of the signal received by the detector panel, which follows the same principle as increasing the ‘brightness’ on the sample. Gain is particularly useful if the resultant greyscale histogram is not well placed but the settings are optimum otherwise. Increasing gain could also spread the histogram out thus increasing contrast

between phases but at the expense of increasing noise. Thus, intermediate voxels may be more difficult to assign to a specific material.

- Filtering:

Filtering is used to preferentially remove low energy X-rays produced by the polychromatic beam, following a Gaussian distribution. Copper filtering is used predominantly in the scanning of meteorites (high filtering). Lower filtering can be provided with aluminium. Tin provides more filtering than copper, and in turn, for very dense materials, silver can be used for higher filtering than tin.

- Projections:

As a standard, 3142 projections are gathered. This is calculated by 'detector width'/2*$\prod$. Theoretically, each tomogram should capture a given feature in a different pixel, which should help to identify individual features more easily, i.e. reducing blur. This has been increased to 6284 in some scans, in order to halve the angle step between each projection, which has the effect of reducing noise, but also doubles the time required for the scan.

- Exposure time:

The exposure selected denotes the time spent gathering each projection. Increasing the exposure has the effect of increasing the flux received at the detector panel, resulting in more X-rays detected and less noise. This is naturally a trade off with scan time.

- Frame averaging:

Frame averaging involves taking multiple projections at each angle and then averaging the data across the projections. This has the effect of reducing noise in the data, but again, doubles the time required for a scan.

2.1.4 Artefacts in the data

Several artefacts are common in CT data, which can introduce errors when thresholding or segmenting a volume, and thus make shape analysis of features impossible. There are some ways to mitigate the impact of artefacts, however these often require compromises. Common artefacts include the following:

- Blurriness arises from several effects including the partial volume effect, a large X-ray focal spot, noise in the system, geometric imprecision, CT reconstruction algorithms, or movement during a scan. Scans must be repeated if significant blurring occurs.
- Ring artefacts result from defective detector elements which cause rings centred on the centre of rotation. Frame averaging for reference images should reduce such artefacts.
- Noise in the data, i.e. a low signal-to-noise ratio, can be reduced by increasing exposure, however this can increase ring artefacts. In data sets significantly affected by noise, frame averaging can also be carried out.
- Partial volume averaging, whereby a voxel that contains two or more different materials presents a greyscale that is an average of the attenuation of the different materials which can make finding the boundary between them challenging.
- Streaking, as seen in Figure 2.4, whereby the high attenuation caused by high-density materials, often Fe-Ni metal, creates streak artefacts that shadow the data around it.
- Beam hardening concerns the use of polychromatic X-rays and is especially important where more dense materials are found. This can result in brightening of the data in some parts of the scan. Softer X-rays are more likely to cause beam hardening but this can be reduced by inserting a copper filter, which removes low-energy photons, between the source and the detector. Generally for ~1cm ordinary chondrites, the Cu 0.25mm filter was used.
- Starbursts, as seen in Figure 2.4, are particularly an issue with meteoritic samples. They arise because there are large attenuation contrasts between materials, combined with low energy X-rays. This manifests in streaky bursts of varying brightness around high-density materials. The effect can be mitigated by increasing the source energy and using additional filtering; however, there is a compromise as this can result in loss of contrast in lower density materials. It is also possible to use a lower angle between the beam and sample, however this sacrifices the resolution.

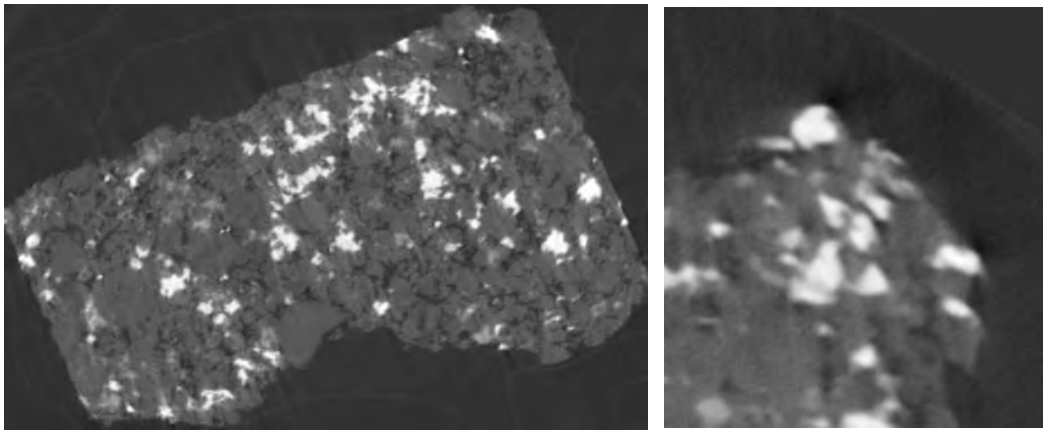

Figure 2.4. XCT tomograms showing streaking (left) and blurring (right) artefacts in CT data of ordinary chondrite samples.

2.1.5 Other CT techniques

There are several other techniques in CT that may prove crucial in the development of the method, as they can provide improved data quality and potentially quantification and delineation of phases. These include: phase contrast, which uses the refraction of X-rays by the sample to highlight the edges of and boundaries in a sample, and dual energy CT, which involves using two sources, at different energies, exploiting the K-edge of a given material, at which there is a spike in attenuation due to the increased photoelectric absorption at levels just above the K-shell binding energy). For example, Tsuchiyama et al. (2013) employed analytical dual-energy microtomography by scanning particles returned by the Hayabusa mission at two energies to discriminate between minerals in a solid solution series. These are currently beyond the scope of this project due to limitations of the instrumentation, however any considerations of the use of XCT should follow advancements in technique development.

2.1.6 Data analysis

Once a scan is complete, the raw projections are loaded into CT Pro, a Nikon program which finds the centre of rotation from two slices, at the top and bottom of the scan. If the software fails to automatically do this, it is possible for the user to manually register the projections, by an interative process, starting with a coarse alignment, and gradually user finer controls to reach the sharpest image. The data are reconstructed using a modified Feldkamp back projection algorithm to generate a volume, which can then be visualised in three dimensions or as single tomogram slices in any orthographic plane.

Data are exported in 16-bit volumes. The bit depth describes the number of bits used to define each pixel, therefore with a greater bit depth, i.e. 16 instead of 8, the greater the number of greyscale tones can be represented. In 8-bit images, 2^8, or 256 tones can be represented. In 16-bit images, this rises to 2^{16}, or 65,536 tones. One must also consider the ability of the human eye to differentiate between such numbers of tones and consider certain compromises. Working in 16-bit requires considerably more processing power and thus additional workstation time. When working with circa 30 gigabyte (GB) volumes, this can sometimes be impractical.

Visualisation of CT data sets can be carried out with various software packages. Their usefulness depends on the information that is required by the user. This can vary from simple visualisation of the interior, to mapping out veins, cracks and fractures, segmentation of the data via thresholding or manual outlining to finding the volumes of selected features or phases. Some programs are preferable for visualisation, e.g. Drishti, whereas others should be utilised for quantitative measurements, e.g. Avizo. As with the hardware, continuing advances in technology are leading to improved capabilities, faster processing speeds and lower costs, making the applications of software ever more effective.

Quantitative software related to geological applications of XCT is rare. University of Texas CT Lab Facility have developed BLOB3D, an “image-processing tool of blob analysis, in which contiguous sets of pixels meeting certain conditions are traced and described” (Ketcham, 2005). Originally designed for the analysis of porphyroblastic rocks, the program has potential applications in quantitative analysis of a variety of geological materials. BLOB3D can be used for the segmentation of CT data, i.e. the assigning of particular voxels to different materials, the automated and manual separation of different features that may be texturally distinct but similar in greyscale, and the extraction of relevant segmented or separated data for quantitative measurements such as volume, aspect ratio and orientation. The BLOB3D program is written in IDL (Interactive Data Language) and available through Exelis Visual Information Solutions.

Data analysis in this study was primary carried out using the FEI Avizo software, after testing of features in several programs. This study used two main methods of segmentation of XCT data: i) manual outlining and interpolation through slices, as used to separate inclusions in *Section 4*; ii) histogram thresholding to separate entire phases

based on their greyscale values, as used to segment porosity and metal grains in *Section 3.* Workflows of XCT data analysis are given in *Appendix 4.*

In order to assess the orientation of metal grains within each sample, a *particle analysis* module was run, in which a bounding box was fit around each grain. Although metal grains are irregular and not easily described geometrically, this approximation can provide a metric for unidirectional elongation (e.g. Friedrich et al. 2008). Each metal grain was then analysed for shape and orientation information, which indicates the degree of preferred orientation observed in the samples.

Stereonets, or stereographic projections, of the data are used to illustrate the fabrics visually. All plots use a lower hemisphere, equal area projection to standardise across stereonets. Each point represents a single major axis of a metal grain. Analysis within the Stereo32 program (Röller and Treppmann, 2007) provides statistical measures of the distribution:

$$\boldsymbol{C = ln\frac{eigenvalue\ 1}{eigenvalue\ 3}}$$

$$\boldsymbol{K = ln\frac{eigenvalue\ 1}{eigenvalue\ 2} / ln\frac{eigenvalue\ 2}{eigenvalue\ 3}}$$

$$\boldsymbol{R\% = \left(\frac{R}{n}\right) x\ 100}$$

where C = strength parameter, a measure of the degree of anisotropy; K = shape parameter, where a girdle distribution (k < 1) indicates a foliation, or a cluster distribution (k >1) indicates a lineation; R% is a normalised mean vector metric, which describes the similarity of the grain orientations and is independent of the number of grains in the sample; R is the mean vector, and n is the number of grains (Röller and Treppmann, 2007). The greater the orientation of the metal grain major axes, the higher the value of R%. For samples that show a foliation, density distributions are included. Such projections are not useful when examining data for samples without any preferred orientation as they can be misconstrued. For example, Figure 2.5 shows the stereogram and associated density distribution for Barwell. The normalised degree of preferred orientation of the metal grains, R%, is 11.5 (fairly low), however the density distribution would immediately give an impression of a strong lineation. The density

distributions are dependent on the number of grains, thus scalebars are variable across samples.

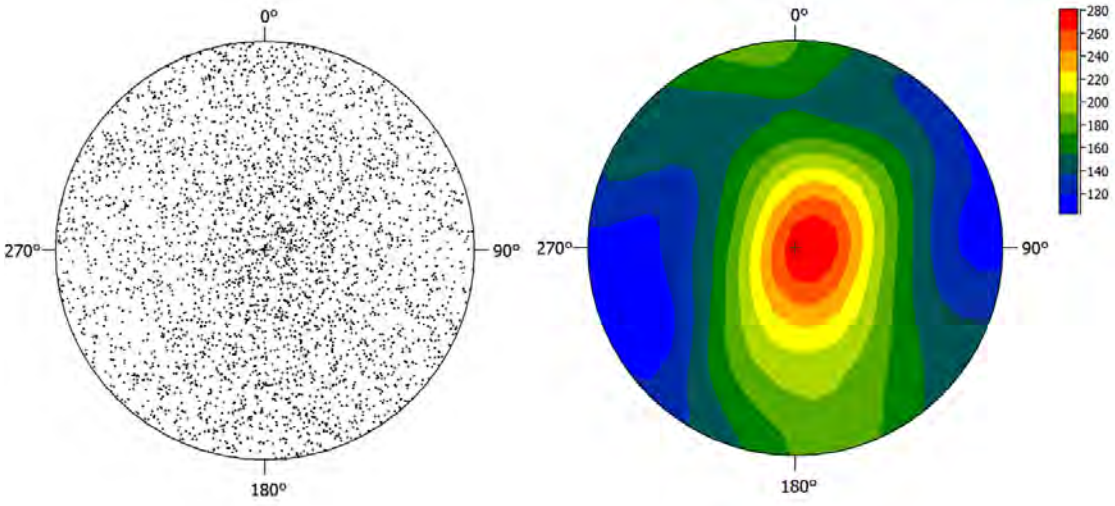

Figure 2.5. A stereogram (left) and associated density distribution (right) showing the orientations of major axes for individual metal grains in the Barwell meteorite. Number of grains: 3463.

2.2 Energy-Dispersive X-ray Scanning Electron Microscopy

Scanning electron microscopy (SEM) was used for the identification and imaging of phases, allowing for petrographic description and the utilisation of chemical compositions as indicators of petrogenetic processes. Energy dispersive X-ray (EDX) SEM mapping was additionally used for measuring phase proportions and to provide context and facilitate accurate electron microprobe (EPMA) analyses using wavelength-dispersive spectrometry (WDS).

2.2.1 Theory

EDX is based on the interactions of a beam of electrons with a sample. This leads to the ejection of an electron from a stable orbit within an element, creating an unstable configuration and subsequently leading to relaxation of an electron in a higher orbit, which releases a characteristic X-ray emission. The energy is dependent on the location of the emitted electron. If an electron is lost from the innermost shell, K, and replaced by an L shell electron, then Kα line emission is detected. If an M shell electron

relaxes, Kβ emission is detected (Figure 2.6). This is a simplistic view of the interaction, since there may be a range of slightly different electron energies within a given shell, however this thesis follows well-established methods of SEM commonly used for geological applications and additional considerations can be found in the literature (Goldstein et al., 1992).

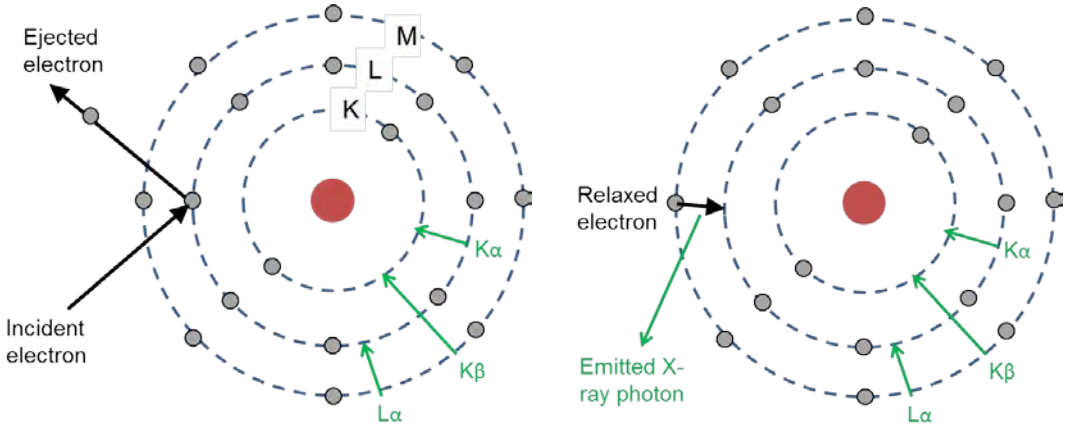

Figure 2.6. A diagram of the interaction between the electron beam and electrons in the atom shell. The incident electron leads to ejection of an orbital electron, which is then replaced by relaxation of an atom from a neighbouring, less-tightly bound shell. Electrons moving from the L to the K shell lead to a Kα emission, from M to K shell, Kβ emission and from M to L shell, Lα emission. Diagrams adapted after Goldstein et al. (1992).

2.2.2 Instrumentation

The Zeiss EVO 15LS SEM was used throughout this study. The vacuum system consists of two rotary pumps and a turbomolecular pump, in high vacuum for quantitative analysis. The electron beam, generated by the electron gun with a tungsten filament, is attracted through the anode, condensed by electromagnetic lenses, and eventually focused, by an objective lens, to a fine point on the sample. The sample and source must be kept within a vacuum as molecules within air can easily absorb or deflect the electron beam. The electron energies that can be selected range from ~ a few hundred electron volts (eV) to approximately 30 KeV. On reaching the sample, the characteristic X-ray emissions (produced by the interaction between the electrons and the constituent elements) are then collected. This instrument is equipped with an EDX spectrometer, thus counts X-rays of a range of energies simultaneously. These are then converted into a charge, in proportion to the energy of the X-ray. This charge is then converted into voltage, and amplified. The output is a plot of intensity against X-ray photon energy.

For quantitative analysis, the following instrument parameters are optimal: working distance of 8.5 mm, accelerating voltage at 20 kV and beam current at 3 nA. Before beginning analysis of the sample, the stability of the system is checked by measuring a known standard composition, Kakanui augite.

Polished sections are required since rough or irregular surfaces can add lead to errors in quantification through differing X-ray generation and escape leading to variable absorption and secondary fluorescence. Sections are carbon coated to prevent charging on the sample, and aid in the removal of surface electrons.

2.2.3 Data analysis

Minerals are essentially crystalline compounds with defined elemental ratios, or stoichiometry, which reflects the arrangement of atoms in their crystal lattice. These ratios are characteristic and can be used to identify minerals through analysis of the EDX data. Element concentrations are quantified by comparing the peak ratios of well-characterised standards to the unknown. Standardisation of the EVO instrument at the Natural History Museum were set up previously, and calibration is regularly carried out. Removal of background counts and matrix corrections are applied within the software, and the concentrations are calculated from the area of each specific X-ray peak. For this reason, low concentrations may not be determined if a low, broad peak is not statistically distinct from the Bremsstrahlung background.

Oxygen is calculated by stoichiometry, i.e. adding ions to the formula based on the oxidation state of other measured components, rather than directly in this method. For example, forsterite contains one Si^{4+} and two Mg^{2+} ions, thus the addition of four O^{2-} ions balances the stoichiometry of the mineral as two molecules of MgO and SiO_2. The user selects the appropriate number of ions to add to the formula, which is then calculated using a quantitative analysis routine available within the SEM software. The stoichiometry of a mineral can then be manually checked by considering substitutions for other common elements (e.g. the common substitution of divalent ions Fe, Mg, Mn, Cr, Ca).

As well as quantitative data on elemental composition, SEM provides high-resolution imagery of the sample petrography. Backscattered electrons result from elastic interaction between beam and sample and are counted using a specific backscatter

detector. They are produced from the entire interaction volume, meaning the images are less sensitive to surface topography than secondary electrons. Since the production of BSEs is dependent on the average atomic number of the material, bright areas on an image correspond to areas with high proportion of BSEs (low electron absorption) and vice versa. Thus, BSE images are a useful reconnaissance tool for investigating the texture of a sample, however the same greyscale value can be produced by two different mineral compositions. Appropriate brightness and contrast levels must be selected for any given site of interest.

2.3 Wavelength-Dispersive Spectrometry: Electron Microprobe

2.3.1 Theory

Similarly to EDS analyses, an electron microprobe provides elemental composition by analysing characteristic X-rays produced by the interaction of an electron beam with a polished sample. However, whilst an EDX spectrometer differentiates X-rays by energy, an electron microprobe disperses X-rays based on their wavelengths using X-ray diffraction. The spectrometer consists of an analysing crystal and a detector. The crystal lattice and its orientation determine the wavelength of X-rays that are diffracted, according to Bragg's Law:

$$n \lambda = 2 d \sin \theta$$

Where n = an integer corresponding to the order of diffraction; λ = the wavelength of the X-ray, d = the lattice spacing of the crystal; θ = the angle between the incident X-ray and the crystal surface.

Selected X-rays then enter the detector, which is tuned to the peak position of an emission line for a given element. Therefore, interference from peaks of other elements in the sample is reduced or eliminated, but each spectrometer collects data for only one element at a time. As a result, analysis by WDS is slower but able to detect lower concentrations than EDX. Quantitative analysis can be obtained for elements with atomic numbers > 5, to within 1 % (Reed, 2005).

2.3.2 Instrumentation

The Cameca SX100 electron microprobe at the Natural History Museum was used throughout this study. The vacuum system consists of rotary, oil diffusion and ion pumps. The electron beam, produced by an electron gun with a tungsten filament, is focused by a series of electromagnetic lenses in the instrument column. The diameter of this beam at the interaction with the sample is referred to as the 'spot size'. The interaction volume of electron scattering is a greater resolution-limiting factor than the incident spot size itself. Monte Carlo simulations of EPMA analysis indicate that the volume of interaction for an electron beam with voltage of 20 kV and spot size of 1 μm leads to the generation of X-rays at depths of up to ~ 3.5 μm and radially extends from the beam centre ~1.5 μm (Figure 2.7). Thus, large grains are preferred for measurements to prevent mixing of analyses with surrounding phases. A BSE image is used for orientation across the sample.

Five wavelength dispersive X-ray spectrometers are used, each with multiple crystals, facilitating a wide range of simultaneous X-ray detection. Crystals used in the Cameca SX100 at the Natural History Museum are: thallium acid phthalate (TAP), pentaerythritol (PET) and lithium fluoride (LIF). Large crystals, e.g. LTAP, are used to provide higher counts, resulting in lower detection limits. For each mineral phase, an element list is created and a method designed that determines: the crystals required, the order in which the elements are determined and their peak positions, the counting time (on both peaks and background), and off-peak spectrometer positions (for measurements of the background avoiding peak overlaps). Specific element lists are necessary, since measuring additional elements requires a longer analysis and increases the potential for peak overlaps. Protocols for different methods (Fe/Mg silicates, feldspar, oxides, FeNi metal) are shown in Table 2.1. Volatile elements are generally measured first, since they are likely to migrate due to beam interaction.

For quantitative analysis carried out in this project (Fe-Mg silicates, oxides and metal grains), the following parameters are optimal: beam spot size of 1 μm, accelerating voltage at 20 kV and beam current at 20 nA. Prior to any analysis, the focus of the sample is checked using a reflected light microscope to maximise counts since even small changes in the sample height can have a significant effect on signal intensity.

Quantitative analysis is acquired by comparison of element peaks against a standard. Measurements of both standard and sample have background subtracted from the

peak value (intensity). The tuning of a spectrometer to the peak position of an emission line is based on scanning across the approximate position during calibration using standards. This calibration can change over time, therefore is carried out close to the time of analysis. The standard is selected to have a similar composition to the unknown, as the peak location can change considerably with valency for some elements, e.g. S. Since many elements generate X-rays with overlapping peak positions, their contributions to peak values are measured and subtracted by ratio (within the software). Standards are measured at the beginning of a run and calibrated daily to account for any instrumental variance.

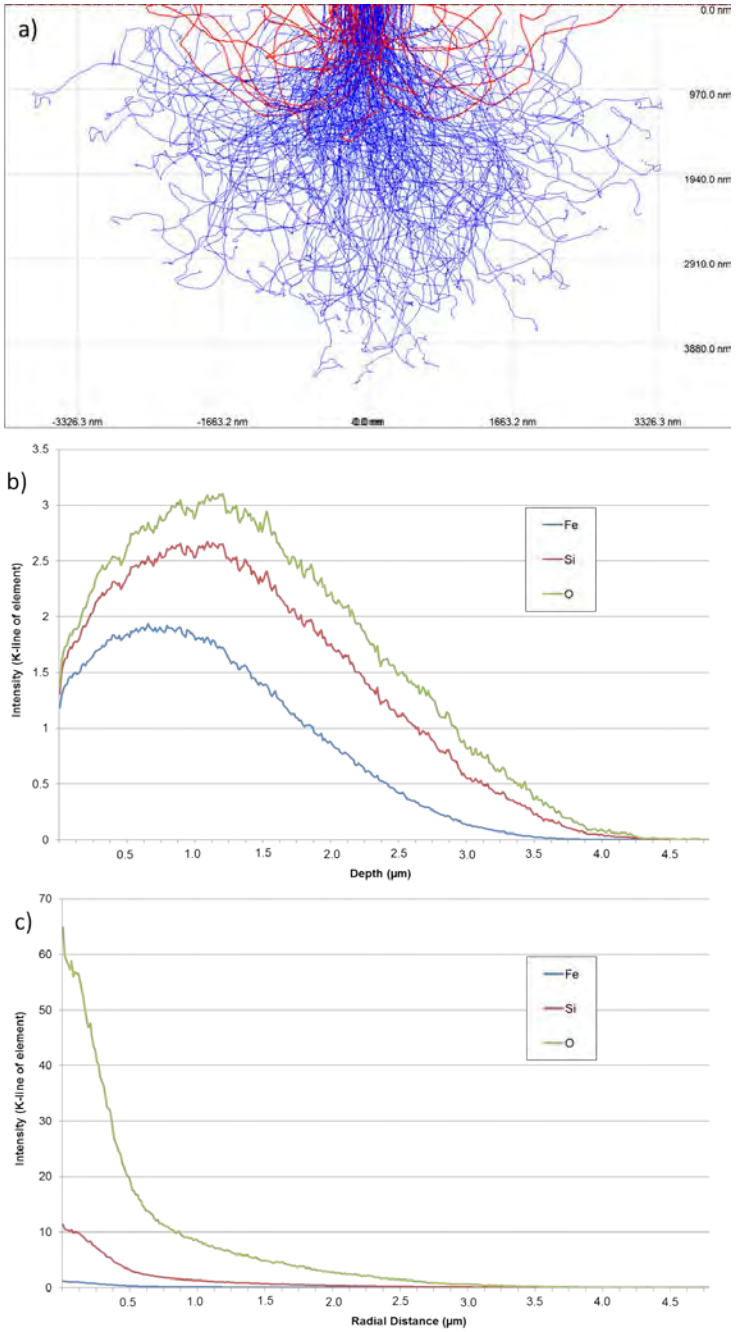

Figure 2.7. A Monte Carlo simulation of an electron beam at 20 kV penetrating fayalite (Fe_2SiO_4), showing: a) the simulated trajectory of electrons (blue: absorbed, red: backscattered); b) the depth of X-ray generation in the sample; c) the radial distribution of X-ray generation in the sample.

Protocol	Element	Crystal	Beam current (nA)	Beam diameter (µm)	Voltage (kV)
Olivine, Pyroxene	Na Ka	LTAP	20	1	20
	Mg Ka				
	Al Ka				
	Si Ka				
	K Ka	PET			
	Ca Ka				
	Ti Ka				
	V Ka	LLIF			
	Mn Ka				
	Fe Ka				
	Co Ka				
	Ni Ka				
	Y La	TAP			
	Cr Ka	LPET			
Feldspar, Glass	Na Ka	TAP	20	5	20
	Si Ka				
	Al Ka				
	Mg Ka				
	Ca Ka	PET			
	Ti Ka				
	Ba La				
	Mn Ka	LLIF			
	Fe Ka				
	K Ka	LPET			
	Sr La				
Metal, Sulphide	S Ka	LPET	20	1	20
	P Ka				
	Cr Ka				
	Ti Ka	PET			
	V Ka	LLIF			
	Mn Ka				
	Fe Ka				
	Co Ka				
	Ni Ka				
	Cu Ka				
	Zn Ka				
	Mg Ka	TAP			
	Si Ka				
Fe oxide	Na Ka	LTAP	20	1	20
	Si Ka				
	P Ka	LPET			
	Ti Ka				
	Cr Ka				
	K Ka	PET			
	Ca Ka				
	V Ka	LLIF			
	Mn Ka				
	Fe Ka				
	Co Ka				
	Ni Ka				
	Al Ka	TAP			
	Mg Ka				

Table 2.1. Protocol for different methods by EPMA, showing the order of elements analysed by different crystals, lithium fluoride (LIF), pentaerythritol (PET), thallium acid phthalate (TAP). The large crystals (LTAP, LPET, LLIF) are used for lower concentrations as they provide more counts. Volatile elements are counted first as their concentrations are artificially affected by the beam.

2.3.3 Data analysis

Matrix corrections are applied to account for interaction with X-rays and the sample. The Cameca software includes the PAP matrix correction (Pouchou and Pichoir, 1987), which is applied to all analyses in this study. Oxygen was not determined directly, but calculated by stoichiometry for minerals containing oxygen (e.g. silicates and Fe-oxides). Data are output in weight % or weight % oxide for each element measured during each analysis.

Before drawing any scientific inferences, the data were examined for robustness, precision and accuracy. Detection limits and errors based on counting statistics are provided for each analysis. Both must be considered to determine the validity of data. For major elements (> 10 wt% oxide), the data are considered statistically valid above 0.1 wt % oxide. Totals between 98 and 102 wt % were deemed acceptable, whilst data outside this range were rejected.

2.4 Laser ablation inductively coupled plasma mass spectrometry (LA-ICP-MS)

2.4.1 Theory

Laser ablation inductively coupled plasma mass spectrometry (LA-ICP-MS) can provide in situ measurements of elements in low concentration in different mineral phases. A thorough review of the technique is given in Longerich (2008). The technique can be considered in three parts. Firstly, the LA system consists of a laser and associated optics, a cell containing the samples, and tubing that connects the cell to the ICP. Material is ablated by the laser and carried by He gas that flows through chamber. Secondly, the sample (now as aerosol) is introduced to the ICP where it is further vaporised and ionised. Finally, the MS, operated under vacuum, separates these ions based on their mass to charge ratio, and the intensity of each ion beam is converted into an electrical signal that reflects the concentration.

In this study, LA-ICP-MS analyses are carried out the obtain siderophile and rare earth element (REE) concentrations of igneous inclusions in the Barwell L6 meteorite.

2.4.2 Instrumentation

Agilent 7500cs ICP-MS coupled to an ESI New Wave UP193FX laser ablation system. The instrument parameters are given in Table 2.2.

Laser	
Instrument	ESI NWR193
Laser type	ArF excimer
Wavelength	193 nm
Pulse duration	20 ns
Repetition rate	10 Hz
Analysis type	Spot
Spot diameter	20 - 45 µm
Fluence	2.5 J/cm^2
Carrier gas (He)	350 ml/min
Primary reference material	NIST 612
Secondary reference material(s)	BCR-2g
Internal Standard	Si

Mass spectrometer	
Instrument	Agilent 7500 ICP-Q-MS
Plasma gas flow (Ar)	1.1 l/min
Analysis duration	60s
Blank duration	30s
Dwell time per element	10ms

Table 2.2. Instrument parameters for LA-ICP-MS analyses of inclusions as conducted in this study.

Backscattered electron maps from SEM analysis were used for orientation around the sample to ensure the correct mineral was selected for analysis. REEs tend to be more abundant in pyroxene than olivine, and again in clinopyroxene rather than orthopyroxene. Thus, these minerals were targeted where possible. Spot sizes varied from 20 to 45 µm depending on the size of the grains available. A fluence of ~2.5 J/cm^2 was used for all meteorite analyses. A spot size of 50 µm and fluence of 3.5 J/cm^2 were used for the standards. NIST612 was used as calibration standard, and BCR-2g as the secondary standard. Microprobe analyses of mineral phases provided accurate concentrations of the internal standard, ^{29}Si.

Some larger areas were rastered during a ~90 second laser ablation run in order to provide an approximation of a 'bulk' measurement. Five areas, of 225 µm^2, were ablated in each inclusion. In order to estimate the contribution from each mineral to the

Si internal standard, BSE images of the rastered area were thresholded, similar to the method of estimation of the modal mineralogy of the inclusions in *Section 4.3*. The internal standard value was then calculated using the silicon wt % of each phase from EPMA analyses. Figure 2.8 shows locations of spot and raster analyses in inclusion B. Similar maps of analyses are provided in *Appendix 11*.

Individual spot analyses of olivine, pyroxene and plagioclase and bulk analyses of the inclusions were all analysed for: ^{29}Si, ^{31}P, ^{43}Ca, ^{45}Sc, ^{51}V, ^{53}Cr, ^{55}Mn, ^{59}Co, ^{60}Ni, ^{65}Cu, ^{66}Zn, ^{69}Ga, ^{72}Ge, ^{75}As, ^{85}Rb, ^{88}Sr, ^{95}Mo, ^{137}Ba, ^{139}La, ^{140}Ce, ^{141}Pr, ^{145}Nd, ^{147}Sm, ^{151}Eu, ^{157}Gd, ^{159}Tb, ^{163}Dy, ^{165}Ho, ^{167}Er, ^{169}Tm, ^{173}Yb, ^{175}Lu, ^{177}Hf, ^{182}W, ^{195}Pt, ^{197}Au, ^{209}Bi, ^{232}Th and ^{238}U.

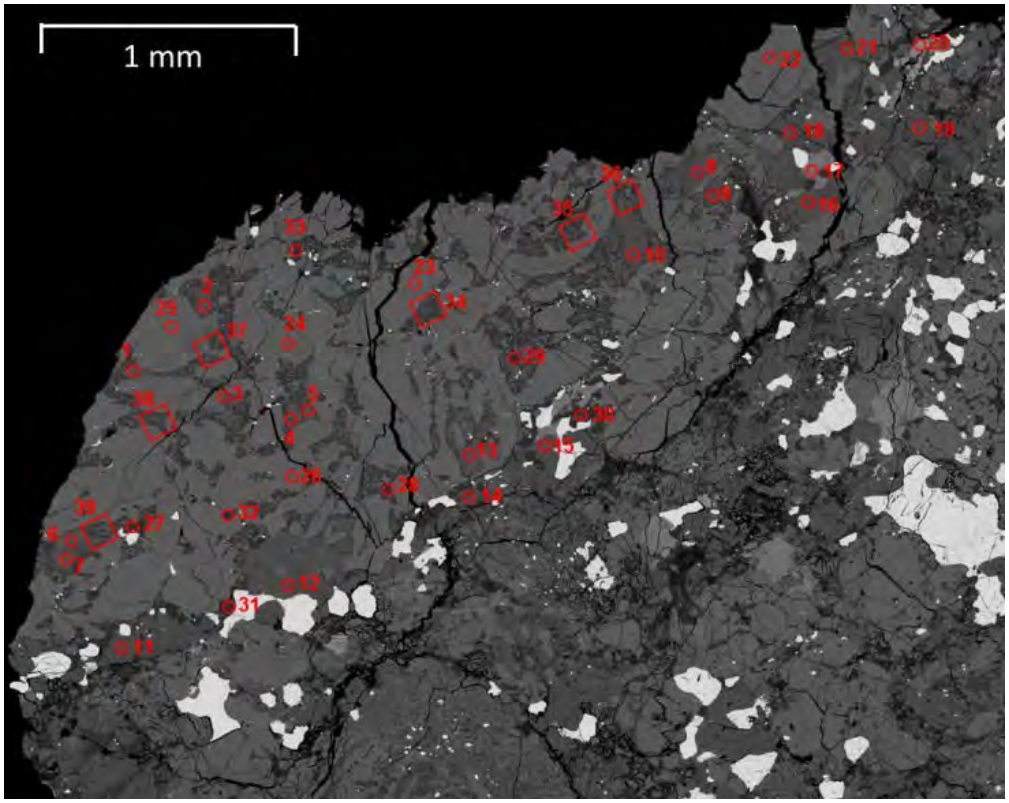

Figure 2.8. A BSE map of an inclusion (B) in Barwell showing the location of LA-ICP-MS individual mineral spot analyses (circles) and bulk rock raster analyses (squares).

2.4.3 Data analysis

The signal integration interval must be selected for each analysis. This is a subjective process, since the user must decide which slices of data are included or not, using the most consistent approach possible. A larger integration interval provides better counting statistics, and therefore lower detection limits, however only analysis of the

target mineral should be included to ensure accuracy of the data which are based on known internal standards. Figure 2.9 shows an example of data gathered for a plagioclase grain in inclusion A. No suitable slices could be found due to the chaotic nature of the data – likely the analysis was contaminated with other minerals, which often occurred in plagioclase analysis since the grains tended to be small. Figure 2.10 shows a mixed analysis, originally olivine, with few appropriate slices selected for analysis (the blue highlighted area shows the signal integration interval).

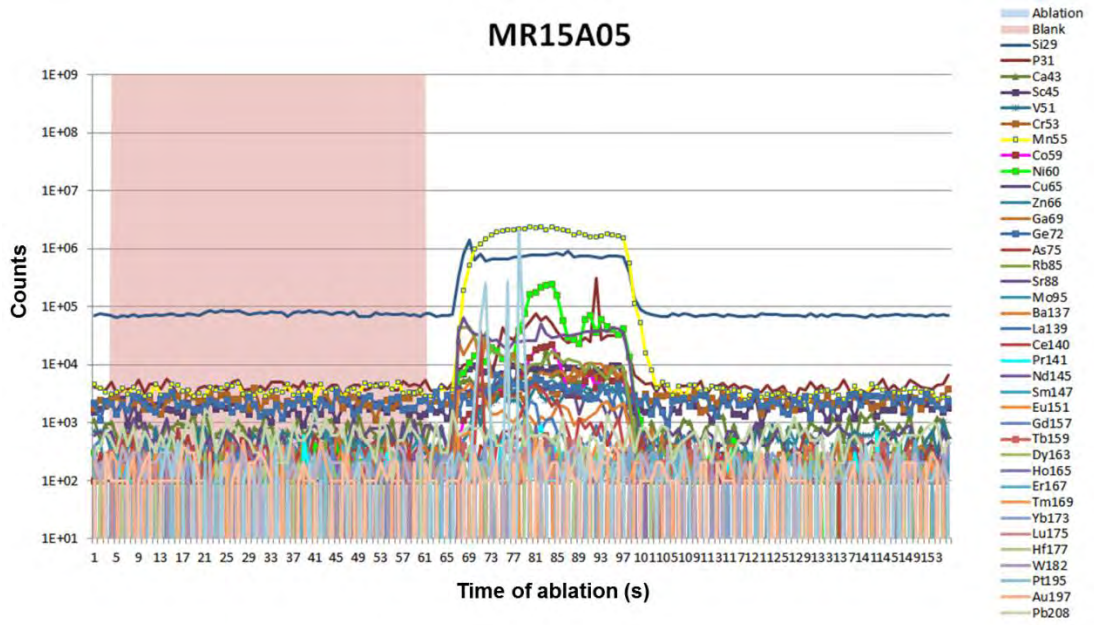

Figure 2.9. An example of plagioclase LA-ICP-MS data in inclusion A (analysis MR15A05). The area coloured in pink shows the pre-firing blank background slices. No suitable slices could be selected for the sample ablation.

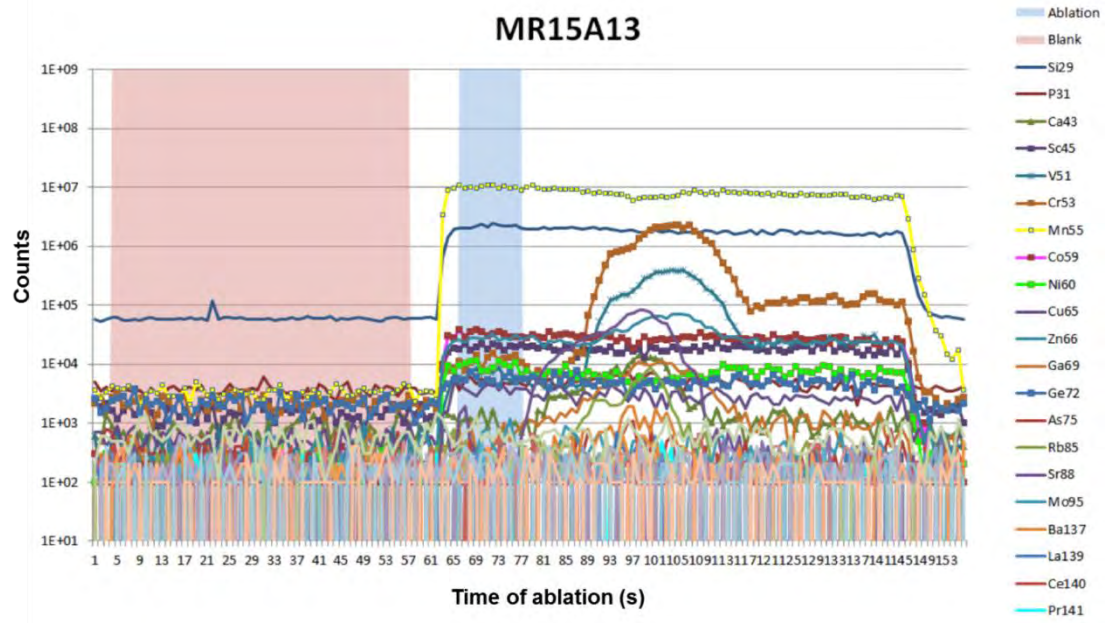

Figure 2.10. An example of a mixed analysis in inclusion A (analysis MR15A13). The laser spot was initially fired into an olivine grain, however the irregular element patterns indicate that more than one phase was sampled, perhaps an inclusion in the olivine. The area coloured blue shows the signal integration interval, i.e. the slices of ablation selected as reliable data.

Data were then processed using ExLAM (© Zacharias, 2008) software, in which element concentrations were calculated from external standard and sample ablations to provide net element intensities, which were corrected for the isotopic abundance of the measured isotope.

$$C_{an} = \frac{I_{an} \cdot C_{is}}{I_{is}} SRR_{an}$$

where C = concentration (in ppm), I = intensity (in cps), an = analyte element, is = internal standard element, SRR = standard reference ratio (Longerich et al., 1996). SRRs were calculated for each element in standards run at both the beginning and the end of each run to correct for instrument drift and the different fractionation of elements.

The limit of detection (LOD) for a given element is calculated as 3σ of the blank measurement, thus:

$$LOD = \frac{3\,\sigma\, R_{net}}{S}$$

where σ R_{net} = standard deviation of the mean background-corrected count rate on the signal in a sample that contains zero analyte, and S = normalised sensitivity (in cps/ppm) (Longerich et al., 1996). This is a 'background/noise' level, i.e. the signal from laser firing must be above this to be distinguished from blank. In many cases, the measurements of the sample were below, or close to, the detection limit. This is the result of several factors, including the grain size limitation, thus combined with low REE and trace element abundances has led to limited success in applying this technique. In the case of small grains, the laser spot size was reduced to the limit of the instrumentation (from a typical 50 μm to 20 μm), which leads to reduced counts, and the limited depth of grains frequently led to mixed analyses when a different mineral was ablated.

The analytical error is represented by the relative standard deviation (RSD) of the BCR-2g standard, and was within acceptable parameters for all elements except Zn and Ga (*Appendix 1*), thus care was taken with interpretation of these element concentrations. Absolute errors for analytes are difficult to calculate with LA-ICP-MS. Often in ore research, measurements are compared with bulk data gathered using a different technique. This was not possible with such limited available material. Ideally,

the quality and accuracy of the data would be compared with already characterised identical or analogous material that could be run in parallel with the samples in question, however, it was outside the scope of this study to pursue alternative techniques. ICP-MS by solution could be one such alternative, however this requires a minimum of approximately 20mg of material, as estimated through discussion with specialists at the NHM (Humphreys-Williams & Strekopytov, pers. comm, 2016).

2.5 The Hafnium-Tungsten isotopic system

2.5.1 Hafnium-Tungsten systematics

The short-lived ^{182}Hf-^{182}W system is used to provide insight into the mechanisms of planetary accretion, specifically the timing of metal-silicate separation (Halliday et al. (1995 and others), Kleine et al. (2002 and others). Hafnium (the parent) and tungsten (the daughter) are both notably refractory elements and should occur in chondritic proportions (Hf/W ~ 1.1) in undifferentiated early Solar System material (Kleine et al. 2004). Where differentiation occurs, the Hf-W ratio is significantly perturbed as the lithophile Hf is strongly partitioned into the silicate portion, whereas siderophile W will be preferentially partitioned into the metallic portion. ^{182}Hf decays via ^{182}Ta to ^{182}W, with a half-life of ~9 million years. If core formation leads to the fractionation of Hf and W during ^{182}Hf activity, i.e. causing an increase in Hf/W ratio, then an excess in radiogenic ^{182}W should be found in the silicate portion of a differentiated body. Similarly, early Solar System metals are deficient in ^{182}W relative to chondritic abundances, if they segregated before the decay of ^{182}Hf. Horan et al. (1998) showed that the core formation of iron meteorite parent bodies occurred within ~ 5 Ma of each other. Further work using Hf-W systematics show that core formation of parent asteroids of iron meteorites occurred prior to chondrule formation, further questioning the standard model that chondrites represent precursor material of differentiated bodies (Kleine et al., 2005; Kruijer et al., 2012).

The correct interpretation of Hf-W data is dependent on the accuracy of the initial abundance of ^{182}Hf in the Solar System, and the W isotope composition of chondritic meteorites. The initial abundance of ^{182}Hf at the start of the Solar System has been estimated at ^{182}Hf/^{180}Hf = (2.75 ± 0.24) x 10^{-4}, by Lee and Halliday (1997, 2000). Kleine et al. (2002) reported a revised value of (1.09 ± 0.09) x 10^{-4}, and this has been further refined by Kruijer et al. (2014b) at (1.018 ± 0.043) x 10^{-4}, in agreement with

comparisons of W isotopes in iron meteorites and chondrites, and internal chondrite isochrons.

Precise timing of core formation can be obtained through analysis of the Hf-W systematics of the silicate portion of differentiated bodies owing to the high Hf/W ratio. The correlation of εW and $^{182}Hf/^{184}W$ is interpreted as an internal Hf-W isochron whose slope corresponds to the initial $^{182}Hf/^{180}Hf$ ratio when the Hf-W system closed.

This method is used to investigate igneous inclusions in the Barwell meteorite. If the proto-parent body/bodies of the inclusions was differentiated prior to their ejection, the inclusions would be expected to have high radiogenic W (a positive εW) created from the decay of Hf, because the silicate portion of the parent body would be enriched in ^{182}Hf due to fractionation during differentiation, which must have occurred whilst ^{182}Hf was still active as it predates the accretion of the L chondrite parent body at ~ 2-5 Ma after CAI, similar to that of the H chondrite body (Kleine et al. 2005).

2.5.2 Methods

2.5.2.1 Sample preparation

Small pieces of the igneous inclusions found in the Barwell meteorite were separated for analysis. These fragments were observed with binocular microscope to check for any remaining host rock before being submerged in ethanol and cleaned in an ultrasonic bath for several minutes. The fragments were then dried under a heat lamp and crushed to a fine powder in an agate mortar, ensuring that any matrix present was removed. All equipment was cleaned with acetone, ethanol and/or HCl between samples to prevent cross-contamination. All further sample preparation was carried out in a clean laboratory. Samples were weighed and dissolved in Savillex® vials in 15 ml $HF\text{-}HNO_3$ (2:1) on a hotplate at 125˚C for 24 hours. In this case, triple-distilled HF (~ 5 times less W than twice-distilled HF) was used to avoid addition of any W blank during digestion since silicates have low W concentrations. A terrestrial standard, BHVO-2 (Hawaiian Basalt, U.S.G.S.) was included to ensure accuracy and reproducibility of measurements. As W is adsorbed by Savillex® Teflon, beakers were thoroughly cleaned prior to the experiment, and two blank samples were also included. For vials used in this study, W blanks were lower than 50 pg. Masses of samples, spike and aliquot are provided in Table 2.3.

sample ID	AQ01	AQ02	AQ07	AQ08	AQ12
sample name	Barwell A	Barwell B	Barwell 3 *	Barwell 4 *	Barwell 6 *
empty vial (g)	76.91487	77.09632	77.90596	75.973	77.69417
vial + sample (g)	77.04551	77.56236	78.02166	76.12905	77.95485
total sample weight (g)	0.13064	0.46604	0.1157	0.15605	0.26068
vial + solution (g)	110.3673	110.8756	111.4888	109.0978	111.112
vial + solution - aliquot (g)	107.0646	107.552	108.1892	106.0507	107.7936
spike weight (g)	0.02314	0.08017	0.01977	0.02694	0.04328
ID aliquot (g)	0.012898	0.045854	0.011368	0.014355	0.025886
nmol W in spike	0.003222	0.011163	0.002753	0.003751	0.006026
nmol Hf in spike	0.013047	0.045202	0.011147	0.015189	0.024402

Table 2.3. Sample preparation information for Hf-W analyses, detailing total masses, aliquots for isotope dilution and spike added. * denotes samples from Bridges and Hutchison (1997).

Once dried (overnight at 100˚C), 1 ml HNO_3 was added to dissolve and dry down, again at ~100˚C. This process was repeated to oxidise the sample and destroy any fluorites (e.g MgF_2 and CaF_2), which form during digestion and could potentially fractionate Hf and W. Finally, 0.5 ml 6M HCl – 0.06M HF and 0.5 ml HNO_3 was added and dried down to ensure complete conversion of fluorites. Lastly, the remaining fractions were redissolved in 30 ml 6M HCl – 0.06 HF to convert samples from nitrates to chlorides and equilibrated at 100˚C overnight. From the final solution, 10% aliquots were taken to determine Hf and W concentrations. The remaining 90% was used to determine W isotope compositions.

2.5.2.2 Chemical separation of tungsten

In order to accurately measure the W isotopic composition of the samples, W must be efficiently separated from the matrix, using a two-stage anion exchange chromatography (after Kleine et al., 2012 and Kruijer et al., 2014). The first stage involves separation of the high field strength elements (HFSE, e.g. Hf, W, Ti and Zr) from the sample matrix. Columns were pre-cleaned and conditioned as per Table 2.4, and filled with 4 ml resin (BioRad® AG1X8, 200-400 mesh). Dried samples (remaining after 10% aliquots taken) were redissolved in 75 ml 0.5 M HCl – 0.5 M HF and centrifuged to remove any remaining particulate organic matter before being loaded onto the columns in two steps. Any remaining matrix was flushed through the columns using an additional 10 ml 0.5 M HCl – 0.5 M HF. Lastly, 15 ml 6 M HCl – 1M HF was added to elute the HFSE, which were then dried at ~120˚C.

Step	Volume (ml)	Acid
Clean	CV	3 M HNO_3
Clean	CV	6 M HNO_3 - 0.2 M HF
Clean	2 x RV	H_2O
Clean	CV	6 M HCl - 1 M HF
Equilibrate	CV + 2	0.5 M HCl - 0.5 M HF
Load sample	75	0.5 M HCl - 0.5 M HF
Rinse	10	0.5 M HCl - 0.5 M HF
Elute HFSE	15	6 M HCl - 1 M HF

Table 2.4. Successive steps in the first stage of chromatography to elute HFSE from samples. CV: column volume = 18 ml, RV: resin volume = 4 ml.

Step	Volume (ml)	Acid
Clean	CV	3 M HNO_3
Clean	CV	6 M HNO_3 - 0.2 M HF
Clean	3	H_2O
Clean	CV	6 M HCl - 1 M HF
Equilibrate	5 + 5	1 M HF
Load HFSE cut	6	0.6 M HF - 0.4% H_2O_2
Rinse (Ti, Hf, Zr)	10	1 M HCl - 2% H_2O_2
Rinse	2 X RV	H_2O
Rinse	9	8 M HCl - 0.01 M HF
Rinse	0.5	6 M HCl - 1 M HF
Elute W	8.5	6 M HCl - 1 M HF

Table 2.5. Successive steps in the second stage of chromatography to elute W from HFSE. CV: column volume = 10 ml, RV: resin volume = 1 ml.

The second stage of chromatography, or 'clean-up chemistry' separates W from the HFSE. Columns were pre-cleaned and conditioned following the procedure outlined in Table 2.5, and filled with 1 ml resin (BioRad® AG1X8, 200-400 mesh). Fractions (HFSE) remaining from the first stage of chromatography were redissolved in 3.6 ml 1 M HF before H_2O and 80 µl 30% H_2O_2 were added (acid composition: 6 ml 0.6 M HF-0.4% H_2O_2), allowing 20 minutes on a hot plate at 100˚C for equilibration. High Field Strength Elements, excluding W, were rinsed from the column using 10 ml 1 M HCl –

2% H_2O_2. Water was flushed through the column to remove any remaining peroxide. Two additional rinses of 9 ml 8 M HCl – 0.01 M HF and 0.5 ml 6 M HCl – 1 M HF were used to clean and prepare the column for the final elution of W, using 8.5 ml 6 M HCl – 1 M HF. The remaining W fractions were dried at ~120˚C before being dissolved in running solution (0.56 M HNO_3–0.24 M HF) for MC-ICP-MS analysis.

2.5.2.3 Elemental concentration by isotope dilution

The concentrations of Hf and W were determined using the isotope dilution method. The 10% aliquots taken from the dissolved samples were spiked with a tracer containing known amounts of ^{180}Hf (101.44 ppb) and ^{183}W (25.474 ppb) that was calibrated against pure Hf and W metal standards (Kleine et al., 2004). Columns were pre-cleaned and conditioned as per Table 2.6, and filled with 1 ml resin (BioRad® AG1X8, 200-400 mesh).

Step	Volume (ml)	Acid
Clean	CV	3 M HNO_3
		6 M HNO_3 - 0.2 M HF
Clean	CV	H_2O
Clean	3	6 M HCl - 1 M HF
Clean	CV	0.5 M HCl - 0.5 M HF
Equilibrate	CV	1 M HCl - 0.5 M HF
Load aliquot	1.5	0.5 M HCl - 0.5 M HF
Rinse	RV	1 M HF
Rinse	5	8 M HCl - 0.01 M HF
Elute Hf	4	6 M HCl - 1 M HF
Elute W	5	

Table 2.6. Successive steps in the anion exchange chromatography to elute Hf and W from sample aliquots. CV: column volume = 10 ml, RV: resin volume = 1 ml.

Aliquots were loaded onto the columns and twice rinsed in 0.5 M HCl – 0.5 M HF before Hf and subsequently W, were eluted using concentrated HCl – HF. These cuts were then dried down before converted in a few drops of concentrated HNO_3 and H_2O_2

to destroy any remaining organics from the resin. Finally, Hf and W were then added to running solution for MC-ICP-MS analysis.

2.5.2.4 Isotopic Composition by Multicollector-Inductively Coupled Plasma Mass Spectrometer (MC-ICP-MS)

MC-ICP-MS utilises ionisation by inductively coupled plasma source with a magnetic sector analyser and multiple collectors for the measurement of ions. The sample (in solution) is introduced into the inductively coupled plasma, which removes electrons thus producing ions that are then accelerated across an electrical potential gradient and focused into a beam. Ions are then separated first by an Electro Static Analyser (ESA) and deflected by a magnetic field, based on their mass to charge ratio, given by:

$$r^2 = 2\ m\ U\ /\ q\ B^2$$

Where r = radius of ion path, m = ionic mass, U = acceleration voltage, q = ionic charge, B = magnetic field strength. Thus, ions with a low mass/charge ratio have a lower path radius and thus are more strongly deflected. These beams are then directed into the Faraday cups accordingly, and converted into voltages, which can then be compared to achieve isotope ratios. Further description of the technique is covered in Rehkämper et al. (2001).

Isotopes were measured on the ThermoScientific® Neptune *Plus* High Resolution MC-ICP-MS at the Westfälische Wilhelms-Universität Münster, following the measurement protocols described by Kruijer et al. (2014). Samples were introduced to the instrument by an ESI PFA nebuliser combined with a Cetac Aridus II® desolvator. Jet sampler and X skimmer cones were used, yielding ion beam intensities of ~ 2 x 10^{11} A at an uptake rate of ~50 µL/min for a 30 ppb W solution. Isotopes ^{178}Hf, ^{180}W, ^{181}Ta, ^{182}W, ^{183}W, ^{184}W, ^{186}W and ^{188}Os were measured simultaneously.

Each measurement consisted of 60 s baseline integrations followed by 100 isotope ratio measurements of 4.2 s each. The masses of the samples were insufficient to allow multiple measurements to increase precision. Measurements were bracketed with 200 cycle measurements of the Alfa Aesar® standard metal of varying W concentration, dependent on the W concentration of the following sample (batch no. 22312; Kleine et al., 2004).

The chemistry to separate W from the matrix is key when using MC-ICP-MS, since all elements are ionised, including doubly charges species and oxides. Thus, the only relevant interference for W isotopes comes from osmium (Os), therefore ^{188}Os is also measured by mass spectrometry, and natural ratios are used to subtract any contribution from other isotopes. Generally, this is negligible, since most Os is removed by volatilisation during dry downs in the preparatory chemistry.

2.5.3 Data analysis

An internal mass bias correction must be applied, using the exponential law by internal normalisation, to account for any fractionation occurring in the column chemistry or instrumentation, which affects ^{183}W. For this, a β factor is calculated from the difference between the natural and measured ratios of ^{186}W/^{184}W (the 6/4 ratio) or ^{186}W/^{183}W (the 6/3 ratio).

$$\beta = \ln [(^{186}W/^{184}W)_{natural} / (^{186}W/^{184}W)_{measured}] / \ln [at.wt. (^{186}W/^{184}W)]$$

Where the naturally occurring ratio of ^{186}W/^{184}W = 1.98594 (6/4) and ^{186}W/^{183}W = 0.92767 (6/3). This can then be used to calculate the corrected ratio, e.g.

$$(^{182}W/^{184}W)_{corrected} = (^{182}W/^{184}W)_{measured} \times [at.wt. (^{182}W/^{184}W)]^{\beta}$$

The data are then expressed in terms of ε^{182}W, which describes the ^{182}W composition relative to the bracketing measurements of the terrestrial standard, Alfa Aesar W, in parts per 10^4.

$$\mathbf{\varepsilon^{182}W = \{ [(^{182}W/^{184}W)_{sample} / (^{182}W/^{184}W)_{standard}] -1 \} \times 10^4}$$

The correlation of ε^{182}W and ^{180}Hf/^{184}W (determined by isotope dilution) is interpreted as an internal Hf-W isochron whose slope corresponds to the initial ^{182}Hf/^{180}Hf ratio when the Hf-W system closed.

The uncertainties (±2σ) reported for measured ε^{i}W values represent the internal standard error (2 s.e.).

2.6 Laser Fluorination: Oxygen Isotopes

2.6.1 Oxygen isotope systematics in chondrites

Oxygen isotope compositions of meteorites can constrain the evolution of planetary bodies. Variations in O isotopic composition are dominated by either heterogeneity, and thus isotopically distinct reservoirs, and physical and chemical processes causing mass-dependent fractionation. There are three oxygen isotopes, ^{16}O, ^{17}O and ^{18}O, which act as tracers of different fractionation processes in the solar nebula. Oxygen, as a light element like hydrogen, carbon and nitrogen, was abundant in the pre-solar nebula, and was predominantly present in gaseous form (including H_2, CO and N_2). Clayton et al. (1973) proposed that such elements were more prone to isotope exchange and interaction with stellar photons and cosmic rays, thus show significant variation in isotopic composition between reservoirs in the Solar System. In contrast, other common elements such as magnesium, are more uniform and do not provide the same record of Solar System formation processes. That is, their isotope compositions are close to terrestrial compositions, and small deviations are due to fractionation through evaporation, condensation, aqueous alteration and other thermal processing. Such processes fractionate isotopes according to nuclear mass. For example, ^{18}O is twice as fractionated as ^{17}O, relative to ^{16}O (Lyon and Young, 2005). Data from CAIs show that ^{17}O and ^{18}O are almost equally fractionated, which indicates that another process must be involved.

The terrestrial fractionation line (TFL) has slope of 0.52, i.e. the ratio of $^{17}O/^{16}O$ to $^{18}O/^{16}O$ is 0.52, indicating the variation in O isotopes is a result of mass-dependent fractionation from a single homogeneous source. This slope is an average of many chemical and physical processes, each with a slightly different slope that is well understood from fundamental physics, and dependent on the differences in mass between the three isotopes. Figure 2.10. shows a schematic of the effect of different processes on the plot. Oxygen isotopic compositions are conventionally expressed in δ units, representing deviations in parts per thousand (per mil, ‰) in the $^{17}O/^{16}O$ and $^{18}O/^{16}O$ ratios from Standard Mean Ocean Water (SMOW) with $^{17}O/^{16}O$ = 0.0003829 and $^{18}O/^{16}O$ = 0.0020052 (McKeegan and Leshin, 2001).

$$\delta^{18}O = \left[\frac{(O^{18}/O^{16})_{\text{sample}}}{(O^{18}/O^{16})_{\text{SMOW}}} - 1\right] x1000$$

$$\delta^{17}O = \left[\frac{(O^{17}/O^{16})_{sample}}{(O^{17}/O^{16})_{SMOW}} - 1\right] x1000$$

Figure 2.11 shows the fields in which different meteorite groups fall on a three oxygen isotope plot. Primitive meteoritic materials plot nearer a line of ^{16}O addition. This deviation in O isotopic composition from the TFL could be a result of pre-existing isotopic heterogeneity in the material that condensed to form the protoplanetary disk, and/or mass independent fractionation processes in the early Solar System. The $\delta^{17}O$ values for ordinary chondrites are significantly higher than both other extraterrestrial material and the TFL. Bulk O isotopes for the ordinary chondrites show similar but still resolvable fields for the H/L/LL groupings (Clayton et al., 1991). Most extraterrestrial materials do not plot on the TFL, with the exception of some enstatite meteorites, and lunar rocks. Indeed this is part of the mounting evidence that the Moon was once part of the Earth. Samples from other planetary bodies that have experienced widespread melting and differentiation, such as Martian meteorites or the HED suite, similarly display narrow ranges of O isotope compositions, plotting on lines parallel to the TFL, indicative of mass dependent isotopic fractionation (e.g. Greenwood et al., 2014). The fields for carbonaceous chondrite groups are much larger than the range of points for ordinary chondrites, due to the effect of low-temperature aqueous alteration and the resultant phyllosilicates (which are enriched in heavier O isotopes).

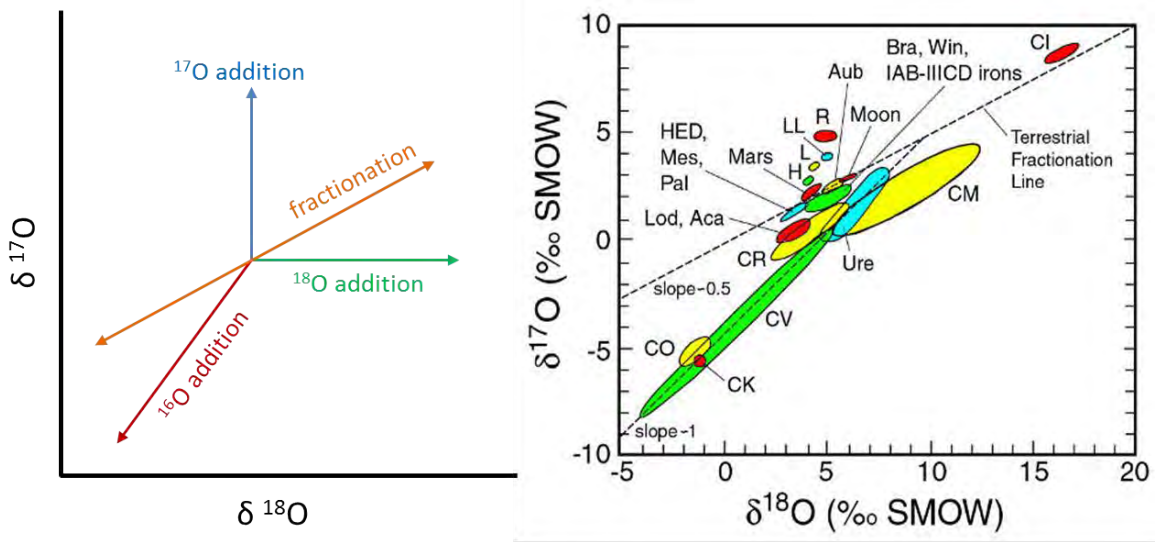

Figure 2.11. Left: A schematic diagram showing the effect of various isotopic processes on the three isotope plot (after Clayton et al. 1991); Right: a three-isotope plot of extraterrestrial material indicating the diagnostic fields for different meteorite groups (from Wittke, 2008)

Measuring the oxygen isotopes of igneous inclusions in the Barwell meteorite can provide insight into the origin of the material, indicating whether they are from the Barwell parent body, or, like the original “Pebble” described by Hutchison et al. (1988),

share an oxygen isotopic composition with material from other bodies. Should the clasts show a similar oxygen isotopic composition to the bulk Barwell material, this data will provide insight into the local differentiation occurring on the parent body. Conversely, should the oxygen isotopic composition indicate a different origin for the clasts, the study will be highlighting mixing in the early Solar System, and provide insight on an early generation of achondrites.

2.6.2 Instrumentation

Oxygen isotope analysis was carried out by R. Greenwood at the Open University, Milton Keynes, using a laser fluorination system (Miller et al. 1999; Greenwood et al., 2016). Laser fluorination is capable of the highest precision measurements of oxygen isotopes currently available, measuring 0.5 to 2 mg samples with a precision of ±0.08 ‰ for $\delta^{17}O$, ±0.16 ‰ for $\delta^{18}O$, and ±0.05 ‰ for $\Delta^{17}O$ (Valley and Kita, 2005; Greenwood et al., 2014, Starkey et al., 2016).

The fluorination system comprises four principle components: an IR or near-IR laser and beam delivery system, a sample chamber, a sample gas clean-up line and a Thermo Fisher MAT 253 isotope ratio mass spectrometer. Detailed discussions of the method and instrumentation at the Open University are provided by Miller et al. (1999) and Greenwood et al. (2016). In brief, samples of the bulk Barwell chondrite and individual inclusions were separated and powdered to provide bulk measurements. Samples are placed in a vacuum chamber, 200 mbar BrF_5 is introduced, and infrared radiation from a 25 W CO_2 laser (10.6 μm, 12-50 W max. power output) heats the powder allowing oxygen to be released. After purification or 'clean-up' via a series of liquid nitrogen "U" tube traps, the oxygen is passed through 13X molecular sieve pellets and introduced into a mass spectrometer for individual isotope analyses.

2.6.3 Data analysis

Isotope measurements are used to derive values for $\delta^{17}O$ and $\delta^{18}O$ (defined in 2.6.1.). The diagram of $\Delta^{17}O$‰ against ^{18}O‰ is used to represent the variation in the isotopic composition irrespective of the fractionation trend. Deviations from the TFL are commonly expressed as:

$$\Delta^{17}O_{SMOW} = \delta^{17}O_{SMOW} - 0.52 \times \delta^{18}O_{SMOW}$$

System precision (2σ) values in this study are $\delta^{17}O$, $\delta^{18}O$ and $\Delta^{17}O$ is ±0.05‰, ±0.09‰, and ±0.02‰, respectively.

2.7 Anisotropy of Magnetic Susceptibility

2.7.1 Theory

Magnetic susceptibility, χ, is the derivative of the intensity of magnetisation induced in a sample with respect to the applied field (Gattacecca et al. 2005). It indicates how strongly a body is magnetised when in the presence of a magnetic field, which is described by:

$$\boldsymbol{M} = \chi \boldsymbol{B}$$

Where M is the magnetic response, χ is the magnetic susceptibility and B is the imposed field. Thus, the susceptibility is a first-order index of the quantity of ferromagnetic minerals within a specimen (e.g. Rochette et al., 2010). Anisotropy of magnetic susceptibility (AMS) has been demonstrated as a reliable proxy for the presence of foliation and lineation in chondrites by the preferred orientation of minerals with a high magnetic susceptibility (e.g. Gattacceca et al., 2005). In ordinary chondrites, the only significant ferromagnetic material is iron nickel metal.

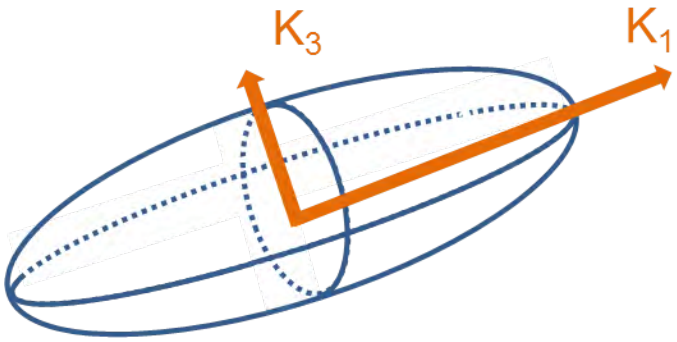

Figure 2.12. A schematic diagram of the magnetic susceptibility ellipsoid indicating the k1 and k3 measurements that define the grain orientation.

The technique involves measuring the magnetic susceptibility along three axes, which allows for the reconstruction of the susceptibility ellipsoid, where $K_1 \geq K_2 \geq K_3$, whose axes correspond to the geometry of the rock fabric. For an anisotropic sample, i.e. an ellipsoid, susceptibility can be visualised as in Figure 2.12. On the application of a magnetic field, the intensity of magnetisation varies with the volume of magnetic components along the direction of the magnetic field. This volume is determined by the preferred orientation of anisotropic ferromagnetic grains, but also by the distribution of

the ferromagnetic material. For example, equant grains of metal arranged preferentially on a plane would elicit a similar foliation. Additionally, measurements of AMS can be used to quantify the intensity of a rock fabric.

Gattacceca et al. (2005) showed that AMS is consistent over a given meteorite through measurements of 22 samples, ranging from <1 g to 50 g, of the Knyahinya L/LL5 chondrite and thus can be considered an intrinsic physical property. That is, foliation and lineation are considered coherent across a given chondrite. The ongoing survey of AMS in chondrites by the Centre de Recherche et d'Enseignement de Géosciences de l'Environnement (CEREGE) group shows that magnetic anisotropy is considerably higher in L chondrites than in terrestrial rocks, and the susceptibility ellipsoid is generally oblate, showing a planar fabric which is consistent with the formation of a foliation by uniaxial compression and compaction (e.g. Rochette et al., 2003; Rochette et al., 2008; Gattacceca et al., 2007; Gattacceca et al. 2005 and references therein).

2.7.2 Instrumentation

AMS analyses were carried out on 17 L chondrite and 11 H chondrite samples, using the MFK1 Agico instrument (low field of 378 μT and frequency of 920 Hz) at CEREGE in Aix-en-Provence, France. The method follows that described by Gattaccecca et al. (2005). The instrument is first calibrated with a standard, before a measurement is collected with only an empty sample holder to account for diamagnetism of the plastic. This value is generally around ~10^{-6}, i.e. so low that the effect would be negligible. Nevertheless, this 'blank' is taken into account for the sample measurements. The ambient temperature of the room is kept constant to prevent any effect on measurements.

The sample is placed in a cubic holder, labelled to ensure each position is measured in turn. The instrument is automated to measure anisotropy across 360° in each position. The sample in the holder is then manually rotated by the user, as per the schematic in Figure 2.13. This instrumentation is specifically accurate because only the deviation from the isotropic ideal is measured in each position, with the total susceptibility, i.e. representing the radius of the isotropic sphere, is measured last.

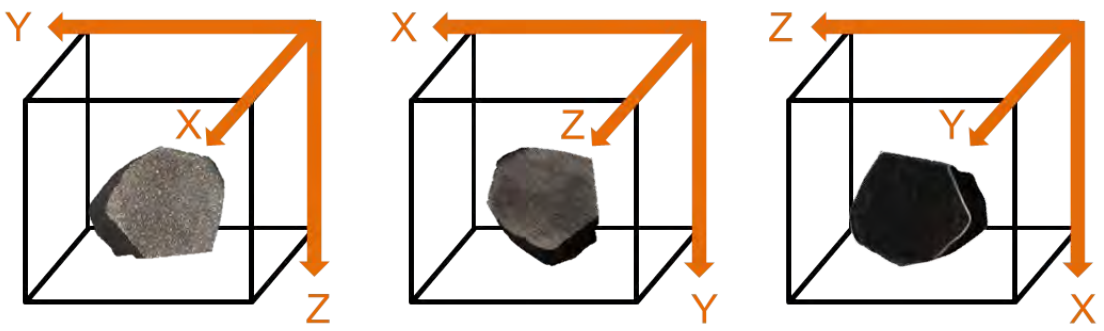

Figure 2.13. A schematic diagram of the three positions of the sample for AMS measurements.

Sources of error in low field susceptibility are outlined in Rochette et al. (2001). Fusion crust has been demonstrated to have a negligible effects for samples with volume > 1 cm^3, where log χ is > 3.5, including all samples in this study. Models indicate that the error in mean log χ is as high as ± 0.1 when measuring along one direction, therefore in this study, χ was averaged from measurements along three perpendicular axes. The uncertainty on the measurements of magnetic susceptibility is ± 5^{-13} m^3 (1σ).

2.7.3 Data analysis

Data are output in tables of volume susceptibility (which is unitless and must be converted into mass magnetic susceptibility, χ, and parameters describing the susceptibility ellipsoid: degree of anisotropy (P), shape parameter (T), and orientation (declination and inclination) for each axis (k1, k2 and k3), as defined below. To describe the fabric of the rock, the magnetic foliation (F) of the sample is defined by the $K_1 \geq K_2$ plane, and the lineation direction (L) is given by the K_1 axis orientation. The shape parameter ranges from +1 for an oblate ellipsoid (well-developed foliation) to -1 for a prolate ellipsoid (well-developed lineation) (Jelinek, 1981). The declination and inclination of major axes are plot onto stereonet projections to allow visual inspection of orientations and comparison with other data sets.

$$\chi = \frac{Kmean\ x\ 10^{-11}}{sample\ mass\ in\ kg}$$

$$P = \frac{k1}{k3}$$

$$T = \frac{(2\ln k2 - \ln k1 - \ln k3)}{\ln k1 - \ln k3}$$

$$F = \frac{k2}{k3}$$

$$L = \frac{k1}{k2}$$

Flat, cut surfaces on small samples may have an effect on the AMS measurements. This is relevant for L chondrites Jackalsfontein, Crumlin, Jhung. Gattacceca et al. (2005) showed that the effect is noticeable on AMS measurements of L chondrite polished sections, however in the case of the morphology of the samples in this study, it will not be a considerable effect (Gattacecca, pers. comm., 2016).

In the case of H chondrites, with an average susceptibility around 0.6 due to greater metal content, the shape of the sample can have a significant effect, therefore isotropic shapes are preferable. In this study, which has focused on non-destructive methodology, this has not been possible. For samples deviating considerably from an isotropic shape, the results must be interpreted in light of this effect.

With L chondrites, the amount of metal present, i.e. their magnetic susceptibility, is sufficiently low that the shape anisotropy is not a factor for samples with an aspect ratio < 5. Furthermore, metal in L chondrites is dominantly kamacite and taenite, which have body-centred cubic and face-centred cubic structures respectively, and are therefore isotropic. This means that the effect of grain shape is dominant over the magnetocrystalline effect. In contrast, tetrataenite, which has a tetragonal structure, is highly anisotropic and its presence has a considerable effect on the AMS measurements. Gattacecca et al. (2005) found that data for L chondrite finds are inconsistent and do not show the correlation between AMS and shock stage seen in data for L chondrite falls. This is attributed to the sensitivity of AMS in metal-bearing meteorites to weathering. In this study, only falls are considered, therefore the effects of weathering are considered minimal. However, it must be recognised that weathering is not completely negated in falls. They may have experienced alteration since their arrival on Earth - either by late collection, poor handling or environmental conditions.

2.8 Helium Pycnometry

2.8.1 Theory

Pycnometry provides a measure of the porosity in a sample without requiring saturation with water, by measuring the grain volume, i.e. the volume of solid material, or the volume in the chamber from which the gas is excluded. Helium is used because it is inert and has the smallest atomic radius of any element, thus can penetrate very fine cracks and small voids. This method, using gas as a displacement medium, is possible due to the ideal gas law:

$$\boldsymbol{P\,V\ =\ n\,R\,T}$$

Where P = pressure of the gas, V = the volume of the gas, n = number of moles of gas, R = gas constant (8.31447 J K^{-1} mol^{-1}) and T = temperature of the gas. In the technique, the temperature and quantity of gas are kept constant, thus the pressure and volume vary together, i.e. PV = constant. This can be written as:

$$\boldsymbol{P_1V_1\ =\ P_2V_2}$$

Or, in the case of a chamber whose volume changes from V_1 to V_2, on the addition of a sample with volume V_s, the volume occupied by the gas is first V_1-V_s and second V_2-V_s, and the equation can be rewritten and rearranged thus:

$$\boldsymbol{P_1\,(V_1 - V_s)\ =\ P_2\,(V_2 - V_s)}$$

$$\boldsymbol{V_s = \frac{(P_1V_1 - P_2V_2)}{P_1 - P_2}}$$

2.8.2 Instrumentation

Pycnometry was carried out using a Quantachrome He stereopycnometer at CEREGE in Aix-en-Provence, France. The instrument consists of two chambers, one which holds the sample, and thus has a gas-tight lid, and the second with a fixed, known volume. A valve between the two chambers is used to control the connection, as per Figure 2.14. Once the sample is placed in the cell, both sample chamber (cell) and reference chamber, are filled with helium. The valve is closed and helium is pumped into cell with

an overpressure. The valve is opened and pressure equilibrates over both chambers, then the final pressure is measured.

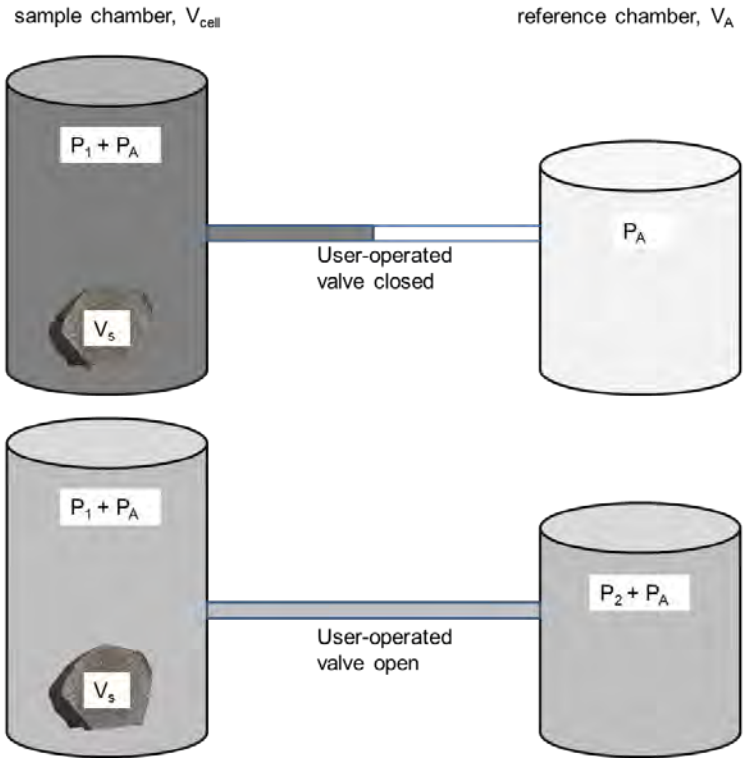

Figure 2.14. A schematic diagram of the two states of the pycnometry instrument. Top: the valve is closed and the chambers are separate. Bottom: the valve is opened and the gas expands to fill both chambers thus the pressure drops and is measured by a transducer attached to the chamber.

Both V_{cell} and V_a must be known precisely. These are measured directly and precisely using calibration spheres. The grain density gradually decreases as helium penetrates the sample. For this reason, multiple measurements are collected, which gradually reach equilibrium. The mean value for the latter analyses (after stabilisation) is then taken. In some circumstances, this was not the case. This was either due to small sample size or to disturbances (e.g. the opening and closing of doors in the room where the analyses were carried out). Figure 2.15 shows two examples of subsequent analyses for Aumale (ideal example, where data were accepted) and Elenovka (poor example, where data were rejected).

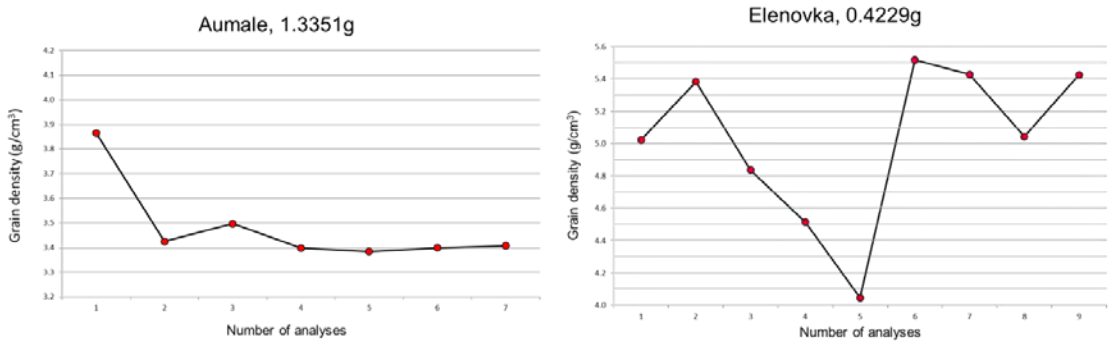

Figure 2.15. Two graphs of grain density measurements using He pycnometry. Left: Aumale – grain density stabilised with increasing number of measurements – data accepted. Right: Elenovka – grain density chaotic with increasing number of measurements – data rejected.

2.8.3 Data analysis

The raw data provided are the initial and final pressures, P1 and P2. Rearranging the ideal gas law given in 2.8.1, the sample volume can be found from:

$$\boldsymbol{V_s = V_{cell} - V_A\left(\frac{P_2}{(P_1 - P_2)}\right)}$$

Once the grain volume is known, the grain density and porosity of the sample can then be calculated, thus:

$$\boldsymbol{\rho_{bulk} = \frac{m}{V_{bulk}}}$$

$$\boldsymbol{\varphi = \left(1 - \left(\frac{V_{grain}}{V_{bulk}}\right)\right) x\ 100}$$

$$\boldsymbol{\varphi = \left(1 - \left(\frac{\rho_{grain}}{\rho_{bulk}}\right)\right) x\ 100}$$

Where ρ_{bulk} = bulk density, ρ_{grain} = grain density, m = mass of the sample, V_{bulk} = bulk volume, V_{grain} = grain volume, and φ = porosity (in %).

The technique requires accurate measurement of both the bulk volume, and the mass of the sample. In this case, the first is provided by segmentation of the sample in the XCT data, and the second, is by weighing with high-precision scales.

2.9 Assessing shock stage with optical microscopy

Shock metamorphism of meteorites is evident in either deformation (such as fracturing, plastic deformation, mosaicism, and twinning), or transformation (such as production of high pressure polymorphs, shock melting to produce melt veins and pockets, and formation of diaplectic glass). High-pressure minerals can form both from solid-state transformation of minerals in the meteorite, or through crystallisation of melted silicates in veins and pockets.

Thin-section optical microscopy is a primary technique to assign shock stage to meteorite samples. Stöffler et al (1991) outlined the features that indicate the shock pressure experienced by a sample.

Shock effects in meteorites and terrestrial rocks have been discussed at length in the literature (e.g. Chao, 1967, 1968; Heymann, 1967; Kieffer, 1971; Scott et al., 1992; Stöffler, 1972, 1974; Stöffler et al., 1991; Ashworth, 1985; Bischoff and Stöffler, 1992; Leroux, 2001; and many more). Table 2.7 provides an overview of the features observed in silicate minerals of ordinary chondrites with increasing shock pressures, according to the Stöffler et al. (1991) scheme of classification. This is the basis for which ~ 50 grains of varying sizes in thin sections of the different ordinary chondrite meteorites were classified. Shock stage was then assigned according to the dominant classification across those grains.

Shock Stage	Effect from equilibrium peak shock pressure (olivine)	Effect from equilibrium peak shock pressure (plagioclase)	Effect from local P-T excursions	Shock pressure (GPa)	Post-shock T increase (°C)	Olivine criteria used by Ruzicka et al. (2015)
S1 (unshocked)	Sharp optical extinction, irregular fractures	Sharp optical extinction, irregular fractures	None	<4-5	10-20	< 2° misorientation
S2 (very weakly shocked)	Undulatory extinction, irregular fractures	Undulatory extinction, irregular fractures	None	5-10	20-50	2-3° misorientation
S3 (weakly shocked)	Planar fractures, undulatory extinction, irregular fractures	Undulatory extinction	Opaque shock veins, incipient formation of melt pockets, sometimes interconnected	15-20	100-150	2-3° misorientation + at least one set of parallel planar fractures
S4 (moderately shocked)	Mosaicism (weak), planar fractures	Undulatory extinction, partially isotropic, planar deformation features	Melt pockets interconnecting melt veins, opaque shock veins	30-35	250-350	3-5° misorientation ≥ two sets of parallel planar fractures
S5 (strongly shocked)	Mosaicism (strong), planar fractures + planar deformation features	Maskelynite	Pervasive formation of melt pockets, veins and dykes; opaque shock veins	45-55	600-850	> 5° misorientation ≥ three sets of parallel planar fractures
S6 (very strongly shocked)	Solid state recrystallisation and straining, ringwoodite, melting	Shocked melted (normal glass)	Pervasive formation of melt pockets, veins and dykes; opaque shock veins	75-90	1500-1750	Recrystallised

Table 2.7. Crystallographic and textural changes in plagioclase and olivine with progressive shock (after Stöffler et al., 1991) and Ruzicka et al. (2015).

3 Three-Dimensional Structure of Ordinary Chondrites

This study explores the use of XCT data for describing and quantitatively measuring the 3D shape and distribution of meteoritic components, specifically porosity and iron-nickel metal, in ordinary chondrites. Complementary techniques, including anisotropy of magnetic susceptibility and gas pycnometry, are used to further clarify the relationship of these phases to the levels of thermal and shock metamorphism, to compare the accuracy of the different methods, and to explore their usefulness in conjunction with one another.

3.1 Porosity and metal distribution in ordinary chondrites

3.1.1 Porosity and density of ordinary chondrites

Meteorites act as ground truth for our understanding of asteroid structure as well as composition, thus it is crucial to measure their density and porosity accurately. These characteristics can be used in the modelling of impact-related phenomena, as the volume and structure of porosity is important when considering parent body processing, e.g. shock propagation, impact-related heating and thermal diffusion (Friedrich et al., 2008). Some robotic and satellite co-orbital observations have been used to infer asteroid density (Britt et al., 2002). However, laboratory analysis of meteorites places constraints on their structure, as well as providing insight into the nature of precursor materials and processes experience since induration. Furthermore, understanding the porosity of meteorite specimens can give indications of their permeability and the potential for aqueous alteration on the parent body. Similarly, determining the timescale of porosity reduction and changes in bulk density is important for understanding the efficiency of thermal processing owing to its effect on a material's conductivity. Britt, Consolmagno and Macke dominate the field of meteorite porosity, regularly updating and improving techniques

for better accuracy in measuring bulk volume, density and porosity, as well as having produced key reviews of the data (e.g. Britt & Consolmagno, 2003).

Porosity in ordinary chondrites can be used to infer characteristics of the parent body (e.g. Fujiwara et al. 2006). However, remote observations of asteroids usually indicate higher porosities than those measured in meteoritic material thought to originate from such bodies (Britt et al., 2002). Jutzi et al. (2008, 2010) provided a detailed view on how porosity structure affects the impact kinetics of asteroidal material. In many cases, asteroidal mass is too low for the observed volume, i.e. there is a significant discrepancy between ordinary chondrite microporosity and asteroidal densities. The 'rubble pile' model of asteroidal structure accounts for this by suggesting that 20-40 % of asteroidal volume is macroporosity voids (Britt et al., 2003). The extent of rubble piles will depend on the petrological grade and compaction history of the material – which then dictates the densities of the agglomerated material. The process of impact on asteroids has many effects, including seismic shaking and fragmentation of constituents (e.g. chondrules) as well as a flow of granular material. It is also probable that meteoritical collections on Earth are subject to an inherent bias because more friable, porous meteorites are unlikely to survive ejection from the parent asteroid, as well as terrestrial entry and landing.

Porosity refers to voids and cracks in a rock, causing the density of the sample to be different from a theoretical value based on its bulk chemical composition. After forming from the accretion of millimetre-size chondrules, metal grains and refractory inclusions and micron-size dust particles, the early solid bodies of the Solar System were likely to have been highly porous (Cuzzi et al., 2008). The considerably higher bulk density of meteorites suggests a process of compaction. Hypotheses include slow gravitiational compaction (e.g. Yomogida and Matsui, 1984), and/or shock compaction through collision (e.g. Consolmagno et al., 2003; Bland et al. 2014). Several other factors may also be important, such as incomplete compaction of crystals and disruption of the fabric through shock or thermal effects (Consolmagno et al., 2008). The location of porosity, i.e. as voids between grains, cracks or microcracks, provides insight into the compaction process. For example, numerical simulations suggest that a shock wave causes anisotropic compaction whereby incomplete compaction occurs on the lee side of chondrules (Davison et al., 2016). The movement of shock waves through a rock medium, causing compression followed by decompression, is thought to be the source of networks of microcracks in ordinary chondrites (Consolmagno et al. 2008, DeCarli et

et al., 2001).

The origin of porosity in meteorites is still not fully understood, but further characterising porosity can add to our understanding of how meteoritic material lithified from the dust of the early Solar System into solid rock. On Earth, rock formation occurs through igneous processes, by sedimentation, by metamorphism, with temperature, pressure and water being the key agents. This is not so clear-cut for chondritic material, much of which has not experienced these agents to the degree necessary to account for their lithification. Therefore, both shock lithification and the gravitational influence of Jupiter in perturbing planetesimals are considered key (Consolmagno et al., 2003). It is unlikely that lithostatic overburden caused the removal of porosity in ordinary chondrites as they originate in parent bodies no more than a few hundreds of kilometres in diameter (McSween et al., 2002). Monnereau et al. (2013) suggested a diameter of 260 km for the H chondrite body, whose centre would have experienced a maximum pressure of ~8 MPa. Sintering, or the compaction and coalescence of material by heat and/or pressure below the melting temperature, is a potential source of porosity reduction. Sintering on asteroids is thought to occur by pressing (either 'cold' at T ≤ 700 K or 'hot' at higher temperatures) of initially porous material as it was heated by the decay of radioactive nuclei. Henke et al. (2012) modelled the effect of sintering to constrain the thermal evolution of the H chondrite parent body, finding that sintering compacted the body and predicting burial depths for Kernouvé (H6) and Richardton (H5) in agreement with their previously constrained cooling histories. Friedrich et al. (2013) have since shown, based on both metal grain and porosity analysis, that Kernouvé experienced both thermal and considerable shock metamorphism leading to metal vein formation.

Porosity provides insight into the physical history of the parent body. Generally, ordinary chondrites have similar porosities, and are thus thought to have undergone similar processes. However, the absence of direct evidence on the nature of porosity prior to any parent body processing constitutes an obstacle. Sasso et al. (2009) proposed that incompletely compacted ordinary chondrites represent primordial material accreted with high microporosity, or that these materials originated as a regolith upon the parent body and were later indurated. This second scenario is similar to that put forward by Wilkison et al. (2003). Experimental and modelled predictions of accretionary materials have estimated post-accretionary, pre-metamorphic porosities ranging from 35-40% to over 85% (Friedrich et al., 2014). Yomogida and Matsui (1984) described several processes

during planetesimal growth including mild static pressure, granular movement and low velocity impact, to estimate a post-accretionary porosity of ~40%. With little to no reduction by burial or thermal metamorphism, it is widely accepted that shock processing is the primary mechanism for the decrease of porosity in chondritic meteorites. Nakamura et al. (2000) carried out experimental shocking of Allende (CV3) and found that an impact of 20 GPa can reduce porosity from 26% to 14% via compression leading to pore collapse. If the experiment is carried out on a heated sample, the effect was significant - at 600°C, the porosity reduced from 20% to just 6%. Thermal metamorphism of ordinary chondrites reached a maximum temperature of ~1175 K, only just below the melting point for a eutectic mixture of metal and sulphide (McSween et al. 1988), thus it is conceivable that shock events on ordinary chondrite asteroids were not cold.

Hirata et al. (1998, 2008) carried out similar experiments on ordinary chondrite analogue material – powders with porosities between 30-35% – and showed that, at room temperature, they retained porosity of ~ 10% with shock pressures of ≤ 5 GPa and had their porosity reduced to < 5% after exposure to shock at 22 GPa. However, the grain sizes (5-100 μm) are considerably smaller than typical ordinary chondrites. Friedrich et al. (2014) used these experiments to conclude that high porosity, incompletely compacted chondrites (e.g. Miller with 20% porosity) experienced an upper limit of 5-10 GPa for a single impact.

Multiscale modelling of impact compaction of chondrite-like material indicates that there is a wide range of temperatures induced. An impact velocity of 1.5 kms^{-1} was shown to be capable of causing variations in pressure and temperature of >10 GPa and >1000 K over ~100 μm. In this situation, the matrix experiences considerable heating and compression, versus the solid chondrules, which are relatively unscathed, acting as heat-sinks (Bland et al., 2014). Indeed, the pre-shock porosity dictates the thermal conductivity. As a shock wave passes through a porous material, extra pressure-volume work is expended to reduce the pore space. When released from the shock wave, this work transfers energy to the surroundings as ‘waste heat’, therefore porous materials reach higher temperatures than non-porous materials undergoing the same shock event. Low-velocity collisions are likely a significant mechanism causing the loss of porosity and lithification of chondrite parent bodies, especially source regions of meteorites with lower petrological grades (type 3-4) where gravitational compaction acts inefficiently (Bland et al. 2014). Gravitational compaction is most efficient in the cores of parent bodies, however impact compaction is most efficient at the surface.

Gravitational compaction is only efficient for small grain sizes (~1 μm) and at high temperatures (>800 K) a different mechanism may be required to explain lithification of parent bodies of meteorites that are unmetamorphosed, such as the carbonaceous chondrites, or dominated by mm-scale chondrules, such as the L chondrites.

Intragranular porosity, e.g. within chondrules, is likely nebular in origin and results from: i) shrinkage of an inner part of the chondrule during cooling, ii) trapping of gas when a chondrule formed from heating of a dust ball, iii) vapour pressure of a volatile element in the chondrules exceeding the nebula pressure, creating a bubble (Tsuchiyama et al., 1997). This porosity is also seen in CT data collected by these authors, who described the pores found in Allende (CV) and Moorabie (L3) as irregular in shape and similar to formation by visco-elastic fingering, and infer that this is a result of the first method – shrinkage due to cooling.

3.1.2 Measuring porosity in ordinary chondrites

There are several standard methods for measuring porosity. Bulk densities of meteorites have been measured using glass beads (approximately 40 μm in diameter), which are chemically inert and leave no residue on the sample. The grain volume can then be found using ideal gas pycnometry (e.g. Macke, 2010). Differences between the average, measured and model porosities arise from either significant heterogeneity in the sample or the need to improve accuracy in these measurements (Britt and Consolmagno, 2003).

In ordinary chondrites, petrological grade appears to have no correlation with porosity. Consolmagno et al. (2008) stated that any porosity-forming events must be subsequent to, and independent of, metamorphism. Nevertheless, there are trends in the data. The grain densities of ordinary chondrites that are fresh falls follow iron content, i.e. H chondrites are more dense than L, which in turn are more dense than LL (Figure 3.1). This is seen in the data of Britt & Consolmagno (2008) in Table 3.1. Consolmagno et al. (2008) found that grain density alone can be used to determine the type (for H and L but not between L and LL as there is an overlap). Generally, H chondrites (model porosity 10.6 ± 4.8 %) tend to be more porous than L chondrites (model porosity 6.9 ± 0.6 %).

Consolmagno et al. (2008) quoted values for average porosity of ordinary chondrite falls at 7.4 ± 5.3 %. The average porosity for OC finds is 4.4 ± 5.1 %, but ranges from fall-like porosities down to zero. This is consistent with weathering studies, whereby metallic grains react with terrestrial oxygen creating oxides, such as goethite, which are about half as dense as the original metal grains and thus expand into pore spaces (Bland et al., 1996). Once the voids are entirely filled, and the grain volume is equal to the bulk volume, weathering can only occur when water and oxygen reach remaining metal by diffusing through minerals (Consolmagno et al., 2008).

	Average	±	Minimum	Maximum	unit
H chondrites					
Based on 265 pieces of 157 meteorites (14.17 kg total reported mass)					
Grain density	3.64	0.12	3.23	3.84	g / cm^3
Bulk density	3.4	0.18	2.8	3.8	g / cm^3
Measured porosity	6.0	4.5	-1.0	18.1	%
Model porosity	10.6	4.8	-0.1	27.2	%
Average porosity	6.4	4.2	-1.0	16.7	%
L chondrites					
Based on 277 pieces of 160 meteorites (20.24 kg total reported mass)					
Grain density	3.51	0.11	3.26	3.75	g / cm^3
Bulk density	3.35	0.16	2.5	3.96	g / cm^3
Measured porosity	5.8	4.7	0.0	19.5	%
Model porosity	6.9	4.6	9.9	30.7	%
Average porosity	4.5	4.6	0.8	19.5	%
LL chondrites					
Based on 149 pieces of 39 meteorites (7.22 kg total reported mass)					
Grain density	3.48	0.08	3.38	3.69	g / cm^3
Bulk density	3.21	0.22	2.38	3.49	g / cm^3
Measured porosity	9.3	8.5	1.0	32.6	%
Model porosity	10.0	6.3	2.1	33.1	%
Average porosity	7.9	4.2	1.6	14.8	%

Table 3.1. Overview of ordinary chondrite porosity with data from Britt & Consolmagno (2003). Reported errors represent 1σ spread among the averages.

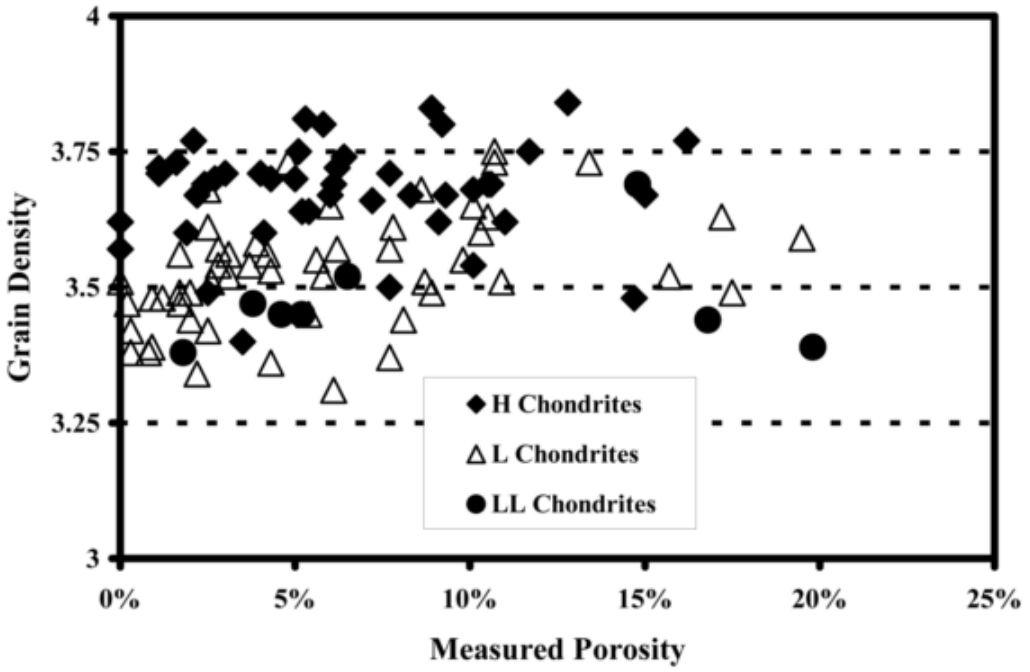

Figure 3.1. Grain density and measured porosity of ordinary chondrites (Britt & Consolmagno, 2003) showing the scatter and overlapping of the groups.

Digital imaging techniques are increasingly being employed for the direct measurement of porosity, such as point-counting of voids in SEM backscatter images. Strait (2011) compared the measurement of porosity by SEM imaging, glass bead/pycnometry, and XCT, finding that the three techniques do not agree well in samples with porosity < 5% but show better agreement in samples of porosity > 10%. Strait (2011) commented that the use of multiple methods is required to evaluate porosity, finding that the pycnometry method is best for reliable whole rock numerical measurements, and CT imaging for visualisation. However, issues were noted in variation across the greyscale range between slices in a single stack, limiting the quality of their CT data. The resolution of the scans were not reported, which could have a considerable effect on the accuracy of their porosity measurement.

3.1.3 Previous studies of porosity using XCT

Ketcham and Iturrino (2005) explored the use of CT in the visualisation of effective porosity. In order to do so, samples were first scanned “dry” (having been dried in a 38°C oven for one day), and then “wet”, i.e. with pore space replaced by a fluid. The concept being that the any voxel containing pore space will have a greyscale value that represents the weighted average of both the air and the solid present. Once the sample

is saturated with a fluid, replacing the pore space, the same voxel should have a higher value due to the greater attenuation of the fluid versus air. The difference between the two values will be proportional to the amount of pore space in the voxel. Whilst this study clearly showed the application of XCT in quantifying porosity, permeability and anisotropy, the methods are invasive and samples thus treated cannot be used for any future investigations.

An increasing number of studies have used the quantitative potential of XCT data to investigate porosity in extraterrestrial samples. Porosity was measured by Russell & Howard (2013), both by selecting threshold values for pore space and comparing to bulk CAI voxels (result 6%), and by point counting random stacks (result ~ 30%). The low figure for the voxel comparison method is attributed to high noise levels in the dataset arising from the low X-ray flux of the technique. Friedrich and Rivers (2013) focused on locating the porosity in ordinary chondrites of variable compaction and shock, carrying out 3D imaging of samples with variable impact histories to visualise microporosity at 2.6 μm resolution. This porosity is present in the form of microcracks and voids between mineral grains. The authors suggested that as much as 5-7% porosity can be reintroduced by microcracking due to impact on the parent body. In the most compacted specimens, porosity is present as sheet-like fractures within brittle silicates, and discrete voids associated with grain boundaries. Bietz et al. (2013) used tomography to measure the porosity of dust rims around chondrules. Dust was accreted onto hot chondrule analogues while levitated in a gas flow to study conditions of dust rim formation. They measured ~60 vol% which is considerably higher than measured porosities of rims around chondrules in Murchison (~10%) which indicates that the rims were compacted.

Benedix et al. (2003) used CT to elucidate the distribution of vesicles and metal/sulphide in the ordinary chondrite PAT 91501. Few ordinary chondrite impact melts have been reported to contain vesicles. This study found that larger vesicles are associated with larger metal/sulphide melt assemblages, indicating that the vesicle-forming gas was SO_2 resulting from the vaporisation of FeS during melting of metal and sulphide. Using a starting abundance of troilite in L chondrites of 4% and an estimation of <1% troilite in the sample from the CT scan, the authors calculated a density of SO_2 as ~3200 kg/m^3. They inferred the pressure at which the bubbles formed and found that vesicular basalts are not formed through impact, but rather can provide insight into asteroidal igneous processes. Quantification of vesicle size distributions in the Ibitira basalt have also been conducted by McCoy et al. (2006) to infer asteroidal formation

conditions. Such methodologies have direct applications to analyses of vesicular basalts in the Apollo suite.

Sasso et al. (2009) exploited CT to derive the size-volume characteristics of porosity in several ordinary chondrites, as well as the distribution of metal particle sizes. They investigated samples of Miller (H5), Mount Tazerzait (L5), NWA 2380 (LL5), Sahara 98034 (H5) and Tjerebon (L5), combining both He-pycnometry and synchrotron XCT, examining and quantifying the phases using Blob3D. The samples were scanned at two resolutions, 8.3 μm/voxel and 16.6 μm/voxel, before being segmented into metal grains, pore space, and sulphide grains. For low-resolution volumes, the authors isolated individual resolvable pores. This proved tedious as each 'isolation' must be user verified within Blob3D, which is further complicated by the interconnectivity of the porosity. For the high-resolution volume, the authors isolated the interconnected solids and subtracted this from the total volume, which gave total void space instead of a size-resolved histogram. In one sample, they also isolated individual pore spaces located within silicate mineral grains. In their cumulative pore space graphs, they used the total porosity as the value achieved through He pycnometry, as this was measured on larger samples than the CT data, and was therefore assumed to be more representative. For the Miller (Arkansas) sample, they found that intragranular pores with volumes > 3.41 $x10^{-6}$ mm^3 that unambiguously reside in silicate grains contribute only 0.95% of the total porosity. This would indicate that such voids, potentially not picked up by He pycnometry, are not plentiful enough to account for the differences in porosity measured by the two techniques, indicating that heterogeneity in the samples (small volume used for CT, large for He) and/or resolution limitation of CT is likely the cause of the discrepancy. Sasso et al. (2009) used only samples of petrological type 5. The petrological type increases with increasing equilibration, which is a result of the degree of heating or rate of cooling; chondrites with greater porosity should have a lower thermal conductivity than those that are more compacted (Clauser and Huenges, 1995). Therefore, assuming the same heat source (i.e. ^{26}Al decay), higher porosity chondrites would either reach a lower peak temperature, or, if they reached the same peak temperature as more compacted rocks, would have cooled more slowly. The authors reasoned that it is likely that the rocks reached a lower peak temperature given an identical heat input is consistent with the samples all being type 5. If the material had cooled more slowly from a given peak temperature, it would be expected to have metamorphosed to a type 6. Potentially therefore, type 5 and type 6 chondrites did not experience the same input of heat.

3.1.4 Metal in ordinary chondrites

Metal grains in ordinary chondrites are typically 100-200 μm in size (Brearley and Jones, 1998). This size range implies that XCT could be used effectively to measure the size distribution pattern in our sample set, to discover if there are any trends with shock or petrological characteristics, or any correlation to be found with results from AMS or He/XCT porosity. Accurate metal grain size distributions for different meteorite groups can also inform a range of wider investigations in the field, for example, interpretation of spectral properties of asteroids (Moretti et al., 2007), or potentially indicate source bodies for micrometeorites. Additionally, samples of low petrological type can provide insight into nebular sorting as they show the closest approximation of metal grain sizes when accreted, with the lowest effect of thermal or impact metamorphism (Kuebler et al., 1999).

The response of metal grain petrography – specifically shape, size and orientation – to metamorphism has not been extensively studied in meteoritics. The primary finding of previous studies is that the most significant change in metal size distribution with increasing petrological type in H and L chondrites occurs between unequilibrated and equilibrated OCs where metal moves from chondrule interiors to surfaces or into the matrix (Afiattalab and Wasson, 1980). The petrological scale for classifying ordinary chondrites is predominantly qualitative; however, quantitative parameters are increasingly being explored with the development of novel techniques and increasing computing power (e.g. Friedrich et al. 2008; Guignard and Toplis, 2015). Previous studies have focused on equilibration with regards to chemical composition but not texture (e.g. Afiattalab and Wasson, 1980). Thorough analysis of metal grain size distributions with increasing metamorphism can also provide insight into the segregation of metal phases from silicate portions of parent bodies.

Guignard and Toplis (2015) quantified textural characteristics of iron-rich phases in ordinary chondrites with increasing petrological type. The parameters measured included: (i) phase proportions, (ii) the length of metal-sulphide contacts, (iii) dihedral angle at contacts with silicate grains, (iv) grain shape and circularity, (v) grain size and size distributions. They found that metal and sulphide grains show considerable variations in textural properties that correlate to metamorphic grade, including increasing mean metal grain size, increasing grain circularity, and increasing separation of metal and sulphide phases as shown by decreasing contact lengths. This

study was conducted on 2D sections of H chondrites, but all aspects lend themselves to quantitative analysis of 3D CT data.

Magnetic properties are increasingly being used to classify meteorites (e.g. Rochette et al. 2003). The measurement of magnetic susceptibility is a key rapid and non-destructive technique, when ~ 1000 new meteorites are discovered each year. Additionally, magnetic properties such as magnetic susceptibility and natural remanent magnetisation of meteorites must be considered in the interpretation of magnetic field measurements of asteroids by space missions (e.g. Acuña et al. 2002). The magnetic susceptibility of a sample describes the ratio of an induced magnetisation of a material to the strength of an applied magnetic field. Thus, the magnetic susceptibility of a meteorite is a function of the abundance of phases containing magnetic elements, iron and nickel, according to their susceptibility. In OC meteorites, the dominant effect is from FeNi alloys, which varies according to geochemical class. Other phases containing these elements (paramagnetic silicates and antiferromagnetic troilite) do not exhibit any remanance and have very low susceptibilities, thus they do not impact the magnetic properties of the meteorite (Rochette et al., 2003).

The proportion of FeNi metal in a chondrite is a key aspect of classification, usually estimated from thin-section, however this method can suffer from sampling bias, not only in terms of whether a section is representative of the whole rock, but also with regards to the plane in which a metal grain is cut, since most are non-spherical in shape. XCT data can be used to ground-truth magnetic susceptibility data with quantitative measurements of metal content in meteorites.

3.1.5 Response of metal grains to shock and development of petrofabric

Sneyd et al. (1988) measured strain and anisotropy of magnetic susceptibility (AMS) in several ordinary chondrites, finding that the magnetic susceptibility ellipsoids indicated progressive foliation development (shortening along the minimum axes) and were almost proportional to the shape anisotropy of the chondrite's metal grains. This was further explored by Gattacceca et al. (2005), who investigated the origin of foliation in OC meteorites by measuring the AMS of 295 meteorites (including carbonaceous and Rumuruti-like chondrites, and achondrites). They found that AMS intensity is correlated with the degree of shock as determined by optical microscopy, and suggested that hypervelocity impacts lead to compaction and lithification of loose material, which

caused the metal grains to deform. It has been demonstrated that deformation and foliation of metal grains in L chondrites is effectively accomplished at peak pressures of 10 - 15 GPa (Friedrich et al., 2008; Gattacceca et al., 2005).

XCT has previously been used to illustrate that both the number and the degree of preferred orientation of metal grains in ordinary chondrites increase with increasing shock metamorphism. Friedrich et al. (2008) conducted the first study of 3D petrofabric measurements as a function of shock loading, using the ratios of ellipsoid tensors to indicate the overall preferred orientation of metal grains. They found that the degree of metal grain orientation is low for the least shocked meteorites, and increases with increasing shock stage, but shows no correlation with petrological type. Additionally, the authors scanned the same sample of L chondrite Tennasilm at two different resolutions to show that higher resolution X-ray CT allowed smaller metal particles to be resolved (13000 more particles, equal to a relative increase in total metal volume by 3.6%), however the resolution had little effect on the size-number results. The authors stated that this underestimation will be more significant at low shock stages since metal grain size coarsens with increasing shock, thus the number of grains visible in XCT increases. Friedrich et al. (2008) also showed that the orientation of metal grains is not dependent on the size fraction analysed, by measuring the degree of preferred orientation in ten different size-sorted groups of Elenovka (L6, S4).

Similarly, Krzesińska et al. (2015) used XCT and AMS to describe the petrofabric of the Pułtusk regolith breccia, finding that this meteorite was dominated by foliation (defined by an oblate ellipsoid similar to Gattacceca et al. 2005), the intensity and orientation of which was consistent across both magnetic and tomographic data sets. Figure 3.2 shows stereographic projects of the metal grain major axes, coloured according to density of data points, and major (K1), intermediate (K2), and minor (K3) axes of the magnetic susceptibility ellipsoid for three different lithologies in the study.

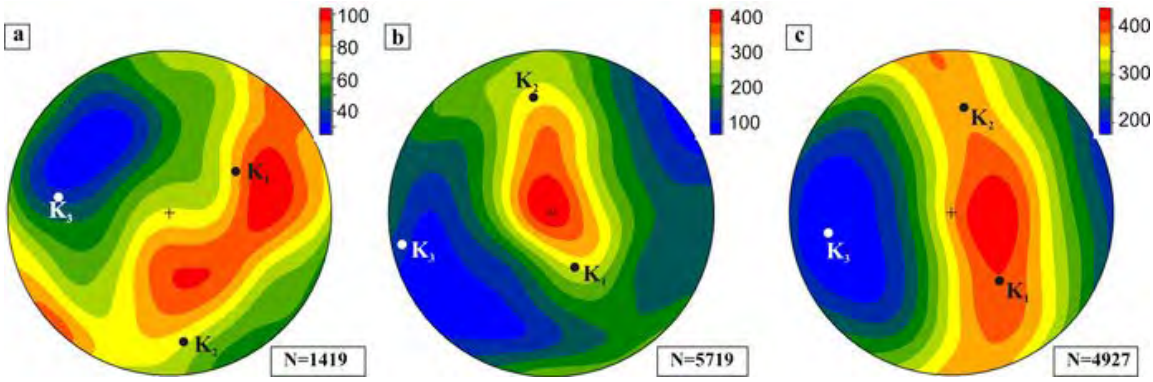

Figure 3.2. Density stereograms of metal grain major axis orientations in three different lithologies of the Pułtusk (H5) breccia showing correlation with the direction of anisotropy of magnetic susceptibility (Krzesińska et al., 2015).

Friedrich et al. (2013) described the petrography of Kernouvé (H5) using XCT at 11.9 μm/voxel and 11.2 μm/voxel. The two samples contain large metallic veins, which have been previously attributed to parent body impact processes (Friedrich et al., 2012). Kernouvé is classified as S1, i.e. displays evidence of low shock. They found that the sample was incompletely compacted, with a porosity of 4.4 ± 1.3% using XCT, and 6.8% using ideal gas pycnometry. The difference was attributed to the presence of pores smaller than the CT resolution. This followed work by Friedrich et al. (2008), whose techniques were used to measure the degree of compaction for Kernouvé and 16 other ordinary chondrites. They found that, like other meteorites with low shock stage, metal grains in Kernouvé do not display significant preferred orientation and have not been compacted by a later event. That the meteorite possesses a low shock stage and high porosity is somewhat surprising, as they imply no significant impact history, whereas the presence of a metal vein indicates that the metal must have been mobilised. The authors have constructed a possible history, after work by Rubin (2003 and 2004), suggesting that the vein was created by an early impact, causing concentration of metal phases “akin to slickenslides”, followed by shearing and annealing, which coalesced the metal vein and removed any preferred orientation of grains.

Figure 3.3 shows the increasing strength factor, or degree of orientation of metal grains, against shock stage for ordinary chondrites. Overall, evidence from multiple studies (Friedrich et al. 2008a; Friedrich et al. 2014; Friedrich and Rivers, 2013; Gattacceca et al. 2005; Krzesińska et al., 2015) indicates that, with increasing shock loading, a petrofabric develops as shown by increasing degrees of preferred orientation of AMS and metal grain major axes.

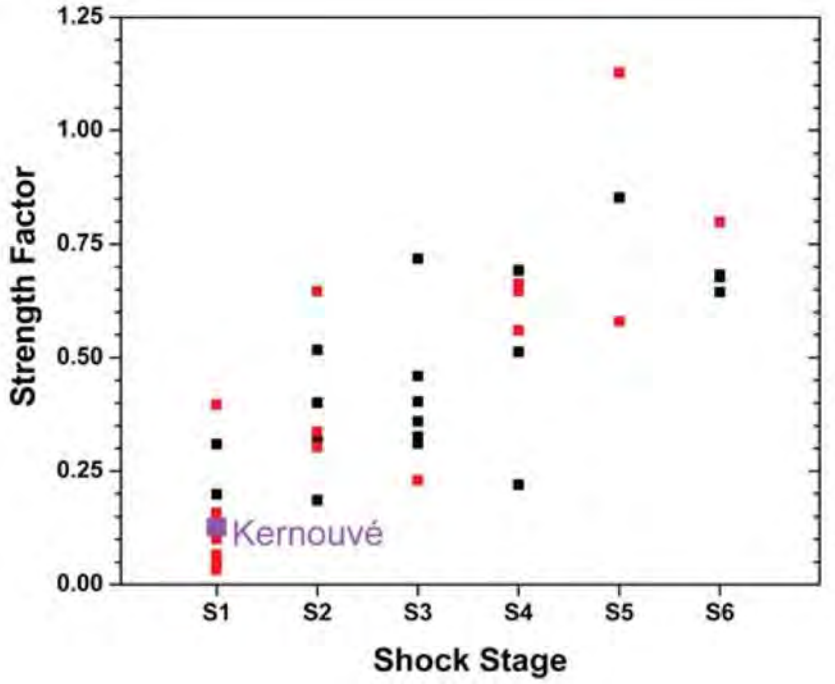

Figure 3.3. Strength factor, representing the degree of compaction, against shock stage for L chondrites (black) and H and LL chondrites (red) (Friedrich et al., 2012; data also from Friedrich et al. 2008a).

3.2 This Study

This study aims to:

- Determine the efficacy of thresholding XCT data as a technique for quantifying porosity and metal grain parameters.
- Investigate the correlation between metal grain orientation in 3D and AMS.
- Elucidate the relationship, if any, between porosity and metamorphism, if any, and evaluate the relevance to the "onion shell" model (after Grimm, 1985).
- Elucidate the relationship between metal grain size and metamorphism, for example, the extent of coalescence as a function of subsolidus heating by thermal or shock metamorphism.
- Elucidate the relationship between metal grain orientation and metamorphism, for example, the extent of petrofabric development as a function of shock stage or petrological grade.
- Determine if metal grain orientation is related to grain size.

3.2.1 Methods

- Samples of 17 L chondrites were selected. Criteria included: falls preferred to minimise the effects of weathering, varying petrological grades, varying shock stages and small samples (on the order of 5-10 mm in each dimension; ~ 0.5 – 2.4 g) to ensure high resolution data (small voxel size). In order to maintain the non-destructive aspect of CT, meteorites were selected if fragments of the right size and shape were already available within the NHM collection, so that no destructive sampling was required.
- All samples were scanned with the HMXST 225 Micro-CT System at the NHM. Nikon 'in-program' beam hardening and noise filters were applied prior to reconstruction. Parameters are described in *Appendix 2.*
- Data analyses were carried out using the FEI Avizo program, including: measurement of bulk volume by separating voxels representing the sample from the surrounding air; quantification of porosity by histogram thresholding and calculating the ratio of pore space to solid material; quantification of metal content by histogram thresholding; volume and orientation of metal grains using a particle analysis module. Grains < 10 voxels in volume (equivalent to ~1250 μm^3) were discarded as noise. The data were then normalised by total metal content to give cumulative volume fraction curves, which highlight the proportion of grains in different size categories.
- Metal grain orientations were converted into trend and plunge for visualisation on stereographic projections and comparison with AMS results.
- Magnetic susceptibility measurements were carried out on the same samples using the MFK1 Agico instrument (low field of 378 μT and frequency of 920 Hz) at CEREGE in Aix-en-Provence, France. The method follows that described by Gattacceca et al. (2005).
- Grain volumes of the same samples were measured using a helium pycnometry system at CEREGE in Aix-en-Provence, France.
- Shock stages for four meteorites (without shock stage classifications in the literature) were predicted based on metal grain analysis then verified with conventional assessment by optical microscopy.

3.3 Results

3.3.1 Bulk density of L chondrites

Table 3.2 shows the bulk volume for L chondrites in this study, given as both number of voxels and calculated as mm^3. The bulk volume was measured twice with a nine-month interval in order to test the reproducibility of segmentation, i.e. if the user selected the same threshold, estimating the same sample boundary and the same results through filling pore spaces. The data show that the maximum deviation between the two sample volume measurements is 3.7 mm^3, equivalent to an error of ~1%, for the Aumale meteorite (Table 3.2).

Meteorite	Bulk volume (voxels) (1)	Bulk volume (mm^3) (1)	Bulk volume (voxels) (2)	Bulk volume (mm^3) (2)	Bulk volume (mm^3) (average)	Error (s.d.) (mm^3)	Error (%)
Aumale	827574477	388.2	816461513	383.0	385.6	3.7	0.96
Aumieres	874158313	413.2	881547158	416.7	415.0	2.5	0.60
Ausson	1051357835	342.4	1042765232	339.6	341.0	2.0	0.58
Barwell	581701171	303.5	585288158	305.3	304.4	1.3	0.43
Bjurbole	858800681	597.3	861370082	599.1	598.2	1.3	0.21
Chervettaz	734154483	163.4	736722698	164.0	163.7	0.4	0.25
Crumlin	647366321	309.6	651205587	311.4	310.5	1.3	0.42
Elenovka	439893102	143.3	438181458	142.7	143.0	0.4	0.28
Farmington	540495632	328.4	540011356	328.1	328.3	0.2	0.06
Hallingeberg	751945916	550.0	751316938	549.5	549.8	0.3	0.06
Holbrook	1132185413	547.7	1131189256	547.2	547.4	0.3	0.06
Jackalsfontein	363730550	329.9	359984128	326.5	328.2	2.4	0.73
Jhung	622761920	277.7	630826626	281.3	279.5	2.5	0.91
Kyushu	1106106100	553.7	1101093542	551.2	552.4	1.8	0.32
Little Piney	1266640600	474.7	1260831957	472.6	473.7	1.5	0.33
Monze	1203850791	558.2	1196965340	555.0	556.6	2.3	0.41
Nikolskoe	1082796512	619.1	1074206534	614.2	616.7	3.5	0.56

Table 3.2. Bulk volumes measured from XCT data, given in voxel count and calculated as mm3. Data were segmented and quantified on two separate occasions, designated (1) and (2), ~ 9 months apart, to assess the repeatability of segmentation.

Table 3.3 shows the bulk density calculated from the volumes measured from XCT data for the L chondrites in this study. Figure 3.4 shows that these bulk density measurements match well to the literature values, which were all carried out by the glass bead method. Jhung is a notable exception – measured in this study as 3.44 g/cm^3 versus 3.19 g/cm^3 (Macke, 2010) and 3.18 g/cm^3 (Kohout et al., 2008). This piece of Jhung has a metal content of 4.02%, which is greater than most L chondrites, indicating that this sample is likely less representative than the pieces in the other studies. Similarly, Chervettaz has a measured density of 3.40 g/cm^3 versus 3.02 g/cm^3 from Macke (2010). The Chervettaz sample in this study does not have a significantly high metal content, nor a particularly low porosity (based on XCT data), therefore the cause for the discrepancy is not clear, however sample heterogeneity is an obvious

factor in the comparison of these data. For example, Elenovka varies from ~ 3.0 to 3.5 g/cm^3 across three data sets. Similarly, Jackalsfontein varies from ~ 3.1 to 3.5 g/cm^3 across three data sets. Measuring the same samples by both methods would elucidate the difference in technique without the effect of sample heterogeneity.

Meteorite	Petrological type	Shock stage	Mass (g)	Bulk volume (mm^3)	Bulk density (g/cm^3)	Bulk density error (s.d.) (g/cm^3)
Aumale	6	4	1.336	386	3.46	0.033
Aumieres	6	4	1.390	415	3.35	0.020
Ausson	5	3	1.144	341	3.36	0.019
Barwell	6	3	0.999	304	3.28	0.014
Bjurbole	4	1	1.765	598	2.95	0.006
Chervettaz	5	3	0.556	164	3.40	0.008
Crumlin	5	4	1.078	310	3.47	0.015
Elenovka	6	2	0.453	143	3.17	0.009
Farmington	5	4	1.163	328	3.54	0.002
Hallingeberg	3	1	1.840	550	3.35	0.002
Holbrook	6	2	1.792	547	3.27	0.002
Jackalsfontein	6	3	1.164	328	3.55	0.026
Jhung	5	2	0.960	280	3.44	0.031
Kyushu	6	5	1.913	552	3.46	0.011
Little Piney	5	2	1.613	474	3.41	0.011
Monze	6	4	1.927	557	3.46	0.014
Nikolskoe	4	2	1.970	617	3.19	0.018

Table 3.3. Bulk density calculated from sample mass and bulk volume (average of two measurements – Table 3.2) from XCT analysis.

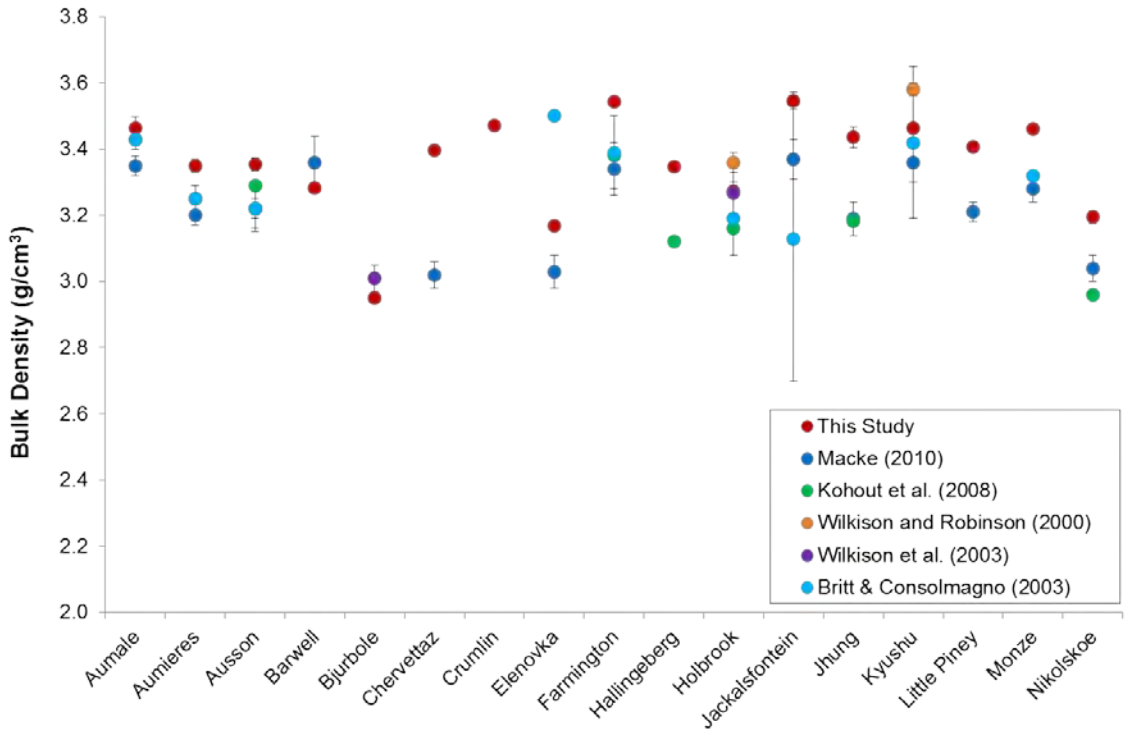

Figure 3.4. Comparison of bulk density measured in this study to literature values for the same L chondrites. All literature data was acquired using the glass bead displacement method.

In some cases, errors may have arisen due to sample preparation. For CT scanning, each sample was wrapped in parafilm to protect against contamination. Figure 3.5 shows a visualisation of the segmentation of the Elenovka sample. This meteorite was particularly friable which meant that selecting all pieces was challenging. Additional errors could come from fragments being lost during weighing.

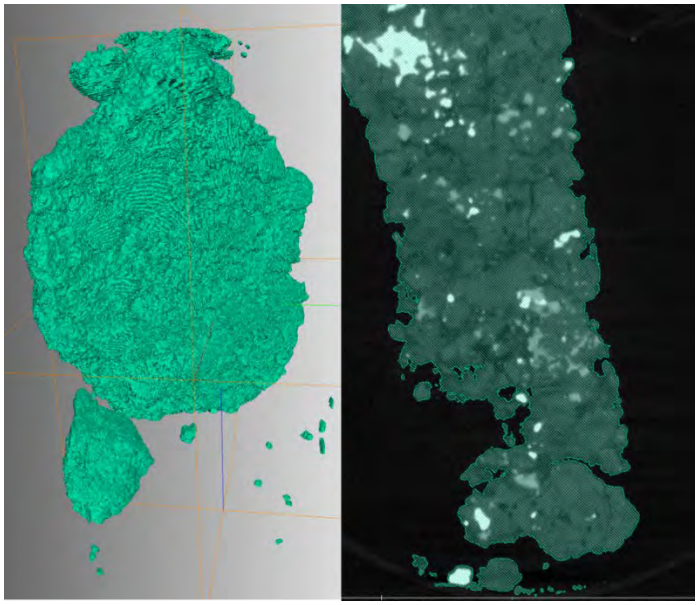

Figure 3.5. A 3D visualisation (left) and a single slice (right) showing the selection of sample from surrounding air within the CT scan of Elenovka, and illustrating the friable nature of the specimen.

3.3.2 Porosity of L chondrites

3.3.2.1 Porosity by XCT

The XCT data show that the porosity of this suite of L chondrites varies widely. Figure 3.6 includes tomograms from five different L chondrites, illustrating the diversity in porosity in these samples. As discussed previously, the greyscale value is dependent on attenuation, thus the darkest areas of the images indicate pore spaces. The most porous are incompletely compacted samples, i.e. Chervettaz, which are characterised by significant intergranular voids, which are irregular in shape and mostly interconnected. They often contain pores within chondrules, and display a 'fluffy' appearance. The next most porous samples show more evidence of compaction but retain high porosity, especially around chondrules and other grains, and within chondrules. Examples include Björbole and Hallingeberg. As specimens decrease in porosity, they appear noticeably compacted. Porosity around chondrules becomes rare, some small voids remain in chondrules, and cracks are more prevalent, e.g. Barwell, Nikolskoe. Very well compacted samples, e.g. Aumale and Ausson, exhibit porosity only in very thin and often long cracks, indicative of fracturing due to shock. Aumale is well compacted with little evidence of intergranular porosity. CT slices show microcracks that, although observable, are too fine for accurate segmentation, thus porosity measurements are likely to be inaccurate.

Figure 3.6 also shows a tomogram of Farmington L5 S4, which appears different to other L chondrites in this study. The specimen looks well compacted in some areas, but interspersed with large void spaces. In many cases, the voids are associated with metal grains.

Figure 3.7 illustrates the challenge of selecting porosity in XCT scans in low porosity specimens. Whilst pores in Elenovka are obvious, and large enough to segment from the surrounding silicates, porosity in Aumale is clearly close to or below the voxel size of the CT scan, appearing mottled or in fine cracks. In such cases, the minimum amount of porosity was thresholded, where it was obvious that not all porosity was selected, but increasing the threshold would include voxels of silicate material (as in Figure 3.7). Quantitative measurements of porosity, where thresholding was successful, are compared with pycnometry and SEM BSE image measurements of porosity later in the chapter (*Section 3.3.2.3*).

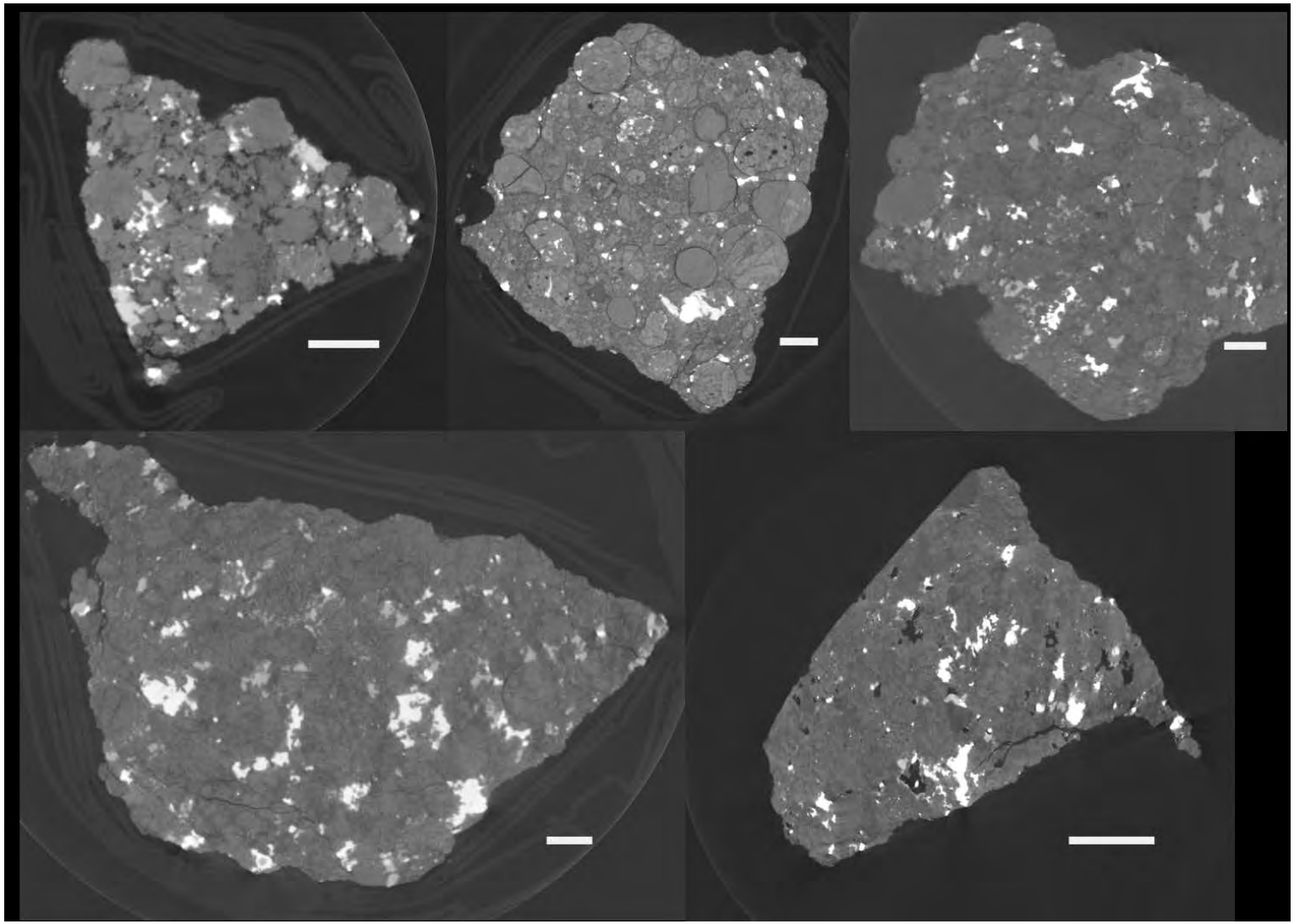

Figure 3.6. Single slice tomograms from XCT data illustrating nature of porosity in L chondrites. Pore spaces are indicated by black/very dark areas corresponding to low attenuation of X-rays. Top (left to right): Chervettaz; Bjürbole; Barwell. Bottom: (left) Aumale; (right) Farmington. Scalebars are 1 mm.

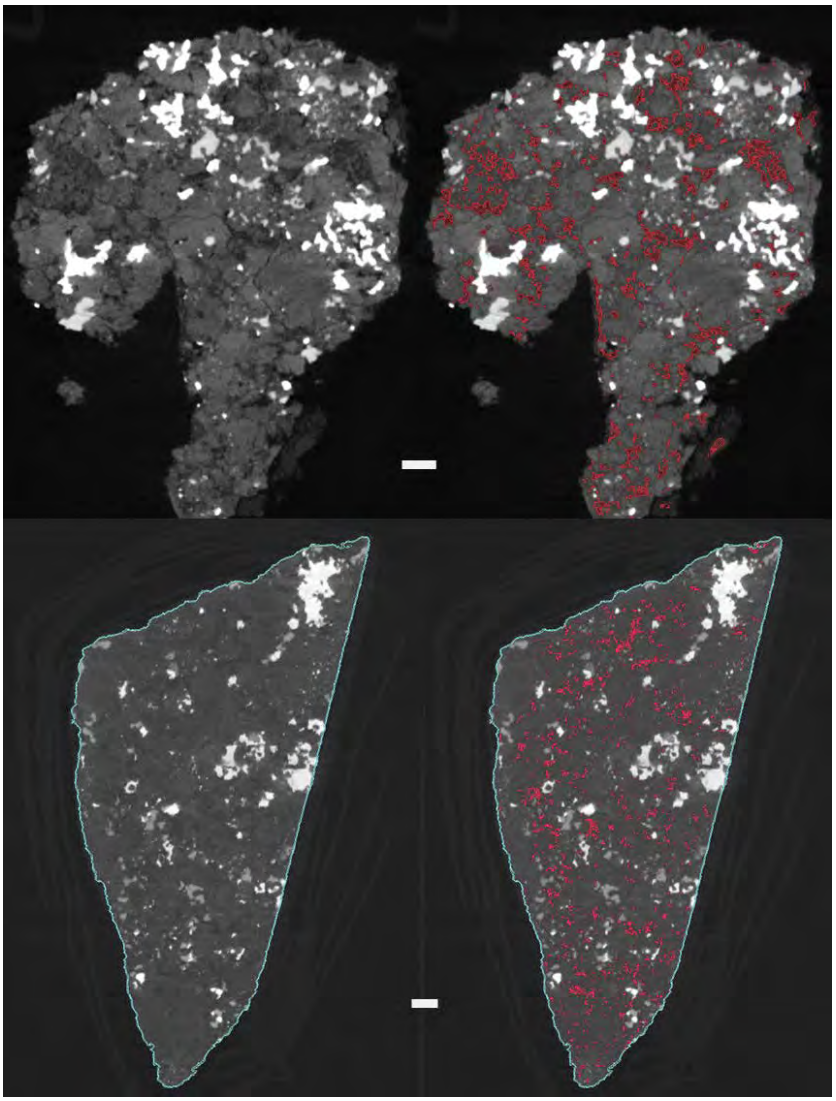

Figure 3.7. Thresholding porosity (shown in red) accurately in incompletely compacted L6 S2 chondrite, Elenovka (top) and inaccurately in the well-compacted L6 S4, Aumale (bottom). Scalebars are 1 mm.

3.3.2.2 Grain density and porosity by gas pycnometry

Grain densities of the L chondrites were measured using helium pycnometry and are compared to literature values in Figure 3.8. Small differences in grain density make very large differences in the calculation of porosity, thus it is likely that the measurement of grain density is where the discrepancy has arisen. For example, a variation of 3.25 – 3.75 g/cm^3 in the grain density of Holbrook measured by four studies is equivalent to a variation in porosity from ~ 3% to 18%. As discussed in *2.8.2. Pycnometry Instrumentation*, the lack of stabilisation of cell volume measurements for three samples (Barwell, Chervettaz, and Elenovka) meant that no grain density calculations were possible.

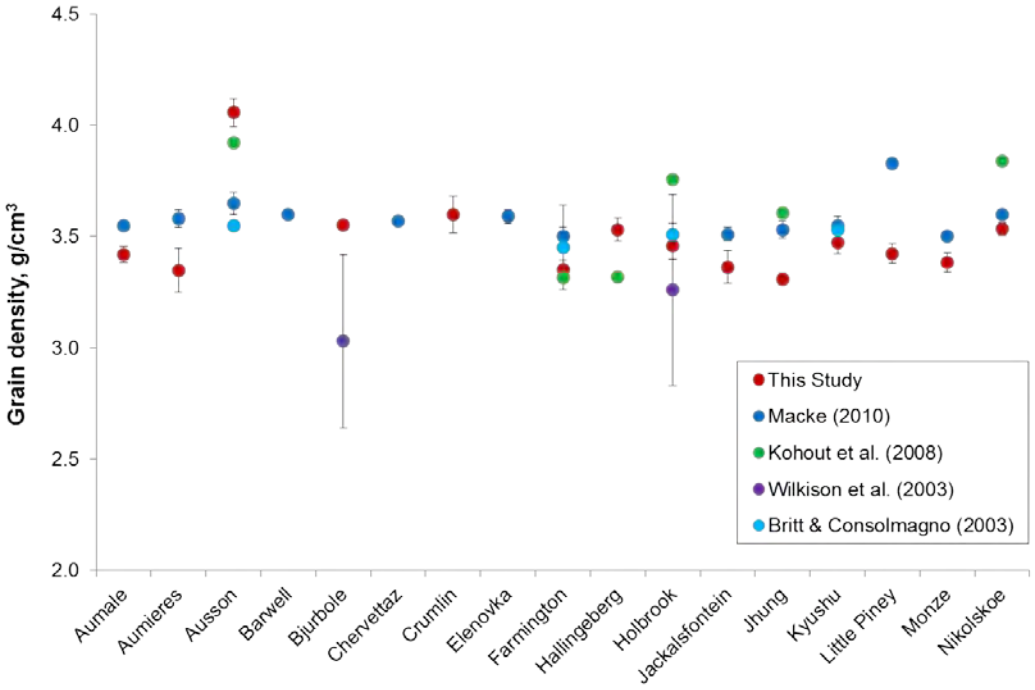

Figure 3.8. Grain densities measured in this study as compared with literature values for the same L chondrites. All measurements made using gas pycnometry. Missing data points represent samples that provided erroneous results as described in *2.8.2. Pycnometry Instrumentation.*

The error in grain volume given by Consolmagno & Britt (1998) is error of repeatability (precision) based on the five measurements taken of each sample. The same error is reported here, but it does not include an estimation of the accuracy. In some cases, e.g. Wilkison et al. (2003), an error can be provided based on manufacturer calibration of the pressure transducers and the error on the parameters defining the calibration curve. This should take into account elevation above sea level and ambient temperature, but in this case, was outside the remit of this project. Based on the variability in the precision of the pycnometry measurements of grain volume, it is unlikely that pycnometry can provide accurate measurements of the porosity of small samples. Examples of the raw data are provided in *2.8.2. Pycnometry Instrumentation*, where the method is fully described.

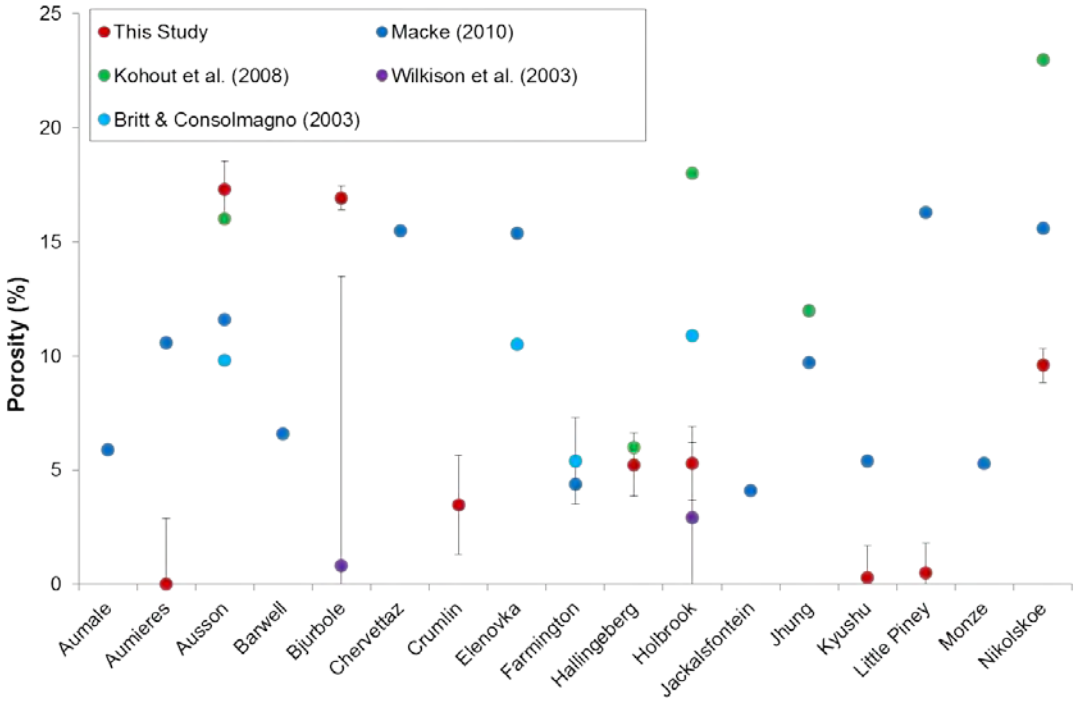

Figure 3.9. Porosity calculated from grain and bulk densities measured in this study compared with literature values for the same L chondrites. Missing data points represent samples that provided erroneous results as described in *2.8.2. Pycnometry Instrumentation*.

Meteorite	Pet. type	Shock stage	Grain density (g/cm^3)	Grain density s.d.	Pycnometry porosity (%)	Pycnometry porosity error (+/-)	CT porosity (%)	CT porosity error (+/-)	SEM porosity (%)	SEM porosity error (+/-)
Aumale	6	4	3.42	0.04	-1.3	1.1	1.9	0.6	n.a.	n.a.
Aumieres	6	4	3.35	0.10	0.0	2.9	3.2	0.5	n.a.	n.a.
Ausson	5	3	4.06	0.06	17.3	1.2	3.0	0.7	22.5	0.8
Barwell	6	3	-	-	-	-	3.1	1.1	19.9	1.1
Bjurbole	4	1	3.55	0.02	16.9	0.5	8.3	1.3	19.0	0.8
Chervettaz	5	3	-	-	-	-	12.9	0.8	n.a.	n.a.
Crumlin	5	4	3.60	0.08	3.5	2.2	<1%	1.0	n.a.	n.a.
Elenovka	6	2	-	-	-	-	9.3	0.8	27.9	0.9
Farmington	5	4	3.35	0.04	-5.7	1.3	1.8	0.1	5.9	0.6
Hallingeberg	3	1	3.53	0.05	5.2	1.4	<1%	1.0	11.0	0.7
Holbrook	6	2	3.46	0.06	5.3	1.6	1.1	0.4	n.a.	n.a.
Jackalsfontein	6	3	3.36	0.07	-5.5	2.3	<1%	1.0	n.a.	n.a.
Jhung	5	2	3.31	0.03	-3.8	0.8	5.8	0.7	n.a.	n.a.
Kyushu	6	5	3.47	0.05	0.3	1.4	<1%	1.0	8.0	1.4
Little Piney	5	2	3.42	0.05	0.5	1.3	<1%	1.0	9.3	1.0
Monze	6	4	3.38	0.04	-2.3	1.3	<1%	1.0	n.a.	n.a.
Nikolskoe	4	2	3.53	0.03	9.6	0.7	<1%	1.0	n.a.	n.a.

Table 3.4. Grain densities and the associated value of porosity by pycnometry, as compared with porosity measured by thresholding XCT data, and by thresholding SEM BSE images. Dashes denote samples that provided erroneous results as described in *2.8.2. Pycnometry Instrumentation*. n.a. = not analysed.

Figure 3.9 shows the porosity calculated in this study along with literature values for the L chondrites in this study. It is evident that porosity is not consistent across a given meteorite, and even samples > ~ 100s grams, although possibly more representative of a whole specimen average, do not provide a value for porosity that reflects the inherent heterogeneity of the meteorite. Table 3.4 includes grain density and porosity measurements by the three different techniques used in this study.

3.3.2.3 Porosity in thin-section by SEM imaging

Backscattered electron montages were made of pre-existing preparations in the NHM collection in order to assess the level of porosity present at scales below that of the XCT resolution. These were: Ausson, Barwell, Bjürbole, Elenovka, Farmington, Hallingeberg, Kyushu and Little Piney. Montages were stitched at the original size to maintain resolution, which was standardised at x 500 magnification, or a pixel size of 1.22 μm, across all samples. Figure 3.10 shows two examples of the original BSE images and the thresholded porosity which was then quantified as a percentage of the total area. Using thresholding of SEM images, whilst effective at measuring microcracks much smaller than could be resolved in the XCT data, still suffers from limited representativeness. This is evident in some of the sections measured here. For example, Ausson, Barwell, Bjürbole, and Little Piney were fairly homogenous across the section; conversely, Farmington, Kyushu, and Jhung all contained inclusions which had to be cropped from the image before porosity could be measured. Additionally, the section of Hallingeberg appeared to show some signs of plucking. The data are included in Table 3.4.

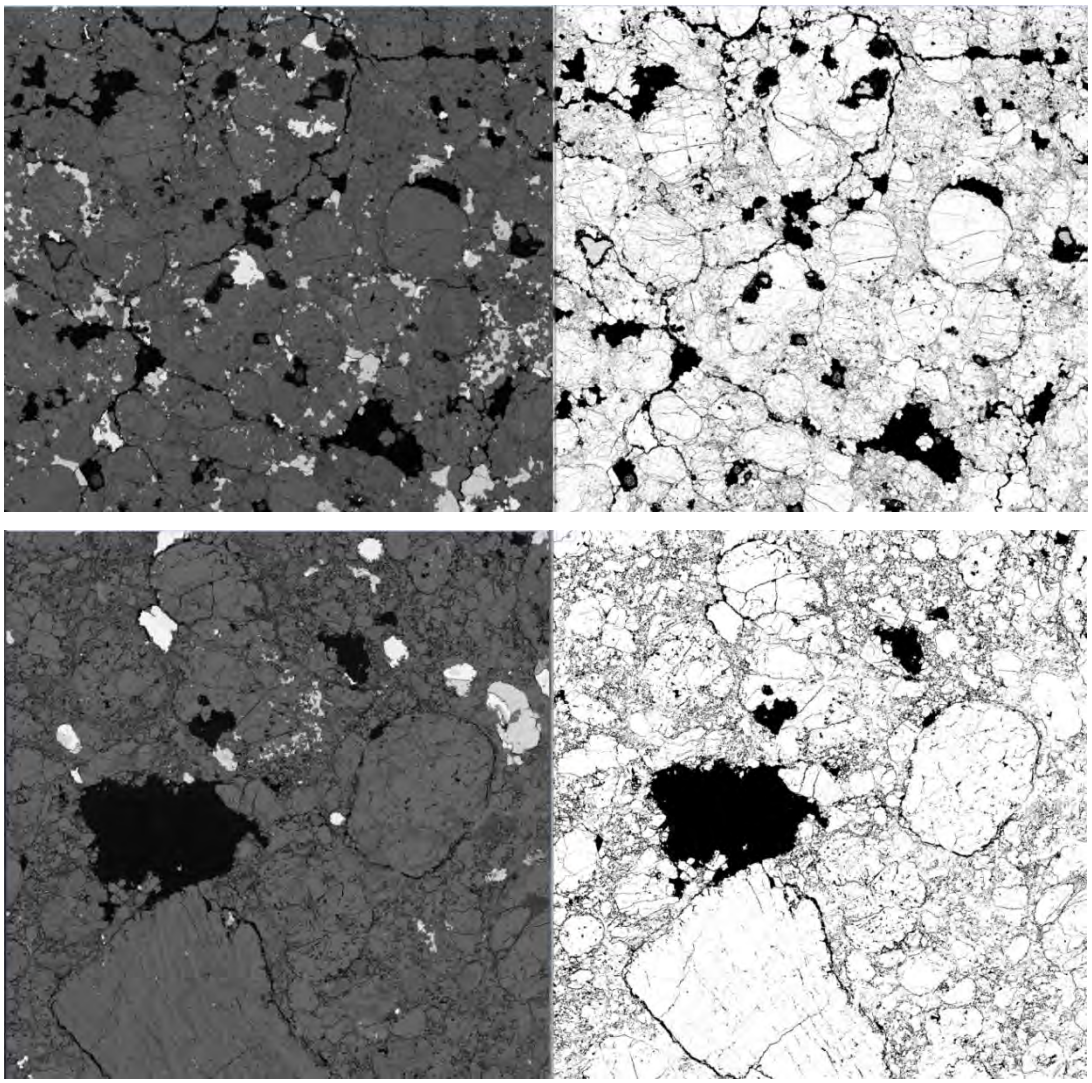

Figure 3.10. Examples of thresholding porosity in SEM BSE images of Ausson (top, FOV = 1 cm) and Bjürbole (bottom, FOV = 400 μm). The greyscale of BSE images is determined by the atomic number of the material therefore pore space appears black.

Figure 3.11 shows the porosity of L chondrites measured by the three techniques in this study. Clearly, there is a large spread in the results. Porosity measurements by thresholding of SEM BSE images are consistently the highest of the three methods, likely due to the greater resolution (pixel size of ~ 1.2 μm versus voxel size of ~ 6-9 μm), thus including smaller microcracks and pores. In most cases, XCT thresholding yields the lowest values for porosity. The difference between the two values can be used to estimate the level of porosity present at sizes between the resolution limits of the two methods. For example, in the case of Barwell, XCT yields a porosity of 3% versus 19% with SEM, indicating that the majority of the porosity in the meteorite is present below ~15-20 μm (two to three times the XCT voxel size), consistent with a well compacted meteorite.

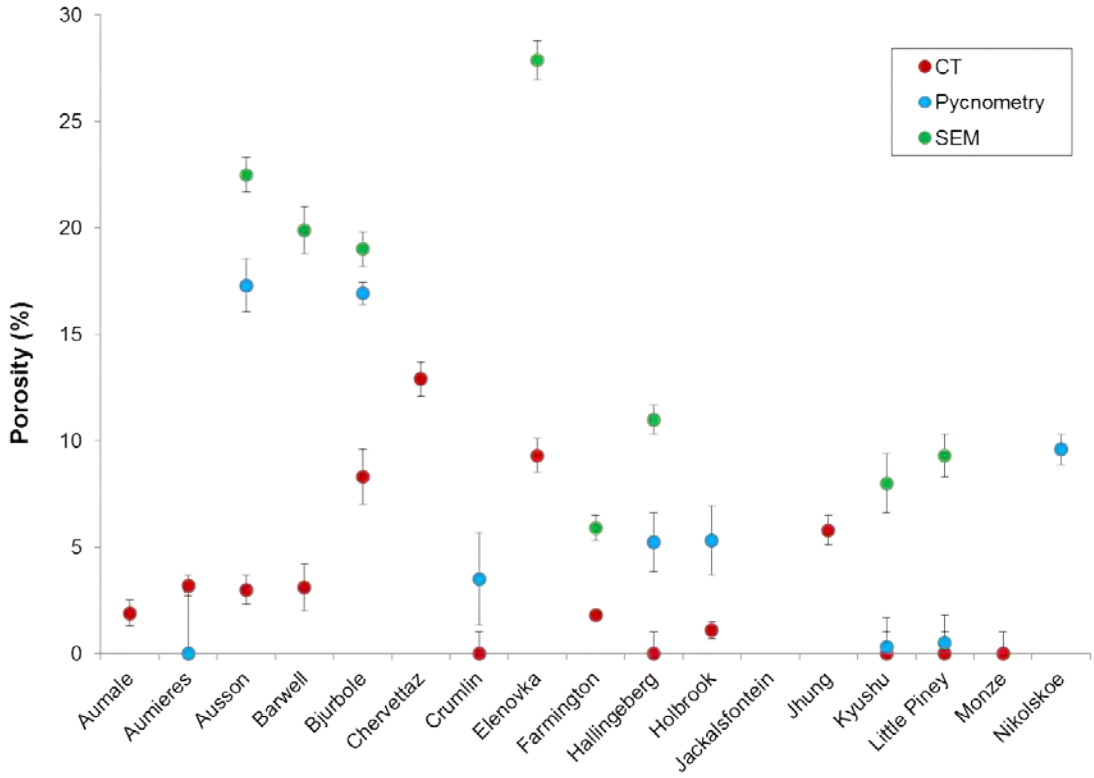

Figure 3.11. Comparison of porosity as measured by three techniques in this study: thresholding of XCT data, thresholding of SEM BSE images, and helium pycnometry. Missing data points represent methods that provided erroneous results or where thin-sections were not available.

3.3.3 Shock stage classification of four L chondrites

For four meteorites – Aumieres, Jackalsfontein, Little Piney and Monze – no shock classification was available in the literature, therefore they were classified in this study, according to the criteria outlined in *Section 2.9. Assessing shock stage with optical microscopy.* This includes identifying evidence of shock such as undulose extinction, sets of planar fractures, or mosaicism in olivine crystals. The results are given in Table 3.5, showing that Aumieries is classified as S4, Jackalsfontein S3, Little Piney S2 and Monze S4. Monze showed almost equal number of grains at S5 therefore is likely intermediary between the two stages. Note that in this section of Jackalsfontein (P4565), there were two lithologies present. One was clearly melted and recrystallized, with muted birefringence colours, strong mosaicism, isotropic glass surrounding rounded grains. This lithology is not represented in CT scanned piece of Jackalsfontein, therefore this part of the section was not included in the shock classification. The meteorite may be a S3/S6 breccia.

Meteorite	Section	Grains (n)	% S1	% S2	% S3	% S4	% S5	% S6	Shock Stage
Aumieres	BM.71575	51	-	6	29	43	22	-	4
Jackalsfontein	BM.1908,431, P4565	58	-	-	50	38	12	-	3
Little Piney	BM.24005, P92	69	16	54	30	-	-	-	2
Monze	BM.1951,101 (b)	56	-	-	20	43	37	-	4

Table 3.5. Olivine shock stage data based on optical microscopy, according to scheme of Stöffler et al. (1991).

3.3.4 Metal grain size of L chondrites

3.3.4.1 Metal content

Table 3.6 shows the results of the XCT data analysis of metal in L chondrites. All metal grains were thresholded from the bulk volume and voxels counted to provide quantitative measure of the FeNi phases. The total metal contents are consistent with their classification as L chondrites apart from Björbole – likely an LL.

Meteorite	Pet. type	Shock stage	Metal content (%)	Metal content (%) present < 11 voxels	Max metal grain vol (mm^3)	Mean metal grain vol (mm^3)	Median metal grain vol (mm^3)	Number of grains > 10 voxels	Number of grains / mm^3
Aumale	6	4	2.97	0.0169	1.222	0.0024	8.7E-05	4733	12.27
Aumieres	6	4	1.99	0.0196	0.303	0.0011	1.8E-04	7583	18.27
Ausson	5	3	2.59	0.0159	0.500	0.0020	6.0E-05	4339	12.72
Barwell	6	3	2.98	0.0186	1.326	0.0026	8.6E-05	3463	11.38
Bjurbole	4	1	1.47	0.0708	0.402	0.0011	8.9E-05	7750	12.96
Chervettaz	5	3	2.71	0.0023	0.223	0.0026	2.4E-04	1685	10.30
Crumlin	5	4	3.42	0.0100	0.869	0.0035	1.6E-04	3027	9.75
Elenovka	6	2	3.05	0.0130	0.923	0.0019	5.9E-05	2254	15.76
Farmington	5	4	2.87	0.0163	2.930	0.0037	1.1E-04	2530	7.71
Hallingeberg	3	1	2.49	0.0967	0.141	0.0009	1.0E-04	14745	26.82
Holbrook	6	2	2.14	0.0289	0.333	0.0014	1.0E-04	8182	14.95
Jackalsfontein	6	3	2.59	0.0818	0.302	0.0014	1.1E-04	5925	18.05
Jhung	5	2	4.03	0.0042	1.287	0.0056	2.5E-04	2023	7.24
Kyushu	6	5	2.67	0.0221	2.004	0.0017	1.2E-04	8777	15.89
Little Piney	5	2	2.85	0.0115	1.008	0.0036	1.7E-04	3802	8.03
Monze	6	4	2.58	0.0122	0.999	0.0021	2.7E-04	6962	12.51
Nikolskoe	4	2	2.69	0.0061	0.722	0.0044	2.7E-04	3735	6.06

Table 3.6. Quantification of metal content in L chondrites in this study.

As the mean metal grain size increases, so the number of grains per mm^3 of bulk volume decreases, as expected for the coalescence of grains due to heating. Individual grains were separated and those < 10 voxels in volume were disregarded as too noisy for quantification of their orientation. Comparing the total volume of all grains with that of the cumulative volumes of those greater than 10 voxels, far less

than 1% of the grains were not represented in the orientation analysis, implying that the results are representative of the fabric as manifested by the metal grains. It should be noted that metal may also be present at sizes below the voxel size of the XCT data. Volumes and orientations were measured for every grain > ten voxels in volume. These data are illustrated and compared with magnetic susceptibility in the following sections.

3.3.4.2 Grain size distribution trends with metamorphism

No trend is obvious in the (volume-normalised) number of grains with shock stage, i.e. it is not clear that the number of grains increases with increased shock loading, as observed by Friedrich et al. (2008). This is likely due to the small sample number in each petrological type. Grain size distribution curves allow a simpler visual assessment of the data. Figure 3.12 shows the grain size distributions for low petrological type and low shock L chondrites. Hallingeberg is the only L3 S1 meteorite in the study and shows the smallest grain sizes, lowest maximum grain volume, and highest grain number density (Table 3.6), consistent with least parent body processing.

To parameterise changes in metal grain size and size distribution between petrological types, data for S1 and S2 chondrites are compared in Figure 3.13. Generally, the data show that metal grain coarsening is correlated with increasing degree of thermal metamorphism from type 3 to 4 to 5, consistent with Afiattalab and Wasson (1980), but there is a change towards smaller grains at type 6. However, Jhung is the only low shock stage L5 chondrite and may not be representative of the petrological type, as explored further in *3.3.5. Metal grain orientation*.

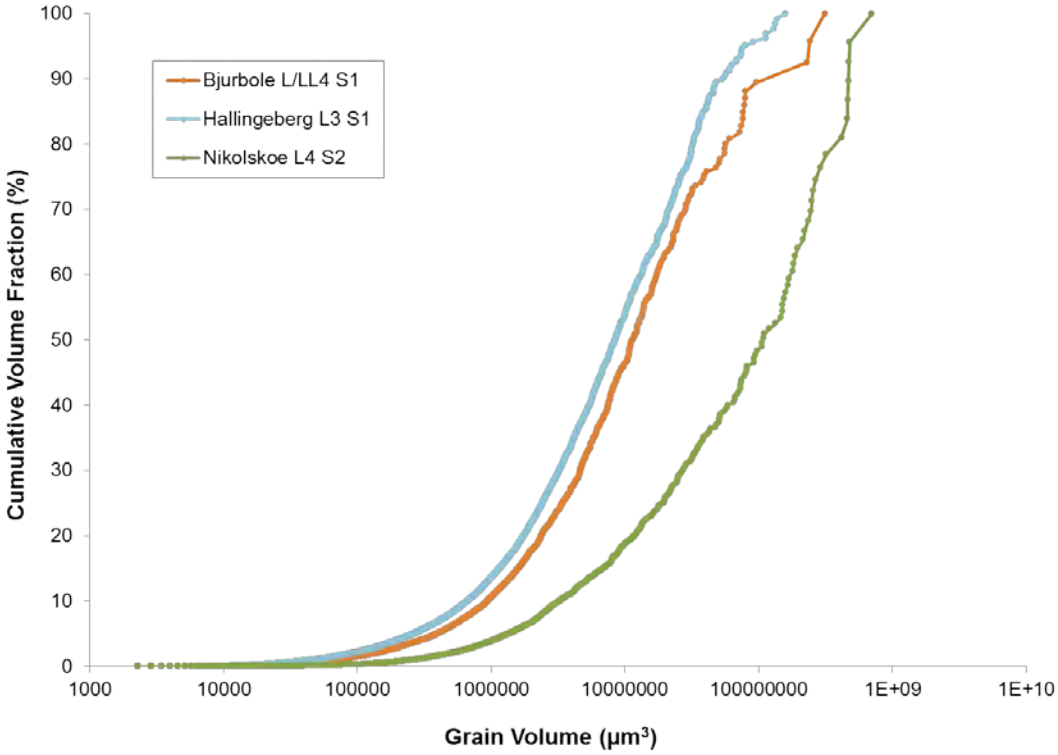

Figure 3.12. Cumulative metal grain size distributions in three L chondrites of low petrological type and shock stage. Each point denotes a grain that has been normalised to provide the percentage of total metal it represents. For example, the largest grain is 3.1 x10^8 µm^3 and accounts for ~ 4% of all the metal in the Bjürbole sample.

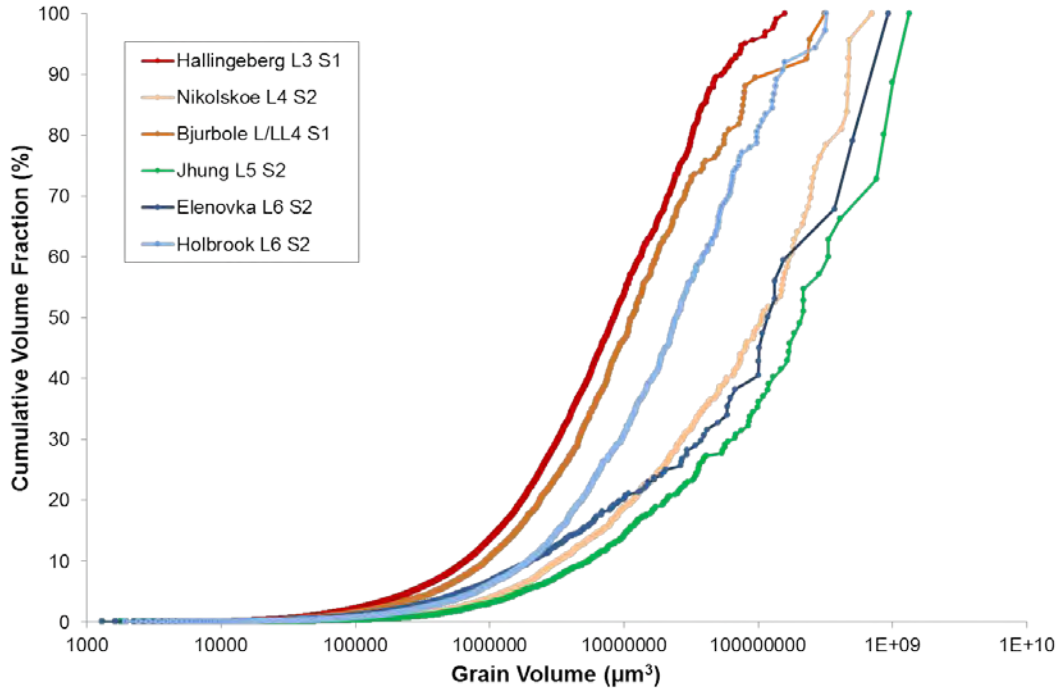

Figure 3.13. Cumulative metal grain size distributions in six L chondrites of low shock stage and varying petrological type.

To compare between shock stages, the metal grain size distribution of chondrites of the same petrological type only are illustrated in Figure 3.14. There is no simple trend with increasing shock pressure. In samples of petrological type 5, the distribution moves toward more, smaller grains between S2 to S3, and then moves towards fewer, larger grains from S3 to S4. However, again Jhung is the only L5 S2 meteorite in the study, and may be anomalous. The bottom image shows type 6 chondrites only; the size distributions of Elenovka (S2) and Aumale (S4) are very similar. Comparing Holbrook (S2) with Jackalsfontein (S3) and Aumieres (S4), there appears to be an increase in smaller grains. Similarly, Kyushu (S5) shows more plentiful, smaller grains but also contains a single large grain that accounts for ~15% of the total metal volume. Monze (S4/5) is somewhat intermediate between Aumieres and Kyushu, fitting with its classification based on optical microscopy carried out in this study. These trends likely represent the different effects of shock in chondrites, initially causing comminution of grains (between S2 and S4) then, on increasing shock to the degree where melting temperatures are reached, coalescence of metal into veins (at S4 and S5).

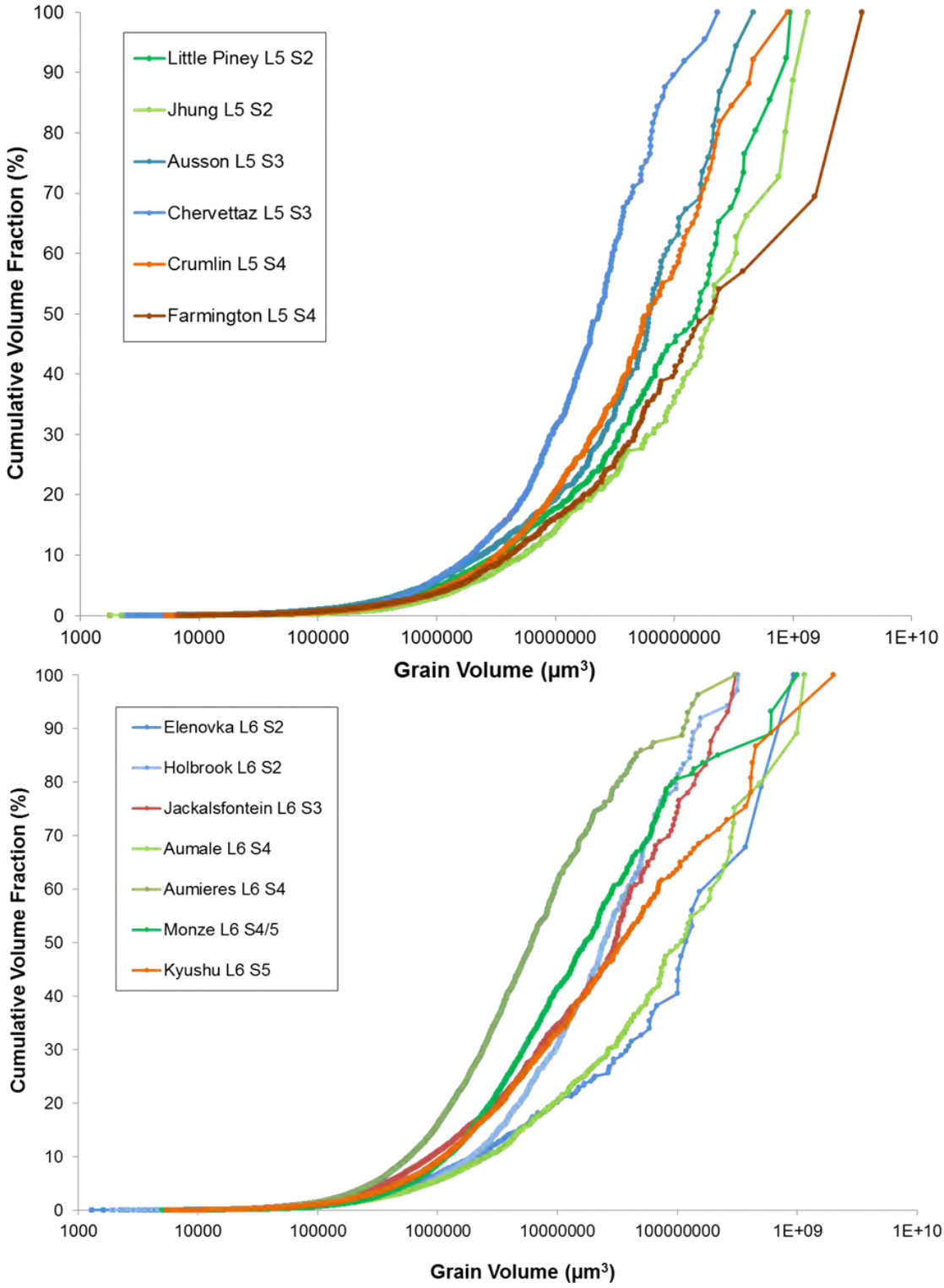

Figure 3.14. Cumulative metal grain size distributions in L chondrites of varying shock stage. Top: petrological type 5; bottom: petrological type 6.

3.3.5 Anisotropy of magnetic susceptibility of L chondrites

Table 3.7 summarises the results from measurements of magnetic susceptibility for the L chondrites in this study. The terms are fully explored in *2.7.3. Anisotropy of Magnetic Susceptibility: Data Analysis*. Briefly, P is the degree of anisotropy, T is the shape parameter, F is the magnetic foliation, L is the lineation and χ is mass susceptibility, also given in log χ for comparison with literature. About half of the analysed samples have P values about 1.5, indicating that AMS is a common feature of L chondrites.

Meteorite	Petrological type	Shock stage	P	T	L	F	χ mean (m^3/kg)	Log χ (10^{-9} m^3/kg)
Aumale	6	4	1.71	0.089	1.277	1.339	8.90E-05	4.95
Aumieres	6	4	1.233	0.597	1.378	1.205	4.15E-05	4.62
Ausson	5	3	1.247	0.224	1.21	1.369	7.60E-05	4.88
Barwell	6	3	1.216	-0.193	1.422	1.119	8.75E-05	4.94
Bjurbole	4	1	1.316	-0.168	1.412	1.124	2.16E-05	4.34
Chervettaz	5	3	1.139	-0.084	1.073	1.472	6.98E-05	4.84
Crumlin	5	4	1.587	-0.495	1.162	1.338	7.49E-05	4.87
Elenovka	6	2	1.53	-0.677	1.428	1.071	1.07E-04	5.03
Farmington	5	4	1.661	-0.264	1.144	1.159	7.86E-05	4.90
Hallingeberg	3	1	1.139	0.106	1.174	1.121	5.72E-05	4.76
Holbrook	6	2	1.256	-0.614	1.202	1.045	4.19E-05	4.62
Jackalsfontein	6	3	1.591	-0.516	1.09	1.145	8.01E-05	4.90
Jhung	5	2	1.657	0.244	1.043	1.182	1.10E-04	5.04
Kyushu	6	5	1.556	0.319	1.124	1.082	6.83E-05	4.83
Little Piney	5	2	1.326	0.046	1.073	1.062	7.41E-05	4.87
Monze	6	4	1.58	0.69	1.06	1.075	7.13E-05	4.85
Nikolskoe	4	2	1.138	-0.814	1.124	1.012	1.02E-04	5.01

Table 3.7. Magnetic susceptibility data for L chondrites in this study, where P is degree of anisotropy, T is the shape parameter, L gives the lineation (k1/k2), F the foliation (k2/k3), and χ is the magnetic susceptibility, usually expressed as a log value in 10^{-9} m^3/kg, to enable comparison with literature. Terms are more fully explained in *2.7.3. AMS Data Analysis*.

Figure 3.15 shows that the magnetic susceptibilities measured for L chondrites in this study compare well to literature values, falling within the ranges of values for these meteorites reported by Rochette et al. (2003). The results show that the Björbole sample in this study has affinity with LL rather than L, with a χ of ~4.33 (mean log χ of LL chondrites = 4.10 ± 0.3 (Rochette et al., 2003)).

Rochette et al. (2003) used stones of the falls Björbole, Holbrook, L'Aigle, Mocs and Pultusk from a range of different institutions to analyse the range in χ dispersion, showing ranges of log χ of ~ 0.25, excluding outliers. This is evidence of heterogeneity in the same meteorites, such as the presence of metal veins or xenoliths, brecciation or variable weathering (oxidation leads to reduced magnetic susceptibility). Thus, values of χ are also somewhat dependent on time of collection and quality of storage of different samples. For example, Rochette et al. (2003) found significant variations in χ between samples of two falls - Pirgunje (L6) and Wiluna (H5) - from the Vatican and Paris museums in comparison to fresher pieces from the NHM, London.

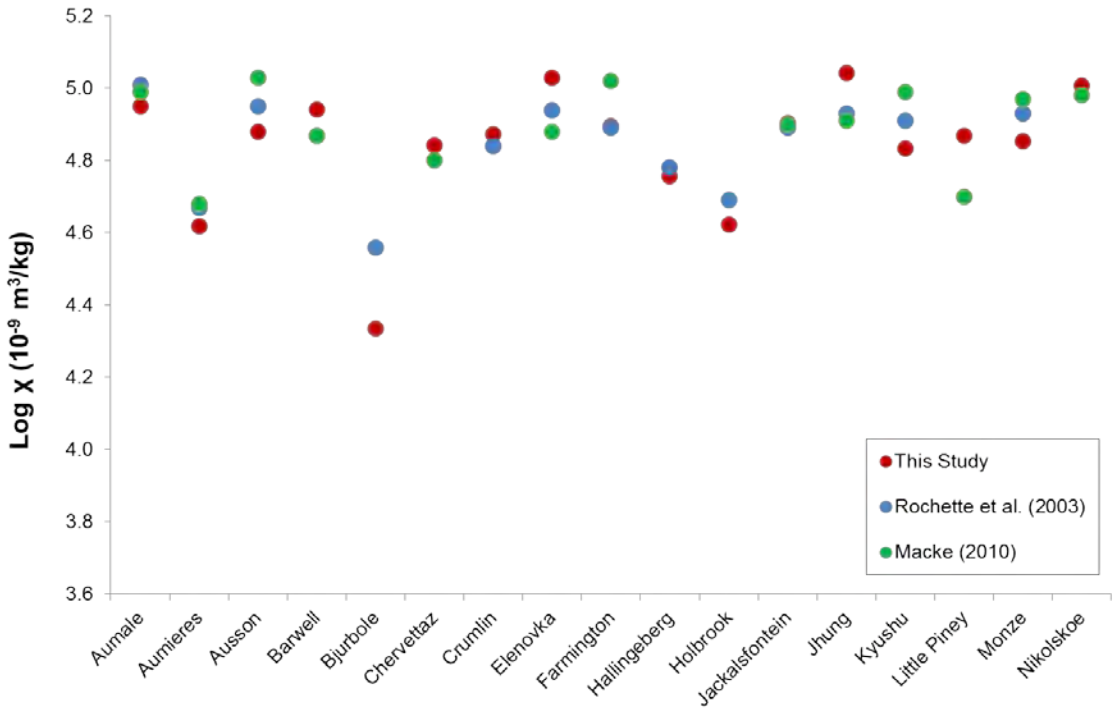

Figure 3.15. Log χ (decimal log of magnetic susceptibility) measured in this study compared with literature values. Errors are 5 x 10^{-13} m^3/kg (1 σ) therefore smaller than the marker size.

Figure 3.16 shows the total metal content, measured by thresholding of XCT data, plotted against the mean magnetic susceptibility of the L chondrite samples in this study. It shows a good correlation between the two factors, as expected given the dependence of χ on the abundance of phases containing Fe and Ni.

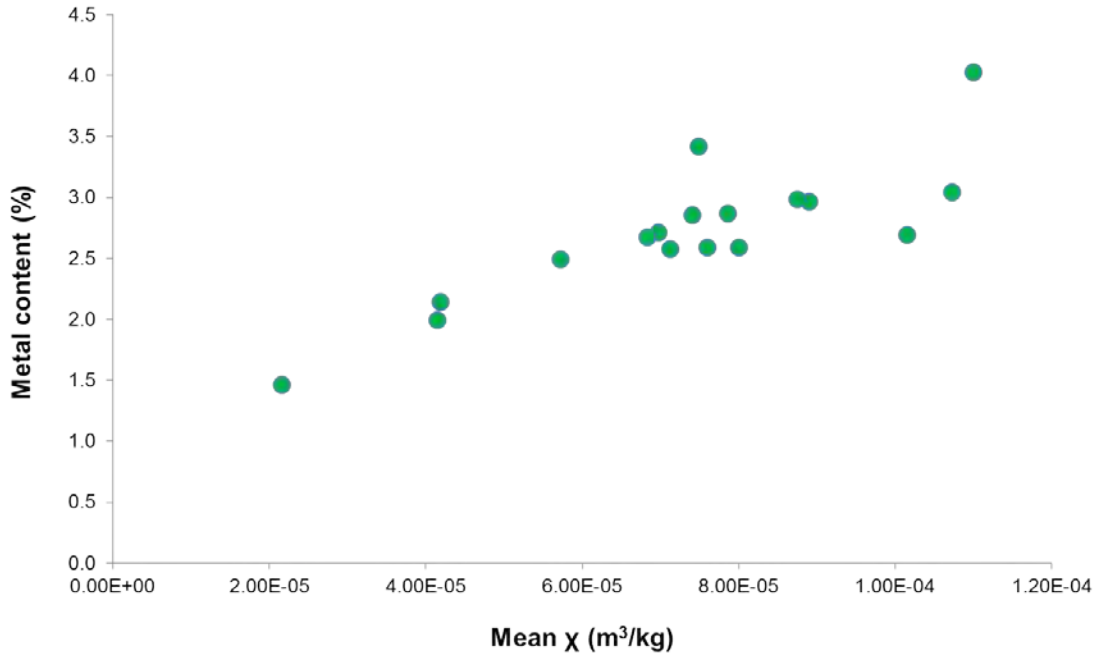

Figure 3.16. Metal content (from thresholding of XCT data – Table 3.6) against mean magnetic susceptibility of L chondrite samples in this study.

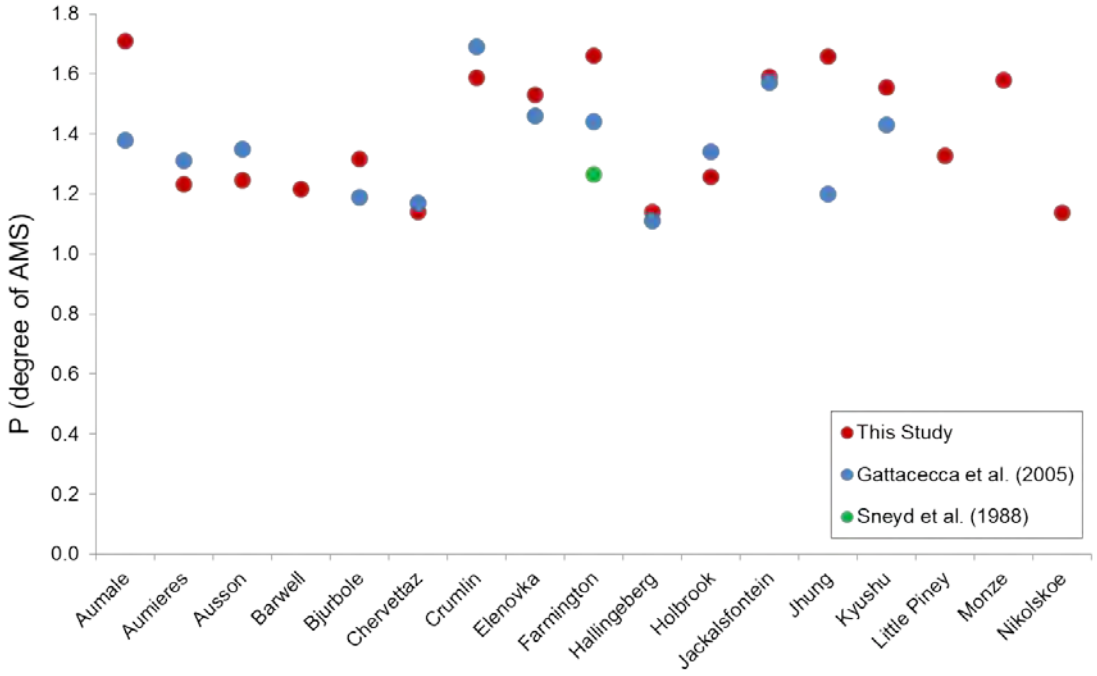

Figure 3.17. Degree of anisotropy of magnetic susceptibility, P, (defined as P = k1 / k3), compared with literature values for the same L chondrites.

Figure 3.17 shows the degree of AMS, P, defined as the ratio of major to minor axes of the susceptibility ellipsoid, for L chondrites in this study compared with literature values. Overall, the data agree well, indicating that foliation is consistent across different samples of the same chondrite. Two notable exceptions are evident: Jhung

and Aumale. As noted in *2.7.,* the physical shape of a sample is known to affect AMS measurements in H chondrites, therefore it is worth considering the effect in this case. The Aumale sample has fairly isotropic shape, therefore the variation in P may be natural (akin to that witnessed in three specimens of Farmington in Figure 3.17). The sample of Jhung used in this study was anisotropic, with an aspect ratio of ~ 2 in one orthogonal plane and ~3 in the other. This may account for the higher P. To understand the discrepancy, the data should also be interpreted with metal grain orientations from XCT and are discussed in the later section. Additionally, small samples may be less representative of a whole meteorite or may contain a few large metal grains that have a greater impact on the AMS.

3.3.6 Metal grain orientation of L chondrites

The collective orientations of metal grains provide an indication of the rock fabric and can be used to identify any foliation or lineation present. The terms used are more fully explored in *2.1.6. Data Analysis.* Briefly, R% is a measure of the similarity of the grain orientations, C provides the degree of anisotropy, K describes the shape of the distribution (<1 = girdle; >1 = cluster). Data are presented in Table 3.8, showing that the strength of fabrics varies widely, from no fabric observed in Hallingeberg (C = 0.185) to the strongest fabric in Monze (C = 1.196).

Figure 3.18 shows the results of metal grain analysis for meteorites with strong foliation fabrics, obvious in the orientations of their major axes, which fall along a great circle. It includes stereograms of major axes directions, density plots of the same data to more easily visualise the direction, and the major, intermediate and minor axes of the magnetic susceptibility ellipsoid. It is clear from Figure 3.18. that Aumale shows a strong preferred orientation of metal grains, indicating that the much higher value for P (degree of magnetic anisotropy) for this sample than Aumale in the literature (P = 1.38 (Gattacecca et al., 2005)), is likely due to sample heterogeneity. Similarly, Jhung (C = 0.77, lineation and foliation) exhibits a strong fabric in its metal grains, which could account for the high measurement of anisotropy in its susceptibility.

Meteorite	Pet. type	Shock stage	Grains >10 voxels (n)	R% (norm. mean vector metric)	C (strength parameter)	K (shape parameter)
Aumale	6	4	4733	19.5	0.836	0.314
Aumieres	6	4	7583	33.8	1.159	0.987
Ausson	5	3	4339	5.5	0.313	0.144
Barwell	6	3	3463	11.5	0.396	0.929
Bjurbole	4	1	7750	8.4	0.288	0.724
Chervettaz	5	3	1685	12.6	0.389	1.371
Crumlin	5	4	3027	16.2	0.749	0.194
Elenovka	6	2	2254	11.5	0.354	2.255
Farmington	5	4	2530	21.9	0.898	0.385
Hallingeberg	3	1	14745	5.5	0.185	0.986
Holbrook	6	2	8182	33.0	1.086	1.191
Jackalsfontein	6	3	5925	17.4	0.971	0.057
Jhung	5	2	2023	25.3	0.77	1.798
Kyushu	6	5	8777	21.2	0.946	0.266
Little Piney	5	2	3802	32.9	0.959	2.356
Monze	6	4	6962	36.3	1.196	1.107
Nikolskoe	4	2	3735	29.1	0.764	6.841

Table 3.8. Results of major axis orientation analysis of metal grains from XCT data of L chondrites in this study. R% is a normalised metric of the similarity of grain orientations; C describes the strength of the fabric (degree of anisotropy), and K describes the shape of the distribution (where <1 = girdle; >1 = cluster).

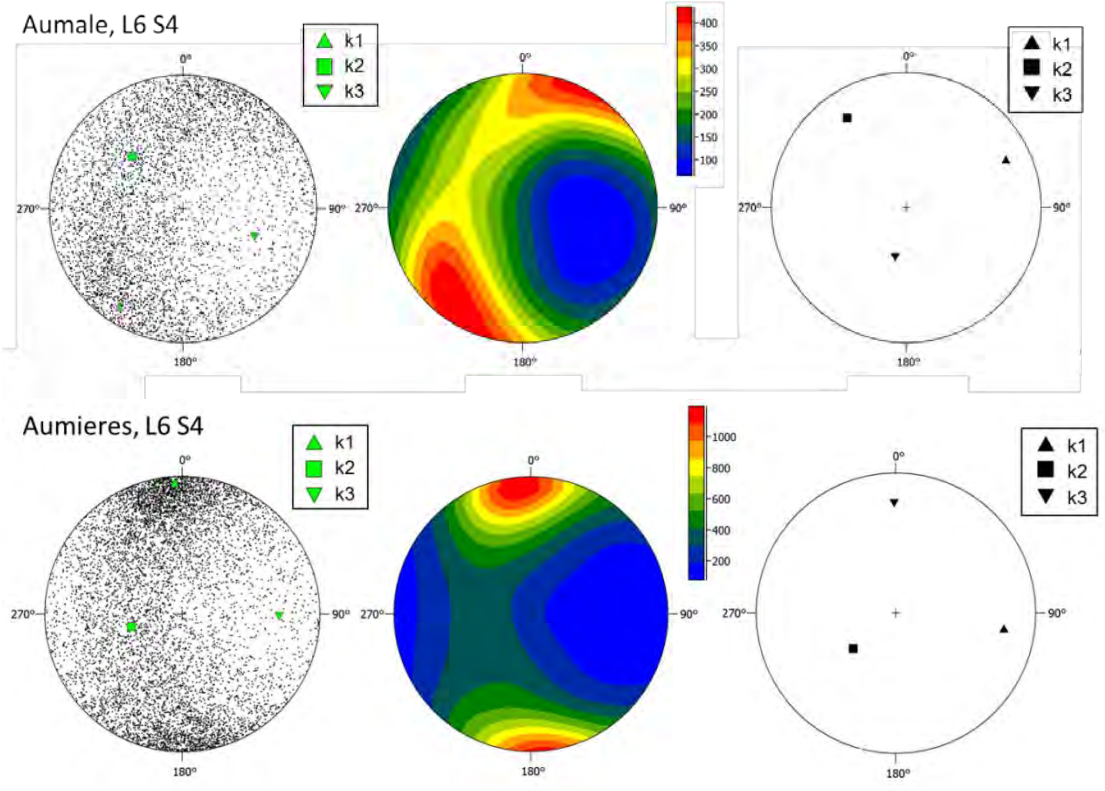

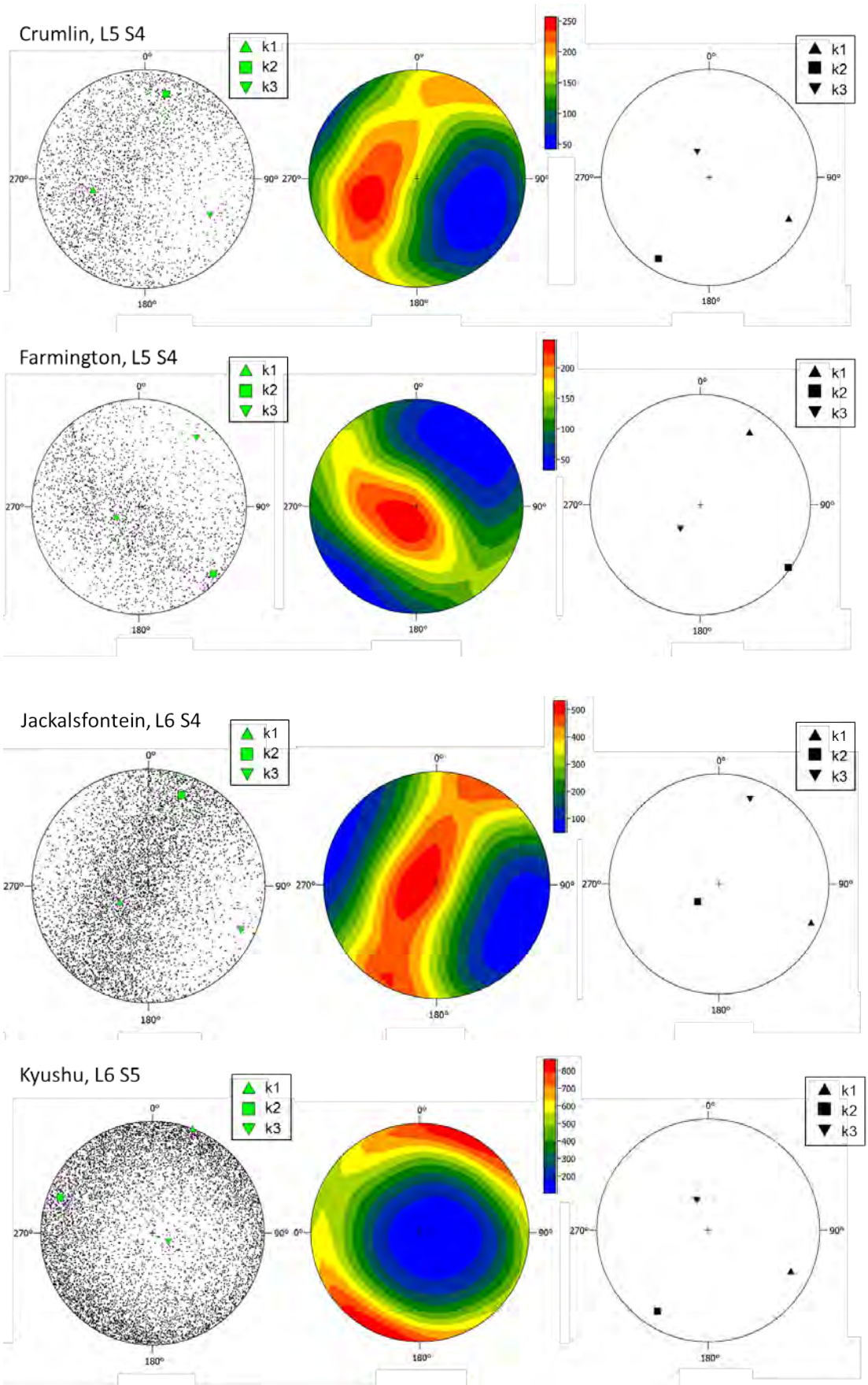

Figure 3.18. Data collected for the Aumale, Aumieres, Crumlin, Farmington, Jackalsfontein and Kyushu meteorites. Left: A stereogram of major axes of metal grains with mean eigenvectors k1, k2, k3; Middle: density stereogram of major axes; Right: k1, k2, k3 axes of the magnetic susceptibility ellipsoid.

Figure 3.19 illustrates the relationship between the degree of AMS and the degree of preferred orientation of metal grains from the XCT data, R%. Hallingeberg shows the least development of a fabric, both in AMS and in orientation of metal grains, fitting with its L3 S1 classification. In general, the graph shows a positive correlation between degree of AMS and R%, however there are exceptions, which are labelled individually in Figure 3.19. Those with the highest degree of preferred orientation of grains show lower than expected anisotropy in magnetics. These samples, Monze, Little Piney, Aumieres, Holbrook and Nikolskoe, are not more anisotropic in shape than other samples (images of each sample are included in *Appendix 6.* Furthermore, the effect of shape anisotropy is considered insignificant below an aspect ratio of 5 for L chondrites (Gattacceca, pers. comm. 2015).

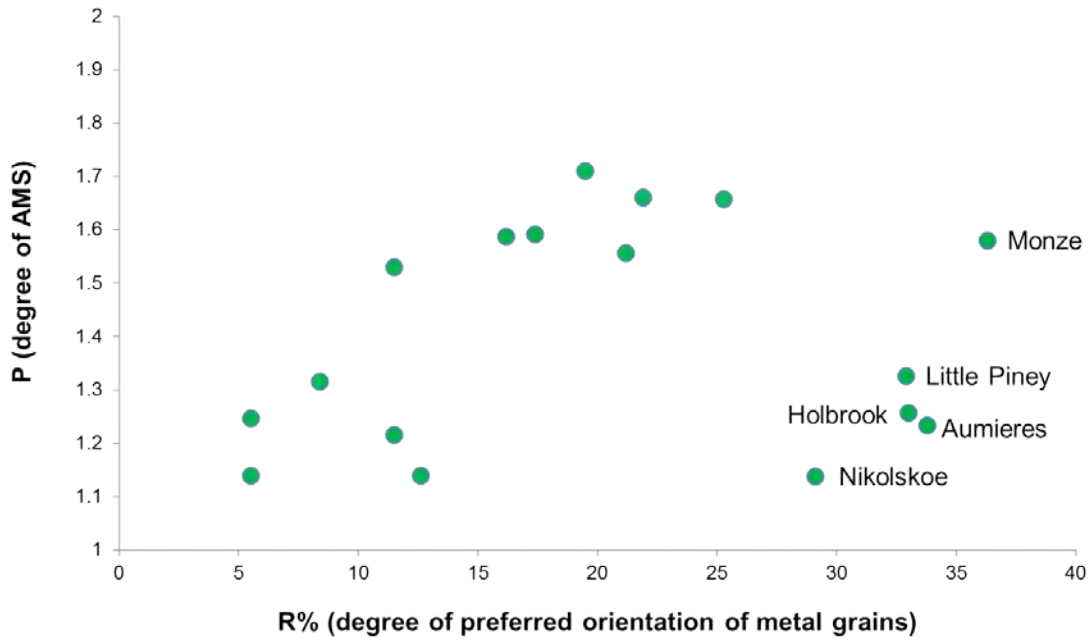

Figure 3.19. Degree of anisotropy of magnetic susceptibility (defined as P = k1 / k3) against mean normalized degree of preferred orientation of metal grains (defined as R% = R / n*100) for the L chondrites in this study.

Figure 3.20 illustrates that there is no discernible relationship between the degree of preferred orientation of metal grains (given by the strength factor, C) and petrological type for L chondrites in this study. However, the samples in this study were mostly types 5 and 6, and the sample number is small, therefore any relationship may be obscured.

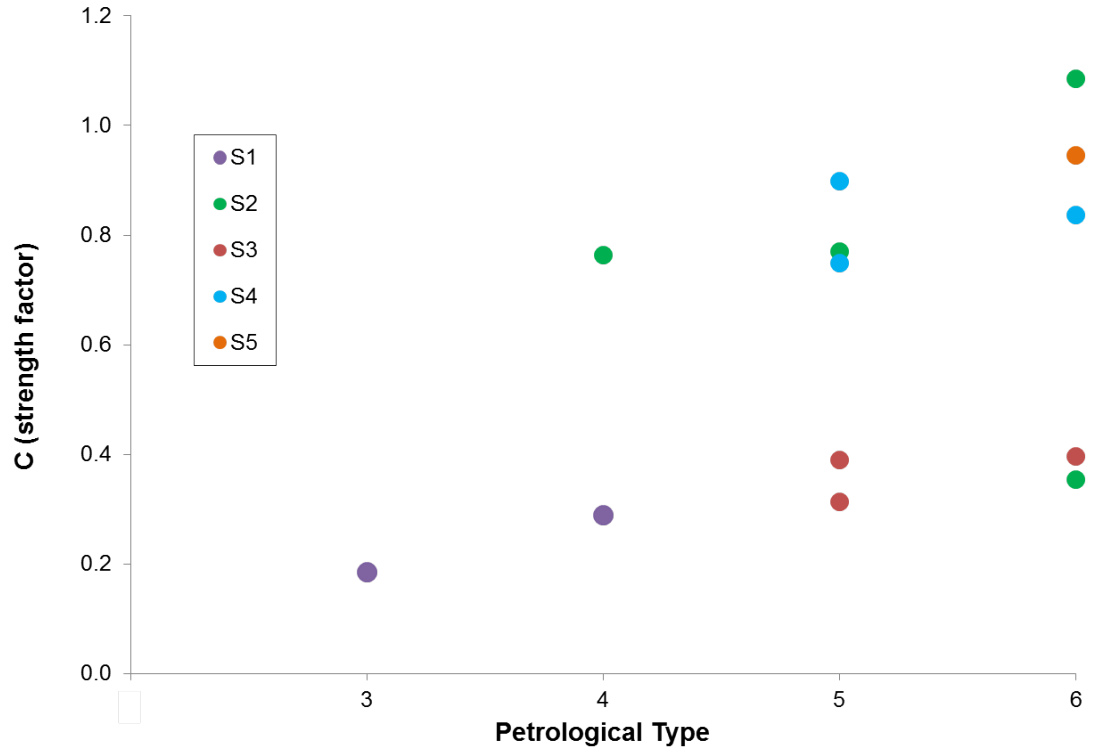

Figure 3.20. Relationship between C (strength factor) and petrological type for L chondrites in this study.

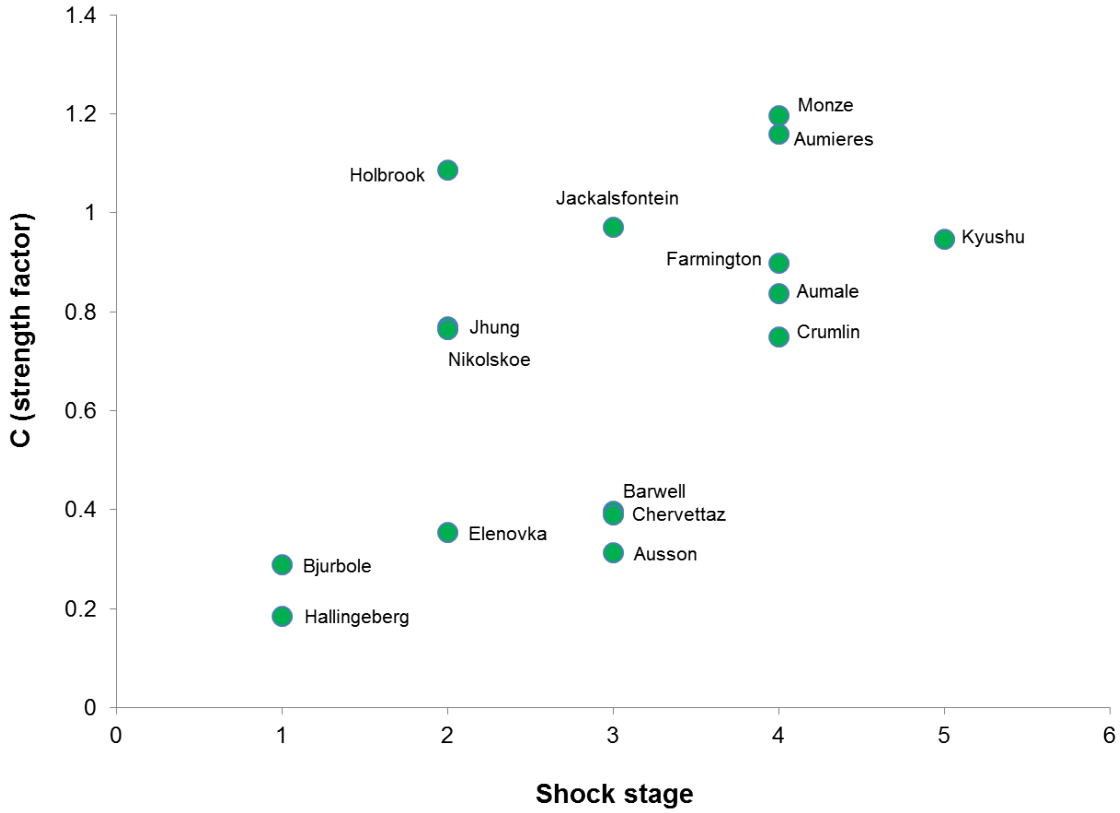

Figure 3.21. Relationship between C (strength factor) and shock stage of L chondrites in this study.

In contrast, Figure 3.21 illustrates the relationship between the degree of preferred orientation of metal grains given by the strength factor, C, and shock stage (from literature) for L chondrites in this study. The figure clearly shows that the higher the shock stage of the meteorite, the greater the degree of preferred orientation of metal grains. Jackalsfontein shows a high strength factor for its shock stage but as shown in Table 3.5, a high proportion (38%) of grains exhibited S4 features in thin-section (versus 50% S3). Similarly, Monze showed 43% S4, and 37% S5 grains, therefore it is likely intermediate between stages. Holbrook, Nikolskoe and Jhung (labelled in Figure 3.21) are outliers to the trend and these measurements are possibly the result of sample heterogeneity. Holbrook (L6, S2) has been suggested to exhibit evidence of brecciation, and shows areas dominanted by shock stages S2, S3 and S4 (Ruzicka et al., 2015).

Holbrook (L6 S2) shows a fairly weak foliation and lineation in AMS (P = 1.256, F = 1.045, L = 1.202), but in contrast, C = 1.086 and R% = 33, which indicates a strong preferred orientation in the metal grains. Figure 3.22 shows that the orientations of the metal grains match well to the AMS ellipsoid, and the density stereogram shows a strong orientation (the scalebar ranges from 100 – almost 1400). The data indicate both a strong lineation and foliation. It is possible this sample is from a similar region to that described as S4 by Ruzicka et al. (2015).

Nikolskoe (L4 S2) shows a low degree of AMS (P = 1.138, F = 1.012, L = 1.124), however, metal grain analysis indicates a strong fabric (C = 0.764, R% = 29.1). Figure 3.22 shows both metal grain and magnetic susceptibility orientations; the data indicate a strong lineation and a weak foliation. There is a slight rotation between the mean eigenvectors of the grains with respect to the magnetic susceptibility ellipsoid, likely due to the difficulty in physically matching the data sets, however they are in general agreement.

Jhung (L5 S2) shows a strong fabric in AMS measurements (P = 1.657, F = 1.187, L = 1.043) as well as in metal grain orientation analysis (C = 0.77, R% = 25.3). Stereographic projections are included in Figure 3.22. show a foliation fabric, although the magnetic susceptibility ellipsoid axes do not match, which is interpreted as a result of poor alignment of the data sets, rather than disagreement between the techniques. Since the value of R% is independent of the number of grains and the orientations of metal grains show a high degree of foliation, it is likely that the AMS measurements are accurate and not subject to inaccuracy due to sample shape

anisotropy as previously suggested. This indicates that this sample is not similar to that measured by Gattacceca et al. (2005), which showed a much lower degree of AMS. Furthermore, the sample in this study may be not similar to the section of Jhung used to classify shock stage, and it is possible that the meteorite is brecciated or experienced shock heterogenously.

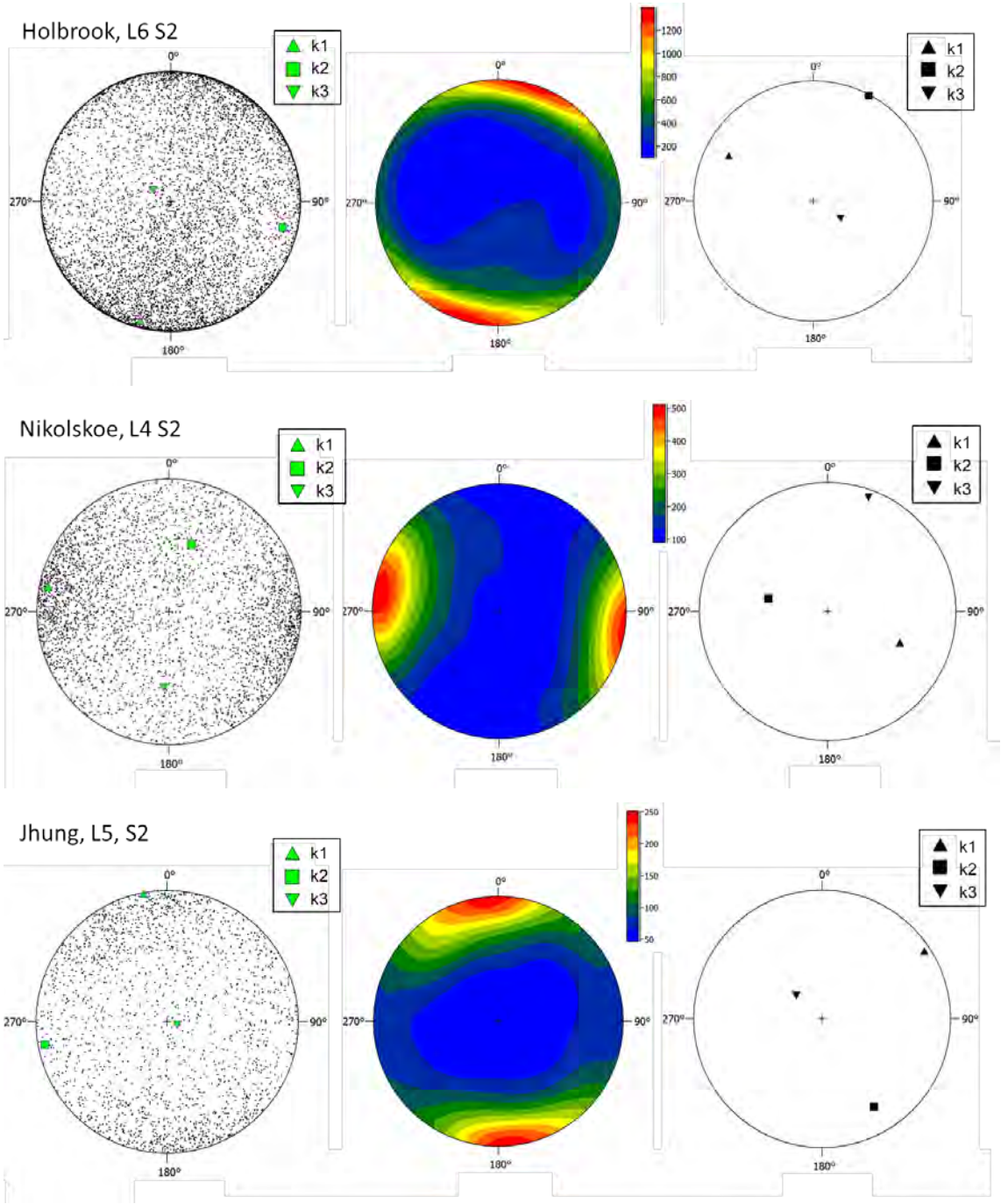

Figure 3.22. Data for outliers (Holbrook, Nikolskoe and Jhung) to trend between metal grain alignment and shock stage (Figure 3.21). Left: stereonet of major axes of metal grains with mean vector eigenvalues k1, k2, k3 plotted in green; Middle: density stereogram of major axes; Right: k1, k2 and k3 axes of the magnetic susceptibility ellipsoid.

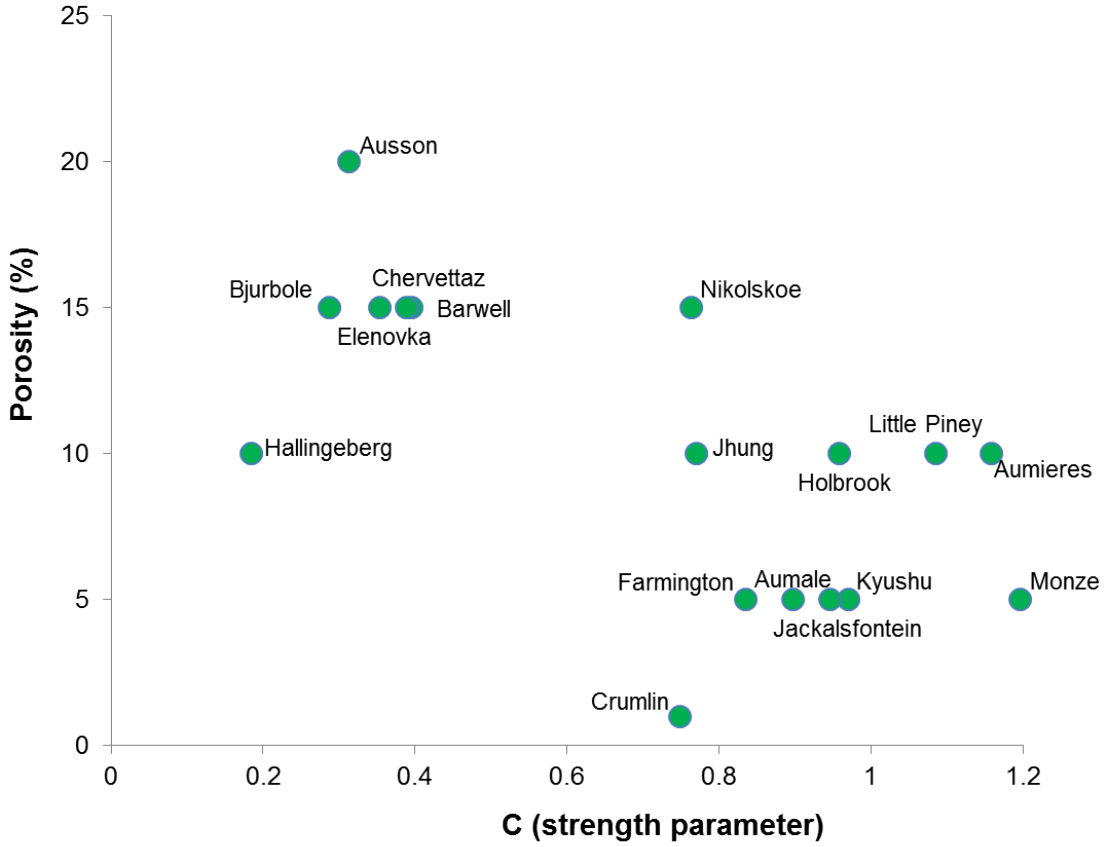

Figure 3.23. Averaged porosity against strength parameter for L chondrites analysed in this study.

Figure 3.23 shows the relationship between averaged porosity and strength parameter, indicating that where the foliation in a meteorite is more developed, the porosity decreases. Due to the lack of reliable accurate data for porosity, values obtained in this study have been averaged with literature values and quoted to the nearest 5%. This is not a precise measurement for porosity, but provides an approximate figure with which to assess the trend with metal orientation.

3.3.7 Metal grain shape of L chondrites

Figure 3.24 compares volume and anisotropy of metal grains in Crumlin (L5, S4), showing that small grains exhibit a wide range of anisotropy (from 0.2 – 1) whereas above ~ 1000 voxels in size (~ 70 μm^3 spherical equivalent) the grains have a more constrained range of anisotropy (> 0.5). Figure 3.25 shows the same graph for all L chondrites in this study, illustrating that metal grains tend to become more anisotropic with increasing volume, and that the trend is seen in all samples.

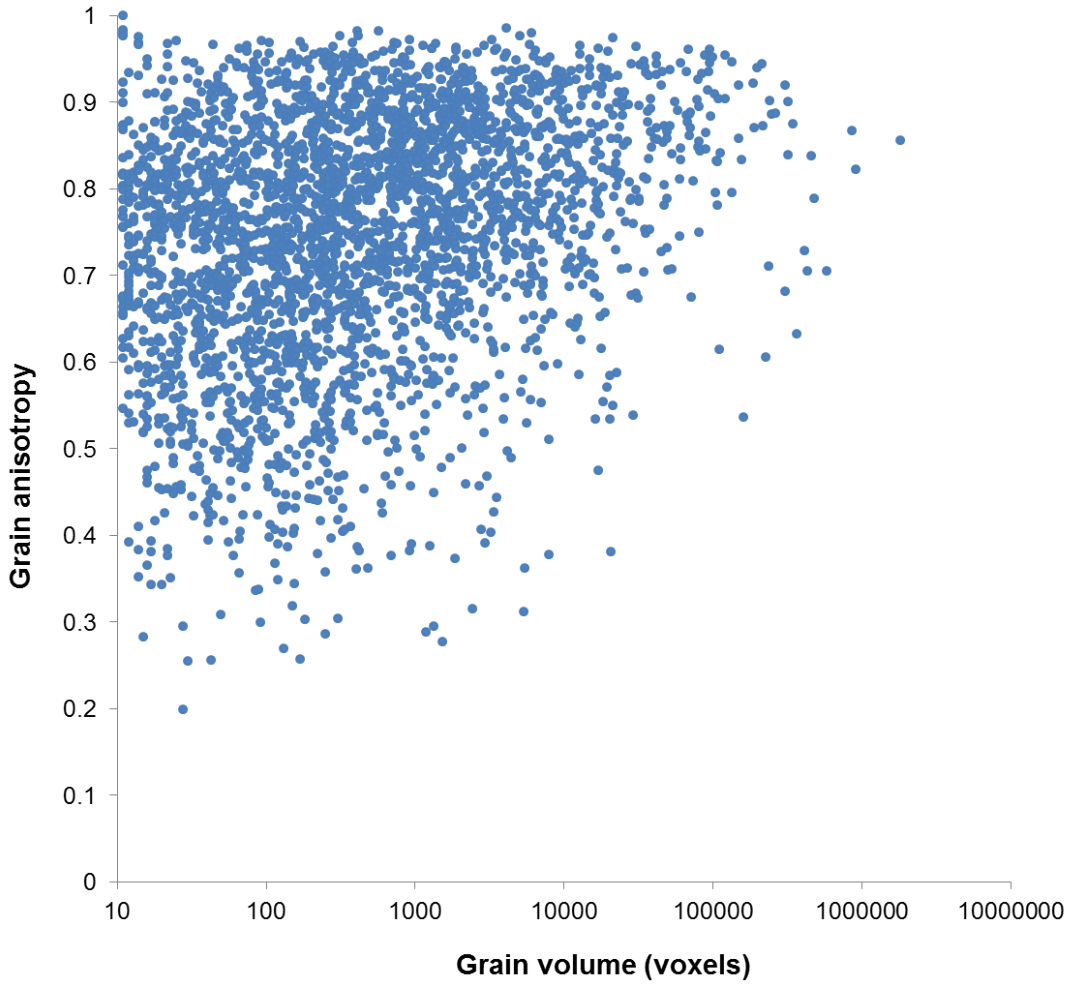

Figure 3.24. Anisotropy against volume for individual metal grains in the Crumlin (L5, S4) meteorite, illustrating that larger grains have a more constrained range of shape anisotropy.

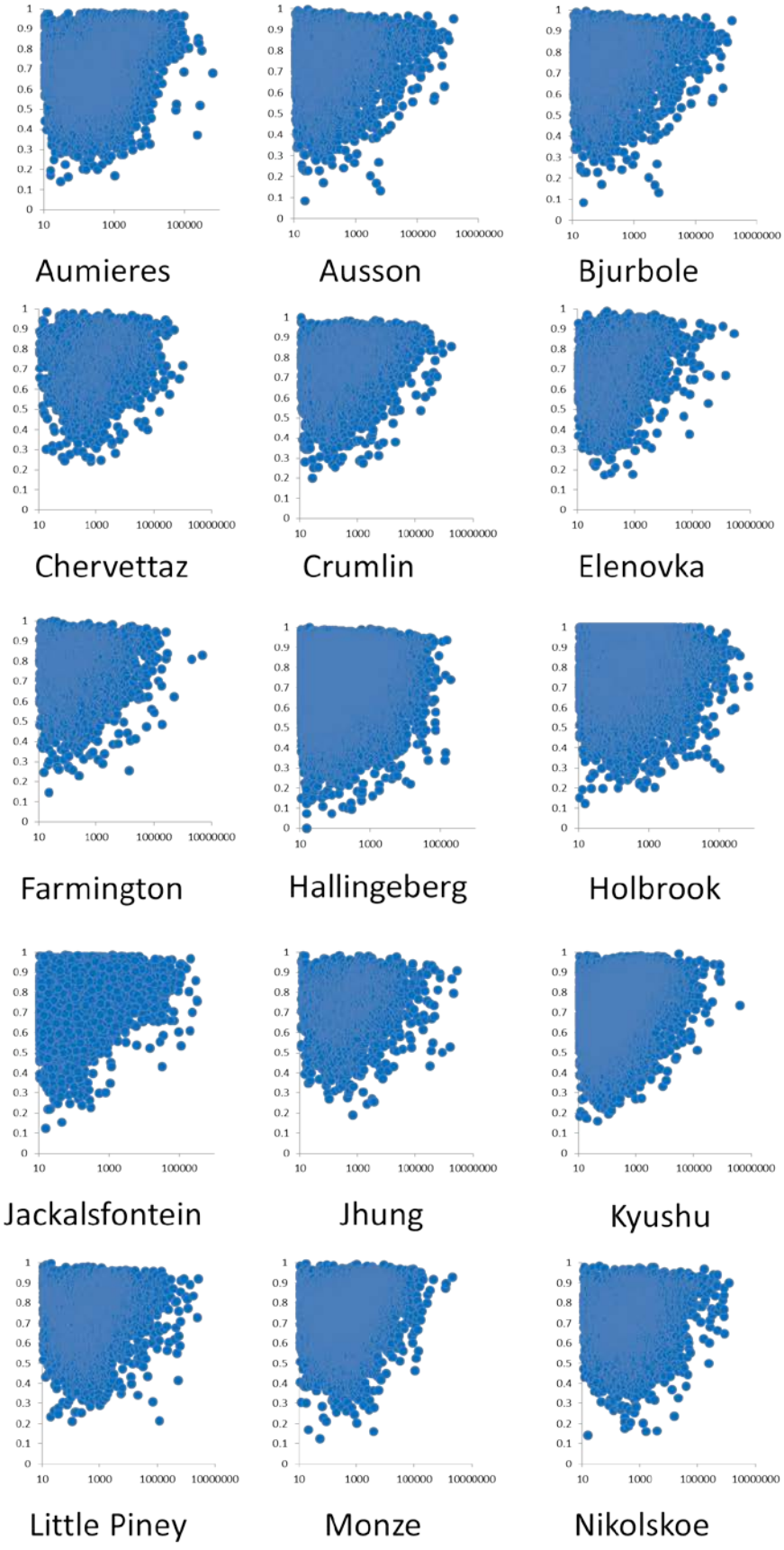

Figure 3.25. Anisotropy (y-axis) against grain volume (logarithmic in voxels on x-axis) for L chondrites analysed in this study. The trend is consistent across all samples, the range of anisotropy decreases with increasing grain size.

This can also be observed in renderings of individual metal grains, colour coded by anisotropy and volume, as shown in Figure 3.26.

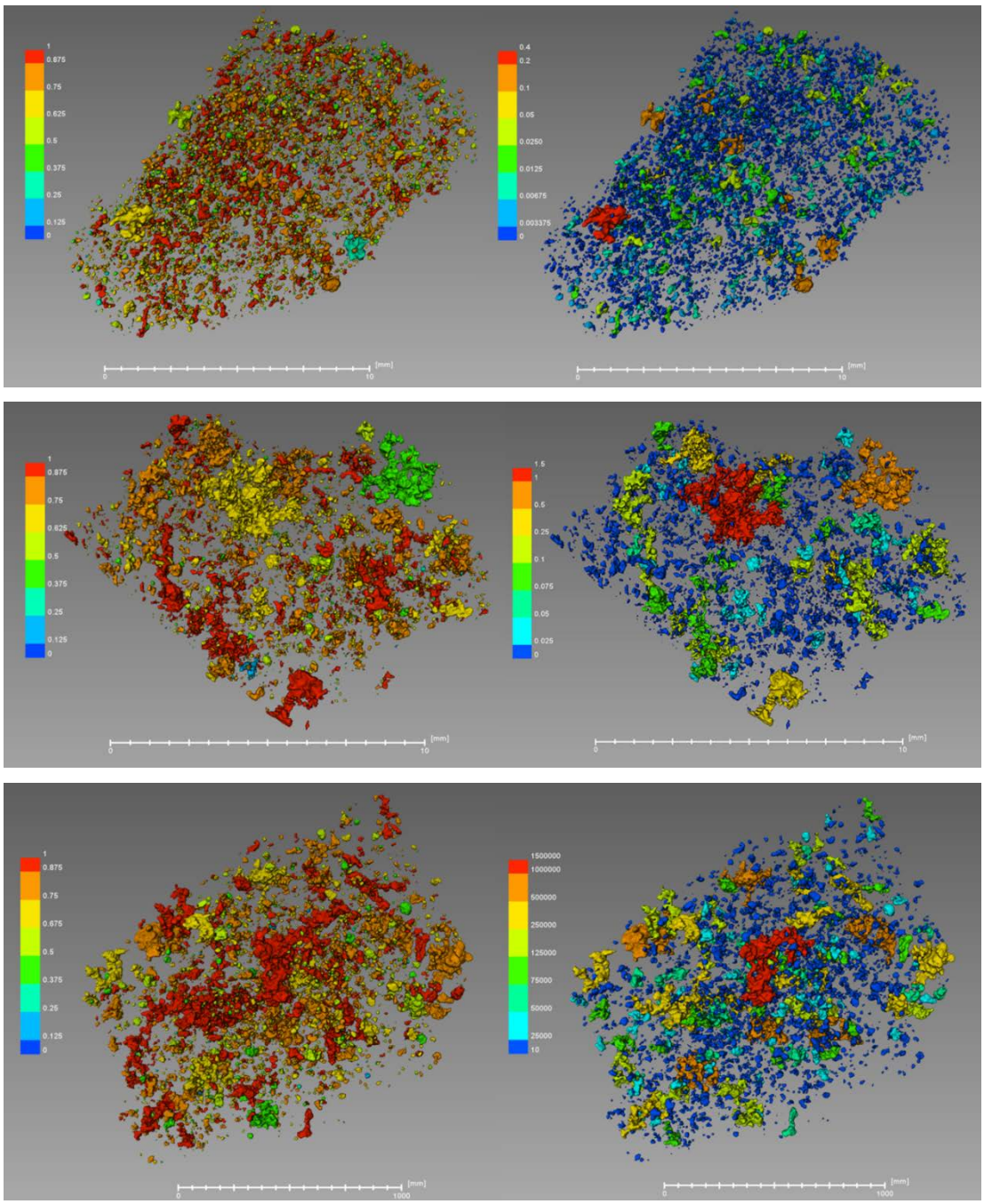

Figure 3.26. Visualisations of individual metal grains in three L chondrites: Aumieres (top), Barwell (middle), and Nikolskoe (bottom). On the left, grains are coloured by their shape anisotropy and on the right, by their volume.

The individual eigenvalues of the grains, i.e. representing the maximum, intermediate and minimum axes, can be used to describe the fabric of the meteorite. In Figure 3.27, metal grain axes in Crumlin (L5 S4) show a tendency towards prolate shapes, indicating a lineation, consistent with AMS measurements of L = 1.162.

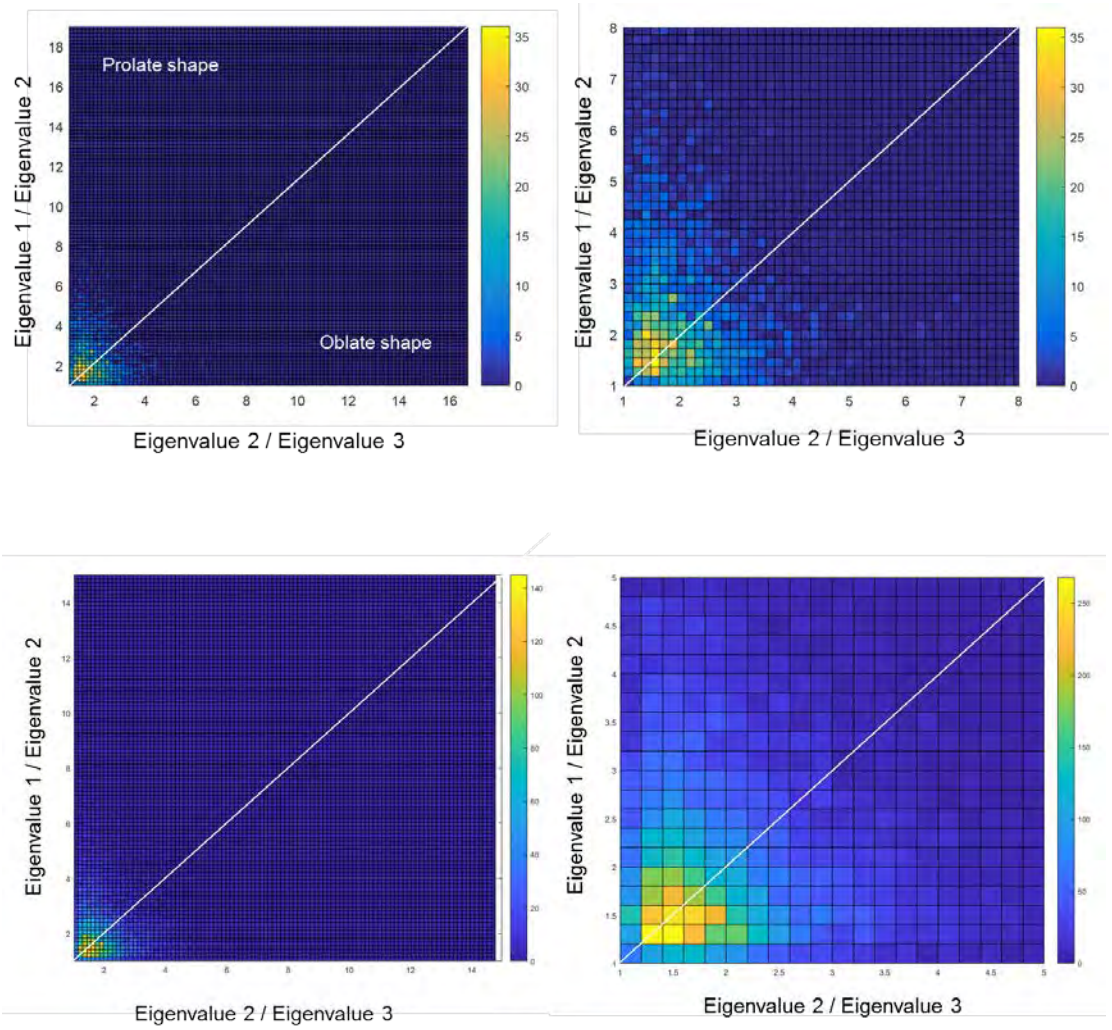

Figure 3.27. Ratios of maximum (eigenvalue 1) and intermediate (eigenvalue 2) axes plotted against ratios of intermediate and minimum (eigenvalue 3) axes of metal grains in the Crumlin L5 S4 meteorite, as segmented from XCT data. Left: full data set of 3027 grains. Right: cropped set that shows the majority of data points.

3.4 Discussion

3.4.1 Porosity

This study illustrates that XCT data with voxel sizes on the order of 5-10 µm cannot provide accurate quantitative measures of porosity in meteorites. This is particularly true for compacted meteorites which contain microcracks that are too thin to be segmented from the surrounding silicate material, but are often visible in the XCT tomograms and evident in SEM BSE imaging. There is a potential trade-off to achieve the resolution required to segment and quantify microporosity by using the

same methodology with a more advanced CT scanning system, e.g. the Zeiss Versa which can achieve a voxel size of 300 nm. However, the maximum sample size would be significantly reduced (< 3 mm) and hence even less representative than the ~1 g samples used in this study, especially in light of the diverse nature of porosity observed in ordinary chondrites.

The results do illustrate that XCT is a useful technique for characterising porosity in meteorites, demonstrating its ability to provide accurate and informed interpretations of porosity quantified by other techniques, but without the limitations inherent in 2D samples or potential errors introduced by sample preparation for thin-section analysis.

The study aimed to compare measurements of porosity by three different techniques in order to understand the strengths and weaknesses of the techniques and assess porosity present on different scales. The results indicate that helium pycnometry is not accurate for the sample size in this study. Grain volume measurements often took a long time to 'settle' or remained erratic. Similarly, calculated porosities were often negative, indicating inaccuracies in the measurements. In some cases, the techniques were successful in yielding results similar to those in the literature, however that alone does not imply reliability.

The results confirm that thresholding of SEM BSE images can illustrate and quantify the level of microfracturing present, which has been shown to account for 5-7% of total porosity by Friedrich and Rivers (2013). This could account for the disparity between porosities measured from XCT and SEM BSE data and may provide a measure for porosity below a certain size. For example, in the case of Bjürbole, gas pycnometry yielded a porosity of 16.9 ± 0.5%, compared with 19 ± 0.8% in SEM BSE thresholding, and 8.3 ± 1.3% in XCT data. Assuming the data are accurate, this would indicate that approximately 10% of the porosity is present on scales below the CT resolution (~ 10-15 μm), and potentially 2% of the porosity is unconnected to the rest of the pore network, and thus not accessed by helium during pycnometry.

The primary finding of this study is that no single technique is capable of accurately characterising porosity in ordinary chondrites, therefore a combined approach is suggested to exploit the benefits of each technique. Helium pycnometry on large samples is widely conceived as the most accurate quantitative measure of grain volume, yet the main errors arise from bulk volume by glass bead displacement.

Grain volume could be quantified using helium pycnometry on very large > 100 g samples, which are more representative. XCT could provide a more accurate, non-contaminating method for measuring bulk volume to combine with pycnometry for a numerical value of porosity, whilst also allowing for characterisation of the nature and three-dimensional distribution of void space and heterogeneity of the samples at varying scales. Although difficult to quantify, observations from XCT data indicate that, for most L chondrites the intragranular, unconnected pore spaces do not constitute a major proportion of the porosity.

These data also suggest that the sample sizes available within meteorite collections may be too small to allow meaningful determinations of the porosity of the parent body. Measurements of porosity vary widely between techniques, as well as between different samples of the same chondrite. One advantage of XCT would be to use virtual subsamples of a specimen to assess this heterogeneity. This inherent variability across samples seen in this study and others is compounded by the error involved in every method employed for measuring porosity. Some ordinary chondrites are likely to have been heterogeneously affected by metamorphism on a scale that means comparison between techniques carried out on different stones/samples may not be possible.

Measurements of bulk density were most similar to literature values where voxels sizes were close to an integer micron value. Whilst discrepancies could be due to specimen heterogeneity, errors in mass measurement, or errors in techniques used in the literature, there may be an error introduced when quantifying volumes using submicron voxel sizes. The data are insufficient to properly test this hypothesis, therefore no conclusion can be made, however it does indicate that testing should be carried out to constrain the errors involved. Ideally, volume measurements should be made using a calibration standard of known mass and volume, at different distances from the X-ray source (i.e. different voxel sizes) to constrain the resolution limitation of the scanner used.

Despite the many issues in the quantification of porosity, the data do support the general conclusion that porosity decreases with increasing shock loading, consistent with the literature (e.g. Gattacecca et al, 2005; Friedrich and Rivers, 2013). Since asteroids would likely have accreted with significant porosity and their small sizes meant that overburden was insufficient to cause compaction, it is broadly accepted that shock through asteroid collision was the key process in the lithification and

processing of ordinary chondrites. Large intergranular pore spaces, like those observed in incompletely compacted Chervettaz or Elenovka, would suggest that their parent bodies experienced only mild shock processing. Bjurbole and Hallingeberg appear to preserve primodial porosity around their chondrules having experienced little processing, either thermal or shock. On the other end of the scale, the lack of intergranular porosity in compacted specimens, such as Aumale or Kyushu, illustrates that from shock stage 4, the only pore space present is in shock-induced cracking.

3.4.2 Metals

This study indicates that metal grains can be used as markers of the temperature-pressure-time path experienced by L chondrites, as a result of their response to metamorphism and strain. Type 3 chondrites show the smallest ranges of grain volume, which is spread from the limits of the technique resolution to a maximum of 1.5 mm^3. There is a fairly linear size-fraction correlation in L5 samples of lower shock stages. With increasing petrological grade, size distribution curves move toward fewer larger grains, consistent with coalescence of metal due to heating. There is no clear trend with increasing shock stage, where the grain size distribution in L5 samples moves towards more small grains between S2 and S3 then reverses to move towards fewer larger grains from S3 to S4. This could represent communition of grains from S2 to S3 and coalescence due to melting from S3 to S4 but the sample size is too small to draw firm conclusions. A much wider survey of L5 chondrites, with well characterised shock histories (e.g. signs of annealing) would be required.

Guignard and Toplis (2015) suggested that mean metal grain size could be a quantitative measure of petrological type and possibly allow calculation of parent body burial depth. However, the data collected in this study show that the response of metal grains to thermal metamorphism is not simple coarsening. For example, although L chondrites show an overall increase in metal grain size up to type 5, there is a change towards smaller grains at type 6. The small number of samples in this study is a limiting factor, and it is possible that some specimens may be atypical, however the results indicate that more work is required before grain size can be considered as an indicator of degree of metamorphism. The data also show that many chondrites contain foliated metal grains, even at fairly low shock stages.

This highlights the bias in measuring the size of metal grains in two-dimensional sections, since most orientations will not sample the maximum diameter of a given grain.

There does not appear to be any clear trend in metal grain orientation with petrological type, however the samples in this study were predominately type 5 and 6, therefore additional samples are required for confirmation. There is a dominant trend of increasing preferred orientation of metal grains with increasing shock stage, with the most significant increase seen between stages S3 and S4. This finding agrees well with literature in which impact has been identified as the primary mechanism leading to foliation in chondrites (Gattacceca et al. 2005, Friedrich et al. 2008a, Friedrich et al., 2016 and references therein).

Despite the general trends observed, there are complexities in the history of every chondrite. For example, Jhung (L5 S2) does not fit well to other L5 S2 grain size distribution curves (including several large grains ~ 1 mm^3), exhibits a strong fabric in metal grain orientations and shows a high degree of AMS. This could indicate that Jhung may have experienced a much higher shock pressure but subsequent annealing (causing healing of olivine crystal lattice and so on) has led to a classification of S2 based on silicates. Alternatively, the sample of Jhung used in this study may have experienced a higher degree of shock than that represented in the thin section used for shock stage classification.

Rubin (2002, 2003, 2004) showed significant evidence for many equilibrated OCs that are classified as shock stage S1 (based on sharp optical extinction in olivine) as having been previously shocked to stages S3 to S5 but subsequently annealed to S1, potentially by heating in the same impact event as caused the shock (and similarly potentially causing the thermal metamorphism to a higher petrological type). This evidence includes features such as chromite-plagioclase assemblages, silicate darkening, glassy silicate melt veins, plessite and others. It stands to reason that the three-dimensional shape and orientation of metal grains may similarly retain evidence to constrain the shock history of a chondrite. This may be the case for Jhung and Holbrook, both classified as S2, but exhibiting high strength factors in their metal grain orientations and appearing compacted in CT images.

It should be noted that correlating between AMS and degree of orientation of metal grains is not simple for samples that are irregular in shape, as rotations can be

introduced during sample preparation and even data sets matched well using registration software show slight misalignments. Additionally, the study should be widened to larger specimens since smaller samples may be less representative of a meteorite as a whole, or may contain a few large metal grains that have a greater impact on the AMS. Regarding metal grain shape, although the best fit ellipsoids prove effective at representing the orientation of major axes and thus illustrate the presence of foliation, the grains are typically complex in shape and new methods and software must be developed for their analysis, e.g. those explored by Friedrich (2008).

The wide variation in the degree of metal grain orientation within shock stages, and the variability of correlation with porosity and shock in silicates, also indicate that it is likely that the shock histories of these chondrites are complex and involved several impacts that led to brecciation on various scales. Many of the samples show evidence of a lineation fabric, which may be caused by multiple impacts and/or non-coaxial strain experienced during impact (Gattacceca et al., 2005). The location of the metal grain with respect to the path of the impactor may also play a role. Where porosity is not correlated to strength factor, e.g. the porosity is low but foliation is weaker than expected for compacted material, other factors should be considered. If the chondrite was shocked at an early stage when the parent body was still hot from endogenous radioactivity, then the material would have compacted more efficiently than shock in a cold medium. Similarly, if the meteorite experienced post-shock annealing, the current shock stage recorded by silicates would be reduced, and foliation in metals may be weakened (Friedrich et al., 2016).

This study suggests that the examination of silicates in thin-section and quantitative measures of porosity are likely insufficient indicators of the shock history of a meteorite. Rather, it suggests that a combined interpretation of several aspects of chondrite petrography is required to understand the meteorite history. XCT is a crucial technique in this characterisation, providing data from which the nature of porosity, shape and orientation of metal grains, and heterogeneity of a specimen can be assessed.

3.5 Future Work

The study would benefit from widening to a larger sample size including a wider range of chondrite falls, particularly of shock stages 1, 5, and 6 to further clarify the trend. Specifically, ordinary chondrites of very low petrological types (<3.5) would provide the best representation of metal grains directly derived from the nebula and provide a baseline for analysing shape and size with respect to metamorphism. The same methods employed in this study could be applied to H chondrites. A such, we have already collected XCT, AMS and He pycnometry data for 20 H chondrites (Almeida et al., 2014).

With regards to porosity and bulk density measurements, the volume of the same samples should be measured by the glass bead method (cf. Macke, 2010; Britt & Consolmagno, 2003; and others) to independently estimate the accuracy of the XCT segmentation method. Similarly, a calibration of XCT instrumentation is suggested. Using a standard of known mass and volume, scanned at different voxel sizes, would allow calculation of the inherent instrumental error when quantifying size parameters from CT data.

Petrological examination of meteorite sections from the same samples that were CT scanned would enable shock stage classification of the relevant piece of meteorite, removing any inaccuracy from sample heterogeneity. Transmission electron microscopy (TEM) would allow for characterisation of dislocation density and other microstructures in olivine which can further elucidate the degree of shock experienced, as well as providing evidence of microstructural recovery by annealing (e.g. presence of subgrain boundaries), as seen in Kernouve, Portales Valley and MIL 99301 by Ruzicka et al. (2015). Evidence for shock deformation at elevated temperatures is also possible using TEM (e.g. Ashworth, 1985).

Radiometric dating using the ^{40}Ar-^{39}Ar system indicates significant shock events experienced by the meteorite as it is especially sensitive to impact metamorphism (Turner, 1988), whereby degassing due to shock and post-shock thermal overprinting can cause diffusive loss of ^{40}Ar. The timing of shock events relative to thermal metamorphism on the ordinary chondrite parent bodies, which is thought to have lasted approximately 100– 200 Ma (Bogard, 2011), can provide context for the interpretation of petrological indicators of shock in these meteorites, i.e. whether

shock occurred before (and thus material was potentially annealed) or during (thus potentially the material was warm) thermal metamorphism.

Interpretation of metal grain orientation and porosity data in light of TEM and radiometric dating would further elucidate the impact histories of these meteorites, especially those appearing incompletely compacted and allow determination of whether porosity is ancient, i.e. remnant of accretion, or impact-induced more recently, cf. the work by Friedrich et al. (2014), providing more understanding of the role of impact in the evolution of the ordinary chondrite parent bodies.

Guignard and Toplis (2015) described iron-rich phases (i.e. metal and sulphide) as more intimately related at lower petrological types but more independent with progressive metamorphism. This concept could be testing using the data set created in this study, by quantifying the contact between sulphide and FeNi metal grains in the samples.

Thorough analysis of metal grain size distributions with increasing metamorphism could provide insight into the segregation of metal phases from silicate portions of parent bodies. Widening the methods employed in this study to primitive achondrite meteorites, which have progressed further in planetary differentiation than metamorphosed ordinary chondrites, would further our understanding of the mechanism of metal-silicate separation.

The XCT data of Farmington showed large pores possibly associated with metal grains. Further exploration of this spatial relationship may glean information on the pore-forming mechanism, i.e. if they are the effect of shadowing from a shock pulse, as predicted by models of Bland et al. (2014).

Since the difficulty in understanding porosity and metal grains in chondrites comes from a lack of knowledge of the starting material characteristics and degree of shock loading experienced, artificially shocking a well-studied sample (i.e. porosity examined by many techniques, metal grain size distribution quantified), at known pressures, would allow examination of the effect on shock on these parameters. This could also be conducted at different orientations to examine the effect of impact direction on the resultant fabric.

4 Igneous Inclusions in Barwell

This study uses micro-CT to determine the abundance of unusual inclusions in the Barwell (L6) meteorite. Such data can indicate where a sample should be cut to expose the inclusions, which can then be investigated to determine their origin and relationship to the bulk meteorite. Igneous-textured inclusions in ordinary chondrites have previously been investigated to provide evidence for early differentiation, timing of thermal metamorphism, and implications for impact history and mixing in the early Solar System.

4.1 Previous work on inclusions in chondritic meteorites

4.1.1 Foreign inclusions in chondrites

Previous work has shown that mixing of material between parent bodies was prevalent in the early Solar System (e.g. Bridges and Hutchison, 1997; Ruzicka et al., 1995, 1998, 2000, 2012). In the literature, the terms clast, inclusion, lithic fragment and xenolith are all used somewhat interchangeably. In this study, such terms are used to describe objects which appear different to the host rock, for example, are larger in size than constituent chondrules. Carbonaceous chondrite fragments have been reported in a variety of other meteorite types, for example ordinary chondrites (Fodor and Keil, 1976), HEDs (Buchanan et al., 1993), and lunar meteorites (Joy et al., 2012). Several authors reported inclusions in ordinary chondrites, some are microporphyritic impact melt clasts, whereas others exhibit textures ranging from quenched glasses to fully crystalline material (e.g. Rubin et al. 1981; Ruzicka et al., 1995 and 2016; Krot and Wasson, 1994; Corrigan and Lunning, 2016 and references therein; Mayeda et al., 1987; Bridges et al., 1995).

Bridges and Hutchison (1997) estimated that metal- and sulphide-poor inclusions occur in ~4% of ordinary chondrites. Several cm-sized igneous-textures inclusions with O isotopes close to equilibrated H chondrites have been found in a variety of L chondrites. For example, Bovedy (L4) contains both a clast with heterogenous

silicates, thought to have formed by impact melting of a chondritic source (Rubin et al. 1981) and a silica-rich orthopyroxenite inclusion (Ruzicka et al., 1995). Y75097 and Y793241 (both L6, possibly paired meteorites) contain olivine-rich clasts, where the olivine is similar in composition to equilibrated L chondrites (Clayton et al., 1984.; Mayeda et al., 1987). Furthermore, the clast within Y793241 contains a relict chondrule, implying a chondritic source (Prinz et al., 1984).

Such inclusions have been investigated by optical microscopy, oxygen isotopes, Ar-Ar dating and trace element composition, to identify their origin and formation mechanisms. Bridges and Hutchison (1997) classified clasts into four groups: macrochondrules (showing similar textures to chondrules, varying only in size), chemically fractionated (i.e. considerably different to chondritic mineral assemblages), microporphyritic (finer in grain size than chondrules and showing no evidence for shock or impact formation), and impact melt (after descriptions by Rubin, 1985 and Stöffler et al., 1991), with those outside these definitions described as indeterminate.

Ruzicka et al. (1998) used the chemistry of large igneous inclusions to separate them into Na-rich (superchondritic abundances of volatiles Na, Mn, K and Na/Al > 0.35 atomic) or Na-poor (sub-chondritic abundances of Na and Na/Al ≤ 0.35 atomic). They suggested that Na-rich inclusions formed through shock-melting, as their compositions overlap with melt-pocket-glasses formed through localised shock-induced melting described by Stöffler et al. (1991), whereas Na-poor inclusions are thought to have originated through melting of vapour-fractionated mixtures.

Armstrong and Ruzicka (2015) described the petrography and major element chemistry of 29 igneous-textured inclusions in ordinary chondrites, finding that none were derived from an igneously-differentiated source. They divided them into three chemical groups: unfractionated, vapour-fractionated, and feldspar-enriched. Based on observations of melt pockets and shock experiments that indicate preferential melting of feldspar, they propose that inclusions exhibiting a pronounced enrichment in potassium are derived from shock melted material. They also found a subset of inclusions which crystallised as free-floating droplets in space, and suffered vapour-fractionation, as evident in lower (Na+K)/Al ratios, resulting from loss of volatiles Na and K. Oxygen isotope measurements of unfractionated inclusions tend to be similar to those of ordinary chondrites, consistent with an impact melt origin (Ruzicka et al., 2016). Vapour-fractionated clasts have been shown to have low $\Delta^{17}O$ values,

suggesting a distinctive process or provenance, possibly exchange with nebular gas (Ruzicka et al., 2016).

Impact melt clasts are formed by impact melting on chondrite parent bodies (e.g. Rubin et al., 1981; Rubin, 1985; Wloztka et al., 1983; Stoffler et al., 1991; Corrigan et al., 2016) and usually have a chondritic bulk composition. They show signs of shock, including glassy veins and undulose extinction in olivine, with a fine-grained groundmass including pyroxene, plagioclase, interstitial glass, globules of FeNi metal, troilite and schreibersite (Corrigan and Lunning, 2013). Corrigan et al. (2012, 2015 and references within) are conducting a systematic classification of clasts in ordinary chondrites to fully characterise this material and to date them using the Ar-Ar system, which is reset by shock.

4.1.2 Origin of foreign inclusions and their formation processes

Understanding the origin and history of foreign inclusions can provide insight into mixing in the early Solar System. Various formation processes have been suggested for igneous-textured silicate inclusions, including differentiation of the chondrite parent body (Hutchison et al., 1988; Ruzicka et al., 1995), chondrule formation with notably large volumes of melt (e.g. Weisberg et al. 1988), melting of vapour-fractionated condensate mixtures (Ruzicka et al., 1998; 2000; 2016), and shock-melting of ordinary chondrite material and associated loss of the metal/ sulphide portion (e.g. Fodor and Keil, 1976; Dodd and Jarosewich, 1976; Jamsja and Ruzicka, 2010).

It has been suggested that some lithic fragments may retain evidence for early igneous differentiation, such as the original Barwell 'Pebble' (Hutchison et al., 1988), also a microgabbroic fragment in Parnallee (Kennedy et al., 1992) and others (e.g. Bridges et al., 1995; Bridges and Hutchison, 1997; Krot and Wasson, 1994; Ruzicka et al, 1995). The role of impact, alongside radiogenic sources, as a cause of heating for planetary differentiation is still not fully understood. Ruzicka et al. (1995) interpreted the texture, form, size and composition of the Bo-1 clast in Bovedy (L3) to indicate that metallic and silicate partial melts were lost during heating by radionuclides or by electromagnetic induction. Ruzicka et al. (2012) described chemical similarities between igneous inclusions in the Buzzard Coulee H4 meteorite and silicate inclusions in IIE and IVA iron meteorite groups. The authors

infer that the inclusions formed through igneous differentiation, with compositions fitting models of a cumulate formed by concurrent crystallisation of low-Ca pyroxene and cristobalite (Ruzicka et al. 2012).

Accretion and differentiation may pre-date or have been contemporaneous with chondrule formation (Kleine et al., 2005; Bizzarro, et al. 2005) and chondrite parent body formation could have been a multi-stage process when ^{26}Al may have been sufficiently abundant to facilitate differentiation of achondrite parent bodies (Bizarro et al. 2005; Huss et al., 2001). During increased impact activity, differentiated material, metamorphosed fragments, and chondritic melt clasts would have been ejected and incorporated into chondritic parent bodies. The discovery of material that has experienced high-grade thermal metamorphism, e.g. granitoidal and andesitic fragments in primitive chondrites Adzhi Bogdo (Bischoff et al., 1993) and Study Butte (Sokol and Bischoff 2006), supports the growing evidence that chondrite meteorites have a complex history involving previous generations of planetesimals, parent body modification and metamorphism, disruption, and reaccretion (Sokol et al., 2014).

Some large chondrules have textures and mineral assemblages similar to normal chondrules, indicating a common origin, and may be more common than studies have suggested, as fragments of broken macrochondrules may be 'disguised' in chondrite matrix (Weisburg et al. 1988). If some igneous inclusions are indeed large chondrules, identifying the range of sizes may shed some light on chondrule formation and add an important constraint on models of such (Gooding, 1983). Weisberg et al. (1988) suggested that macrochondrules are unusual in size as they originated in very dust-rich areas of the nebula, or regions with a greater dust/gas ratio, and/or a higher electrostatic attraction between particles, i.e. when there was more material to melt, or a higher probability of molten droplets colliding. Such macrochondrules would have remained molten for longer than typical chondrules (Weisburg et al. 1988; Weyrach and Bischoff, 2012).

The peak in ages of melted Solar System material at 3.9 Ga is of particular interest in Solar System evolution, as it may represent either a giant cataclysmic event that caused widespread resetting of isotopic chronometers, or a peak that represented the end of a decrease in impact cratering (Corrigan et al., 2012; Gomes et al., 2005; Kring and Cohen, 2002). The dating of impact melt clasts can provide insight into

mixing between ordinary chondrite parent bodies and the effect of impact bombardment and small body scattering on the asteroid belt.

4.1.3 The Barwell meteorite

Barwell, an equilibrated L6 chondrite, fell as a shower of stones, totalling 44 kg, in Leicestershire, UK, on Christmas Eve, 1965. The Barwell "Pebble" refers to an object found within one stone that carries the isotopic signature matching H-group chondrites while exhibiting the texture, mineralogy and trace element concentrations of an igneous rock (Hutchison et al., 1988). It is a dark grey object, 15 by 12mm in cross section, protruding about 10mm from a flat broken surface on one piece of BM1966, 59. The cracks surrounding the "Pebble" show that it is not welded to the main mass.

In Hutchison's original study, the object was cut and two polished thin sections (total area 2 cm^2) were made. Olivine (Fo 75.5) is the dominant mineral, occurring as elongate euhedral crystals up to 1.0mm long (although in one extreme case, 4.0mm) or as subhedral grains 0.2 – 1.0mm in diameter. The mean grain-size varies randomly from one area to another. Between the olivine crystals lie dark brown to opaque, turbid plagioclase crystals 0.1-0.4 mm long, with a length to breadth ratio of 6:1 or more. These are often surrounded by a granular mosaic of clear, crystalline plagioclase. The elongate turbid crystals may occur as groups with a sub-parallel alignment, individuals being separated from each other by clear plagioclase. The turbidity is due to the presence of innumerable tiny voids. The plagioclase composition is described as An 74-70 in the centre of the inclusions and An 20 towards the margin. There are three almost parallel fractures, visible on the sawn face of the "Pebble", that do not continue into the host rock. This igneous-textured "pebble" also exhibits oxygen isotopes indicative of an H chondrite parent body (Figure 4.1) (Hutchison et al., 1988).

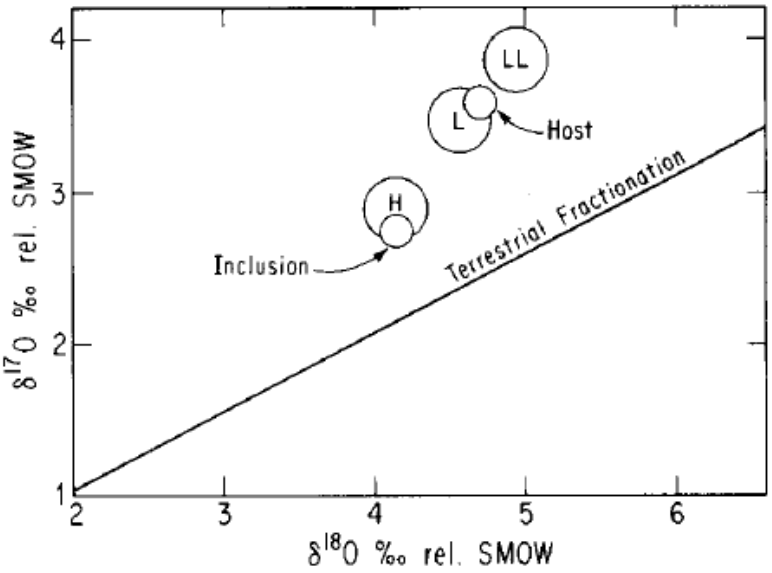

Figure 4.1. A three isotope plot for oxygen for both host and inclusion compared to ordinary chondrite fields, from Hutchison et al. (1988)

I-Xe dating has shown very similar ages (~4566Myr) of these clasts and the bulk Barwell material (Crowther et al. 2014). Ar-Ar, Pb-Pb, and U-Pb ages are close to 4.5 Ga which indicate that this meteorite has remained thermally unaltered (Unruh et al., 1979). The presence of these objects supports the paradigm of an early generation of differentiated planetesimals, indicating that complex processes were occurring at the same time as chondrule formation.

Bridges and Hutchison (1997) described a further seven clasts in the Barwell meteorite. Five they described as macrochondrules, three as indeterminate (including the Pebble from Hutchison et al.,1988). Table 4.1 provides descriptions on the inclusions as described by Bridges and Hutchison (1997). Macrochondrules are described as porphyritic (olivine, albite, enstatite) (2); barred olivine and porphyritic (olivine, albite) (4); barred olivine with enstatite and albite (5); coarse porphyritic (olivine, albite, apatite, clinopyroxene) (6); porphyritic (olivine, enstatite, albite) (7). Indeterminate clasts are described as porphyritic, skeletal (olivine, pyroxene, chromite) (1); olivine grain enclosing enstatite and albite (3); Barwell Pebble described by Hutchison et al. (1988): olivine-plagioclase cumulate (olivine, anorthite, albite, apatite, chromite) (8). Ruzicka et al. (2000) classified the Barwell 'Pebble' as a Na-poor inclusion, however supposed that the relatively high Na/Al value is due to metasomatism event which enriched the margins of the inclusion.

Number in Study	Specimen	Section	Type	Size (mm)	Appear-ance	Weight (before sectioning)	Petrography	Mineral compositions	d17O, d18O	Other
1	1985,M68	P5174	indeterminate clast	10	rounded clast	1.63	porphyritic skeletal olivine, pyx, cr	Fo75	2.9, 4.6	Ar-Ar 4.48 Ga
2	1985,M68	P5206	macrochondrule	3		0.18	porphyritic ol, ab, en	Fo75		
3	1985,M68	P5175	indeterminate clast	5		1.05	ol grain enclosing en, ab	Fo75		
4	1985,M68	P5203	macrochondrule	5		0.8	barred ol and porphyritic, ol, ab	Fo75		
5	1985,M71	P5202	macrochondrule	4		0.13	barred ol, en ab	Fo75		
6	1985,M68	P5207	macrochondrule	4		0.71	coarse porphyritic ol, ab, ap, cpx	Fo75		
7	1985,M68	P5204	macrochondrule	5		0.14	porphyritic ol, en, ab	Fo75		S3
8	1966,59	P3118	indeterminate clast ('Hutchison's Pebble')	15	oval, cracked		Ol-plagioclase cumulate ol, an, ab, ap, cr	Fo75.5, An70-74	2.7, 4.1	Ar-Ar 4.44 Ga

Table 4.1. Inclusions in NHM specimens of Barwell, as described in Table 1 of Bridges and Hutchison (1997).

4.2 This Study

This study tests the argument for early differentiation and mixing in the Solar System by seeking out additional inclusions within the Barwell meteorite.

4.2.1 Aims

This study aims to:

- Discover how common these “pebbles” are.
- Determine if XCT can provide insight into their formation and incorporation processes through visualisation of their shapes and orientations.
- Determine if the inclusions thus exposed are similar in mineralogy and composition to those discovered by previous studies.
- Provide insight into the origin of exotic material within the Barwell meteorite and the implications for early Solar System processes.

4.2.2 Methods

- The original “Pebble” sample (BM.1966,59) was scanned with the HMXST 225 Micro-CT System at the NHM. The scan revealed the presence of multiple inclusions, prompting the study of a further seven samples. Parameters are described in *Appendix 3.*
- Inclusions similar in morphology and greyscale to the “Pebble” were segmented and their volumes calculated according to the workflow given in *Appendix 6*.
- Using the visualisations of the sample interior, a suitable area of a different piece of BM1966, 59 (441g) was selected for slicing, thus minimising material loss and ensuring that inclusions would be exposed.
- Subsampling of the 441g Barwell fragment resulted in the exposure of several inclusions. Three polished blocks were made, named B1, B2 and B3. Two additional inclusions were separated out mechanically from smaller fragments of Barwell in the NHM collection.
- Polished blocks were created and four inclusions were analysed using the EDX detector on the Zeiss EVO 15LS SEM. Backscattered electron images and chemical phase maps were obtained for each inclusion for petrographic study and to determine modal abundance.
- Each inclusion was further investigated with the Cameca SX100 WDS microprobe to obtain major phase compositions and determine bulk chemistry by modal reconstruction.
- Subsamples of the four inclusion and matrix material were sent for irradiation in preparation for I-Xe isotopic analysis, using the RELAX instrument at the University of Manchester. Isotopic dating to provide insight into timing of crystallisation and potentially constraining early differentiation of the material.
- Oxygen isotopes were measured in subsamples of the four clasts and matrix material, using laser fluorination method at the Open University, described in *Section 2.6*. Note that this was carried out by R. Greenwood, not the author of this thesis.
- LA-ICP-MS analyses were carried out on three inclusions, both within individual mineral grains, and larger rasters to cover bulk areas. This work was undertaken using the ESI New Wave NWR193 Laser Ablation system coupled to an Agilent 7500cs Inductively Coupled Plasma Mass Spectrometer, described in *Section 2.4*.

- Samples of five inclusions were analysed by high-precision isotope ratio mass spectrometry at the Institut für Planetologie at the Westfälische Wilhelms-Universität Münster, to determine if the source parent bodies were differentiated, and to date core formation. Inclusions A and B from this study and inclusions 3, 4, and 6 from previous work by Bridges and Hutchison (1997) were selected as a minimum of ~ 100 mg of material was required based on estimated W concentrations. The method is fully described in *Section 2.5.*

4.3 Results

4.3.1 XCT of Barwell specimens

The host meteorite Barwell, L6, has a fairly uniform texture with approximately 3.5% metal, 7.5% Fe-oxides and sulphides, and 89% silicates. The original Pebble (volume = 0.731 cm^3) has an irregular but well-rounded shape and accounts for 1% of the bulk volume. Nineteen additional inclusions similar to the Pebble in both morphology and CT greyscale range (i.e. density) have been found, with volumes given in Table 4.2. Of the 285.5 cm^3 scanned in the three largest samples for this study, a total of 1.94 cm^3 (0.7%) is material that exhibits similar characteristics (in terms of X-ray attenuation) to the "Pebble". Only the three largest are included in this estimation, as they are likely most representative of the host meteorite whereas smaller fragments may have evidence of unusual material on the surface, therefore are somewhat 'preselected'.

Specimen	Mass (g)	Bulk Volume (cm^3)	Inclusion Volumes (cm^3)	∑ Inclusion Volume (cm^3)
BM1966,59	232.7	72.98	0.731, 0.190, 0.109, 0.040, 0.027	1.097
BM1966,59	441	145.79	0.099, 0.097, 0.090, 0.084 (C), 0.064 (D), 0.057	0.491
BM1966,58b	203	66.70	0.118, 0.080, 0.056, 0.046, 0.043, 0.013	0.356
BM1985, M68	9.961	3.08	0.241 (B), 0.017	0.259
BM1985, M68	2.286	0.65	0.085 (A)	0.085

Table 4.2. Specimen masses and volumes of inclusions found within using XCT.

Figure 4.2 shows single slices from the raw CT data, showing the appearance of the original “Pebble” (on the left side of the images) and similar clasts. The inclusions show very similar greyscales, within narrow ranges. They exhibit smooth, rounded shapes. Sub-parallel fractures that do not continue into the host, as noted by Hutchison et al. (1988), are also visible in many of them. The feature circled in yellow is possibly a macrochondrule. It is notable because of the sharp delineation with the main host, and is exceptionally large compared to other chondrules in the sample, and for its significant metal/sulphide content.

Figure 4.2 also shows an unidentified feature within the Barwell host. This rounded, broadly rectangular shaped inclusion appears to be significantly different from both the main mass and other inclusions. Although not investigated in this study, it may be of future interest and contribute to understanding of diversity of material in ordinary chondrites.

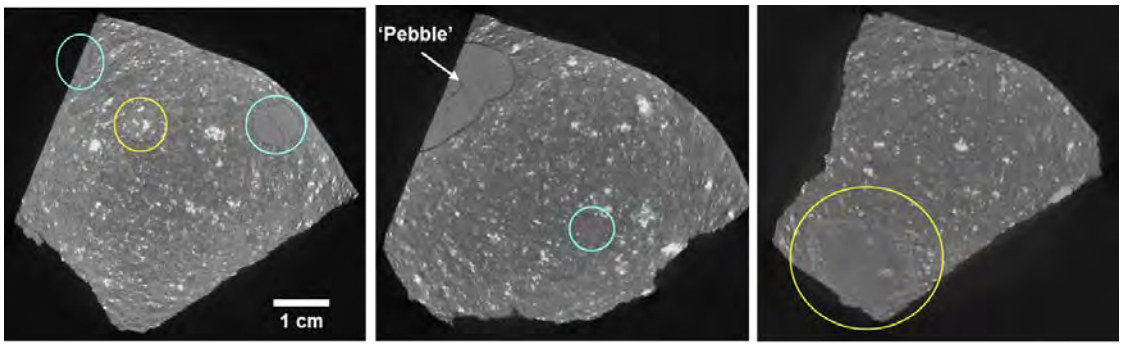

Figure 4.2. XCT slices from 232.7 g Barwell fragment BM1966,59. Left: Slice 655, with large chondrule circled in yellow and inclusions in blue. Middle: Slice 1272, showing the Barwell “Pebble” at its largest extent (left) and the appearance of another clast (circled). Right: Slice 363. Unidentified feature in host rock.

Figure 4.3 shows two perpendicular views in slices of the XCT data of a 2.286g fragment from BM1985, M68. This clast, referred to as ‘Inclusion A’, is very clear in the CT data, which was used to inform manual picking of the inclusion for other techniques. The XCT images also show the characteristic subparallel fractures observed in other inclusions in Barwell.

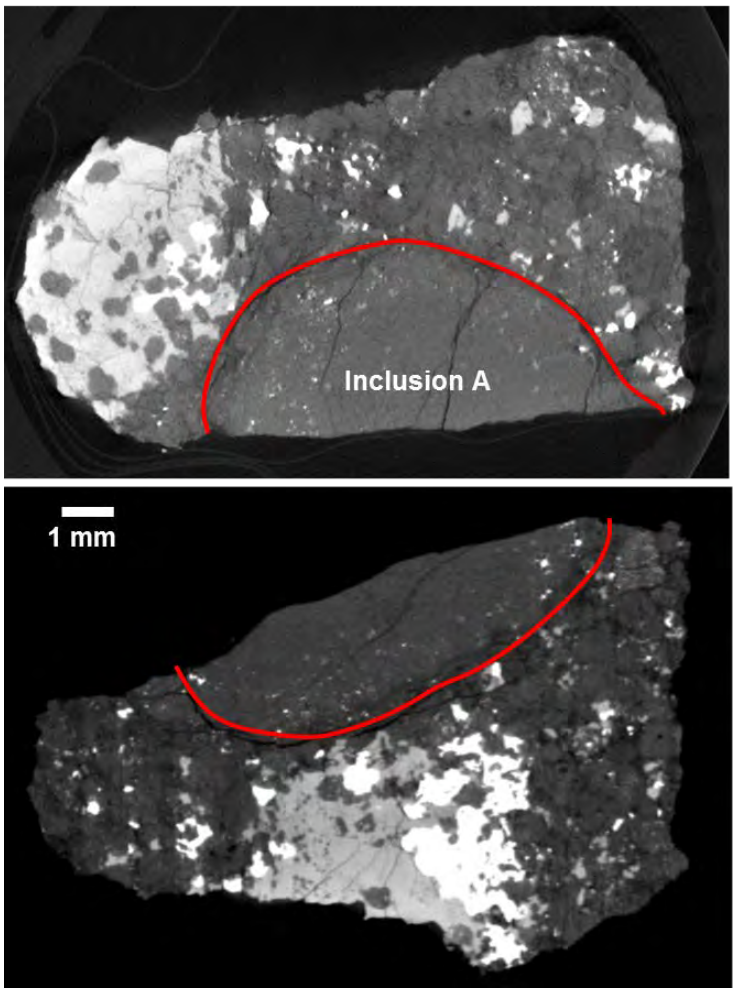

Figure 4.3. XCT slices from 2.286 g Barwell fragment BM.1985,M68. Top: Slice 1050 showing the location of partial inclusion A in this fragment of Barwell. Bottom: Slice perpendicular to top image.

Figure 4.3 also shows a potential relationship between A and a sulphide/metal inclusion in close proximity. Observations of the image stack indicate that the metal is concentrated at the margin of the predominantly sulphide inclusion. The lower image in Figure 4.3, cut perpendicular to the upper image, shows an interesting feature in the bottom right. This mottled texture may indicate an area where the differentiation of metal and sulphide from silicate is incomplete, i.e. showing blebs of metal and sulphide, potentially 'trapped' within a silicate glass, that did not have time to migrate before solidification. Both images show that the more dense phases are concentrated at the margins of the inclusion, but that on the whole and similar to others, inclusion A is depleted in metal.

Figure 4.4 shows three-dimensional visualisations of the three largest Barwell samples scanned. Each coloured object represents an inclusion that was manually segmented from the bulk in the CT data. These visualisations were used to subsample the stones, as well as understand their shape.

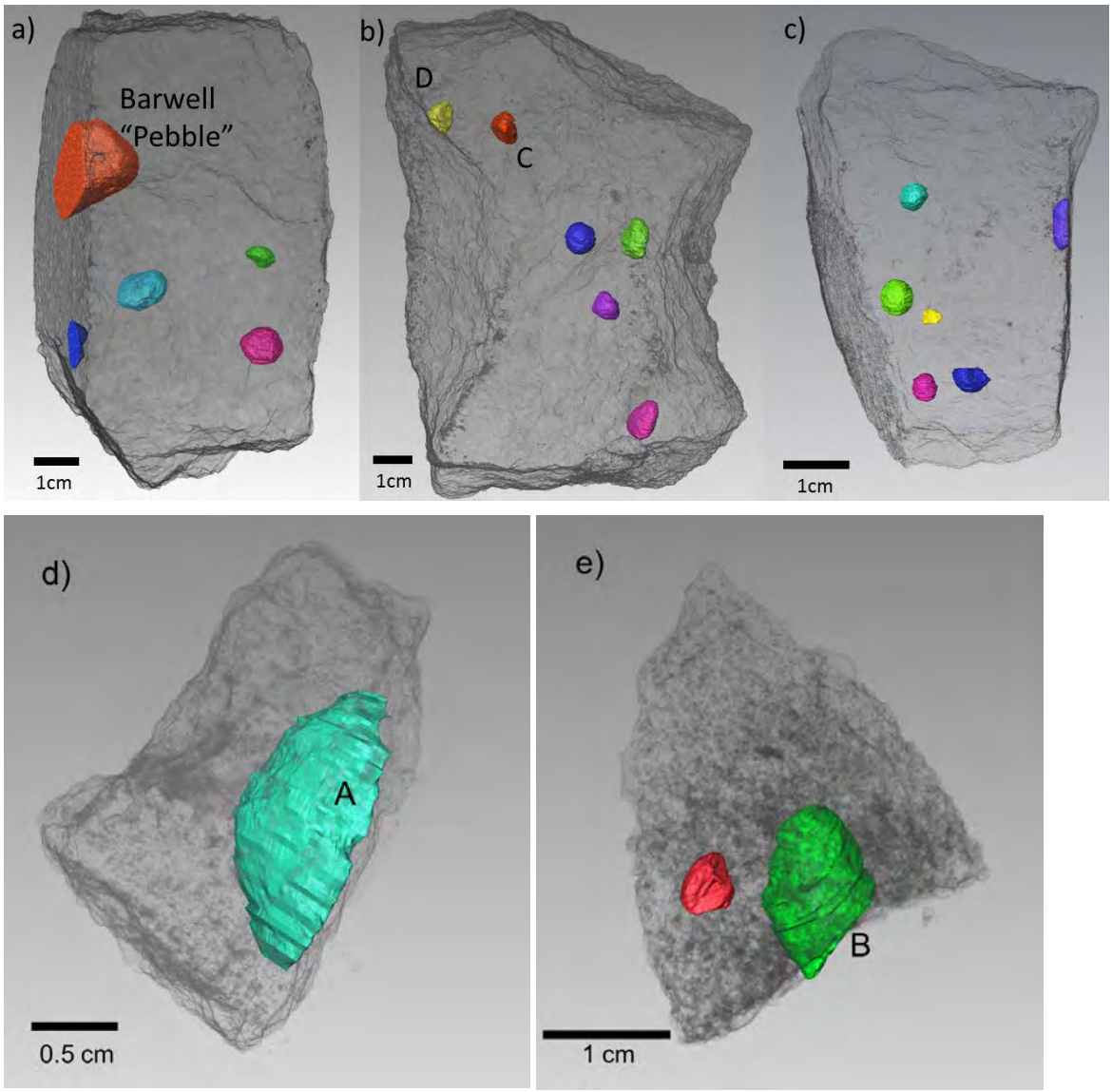

Figure 4.4. Visualisations of XCT data of the segmented inclusions in: (a) BM.1966,59, The 'Pebble' sample, 232.7 g; (b) BM.1966,59, 441 g – which was later subsampled and inclusions C and D were extracted; (c) BM.1966,58b, 203 g; d) BM.1986, M68, 2.286 g – from which inclusion A was extracted; e) BM.1986, M68, 9.961 g – from which inclusion B was extracted.

4.3.2 Mineralogy of Barwell inclusions

From the XCT data, four inclusion (A, B, C, and D) were physically separated from the host rock and fragments embedded in resin blocks. Each of the four inclusions, and some randomly selected areas of the host meteorite, were mapped by scanning electron microscopy to provide both textural information and modal mineralogy. This also provided reconnaissance data for the selection of microprobe analysis sites. Each inclusion is first described individually, followed by a comparison of their geochemistry.

4.3.2.1 Inclusion A

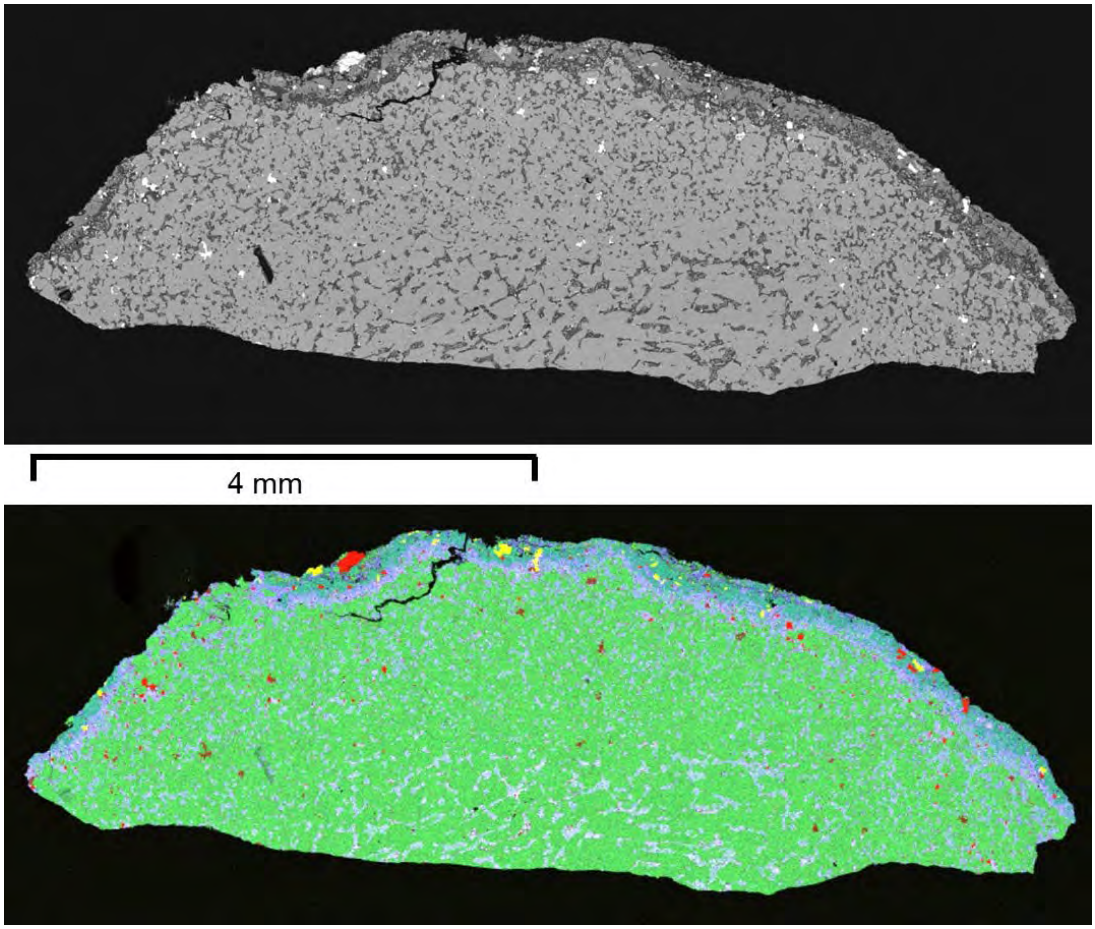

Figure 4.5. Top: Montaged BSE of inclusion A showing variation in texture from centre to rim. Bottom: Montaged EDX map of inclusion A, with Fe in Red, Ca in Yellow, Si in Blue, Mg in Green and Al in White. Scale bar is 4mm.

Inclusion A, shown in the backscattered electron (BSE) and false-colour EDX images in Figure 4.5, was separated from a 2.286g piece of Barwell BM1985, M68. The BSE image (Figure 4.6, top) is typical of the interior. Crystals in the core of the inclusion are larger (olivine, up to 500 μm), whereas those closer to the rim are considerably smaller (maximum 200 μm – Figure 4.6, bottom), indicating different cooling rates experienced. The inclusion is dominated by large olivine crystals with an equilibrium texture, exhibiting 120° angles between crystals, indicating slow cooling. There is no indication of preferential crystallisation orientations. The darker interstitial silicate phase is plagioclase. occurring as a late-stage crystallisation phase, in textural equilibration with olivine as seen in the embayment features. Small olivine crystals occur within the plagioclase. Inclusion A could petrographically be interpreted as a 'megachondrule' by the textural guidelines of Ruzicka et al. (1998) – partly-to-wholly curved surfaces, radial variations in textures – that support crystallisation as a free-floating droplet, i.e. cooled from outside-in.

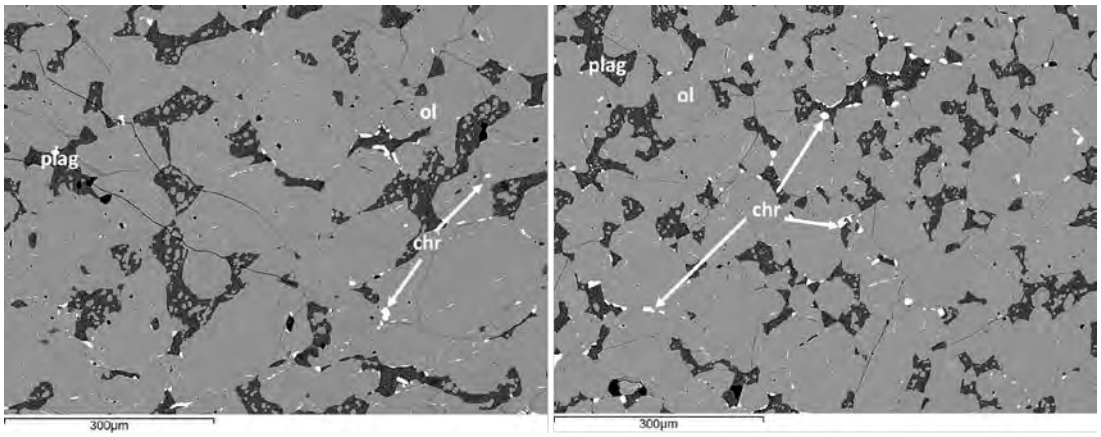

Figure 4.6. Left: Tile 61, from the most central part of the inclusion, taken from a montaged BSE map of inclusion A. Right: Tile 34 from interior of inclusion close to the edge, taken from a montaged BSE map of inclusion A.

Non-silicate Fe in inclusion A is present in chromite and rare sulphide as illustrated in Figure 4.7. Chromite is present in rounded blebs (10-30 µm) as well as linear features. The rounded grains are indicative of thermal metamorphism, whereas linear features likely arose when chromite was mobilised and infilled impact-formed cracks which have subsequently healed. The Ca map in Figure 4.7 shows an enrichment at the edge of the inclusion, where apatite occurs.

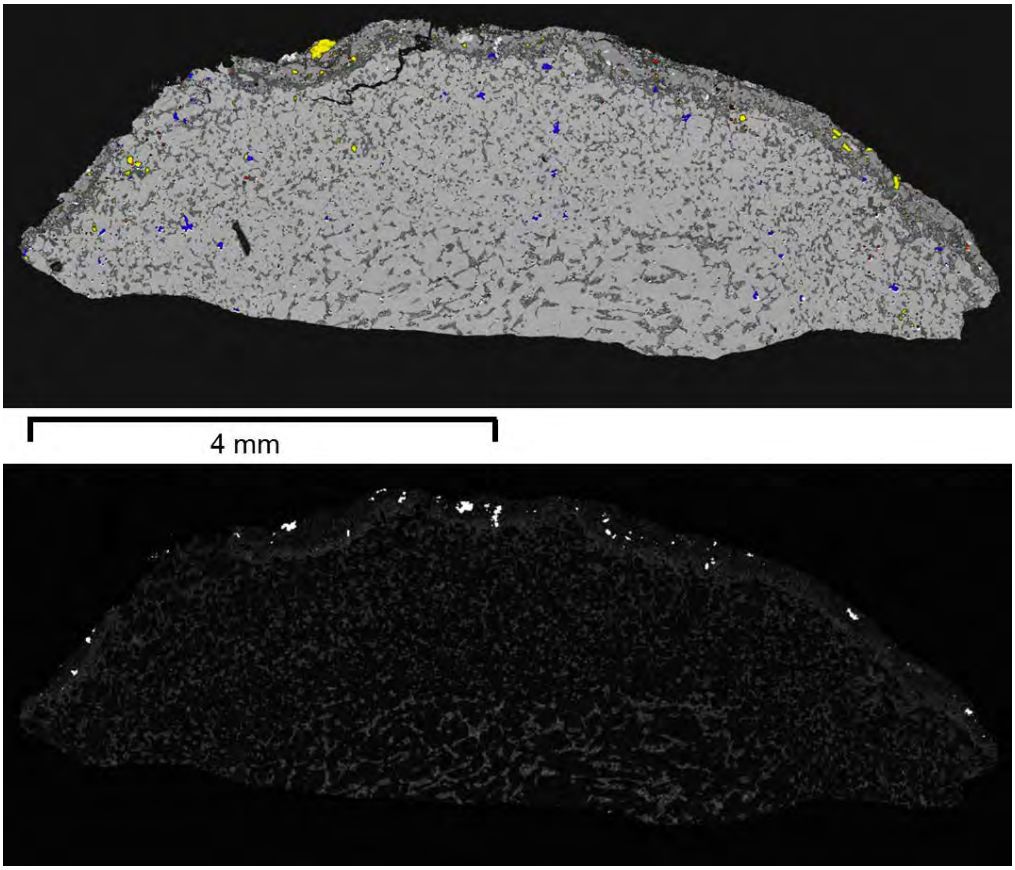

Figure 4.7. Top: EDX element map of inclusion A, where S is Yellow, Cr is Blue and Ni is Red with a BSE montage in greyscale in the background. Bottom: Montaged EDX map of calcium in inclusion A. Scale bar is 4mm.

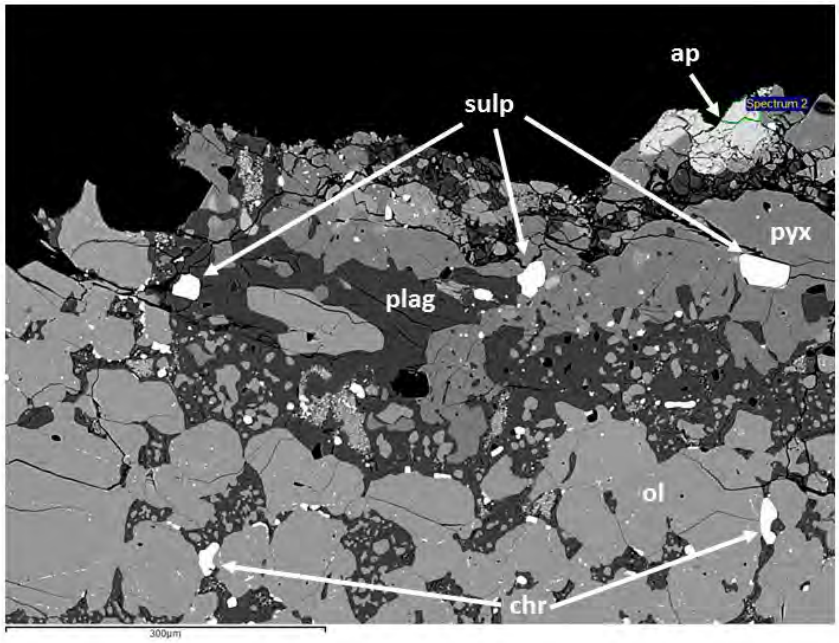

Figure 4.8. Tile 23 from a montaged BSE map of inclusion A, showing the mineralogy of the inclusion edge, where sulp: sulphide, chr: chromite, ol: olivine, pyx: pyroxene, plag: plagioclase, ap: apatite. Scale bar is 300µm.

The BSE image in Figure 4.8, shows a region typical of the edge of the inclusion. The brightest phase is chromite, followed by apatite, olivine, pyroxene and feldspar. Porosity is present both in cracks and in pores. Large pores may have formed by reduction in solid volume due to melt crystallisation, however, the origin of the small pores within the interstitial plagioclase is questionable. Such small, rounded pores may have formed through dissolution or degassing/loss of volatiles, possibly through impact. This is also seen in the plagioclase composition in inclusion A, which is sodium-poor (oligoclase/andesine) compared with host Barwell plagioclase (albite). The texture, for example the linear chromite trails within olivine grains, the pores along cracks and the triple junctions visible between some olivine grains, suggests that the inclusion experienced some annealing.

The modal mineralogy of this inclusion has been estimated using image thresholding. As the mineralogy is fairly simple, it is legitimate to use BSE images where all phases – olivine, plagioclase, opaques (chromite) and the sample porosity, are represented by obvious greyscale differences. Eleven tiles from the BSE montage of the inclusion (Figure 4.5) were used at their full resolution – 1024 by 800 pixels. The greyscale ranges selected, based on an 8-bit 0-255 scale, were: porosity 0-38, plagioclase 40-90, olivine 95-175, opaques 180-255. Figure 4.9 shows the process of taking the original BSE map and thresholding before binarising the image to calculate area of each phase. The same process was applied to other

tiles, which were selected from the centre of the montaged area. Some tiles were excluded due to the presence of contaminants on the surface which would skew the thresholded areas. As seen in Table 4.3, the modal mineralogy does not change significantly, despite the reduction of grain size with increasing distance from the centre, as is evident in Figure 4.5 and Figure 4.6.

Microprobe (WDS) data from inclusion A are shown in Table 4.4. Olivine is homogenous and forsteritic, with Fo 74.5 (s.d. = 0.14, n=25). Chrome number (Cr/ Cr+Al) of chromite is 78.9 (s.d. = 0.01, n=34). Microprobe analyses of plagioclase show good totals between 99–101%, indicating it is crystalline, not glassy, falling mostly in the oligoclase field compositionally, defined by the Na/C ratio, i.e. low in K (Figure 4.10). Plagioclase is more calcic towards the centre of the inclusion, increasing in Na and K moving towards the rim.

Note that *Appendix 10* includes full EPMA data for all inclusions.

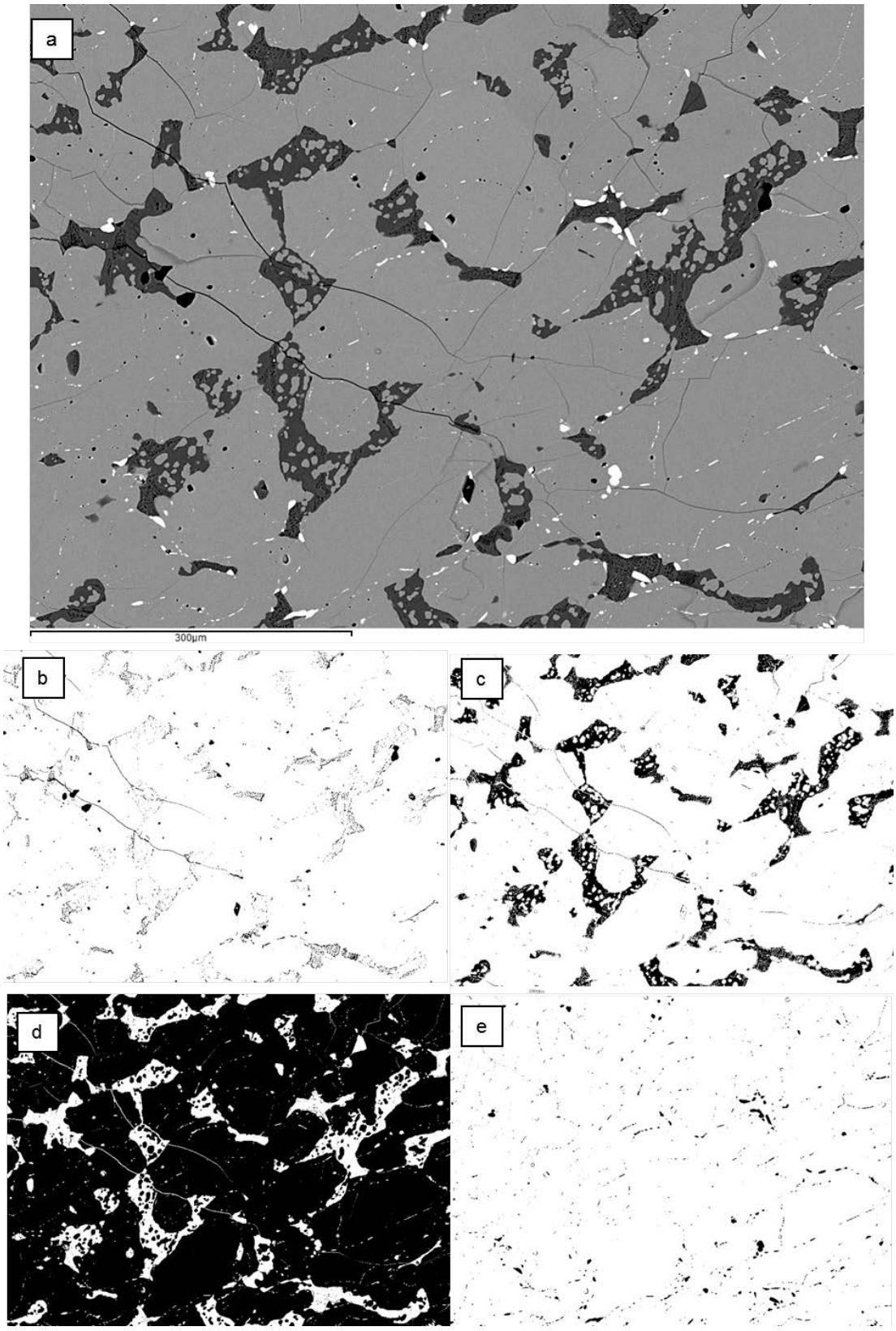

Figure 4.9. Thresholding modal mineralogy of inclusion A: a) original BSE image of Tile 61 from inclusion A; b) segmented porosity; c) segmented plagioclase; d) segmented olivine; e) segmented opaques.

Tile	Porosity (%)	Plagioclase (%)	Olivine (%)	Opaques (%)
32	3.1	13.6	79.5	2.9
34	2.4	11.5	83.6	1.8
36	2.3	12.4	82.0	2.5
44	2.7	10.8	84.7	1.1
45	2.6	9.5	85.7	1.7
46	2.2	8.5	86.6	2.3
47	2.8	10.2	84.9	1.5
57	3.3	14.1	80.5	1.5
58	2.5	13.0	82.2	1.6
60	2.1	11.9	84.0	1.4
61	2.1	11.5	84.3	1.3
Average	2.6	11.6	83.5	1.8
s.d.	0.40	1.72	2.18	0.55

Table 4.3. A table of modal mineralogy based on thresholding of BSE images of inclusion A. Tiles 32, 34, 36 are closer to the rim, with tiles 44, 45, 46, 47 in between, and tiles 57, 58, 60, 61 closest to the centre.

	Olivine		Plagioclase		Chromite	
Oxide	**(n=24)**	**s.d.**	**(n=31)**	**s.d.**	**(n=36)**	**s.d.**
SiO_2	38.466	0.411	60.618	1.041	b.d.l	
MgO	38.977	0.285	0.274	0.609	2.544	0.117
FeO	23.198	0.090	0.834	0.677	31.876	0.485
TiO_2	0.060	0.038	0.059	0.014	3.320	0.450
Cr_2O_3	0.031	0.042	n.a.		51.066	0.759
MnO	0.496	0.016	0.015	0.016	0.581	0.021
CaO	0.019	0.008	5.318	0.778	b.d.l	
Na_2O	b.d.l		8.584	0.380	n.a.	
Al_2O_3	b.d.l		24.050	0.794	9.154	0.586
K_2O	n.a.		0.479	0.097	n.a.	
V_2O_5	b.d.l		n.a.		0.751	0.024

Table 4.4. EPMA data in wt% oxide for phases in inclusion A. [b.d.l. – below detection limit; n.a. – not analysed].

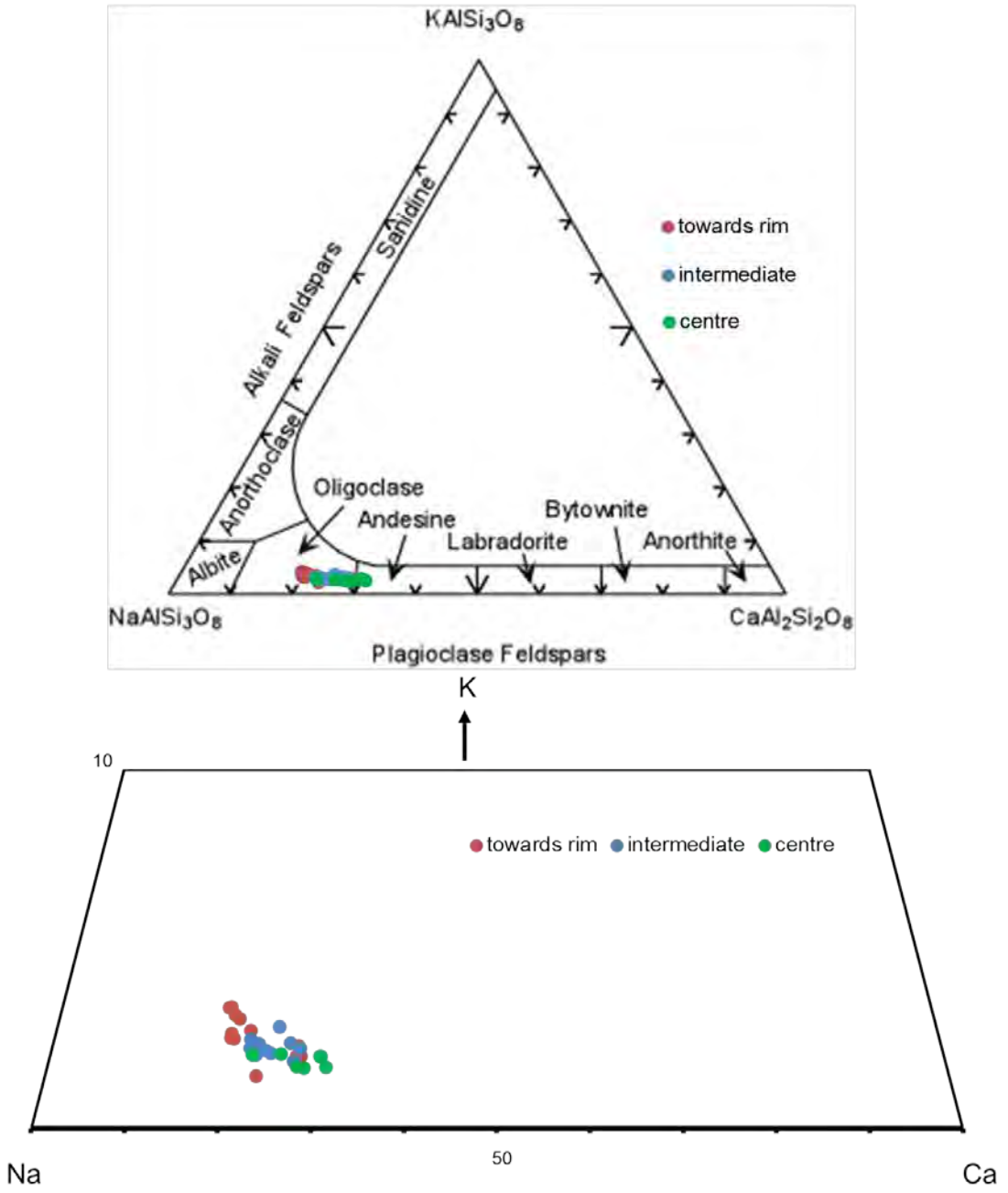

Figure 4.10. Top: Feldspar tri-plot showing EPMA data points for inclusion A. Bottom: Reduced view (up to 0.1 K) of the same data set showing the variation in plagioclase composition with distance from centre of the inclusion.

4.3.2.2 Inclusion B

Figure 4.11 shows that this inclusion is dominated by large olivine crystals (~300-500 µm), consistent with a period of slow cooling early in the object's history. Similar to inclusion A, there is some embayment of olivine edges. Small crystals of pyroxene and olivine are poikilitically enclosed within plagioclase, representing a subsequent period of faster cooling. Two possible relict chondrules can be seen towards the top of the clast. No difference in size of crystals between the edge and core of the clast is evident, however only part of the entire inclusion is visible in this block.

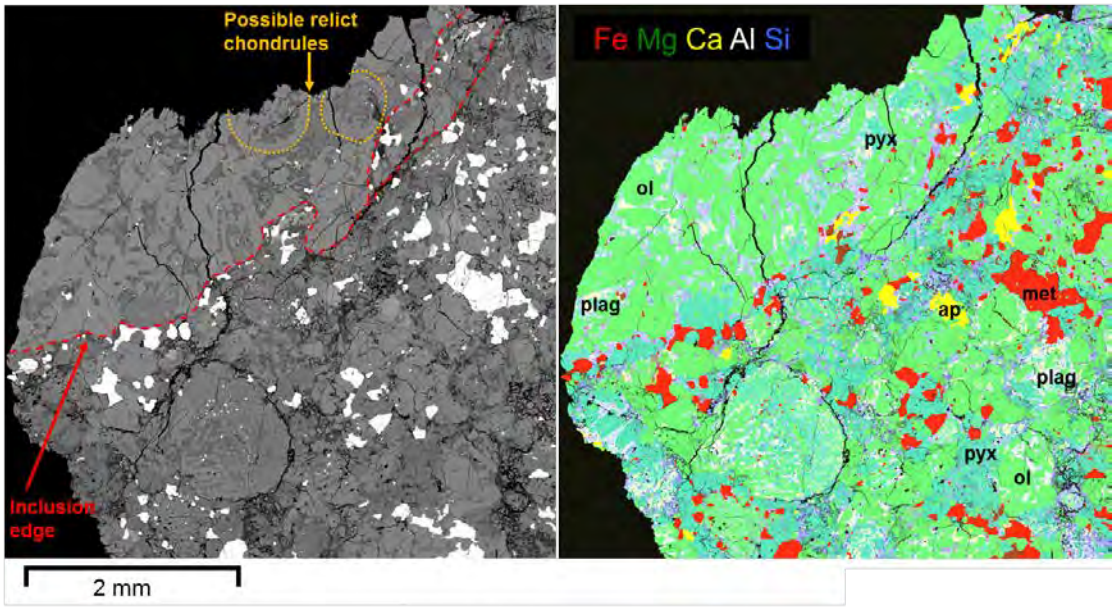

Figure 4.11. i) Montaged BSE of inclusion B within bulk Barwell with inclusion edge and possible relict chondrules marked. ii) Montaged EDX map of inclusion B, left, and host Barwell, right, with Fe in Red, Ca in Yellow, Si in Blue, Mg in Green and Al in White.

The inclusion does not appear as highly shocked as the host rock, with considerably fewer microcracks evident. FeNi metal may be concentrated at the edges of the inclusion, which could be a result of clast-host interaction, however the abundance is not signficantly higher than bulk Barwell. The inclusion is almost devoid of FeNi metal, except for rare very small grains, such as those visible in Figure 4.11, which also shows small phosphate crystals around the edge of the inclusion. Larger phosphates are visible in the host rock, but not found within the inclusion. Figure 4.11 shows the interpreted contact between inclusion B and the host Barwell. Unlike inclusions A, C, and D which show broken edges or mantles, inclusion B has an indistinct margin with the host, suggestive of in situ recrystallisation during thermal metamorphism.

Chromite is present as both rounded blebs and linear features; the latter are symptomatic of annealing, whereas rounded grains indicate thermal metamorphism. Within plagioclase, there is a very fine intergrowth of chromite, feldspathic mesostasis and porosity that appears to have replaced olivine or pyroxene, and may be a quench texture. Figure 4.12 includes both BSE and element maps of this area. The centre contains tabular chromites in mestostasis, which is surrounded by a glassy vesicular mantle. This in turn, is surrounded by plagioclase feldspar. Chromite-plagioclase assemblages are consistent with significant temperature excursions and indicate formation during shock (Rubin, 2003).

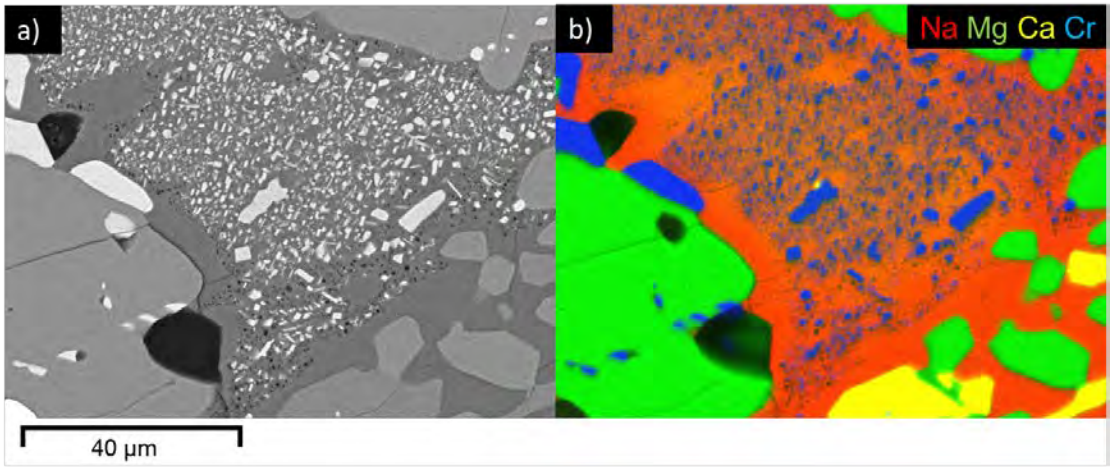

Figure 4.12. (a) BSE and (b) element map of chromite-plagioclase assemblage in inclusion B.

Figure 4.13 shows BSE images of the most central part of the inclusion, and indicate a texture more similar to that seen in inclusion A, however with both olivine and pyroxene enclosed in plagioclase. The variation in textures within this inclusion indicates a complicated cooling history, potentially slow at first with a subsequent faster cooling period. Porosity is present mostly in cracks however there are some small rounded pores (~20 µm) that may be a result of dissolution, e.g. in Figure 4.13 (top right), where rounded pores are concentrated around a grain of olivine.

The modal mineralogy was estimated in different regions of the inclusion, as with inclusion A previously. With increasing distance from the contact with the host, there is a decrease in the modal content of plagioclase and pyroxene, coupled by an increase in olivine (Table 4.5).

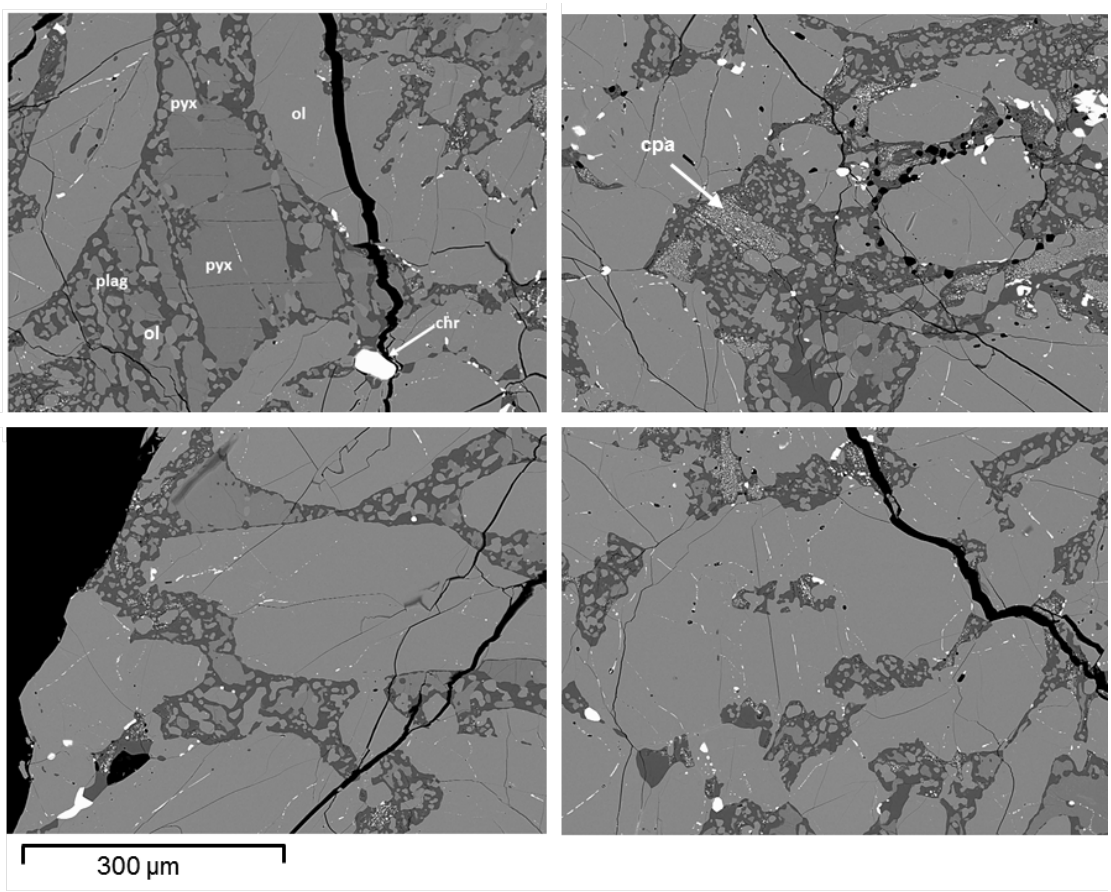

Figure 4.13. Tiles of a montaged BSE map of inclusion B. Top: left, tile 35 near the edge of the inclusion; right, tile 46 just below 35. Bottom: left, tile 69, right, tile 68 – both closer to the centre of the inclusion.

Tile	Porosity (%)	Plagioclase (%)	Pyroxene (%)	Olivine (%)	Opaques (%)
35	3.6	16.1	24.9	52.6	1.1
46	1.8	23.5	10.3	62.1	2.3
68	3	14.6	6.9	74.2	1.4
79	2.3	12.4	7.2	73.3	2.8
69	3	12.4	6.5	76.8	1.3
Average	2.74	15.80	11.16	67.80	1.78
s.d.	0.70	4.58	7.83	10.19	0.73

Table 4.5. Modal mineralogy of Barwell inclusion B, based on thresholding of BSE images. Tiles 35, 46 are closer to the host, tiles 68 and 69 are intermediary, and tile 79 is in the centre most part exposed in the block.

EPMA data from inclusion B are shown in Table 4.6. Olivine is homogenous and forsteritic, with Fo 74.5 (s.d. = 0.13, n=45). Chrome number (Cr/Cr+Al) of chromite is 80.0 (s.d. = 0.01, n=32). Pyroxene is present in two populations – diopside and enstatite (Figure 4.14). Microprobe analyses of plagioclase show good totals between 99–101%, indicating it is crystalline, not glassy, falling mostly in the oligoclase field compositionally (Figure 4.15).

Oxide	Olivine (n=45)	s.d.	Plagioclase (n=22)	s.d.	High-Ca Pyroxene (n=31)	s.d.	Low-Ca Pyroxene (n=31)	s.d.	Chromite (n=31)	s.d.
SiO_2	38.50	0.20	63.47	1.93	54.70	0.24	55.86	0.35	b.d.l.	
MgO	38.83	0.17	0.27	0.43	16.51	0.30	28.64	0.19	2.41	0.40
FeO	23.17	0.11	0.64	0.19	4.96	0.25	13.97	0.12	31.13	0.90
TiO_2	0.03	0.02	0.05	0.02	0.52	0.09	0.33	0.12	3.33	1.89
Cr_2O_3	0.01	0.02	n.a.		0.79	0.05	0.23	0.11	55.48	2.06
MnO	0.49	0.01	b.d.l		0.23	0.01	0.49	0.02	0.62	0.04
CaO	0.02	0.01	3.16	0.89	22.02	0.51	0.88	0.09	b.d.l.	
CoO	0.02	0.01	n.a.		n.a.		n.a.		n.a.	
Na_2O	b.d.l		9.56	0.65	0.57	0.04	b.d.l		n.a.	
Al_2O_3	b.d.l		21.52	1.45	0.58	0.09	0.29	0.13	5.68	0.71
K_2O	n.a.		0.78	0.18	n.a.		n.a.		n.a.	
V_2O_5	b.d.l		n.a.		n.a.		n.a.		0.70	0.05

Table 4.6. EPMA data in wt% oxide for phases in inclusion B. [b.d.l. – below detection limit; n.a. – not analysed].

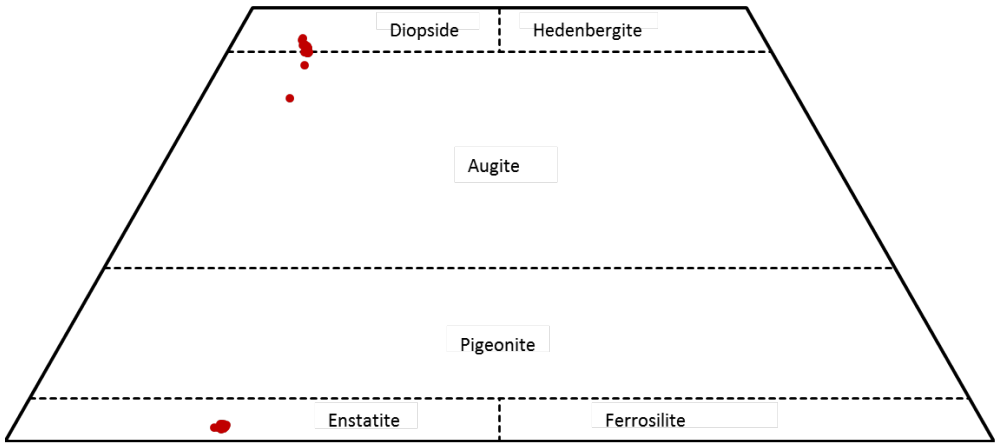

Figure 4.14. Pyroxene quadrilateral showing EPMA data points for inclusion B.

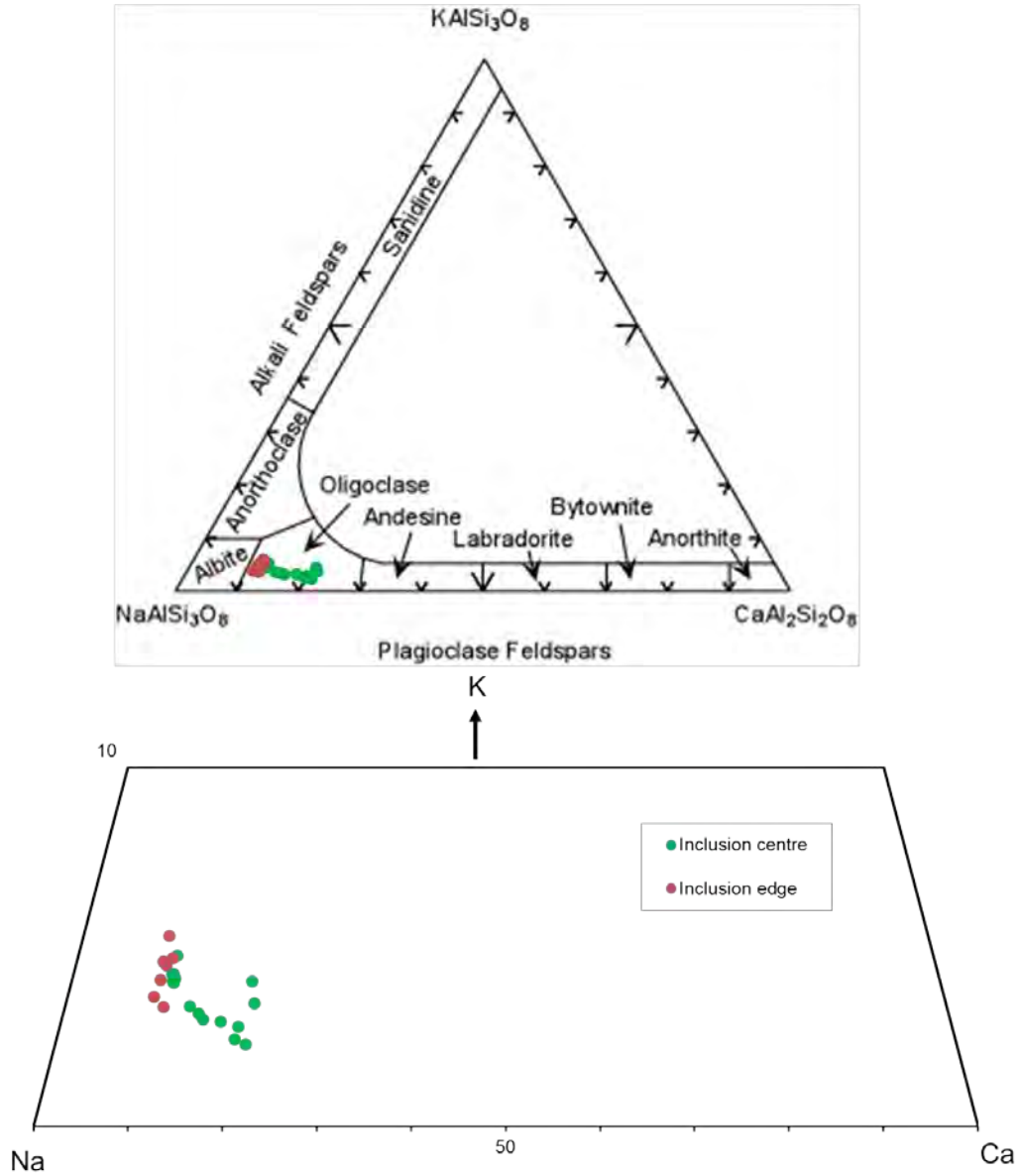

Figure 4.15. Top: Feldspar tri-plot showing EPMA data points for inclusion B. Bottom: Reduced view (up to 10% K) of the same data set showing the variation in plagioclase composition with distance from centre of the inclusion.

4.3.2.3 Inclusion C

As shown in the BSE montage, Figure 4.16, inclusion C exhibits a spinifex texture, with lath-like acicular crystals (up to ~500 μm) of olivine and pyroxene, and interstitial plagioclase, indicative of rapid crystallisation from undercooling of melt. This texture is entirely different to that observed in inclusions A, B and D.

There is no indication of alignment or preferred orientation of the crystals in the interior of the inclusion, however there do appear to be some radial features which resemble an open spherulitic texture. Minor chromite is also present in very small grains (maximum ~15 μm). This SEM montage image also shows the presence of

subparallel fractures, noted by Hutchison et al. (1988) and visible in the CT data previously described.

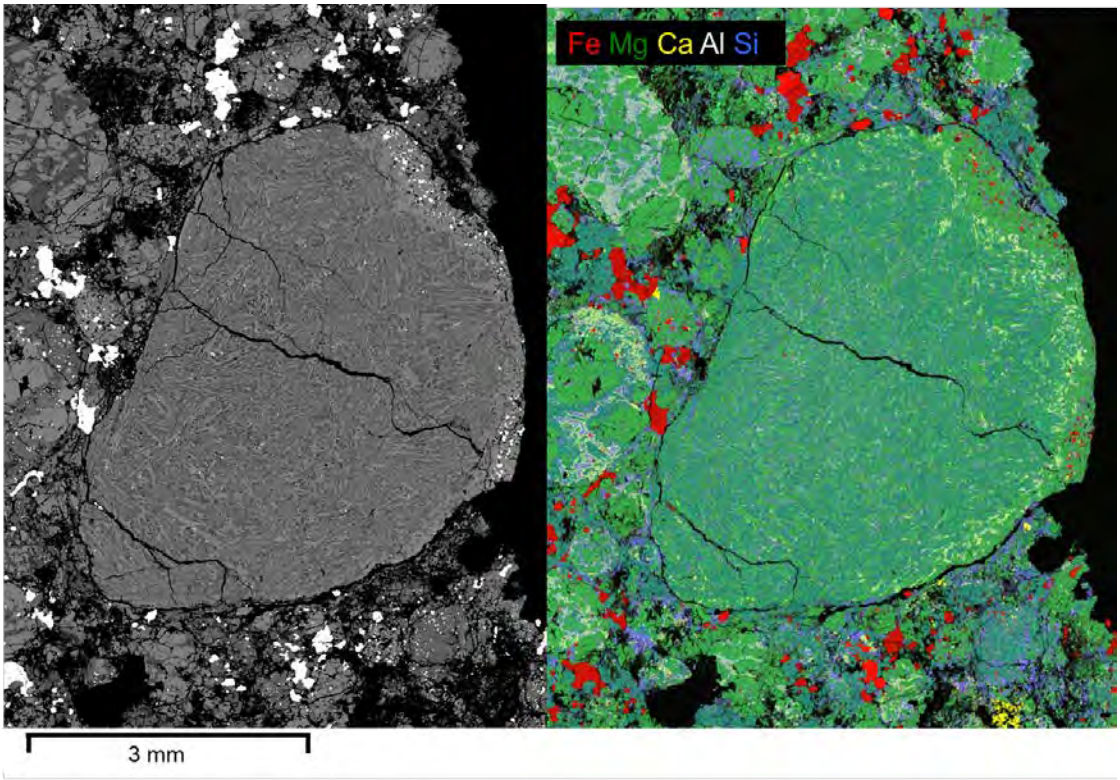

Figure 4.16. Montaged BSE and EDX maps of inclusion C, with Fe in Red, Ca in Yellow, Si in Blue, Mg in Green and Al in White.

The elemental maps of inclusion C, combined in Figure 4.16, show that it is enriched in Ca and Al towards the edge. This image also shows the presence of a mantle around part of C that has been partially removed before incorporation into the Barwell parent body. Another potential origin of the partial contact is metamorphism with the Barwell host. Figure 4.17 (bottom right) shows a representative part of the inclusion mantle with minerals labelled. Unlike the centre of the inclusion, the mantle of has a coarser, more equant grain size and is dominated by olivine. Iron nickel metal is present in the mantle but absent from the inclusion centre. The presence of taenite in the mantle could indicate unequilibrated material was accumulated in the nebula prior to incorporation in the Barwell parent body. Chromite is present in both locations, but is found in considerably smaller grain sizes in the clast centre.

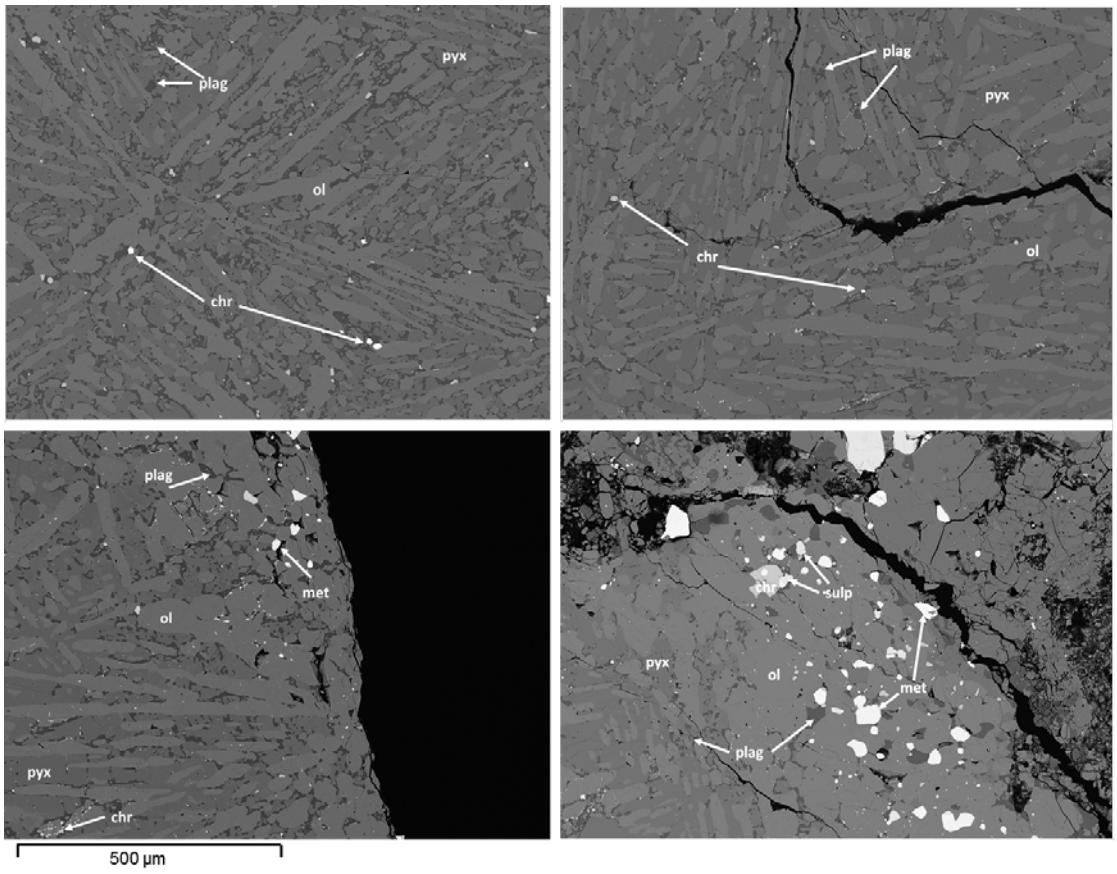

Figure 4.17. BSE images from montage of inclusion C. Top left and right: interior of inclusion, showing spinifex texture of olivine (ol), pyroxene (pyx) and interstitial plagioclase (plag) with tiny chromite grains (chr); bottom left: example area of inclusion edge without mantle; bottom right: example area of the inclusion C mantle, showing diversity of mineralogy, including metal (met) and sulphides (sulp).

Similar to previous inclusions, the modal mineralogy was calculated by thresholding of several areas (Table 4.7; Figure 4.18), indicating that pyroxene is more plentiful in the centre of the inclusion, decreasing by ~5-10% modally towards to edge. EPMA data from inclusion C are shown in Table 4.8. Olivine is forsteritic, with Fo 74.5 (s.d. = 0.09, n=44) and is similar in the clast mantle. There are two populations of pyroxene in the mantle – both diopside and enstatite, whereas only enstatite is seen in the inclusion centre, accounting for the enrichment in Ca (Figure 4.19). Microprobe analyses of plagioclase in the inclusion show good totals between 99–101%, indicating that it is crystalline rather than glassy, and are mostly oligoclase compositionally (Figure 4.20). Chromite has (Cr/Cr+Al) of 87.5 (s.d. = 0.004, n=10). The particularly small grain size of chromites made accurate analysis challenging. Individual chromites were identified and spot analyses collected after using the EDX detector on the microprobe to confirm composition by checking for fluorescence. Although the volume of interaction is smaller than for silicate analyses due to the higher atomic number, most grains were still too small (<5 µm). For this reason, only

ten analyses of chromite have been collected – representing almost all grains of a sufficient size – as many others were mixed, based on the presence of silicon.

Tile	Porosity (%)	Plagioclase (%)	Pyroxene (%)	Olivine (%)	Opaques (%)
81	0.36	9.8	47.4	42.2	0.3
125	0.1	11.4	46	42.3	0.2
92	0.8	14	40.1	44.6	0.4
115	0.1	16.3	38.6	44.6	0.3
Average	0.34	12.88	43.03	43.43	0.30
s.d.	0.33	2.87	4.33	1.36	0.08

Table 4.7. A table of modal mineralogy based on thresholding of BSE images of inclusion C. Tiles 92 and 115 are more central in the inclusion, whereas 81 and 125 are closer to the edge.

Oxides	Olivine (n=44)	s.d.	Plagioclase (n=24)	s.d.	Pyroxene (n=31)	s.d.	Chromite (n=10)	s.d.
SiO_2	38.378	0.148	64.13	0.80	55.224	0.200	0.18	0.24
MgO	38.492	0.111	0.55	0.78	28.251	0.170	1.88	0.18
FeO	22.999	0.091	1.00	0.62	14.033	0.121	31.10	0.40
TiO_2	b.d.l		0.05	0.02	0.404	0.104	2.53	0.29
Cr_2O_3	0.029	0.035	0.02	0.02	0.232	0.065	55.58	0.77
MnO	0.484	0.016	0.03	0.02	0.488	0.014	0.62	0.02
CaO	0.025	0.017	2.37	0.36	0.913	0.162	0.08	0.05
Na_2O	b.d.l		9.70	0.17	b.d.l		0.03	0.04
Al_2O_3	b.d.l		21.02	0.57	0.378	0.118	5.29	0.13
V_2O_5	b.d.l		b.d.l		n.a.		0.87	0.04
K_2O	n.a.		0.98	0.12	n.a.		b.d.l	

Table 4.8. EPMA data in wt% oxide for phases in inclusion C. [b.d.l. – below detection limit; n.a. – not analysed].

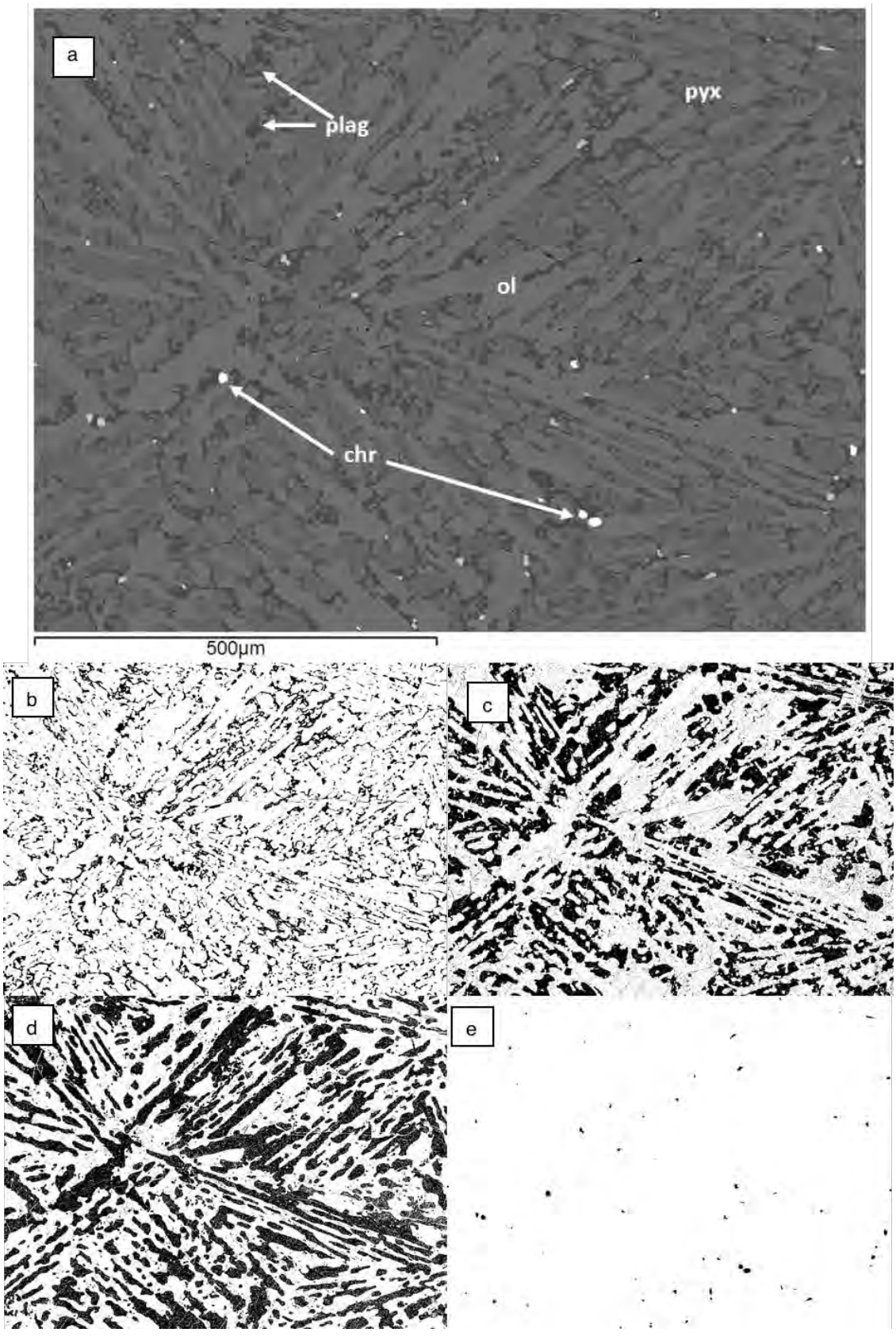

Figure 4.18. Thresholding modal mineralogy of inclusion C: a) original BSE image of Tile 115 from inclusion C; b) segmented plagioclase; c) segmented pyroxene; d) segmented olivine; e) segmented opaques.

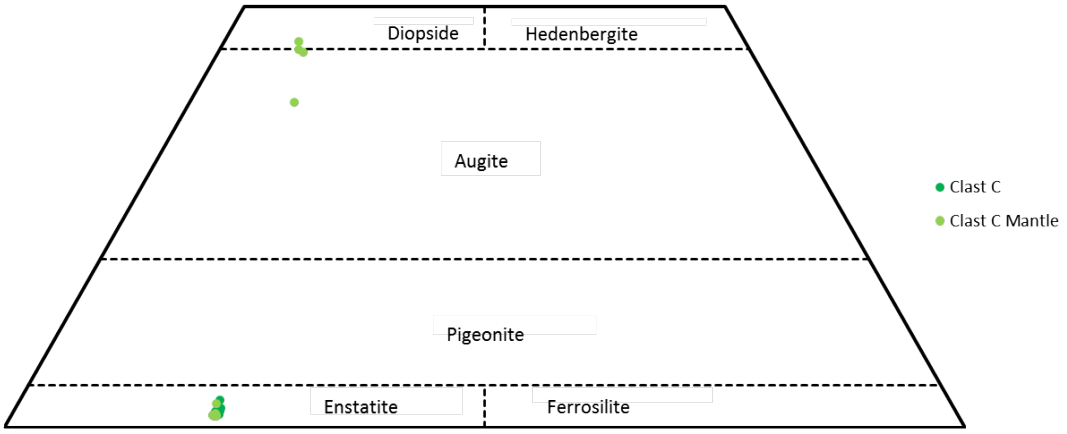

Figure 4.19. Pyroxene quadrilateral showing EPMA data points for inclusion C. Pyroxene within the clast is homogenised and only enstatite, whereas two populations (diopside and enstatite) are found in the mantle.

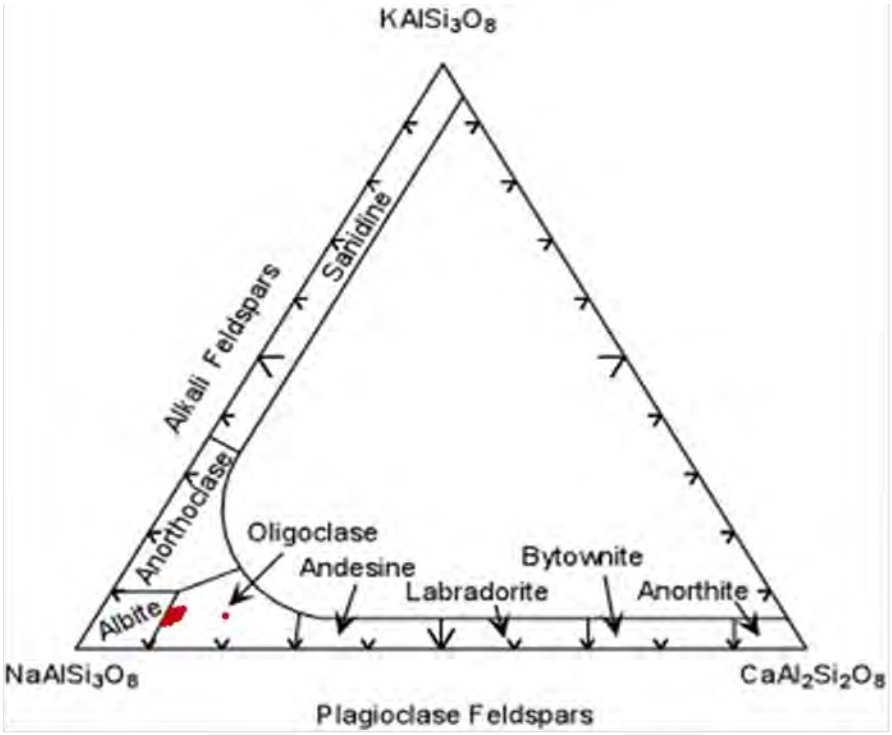

Figure 4.20. Feldspar tri-plot showing EPMA data points for inclusion C.

4.3.2.4 Inclusion D

Like inclusions A and B, inclusion D is dominated by olivine, with some pyroxene and interstitial feldspar (see element map and BSE montage in Figure 4.21). Olivine is predominantly very fine-grained (~20 µm) but very occasionally occurs as larger grains (~ 200 µm). Unlike other inclusions, FeNi metal is present but occurs only in

very small grains (~ 10-20 μm). Chromite is also present in a similar abundance (<10 μm). Inclusion D exhibits more of a feathered, quench texture than other inclusions in this study. The texture is most similar to inclusion C, however it lacks radial textures or elongated features.

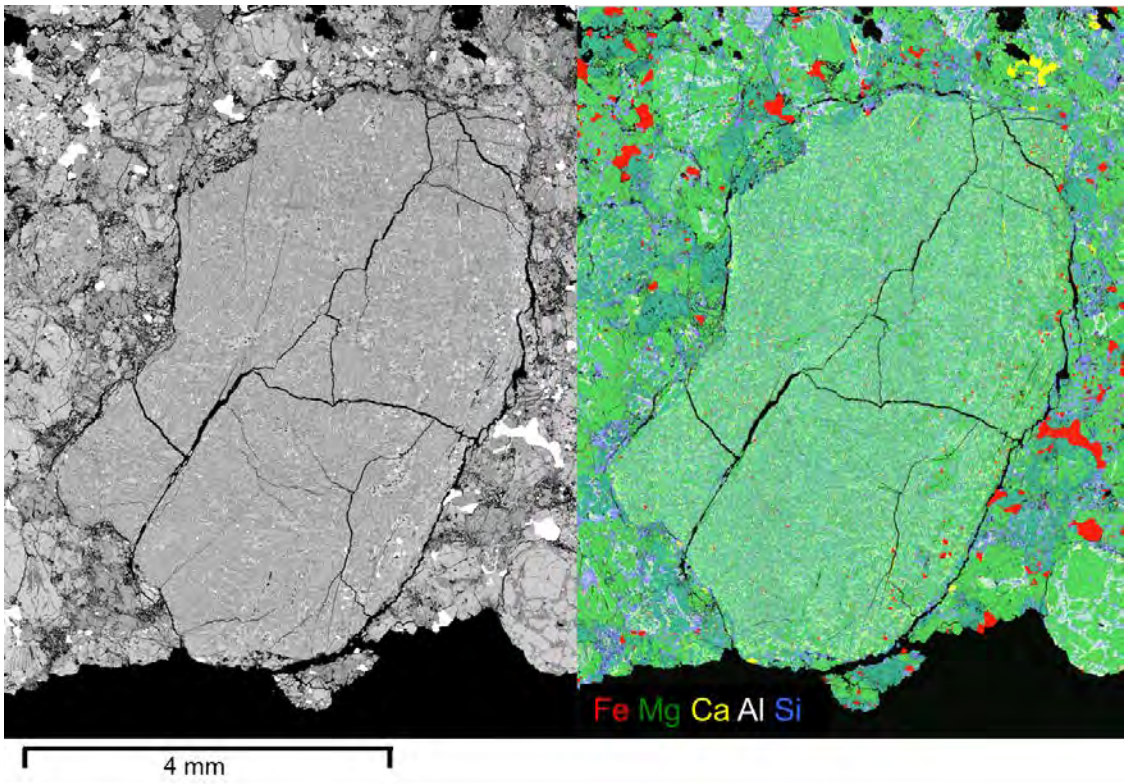

Figure 4.21. Montaged BSE (with high contrast to illustrate the texture) and EDX map of inclusion D, with Fe in Red, Ca in Yellow, Si in Blue, Mg in Green and Al in White.

The clast has broken edges and no mantle is present, indicating it was once part of a larger mass. The brittle appearance of the cracks in this clast, which often include fragments within the pore space created, imply that fracturing occurred on a cold rock, therefore not in the early history of the inclusion; however, as they do not extend into the sample, this must have occurred prior to accretion into the Barwell parent body. On the whole, the inclusion appears less shocked that the Barwell host, with fewer microcracks present. Backscattered electron images show that some cracks within the inclusion have been annealed. Apatite is present and associated with these partially healed cracks, specifically as shown in Figure 4.22, to the top right of the inclusion. It is only seen in this clast and in the bulk Barwell, and may be related to the larger apatite grain at the top right of the clast. Apatite occurs as a result of some fluid interaction, likely emplacing the mineral in pre-existing cracks. Figure 4.23 illustrates that the clast is devoid of sulphur, and contains very minor kamacite, taenite and chromite.

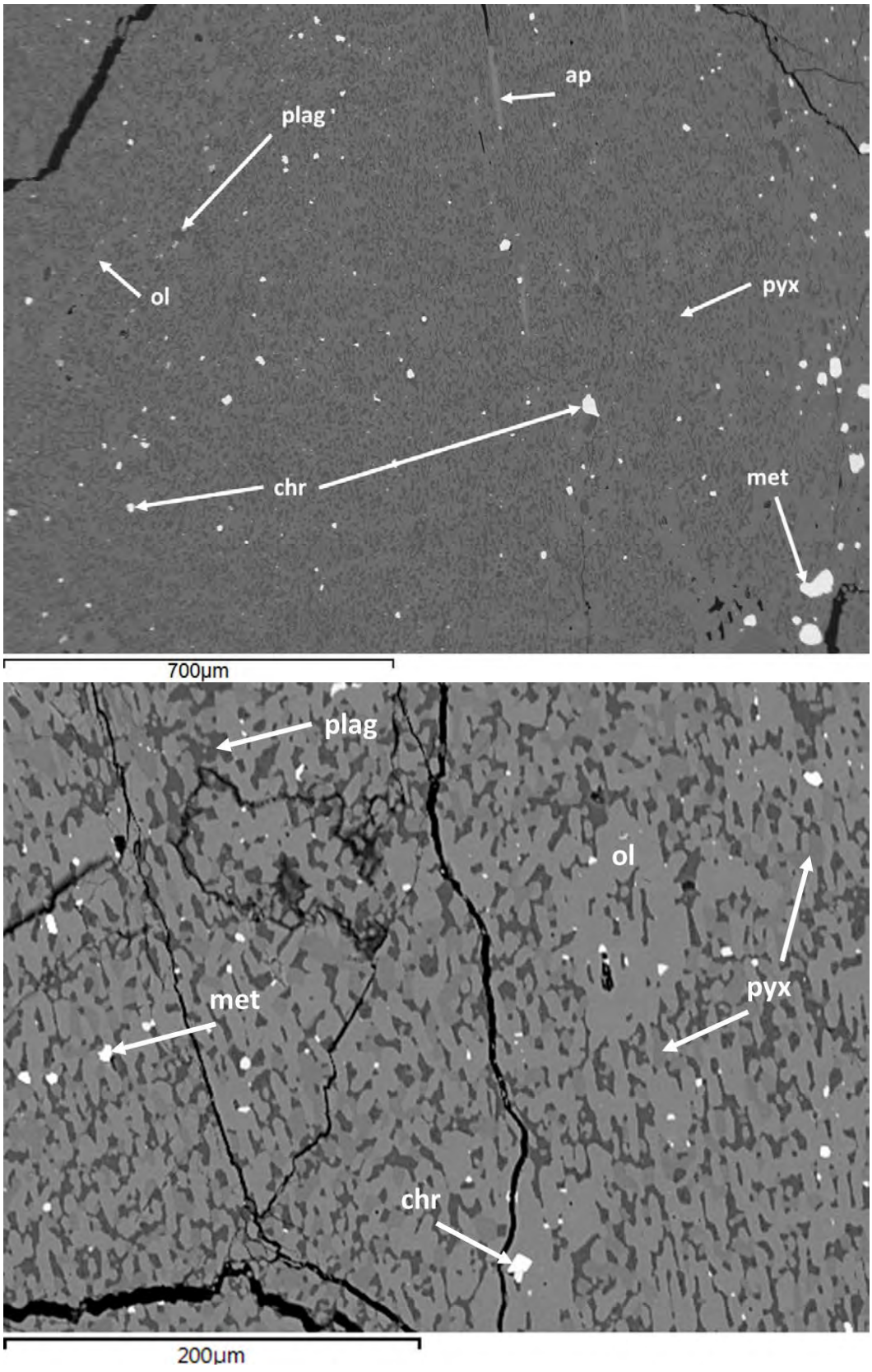

Figure 4.22. Top: Tile 12 from montaged BSE map of Barwell inclusion D, showing the feathery fine-grained texture of the inclusion and the presence of apatite infilling cracks. Bottom: Higher magnification BSE image from interior of inclusion D. Ol = olivine; pyx = pyroxene; plag = plagioclase; ap = apatite; chr = chromite; met = metal.

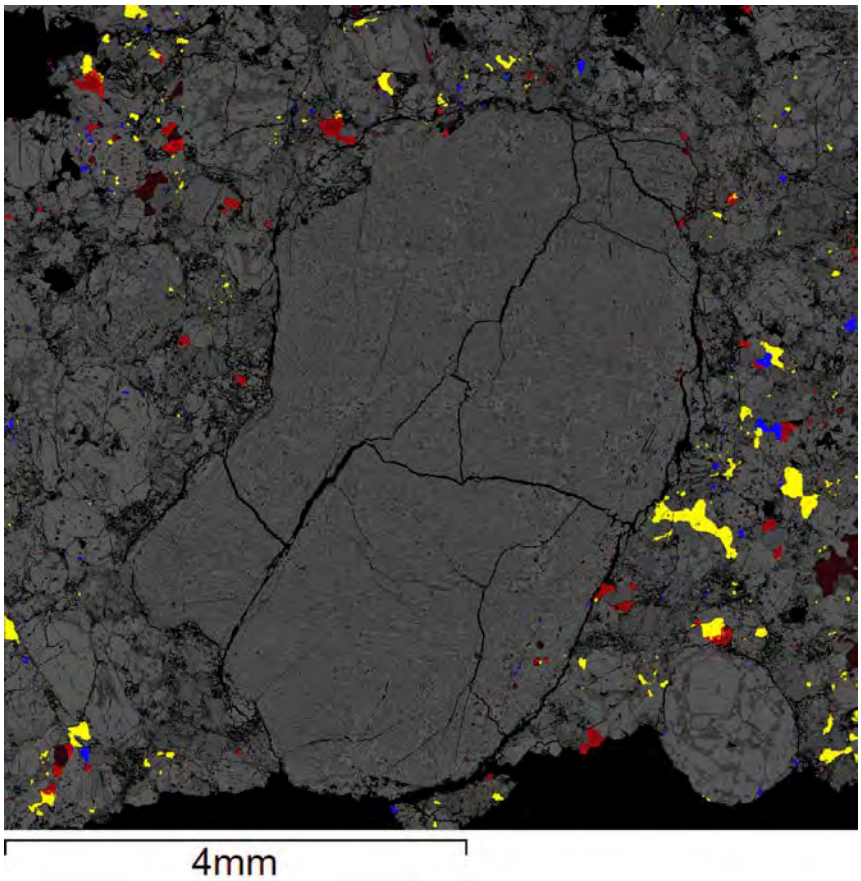

Figure 4.23. Element map showing S in yellow, Ni in red, Cr in blue overlaid on a BSE montage of the inclusion, illustrating the inclusion is devoid of sulphur, and contains very minor kamacite, taenite and chromite.

As with other inclusions, the modal mineralogy was estimated by thresholding of several areas (see example in Figure 4.24), which show good agreement across the inclusion (Table 4.9), as expected since this clast has broken edges and no evidence of a mantle and is likely a piece of a larger mass.

EPMA data from inclusion D are shown in Table 4.10. Olivine is forsteritic, with Fo 74.4 (s.d. = 0.24, n=55). Pyroxene within the inclusion is less uniform than in other inclusions, with compositions ranging from enstatite to diopside (Figure 4.25). Microprobe analyses of plagioclase show good totals between 99–101%, indicating it is crystalline, not glassy. Compositionally, plagioclase is much more uniform than other inclusions, falling mostly on the boundary between albite and oligoclase fields (Figure 4.26). Chromite grains were too small for analysis by microprobe. The small size of the metal grains made analysis challenging, with poor totals or mixed analyses (with Mg/Si present) due to sampling adjacent silicates. Any metal grains large enough were attempted, thus should provide a representative indication of the composition. Both kamacite and taenite are present.

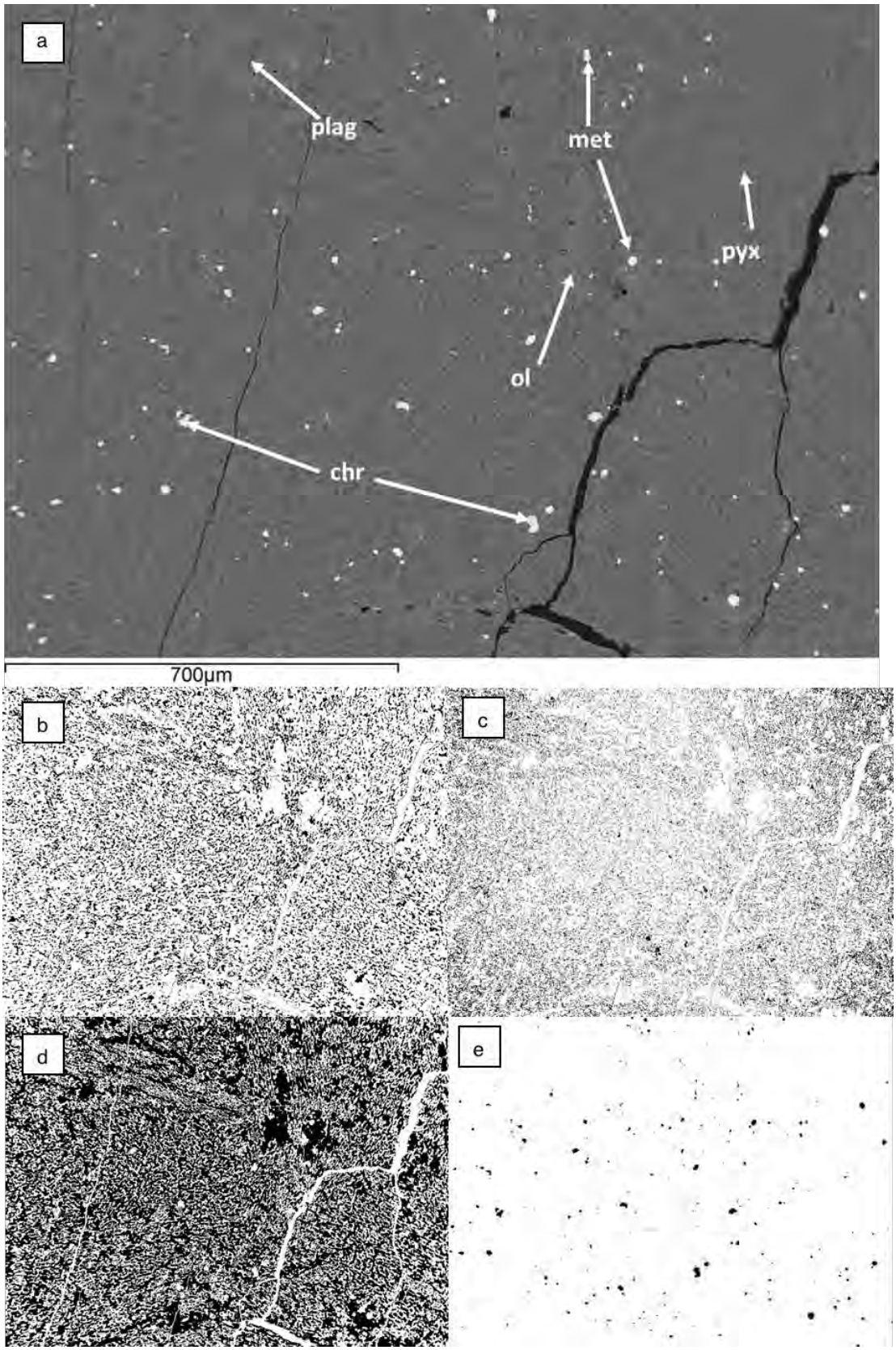

Figure 4.24. Thresholding modal mineralogy of inclusion D: a) original BSE image of Tile 13 from inclusion D; b) segmented plagioclase; c) segmented pyroxene; d) segmented olivine; e) segmented opaques (chromite + metal).

Tile	Porosity (%)	Plagioclase (%)	Pyroxene (%)	Olivine (%)	Opaques (%)	Metal (%)
12	1.0	18.3	19.8	60.0	0.4	0.6
13	2.1	21.4	16.3	59.5	0.4	0.6
18	3.5	20.0	16.7	59.3	0.3	0.3
23	1.4	20.3	18.7	59.1	0.3	0.4
Average	2.0	20.0	17.9	59.5	0.4	0.5
s.d.	1.10	1.28	1.66	0.39	0.06	0.15

Table 4.9. Modal mineralogy based on thresholding of BSE images of inclusion D.

Oxide	Olivine (n=54)	s.d.	Plagioclase (n=13)	s.d.	High-Ca Pyroxene (n=40)	s.d.	Low-Ca Pyroxene (n=6)	s.d.
SiO_2	38.87	0.30	65.10	1.03	53.98	0.59	55.44	0.42
MgO	38.24	0.25	0.25	0.40	16.71	0.55	29.30	0.16
FeO	22.95	0.17	0.70	0.27	5.18	0.41	14.22	0.17
TiO_2	0.01	0.01	0.03	0.02	0.47	0.04	0.19	0.01
Cr_2O_3	0.05	0.09	0.02	0.03	0.82	0.05	0.10	0.02
MnO	0.48	0.02	0.02	0.01	0.24	0.01	0.50	0.02
CaO	0.05	0.07	2.21	0.16	21.66	0.71	0.68	0.10
Na_2O	b.d.l		10.06	0.26	0.64	0.13	0.04	0.05
Al_2O_3	b.d.l		21.30	0.25	0.70	0.51	0.24	0.20
K_2O	n.a.		1.12	0.15	n.a.		n.a.	
V_2O_3	b.d.l		b.d.l		n.a.		n.a.	

Table 4.10. EPMA data in wt% oxide for phases in inclusion D. [b.d.l. – below detection limit; n.a. – not analysed].

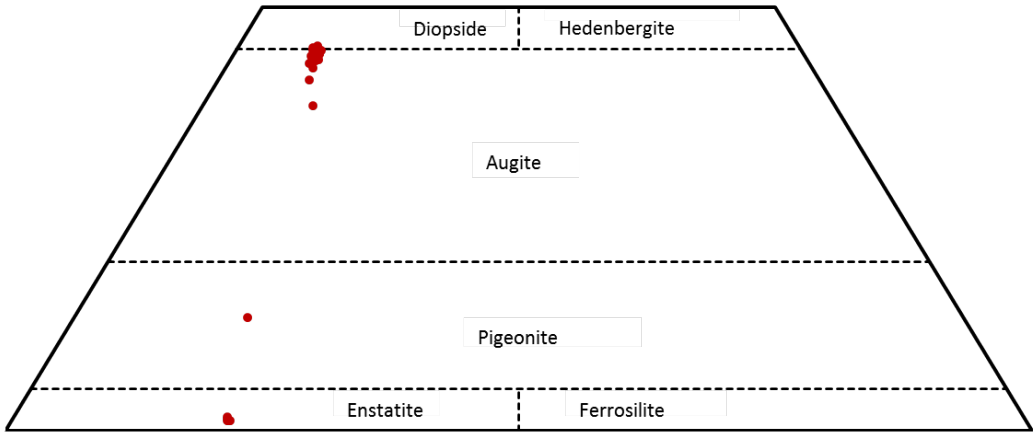

Figure 4.25. Pyroxene quadrilateral showing EPMA data points for inclusion D. Pyroxene within the clast is less uniform than in other inclusions, with compositions ranging from enstatite to diopside.

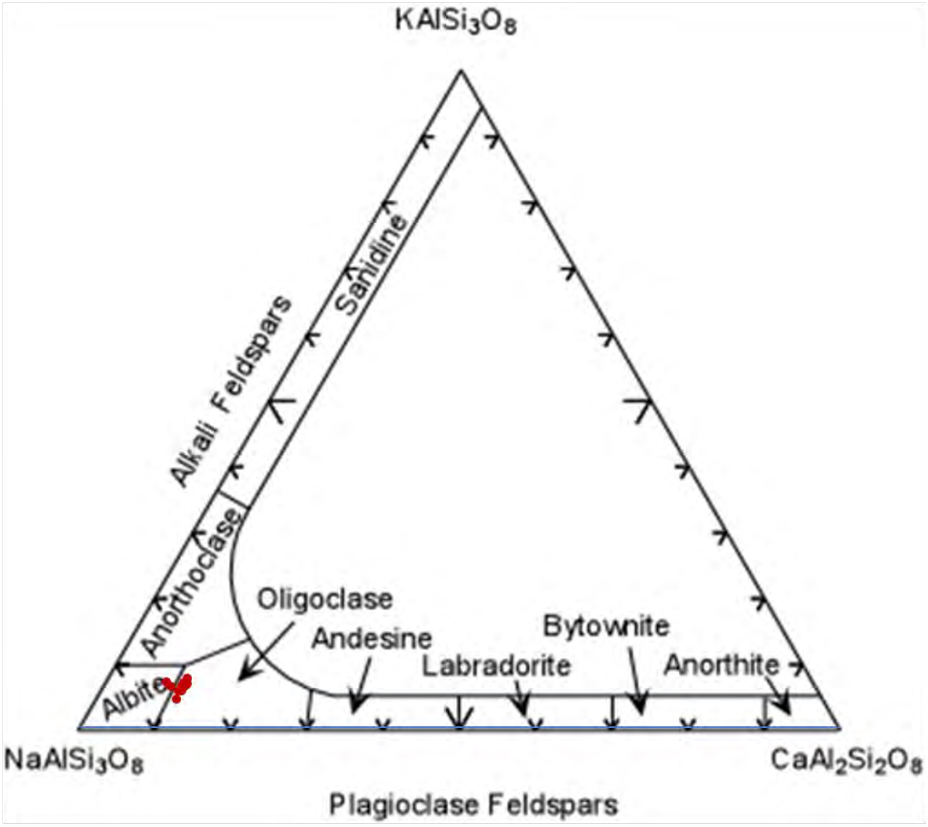

Figure 4.26. Feldspar tri-plot showing EPMA data points for inclusion D, showing that plagioclase has equilibrated across the inclusion.

4.3.2.5 Original “Pebble”

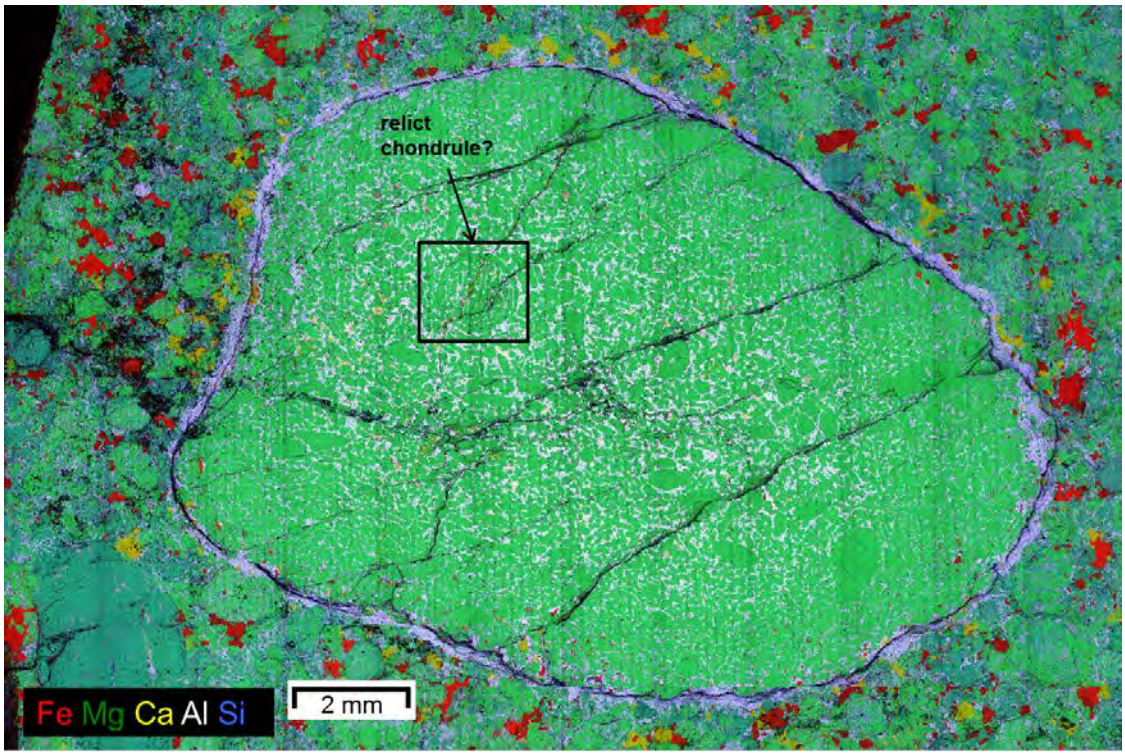

Figure 4.27. Montaged false colour EDX element map of the original Barwell “Pebble”. Green: Mg, Red: Fe, Yellow: Ca, Blue: Si, White: Al. Note that the Al enrichment in the cracks around the edge of the inclusion is not inherent, but likely a result of aluminium oxide used in preparation/slicing of the sample.

The sawn surface exposing the original Barwell “Pebble” was analysed with the FEI Quanta 650 SEM. (Figure 4.27). This instrument is notable in that no sample preparation was required, a crucial point when dealing with this most precious sample. Elemental maps were acquired at low vacuum, thus the sample did not require a carbon coat. The results show an olivine- and plagioclase-rich inclusion, with some spinel and no FeNi metal evident. Olivine (Fo 75.5) is the dominant mineral, occurring as elongate euhedral crystals up to 1.0mm long (although in one extreme case, 4.0mm) or as subhedral grains 0.2 – 1.0mm in diameter (Hutchison et al., 1988). The mean grain-size varies randomly from one area to another (Hutchison et al., 1988). Between the olivine crystals lie dark brown to opaque, turbid plagioclase crystals 0.1-0.4 mm long, with a length to breadth ratio of 6:1 or more, which are often surrounded by a granular mosaic of clear, crystalline plagioclase. The elongate turbid crystals may occur as groups with a sub-parallel alignment, individuals being separated from each other by clear plagioclase. The plagioclase composition varies from An 74-70 in the centre of the inclusions to An 20 towards the margin (Hutchison et al., 1988), and is compared to plagioclase from

inclusions in this study in the following section. Spinel is markedly more aluminous than L chondrites and the inclusions in this study. Hutchison et al. (1988) found ~ 27 wt % Al_2O_3 in the centre of the inclusion, declining to 10.5 wt % near the margin, and Cr number (Cr / (Cr + Al)) increased from 47 in the centre to 80 at the edge. This inclusion is devoid of pyroxene, similar to inclusion A in this study. Sub-parallel fractures, which do not continue into the host, are clear. The element map also shows the clear distinction between the core of the "Pebble" and the smaller grains towards the edge. No modal abundances were given by Hutchison et al. (1988) and could not be calculated accurately in this study since BSE imaging was not viable on large unpolished surface due to charging.

Texturally, there are no similarities with the inclusions exposed in this study, however, similar to inclusion B, there is a feature that is reminiscent of a barred olivine chondrules, as seen in Figure 4.28.

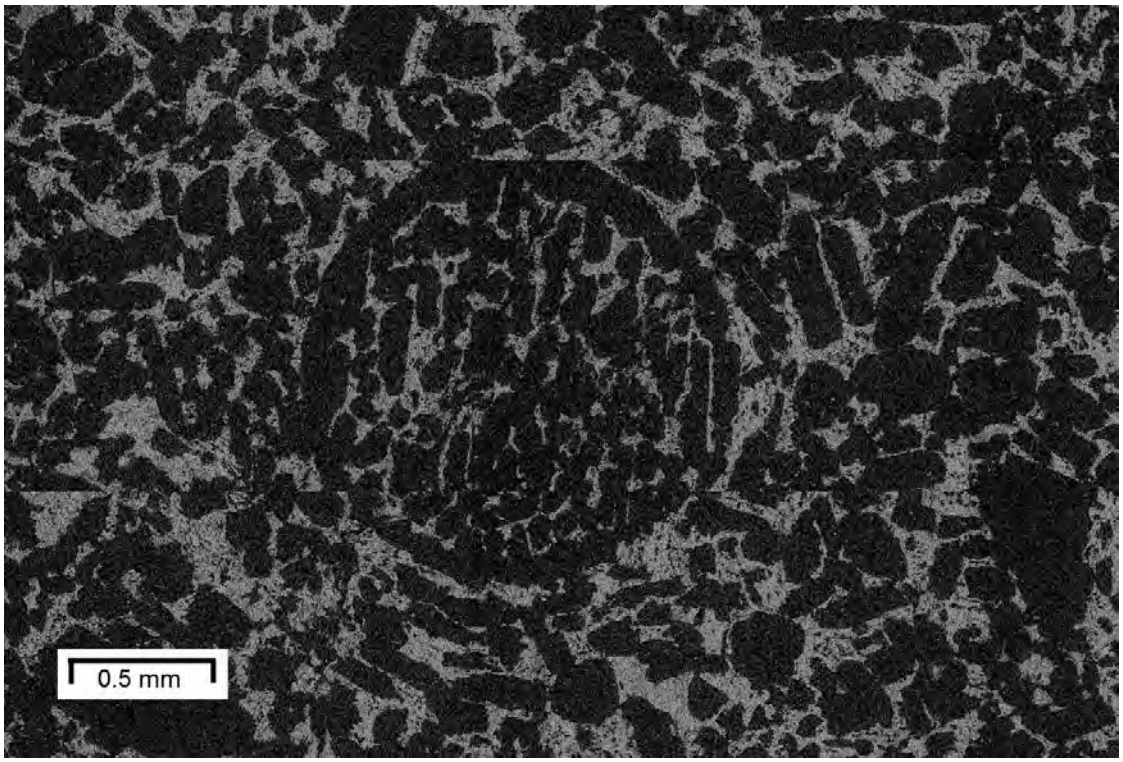

Figure 4.28. Aluminium EDX map of the possible barred chondrule in the Barwell "Pebble".

4.3.3 Comparison of modal mineralogy and major element composition of inclusions

As Table 4.11 shows, the inclusions are similar to each other in their porosity, which is mostly present in large cracks, and their chromite content. Figure 4.29 shows that on removing these and normalising the contents of olivine, plagioclase and pyroxene, the modal mineralogies vary widely. Olivine is the dominant mineral in A, B, and D and compositions are equilibrated (Figure 4.30). Inclusion B shows equal content in olivine and pyroxene. Pyroxene compositions are similar across all inclusions, apart from A, which lacks pyroxene entirely (Figure 4.31). Inclusions B and D contain native metal, though at very low abundances (≤ 0.5 % modally). EPMA results are given in full in *Appendix 10*.

Chromite is similar in all elements across the inclusions, apart from Al, which varies in composition from ~5.5 wt. % oxide in B and C to 9.2 wt. % oxide in inclusion A. Plagioclase in inclusion A is also more aluminous than in the other three inclusions (24 wt. % oxide versus 21 wt. % oxide). Most feldspar is oligoclase, however, A and B show enrichment in calcium relative to the host Barwell, with compositions similar to plagioclase at the edge of the Barwell “Pebble” (Figure 4.32). This may represent an igneous fractionation trend, or a trend towards thermal equilibration, indicating that plagioclase in inclusions A and B has not fully equilibrated with the host, whereas plagioclase in C and D has.

Phase	A	B	C	D
Porosity	2.5	3.0	0.5	2.0
Plagioclase	11.5	16.0	13.0	20.0
Pyroxene	-	11.0	43.0	18.0
Olivine	83.5	68.0	43.5	59.5
Chromite	2.0	2.0	0.5	0.5
Metal	-	-	-	0.5

Table 4.11. Modal abundance of minerals for all four inclusions for comparison, based on BSE image thresholding in ImageJ, given to closest 0.5%.

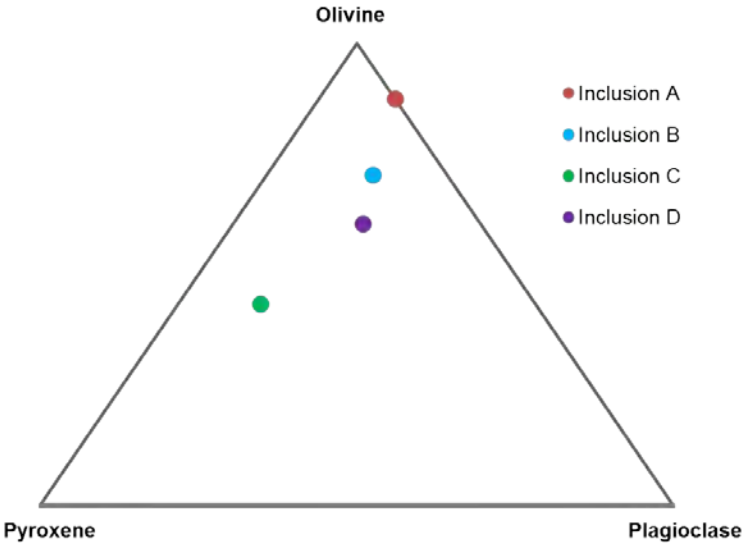

Figure 4.29. Comparison of the normalised olivine, pyroxene and plagioclase modal proportions in the four inclusions.

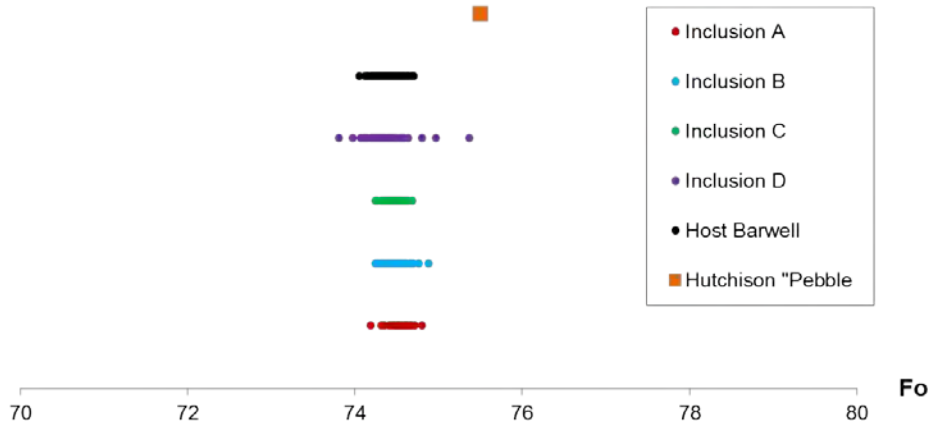

Figure 4.30. Olivine compositions of inclusions A, B, C, D, host Barwell, and the “Pebble” (Hutchison et al. 1988).

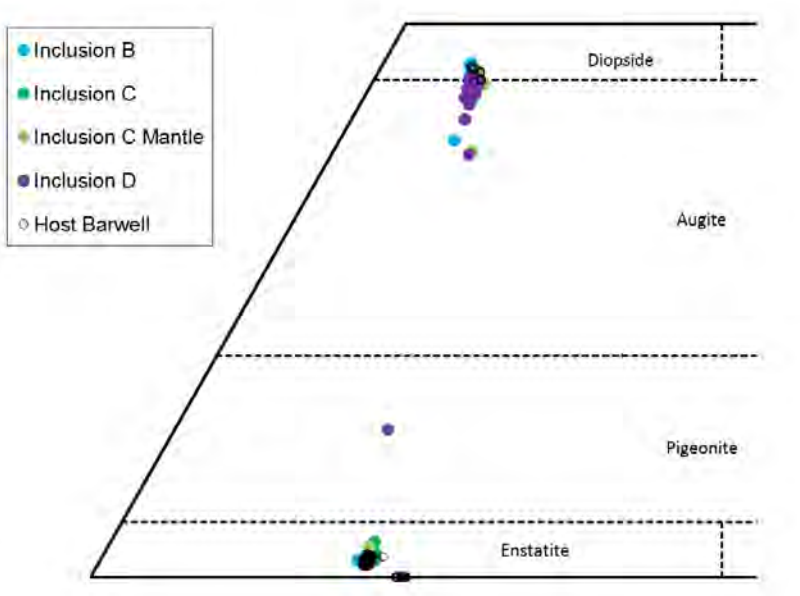

Figure 4.31. Pyroxene compositions of inclusions A, B, C, D and host Barwell, by EPMA.

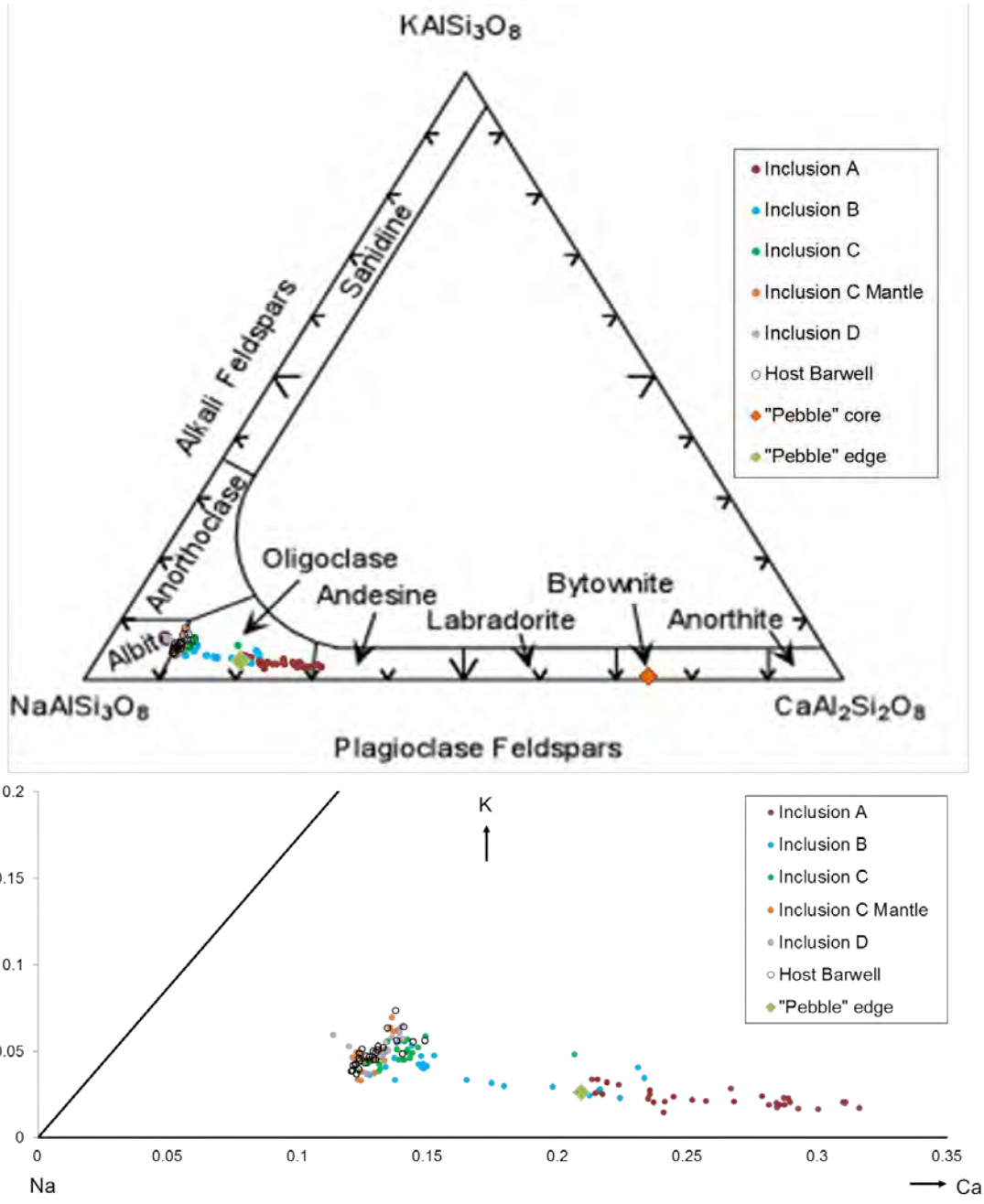

Figure 4.32. Feldspar tri-plots from EPMA analyses of inclusions and host Barwell. “Pebble” analyses from Hutchison et al. (1988).

Chromite compositions in inclusions A, B, C, and the host Barwell are all very similar (e.g. Cr varies by ~2 wt%, Fe varies by 1 wt%), as are those of silicate minerals, therefore showing the inclusions as equilibrated with the host Barwell. For this reason, all chromite analyses for the three inclusions and host rock were averaged to provide a chromite composition for inclusion D, for use in reconstructing a bulk rock composition. However, as shown in Figure 4.33, the Al_2O_3 concentration in chromite in inclusion A is considerably higher than in the

other inclusions, showing more affinity with the edge of the Barwell "Pebble". Inclusions B and C are close to host Barwell chromite compositions, indicating this is a trend with thermal equilibration, again indicating that inclusion A is less equilibrated than the others.

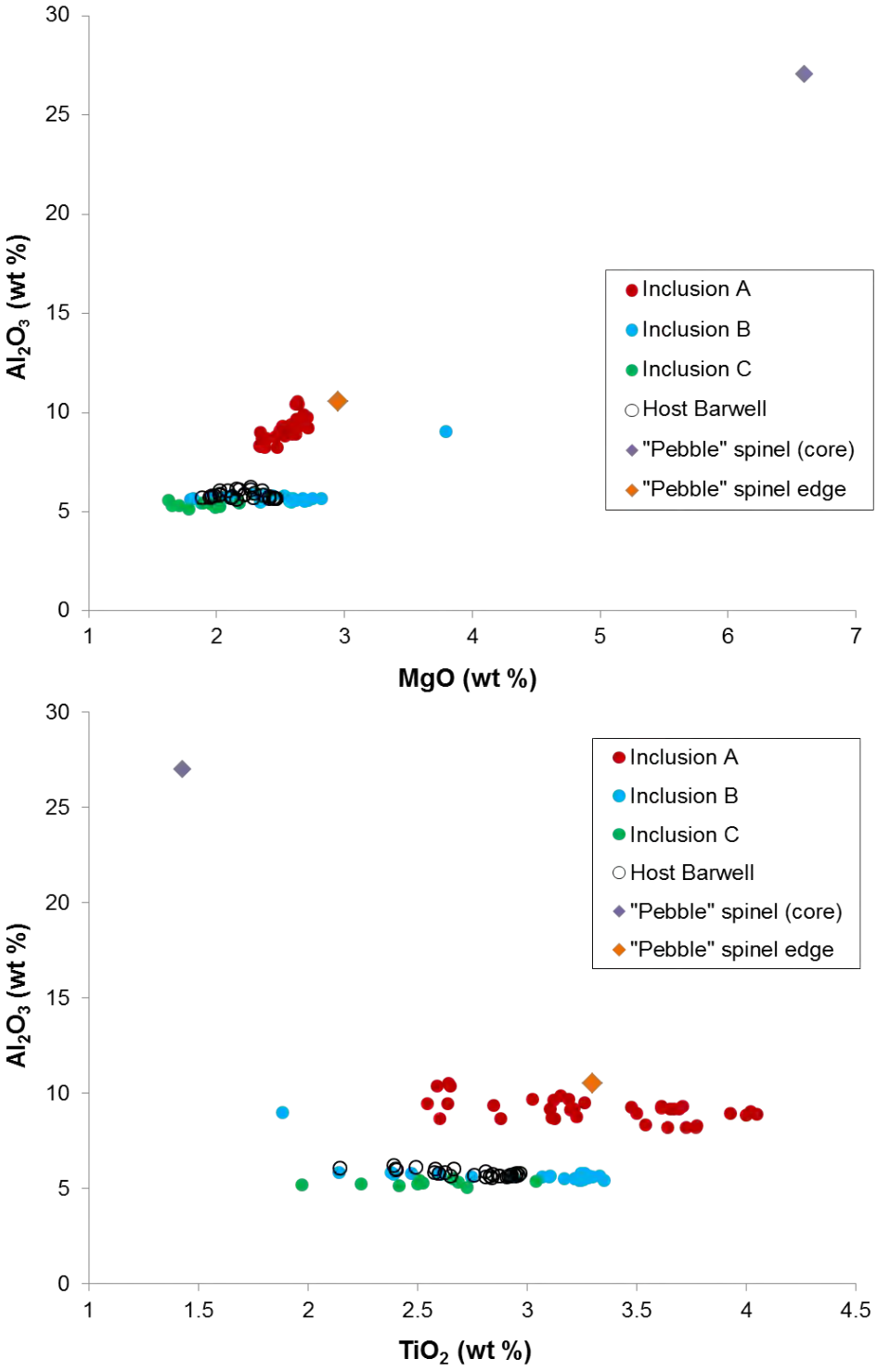

Figure 4.33. Comparison of Al_2O_3 and MgO (top) and Al_2O_3 and TiO_2 (bottom) in chromite in inclusions and host Barwell from EPMA analyses. "Pebble" analyses from Hutchison et al. (1988).

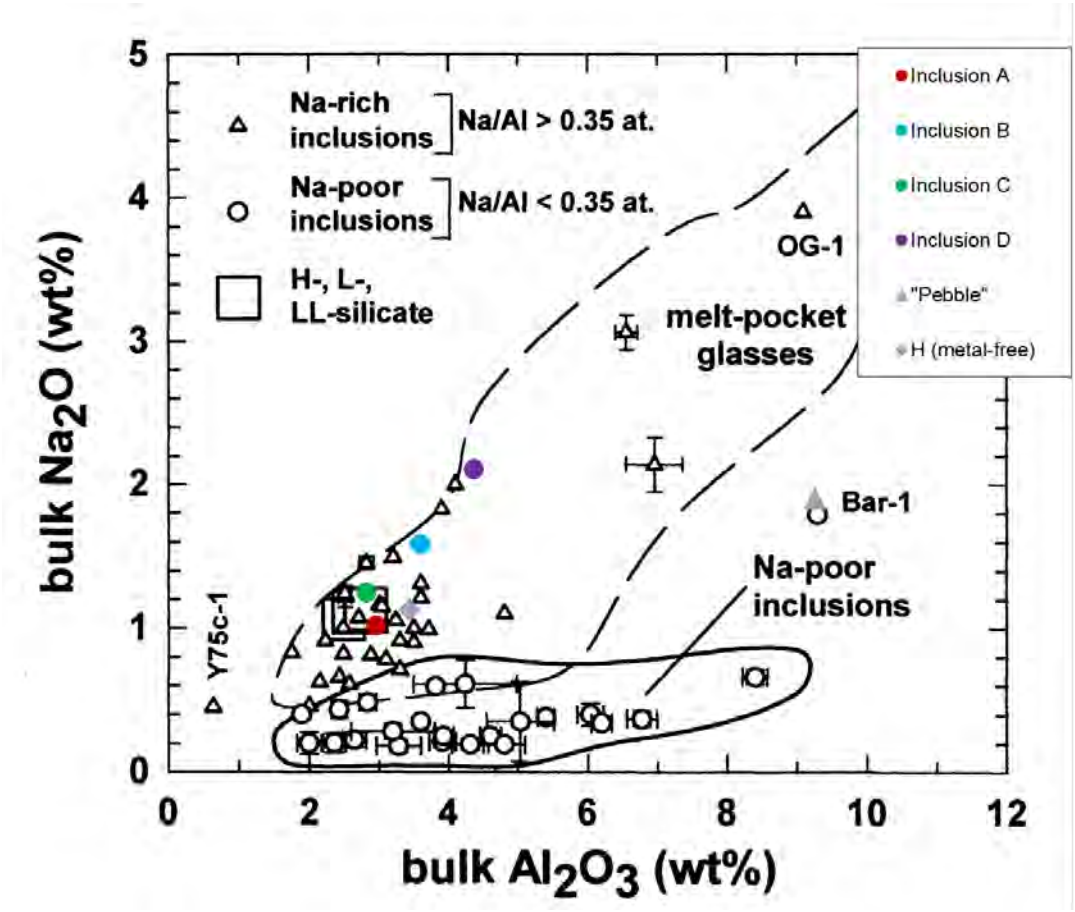

Figure 4.34. Bulk Na_2O against Al_2O_3 for inclusions in this study, superimposed on Figure 2 from Ruzicka et al. (2000), H (metal-free) values from Mason (1965). Melt-pocket glass data from Dodd and Jarosewich (1982) and Dodd et al. (1983). H/L/LL chondrite data from Jarosewich (1990).

Figure 4.34 compares soda and alumina abundances from inclusions in this study and the Barwell “Pebble” with those analysed by Ruzicka et al. (2000), similarly to Na-rich inclusions described by those authors, and further indicating a relationship between OC silicates and inclusions A and C although B and D are more sodium-rich. All fall in the wide range of melt-pocket glasses.

Bulk compositions of each inclusion (Table 4.12) were calculated based on the modal mineralogy and average mineral compositions from EPMA data. Note that for inclusion D, chromite grains were too small for analysis by microprobe, therefore an estimation of the composition has been made.

	INCLUSION A			INCLUSION B			INCLUSION C			INCLUSION D		
Element	Bulk wt%	Bulk wt % normalised*	Atomic %	Bulk wt%	Bulk wt % normalised*	Atomic %	Bulk wt%	Bulk wt % normalised*	Atomic %	Bulk wt%	Bulk wt % normalised*	Atomic %
Si	18.87	31.88	34.99	20.44	35.02	38.16	22.76	40.25	43.12	21.86	37.87	40.87
O	41.80			42.44			43.21			42.95		
Mg	20.31	34.31	43.51	18.15	31.09	39.15	17.46	30.87	38.22	16.53	28.64	35.71
Fe	16.07	27.14	14.98	14.08	24.12	13.21	12.63	22.33	12.03	12.79	22.16	12.03
Ti	0.07	0.12	0.08	0.08	0.14	0.09	0.11	0.20	0.13	0.05	0.09	0.06
Cr	0.65	1.09	0.65	0.73	1.24	0.73	0.19	0.33	0.19	0.21	0.37	0.21
Mn	0.34	0.57	0.32	0.31	0.53	0.30	0.33	0.58	0.32	0.28	0.49	0.27
Ca	0.45	0.76	0.59	1.33	2.28	1.74	0.51	0.90	0.67	1.80	3.11	2.35
Na	0.76	1.28	1.72	1.18	2.02	2.69	0.93	1.64	2.15	1.57	2.72	3.58
Al	1.60	2.71	3.09	1.94	3.32	3.76	1.53	2.70	3.01	2.36	4.08	4.58
K	0.05	0.08	0.06	0.11	0.18	0.14	0.11	0.19	0.14	0.19	0.33	0.26
Sr	0.00	0.01	0.00	0.00	0.01	0.00	0.00	0.01	0.00	0.00	0.00	0.00
Co	0.02	0.03	0.02	0.01	0.02	0.01	0.00	0.00	0.00	0.02	0.03	0.01
V	0.01	0.02	0.01	0.01	0.01	0.01	0.00	0.00	0.00	0.00	0.00	0.00
Total	100.99			100.81			99.75			100.67		

Table 4.12. Bulk major element composition of all four inclusions for comparison. Bulk weight % calculated from modal mineralogy and EPMA data. * = bulk wt% without oxygen, normalised. Atomic % calculated from this to allow comparison with atomic ratios in the literature (Table 4.13).

Figure 4.35 shows the CI-normalised abundances of major elements in the calculated bulk inclusions in comparison with H and L chondrite averages from Wasson and Kallemeyn (1988). The inclusions show considerable variation in bulk elemental composition from that of H and L chondrites. Most elements are enriched, with some exceptions; both A and C are depleted in Ca, whilst C and D are depleted in Cr and inclusion A is also depleted in K. Depletion in K may indicate vapour fractionation as K is volatile, however this does not explain the loss of Ca. The apparent depletion of Cr in clast D could be an artefact of the data since EPMA data collection was not possible. The inclusions are not depleted in Na [Na/Al = 0.56 (A); 0.72 (B); 0.71 (C) and 0.78 (D)], thus fit into the 'Na-rich' classification of Ruzicka et al. (1998).

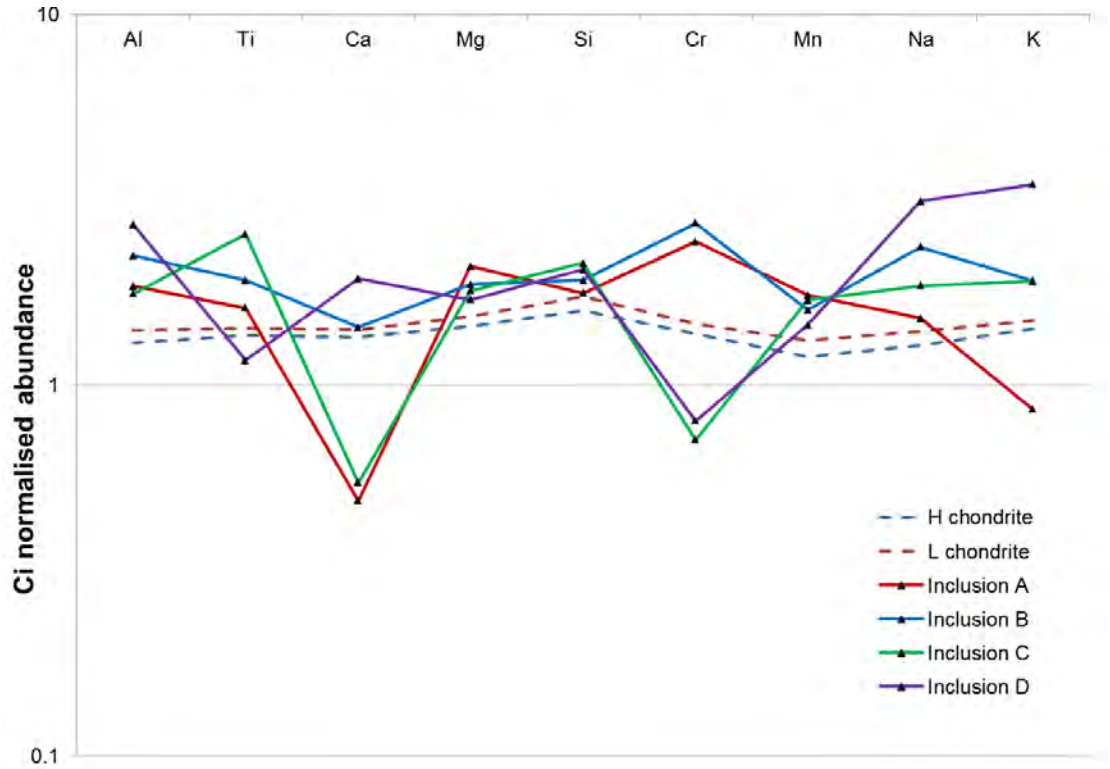

Figure 4.35. A graph of CI-normalised major element chemistry for inclusions in this study and H and L chondrite averages (Wasson and Kallemeyn, 1988).

Bulk data (Table 4.12) were then normalised without oxygen, and atomic % recalculated for comparison with ordinary chondrite bulk atomic ratios from Hutchison (2004), since inter-element ratios are more diagnostic of meteorite class than the elemental abundances alone. These ratios are given in Table 4.13.

Ratios	Inclusion A	Inclusion B	Inclusion C	Inclusion D	Barwell "Pebble"	H chondrite	L chondrite
Mg/Si	1.24	1.03	0.89	0.87	0.95	0.96	0.93
Al/Si (x 10^4)	883	986	699	1122	259	694	685
Ca/Si (x 10^4)	168	455	156	576	67	520	498
Fe/Si	0.43	0.35	0.28	0.29	0.33	1.63	1.16
Ca/Al	0.19	0.46	0.22	0.51	0.26	0.75	0.73
Na/Al	0.56	0.72	0.71	0.78	0.34	0.67	0.67
Na+K/Al	0.58	0.75	0.76	0.84	0.34	0.71	0.72
Si/Al	11.33	10.14	14.31	8.91	3.86	14.41	14.6
Fe/Mn	46.57	44.7	37.68	44.51	49.36	117.5	81.67
Fe/Mg	0.34	0.34	0.31	0.34	0.34	0.85	0.63

Table 4.13. Major element ratios calculated from atomic % for Barwell inclusions in this study, compared with the Barwell “Pebble” (calculated from bulk analyses in Hutchison et al. 1988), and H and L chondrites (Hutchison, 2004, after Wasson and Kallemeyn, 1988).

Refractory lithophile elements Al and Ca show near perfect correlation between chondrite groups. Figure 4.36 shows data from Hutchison (2004) (after Wasson and Kallemeyn, 1988) for the 13 chondrite groups, with added bulk data from this study for the igneous inclusions in Barwell. All inclusions show considerable depletion in Ca. A and B also show enrichment in Al compared with the ordinary chondrites.

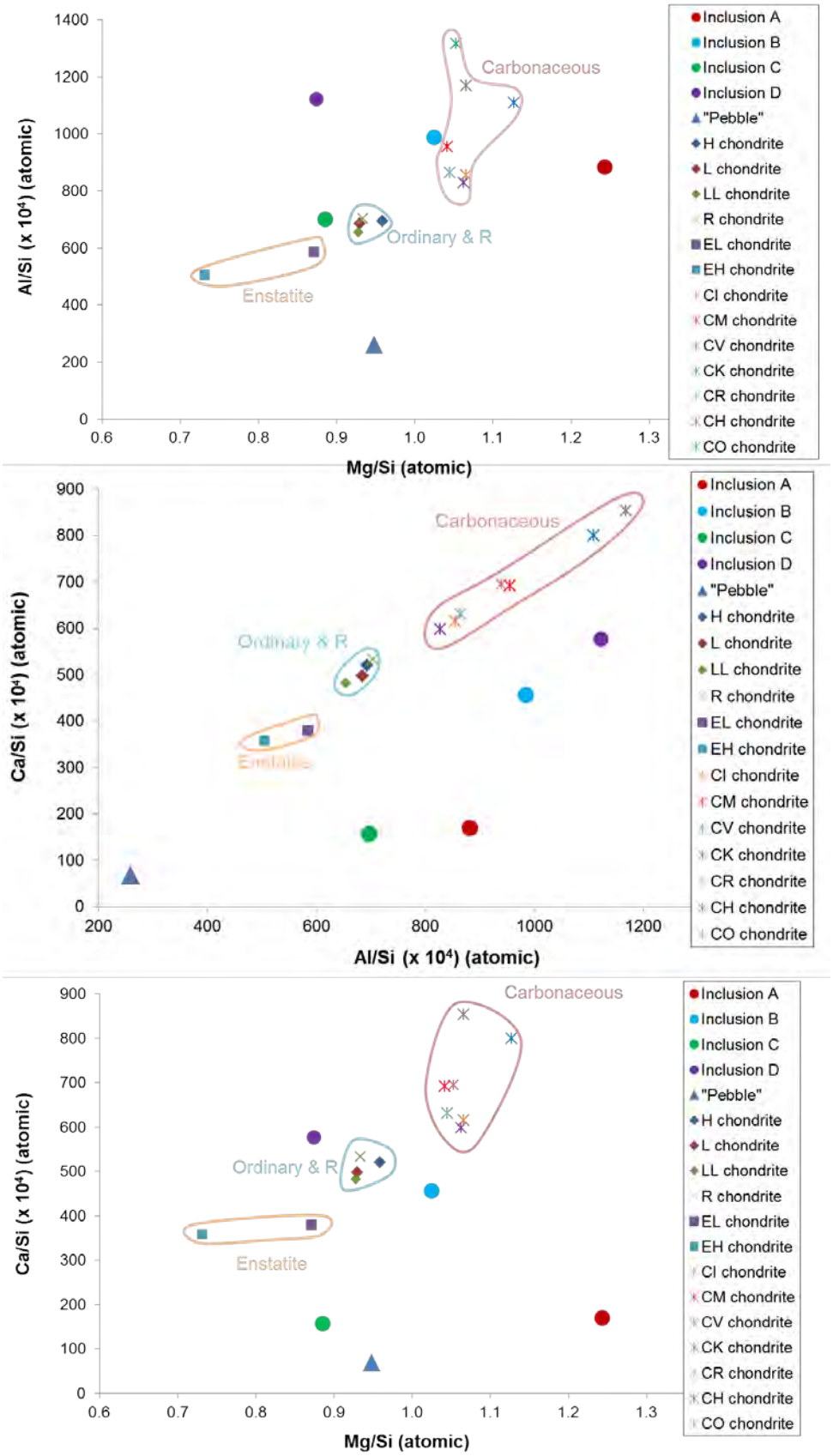

Figure 4.36. Ratios calculated from bulk rock compositions of igneous inclusions in this study (Table 4.13) compared with 13 chondrite groups (Hutchison, 2004) and the Barwell "Pebble" recalculated from Hutchison et al. (1988). Top: Mg/Si against Al/Si (x10^4); middle: Al/Si (x10^4) against Ca/Si (x10^4); bottom: Mg/Si against Ca/Si (x10^4).

The inclusions in this study plot similarly to silicate portions of ordinary chondrites in Figure 4.36, which indicates a loss of Fe. There is some increase in Fe/Mg ratio, which could be a result of igneous fractionation. This does not cause considerable change in Fe/Mn ratio due to the similar behaviour of Fe^{2+} and Mn^{2+} (Goodrich and Delaney, 2000). The inclusions in this study still fall within chondrite ratios as bounded by CI and CH values (Figure 4.37).

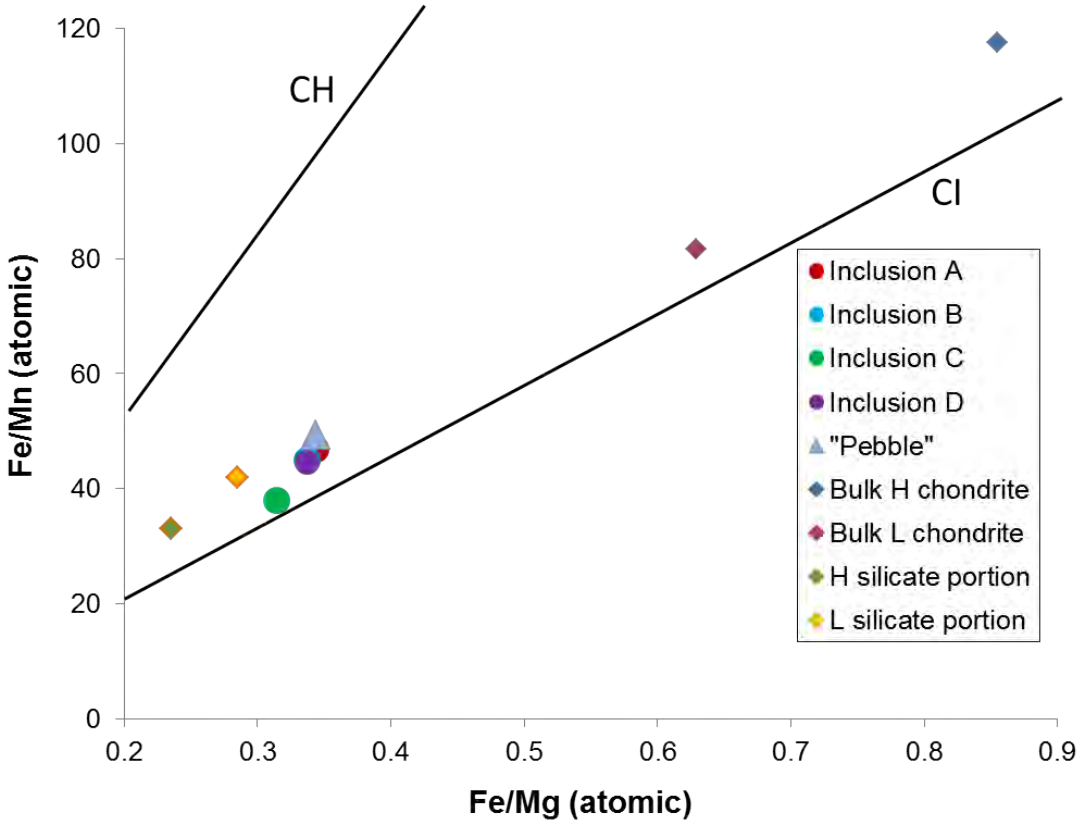

Figure 4.37. Fe/Mg against Fe/Mn for inclusion in this study (note overlap of inclusion B and D) and H and L chondrites (calculated from Wasson and Kallemeyn, 1988) and silicate portions of H and L chondrites (from Goodrich and Delaney, 2000, after Jarosewich, 1990). The area bounded by CI and CH chondrites indicates chondritic values of Fe/Mn and Fe/Mg.

Figure 4.38 is adapted from the Hezel et al. (2006) study of silica-rich components (SRCs) in OCs. The plot shows SRCs from other studies, as well as individual chondrules analyses, and some terrestrial rocks for comparison. The inclusions in this study, and the Barwell “Pebble” fall in a similar field to type II chondrules.

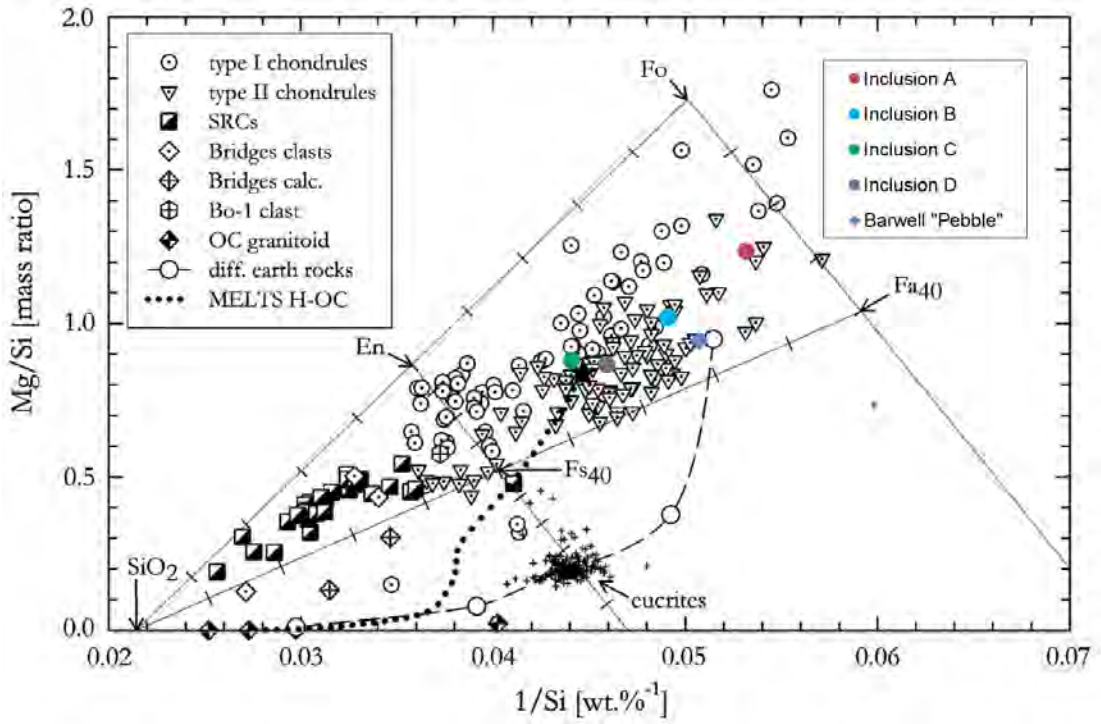

Figure 4.38. Diagram adapted from Hezel et al. (2006). A comparison of bulk Mg/Si ratio and silicon content for the inclusions in this study, and the Barwell "Pebble" (Hutchison et al., 1988) compared with chondrules (Dodd, 1978; Grossman and Wasson, 1983; Olsen, 1983; Sears et al., 1984; Rubin and Pernicka, 1989; Jones, 1990, 1994, 1996; McCoy et al., 1991; Matsunami et al., 1993; Bridges et al., 1995; Ruzicka et al., 1995; Huang et al., 1996; Tachibana et al., 2003; Hezel et al., 2004, silica-rich components (SRCs; Hezel et al. 2006), clasts from Parnallee (Bridges et al. 1995), a silica-rich clast in Bovedy (Ruzicka et al., 1995), a granitoid clast in Adzhi Bogdo (Bischoff et al., 1993) . The four straight lines are scaled mixing lines between Fo-SiO_2, Fo-Fa, Fa_{40} – SiO_2 and En-Fs, where Fo = forsterite, En = enstatite, Fa = fayalite and Fs = ferrosilite. "Diff Earth rocks" are terrestrial data from Hughes (1982); In order of increasing SiO2: komatiitic peridotite – basanite – tholeiitic basalt – andesite – granite. "MELTS H-OC" describes a fractionation trend as calculated by the authors in the MELTS program, using a starting composition of H chondrites (black star) from Mason (1965).

The CIPW norm, developed by petrologists Cross, Iddings, Pirsson, and Washington (1902), is used to compare rock types independently of their modal mineral assemblages. The calculation produces 'normative constituents' which are water-free standard mineral compounds, and eliminate the effects of pressure, allowing comparison of original melt chemistry. Figure 4.39 shows normative compositions of inclusions A through D superimposed on a diagram from Armstrong and Ruzicka (2015), indicating that, as the calculated compositions do not plot near cotectics or reaction curves, the source of these inclusions was not fully differentiated.

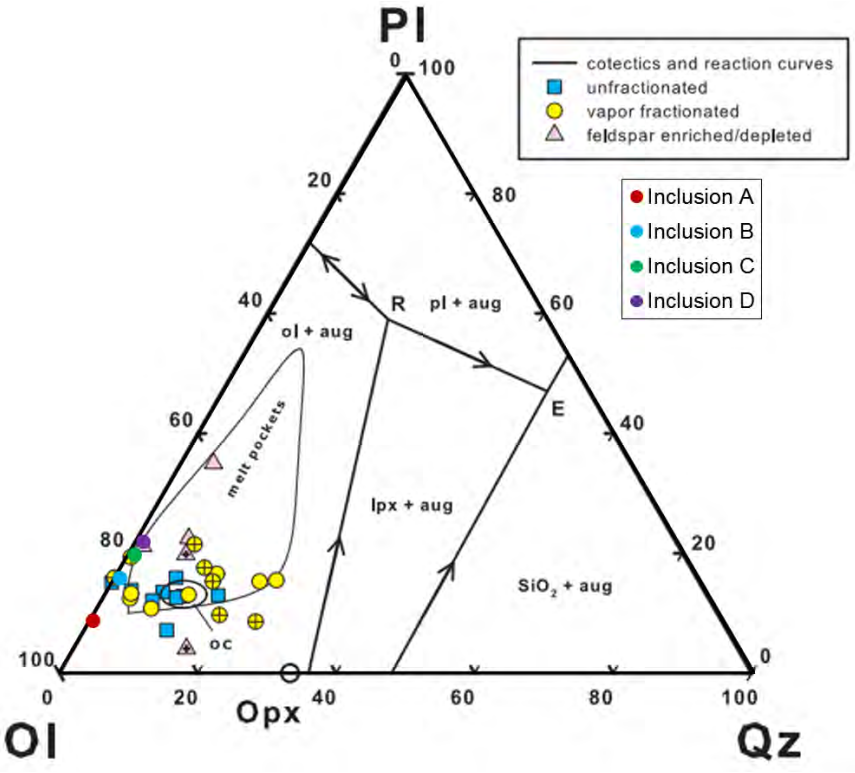

Figure 4.39. CIPW normative ternary diagram for olivine, quartz and plagioclase, adapted from Armstrong and Ruzicka (2015) with data for inclusions in this study superimposed.

4.3.4 Trace element analysis of Barwell inclusions

LA-ICP-MS analyses were carried out on individual grains of each silicate mineral in inclusions A, B, and C, with spot sizes ranging from 15 to 40 μm, depending on the availability of grains of sufficient size. Some larger areas were rastered during a ~ 90 second laser ablation run in order to provide an approximation of a 'bulk' measurement. Five areas, each of 225 μm^2, were ablated in each inclusion. The element list and information on internal standards is provided in the method description in *Section 2.4*. Figure 4.40 shows an example of the locations of both spot and bulk analyses of inclusion A.

Note that *Appendix 12* includes full LA-ICP-MS data for all inclusions.

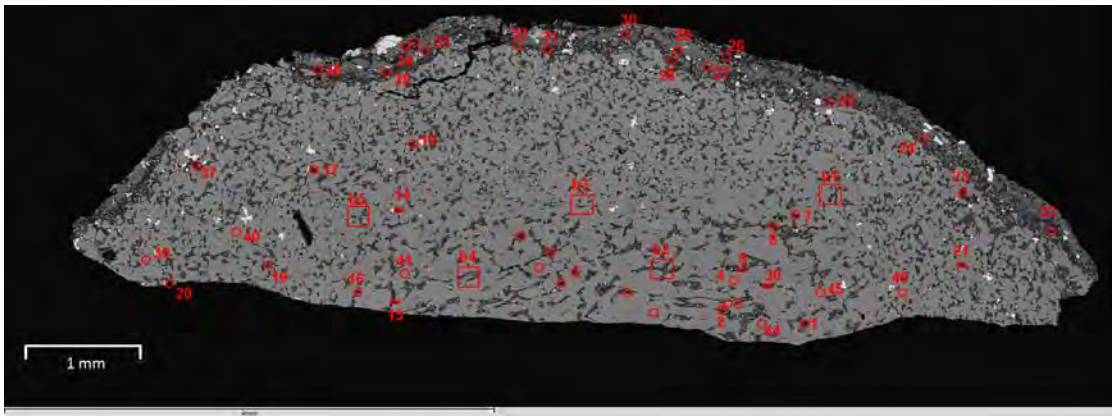

Figure 4.40. LA-ICP-MS spot analyses and bulk raster analyses marked on a BSE montage of inclusion A.

Mn was measured by both EPMA (bulk calculated from modal mineralogy) and LA-ICP-MS and shows good agreement for bulk analyses: inclusion A, 3400 ppm by EPMA versus 3361 ppm by LA-ICP-MS; inclusion B, 3100 ppm versus 2707 ppm; C, 3300 ppm versus 3445 ppm.

Owing to their affinity for metal, highly siderophile elements (Os, Ir, Ru, Rh, Pt, Pd, Re and Au) can be used as indicators of differentiation on planetary bodies (Day et al., 2016). Depletions in siderophile and chacophile elements would indicate efficient removal of metal and sulphide. However, as a result of limitations of the instrumentation, it was not possible to measure abundances of several HSEs, including Ru, Rh, Pd, Re, Os, Ir, and Pt. Au was measured as below detection limit (maximum of 0.048 ppm), however, bulk H and L chondrites have concentrations of 0.215 ppm and 0.162 ppm respectively, therefore the data indicate that the inclusions are depleted in HSE, in keeping with their low metal contents. However, Figure 4.41 shows the CI normalised bulk abundances of siderophile elements in each inclusion, measured by EPMA and LA-ICP-MS, with bulk H and L chondrite concentrations for reference.

In comparison to average bulk H and L chondrites, inclusions are depleted in all siderophile elements analysed apart from Mn, where they have chondritic abundances. These results indicate that the inclusions have lost iron and siderophile elements, presumably as part of a FeNi melt prior to accretion into the Barwell parent body. Nickel is especially depleted in all samples, with inclusion C showing a thousand-fold decrease in comparison with H and L OC bulk concentrations.

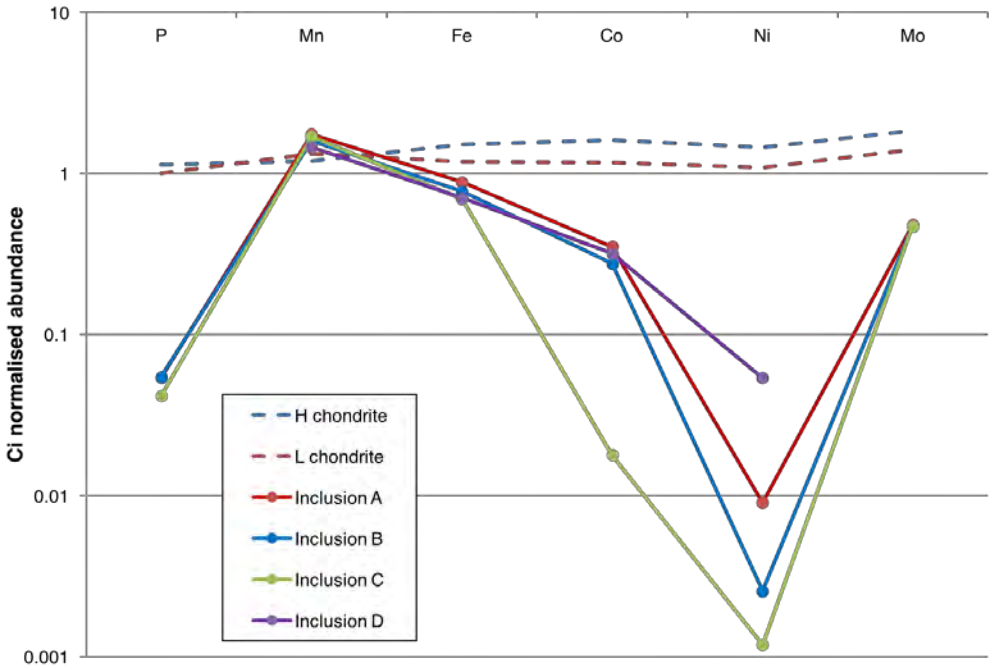

Figure 4.41. Chondrite-normalised siderophile abundances in inclusions A to D, compared with average bulk H and L chondrite values (calculated from Wasson and Kallemeyn, 1988). Mn, Fe, Co from EPMA data, P, Ni and Mo from LA-ICP-MS. CI composition from Lodders (2003).

Rare earth element (REE) patterns can also be used to indicate fractionation. Such elements are incompatible in silicate minerals, thus depletion relative to H or L chondrite may indicate that the inclusions formed from an ordinary chondrite precursor that had lost a partial melt that was enriched in these incompatibles. It was not possible to measure the REE abundances within individual minerals. In many cases, the entire analysis was corrupted. The primary limiting factor in this case is grain size. In all the inclusions, olivine was the most coarse-grained mineral, however does not tend to accommodate these larger atoms into its crystal structure. For inclusion A, the only alternative mineral was plagioclase, which does host some trace elements, however in most cases, was too small, or too shallow, and thus we could not achieve a reasonable duration of ablation (see *Section 2.4.3* for examples of data reduction).

Figure 4.42 shows both detection limits and bulk raster averages (across the five analyses, for elements with concentrations above detection limits) for inclusions A and C indicating that, for the majority of lanthanide elements, the measurements were close to, or below the detection limits. Rare exceptions are Ce, Eu and Yb, however the data are generally poor and potentially unreliable (pers. comm. Jeffries, 2016). Figure 4.43 shows the maximum detection limits for the lanthanides in the bulk raster analyses for inclusions A and C, against average H and L chondrites. Although the measurements were mostly unsuccessful, the detection limits allow a tentative suggestion that the inclusions are both depleted in these elements.

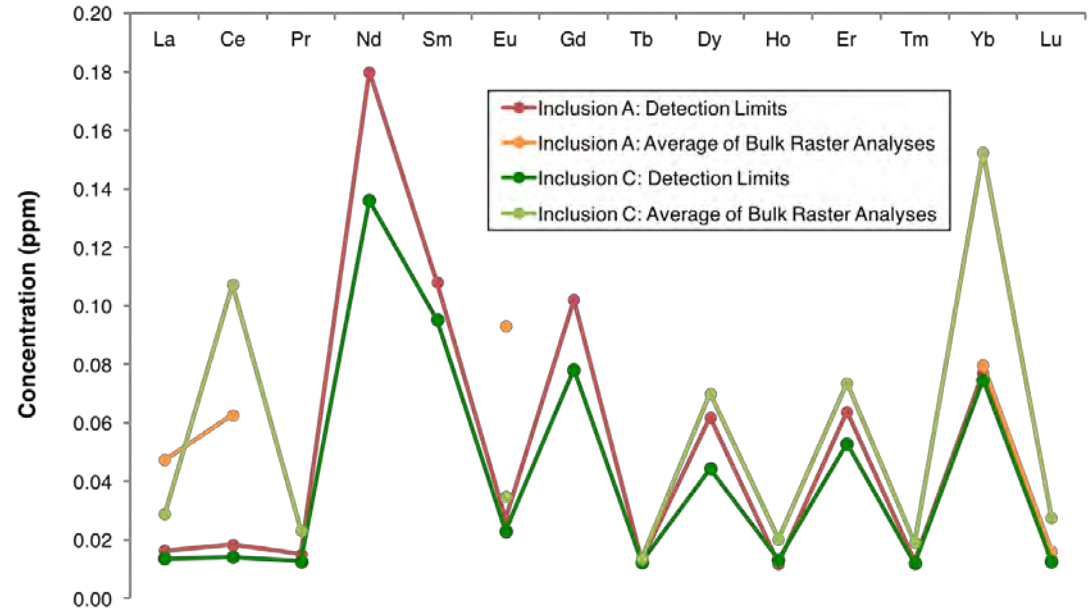

Figure 4.42. Detection limits and bulk raster averages for inclusions A and C, indicating that apart from a few elements (La, Ce, Eu, Yb), the bulk LA-ICP-MS analyses are close to detection limits and thus unreliable.

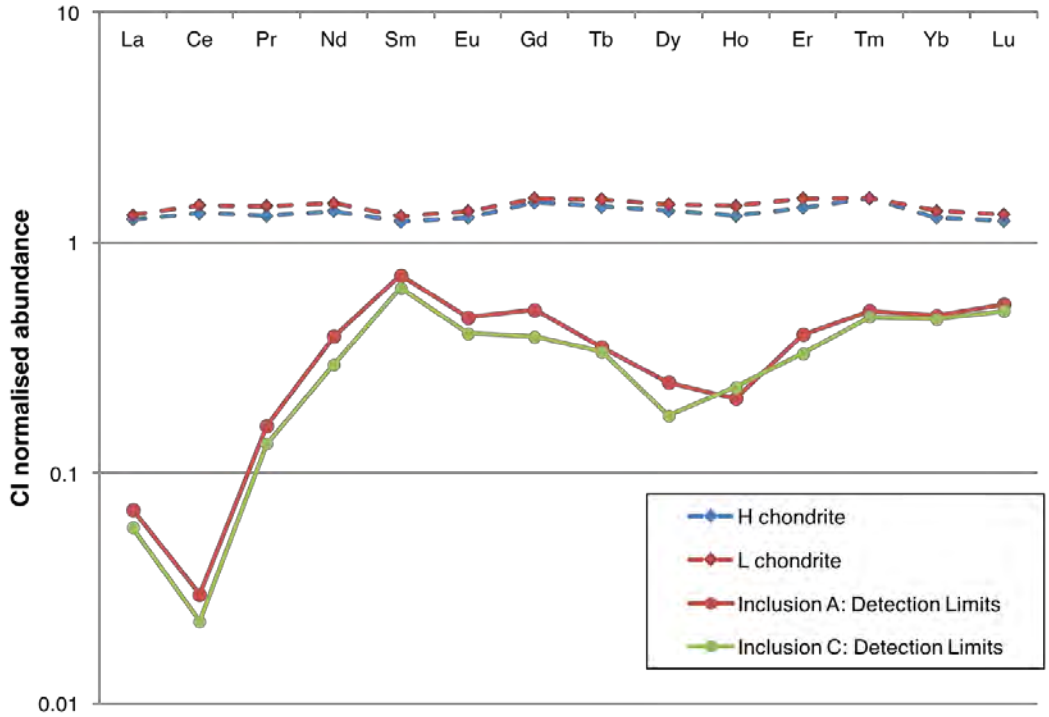

Figure 4.43. Maximum detection limits for REEs in bulk raster analyses for inclusions A and C, against H and L bulk chondrite concentrations from Wasson and Kallemeyn (1988). CI composition from Lodders (2003).

Figure 4.44 shows the CI-normalised REE pattern for inclusions A, B, and C compared with those of bulk H and L chondrite (Wasson and Kallemeyn, 1988). It is likely that inclusion B provides the clearest results due to the presence of clinopyroxene, which

tends to host REEs. Bulk data for inclusion B indicate that the clast is depleted in light REE, and enriched in middle REE. This may indicate that the igneous inclusion is a residue since the more refractory elements should partition into the melt.

Individual analyses of clinopyroxene show a negative Eu anomaly (Table 4.14; Figure 4.45), which agrees with increased Eu measured in most plagioclase. REE patterns for plagioclase analysis shown in Figure 4.45 are detection limits and thus reflect the highest possible value for that element, apart from Eu, therefore the patterns do not provide enough information for meaningful interpretation.

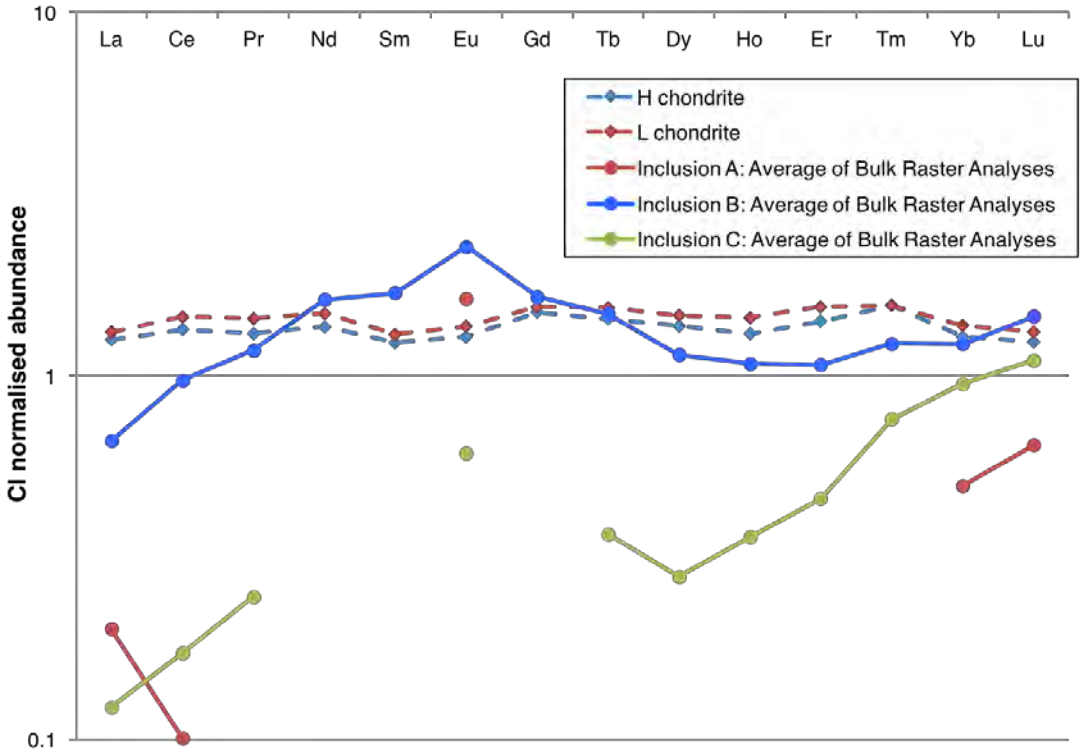

Figure 4.44. Cl-normalised REE patterns for bulk raster analyses in inclusions A, B, and C alongside average REE concentrations for bulk H and L chondrites from Wasson and Kallemeyn (1988). Cl composition from Lodders (2003). REE data for inclusions A and C includes only measurements above detection limit, however most analyses were close (Figure 4.41).

Analysis No.	La	Ce	Pr	Nd	Sm	Eu	Gd	Tb	Dy	Ho	Er	Tm	Yb	Lu
1	1.355	5.915	1.184	7.171	2.374	0.074	3.773	0.624	3.644	0.859	1.797	0.233	1.505	0.233
2	1.645	7.359	1.352	7.252	2.315	<0.0604	3.350	0.543	3.138	0.569	1.556	0.189	1.399	0.231
3	1.008	4.530	0.895	5.596	1.891	0.113	2.946	0.480	3.019	0.567	1.396	0.206	1.308	0.187
4	1.258	6.255	1.196	6.062	2.565	<0.093	2.760	0.428	2.830	0.481	1.201	0.204	1.244	0.164
5	1.147	5.367	1.066	6.268	1.579	0.139	2.930	0.404	2.544	0.467	1.266	0.163	0.990	0.135
6	0.580	2.580	0.498	2.959	1.429	0.035	1.998	0.330	2.248	0.415	1.302	0.166	1.156	0.167
7	0.555	2.462	0.522	2.868	1.051	0.057	1.914	0.323	2.076	0.454	1.132	0.148	1.011	0.183

Table 4.14. Individual analyses of clinopyroxene grains in inclusion B. All values in ppm. Values in red are detection limits.

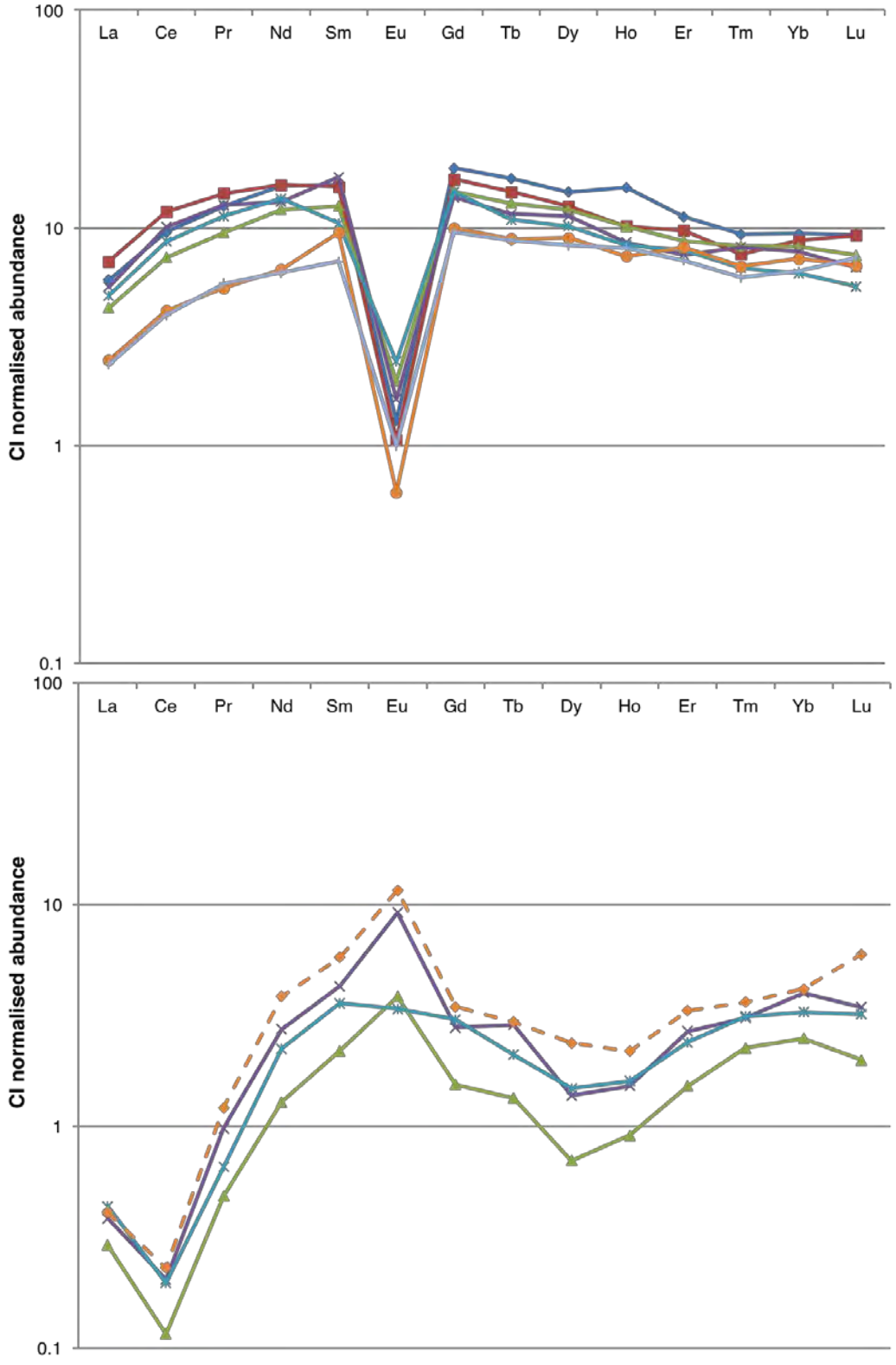

Figure 4.45. CI-normalised REE patterns for individual clinopyroxene (top) and plagioclase (bottom) analyses in inclusion B. Note that for plagioclase analyses, only Eu measurement was above detection limit. Data points for other elements are detection limits, therefore only provide the highest possible concentration for that element. CI composition from Lodders (2003).

4.3.5 Oxygen Isotopes of Barwell inclusions

Subsamples of each inclusion, ranging from 29.8 mg to 58.5 mg, were analysed by laser fluorination and mass spectrometry to measure their oxygen isotopes, by Richard Greenwood at the Open University. Similarly, two 'bulk host' samples were analysed from two different stones in order to be representative of whole-rock Barwell. Oxygen isotopic composition provides insight into the origin of the material, indicating whether they are from the Barwell parent body or, like the original "Pebble" described by Hutchison et al. (1988), share an oxygen isotopic composition with H chondrites. The method is described in *Section 2.6*.

Results are shown in Table 4.15. The data show a wide range in oxygen isotopic composition of Barwell inclusion A through D. B exhibits the lowest $\delta^{17}O$ value at 2.68 ‰ (average of two measurements, 1σ=0.006). The highest $\delta^{17}O$ value is for inclusion D, at 3.75 ‰ (average of two measurements, 1σ=0.027). Measurements of bulk Barwell subsamples from two separate stones fall clearly in the L chondrite field (from Clayton et al., 1991) and are in very good agreement, respectively and with host rock measurements by Hutchison et al. (1988) (Figure 4.46).

Sample	$\delta^{17}O$ ‰	1σ	$\delta^{18}O$ ‰	1σ	$\Delta^{17}O$ ‰	1σ	$\Delta^{17}O$ ‰ linear	1σ
Inclusion A	2.921		4.536		0.562		0.542	
	2.880		4.484		0.548		0.528	
AVERAGE	2.901	0.029	4.510	0.037	0.555	0.010	0.535	0.010
Inclusion B	2.687		4.418		0.390		0.370	
	2.679		4.389		0.397		0.378	
AVERAGE	2.683	0.006	4.404	0.021	0.393	0.005	0.374	0.005
Inclusion C	3.165		4.803		0.667		0.646	
	3.225		4.853		0.701		0.680	
AVERAGE	3.195	0.042	4.828	0.035	0.684	0.024	0.663	0.024
Inclusion D	3.733		5.430		0.909		0.885	
	3.771		5.452		0.936		0.911	
AVERAGE	3.752	0.027	5.441	0.016	0.923	0.019	0.898	0.019
Bulk 1	3.661		4.813		1.158		1.135	
	3.665		4.814		1.162		1.138	
AVERAGE	3.663	0.003	4.814	0.001	1.160	0.002	1.137	0.002
Bulk 2	3.690		4.910		1.137		1.113	
	3.636		4.805		1.137		1.114	
AVERAGE	3.663	0.038	4.858	0.074	1.137	0.000	1.114	0.001

Table 4.15. Oxygen isotope compositions of subsamples from the four inclusions and two host Barwell stones.

Inclusions span a range in $\delta^{18}O$ from 4.39 ‰ to 5.44 ‰ (Table 4.15, Figure 4.46). Increases in $\delta^{18}O$‰ can be explained by mass-dependent fractionation, i.e. igneous processing, on the parent body or by fractionation of the lighter isotopes in the nebula.

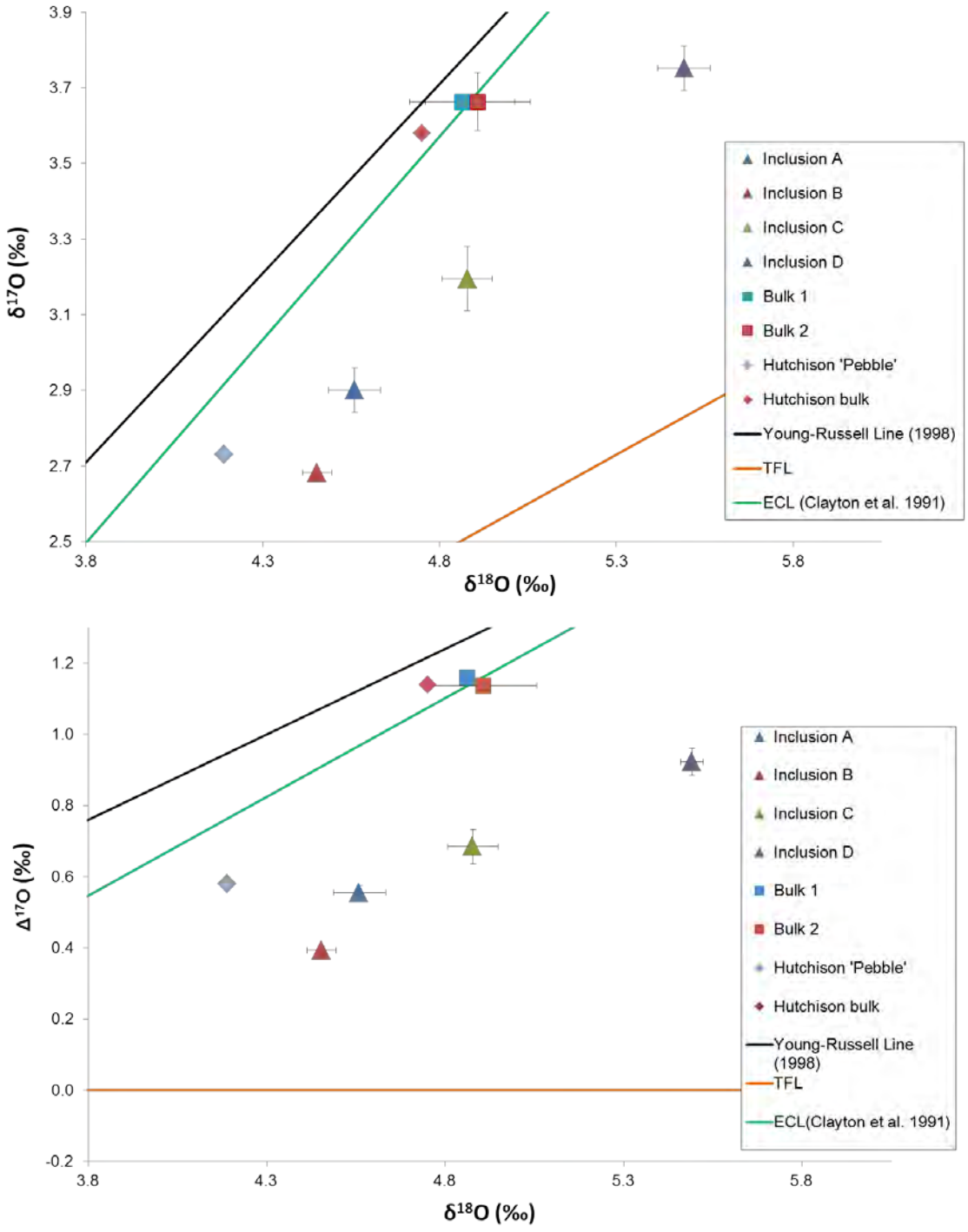

Figure 4.46. Top: $\delta^{17}O$ against $\delta^{18}O$ for Barwell inclusions A, B, C and D, bulk Barwell 1 and 2, alongside data on Barwell from Hutchison et al. (1988). Error bars are 2σ for results in this study. No errors given in literature. Bottom: $\Delta^{17}O$ against $\delta^{18}O$ for Barwell inclusions A, B, C and D, bulk Barwell 1 and 2, alongside data on Barwell from Hutchison et al. (1988). Error bars are 2σ.

Variations in Δ ^{17}O‰ suggest different sources for the material in these clasts. The Δ^{17}O‰ value for inclusion D could still support an L chondrite parent body, however values for inclusions A, B and C are suggestive of source with an oxygen isotopic composition similar to H chondrites (Figure 4.47). Considering the offset between measurements of host rock Barwell in this study and in Hutchison et al. (1988), a similar offset applied to the 'Pebble' would bring it closer to agreement with inclusions A and B analysed in this study.

The oxygen isotope compositions of the four inclusions are offset from that of their host, Barwell, suggesting large-scale transport processes were involved, and preservation of primitive signatures, maintaining isotopic heterogeneity despite considerable metamorphism. They do not derive from any known differentiated parent bodies that are represented by achondrite meteorite groups.

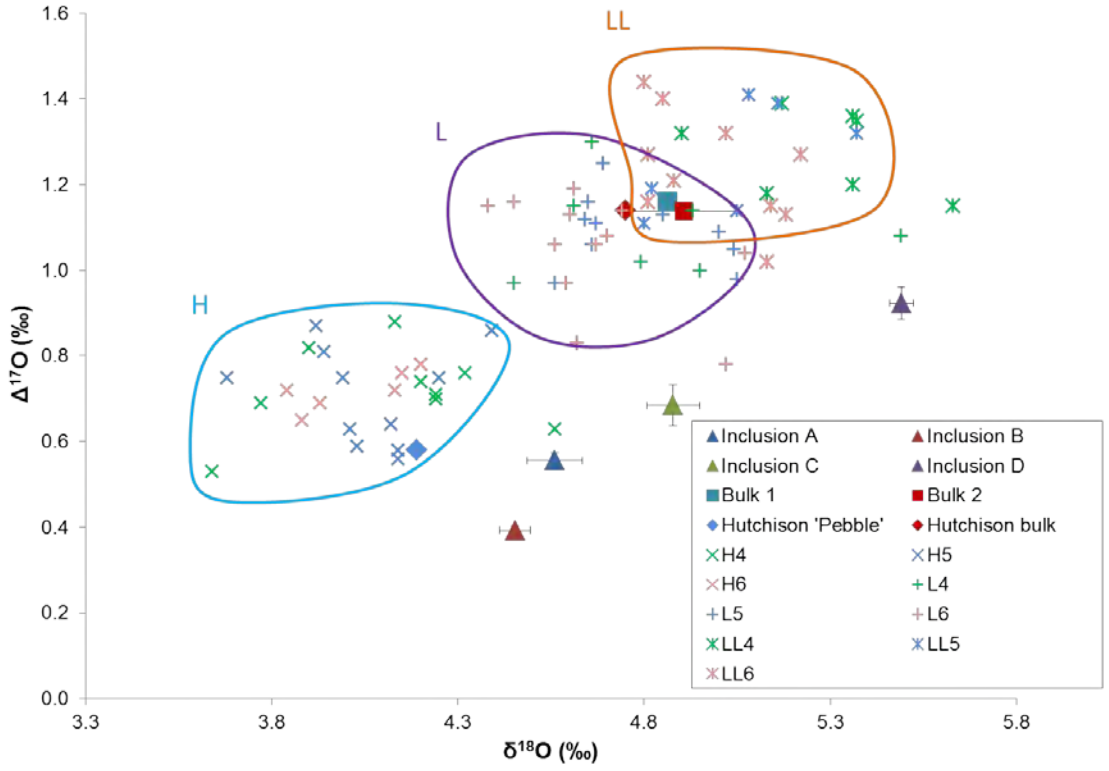

Figure 4.47. An oxygen three-isotope plot of Δ^{17}O against δ^{18}O for Barwell inclusions A, B, C and D, bulk Barwell 1 and 2, alongside data on Barwell from Hutchison et al. (1988) and ordinary chondrite data from Clayton et al. (1991).

Figure 4.48 shows that the inclusions have oxygen isotope compositions similar to those of individual chondrules in low petrological type OC meteorites (Clayton et al., 1991; Bridges et al, 1998). This may imply that they are derived from the same

reservoir as chondrules that were accreted onto OC parent bodies but have retained their original compositions, despite the metamorphism that led to Barwell being a type 6 and the silicate minerals equilibrating with the host. For a type 6 OC meteorite reaching peak temperatures of 850 – 950°C (Huss et al., 2006), exchange and homogenisation would be expected, i.e. the oxygen isotopic composition should converge on the whole rock values.

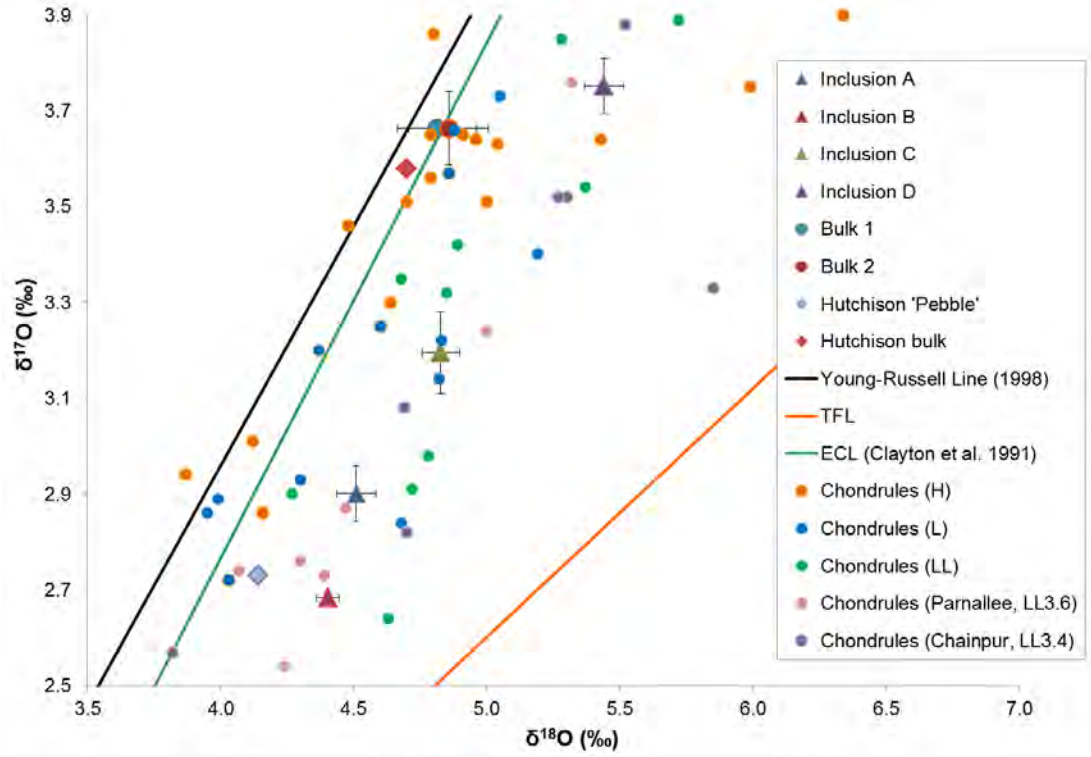

Figure 4.48. An oxygen three-isotope plot showing $\delta^{17}O$ against $\delta^{18}O$ for Barwell inclusions A, B, C and D, bulk Barwell 1 and 2, alongside data for individual chondrules in low petrological type OC meteorites from Clayton et al. (1991), and individual chondrules from Parnallee and Chainpur from Bridges et al. (1998).

Another aspect to the interpretation of the results is that the oxygen isotope compositions of the inclusions appear to define a mixing line (Figure 4.49), indicating exchange between reservoirs of different $\delta^{17}O$ compositions, i.e. a distinctive provenance and possibly a result of exchange with nebular gas. Mass fractionation of host Barwell material would result in compositions lying along the purple fractionation line in Figure 4.49.

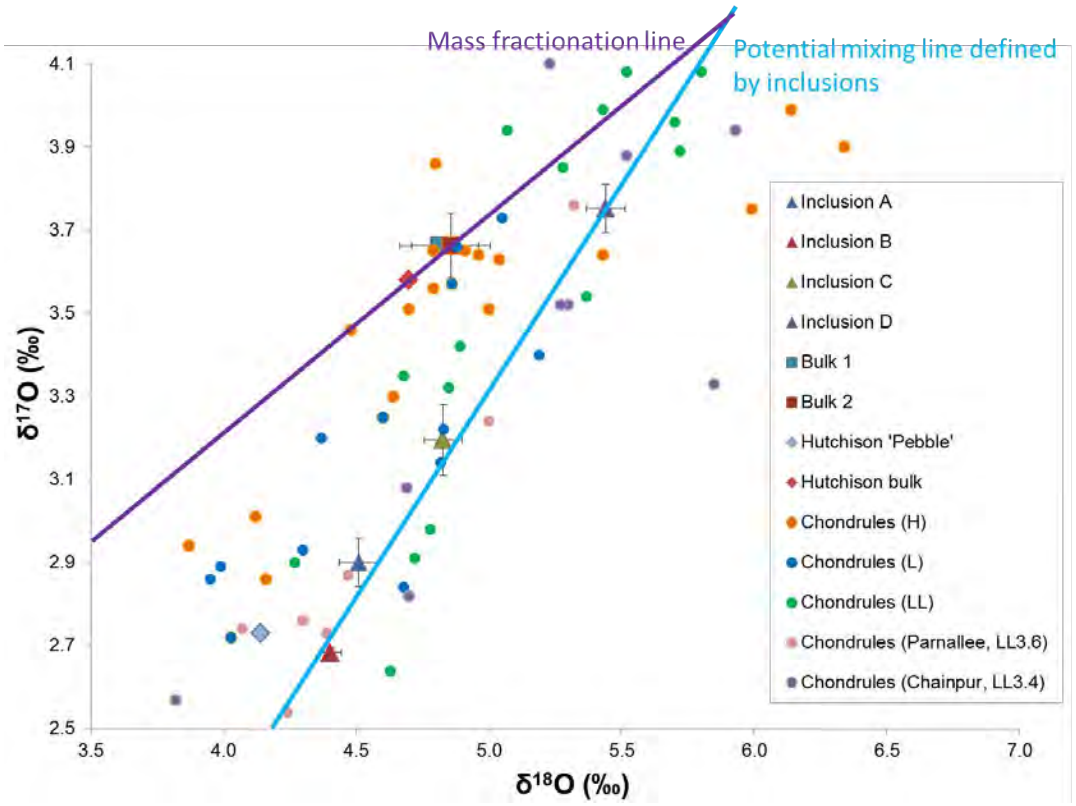

Figure 4.49. An oxygen three-isotope plot showing $\delta^{17}O$ against $\delta^{18}O$ for Barwell inclusions A, B, C and D, bulk Barwell 1 and 2, alongside data for individual chondrules in low petrological type OC meteorites from Clayton et al. (1991), and individual chondrules from Parnallee and Chainpur from Bridges et al. (1998). The blue line indicates a possible mixing line defined by the compositions of the inclusions. The purple line (slope 0.52) indicates mass fractionation from the host Barwell bulk rock value.

4.3.6 Hf-W dating of Barwell inclusions

Samples of five inclusions in the Barwell meteorite were analysed by high-precision isotope ratio mass spectrometry, as per the method outlined in *Section 2.5*. These samples correspond to inclusions A and B from this study, and clasts 3, 4, and 6 from Bridges and Hutchison's study (1997), which were selected due to minimum mass requirements of the technique. See Table 4.1 for descriptions of the inclusions.

Tungsten abundances were estimated at 2 ng per gram, therefore at least 100 mg of powder was required for sufficient detection. Results of MC-ICP-MS measurements are provided in Table 4.16. As explained in *Section 2.5.1*, the interpretation of the Hf-W isotopic evolution of the inclusions is dependent on both the bulk Hf/W ratio, and the initial isotopic composition. The correlation of $\varepsilon^{182}W$ (the deviation of $^{182}W/^{184}W$ from the mean value of the bracketing measurements of the Alfa Aesar W standard in parts per 10^4) and $^{180}Hf/^{184}W$ is interpreted as an internal Hf-W isochron whose slope represents

the initial $^{182}Hf/^{180}Hf$ ratio, corresponding to an age for Hf-W system closure relative to CAI formation (Figure 4.50).

Sample	Mass (g)	W (ppb)	Hf (ppb)	$^{180}Hf/^{184}W$ (±2σ)	$\varepsilon^{182}W$ (6/3) (±2σ)	$\varepsilon^{182}W$ (6/4) (±2σ)	$\varepsilon^{183}W$ (6/4) (±2σ)	$\varepsilon^{184}W$ (6/3) (±2σ)
Inclusion A	0.1306	48.6	77.7	1.887 ± 0.016	0.15 ± 0.25	-0.48 ± 0.32	-0.49 ± 0.27	0.32 ± 0.18
Inclusion B	0.4660	74.2	205	3.261 ± 0.018	0.14 ± 0.14	-0.04 ± 0.16	-0.15 ± 0.14	0.10 ± 0.09
Inclusion 3*	0.1157	38.9	328	9.941 ± 0.107	6.00 ± 0.32	5.92 ± 0.29	-0.09 ± 0.27	0.06 ± 0.18
Inclusion 4*	0.1561	44.3	70.8	1.886 ± 0.016	-0.06 ± 0.26	-0.13 ± 0.33	-0.05 ± 0.27	0.03 ± 0.18
Inclusion 6*	0.2607	67.3	368	6.450 ± 0.038	2.95 ± 0.23	3.24 ± 0.22	0.18 ± 0.22	-0.12 ± 0.15

Table 4.16. Results of W isotope measurements by MC-ICP-MS. Internal mass bias fractionation was corrected using the exponential law by internal normalisation to $^{186}W/^{183}W$ = 1.98594 (6/3 ratio) or $^{186}W/^{184}W$ = 0.92767 (6/4 ratio). The uncertainties (±2 σ) reported for measured ε iW values represent the internal standard error (2 s.e.). *denotes samples first described by Bridges & Hutchison (1997). BHVO-2 = Basalt, Hawaiian Volcanic Observatory standard. The data are expressed in terms of $\varepsilon^{i}W$, which describes the W isotopic composition ($^{182}W/^{183}W$, $^{182}W/^{184}W$, $^{183}W/^{184}W$ and $^{184}W/^{183}W$) relative to the bracketing measurements of the terrestrial standard, Alfa Aesar W, in parts per 10^4.

There is mass-independent fractionation of ^{183}W from ^{182}W, ^{184}W and ^{186}W induced during the analytical procedure (possibly during evaporation in Teflon vials) which leads to a deficit in ^{183}W (Willbold et al., 2011; Kruijer et al., 2014b). Since the $\varepsilon^{182}W$ (6/4) values are unaffected by this, the data were corrected for internal mass bias fractionation using the $^{186}W/^{184}W$ ratio, therefore $\varepsilon^{182}W$ is used to describe $\varepsilon^{182}W$ (6/4) hereafter.

Table 4.17 gives initial $\varepsilon^{182}W$ ratios and initial $^{182}Hf/^{180}Hf$ ratios and their corresponding ages, relative to CAI. Calculation of a model age from the Hf-W systematics is based on a two-stage model, i.e. that the Hf and W were fractionated, and the system subsequently closed. The model uses L chondrite averages ($^{182}Hf/^{180}Hf$ = 1.59 ± 0.19; $\varepsilon^{182}W$ = -1.83 ± 0.14) for the anchor point of a two point model isochron (Hellman and Kleine, unpublished). These ages have been calculated by the following equation, using an initial $^{182}Hf/^{180}Hf$ ratio for CAIs of (1.018 ± 0.043) x 10^{-4} (Kruijer et al., 2014) and a decay constant, λ, of 0.078 ± 0.02 Myr^{-1} (Vockenhuber et al., 2004):

$$\Delta t = \frac{1}{\lambda} \times \ln \left[\frac{(^{182}Hf/^{180}Hf)^{i}_{sample}}{(^{182}Hf/^{180}Hf)^{i}_{CAI}} \right]$$

The closure temperature of the Hf-W system is dependent on several factors. In highly metamorphosed ordinary chondrite groups, this temperature is close to the peak temperature experiences by the meteorite, thus $^{182}Hf/^{180}Hf$ isochron ages may date

crystal growth from metamorphism, or cooling from peak temperature below closure temperature (Kleine et al., 2008).

Sample	$^{180}Hf/^{184}W$	2σ	$\varepsilon^{182}W$ (6/4)	2σ	$^{182}Hf/^{180}Hf$ x10^{-4}	2σ	Myr after CAI	2σ
Inclusion A	1.887	0.016	-0.48	0.32	3.93	-	-17.3	-
Inclusion B	3.261	0.018	-0.04	0.16	0.93	0.15	1.2	2.1
Inclusion 3*	9.941	0.107	5.92	0.29	0.80	0.04	3.1	0.8
Inclusion 4*	1.886	0.016	-0.13	0.33	4.97	-	-20.3	-
Inclusion 6*	6.450	0.038	3.24	0.22	0.90	0.06	1.5	1.0

Table 4.17. ε182W, initial 182Hf/180Hf ratios and their corresponding ages, relative to CAI, for inclusions in this study, using L chondrite averages for the anchor point of a two point model isochron.

The $\varepsilon^{182}W$ values of inclusions measured in this study range from ~-0.5 to ~6. These values are not exceptionally high as might be expected from silicates in a parent body that experienced significant core formation leading to the fractionation of Hf and W. For example, basaltic eucrites show a range of $\varepsilon^{182}W$ from 14 – 26 (Kleine et al., 2004).

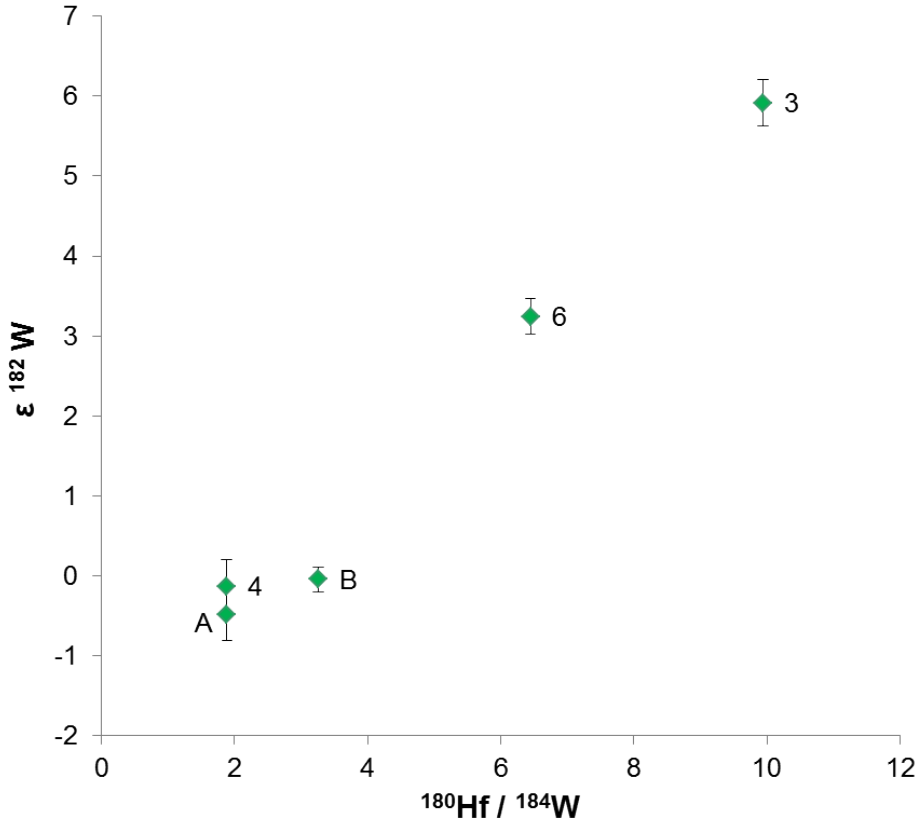

Figure 4.50. $\varepsilon^{182}W$ against $^{182}Hf/^{184}W$ for the five inclusions measured in this study. The slope gives the initial $^{182}Hf/^{180}Hf$ – the closure time of the system. Errors are 2 σ.

Two inclusions, 'A' from this study and '4' first described by Bridges and Hutchison (1997) show unexpectedly low concentrations of Hf (~70-80 ppb) and relatively high concentrations of W (~45 ppb). Based on visual inspection, it is likely that A and 4 are in fact the same inclusion, which is supported by Hf and W concentrations. Moreover, the model ages calculated are -17.3 Ma (after CAI) and -20.3 Ma (after CAI). Thus, the Hf-W evolution of these two inclusions was more complex, e.g. a multi-stage process that likely involved more than one event of Hf-W fractionation, indicating that the two stage model is not applicable and no meaningful age can be calculated for these inclusions. There are two possible causes of these results. Such concentrations could arise from multi-stage parent bodies processes thus: a primitive body undergoes widespread melting → silicate differentiation leads to loss of Hf from the residue → a core begins to form, i.e. metal is lost from residue leading to reduction of W → parent body cools and core formation is not complete, thus some W remains in the residue. In order to be incorporated in an L chondrite parent body, this must have occurred, and been ejected, within the first ~2 Ma of Solar System history. However, it may not be necessary to invoke a complicated story. The second potential cause of these results calls into question how representative these pieces are. The inclusion is described as 5 mm in size by Bridges and Hutchison (1997), however XCT and SEM imaging in this study shows the fragment to be > 8 mm across (which would extrapolate to a sphere ~ 10-12 mm in diameter). This illustrates why it is key to sample from the most central part of any inclusion to achieve the most representative piece, since areas closer to the edges are likely to have suffered more from overprinting or resetting by exchange with the host through thermal metamorphism. In this case, since the inclusion was only partly present in the piece when this study began, it is not possible to know where the subsample was taken from, but likely that it is not from the centre of the inclusion. Therefore, these results are discarded.

Three inclusions, 'B' from this study, and '3' and '6' from Bridges and Hutchison (1997) show superchondritic Hf/W ratios ($^{180}Hf/^{184}W$ = 3.261 ± 0.018; 9.941 ± 0.107 and 6.450 ± 0.038 respectively), which are similar to that measured for chondrule fractions of ordinary chondrites (Kleine et al., 2002; Hellmann et al., 2017). Assuming a chondritic source, they provide model ages of ~1.2 ± 2.1 Ma, ~1.5 ± 1.0 Ma and ~3.1 ± 0.8 Ma after CAI formation (Table 4.17) – similar to chondrule formation ages (e.g. Kita et al., 2000; Rudraswami and Goswami, 2007; Amelin et al., 2002; see *Section 1.4.2*). The high Hf concentrations (~330 ppm and ~370 ppm respectively) and old model ages indicate the inclusions were sufficiently large to remain isolated

and retain their original signatures that predate metamorphism on the Barwell parent body. Typically, L chondrites that have been metamorphosed to petrological type 6 give ages of ~9-11 Ma after CAI (Hellmann et al., 2017).

Furthermore, as these inclusions show variable Hf/W and W isotopic compositions, the results can be used to define a 'bulk inclusion' isochron. Figure 4.51 shows that these three inclusions define a single Hf-W isochron with a slope of 0.957 ± 0.054, which corresponds an age of ~2.7 ± 0.9 Ma after CAI formation. The data are significant, with MSWD = 1.8, where MSWD describes the mean square weight deviation – an expression of the scatter that takes the analytical errors into account. This isochron makes it possible to date Hf/W fractionation among bulk inclusions directly without the assumption of a single fractionation from a chondritic source. This 'bulk inclusion' Hf-W isochron passes through the bulk chondritic composition, therefore the bulk isochron and model ages (Table 4.17) are very similar. Since the age determined via the isochron method is based on several samples, it is much more precise than the model ages calculated for individual samples.

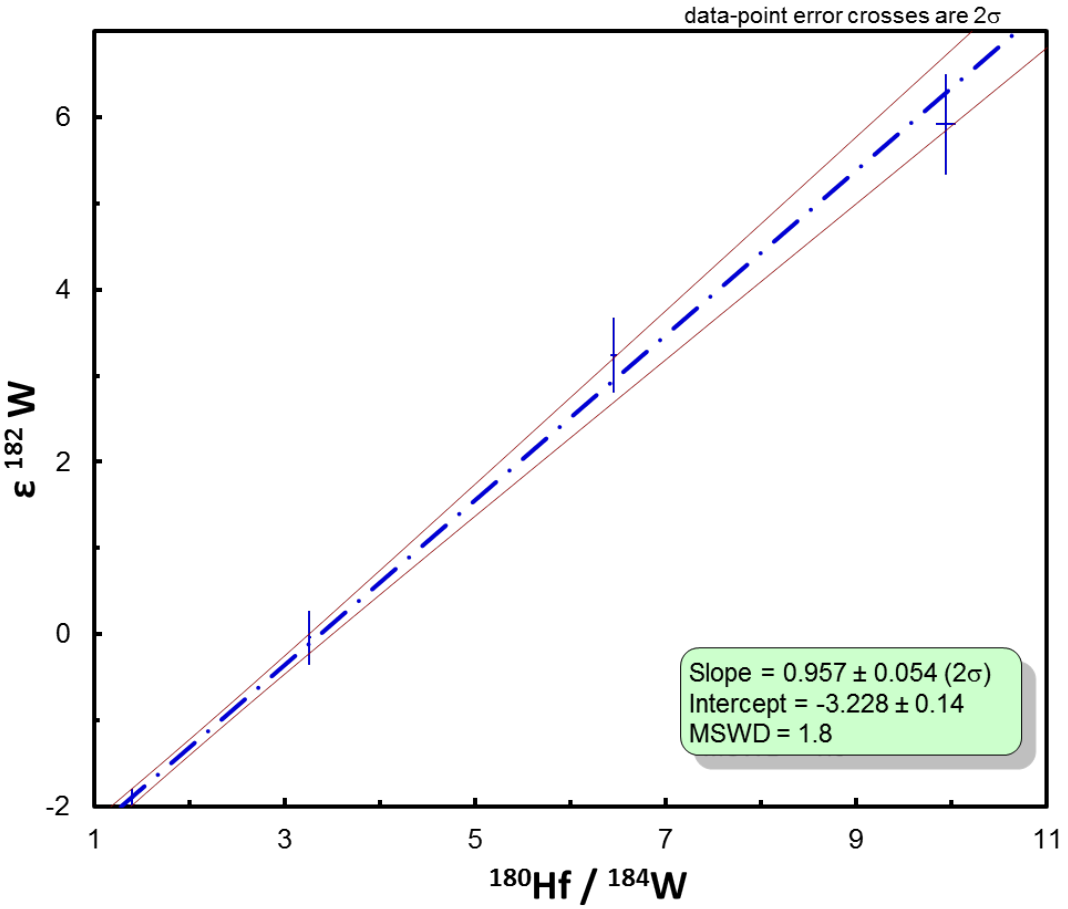

Figure 4.51. A bulk isochron from three inclusions in this study and bulk L chondrite (Kleine et al. 2009) Hf-W systematics. Where the slope gives the initial $^{182}Hf/^{180}Hf$ – the closure time of the system. Errors are 2 σ.

Moreover, Figure 4.52 demonstrates that the three points also define an isochron which agrees with L3 chondrule fractions (recent data from Budde, unpublished) and an additional inclusion found in another L6 host, NWA 7871 (measured at the same time as this study, as yet unpublished). Although these are preliminary unpublished data, the results are promising and may demonstrate that the timing of inclusion formation can be dated using a bulk inclusion Hf-W isochron.

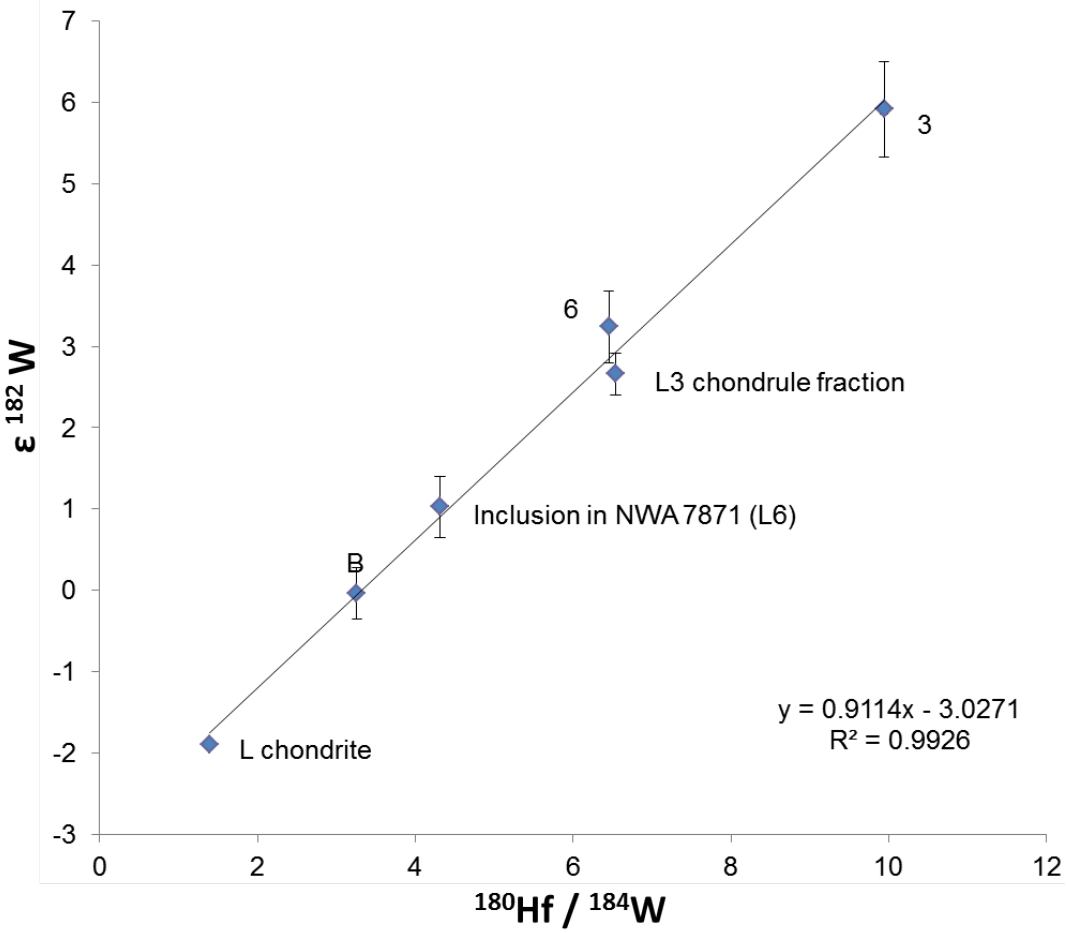

Figure 4.52. $\varepsilon^{182}W$ against $^{182}Hf/^{184}W$ for three inclusions measured in this study (B, 3, and 6). The slope gives the initial $^{182}Hf/^{180}Hf$ – the closure time of the system. Errors are 2 σ. Inclusion in NWA 7871 measured at the same time as this study but unpublished (Ruzicka and Hellmann). Chondrule fractions from GRO 95502 (L3) also unpublished as yet (Budde).

4.4 Discussion

The canonical theory states that parent bodies of the ordinary chondrites accreted after the formation of CAIs and chondrules, forming after ^{26}Al and other radionuclides had decayed past levels adequate to cause total melting of an asteroid (e.g. Brearley and Jones, 1998; Bennett and McSween, 1996; Kleine et al. 2005). The presence of

inclusions like the Barwell “Pebble” challenged this perception. Hutchison et al. (1988) asserted that, assuming ordinary chondrites accreted directly from the protoplanetary disk and remained largely unaltered since, this would indicate that the constituents of ordinary chondrites co-existed in the disk, i.e. that chondrules, metal, mineral grains, and igneous fragments all co-existed. Hutchison (2011) advocated that chondrules formed through the breaking up of partly molten differentiated planetesimals, and argued that the presence of igneous objects, like the Barwell “Pebble” and fractionated chondrules observed in ordinary chondrites, implies that they arose from differentiated parent bodies.

This study shows that additional inclusions, similar to the “Pebble”, are present in Barwell. In the three largest specimens of the meteorite scanned (285 cm^3), a total of 0.7% is inclusion-like material, however it is possible that not all inclusions are similar in origin or type, merely exhibit similar features of attenuation in XCT data. They are all united by a lack of metal and sulphide, and a size considerably larger than typical Barwell chondrules. The XCT data shows that the host meteorite Barwell has a uniform texture and mineralogy without evidence of brecciation.

Taking into account all the evidence from this investigation, the new inclusions are closest to the ‘microporphyritic clast’ subdivision of Bridges and Hutchison (1997). They lack features that could categorise them as macrochondrules (no typically chondrule-like texture, appearing as fragments of larger objects) or impact melt (no glassy veins, no metal/sulphide globules) but exhibiting a somewhat chondritic mineral assemblage, and are only marginally enriched in Si, thus not fitting into the chemically fractionated class. Bridges and Hutchison (1997) that the origins of microporphyritic clasts are unclear but may have formed from small melt ponds, like impact melt clasts, but did not suffer significant shock.

4.4.1 Proposed series of events

This study suggests that the inclusions arise following this set of events: i) accretion of a planetesimal early in Solar System history; ii) onset of melting on the initial parent body due to shock (localised segregation) or radiogenic heating (leading to large-scale differentiation); iii) disruption of the planetesimal leading to ejection of metal-depleted material that may or may not have melted; iv) solidification of this material in the nebula, and acquisition of mantle material; v) contact with other material in the nebula leading to cracking and fragmentation; vi) accretion of the inclusions onto the Barwell

parent body; vii) burial and thermal metamorphism. The evidence for these possible events is explored below.

4.4.2 Accretion of a planetesimal early in Solar System history

A three-isotope plot of oxygen isotopes provides a way to distinguish between ordinary chondrite groups. Although the whole-rock O isotopic compositions of H, L and LL chondrites are similar, they are still distinguishable (Clayton et al., 1991). O isotopic compositions of chondrules within ordinary chondrites do not show group-specificity; that is, chondrules within these meteorites are drawn from a single population. Broadly, the oxygen isotopic compositions of all four inclusions suggest they are derived from the same reservoir as the material that formed the ordinary chondrite meteorites. The oxygen isotope data gathered on Barwell inclusions show a clear disparity with that of the host meteorite. All inclusions are enriched in ^{18}O compared with the bulk host. This could imply mass-dependent fractionation, or exchange with an isotopically heavy reservoir (Franchi et al., 2001). There is no petrological indication of aqueous alteration, which would also cause enrichment in the heavier isotope. The inclusions are also depleted in ^{17}O, relative to the bulk chondrite, which puts inclusions A, B, and C, closer to the H chondrite field, as defined by survey work by Clayton et al. (1991). Inclusion D is closer to a boundary between the H and L fields.

During metamorphism, an inclusion can retain its original oxygen isotopic signature (with equilibration only taking place over small distances), despite convergence of Fe/Mg ratio in pyroxene and other indicators of equilibration between origin and host (Nakamura et al., 1994). Some iron meteorites have oxygen isotopic compositions indistinguishable from ordinary chondrites (Clayton et al., 1983), leading to the question if it is possible that the inclusions have originated from additional asteroids with oxygen isotopic compositions similar to that of OC parent bodies. Ruzicka et al. (2000) found that often inclusions with equilibrated Fe-Mg compositions lie close to the ordinary chondrite fields within an oxygen three-isotope plot, but not always in the appropriate host field, e.g. a clast with L-like silicates but $\Delta^{17}O$ values in the LL field (8645-I1) or an inclusion with L-like silicate compositions but fitting better with the oxygen field of H-chondrites (7871-I1). They found that inclusions with unequilibrated Fe-Mg compositions lie far from the host L or LL fields, with $\Delta^{17}O$ values between H chondrites and the terrestrial fractionation line. Considering the degree of thermal metamorphism experienced on the L chondrite parent body, it is feasible that the inclusions did experience some equilibration with the host, implying that their original isotopic

composition may have been even more enriched in ^{18}O, or even more depleted in ^{17}O, than the present composition.

The simplest interpretation of oxygen isotopes is that they indicate preservation of primitive signatures, maintaining isotopic heterogeneity despite considerable metamorphism (Barwell is a type 6 OC). Inclusions span a range in $\delta^{18}O$ from 4.40 ‰ to 5.44 ‰ and in $\Delta^{17}O$ from 0.37 ‰ to 0.90 ‰. These inclusions are depleted in ^{17}O compared with bulk Barwell measurements ($\delta^{18}O \approx 4.83$ ‰ and $\Delta^{17}O \approx 1.15$ ‰), possibly indicating fractionation from a H chondrite-like source, but also exhibiting oxygen compositions similar to those reported for individual chondrules in low petrological type L and LL chondrites (Clayton et al., 1991). This indicates that the source planetesimal(s) that the inclusions originate from was, 1) formed in the same reservoir as ordinary chondrites, and, 2) not homogenised in oxygen isotopes.

4.4.3 Onset of melting due to radiogenic heating or shock

It is not possible to estimate the original composition of this material based on the equilibration with the host, obvious from the homogenised silicate compositions. However, the inclusions show chemical fractionation from typical chondrule composition, e.g. increasing in Fe/Mg ratio. Although bulk lithophile element compositions are broadly similar to silicates in ordinary chondrites, the low content of metal and sulphide in the inclusions, as well as low abundances of siderophile and chalcophile elements, indicate that metal and sulphide were removed from the parent material. Additionally, trace element analysis on fine-grained material was challenging and largely unsuccessful, however there is a broad indication that the REE patterns are somewhat fractionated, and the inclusions are depleted in REE.

There are some clues to the starting material that the inclusions formed from. In the centres of inclusions A and B, plagioclase shows more calcic compositions, similar to that found at the edge of the “Pebble” but not nearly as calcic as plagioclase in the “Pebble” core (~An 74). Chromites within B and C appear to be converging on the host composition, however are considerably more aluminous in inclusion A, though not as high as that reported within the “Pebble” inclusion (Hutchison et al., 1988). Likely this is due to easier diffusion of Fe^{2+} and Mg^{2+} than elements bonded within the silica tetrahedra. The higher Mg content of chromite and An content of plagioclase are a closer representation of the original source material from the inclusions, indicating a more mafic, higher temperature and more reduced environment.

As explored in *Section 1.2*, there is evidence that radiogenic heating was prevalent due to decay of short-lived isotopes, e.g. ^{26}Al (Weiss & Elkins-Tanton, 2013). Similarly, there is evidence from magmatic iron meteorites that large differentiating planetesimals had already accreted and begun to differentiate (Kruijer et al. 2014). As well as the contribution of radioactivity to heating of parent bodies, the Solar System was likely a chaotic environment during the first few million years after CAI, with impacts on various scales, at various speeds (e.g. Melosh, 1989). These impacts may have driven the heating and segregation of metal/sulphide from silicate.

Hf-W systematics indicate a common age (~2.7 Ma after CAIs) of inclusions B, 3 and 6 from Bridges and Hutchison (1997), which, although having superchondritic Hf/W ratios and radiogenic ^{182}W excesses, are more in line with silicate fractions of ordinary chondrites, than material from planetesimals that had experienced significant differentiation, such as eucrites from 4 Vesta.

4.4.4 Disruption of the planetesimal, ejection of metal-depleted material and solidification in the nebula

The three-dimensional shapes visible in the CT data would imply that these inclusions experienced a rounding process prior to their incorporation into the Barwell parent body, similar to the original “Pebble” described by Hutchison et al. (1988). Where rounded, rims, or mantles, of different compositions can be seen in X-ray tomograms and EDX maps of some inclusions and likely represent the actual edge of the clast. The mantle formation process is undetermined. Potentially this material was accreted in the nebula, after ejection from the inclusion parent body, and prior to accretion into the Barwell parent body. This may have occurred in chondrule-forming regions, as indicated by the mineralogy (including sulphides and metal) of the mantle of inclusion C. In some cases, angular edges to the inclusions are present, for example D, indicating that it is a clast broken from a larger object.

The textures suggest that these inclusions have formed from melts, with varying cooling rates. All cooled slowly enough that they could crystallise, however mostly too fast to attain equilibrium. The variation in grain size in A, from coarse in the centre, to more fine-grained closer to the edge, is indicative of an igneous rock that cooled from the outside, i.e. possibly in a nebula rather than planetary environment. Chromite veinlets in A are likely the result of impact-melting of plagioclase, followed by injection

of a chromite-plagioclase melt into fractures of silicate grains. The chromite crystallised within the fractures whilst the plagioclase continued to flow before pooling in a void. The texture of inclusion B does not exhibit any radial changes, but shows a period of slow cooling (with large olivine and pyroxene crystals) coupled with chromite plagioclase assemblages which are consistent with significant temperature excursions and indicate formation during shock. Rubin (2003) suggested that these formed through shock-melting of plagioclase, with a low impedance to shock compression, leading to the melting of adjacent chromite. This indicates that the inclusion, or the body from which the inclusion originated, suffered significant shock of at least S3 (Rubin, 2003), followed by annealing, potentially as a result of residual heat from the impact that caused the shock effects. For silicate melting to have occurred, the local temperatures must have exceeded the solidus temperature of ordinary chondrite material (1100°C; Jurewicz et al., 1995). Inclusion B also hosts two smaller chondrules, supporting incomplete melting/differentiation of a precursor similar to the OC parent bodies. Similarly, their presence would indicate that the material was not fully melted on ejection from the original parent body.

The textures of inclusions C and D indicate rapid cooling i.e. melting and cooling in space on ejection from the parent body. The spinifex texture in clast C, resulting from undercooling, is not similar to that observed in impact melt clasts, and quench textures generally, where the olivine appears smaller, due to increased nucleation sites, and is often zoned (where Mg-rich olivine forms at higher temperatures, followed by more fayalitic olivine in rims at low temperatures). This zoning may also not be seen if thermal overprinting allowed cation exchange between the zones, which may be the case as host Barwell has reached a high petrological grade.

All inclusions, apart from B, appear non-welded to the host, including cracks surrounding the inclusions and subparallel fractures that do not propagate into the bulk Barwell material. This could have two causes: i) the cracks were formed before the incorporation into Barwell, e.g. by collision with other inclusions, chondrules or metal grains in the nebula; or ii) the crack-forming shock event occurred after incorporation, but the cracks do not extend into the matrix due to lithological differences, i.e. the more fine-grained texture of the clasts, or the presence of metal grains that serve to constrain the crack. This soon after solar system formation, the protoplanetary disk was turbulent (Cuzzi and Weidenschilling, 2006), causing rapid mixing and homogenisation of small particles like chondrules (Alexander et al., 2008), thus it is thought that chondrite parent bodies must have accreted soon after chondrule production. For

example, Hf-W systematics of Allende chondrules and matrix indicate formation at ~ 2.2 Ma after CAI with accretion occurring soon after (Budde et al., 2016). Damage to the inclusions, e.g. these cracks, and/or separation from a larger fragment, is unsurprising in this environment.

4.4.5 Accretion on the Barwell parent body – burial and metamorphism

The inclusions were found within the Barwell meteorite, therefore must have accreted on to the L chondrite parent body at some point. The inclusions are mafic in composition, dominated by olivine, pyroxene and plagioclase, except A, which contains no pyroxene. Olivine and pyroxene are Mg-rich and are equilibrated with the host in all inclusions. Similarly, plagioclase is equilibrated in inclusions C and D, and at the edges of inclusions A and B. Therefore, although these minerals cannot provide insight into the source material of the inclusions, this is evidence that the inclusions were incorporated into the Barwell parent body prior to the thermal metamorphism. That is, the similarities in mineral chemistry between the inclusions and the bulk meteorite are likely the result of homogenisation, i.e. elemental mobilisation, during the heating that metamorphosed Barwell to petrological type 6. Olivine within the “Pebble” (Hutchison et al., 1988) and inclusions described by Bridges and Hutchison (1997) also had olivine compositions of Fo 75, indicating they too were incorporated prior to thermal metamorphism.

Metamorphism and recrystallisation leads to redistribution of oxygen isotopes amongst mineral phases, based on the mass-dependent equilibrium fractionation that corresponds to the peak temperature experienced during metamorphism. Since Olsen et al. (1981) showed that the isotopic equilibration, i.e. the transport of oxygen atoms, in Type 6 chondrites occurs over only a few millimetres, it is possible that the cations in the minerals homogenised, explaining the similarity in olivine and pyroxene chemistry, but the size of the inclusions isolated the O isotopes, fitting with very slow rates of oxygen self-diffusion in silicate minerals (Farver, 2010). That is, these exotic inclusions in Barwell were metamorphosed in-situ but preserved their oxygen composition.

4.4.6 Implications for chondrule formation?

As one of the most hotly contested subjects in meteoritics, (e.g. Lauretta et al, 2006; Wood, 1996; Hewins, 1997; Connelly and Jones, 2016) with no acceptable formation model established as accounting for the majority of chondrule characteristics (Connelly and Desch, 2004; Desch et al., 2012), questioning the formation mechanism of chondrules is somewhat outside of the remit of this study. However, the data indicate that igneous inclusions share many characteristics with chondrules in OCs, despite their size and apparent exotic nature. Based on Hf-W systematics, their common age of ~ 2.7 Ma after CAI formation is similar to chondrules, indicating a contemporaneous formation. Chondrules have been shown to form over wide timescales with Pb-Pb ages of individual chondrules suggest that their formation was contemporaneous with CAI formation and continued for over 3 Ma (Connelly et al., 2012; Kita et al., 2013). Nevertheless, similar ages do not themselves imply a similar formation mechanism.

The size of the inclusions indicates that a considerable amount of material was available for their production. The difference between the size of the inclusions and the average size of chondrules in L chondrites, combined with the lack of metal in the inclusions points to a different formation process. The loss of metal from chondrules has been shown to occur through parent body metamorphism. In some respects, this study brings up more queries about the origin of this material, and speculation of the implications for chondrule formation may elucidate future avenues of research related to these inclusions. For instance, these inclusions may point to chondrules being more diverse in size and composition than previously recognized, and thus have implications for chondrule formation processes. If these inclusions are ‘macrochondrules’, the question remains as to why inclusions of this size (an order of magnitude > typical OC chondrules) are seen. Cuzzi et al. (2001) suggested that aerodynamic sorting accounted for the chondrule size differences between chondrite groups, however to explain these inclusions would invoke a complicated history. The inclusions would have to form in the same reservoir as OC chondrules (acquiring an oxygen isotopic composition similar to OC chondrules), being size sorted, and once again being added to the same reservoir as OC chondrules in order to be accreted onto the L parent body. Alternatively, Rubin (2010) suggested that the difference in chondrule sizes amongst different groups was a result of variations in the number of remelting events experienced by chondrules in different parts of the solar nebula. Potentially, these inclusions could arise from the remelting of compound chondrules, or collision of still molten chondrules. However, the mechanism of metal/sulphide depletion is

unexplained. Future research into the possibility of this material forming in the nebula is warranted, for example, possible methods of metal depletion in free-floating droplets of melt (such as centrifugal forces from rapid spinning).

There is also the consideration that chondrules may have formed in an impact scenario (Sanders and Scott, 2012; Asphaug et al., 2011). Chondrules in CB meteorites have been shown to form in a vapour-melt plume (Krot et al. 2005), and some studies have suggested that impact jetting would have melted and ejected near-surface material at high velocity, implying that chondrules were a 'by-product of planetary formation rather than leftover building material' (Johnson et al., 2015). Ejection of previously molten/differentiated material is unlikely to have produced chemically unfractionated chondrules (Taylor et al. 1983). However, some differentiated planetesimals had veneers of undifferentiated material (Weiss and Elkins-Tanton, 2013), so a diversity of compositions could originate. Indeed, it could be that the earliest planetesimals were formed from chondrules, and that the earliest differentiated parent bodies (e.g. those formed < 1 Ma after CAI as described by Kleine et al. (2009) and Kruijer et al. (2014)) underwent processing in chondrule-forming events (Connelly and Jones, 2016). The similarity in age and isotopic composition of the inclusions to OC chondrules may point to them forming by a similar mechanism, but they must have formed from siderophile-depleted precursors.

4.5 Future Work

This study has indicated that XCT is a useful tool in identifying and subsampling of material to expose igneous inclusions. Widening the work to additional stones of Barwell would provide better statistics on the frequency of this material, and allow targeting of inclusions that are of sufficient size for characterisation by the techniques in this study and others that may provide more information, for example, whole rock geochemistry by atomic emission spectroscopy (ICP-AES) thus reducing inaccuracies from modal recalculation of bulk compositions, or absolute ages using the Pb-Pb system. Additionally, we intend to separate more inclusions to conduct Hf-W analysis to further constrain the bulk inclusion isochron and better understand the degree of metal-silicate fractionation experienced by the material. Similarly, analysis of the Hf-W isotope compositions of both metal and non-metal fractions of the host chondrite would further inform about the thermal history of the host chondrite. Since Barwell is an L6 chondrite, the Hf-W metal-silicate isochron will date the cooling below the Hf-W closure

temperature of ~800 °C, as well as providing a more accurate ‘bulk chondrite’ anchor to calculate model ages of the inclusions.

The trace-element abundances were inconclusive due to instrument and sample limitations however accurate data could prove crucial in determining if the clasts are formed through planetary, igneous processes, indicating if the patterns result from crystal-liquid fractionation or different element volatilities (Ruzicka et al., 1995; Bridges et al., 1995). Improved data on REE patterns of the inclusions would further elucidate the degree of similarity between the igneous inclusions and ordinary chondrites. Leftover bulk cuts, remaining after the removal of high field strength elements for W isotope compositions, were retained in the hope of conducting this by solution ICP-MS.

Furthermore, the same method outlined here could be applied to additional inclusions found in other ordinary chondrites. It would be prudent to search for such igneous inclusions in unequilibrated OCs, which would lack the overprinting of metamorphism and add further constraints on our understanding of the origin of this material.

5 Conclusions

5.1 Three-dimensional analysis of extraterrestrial material

5.1.1 3D structure of ordinary chondrites

Ordinary chondrites are amongst the most primitive materials we have for the study of the early Solar System. Their evolution has been dominated by thermal and shock metamorphism, which has led to the classification schemes in place today, i.e. petrological type and shock stage designations, which indicate the degree to which a meteorite was subject to these processes. It is evident that the effects are highly variable as the degree of porosity of a precursor greatly affects the response to impact (e.g. Bland et al., 2014; Beitz et al., 2013).

As shown in *Section 3.3*, for ordinary chondrites, the size distribution of metal grains can reflect whether the sample is texturally equilibrated or not. We can separate trends that relate to reaching textural equilibrium due to static metamorphism, as well as the loss of equilibrium due to impact events and the onset of shock melting. It is not possible to predict or model the metal grain size distribution, as there is clearly significant variation between meteorites of the same shock stage and petrological type. Other factors may influence the metal grain size distribution, for example, the duration of the shock pulse, melting due to peak shock temperatures achieved or frictional melting, any subsequent post-shock annealing, and differences in rheology between H and L chondrites. The results show that metal grain size distributions register the temperature-pressure-time path of the chondrite.

Prior to their classification by observations of effects of shock on olivine in thin-section (Table 3.5), the shock stage of four meteorites (that lacked shock classification in the literature) were predicted based on their metal grain orientations, AMS, appearance in CT data, and porosity observations by different techniques. Little Piney, Aumieres and Monze all exhibited higher than expected strength factors of their metal grain orientations when compared with degree of anisotropy in their magnetic susceptibilities – the reason for which is not fully understood. Little Piney still preserves some

intergranular porosity, though most void space is present as microcracks. Metal grains show a prevalent lineation but this is not strongly reflected in the AMS data. Therefore, Little Piney was predicted to be shock stage 2. Aumieres shows evidence of lineation and foliation in both metal grain orientation and AMS. It appears well compacted in XCT images, indicating that porosity measured by helium pycnometry is likely present as microcracks. Therefore, it was predicted to be shock stage 3 - 4. Jackalsfontein was predicted to be of shock stage 4 as it appears compacted in CT images, clearly displays a strong foliation fabric in metal, and has high degree of AMS. Monze exhibits low porosity and a strong fabric in both metal grain orientation and AMS. It was therefore predicted to be shock stage 5. On comparison with classification of shock by traditional methods (Table 3.5), these predictions are similar, suggesting that the degree of similarity in the orientation of major axes of metal grains is a reliable indicator for the degree of shock experienced by an OC.

As discussed in *Section 3.3*, porosity is present in many different forms in these samples of OCs. Visualisation of porosity appears to show evidence of both primordial and secondary porosity – interstitial, intragranular, and shock cracks/sheets. Some samples appear incompletely compacted, i.e. with considerable intergranular porosity. These samples are often low shock (S1/2), and may conserve primordial porosity that has been retained due to no significant shock or compaction through metamorphism. Some samples have very low visible porosity, which is mostly found in microcracks in and around silicate grains, which are more prevalent in samples of higher shock stage. The disagreement between the porosity values from this study and those by He pycnometry in the literature could be due to several factors, either related to the samples, or the techniques, or both. One possibility is heterogeneity in the porosity of samples. Sample sizes in He pycnometry studies ranged from 10 g to 1.2 kg, which would be more representative of the bulk meteorite, potentially sampling larger cracks that would not be found in 1 to 2 g samples. Potentially the samples experienced different terrestrial weathering conditions as even falls can be subject to alteration.

There is no evidence in any of the XCT data gathered in this study that the shock waves have led to incomplete compaction on the lee side of chondules (as suggested by the models of Bland et al., 2014 and Davison et al., 2016). This would suggest that the meteorites experienced multiple impacts, with shock waves originating from different directions, which would have homogenised the distribution of porosity. There is no clear trend between porosity and petrological grade. Meteorites of the same grade can exhibit very different porosity types. To further explore this, other features

should be investigated to understand if this lack of a trend is a result of the formation of porosity after metamorphism, the diversity of initial porosities leading to non-uniform effects of metamorphism, or the lack of sufficient overburden pressure to cause compaction in samples of higher petrological type.

The data suggest that shock reduces porosity but the number of samples so far analysed is insufficient. It is also necessary to consider the action of shock contributing to porosity in the form of microcracks. As a shock wave moves through a solid, the passing wave first compresses, then decompresses, thus leaving cracks. However, exactly how shock affects different sample types is not well constrained. Potentially, in more porous meteorites, shock removes porosity. If the slight increase in porosity between S5 and S6 shown in this data is reliable, potentially this indicates that in very low porosity samples, increasing shock contributes to porosity through the generation of microcracks.

The relationship between the meteorites also deserves more consideration. Do the non-compacted samples represent compacted samples prior to shock? That is, do the different groups represent two OC chondrite parent bodies that had different shock histories? Despite the general trends observed, there are complexities in the history of every chondrite. The results illustrate how shock stage classification, whilst a useful tool, is a simplification of the properties of a chondrite. It is clear that grains in the same chondrite, even in the same section, experienced and responded to shock differently. Shock acts heterogeneously depending on grain size, porosity, contacts between different materials, initial temperature, and various other factors.

5.1.2 Igneous inclusions in Barwell

In *Section 4*, this project followed up on the identification of a large differentiated “Pebble” by Hutchison et al. (1988). The study has indicated that inclusion-like material is common in Barwell, with at least 20 additional objects observed. They are varied in their texture but broadly similar in their mineralogy and composition, depleted in metal and sulphides with respect to OC material. These inclusions do not show the same degree of zonation as that observed by Hutchison et al. (1988), however there is evidence that this is a result of mineral equilibration, which is likely to have been more efficient across these inclusions owing to their smaller size than the original ‘Pebble’. REEs are depleted and potentially exhibit fractionated patterns, which may be related to whichever process led to the

loss of metal and sulphide. The inclusions appear to retain their oxygen isotopic signature, which shows a similarity with individual chondrule compositions from unequilibrated OC meteorites. This would support a similar formation region to chondrules, if not a similar formation process.

Hf-W isotopes have similarly remained isolated, based on comparison with other L chondrite data, however this should be further investigated by Hf-W systematics on metal and silicate fractions of Barwell (planned for the near future). The inclusions are characterised by superchondritic Hf/W ratios and radiogenic ^{182}W excesses, consistent with metal-silicate separation, however not as pronounced as differentiated crustal material (e.g. HEDs from Vesta). The isochron defined by three of the inclusions indicates a common age ~2.7 Ma after CAIs, which is in line with evidence of differentiated planetesimals (e.g. Kruijer et al. 2014), but also similar to some chondrule ages, though perhaps whether this is primary formation or a result of subsequent remelting episodes cannot be certain.

A possible scenario for the formation of these inclusions was put forward in *Section 4.4*, whereby an early accreted planetesimal experienced some differentiation – possibly due to radiogenic heating or more localised impact melting – and subsequently experienced collision leading to the ejection of metal-depleted material. This material either completely or partially melted, before solidifying in the nebula and being accreted onto the Barwell parent body.

As discussed in *Section 4.4.8*, the potential genetic link between igneous inclusions and chondrules warrants further investigation, since the existence of these intriguing objects may have implications for our understanding of chondrule formation. For some analyses, this is not possible due to the small size of chondrules. For example, single chondrules in OC chondrites do not contain enough W for Hf-W systematics.

5.2 The use of XCT as a technique for the study of extraterrestrial material

5.2.1 Successes of XCT analysis

The results highlight the potential of XCT as an analytical technique, providing quantitative data that can be further interrogated for other applications. It is possible to measure the size, shape and orientation of thousands of individual metal grains in 3D, providing a more accurate representation of this phase in OC meteorites. The correlation with magnetic susceptibility and AMS data supports this assertion.

The study aimed to compare measurements of porosity by three different techniques in order to understand the strengths and weaknesses of the techniques and assess porosity present on different scales. XCT may be able to provide quantitative measurements for porosity for certain meteorites (i.e. high porosity small samples) but it is difficult to verify with pycnometry because the results indicate that this technique is not accurate for the sample size in this study. Grain volume measurements often took a long time to 'settle' or remained erratic. Similarly, calculated porosities were often negative, indicating inaccuracies in the measurements. In some cases, the techniques were successful in yielding results similar to those in the literature, however that alone does not imply reliability. It is also likely that errors in other methods are contributing to the disparity, e.g. errors in the bulk volume of the sample by the microbead (which acts as an approximation for a fluid) displacement method. Furthermore, this study and other visualisations show that porosity often exists in discrete voids, and it is possible that the helium gas used in pycnometry is unable to reach these voids.

The results do illustrate that XCT is a useful technique for characterising porosity in meteorites, demonstrating its ability to provide accurate and informed interpretations of porosity quantified by other techniques, but without the limitations inherent in 2D samples or potential errors introduced by sample preparation for thin-section analysis.

Furthermore, this study has indicated that XCT is a useful tool in identifying and subsampling of material to expose igneous inclusions. The subsampling of a 441 g piece of the Barwell meteorite to expose two inclusions first observed in the XCT data shows that such visualisations can be used to inform accurate subsampling.

Similarly, manual segmentation of the features facilitates observation of shapes and volumes in 3D, which would otherwise would be subject to misrepresentation in 2D sectioning.

5.2.2 Limitations of XCT analysis

Resolution seems to be the biggest limitation as porosity is present on smaller scales than 5 μm (the limit of our system and many cabinet scanners). Based on SEM observations, it is likely that every meteorite has microporosity below resolution limit, which could explain some disagreements with He pycnometry values. A solution would be to use synchrotron CT, or a newer cabinet scanner such as the Zeiss Versa, however, this would mean even greater sacrifices in representation of the meteorite due to small sample sizes. On the whole, the resolution limit of 5-10 μm is insufficient for accurate quantification of porosity of compacted meteorites.

Artefacts in CT data, such as beam hardening, starbursts, and streaking, can also cause inaccuracies in the quantification of phases and therefore must be identified early on, ideally at the time of reconstruction so that appropriate correction algorithms can be applied. Various parameters can be optimised to mitigate against this and each scan should be qualitatively assessed before being thresholded and samples rescanned if necessary.

Additionally, errors related to the quantification of phases are complex and hard to determine in XCT data. For example, this study utilised user-based thresholding estimations of error by repeating analyses at different time intervals (for reproducibility estimates) and by quantifying phases at bracketing greyscales where visible differences were observed. However, this is only a measure of user error. Realistically, the error is also dependent on the actual data. For example, partial volume – the effect of averaging greyscale of voxels containing one or more material – is complex to estimate as a given voxel on the boundary of pore space and minerals could contain multiple compositionally heterogeneous phases. Thus, this effect is only compounded by the complexity of meteoritic material.

The bit depth of the data may have an impact and it could be worth investigating this more fully. After initially working with both 8- and 16-bit versions of a single scan, weighing up visual improvements in the data with the increase in processing time, the decision was made to uniformly use 8-bit data. In hindsight, using 8-bit

data can provide less accurate measurements of porosity in particularly porous samples. For example, in the case of the Allegan meteorite, selecting a porosity range of 0-51, which appears to be the most accurate to the user, yields a modal porosity of 14.2%. When the greyscale value range is selected at 0-50, the modal porosity is 11.4%, and when one greyscale above the ideal is selected, at 0-52, the modal porosity is 17.6%. Therefore, the user can only select a level of porosity with an accuracy of 2-3%. In these cases, it is worth revisiting the volume using 16-bit data, in order to increase the number of greyscales available, and enabling the user to be more precise.

Lastly, through investigation of available software packages, it is clear that there are no specific programs designed to address the needs of the meteoritical community. It is often the case that existing software can be utilised in novel ways; however, many of the available packages are either considerably costly and often with 'black box' features that are not open to the user, or open-source and thus lacking rigorous maintenance. Knowledge and experience of programming and software development would be a key skill for any researcher embarking on an involved XCT study. Only through experience in using the technique is it apparent that the time taken for data analysis is sometimes prohibitive, and this could be improved with investigation of new software capabilities, utilising machine-learning or automated segmentation tools. In this respect, it would be more productive to work with a programming specialist to develop tools that are specific to the investigation, rather than attempting to apply an existing tool to the problem.

5.3 Future work

5.3.1 3D structure of ordinary chondrites

Proposals for expanding on the work in this study are included within the relevant chapters (Section 3.5 and Section 4.5). To summarise, a key limitation is the sample number studied. Surveys of properties, such as porosity and metal grain size distribution, are susceptible to skewed interpretation as a result of low sample number, i.e. outliers will have a greater effect. A wider sample set would provide more statistically significant and naturally representative overview of the effects of metamorphism in OCs. This is particularly relevant for meteorites with very low and very high shock stages. Furthermore, performing metal grain analysis on primitive achondrites could elucidate the mechanism of metal-silicate separation.

Similarly to metal, XCT data show clear differentiation between sulphide phases and silicates, therefore using existing data sets, this study could be widened to include analysis of sulphide grains, both in terms of their shape and orientation, and their relationship to metal. Additionally, building on the data in this study with analysis by additional techniques could further explain the observations, for example, ^{40}Ar-^{39}Ar dating of degassing to determine the order of shock events with respect to thermal metamorphism on the parent body, or performing the same XCT analysis prior and subsequent to laboratory impact experiments.

As noted earlier, owing to the heterogeneity often observed across a single meteorite, petrological examination of sections from the same samples that were CT scanned would enable shock stage classification of the relevant piece of a specimen, meaning shock experienced should be directly comparable between techniques. With regards to further testing the accuracy of the technique, bulk volume measurements should be made using the glass bead method, and possibly also by 3D laser scanning.

5.3.2 Igneous inclusions in Barwell

This study has indicated that inclusion-like material is common in Barwell, with at least 20 additional objects observed. Continuing the survey to include more stones would better constrain their size ranges, and would indicate where further subsampling could expose more inclusions. With regards to characterising existing material, very little of the inclusions remains (*see Appendix 8*), however, work thus far has indicated how much material is required for different analyses and inclusions of a sufficient size could be targeted. Additionally, polished block preparations are kept for potential future analysis. The lack of reliable REE data from LA-ICP-MS due to the crystal size of these inclusions indicates that this should be carried out by solution ICP-MS, which will be incorporated into Hf-W chemistry workflows to make most efficient use of the material.

The study of these inclusions has indicated that comparisons should also be drawn directly with individual chondrule and/or chondrule fraction data, to further investigate their possible genetic link. There are inherent analytical limitations, since chondrules are relatively small, however ongoing technical advances are improving sensitivity and resolution, and additional data are likely in the near future.

Lastly, Barwell is not unique in containing these igneous inclusions (e.g. Ruzicka et al. 1998, 2000, 2012, 2016). As we see considerable overprinting on the original properties of the inclusions as a result of parent body metamorphism, such inclusions should be sought in unequilibrated chondrites.

5.3.3 XCT

There are many aspects still not fully understood in XCT, specifically those leading to errors in quantification of phases and/or object parameters. Some effects are instrument specific therefore, prior to additional XCT acquisition, it would be beneficial to carry out a comprehensive study of the effect of factors such as location of sample within the cone beam. Using a calibration standard of known mass and volume, scanned at different voxel sizes, would allow calculation of the inherent instrumental error when quantifying size parameters from XCT data. However, applying this error is still subject to the complications of dealing with complex shapes and relationships between phases as seen in meteorites.

This study illustrates XCT is a useful tool in measuring volume and characterising shape of inclusions within precious meteorites. It can be used to accurately locate these areas of interest to inform subsampling, however, one important observation from this experience is that as XCT provides a measure of attenuation, visualisation of the surface of a specimen is not necessarily comparable to the real physical appearance. Future collaboration with software developers to investigate the potential of combining XCT data with photogrammetry (i.e. 3D meshes with surface imagery), which would enable more accurate and simpler sampling.

Across the duration of this study, advances in XCT technologies have been considerable. The introduction of optical lenses to cabinet scanners has meant that smaller voxel sizes, previously only attainable using synchrotron sources, are accessible in a small lab scenario, as with the introduction of the Zeiss Versa instrument at the NHM. Advances in hardware, e.g. detector efficiency and sensitivity, or size of detector elements, are further explored in Hanna and Ketcham (2017). Their lab, UTCT, at the University of Texas at Austin, has long been at the vanguard of geological applications of XCT and they continue to develop both hardware and software in this field. One particularly exciting development is in X-ray detectors that are capable of facilitating chemical characterisation. This may be possible by using

hyperspectral detectors that measure the energy of the incoming X-ray photons (e.g., Egan et al., 2015), or by combining XCT with existing techniques such as X-ray diffraction (XRD) (e.g. Uesugi et al., 2013) or X-ray fluorescence (XRF) (e.g. Wildenschild and Sheppard, 2013).

Additionally, decreasing costs and increasing capabilities of computing equipment have enabled advances in data processing and handling, from more accurate iterative reconstruction algorithms to more complex automatic segmentation or analysis tools (e.g. Deng et al., 2016). Furthermore, advances in software will surely uncover additional ways in which XCT data can be used. For example, preliminary investigations of the Zeiss Atlas package indicates it will be possible to directly correlate between XCT data and EDX element mapping of sections, and infer the chemical composition of the interior. This is especially of interest in its applications the investigation of rare extraterrestrial material. Another area yet to be explored is the use of mineral standards, i.e. including pieces of representative minerals in the same scan and using the attenuation to indicate where these minerals are present in the sample. This is complicated by grain size, crystal zonation, microporosity, and other factors, but would warrant further investigation.

Lastly, there have been recent studies indicating that XCT is not a completely non-destructive technique, having an effect on the natural thermoluminescence of a meteorite, or potentially affecting any organics present. This area must be further investigated, not only for the long term protection of our collections, and for understanding the potential impact on future research, but also because XCT is increasingly identified as an ideal tool for the characterisation of material returned by space missions.

Essentially, XCT is a powerful technique that has its limitations. As is often the case, several analytical approaches must be used in conjunction, and with full consideration of the limitations and trade-offs in each case, as well as a thorough understanding of the impact of each method on the sample. Despite the inferences possible from attenuation differences in the data, XCT does not provide chemical information, however does provide a tool for assessing homogeneity across a material without sampling bias. Conversely, most geochemical techniques (EPMA, LA-ICP-MS, ICP-AES, XRF etc.), although higher resolution, are limited by their 2D and/or destructive nature. Nevertheless, XCT is proving ever more prevalent and relevant as an analytical technique in the natural sciences.

6 References

Abel, R. L., Laurini, C. R., & Richter, M., (2012), A palaeobiologist's guide to 'virtual' micro-CT preparation, *Palaeontologia Electronica*, 15, 2, 17.

Acuña, M. H., Anderson, B. J., Russell, C. T., Wasilewski, P., Kletetschka, G., Zanetti, L., & Omidi, N. (2002), NEAR magnetic field observations at 433 Eros: First measurements from the surface of an asteroid. *Icarus*, *155*(1), 220-22.

Afiattalab, F., & Wasson, J. T. (1980), Composition of the metal phases in ordinary chondrites: Implications regarding classification and metamorphism. *Geochimica et Cosmochimica Acta*, *44*(3), 431445-443446.

Alexander C. M. O'D., Barber D. J., & Hutchison R. H. (1989) The microstructure of Semarkona and Bishunpur, *Geochimica et Cosmochimica Acta*, 53, 3045–3057.

Alexander, C. M. O'D., Grossman, J. N., Ebel, D. S., & Ciesla, F. J. (2008). The formation conditions of chondrules and chondrites. *Science*, *320*(5883), 1617-1619.

Allen, C., Allton, J., Lofgren, G., Righter, K., Zeigler, R. & Zolensky, M., (2013), Curating NASA's Extraterrestrial Samples, *Eos Trans. AGU*, 94, 29, 253.

Almeida, N.V., Smith, C.L., Sykes, D., Downes, H., Ahmed, F., Russell, S.S., (2015), Quantifying the deformation of Leoville chondrules in 3D: Implications for the post-accretional history of the CV3 parent body.*,78th Annual Meeting of the Meteoritical Society, Berkeley, CA,* #5112.

Als-Nielsen, J., & McMorrow, D., (2011), Elements of modern X-ray physics. John Wiley & Sons.

Akaki T. & Nakamura T., (2005), Formation processes of compound chondrules in CV3 carbonaceous chondrites: constraints from oxygen isotope ratios and major element concentrations, *Geochimica et Cosmochimica Acta*, 69, 2907–2929.

Amelin, Y., Krot, A. N., Hutcheon, I. D., & Ulyanov, A. A., (2002), Lead isotopic ages of chondrules and calcium-aluminum-rich inclusions. *Science*, *297*(5587), 1678-1683.

Andreasen, R., & Sharma, M., (2007), Mixing and homogenization in the early solar system: clues from Sr, Ba, Nd, and Sm isotopes in meteorites. *The Astrophysical Journal*, 665(1), 874.

Armstrong, K., & Ruzicka A., (2015), Major-Element Geochemistry of Large, Igneous-Textured Inclusions in Ordinary Chondrites, *46th Lunar and Planetary Science Conference*, #1572.

Arnold J. R., Testa J. P., Friedman P. J., & Kambic G. X., (1983), Computed tomographic analysis of meteorite inclusions, *Science*, 219, 383–384.

Ashworth, J. R., (1985), Transmission electron microscopy of L-group chondrites, 1. Natural shock effects. *Earth and Planetary Science Letters*, *73*(1), 17-32.

Asphaug, E., Jutzi, M., & Movshovitz, N., (2011), Chondrule formation during planetesimal accretion. *Earth and Planetary Science Letters*, *308*(3), 369-379.

Bechtel, H.A., Flynn, G.J., Allen, C., Anderson, D., Ansari, A., Bajt, S., Bastien, R.K., Bassim, N., Borg, J., Brenker, F.E., Bridges, J., Brownlee, D.E., Burchell, M., Burghammer, M., Butterworth, A.L., Changela, H., Cloetens, P., Davis, A.M., Doll, R., Floss, C., Frank, D.R., Gainsforth, Z., Grün, E., Heck, P.R., Hillier, J.K., Hoppe, P., Hudson, B., Huth, J., Hvide, B., Kearsley, A., King, A.J., Lai, B., Leitner, J., Lemelle, L., Leroux, H., Leonard, A., Lettieri, R., Marchant, W., Nittler, L.R., Ogliore, R., Ong, W.J., Postberg, F., Price, M.C., Sandford, S.A., Tresseras, J.-A.S., Schmitz, S., Schoonjans, T., Silversmit, G., Simionovici, A.S., Solé, V.A., Srama, R., Stadermann, F.J., Stephan, T., Sterken, V.J., Stodolna, J., Stroud, R.M., Sutton, S., Trieloff, M., Tsou, P., Tsuchiyama, A., Tyliszczak, T., Vekemans, B., Vincze, L., Von Korff, J., Westphal, A.J., Wordsworth, N., Zevin, D., & Zolensky, M.E., (2014), Stardust interstellar preliminary examination III: infrared spectroscopic analysis of interstellar dust candidates, *Meteoritics & Planetary Science*. 49, 1548–1561.

Beitz, E., Güttler, C., Nakamura, A. M., Tsuchiyama, A., and Blum, J., (2013), Experiments on the consolidation of chondrites and the formation of dense rims around chondrules. *Icarus*, 225, 558-569.

Beitz, E., Blum, J., Parisi, G., (2014), Impact Induced Compaction of Chondrites and the Porosity Evolution of Chondritic Parent Bodies, *77th Annual Meeting of the Meteoritical Society*, #5452.

Benedix, G. K., Ketcham, R. A., Wilson, L., McCoy, T. J., Bogard, D. D., Garrison, D. H., Herzog, G. F., Xue, S., Klein, J., & Middleton, R., (2008), The formation and chronology of the PAT 91501 impact-melt L chondrite with vesicle–metal–sulfide assemblages. *Geochimica et Cosmochimica Acta,* 72, 9, 2417-2428.

Bennett, M. E., & McSween, H. Y. (1996a). Shock features in iron-nickel metal and troilite of L-group ordinary chondrites. *Meteoritics & Planetary Science*, *31*(2), 255-264.

Bennett, M. E., & McSween, H. Y., (1996b), Revised model calculations for the thermal histories of ordinary chondrite parent bodies. *Meteoritics & Planetary Science*, *31*(6), 783-792.

Binzel, R.P., Rivkin, A.S., Bus, S.J., Sunshine, J.M., & Burbine, T.H., (2001), MUSES-C target asteroid (25143) 1998 SF36: A reddened ordinary chondrite, *Meteoritics & Planetary Science,* 36, 1167-1172.

Bischoff, A., Vogel, N., & Roszjar, J., (2011), The Rumuruti chondrite group. *Chemie der Erde - Geochemistry*, *71*(2), 101-133.

Bischoff, A., Geiger, T., Palme, H., Spettel, B., Schultz, L., Scherer, P., & Lkhamsuren, J. (1993). Mineralogy, chemistry, and noble gas contents of Adzhi-Bogdo–an LL3–6 chondritic breccia with L-chondritic and granitoidal clasts. *Meteoritics*, *28*(4), 570-578.

Bischoff, A., Rubin, A. E., Keil, K., & Stöffler, D. (1983). Lithification of gas-rich chondrite regolith breccias by grain boundary and localized shock melting. *Earth and Planetary Science Letters*, *66*, 1-10.

Bizzarro M., Baker J. A., & Haack H., (2005), Rapid time scales for accretion and melting of differentiated planetesimals inferred from 26Al-26Mg chronometry, *The Astrophysical Journal,* 632, L41–L44.

Bland, P.A., Muxworthy, A. R., Collins, G. S., Moore, J., Davison, T. M., Prior, D. J., Wheeler, J., Ciesla, F. J., & Dyl, K. A., (2012), Effect of Low Intensity Impacts on Chondrite Matrix, *43rd Lunar and Planetary Science Conference*, #2005.

Bland, P.A., Zolensky, M. E., Benedix, G. K., & Sephton, M. A., (2006), Weathering of Chondritic Meteorite, *Meteorites and the Early Solar System II*, 853-858.

Bland P. A., Berry, F. J., Smith T. B., Skinner S. J., and Pillinger C. T., (1996), The flux of meteorites to the Earth and weathering in hot desert ordinary chondrite finds, *Geochimica et Cosmochimica Acta*, 60, 2053-2059.

Bland P.A., Howard L. E., Prior D. J., Wheeler J., Hough R. M., and Dyl K., (2011), Earliest rock fabric formed in the Solar System preserved in a chondrule rim, *Nature Geoscience*, 4, 244-247.

Bland P.A., Collins G.S., Davison T.M., Abreu N.M., Ciesla F.J., Muxworthy A.R., & Moore J., (2014), Pressure-temperature evolution of primordial solar system solids during impact-induced compaction, *Nature Communications*, 5, 2041-172.

Blumenfeld, E.J., C.A. Evans, E.R. Oshel, D.A. Liddle, K. Beaulieu, R. Zeigler, R.D. Hanna, & R.A. Ketcham, (2015), Comprehensive non-destructive conservation documentation of lunar samples using high-resolution 3D reconstructions and X-ray CT data, *Lunar and Planetary Science Conference XLVI*, #2740.

Bobrovnikoff, N.T., (1929), The spectra of minor planets, *Lick Observatory Bulletin*, 407, 18-27.

Bouvier, A., & Wadhwa, M., (2010), The age of the Solar System redefined by the oldest Pb–Pb age of a meteoritic inclusion, *Nature Geoscience*, *3*(9), 637-641.

Brearley, A. J. and Jones, R. H., (1998), Chondritic meteorites, *Reviews in Mineralogy and Geochemistry,* 36, 3.1-3.398.

Bridges, J. C. & Hutchison, R., (1997), A survey of clasts and large chondrules in ordinary chondrites, *Meteoritics and Planetary Science*, 32, 389-394.

Bridges, J. C., Hutchison, R., Franchi, I. A., Alexander, C. M., & Pillinger, C. T., (1995), A feldspar-nepheline achondrite clast in Parnallee, *Antarctic Meteorite Research*, *8*, 195.

Bridges, J. C., Franchi, I. A., Hutchison, R., Sexton, A. S., & Pillinger, C. T., (1998), Correlated mineralogy, chemical compositions, oxygen isotopic compositions and size of chondrules, *Earth and Planetary Science Letters*, *155*(3), 183-196.

Britt, D. T., Yeomans, D., Housen, K., and Consolmagno, G., (2002), Asteroid Density, Porosity, and Structure, *Asteroids III,* University of Arizona Press, 485-500.

Britt, D. T., and Consolmagno, G. J., (2003), Stony meteorite porosities and densities: A review of the data through 2001. *Meteoritics and Planetary Science*, 38, 1161-1180.

Bruck Syal, M., Schultz, P. H., Dearborn, D. S. P. Managan, R. A., (2012), Porosity Controls on Asteroid Defense Strategies, *43rd Lunar and Planetary Science Conference*, #2480.

Budde, G., Kleine, T., Kruijer, T. S., Burkhardt, C., & Metzler, K. (2016). Tungsten isotopic constraints on the age and origin of chondrules. *Proceedings of the National Academy of Sciences*, 2886-2891.

Budde, G., Kruijer, T. S., Fischer-Gödde, M., Irving, A. J., & Kleine, T. (2015). Planetesimal differentiation revealed by the Hf–W systematics of ureilites. *Earth and Planetary Science Letters*, 430, 316-32.

Bus, S. J., & Binzel, R. P. (2002). Phase II of the small main-belt asteroid spectroscopic survey: A feature-based taxonomy. *Icarus*, 158(1), 146-177.
Buchanan, P. C., Zolensky, M. E., & Reid, A. M. (1993). Carbonaceous chondrite clasts in the howardites Bholghati and EET87513. *Meteoritics*, *28*(5), 659-669.

Cain, P. M., McSween, H. Y., & Woodward, N. B., (1986), Structural deformation of the Leoville chondrites, *Earth and Planetary Science Letters*, 77, 2, 165 – 175.

Carlson, W. D., Rowe, T., Ketcham, R. A. & Colbert, M. W., (2003), Applications of high-resolution X-ray computed tomography in petrology, meteoritics and palaeontology, *Special Publications, Geological Society, London*, 215:7-22.

Cifelli, R.L., Rowe, T.B., Luckett, W.P., Banta, J., Reyes, R., & Howes, R.I., (1996), Fossil evidence for the origin of the marsupial pattern of tooth replacement, *Nature*, 379, 715–718.

Chaumard, N., Humayun, M., Zanda, B., & Hewins, R. H., (2014), Cooling Rate of a Type I Chondrule from the Renazzo CR2 Chondrite Inferred from Cu and Ga Diffusion Profiles in Metal Grains, *45th Lunar and Planetary Science Conference*, #2448.

Clauser, C., & Huenges, E., (1995), Thermal conductivity of rocks and minerals, *Rock physics and phase relations: A handbook of physical constants*, 105-126.

Clayton, R. N., Onuma, N., & Mayeda, T. K. (1976). A classification of meteorites based on oxygen isotopes. *Earth and Planetary Science Letters*, *30*(1), 10-18.

Clayton, R. N., Mayeda, T. K., Goswami, J. N., & Olsen, E. J. (1991). Oxygen isotope studies of ordinary chondrites. *Geochimica et Cosmochimica Acta*, *55*(8), 2317-2337.

Cloutis, E. A., Binzel, R. P., & Gaffey, M. J. (2014). Establishing asteroid–meteorite links. *Elements*, *10*(1), 25-30.

Connelly, J. N., Bizzarro, M., Krot, A. N., Nordlund, Å., Wielandt, D., & Ivanova, M. A. (2012). The absolute chronology and thermal processing of solids in the solar protoplanetary disk. *Science*, *338*(6107), 651-655.

Connolly, H. C., & Desch, S. J. (2004). On the origin of the “Kleine Kügelchen” Called chondrules. *Chemie der Erde-Geochemistry*, *64*(2), 95-125.

Connolly, H. C., & Jones, R. H. (2016). Chondrules: The Canonical and Non-canonical View. *Journal of Geophysical Research: Planets.*121(10), 1885-1899.

Consolmagno, G. J., Britt, D. T., & Stoll, C. P., (1998, The porosities of ordinary chondrites: Models and interpretation. *Meteoritics and Planetary Science*, 33, 1221-1229.

Consolmagno, G.J., & Britt, D. T. (2004). Meteoritical evidence and constraints on asteroid impacts and disruption. *Planetary and Space Science*, *52*(12), 1119-1128.

Consolmagno, G. J., Weidenschilling, S. J., & Britt, D. T., (2003), Forming well-compacted meteorites by shock events in the solar nebula, *66th Annual Meeting of the Meteoritical Society*, #5247.

Corrigan C. M., & Lunning, N. G., (2016), A Variety Of Melt Clasts In Ordinary Chondrite Breccia Meteorite Hills (MET) 01004, *47th Lunar and Planetary Science Conference*, #2729.

Corrigan, C.M., Lunning, N.G. & Zeigler K. (2015), An H Chondrite Melt Clast in an LL Chondrite: Evidence for Mixing of Ordinary Chondrite Parent Bodies, *46th Lunar and Planetary Science Conference*, #2678.
C. M. Corrigan, N. G. Lunning, J. M. Friedrich, & T. J. McCoy, (2015), An H Chondrite Clast In An LL Chondrite: Impact Melt Or Incipient Partial Melt? *78th Annual Meeting of the Meteoritical Society (2015), #5283.*

Corrigan, C. M., Cohen, B. A., Hodges, K., Lunning, N., & Bullock, E., (2012), 3.9 Billion Years Ago And The Asteroid Belt: Impact Melts In Ordinary Chondrites, *43rd Lunar and Planetary Science Conference*, Abstract #1577.

Cross W., Iddings J.P., Pirsson L.V., & Washington H. S., (1902) A quantitative chemicomineralogical classification and nomenclature of igneous rocks, *Journal of Geology*, 10, 555–690.

Crowther, S. A., Filtness, M. J., & Gilmour, J. D., (2014), Early I-Xe Ages Of Clasts And Chondrules From The L6 Chondrite Barwell, *45th Lunar and Planetary Science Conference*, #2031.

Cuzzi, J. N., Hogan, R. C., & Shariff, K., (2008), Toward planetesimals: Dense chondrule clumps in the protoplanetary nebula. *The Astrophysical Journal*, *687*(2), 1432.

Davison, T. M., Collins, G. S., & Bland, P. A. (2016). Mesoscale Modeling of Impact Compaction of Primitive Solar System Solids. *The Astrophysical Journal*, *821*(1), 68.

DeCarli, P. S., Bowden, E., & Seaman, L., (2001), Shock-induced compaction and porosity in meteorites, *64th Annual Meeting of the Meteoritical Society*, #5171.

Deng, H., Fitts, J. P., & Peters, C. A. (2016). Quantifying fracture geometry with X-ray tomography: Technique of Iterative Local Thresholding (TILT) for 3D image segmentation. *Computational Geosciences*, 20(1), 23.

Desch, S. J., Morris, M. A., Connolly, H. C., & Boss, A. P. (2012). The importance of experiments: Constraints on chondrule formation models. *Meteoritics & Planetary Science*, *47*(7), 1139-1156.

Desch, S. J., & Connolly, H. C. (2002). A model of the thermal processing of particles in solar nebula shocks: Application to the cooling rates of chondrules. *Meteoritics & Planetary Science*, *37*(2), 183-207.

Dodd, R. T., & Jarosewich, E. (1979). Incipient melting in and shock classification of L-group chondrites. *Earth and Planetary Science Letters*, *44*(2), 335-340.

Doube, M., Kłosowski, M. M., Arganda-Carreras, I., Cordelières, F. P., Dougherty, R. P., Jackson, J. S., & Shefelbine, S. J., (2010), BoneJ: Free and extensible bone image analysis in ImageJ. *Bone*, 47, 6, 1076-1079.

Ebel, D. S., Leftwich, K., Brunner, C. E. & Weisberg, M. K., (2009), Abundance and Size Distribution of Inclusions in CV3 Chondrites by X-ray Image Analysis, *40th Lunar and Planetary Science Conference,* #2065.

Ebel, D. S., Yin, Q-Z., Friedrich, J. M., Jenniskens, P., Fries, M. & Hill, M. G., (2012), X-Ray Tomographic Study of the Sutter's Mill CM Chondrite Breccia, *75th Annual Meeting of the Meteoritical Society*, #5380.

Eisenhour, D. D., (1996), Determining chondrule size distributions from thin-section measurements. *Meteoritics and Planetary Science*, 31, 2, 243-248.

Fish RA, Goles GG, & Anders E. (1960). The record in meteorites. III. On the development of meteorites inasteroidal bodies, *The Astrophysical Journal,* 132, 243–258.

Fodor, R. V., & Keil, K. (1976). Carbonaceous and non-carbonaceous lithic fragments in the Plainview, Texas, chondrite: origin and history. *Geochimica et Cosmochimica Acta*, *40*(2), 177-189.

Franchi, I.A., Baker, L., Bridges, J.C., Wright, I.P., & Pillinger, C.T. (2001). Oxygen isotopes and the early Solar System. *Philosophical Transactions of the Royal Society of London Series A - Mathematical Physical and Engineering Sciences*, 359: 2019–2034.

Friedrich, J. M. (2008). Quantitative methods for three-dimensional comparison and petrographic description of chondrites. *Computers & Geosciences*, 34(12), 1926-1935.

Friedrich J. M., Wignarajah D. P., Chaudhary S., Rivers M. L., Nehru C. E., & Ebel D. S., (2008a), Three-dimensional petrography of metal phases in equilibrated L chondrites – effects of shock loading and dynamic compaction, *Earth and Planetary Science Letters*, 275, 172-180.

Friedrich, J. M., Macke, R. J., Wignarajah, D. P., Rivers, M. L., Britt, D. T., & Ebel, D. S., (2008b), Pore size distribution in an uncompacted equilibrated ordinary chondrite. *Planetary and Space Science*, 56, 7, 895-900.

Friedrich, J. M., Ruzicka, A., Ebel, D. S., Thostenson, J., Rudolph, R. A., Rivers, M. L., Macke, R. J., & Britt, D. T., (2012), Three Dimensional Petrography of Kernouvé:

A Story of Vein Formation, Compaction, and Metamorphism, *43rd Lunar and Planetary Science Conference,* #1197.

Friedrich J. M. & Rivers M. L., (2013), Three-dimensional imaging of ordinary chondrite microporosity at 2.6 micrometer resolution. *Geochimica et Cosmochimica Acta*, 116, 63-70.

Friedrich, J. M., Ruzicka, A., Rivers, M. L., Ebel, D. S., Thostenson, J. O., & Rudolph, R. A. (2013). Metal veins in the Kernouvé (H6 S1) chondrite: Evidence for pre-or syn-metamorphic shear deformation. *Geochimica et Cosmochimica Acta*, *116*, 71-83.

Friedrich, J.M., Glavin, D.P., Rivers, M.L., & Dworkin, J.P., (2016). Effect of a synchrotron X-ray microtomography imaging experiment on the amino acid content of a CM chondrite. *Meteoritics and Planetary Science,* 51, 429–437.

Fujimura, A., Abe, M., Yada T., Nakamura, T., Noguchi, T., Okazaki, R., Ishibashi, Y., Shirai, K., Okada, T., Yano, H., Zolensky, M. E., Sandford, S., Ueno, M., Mukai, T., Yoshikawa M., & Kawaguchi, J., (2011), Processes to open the container and the sample catcher of the Hayabusa returned capsule in the planetary material sample curation facility of JAXA, *42nd Lunar and Planetary Science Conference*, #1829.

Fujiwara, A., Kawaguchi, J., Yeomans, D. K., Abe, M., Mukai, T., Okada, T., Saito, J., Yano, H., Yoshikawa, M., & Scheeres, D. J., (2006), The Rubble–Pile Asteroid Itokawa as observed by Hayabusa. *Science*, 312, 1330–1334.

Gaffey, M. J., & Gilbert, S. L. (1998). Asteroid 6 Hebe: The probable parent body of the H-type ordinary chondrites and the IIE iron meteorites. *Meteoritics & Planetary Science*, *33*(6), 1281-1295.

Garwood, R.J., Dunlop, J.A., & Sutton, M.D., (2009), High-fidelity X-ray micro tomography reconstruction of siderite-hosted Carboniferous arachnids. *Biology Letters*, 5, 841-844.

Gattaceca J., Rochette P., Denise M., Consolmagno G., & Folco L., (2005), An impact origin for the foliation of chondrites, *Earth and Planetary Science Letters*, 234, 351-368.

Gattacceca, J., Lamali, A., Rochette, P., Boustie, M., & Berthe, L. (2007). The effects of explosive-driven shocks on the natural remanent magnetization and the magnetic properties of rocks. *Physics of the Earth and Planetary Interiors*, *162*(1), 85-98.

Ghosh A. & McSween H. Y. Jr. (1998) A thermal model for the differentiation of asteroid 4 Vesta based on radiogenic heating. *Icarus*, 134, 187–206.

Gilmour J.D., Hewitt, S. S., Lyon, I. C., Stringer, M., & Turner, G., (1991), A Resonance Ionization Mass Spectrometer for Xenon, *Measurement Science and Technology*, 589-595.

Goldman, R. T., Crapster-Pregont, E. J., & Ebel, D. S., (2014), Comparison of Chondrule and CAI Size Measured by Electron Microprobe (2D) and Computed Tomography (3D), *45th Lunar and Planetary Science Conference*, #2263.

Gomes, R., Levison, H. F., Tsiganis, K., & Morbidelli, A. (2005). Origin of the cataclysmic Late Heavy Bombardment period of the terrestrial planets. *Nature*, *435*(7041), 466-469.

Goodrich, C. A., & Delaney, J. S. (2000). Fe/Mg–Fe/Mn relations of meteorites and primary heterogeneity of primitive achondrite parent bodies. *Geochimica et Cosmochimica Acta*, *64*(1), 149-160.

Goodrich, C. A., & Kring, D. A. (2016). A Large Igneous Clast in the Northwest Africa 092 Chondrite (L3. 7): Xenolith from a Differentiated Parent Body or Product of an Ordinary Chondrite-Related Melt?. *47th Lunar and Planetary Science Conference,* 1233.

Greenwood, R.C., Barrat, J.-A., Yamaguchi, A., Franchi, I.A., Scott, E.R.D., Bottke, W.F., & Gibson, J.M., (2014). The oxygen isotope composition of diogenites: Evidence forearly global melting on a single, compositionally diverse, HED parent body, *Earth and Planetary Science Letters*, 390, 165–174.

Greenwood, R. C., Schmitz, B., Bridges, J. C., Hutchison, R., & Franchi, I. A. (2007). Disruption of the L chondrite parent body: New oxygen isotope evidence from Ordovician relict chromite grains. *Earth and Planetary Science Letters*, *262*(1), 204-213.

Grimm, R. E., (1985), Penecontemporaneous metamorphism, fragmentation and reassembly of ordinary chondrite parent bodies, Journal of Geophysical Research, 90, 2022-2028.

Grossman, J. N., & Brearley, A. J. (2005). The onset of metamorphism in ordinary and carbonaceous chondrites. *Meteoritics & Planetary Science*, *40*(1), 87-122.

Guignard, J., & Toplis, M. J. (2015). Textural properties of iron-rich phases in H ordinary chondrites and quantitative links to the degree of thermal metamorphism. *Geochimica et Cosmochimica Acta*, *149*, 46-63.

Haack, H., Farinella, P., Scott, E. R., & Keil, K. (1996). Meteoritic, Asteroidal, and Theoretical Constraints on the 500 Ma Disruption of the L Chondrite Parent Body. *Icarus*, *119*(1), 182-191.

Hamano Y., & Yomogida K., (1982), Magnetic anisotropy and porosity of Antarctic chondrites. Proceedings of the Seventh Symposium on Antarctic Meteorites, 281–290.

Hanna, R. D., & Ketcham, R. A., (2013), Estimation of Pre-Deformation Bulk Microporosity Using 3D Measurement of Deformed Chondrules in CM2 Murchison. *76th Annual Meeting of the Meteoritical Society*, #5031.

Hanna, R.D., & Ketcham, R.A.,(2015). 3D measurement of fine-grained rims in CM murchison using XCT. *78th Annual Meeting of the Meteoritical Society*, #5350.

Hanna, R.D., Ketcham, R.A., Zolensky, M., & Behr, W., (2015). Impact-induced brittle deformation, porosity loss, and aqueous alteration in the Murchison CM chondrite, *Geochimica et Cosmochimica Acta,* 171, 256–282.

Hanna, R. D., & Ketcham, R. A. (2017). X-ray computed tomography of planetary materials: A primer and review of recent studies. *Chemie der Erde - Geochemistry*.

Hanna, R. D., & Ketcham, R. A. (2016). 3D Morphology of Fine-Grained Rims in CM Murchison, In 47th *Lunar and Planetary Science Conference*, # 2185.

Harvey R. P., Bennett M. L., & McSween H. Y. Jr. (1993) Pyroxene equilibration temperatures in metamorphosed ordinary chondrites, *Lunar and Planetary Science XXIV*, 615–616.

Hellmann, J. L., Kruijer T.S., & Kleine, T., (2017),Constraining The Timescale Of Solar Nebula Metal-Silicate Fractionation Using Hf-W Chronometry Of Ordinary Chondrites, *Lunar and Planetary Science XLVIII,* #2046.

Herndon, J. M. & Herndon, M. A. (1977), Aluminium-26 as a planetoid heat source in the early solar system. *Meteoritics* 12, 459-465.

Heymann, D. (1967), On the origin of hypersthene chondrites: Ages and shock effects of black chondrites. *Icarus*, 6, 189–221.

Heymann, D., Smith, M. J., and Anderson, J. B., (1985), X-Radiography Of Slabs Of The Allende Meteorite. *Meteoritics*, 20, 3, 559-569.

Hewins, R. H. (1997). Chondrules. *Annual Review of Earth and Planetary Sciences*, *25*(1), 61-83.

Hewins, R. H. (1983). Impact versus internal origins for mesosiderites. *Journal of Geophysical Research: Solid Earth*, *88*, S01.

Hezel, D. C., Elangovan, P., Viehmann, S., Howard, L., Abel, R. L., & Armstrong, R., (2013), Visualisation and quantification of CV chondrite petrography using micro-tomography. *Geochimica et Cosmochimica Acta*, 116, 33-40.

Hirata N., Kurita K., & Sekine T., (1995), Shock deformation and melting in the silicate-metal powder mixture, *26th Lunar and Planetary Science Conference*, #1305.

Hirata N., Kurita K., & Sekine T., (1998), Experimental shock lithification of porous powder mixture, *29th Lunar and Planetary Science Conference*, #1345.

Hörz, F., Cintala, M. J., See, T. H., & Le, L. (2005). Shock melting of ordinary chondrite powders and implications for asteroidal regoliths. *Meteoritics & Planetary Science*, 40(9-10), 1329-1346.

Hughes, D.W., (1978), A disaggregation and thin section analysis of the size and mass distribution of the chondrules in the Bjurböle and Chainpur meteorites, *Earth and Planetary Science Letters*, 38, 391-400.

Hunt, A. C., Benedix, G. K., & Howard, L., (2011), Pontlyfni, the Inside Story: Distribution of Metal and Sulfide Revealed by Micro-Computed Tomography, *74th Annual Meeting of the Meteoritical Society*, #5136.

Huss, G. R., Rubin, A. E., & Grossman, J. N. (2006). Thermal metamorphism in chondrites. *Meteorites and the Early Solar System II*, 567-586.

Huss, G. R., MacPherson, G. J., Wasserburg, G. J., Russell, S. S., & Srinivasan, G. (2001). Aluminum-26 in calcium-aluminum-rich inclusions and chondrules from unequilibrated ordinary chondrites. *Meteoritics & Planetary Science*, 36(7), 975-997.

Hutchison, R., Williams, C. T., Din, V. K., Clayton, R. N., Kirschbaum, C., Paul, R. L., & Lipschutz, M. E., (1988), A planetary, H-group pebble in the Barwell, L6, unshocked chondritic meteorite. *Earth and Planetary Science Letters*, 90, 2, 105-118.

Hutchison, R., (2011), Chondrules and their associates in ordinary chondrites: a planetary connection?, *In Chondrules and the Protoplanetary Disk*, Cambridge University Press, 311-317.

Hutchison, R., (2004), *Meteorites: A Petrologic, Chemical and Isotopic Synthesis*, Cambridge University Press.

Ireland, T. R., Salmeron, R., & Wardle, M. (2016). Isotopic and Chemical Fractionations Caused by Disk Winds in the Protoplanetary Disk. *LPI Contributions*, *1921*.

Jamsja, N., & Ruzicka, A. (2010). Shock and thermal history of Northwest Africa 4859, an annealed impact-melt breccia of LL chondrite parentage containing unusual igneous features and pentlandite. *Meteoritics & Planetary Science,* 45(5), 828-849.

Jelinek, V., (1981), Characterization of the magnetic fabric of rocks, *Tectonophysics*, 79, 63–67.

Johnson, B. C., Minton, D. A., Melosh, H. J., & Zuber, M. T. (2015). Impact jetting as the origin of chondrules. *Nature*, 517(7534), 339-341.

Jones, R., & Scott, E. (1996). *Chondrules and the protoplanetary disk*. Cambridge University Press.

Jones, R. H., Grossman, J. N., & Rubin, A. E. (2005). Chemical, mineralogical and isotopic properties of chondrules: Clues to their origin. In *Chondrites and the protoplanetary disk*, 341, 251.

Jones, R. H. (2012). Petrographic constraints on the diversity of chondrule reservoirs in the protoplanetary disk. *Meteoritics & Planetary Science*, 47(7), 1176-1190.

Jones, R. H. (1998). A Compilation of Olivine and Low-Ca Pyroxene Compositions in Type 4-6 Ordinary Chondrites. *29th Lunar and Planetary Science Conference*, #1397

Joy, K. H., Zolensky, M. E., Nagashima, K., Huss, G. R., Ross, D. K., McKay, D. S., & Kring, D. A. (2012). Direct detection of projectile relics from the end of the lunar basin–forming epoch. *Science*, 336(6087), 1426-1429.

Jurewicz, A. J. G., Mittlefehldt, D. W., & Jones, J. H. (1995). Experimental partial melting of the St. Severin (LL) and Lost City (H) chondrites. *Geochimica et Cosmochimica Acta*, 59(2), 391-408.

Jutzi, M., Michel, P., Hiraoka, K., Nakamura, A. M., & Benz, W., (2009), Numerical simulations of impacts involving porous bodies: II. Comparison with laboratory experiments, *Icarus*, 201, 2, 802-813.

Jutzi, M., Michel, P., Benz, W., & Richardson, D. C., (2010), Fragment properties at the catastrophic disruption threshold: The effect of the parent body's internal structure. *Icarus*, 207, 1, 54-65.

Kallemeyn, G. W., & Wasson, J. T. (1986). Compositions of enstatite (EH3, EH4, 5 and EL6) chondrites: Implications regarding their formation. *Geochimica et Cosmochimica Acta*, 50(10), 2153-2164.

Kallemeyn, G. W., Rubin, A. E., & Wasson, J. T. (1996). The compositional classification of chondrites: VII. The R chondrite group. *Geochimica et Cosmochimica Acta*, 60(12), 2243-2256.

Kant, I., (1755) *Universal Natural History and Theories of the Heavens* (Zeitz: Bei w Webel)

Kennedy, A. K., Hutchison, R., Hutcheon, I. D., & Agrell, S. O. (1992). A unique high Mn/Fe microgabbro in the Parnallee (LL3) ordinary chondrite: nebular mixture or planetary differentiate from a previously unrecognized planetary body?, *Earth and Planetary Science Letters*, 113(1-2), 191-205.

Kessel R., Beckett J. R., & Stolper E. M. (2002) The thermal history of equilibrated ordinary chondrites and the relationship between textural maturity and temperature (abstract). In *Lunar and Planetary Science XXXIII*, #1420.

Ketcham, R. A., & Iturrino, G. J., (2005), Nondestructive high-resolution visualization and measurement of anisotropic effective porosity in complex lithologies using high-resolution X-ray computed tomography, *Journal of Hydrology*, 302, 1, 92-106.

Keil K., Stöffler D., Love S. G., & Scott E. R. D. (1997), Constraints on the role of impact heating and melting in asteroids. *Meteoritics& Planetary Science* 32:349–363.

King, E.A, King, T. V. V., Arndt, J. & Hornemann, U., (1978), Experimental investigation of the textures of CV3 carbonaceous chondrites, *Meteoritics*, 13, 549-550.

Kita, N.T., Yin, Q.Z., MacPherson, G.J., Ushikubo, T., Jacobsen, B., Nagashima, K., Kurahashi, E., Krot, A.N. & Jacobsen, S.B., (2013). ^{26}Al-^{26}Mg isotope systematics of the first solids in the early solar system. *Meteoritics & Planetary Science*, *48*(8),1383-1400.

Kleine, T., Münker, C., Mezger, K., & Palme, H. (2002). Rapid accretion and early core formation on asteroids and the terrestrial planets from Hf–W chronometry. *Nature*, *418*(6901), 952-955.

Kleine, T., Mezger, K., Palme, H., Scherer, E., & Münker, C., (2005a), Early core formation in asteroids and late accretion of chondrite parent bodies: Evidence from 182 Hf-182 W in CAIs, metal-rich chondrites, and iron meteorites. *Geochimica et Cosmochimica Acta*, 69, 24, 5805-5818.

Kleine T., Mezger K., Palme H., Scherer E. & Münker C. (2005b) The W isotope composition of eucrites metal: constraints on the timing and cause of the thermal metamorphism of basaltic eucrites, *Earth and Planetary Science Letters,* 231, 41–52.

Kleine T., Mezger K., Palme H., & Scherer E., (2005c), Tungsten isotopes provide evidence that core formation in some asteroids predates the accretion of chondrite parent bodies, *36th Lunar and Planetary Science Conference*. #1431.

Kleine, T., Mezger, K., Münker, C., Palme, H., & Bischoff, A. (2004). 182 Hf-182 W isotope systematics of chondrites, eucrites, and martian meteorites: Chronology of core formation and early mantle differentiation in Vesta and Mars. *Geochimica et Cosmochimica Acta*, *68*(13), 2935-2946.

Kleine, T., Touboul, M., Van Orman, J. A., Bourdon, B., Maden, C., Mezger, K., & Halliday, A. N. (2008). Hf–W thermochronometry: closure temperature and constraints on the accretion and cooling history of the H chondrite parent body. *Earth and Planetary Science Letters*, *270*(1), 106-118.

Kleine T., Touboul M., Halliday A., Zipfel J. & Palme H. (2007) Cosmochemical fractionation of Hf and W in the solar nebula: evidence from W isotopes in chondrites. *38th Lunar and Planetary Science Conference.*

Kring, D. A., Swindle, T. D., Britt, D. T., & Grier, J. A. (1996). Cat Mountain: A meteoritic sample of an impact-melted asteroid regolith. *Journal of Geophysical Research: Planets*, 101, (E12), 29353-29371.

Kring, D.A., Hill, D.H., Gleason, J.D., Britt, D.T., Consolmagno, G.J., Farmer, M., Wilson, S. & Haag, R., (1999). Portales Valley: A meteoritic sample of the brecciated and metal-veined floor of an impact crater on an H-chondrite asteroid. *Meteoritics & Planetary Science*, *34*(4), pp.663-669.

Krot, A. N., & Wasson, J. T. (1994). Silica-merrihueite/roedderite-bearing chondrules and clasts in ordinary chondrites: New occurrences and possible origin. *Meteoritics*, *29*(5), 707-718.

Krot, A.N., Fagan, T.J., Keil, K., McKeegan, K.D., Sahijpal, S., Hutcheon, I.D., Petaev, M.I. and Yurimoto, H., (2004) Ca, Al-rich inclusions, amoeboid olivine aggregates, and Al-rich chondrules from the unique carbonaceous chondrite Acfer 094: I. mineralogy and petrology. *Geochimica et Cosmochimica Acta*, 68(9), 2167-2184.

Krot, A. N., Amelin, Y., Cassen, P. & Meibom, A. (2005), Young chondrules in CB chondrites from a giant impact in the early Solar System. *Nature,* 436, 989–992.

Kring, D. A., & Cohen, B. A. (2002). Cataclysmic bombardment throughout the inner solar system 3.9–4.0 Ga. *Journal of Geophysical Research: Planets*, 107(E2).

Kruijer, T. S., Sprung, P., Kleine, T., Leya, I., Burkhardt, C., & Wieler, R. (2012). Hf–W chronometry of core formation in planetesimals inferred from weakly irradiated iron meteorites. *Geochimica et Cosmochimica Acta,* 99, 287-304.

Kruijer, T. S., Fischer-Gödde, M., Kleine, T., Sprung, P., Leya, I., & Wieler, R. (2013). Neutron capture on Pt isotopes in iron meteorites and the Hf–W chronology

of core formation in planetesimals. *Earth and Planetary Science Letters*, 361, 162-172

Kruijer, T. S., Touboul, M., Fischer-Gödde, M., Bermingham, K. R., Walker, R. J., & Kleine, T. (2014a). Protracted core formation and rapid accretion of protoplanets, *Science*, 344(6188), 1150-115.

Kruijer, T. S., Kleine, T., Fischer-Gödde, M., Burkhardt, C., & Wieler, R. (2014b). Nucleosynthetic W isotope anomalies and the Hf–W chronometry of Ca–Al-rich inclusions. *Earth and Planetary Science Letters*, 403, 317-327.

Krzesińska, A., Gattacceca, J., Friedrich, J. M., & Rochette, P., (2015), Impact-related noncoaxial deformation in the Pułtusk H chondrite inferred from petrofabric analysis. *Meteoritics and Planetary Science*, 50, 3, 401-417.

Kuebler, K.E., McSween, H.Y., Carlson, W.D., & Hirsch, D., (1999), Sizes and masses of chondrules and metal-troilite grains in ordinary chondrites: Possible implications for nebular sorting, *Icarus*, 141, 96-106.

Laplace P. S. (1796) *Mécanique Céleste* (Paris: Chez J. B. M. Duprat).

Lauretta, D. S., Buseck, P. R., & Zega, T. J. (2001). Opaque minerals in the matrix of the Bishunpur (LL3. 1) chondrite: Constraints on the chondrule formation environment. *Geochimica et Cosmochimica Acta*, *65*(8), 1337-1353.

Lauretta D.S., Nagahara, H., & Alexander C.M.O'D., (2006), Petrology and origin of ferromagnesian silicate chondrules. In *Meteorites and the Early Solar System II*, eds. Lauretta, D.S. and McSween, H.Y., Jr., University of Arizona Press, 431-462.

Lauretta, D. S., & McSween, H. Y. (Eds.). (2006). *Meteorites and the early solar system II*. University of Arizona Press.

Lindgren, P., Hanna, R. D., Dobson, K. J., Tomkinson, T., & Lee, M. R., (2015), The paradox between low shock-stage and evidence for compaction in CM carbonaceous chondrites explained by multiple low-intensity impacts, *Geochimica et Cosmochimica Acta*, 148, 159-178.

Lobo, A., Wallace, S. W., & Ebel, D. S., (2014), Modal Abundances, Chemistry and Sizes of Clasts in the Semarkona (LL3.0) Chondrite by X-Ray Map Analysis, *45th Lunar and Planetary Science Conference*, #1423.

Lodders, K., (2003), Solar system abundances and condensation temperatures of the elements. *The Astrophysical Journal*, 591(2),1220.

Long, H., Swennen, R., Foubert, A., Dierick, M., & Jacobs, P., (2009), 3D quantification of mineral components and porosity distribution in Westphalian C sandstone by microfocus X-ray computed tomography, *Sedimentary Geology*, 220, 1, 116-125.

Longerich, H. P., Jackson, S. E., & Günther, D. (1996). Inter-laboratory note. Laser ablation inductively coupled plasma mass spectrometric transient signal data acquisition and analyte concentration calculation. *Journal of Analytical Atomic Spectrometry*, *11*(9), 899-904.

Longerich, H.P. (2008) Laser Ablation- Inductively Couple Plasma-Mass Spectrometry (LA-ICP-MS): An Introduction. In *Laser Ablation ICP-MS in the Earth Sciences: Current Practices and Outstanding Issues.* Edited by Paul Sylvester. Published by: Mineralogical Association of Canada, Vancouver.

Macke, R. J., & Consolmagno, G. J., (2014), Porosity and Pore Geometry Influence on Meteorite Thermal Conductivities*, 77th Annual Meeting of the Meteoritical Society*, #5045.

Macke, R. J., (2010), Survey of Meteorite Physical Properties: Density, Porosity and Magnetic Susceptibility, *Ph.D. Thesis*, University of Central Florida.

Macke, R. J., Britt, D. T., & Consolmagno, G. J., (2010), Analysis of systematic error in "bead method" measurements of meteorite bulk volume and density, *Planetary and Space Science*, 58, 3, 421-426.

Maharaj, S. V. & Hewins, R. H., (1998), Chondrule Precursor Minerals as Anhydrous Phases. *Meteoritics & Planetary Science*, v. 33, p. 881-887.

Martin, P. M., and Mills, A. A., (1980), Preferred chondrule orientations in meteorites, *Earth and Planetary Science Letters*, 51, 1, 18-25.

Mason, B., (1965). The chemical composition of olivine-bronzite and olivine hypersthene chondrites. *American Museum Novitates,* No. 2223.

Matsui T., Hamano Y. and Honda M., (1980), Porosity and compressional- wave velocity measurement of Antarctic meteorites, *Memoirs of National Institute of Polar Research*, 17, 268-275.

Mayeda, T. K., Clayton, R. N., & Yanai, K. (1987). Oxygen isotopic compositions of several Antarctic meteorites. *Memoirs of National Institute of Polar Research.* Special issue, 46, 144-150.

McCord T.B., Adams J.B., Johnson T.V., (1970) Asteroid Vesta: Spectral reflectivity and compositional implications, *Science*, 168, 1445-1447.

McCoy, T. J., Ketcham, R. A., Wilson, L., Benedix, G. K., Wadhwa, M., & Davis, A. M. (2006). Formation of vesicles in asteroidal basaltic meteorites. *Earth and Planetary Science Letters*, *246*(1), 102-108.

McSween, H. Y., Binzel, R. P., De Sanctis, M. C., Ammannito, E., Prettyman, T. H., Beck, A. W., & Raymond, C. A. (2013). Dawn; the Vesta–HED connection; and the geologic context for eucrites, diogenites, and howardites. *Meteoritics & Planetary Science*, *48*(11), 2090-2104.

McSween H. Y. Jr. (1987) Aqueous alteration in carbonaceous chondrites: Mass balance constraints on matrix mineralogy. *Geochimica et Cosmochimica Acta,* 51, 2469–2477

Mees, F., Swennen, R., Van Geet, M., Jacobs, P., 2013, *Applications of X-ray Computed Tomography in the geosciences*, Geological Society, London, Special Publications, Volume 215.

Melosh, H. J. (1989). Impact cratering: A geologic process*, Oxford University Press, Oxford Monographs on Geology and Geophysics,* No. 11, 1989, 253

Miller, M.F., Franchi, I.A., Sexton, A.S., & Pillinger, C.T., (1999). High precision δ17Oisotope measurements of oxygen from silicates and other oxides: Methods andapplications, *Rapid Communications in Mass Spectrometry*, 13, 1211–1217.

Mittlefehldt, D. W., & Lindstrom, M. M. (2001). Petrology and geochemistry of Patuxent Range 91501, a clast-poor impact melt from the L-chondrite parent body and Lewis Cliff 88663, an L7 chondrite. *Meteoritics & Planetary Science*, 36(3), 439-457.

Miyamoto, M., Fujii, N. & Takeda, H., (1981) Ordinary chondrite parent body: an internal heating model. In *Proceedings of the Lunar & Planetary Science Conference,* 12B, 1145-1152

Morris, M. A., Boley, A. C., Desch, S. J., & Athanassiadou, T. (2012) Chondrule Formation in Bow Shocks Around Eccentric Planetary Embryos, *The Astrophysical Journal,* v. 752:27

Muller, W. F., & Wlotzka, F., (1982), Mineralogical study of the Leoville meteorite (CV3): macroscopic texture and transmission electron microscopic observations, *13th Lunar and Planetary Science Conference*, 558-559.

Nakamura, T., Tomeoka, K., & Takeda, H., (1992), Shock effects of the Leoville CV carbonaceous chondrites: A transmission electron microscope study, *Earth and Planetary Science Letters,* 114,159-170.

Nakamura, T., Tomeoka, K., Sekine, T., & Takeda, H., (1993), Shock metamorphism of carbonaceous chondrites: Textural diversity of experimentally shocked various conditions, *Meteoritics*, 28, 408.

Nakamura, T., Tomeoka, K., Takaoka, N., Sekine, T., & Takeda, H., (2000), Impact-induced textural changes of CV carbonaceous chondrites: experimental reproduction, *Icarus*, 146, 1, 289-300.

Nakamura, T., Noguchi, T., Tanaka, M., Zolensky, M. E., Kimura, M., Tsuchiyama, A., & Kawaguchi, J., (2011), Itokawa dust particles: a direct link between S-type asteroids and ordinary chondrites, *Science*, 333, 6046, 1113-1116.

Nakamura, N., Morikawa, N., Hutchison, R., Clayton, R.N., Mayeda, T.K., Nagao, K., Misawa, K., Okano, O., Yamamoto, K., Yanai, K. & Matsumoto, Y. (1994). Trace element and isotopic characteristics of inclusions in the Yamato ordinary chondrites Y-75097, Y-793241 and Y-794046, *Antarctic Meteorite Research*, *7*, 125

Nelson, V. E., & Rubin, A. E., (2002), Size-frequency distributions of chondrules and chondrule fragments in LL3 chondrites: Implications for parent-body fragmentation of chondrules. *Meteoritics and Planetary Science*, 37, 10, 1361-1376.

Petrovic, A. M., Siebert, J. E., & Rieke, P. E., (1982), Soil bulk density analysis in three dimensions by computed tomographic scanning. *Soil Science Society of America Journal*, 46, 3, 445-450.

Pouchou, J. L., & Pichoir, F. (1987). Basic expression of “PAP” computation for quantitative EPMA. *Proceedings of ICXOM*, *11*, 249-253.

Prinz, M., Nehru, C.E., Weisberg, M.K., Delaney, J.S., Yanai, K., & Kojima, H., (1984), H chondritic clasts in a Yamato L6 chondrite: Implications for metamorphism. *Meteoritics*, 19, 292-293

Rehkämper, M., Schönbächler, M. & Stirling, C. H. (2001), Multiple Collector ICP-MS: Introduction to Instrumentation, Measurement Techniques and Analytical Capabilities. *Geostandards Newsletter*, 25: 23–40.

Rochette, P., Sagnotti, L., Bourot-Denise, M., Consolmagno, G., Folco, L., Gattacceca, J., Osete, M.L., & Pesonen, L., (2003), Magnetic classification of stony meteorites: 1. Ordinary chondrites, *Meteoritics and Planetary Science*, 38, 251–268.

Rochette, P., Gattacceca, J., Bonal, L., Bourot-Denise, M., Chevrier, V., Clerc, J. P., & Pesonen, L. (2008). Magnetic classification of stony meteorites: 2. Non-ordinary chondrites. *Meteoritics & Planetary Science*, *43*(5), 959-980

Röller, K., & Treppmann, C., (2007). *Stereo32* version 0.9.4., http://www.ruhr-uni-bochum.de/hardrock/downloads.htm.

Ross, A. J., Hezel, D. C., Howard, L. E., Smith, C. L., Downes, H., Herrin, J. S., Jenniskens, P., & Shaddad, M., (2011, Petrography and Modal Abundance of Metal in Ureilites: A Combined 2D and 3D Study*, 74th Annual Meteoritical Society Meeting*, #5193.

Rowe, T., Carlson, W.D., Ketcham, R.A., Denison, C., & Kappelman, J., (1997), High-resolution computed tomography - a breakthrough technology for earth scientists, *Geotimes*, 42, 23– 27.

Rubin, A. E., Keil, K., Taylor, G. J., Ma, M. S., Schmitt, R. A., & Bogard, D. D. (1981). Derivation of a heterogeneous lithic fragment in the Bovedy L-group chondrite from impact-melted porphyritic chondrules. *Geochimica et Cosmochimica Acta*, *45*(11), 2213-2228.

Rubin, A. E., (1990), Kamacite and olivine in ordinary chondrites: Intergroup and intragroup relationships, *Geochimica et Cosmochimica Acta*, 54, 5, 1217-1232.

Rubin, A. E., (2003), Chromite-plagioclase assemblages as a new shock indicator; implications for the shock and thermal histories of ordinary chondrites. *Geochimica et Cosmochimica Acta*, 67, 14, 2695-2709.

Rubin, A. E., (2004), Postshock annealing and postannealing shock in equilibrated ordinary chondrites: Implications for the thermal and shock histories of chondritic asteroids. *Geochimica et Cosmochimica Acta*, 68, 3, 673-689.

Rubin, A. E., (2005), Relationships among intrinsic properties of ordinary chondrites: Oxidation state, bulk chemistry, oxygen-isotopic composition, petrologic type, and chondrule size. *Geochimica et Cosmochimica Acta*, 69, 20, 4907-4918.

Rubin, A. E., (2010), Physical properties of chondrules in different chondrite groups: Implications for multiple melting events in dusty environments. *Geochimica et Cosmochimica Acta,* 74, 16, 4807-4828.

Russell, S. S., & Howard, L., (2013), The texture of a fine-grained calcium–aluminium-rich inclusion (CAI) in three dimensions and implications for early solar system condensation. *Geochimica et Cosmochimica Acta*, 116, 52-62.

Ruzicka, A., Kring, D. A., Hill, D. H., Boynton, W. V., Clayton, R. N., & Mayeda, T. K. (1995). Silica-rich orthopyroxenite in the Bovedy chondrite. *Meteoritics*, *30*(1), 57-70.

Ruzicka, A., Snyder, G. A., & Taylor, L. A., (1998), Mega-chondrules and large, igneous-textured clasts in Julesberg (L3) and other ordinary chondrites: Vapor-fractionation, shock-melting and chondrule formation, *Geochimica et Cosmochimica Acta*, 62, 8, 1419-1442.

Ruzicka, A., Hutson, M., Floss, C., & Hildebrand, A. (2012). Large silica-rich igneous-textured inclusions in the Buzzard Coulee chondrite: Condensates, differentiates, or impact melts?. *Meteoritics & Planetary Science*, *47*(11), 1809-1829.

Ruzicka, A., Hugo, R., & Hutson, M. (2015). Deformation and thermal histories of ordinary chondrites: Evidence for post-deformation annealing and syn-metamorphic shock. *Geochimica et Cosmochimica Acta*, *163*, 219-233.

Ruzicka, A. M., Schepker, K. L., Greenwood, R. C., & Franchi, I. A. (2016). Combined Chemical-Oxygen Isotope Study of Large Igneous Inclusions in Ordinary Chondrites. In *47th Lunar and Planetary Science Conference*, 2230.

Ruzicka, A., Snyder, G. A., & Taylor, L. A. (2000). Geochemical and isotopic evidence bearing on the origin of large igneous-textured inclusions in ordinary chondrites. *Antarctic Meteorite Research*, 13, 19-38.

Ruzicka, A., Killgore, M., Mittlefehldt, D. W., & Fries, M. D. (2005). Portales Valley: Petrology of a metallic-melt meteorite breccia. *Meteoritics & Planetary Science*, 40(2), 261-295.

Sanders, I. S., & Scott, E. R. (2012). The origin of chondrules and chondrites: Debris from low-velocity impacts between molten planetesimals?, *Meteoritics & Planetary Science*, 47(12), 2170-2192.

Sasso, M. R., Macke, R. J., Boesenberg, J. S., Britt, D. T., Rivers, M. L., Ebel, D. S., & Friedrich, J. M., (2009), Incompletely compacted equilibrated ordinary chondrites. *Meteoritics & Planetary Science*, 44, 11, 1743-1753.

Schmitz, B., Harper, D.A., Peucker-Ehrenbrink, B., Stouge, S., Alwmark, C., Cronholm, A., Bergström, S.M., Tassinari, M. & Xiaofeng, W., (2008). Asteroid breakup linked to the Great Ordovician biodiversification event. *Nature Geoscience*, 1(1), pp.49-53.

Schrader, D. L., Connolly, H. C., & Lauretta, D. S. (2008). Opaque phases in type-II chondrules from CR2 chondrites: Implications for CR parent body formation. *Geochimica et Cosmochimica Acta*, *72*(24), 6124-6140.

Schmitt, R. T. (2000). Shock experiments with the H6 chondrite Kernouvé: Pressure calibration of microscopic shock effects. *Meteoritics & Planetary Science*, *35*(3), 545-560.

Scott, E.R.D., Keil, K., & Stoffler, D., (1992), Shock metamorphism of carbonaceous chondrites, *Geochimica et Cosmochimica Acta*, 56, 12, 4281–4293.

Scott, E. R., & Wilson, L. (2005). Meteoritic and other constraints on the internal structure and impact history of small asteroids. *Icarus*, *174*(1), 46-53.

Scott, E.R.D., Greenwood, R.C., Franchi, I.A., & Sanders, I. S., (2009), *Geochimica et Cosmochimica Acta*, 73, 19, 5835–5853.

Scott, E. R., & Wasson, J. T. (1975). Classification and properties of iron meteorites. *Reviews of Geophysics*, *13*(4), 527-546.

Sears D. W. G., Grossman J. N., Melcher C. L., Ross L. M., & Mills A. A. (1980) Measuring metamorphic history of unequilibrated ordinary chondrites. *Nature*, 287, 791–795.

Sears, D. W., & Dodd, R. T. (1988). Overview and classification of meteorites, *Meteorites and the Early Solar System*, 3-31.

Sears D. W. G., Hasan E. A., Batchelor J. D., & Lu J. (1991b) Chemical and physical studies of type 3 chondrites — XI: Metamorphism, pairing, and brecciation of ordinary chondrites. *Proceedings of the Lunar & Planetary Science Conference,* 21, 493–512.

Sears, D., Ebel, D.S., Wallace, S.W., & Friedrich, J.M., (2015). X-ray computed tomography and the radiation history of meteorites, *78th Annual Meeting of the Meteoritical Society*, #5156.

Sears, D. W., Sears, H., Ebel, D. S., Wallace, S., & Friedrich, J. M. (2016). X-ray computed tomography imaging: A not-so-nondestructive technique. *Meteoritics & Planetary Science*, *51*(4), 833-838.

Sharp, T. G., & DeCarli, P. S. (2006). Shock effects in meteorites. *Meteorites and the Early Solar System II*, *943*, 653-677.

Sherman, K. M., Ebel, D. S., Friedrich, J. M., Greenberg, M. D., & Rivers, M. L., (2010), 3-Dimensional Chondrule Size Measurement, *73rd Annual Meeting of the Meteoritical Society*, #5431.

Shu, F. H., Shang, H., & Lee, T., (1996), Toward an astrophysical theory of chondrites. *Science*, 1545-1551.

Shu, F. H., Shang, H., Glassgold, A. E., & Lee, T. (1997). X-rays and fluctuating X-winds from protostars. *Science*, 277(5331), 1475-1479.

Shu, F. H., Shang, H., Gounelle, M., Glassgold, A. E., & Lee, T. (2001). The origin of chondrules and refractory inclusions in chondritic meteorites. *The Astrophysical Journal*, 548(2), 1029.

Sokol, A. K., Bischoff, A., Marhas, K. K., Mezger, K., & Zinner, E. (2007). Early Solar System Chronology: Simultaneous Accretion of Differentiated and Metamorphosed Asteroidal Clasts and Chondrules?. In *38th Lunar and Planetary Science Conference,* 1296.

Sorby, H. (1877), On the structure and origin of meteorites, *Nature*, 15, 405–498.

Sneed, E. D., & Folk, R. L., (1958), Pebbles in the lower Colorado River, Texas a study in particle morphogenesis, *The Journal of Geology*, 114-150.

Sneyd, D. S., McSween, H. Y., Sugiura, N., Strangway, D. W., & Nord, G. L., (1988), Origin of petrofabrics and magnetic anisotropy in ordinary chondrites, *Meteoritics*, 23, 2, 139-149.

Spicuzza, M.J., Day, J.M.D., Taylor , L. A., & Valley, J.W., (2007), Oxygen isotope constraints on the origin and differentiation of the Moon, *Earth and Planetary Science Letters*, 253, 254–265.

Srinivasan, P., Simon, J. I ., & Cuzzi, J. N., (2013), Refractory Inclusion Size Distribution And Fabric Measured In A Large Slab Of The Allende Cv3 Chondrite, *44th Lunar and Planetary Science Conference*, #2580.

Starkey, N.A., Jackson, C.R.M., Greenwood, R.C., Parman, S., Franchi, I.A., Jackson, M.,Fitton, J.G., Stuart, F.M., Kurz, M., & Larsen, L.M., (2016). Triple oxygen isotopiccomposition of the high3He/4He mantle. *Geochimica et Cosmochimica Acta*, 176, 227–238.

Stöffler, D., & Keil, K., (1991), Shock metamorphism of ordinary chondrites. *Geochimica et Cosmochimica Acta*, 55, 12, 3845-3867.

Strait, M. M, (2011), A comparison of porosity using different measurement techniques, *74th Annual Meeting of the Meteoritical Society*, #5439.

Strait, M. M, Lipman, M. D., & McCausland, P. J., (2011), A comparison of porosity using different measurement techniques, *42nd Lunar and Planetary Science Conference*, #2052.

Strait, M. M., & Lipman, M. D., (2013), Changes in Porosity During Impact Processes, *76th Annual Meeting of the Meteoritical Society*, #5286.

Sugiura, N., & Strangway, D. W., (1983), Magnetic anisotropy and porosity of chondrites. *Geophysical Research Letters*, 10, 1, 83-86.

Sutton, M.D., Rahman, I. & Garwood, R.J., (2013), *Techniques for Virtual Palaeontology*, Wiley-Blackwell.

Tait, A. W., Tomkins, A. G., Godel, B. M., Wilson, S. A., & Hasalova, P., (2014a), Investigation of the H7 ordinary chondrite, Watson 012: Implications for recognition and classification of Type 7 meteorites. *Geochimica et Cosmochimica Acta*, 134, 175-196.

Tait, A. W., Fisher, K. R., & Simon, J. I., (2014b), Strain Measurements of Chondrules and Refractory Inclusions in Allende, *45th Lunar and Planetary Science Conference*, #1309.

Taylor, S., Jones, K. W., Hornig, C., & Herzog, G. F., (2010), Porosity of Micrometeorites Measured by Tomography, *41st Lunar and Planetary Science Conference*, #1909.

Taylor G. J., Maggiore P., Scott E. R. D., Rubin A. E., & Keil K. (1987) Original structures, and fragmentation and reassembly histories of asteroids: Evidence from meteorites. *Icarus*, 69, 1–13.

Taylor, H. P., Duke, M. B., Silver, L. T., & Epstein, S. (1965). Oxygen isotope studies of minerals in stony meteorites. *Geochimica et Cosmochimica Acta*, *29*(5), 489-51.

Teitler, S. A., Paque, J. M., Cuzzi, J. N., & Hogan, R. C., (2010), Statistical tests of chondrule sorting, Meteoritics and Planetary Science, 45, 7, 1124-1135.

Trieloff, M., Jessberger, E.K., Herrwerth, I., Hopp, J., Fiéni, C., Ghélis, M., Bourot-Denise, M. & Pellas, P., (2003). Structure and thermal history of the H-chondrite parent asteroid revealed by thermochronometry. *Nature*, 422, 6931, 502-506.

Tsiganis, K., Gomes, R. Morbidelli, A., & Levison, H. F., (2005) Origin of the orbital architecture of the giant planets of the Solar System, *Nature,* 435, 7041, 459-461.

Tsuchiyama A., (2014) Asteroid Itokawa—A source of ordinary chondrites and a laboratory for surface processes, *Elements*, 10, 45-50.

Tsuchiyama, A., Kondo, M., Hirai, H., & Koishikawa, A., (1997), High Resolution X-ray CT Images of Chondrites and Chondrules, and Their Three-Dimensional Structures, *28th Lunar and Planetary Science Conference*, #1055.

Tsuchiyama, A., Nakamura, T., Nakano, T., & Nakamura, N., (2002), Three-dimensional description of the Kobe meteorite by micro X-ray CT method: Possibility of three-dimensional curation of meteorite samples*, Geochemical Journal*, 36, 369 – 390.

Tsuchiyama, A., Nakano, T., Uesugi, K., Uesugi, M., Takeuchi, A., Suzuki, Y., Noguchi, R., Matsumoto, T., Matsuno, J., Nagano, T., Imai, Y., Nakamura, T., Ogami, T., Noguchi, T., Abe, M., Yada, T., & Fujimura, A., (2013), Analytical dual-energy microtomography: A new method for obtaining three-dimensional mineral phase images and its application to Hayabusa samples, *Geochimica et Cosmochimica Acta*, 116, 5–16.

Uesugi, M. Uesugi, K, Takeuchi, A., Suzuki, Y. Hoshino, M., & Tsuchiyama, A., (2012), Development of a new X-ray CT for the observation of meteorites and returned sample of future missions, *Asteroids, Comets, Meteors*, #6181104.

Uesugi, M., Uesugi, K., Takeuchi, A., Suzuki, Y., Hoshino, M., & Tsuchiyama, A. (2013). Three-dimensional observation of carbonaceous chondrites by synchrotron radiation X-ray CT–Quantitative analysis and developments for the future sample return missions. *Geochimica et Cosmochimica Acta*, 116, 17-32

Unruh D. M., Hutchison, R, & Tatsumoto, M., (1979), U-Th-Pb systematics and uranium isotopic composition of chondrites, *10th Lunar and Planetary Science Conference*, #1442.

Vockenhuber, C., Oberli, F., Bichler, M., Ahmad, I., Quitté, G., Meier, M., & Gehrke, R. J. (2004). New Half-Life Measurement of Hf 182: Improved Chronometer for the Early Solar System. *Physical Review Letters*, 93(17), 172501.

Wallace, S. W., Ebel, D. S., & Hill, M. G., (2013), Sutter's Mill: Using Computed Tomography to Curate Scientifically Important Meteorites*, 44th Lunar and Planetary Science Conference*, #2297.

Wasson, J. T., Krot, A. N., Lee, M. S., & Rubin, A. E., (1995), Compound chondrules. *Geochimica et Cosmochimica Acta*, 59, 9, 1847-1869.

Wasson, J. T., & Choi, B. G. (2003). Main-group pallasites: Chemical composition, relationship to IIIAB irons, and origin. *Geochimica et Cosmochimica Acta*, *67*(16), 3079-3096.

Wasson J. T. & Kimberlin J. (1967) The chemical classification of iron meteorites; II, Irons and pallasites with germanium concentrations between 8 and 100 ppm. *Geochimica et Cosmochimica Acta*, 31, 149–178.

Wasson J. T. & Kallemeyn G. W. (2002) The IAB iron-meteorite complex: A group, five subgroups, numerous grouplets, closely related, mainly formed by crystal segregation in rapidly cooling melts. *Geochimica et Cosmochimica Acta*, 66, 2445–2473.

Weisberg, M. K., Prinz, M., & Nehru, C. E. (1988). Macrochondrules in ordinary chondrites: Constraints on chondrule forming processes. *Meteoritics*, *23*, 309.

Weisberg, M. K., Prinz, M., Clayton, R. N., Mayeda, T. K., Grady, M. M., Franchi, I., Pillinger, C. T., & Kallemeyn, G. W. (1996). The K (Kakangari) chondrite grouplet. *Geochimica et Cosmochimica Acta*, 60(21), 4253-4263.

Weisberg, M. K., McCoy, T. J., & Krot, A. N. (2006). Systematics and evaluation of meteorite classification. *Meteorites and the Early Solar System II*, 19.

Weiss, B. P., & Elkins-Tanton, L. T. (2013). Differentiated planetesimals and the parent bodies of chondrites. *Annual Review of Earth and Planetary Sciences*, 41, 529-560.

Wellington, S. L., & Vinegar, H. J., (1987), X-ray computerized tomography, *Journal of Petroleum Technology*, 39, 8, 885-898.

Wildenschild, D., & Sheppard, A. P. (2013). X-ray imaging and analysis techniques for quantifying pore-scale structure and processes in subsurface porous medium systems. *Advances in Water Resources*, 51, 217-246

Wilkison, S. L., & Robinson, M. S. (2000). Bulk density of ordinary chondrite meteorites and implications for asteroidal internal structure. *Meteoritics & Planetary Science*, *35*(6), 1203-1213.

Wilkison, S. L., McCoy, T. J., McCamant, J. E., Robinson, M. S., & Britt, D. T., (2003), Porosity and density of ordinary chondrites: Clues to the formation of friable and porous ordinary chondrites. *Meteoritics and Planetary Science*, 38, 10, 1533-1546.

Willbold, M., Elliott, T., & Moorbath, S., (2011), The tungsten isotopic composition of the Earth/'s mantle before the terminal bombardment. *Nature*, 477(7363), 195-198

Wright-Clark, J., & Goles, G. G., (1983), Structural fabric elements observed in Leoville (CV3), *14th Lunar and Planetary Science Conference*, 863-864.

Wurm, G., & Krauss, O., (2006), Concentration and sorting of chondrules and CAIs in the late Solar Nebula, *Icarus*, 180, 2, 487-495.

Yomogida, K., & Matsui, T. (1984). Multiple parent bodies of ordinary chondrites. *Earth and Planetary Science Letters*, 68(1), 34-42.

Zeigler, R., Almeida, N.V., Sykes, D., & Smith, C.L., (2014), X-ray micro-computed tomography of Apollo samples as a curation technique enabling better research. *77th Annual Meteoritical Society Meeting*, #5436.

1. Accuracy for LA-ICP-MS analyses of standard

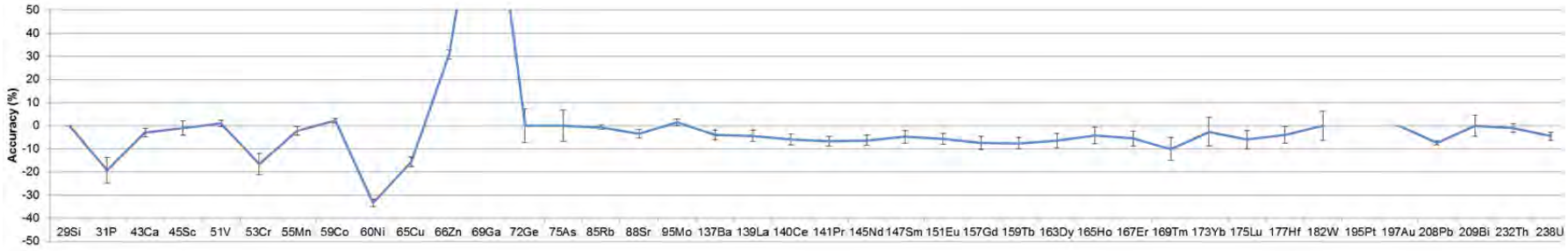

Figure A.1. Accuracy of analyses of USGS Columbia River standard (BCR-2g) by LA-ICP-MS, indicating results are within acceptable limits (20%) for most elements.

	29Si	31P	43Ca	45Sc	51V	53Cr	55Mn	59Co	60Ni	65Cu	66Zn	69Ga	72Ge	75As	85Rb	88Sr	95Mo	137Ba	139La	140Ce
Reported Values	252882	1527	50887	33	416	18	1520	37	18	21	127	23			46.9	340	250	677	24.9	52.9
Average from this study	252882	1231	49416	33	420	15	1487	38	12	18	166	52	3	1	47	328	253	650	24	50
RSD	0.0	5.6	1.9	3.0	1.3	4.5	1.9	1.0	1.7	2.2	2.0	10.6	7.4	6.9	0.9	1.9	1.3	2.1	2.4	2.3
Accuracy (%)	0.0	-19.4	-2.9	-1.0	0.9	-16.6	-2.2	2.2	-33.4	-15.6	30.9	127.5			-0.6	-3.5	1.4	-4.0	-4.3	-5.8
n	9	9	9	9	9	9	9	9	9	9	9	9	9	9	9	9	9	9	9	9
Representative Det Limits	185.000	10.506	113.756	0.173	0.090	1.759	0.222	0.049	0.191	0.302	0.387	0.062	0.452	0.239	0.031	0.021	0.126	0.146	0.016	0.017

	141Pr	145Nd	147Sm	151Eu	157Gd	159Tb	163Dy	165Ho	167Er	169Tm	173Yb	175Lu	177Hf	182W	195Pt	197Au	208Pb	209Bi	232Th	238U
Reported Values	6.7	28.7	6.58	1.96	6.75	1.07	6.41	1.28	3.66	0.54	3.38	0.503	4.9				11		5.7	1.69
Average from this study	6	27	6	2	6	1	6	1	3	0	3	0	5	0	0	0	10	0	6	2
RSD	2.1	2.2	2.6	2.3	2.7	2.5	3.1	3.6	3.2	4.9	6.1	3.9	3.6	6.2	29.0		1.0	4.6	1.9	1.6
Accuracy (%)	-6.7	-6.4	-4.8	-5.7	-7.4	-7.6	-6.5	-4.2	-5.5	-10.1	-2.7	-6.0	-4.0				-7.4		-0.9	-4.6
n	9	9	9	9	9	9	9	9	9	9	9	9	9	9	9	1	9	7	9	9
Representative Det Limits	0.015	0.172	0.097	0.028	0.099	0.014	0.059	0.014	0.062	0.014	0.080	0.015	0.070	0.074	0.080	0.042	0.067	0.026	0.017	0.015

Table A.1. Analyses of USGS Columbia River standard (BCR-2g) by LA-ICP-MS, compared with reported values (USGS) indicating results are within acceptable limits (20%) for most elements.

2. Scanning parameters for micro-CT analyses of L chondrite specimens

Meteorite	Sample	Mass (g)	Voxel size (mm)	Voltage (kV)	Current (µA)	Filter (mm)	Exposure (ms)	Frames per projection
Aumale	1985,M63	1.336	0.00777	190	180	0.25 Cu	500	1
Aumieres	1985,M64	1.3897	0.00780	200	200	0.5 Cu	708	1
Ausson	1985,M65	1.144	0.00689	190	180	0.25 Cu	500	1
Barwell	1966,59	0.9991	0.00806	190	180	0.25 Cu	708	1
Bjurbole	1927,11	1.7647	0.00886	190	180	0.25 Cu	500	1
Chervettaz	86761	0.5561	0.00606	200	200	0.5 Cu	708	1
Crumlin	86115	1.078	0.00783	190	180	0.25 Cu	500	1
Elenovka	1956,166	0.453	0.00689	190	180	0.25 Cu	500	1
Farmington	66200	1.163	0.00848	190	180	0.25 Cu	500	1
Hallingeberg	1974,M24	1.84	0.00901	190	180	0.25 Cu	500	1
Holbrook	1912,677	1.792	0.00786	190	180	0.25 Cu	500	1
Jackalsfontein	1908,431	1.164	0.00969	190	180	0.25 Cu	500	1
Jhung	51190	0.9604	0.00765	200	200	0.5 Cu	708	1
Kyushu	1905,67	1.913	0.00795	190	180	0.25 Cu	500	1
Little Piney	1985,M107	1.6132	0.00721	200	200	0.5 Cu	708	1
Monze	1951,103	1.927	0.00774	200	200	0.5 Cu	708	1
Nikolskoe	1956,326	1.9702	0.00831	200	200	0.5 Cu	708	1

Table A.2. Scanning parameters for samples of L chondrites used in this study (*Section 3*).

3. Scanning parameters for micro-CT analyses of Barwell specimens

Sample	Mass (g)	Voxel size (mm)	Voltage (kV)	Current (μA)	Filter (mm)	Exposure (ms)	Frames per projection
BM1966, 59	232.7	0.0380	220	200	2 Cu	1415	8
BM1966, 59	441	0.0500	220	190	2.5 Cu	1000	4
BM1966, 58b	203	0.0390	210	190	2.5 Cu	1415	1
BM1971, 209	2.178	0.0093	170	180	0.1 Cu	708	4
BM1985, M68	1.833	0.0081	200	170	0.25 Cu	708	1
BM1985, M68	2.286	0.0080	200	160	0.25 Cu	708	1
BM1985, M68	9.961	0.0173	200	190	1.0 Cu	708	1
BM1985, M68	19.359	0.0186	215	200	1.5 Cu	708	1
BM1985, M68	60.42	0.0284	200	190	2.0 Cu	708	1
BM1985, M68	82.6	0.0292	210	190	2.5 Cu	708	1
BM1985, M70	104.71	0.0355	220	200	2.5	708	2
BM.1966, 59	243.06	0.0379	215	160	1 Sn	708	2
BM.1966, 286	382	0.0476	220	200	1.25 Ag	708	2

Table A.3. Scanning parameters for samples of Barwell meteorite used in this study (*Section 4*).

4. Workflow for micro-CT analyses of L chondrites

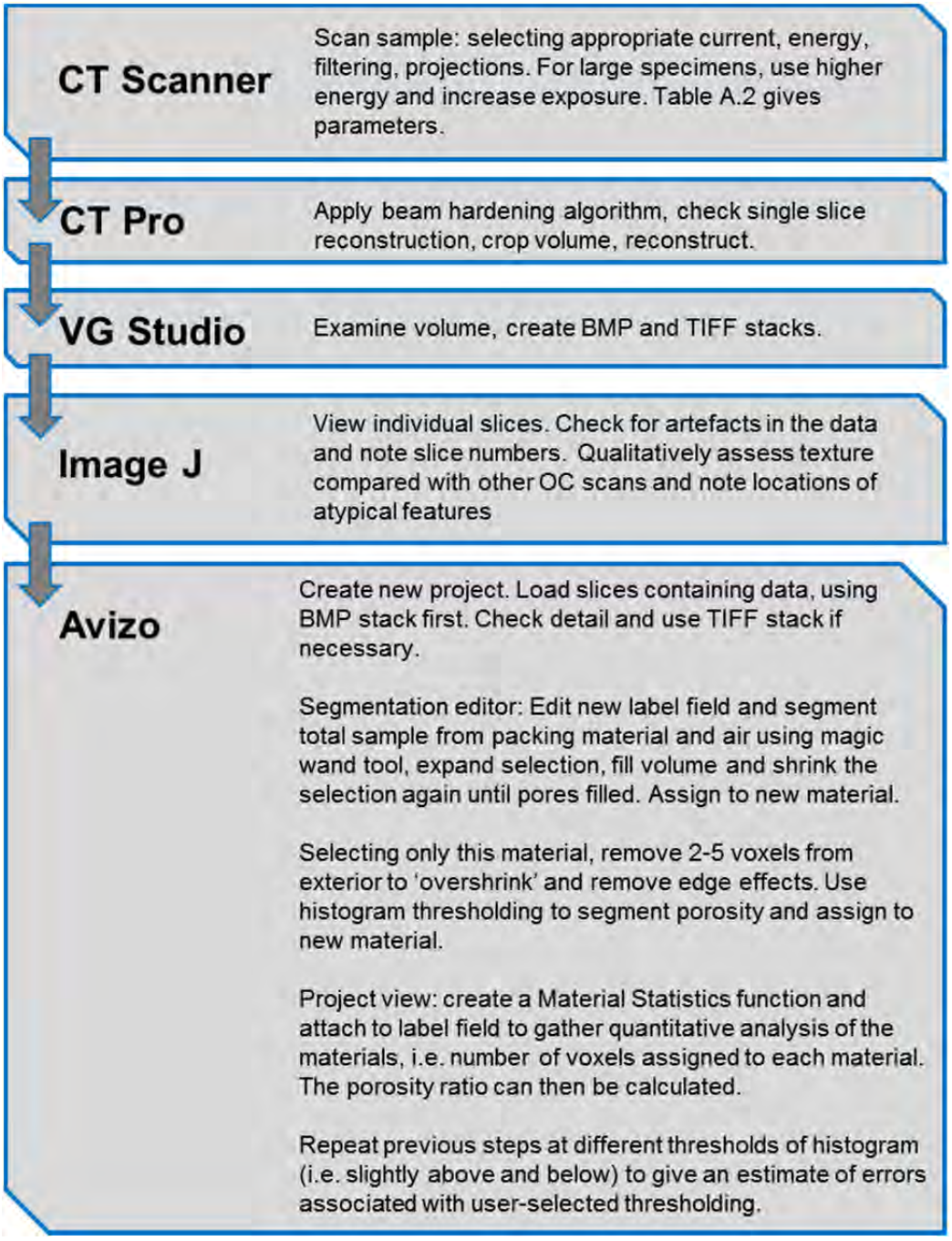

Figure A.2. Workflow for handling of micro-CT for the segmentation of porosity in L chondrites (*Section 3*).

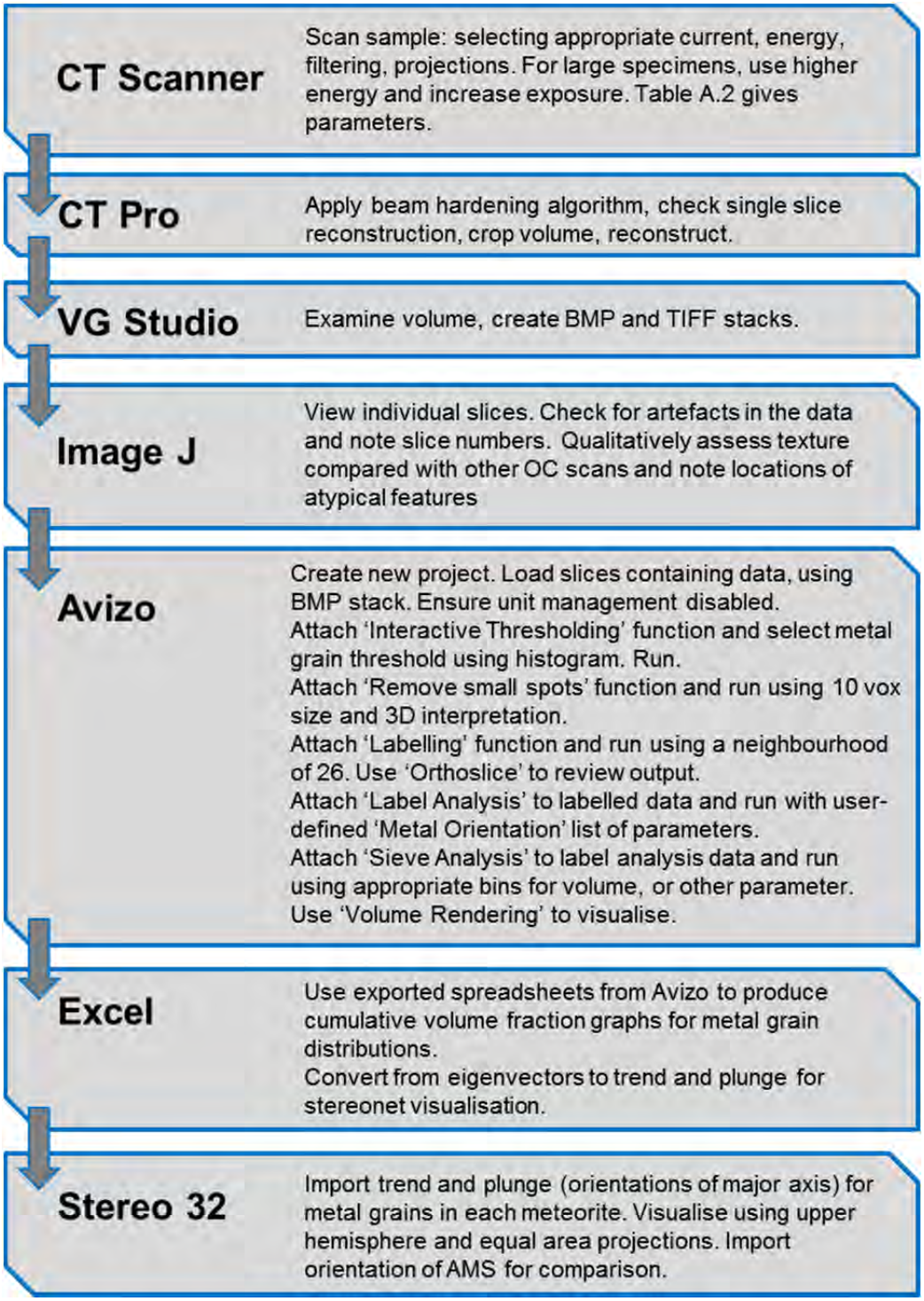

Figure A.3. Workflow for handling of micro-CT for the segmentation and quantitative analysis of metal grains in L chondrites (*Section 3*).

5. Workflow for handling of micro-CT data for Barwell analyses

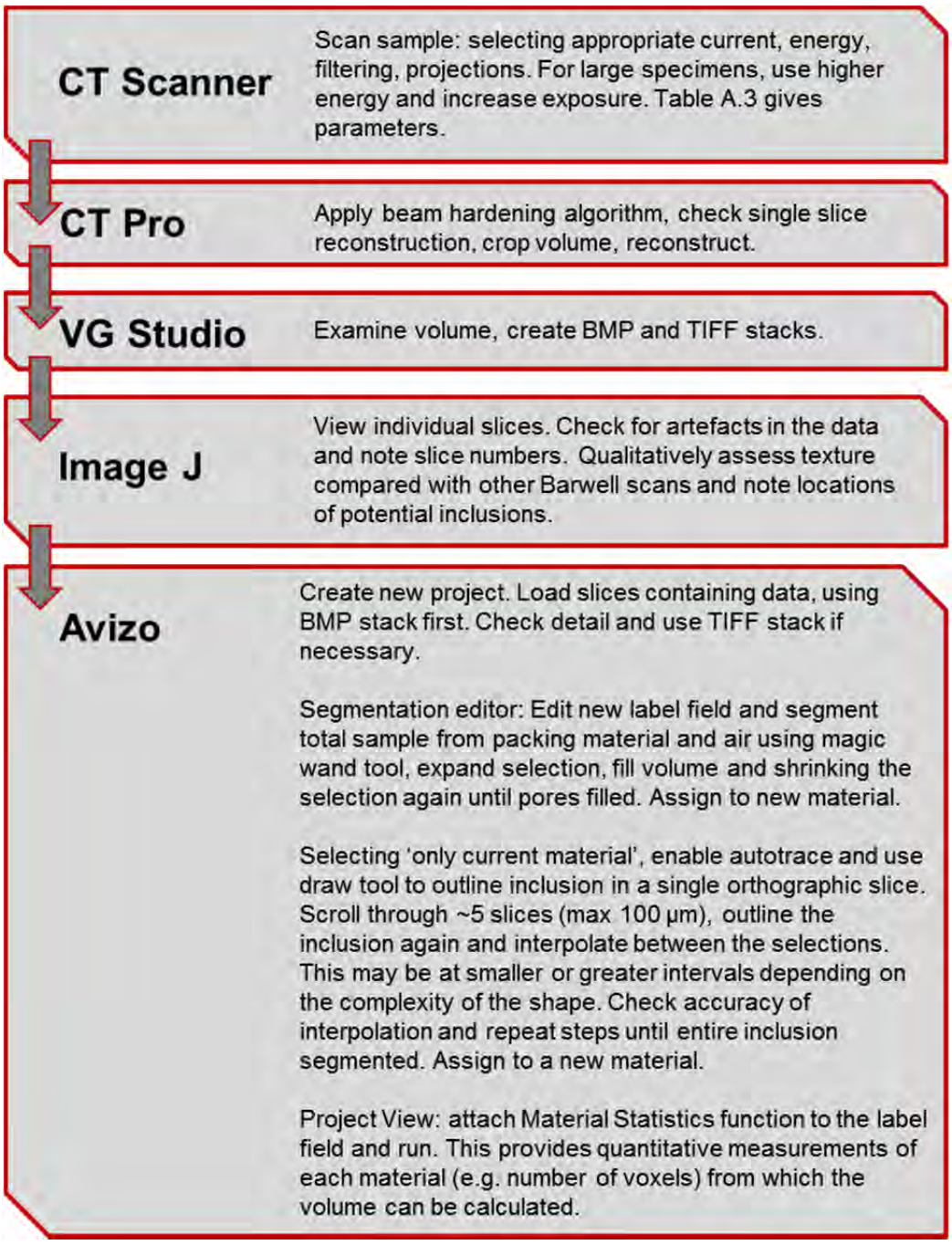

Figure A.4. Workflow for handling of micro-CT for the segmentation of inclusions in Barwell (*Section 4*).

6. Images of L chondrites in this study

Figure A.5. Images of the L chondrites in this study (*Section 3*), in the same orientation as used for AMS measurements and aligned to micro-CT datasets.

7. Polished block preparations of Barwell host and inclusions

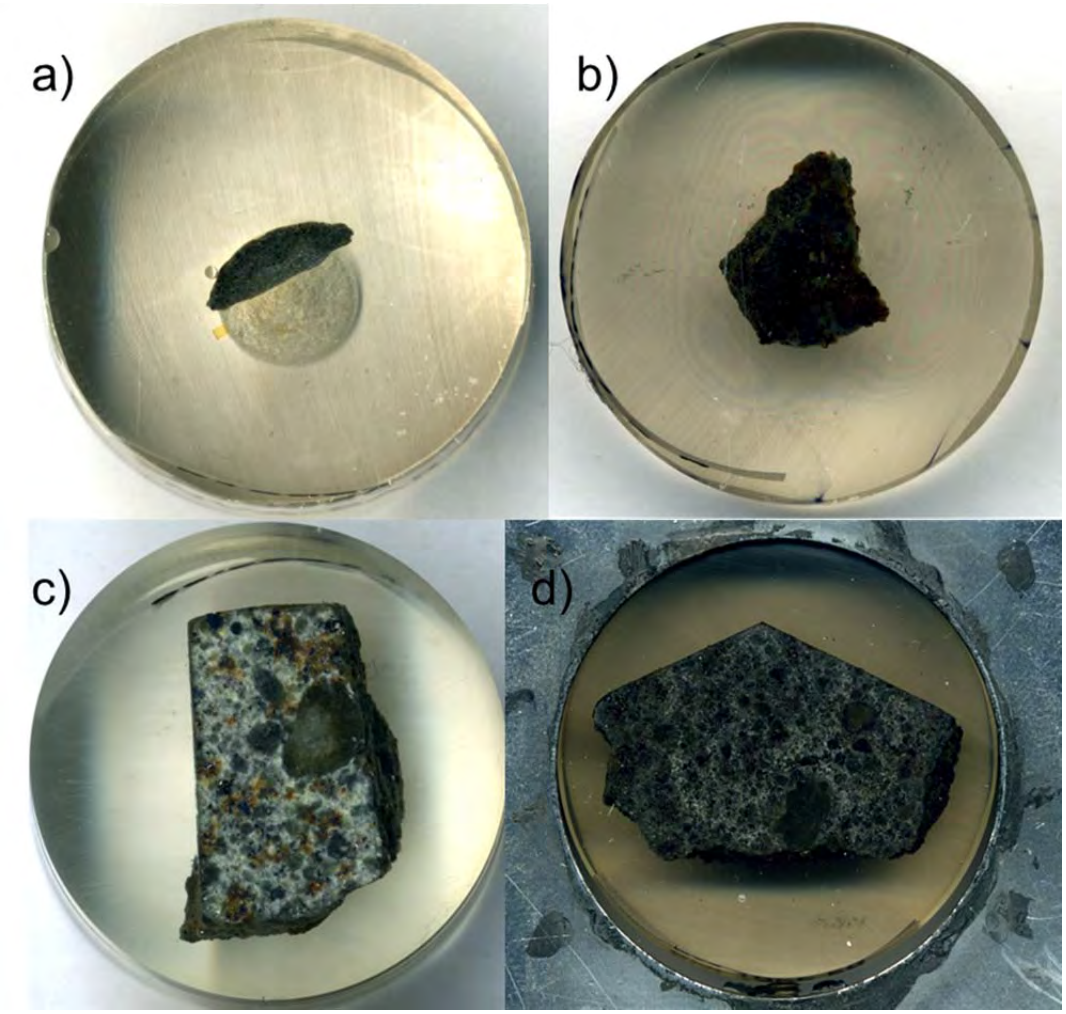

Figure A.6. Scanned images of Barwell preparations used in this study (*Section 4*): a) BM.1985,M68, P19986, containing inclusion A; b) BM 1985,M68, P19987 containing inclusion B; c) BM.1966,59, B1 containing inclusion C; d) BM.1966,59, B3 containing inclusion D.

8. Masses of inclusions used for different analyses

	A	B	C	D	Host BM.1985,M68 (near A)	Host BM.1985,M68 (near B)	Host BM.1966,59 (near C)
Hf-W	133.25	605.04	-	-			
I-Xe	5.75 + 2.10	4.22 + 3.73	3.42	-	3.16	6.06	3.66
Polished block	85.68	small fragment with host attached	already in B1	already in B3			
O	46.13	59.65	29.8	45.58	350.46		602.28
Remaining	tiny fragments with host attached	10.42	12	33			

Table A.4. Masses of inclusions of Barwell used for different techniques in this study (*Section 4*). All masses in mg.

9. Locations of EPMA analyses of inclusions in Barwell meteorite

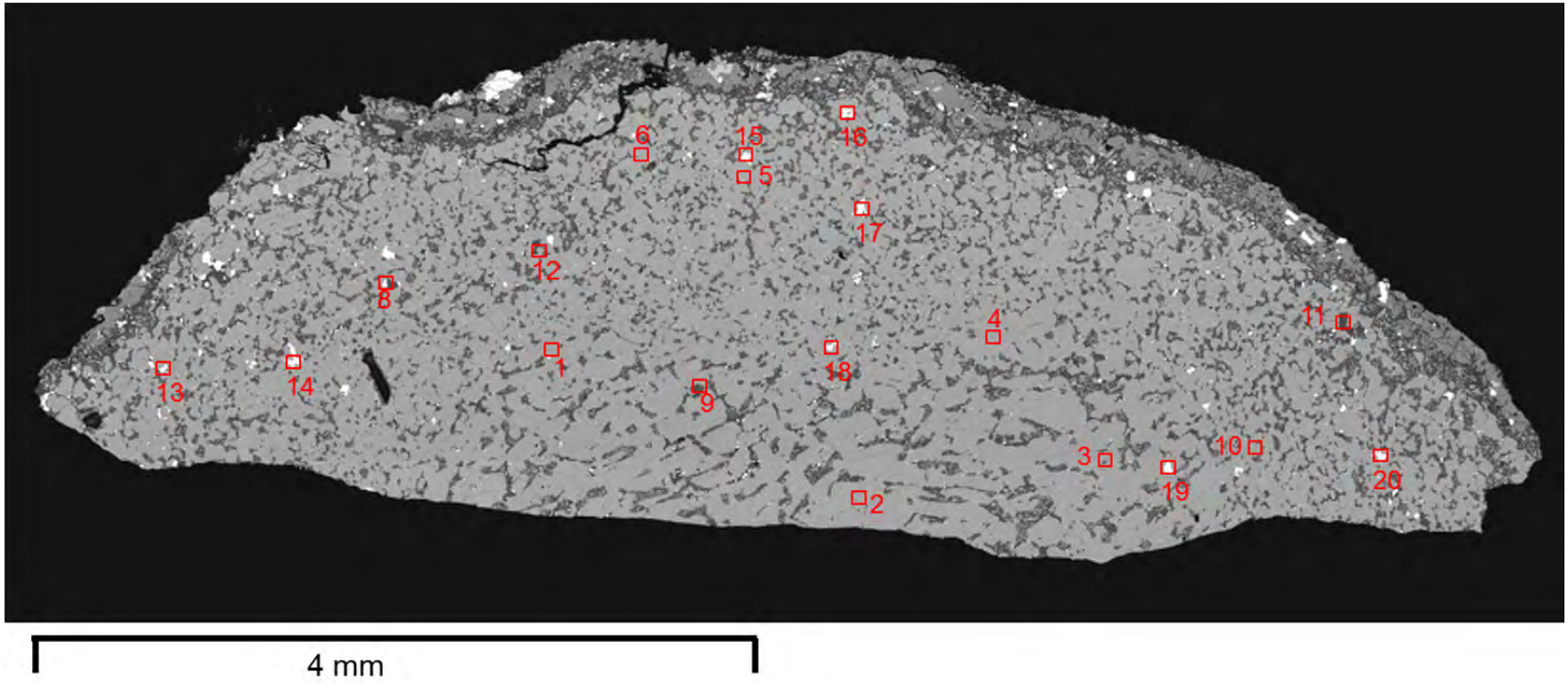

Figure A.7. Locations of EPMA analyses in inclusion A.

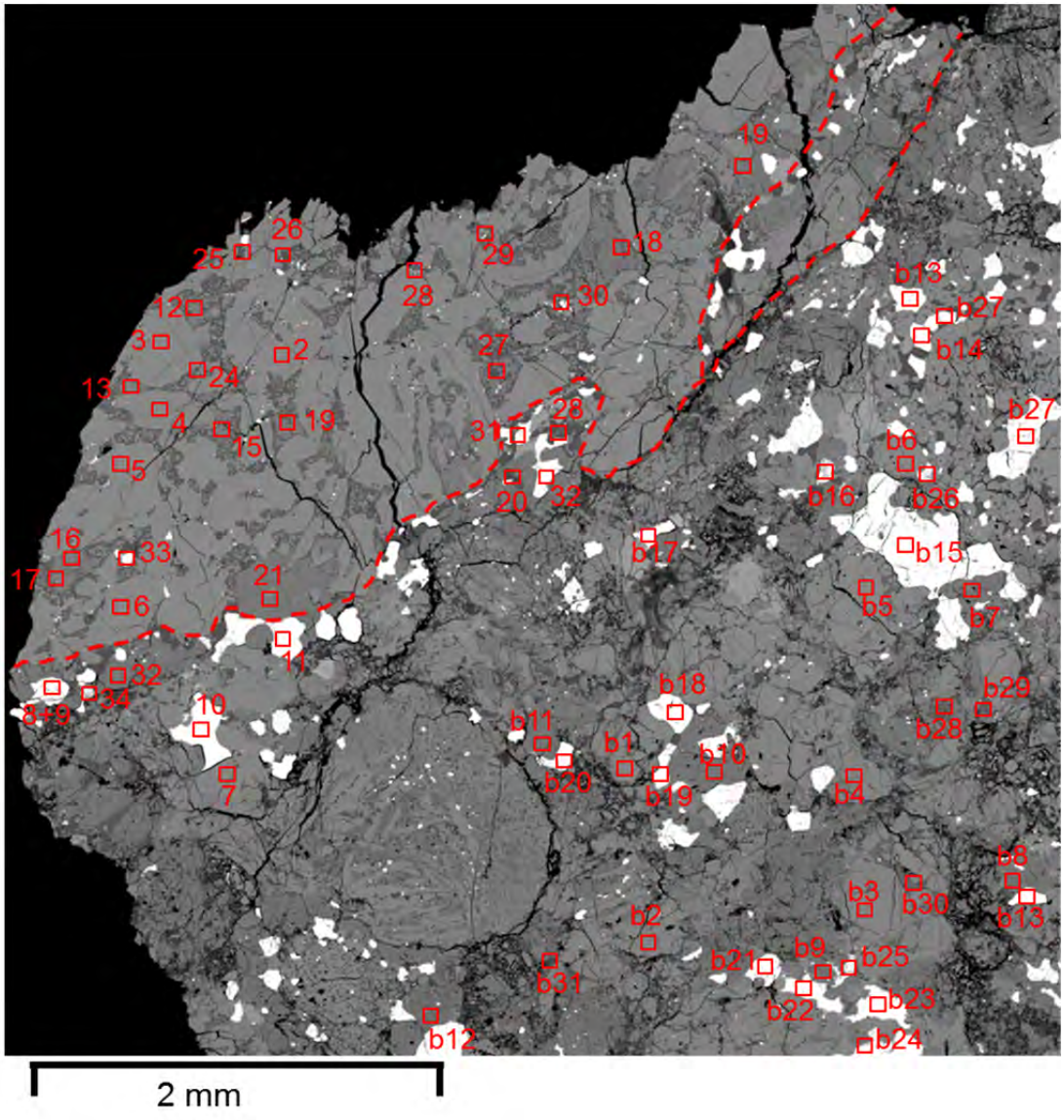

Figure A.8. Locations of EPMA analyses in inclusion B and host Barwell.

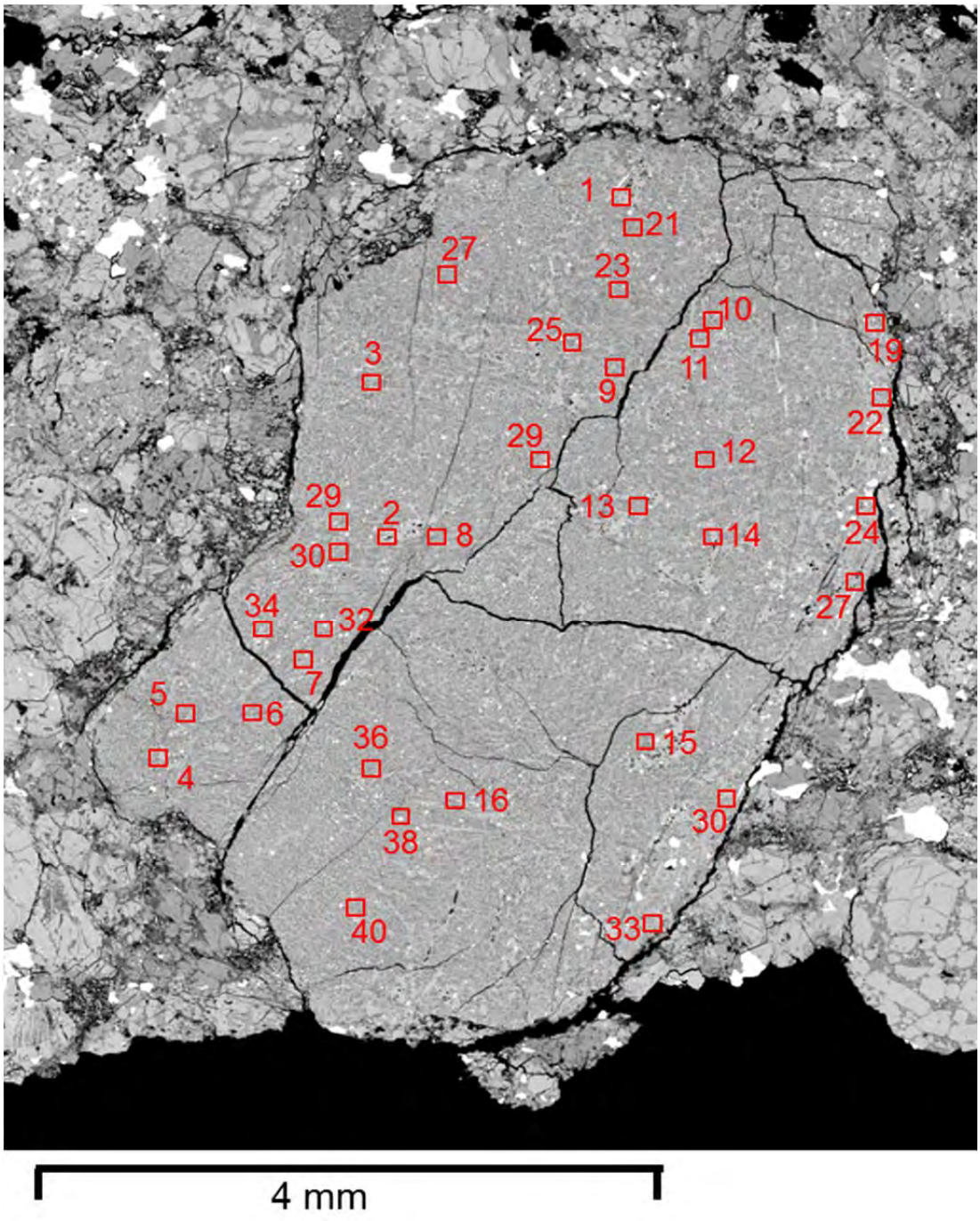

Figure A.9. Locations of EPMA analyses in inclusion D.

10. Data tables for EPMA analyses of inclusions in Barwell meteorite

Site	Point	Mineral	Element													Total
			Na_2O	MgO	Al_2O_3	SiO_2	K_2O	CaO	TiO_2	V_2O3	Cr_2O_3	MnO	FeO	CoO	NiO	Y_2O_3	
BAR_A_01	1 / 1 .	Olivine	b.d.l.	39.11	b.d.l.	38.76	b.d.l.	0.02	0.06	b.d.l.	0.03	0.49	23.20	0.01	b.d.l.	b.d.l.	101.64
	1 / 2 .		b.d.l.	39.17	b.d.l.	38.65	b.d.l.	0.01	0.03	b.d.l.	0.04	0.51	23.33	0.04	b.d.l.	b.d.l.	101.74
	1 / 3 .		b.d.l.	38.98	b.d.l.	38.66	b.d.l.	0.01	0.07	b.d.l.	0.00	0.52	23.29	0.03	b.d.l.	b.d.l.	101.48
BAR_A_02	1 / 1 .		b.d.l.	38.48	b.d.l.	37.93	b.d.l.	0.02	0.07	b.d.l.	0.03	0.46	23.10	0.04	b.d.l.	b.d.l.	100.06
	1 / 2 .		b.d.l.	38.43	b.d.l.	37.82	b.d.l.	0.03	0.03	b.d.l.	0.02	0.49	23.12	0.03	b.d.l.	b.d.l.	99.95
	1 / 3 .		b.d.l.	38.41	b.d.l.	37.70	b.d.l.	0.02	0.08	b.d.l.	0.10	0.49	23.22	0.03	b.d.l.	b.d.l.	100.02
	1 / 4 .		b.d.l.	38.77	b.d.l.	37.78	b.d.l.	0.03	0.06	b.d.l.	0.02	0.52	23.06	0.03	b.d.l.	b.d.l.	100.20
	1 / 5 .		b.d.l.	38.78	b.d.l.	37.85	b.d.l.	0.03	0.06	b.d.l.	0.04	0.49	23.18	0.04	b.d.l.	b.d.l.	100.40
	1 / 6 .		b.d.l.	38.58	b.d.l.	37.66	b.d.l.	0.01	0.04	b.d.l.	0.01	0.52	23.18	0.03	b.d.l.	b.d.l.	99.99
BAR_A_03	1 / 1 .		b.d.l.	39.32	b.d.l.	38.58	b.d.l.	0.02	0.06	b.d.l.	0.02	0.51	23.34	0.04	b.d.l.	b.d.l.	101.86
	1 / 2 .		b.d.l.	39.12	b.d.l.	38.48	b.d.l.	0.01	0.06	b.d.l.	0.01	0.49	23.29	0.03	b.d.l.	b.d.l.	101.44
	1 / 3 .		b.d.l.	38.93	b.d.l.	38.56	b.d.l.	0.01	0.05	b.d.l.	0.02	0.50	23.37	0.03	b.d.l.	b.d.l.	101.42
	1 / 4 .		b.d.l.	38.91	b.d.l.	38.56	b.d.l.	0.02	0.06	b.d.l.	0.00	0.51	23.19	0.02	b.d.l.	b.d.l.	101.21
	1 / 5 .		b.d.l.	38.85	b.d.l.	38.70	b.d.l.	0.02	0.04	b.d.l.	0.02	0.48	23.13	0.02	b.d.l.	b.d.l.	101.26
BAR_A_04	1 / 1 .		b.d.l.	39.10	b.d.l.	38.82	b.d.l.	0.02	0.08	b.d.l.	0.01	0.48	23.13	0.03	b.d.l.	b.d.l.	101.64
	1 / 2 .		b.d.l.	38.92	b.d.l.	38.83	b.d.l.	0.02	0.05	b.d.l.	0.01	0.48	23.27	0.02	b.d.l.	b.d.l.	101.53
	1 / 3 .		b.d.l.	39.17	b.d.l.	38.74	b.d.l.	0.03	0.02	b.d.l.	b.d.l.	0.49	23.21	0.03	b.d.l.	b.d.l.	101.64
	1 / 4 .		b.d.l.	39.00	b.d.l.	38.70	b.d.l.	0.02	0.08	b.d.l.	b.d.l.	0.51	23.23	0.02	b.d.l.	b.d.l.	101.48
	1 / 5 .		b.d.l.	39.25	b.d.l.	38.74	b.d.l.	0.02	0.05	b.d.l.	b.d.l.	0.50	23.25	0.02	b.d.l.	b.d.l.	101.75
BAR_A_05	1 / 1 .		b.d.l.	39.25	b.d.l.	38.79	b.d.l.	0.03	0.04	b.d.l.	0.19	0.48	23.02	0.03	b.d.l.	b.d.l.	101.77
	1 / 2 .		b.d.l.	39.32	b.d.l.	38.80	b.d.l.	b.d.l.	0.06	b.d.l.	0.04	0.51	23.15	0.02	b.d.l.	b.d.l.	101.87
	1 / 3 .		b.d.l.	39.25	b.d.l.	38.73	b.d.l.	0.02	0.07	b.d.l.	0.07	0.52	23.11	0.02	b.d.l.	b.d.l.	101.72
	1 / 5 .		b.d.l.	39.33	b.d.l.	38.76	b.d.l.	0.01	0.05	b.d.l.	0.03	0.49	23.26	0.03	b.d.l.	b.d.l.	101.93
	1 / 7 .		b.d.l.	39.03	b.d.l.	38.60	b.d.l.	0.02	0.22	b.d.l.	0.03	0.48	23.17	0.01	b.d.l.	b.d.l.	101.49

Table A.5. EPMA analysis of olivine in Barwell Inclusion A

Site	Point	Mineral	Element											Total
			Na_2O	SiO_2	Al_2O_3	MgO	CaO	TiO_2	MnO	FeO	K_2O	SrO	BaO	
BAR_A_07 (rim)	1 / 2 .	Plagioclase	8.18	59.60	24.29	1.53	5.74	0.04	0.04	2.03	0.41	0.04	b.d.l.	101.90
	1 / 3 .		8.15	59.72	24.52	0.66	5.87	0.03	0.04	1.21	0.41	0.04	0.03	100.67
	1 / 4 .		8.54	60.65	25.18	0.13	6.10	0.05	0.01	0.68	0.40	0.01	0.01	101.74
	1 / 5 .		8.41	59.87	24.67	0.31	5.96	0.05	0.02	2.10	0.49	0.01	b.d.l.	101.88
	1 / 6 .		8.15	59.17	23.97	2.06	5.76	0.06	0.04	2.37	0.38	0.05	b.d.l.	101.99
BAR_A_08 (centre)	1 / 1 .		8.38	60.45	24.82	b.d.l.	5.91	0.08	0.01	0.55	0.36	b.d.l.	0.02	100.57
	1 / 2 .		8.39	60.28	24.86	b.d.l.	6.16	0.09	b.d.l.	0.56	0.36	0.05	0.04	100.79
	1 / 3 .		8.58	60.98	24.47	b.d.l.	5.52	0.07	b.d.l.	0.58	0.44	0.02	b.d.l.	100.64
	1 / 4 .		8.99	61.60	23.87	b.d.l.	4.89	0.06	0.01	0.68	0.43	0.03	b.d.l.	100.55
BAR_A_09 (centre)	1 / 1 .		8.02	59.30	25.40	0.06	6.60	0.07	0.02	0.58	0.36	0.02	0.01	100.44
	1 / 2 .		8.04	59.63	25.10	0.03	6.43	0.04	0.02	0.55	0.42	0.03	b.d.l.	100.28
	1 / 3 .		8.01	59.61	25.15	0.03	6.41	0.05	0.01	0.56	0.41	0.05	b.d.l.	100.28
	1 / 4 .		8.11	59.62	25.17	0.02	6.46	0.05	0.01	0.60	0.42	0.05	b.d.l.	100.50
BAR_A_10 (intermediate)	1 / 1 .		8.98	61.31	23.67	0.03	5.00	0.06	0.01	0.68	0.43	0.02	b.d.l.	100.18
	1 / 2 .		8.76	61.39	24.17	0.03	5.16	0.07	0.01	0.64	0.46	0.04	0.03	100.76
	1 / 3 .		8.87	61.35	23.50	0.24	4.74	0.05	0.02	0.83	0.52	0.03	b.d.l.	100.14
	1 / 4 .		8.74	61.41	23.62	0.11	4.93	0.04	0.01	0.76	0.49	0.06	0.01	100.18
BAR_A_11 (near rim)	1 / 1 .		9.12	62.08	23.21	b.d.l.	4.30	0.06	b.d.l.	0.42	0.55	0.05	b.d.l.	99.78
	1 / 2 .		9.17	61.94	23.25	b.d.l.	4.39	0.06	0.01	0.41	0.53	0.01	b.d.l.	99.75
	1 / 3 .		9.11	61.81	23.18	b.d.l.	4.28	0.05	0.01	0.43	0.52	0.01	b.d.l.	99.39
	1 / 4 .		8.87	61.15	23.45	b.d.l.	4.72	0.07	0.01	0.47	0.57	0.02	0.01	99.35
	1 / 5 .		9.12	61.76	23.19	b.d.l.	4.17	0.06	0.01	0.43	0.70	0.02	0.02	99.49
	1 / 6 .		9.08	62.00	23.10	b.d.l.	4.21	0.08	0.01	0.39	0.70	0.03	b.d.l.	99.59
	1 / 7 .		8.83	61.68	23.15	b.d.l.	4.34	0.07	0.01	0.48	0.62	0.01	b.d.l.	99.22
	1 / 8 .		8.94	61.74	23.08	b.d.l.	4.26	0.06	b.d.l.	0.45	0.65	0.05	0.04	99.28
BAR_A_12 (intermediate)	1 / 1 .		8.29	60.01	24.66	b.d.l.	5.93	0.07	0.01	0.49	0.47	0.04	0.03	99.99
	1 / 2 .		8.25	60.04	24.27	0.02	5.60	0.08	0.02	0.48	0.49	0.02	0.02	99.29
	1 / 3 .		8.75	60.91	24.24	0.02	5.32	0.06	0.01	0.48	0.44	0.03	b.d.l.	100.25
	1 / 4 .		8.58	60.80	24.32	0.02	5.43	0.06	b.d.l.	0.51	0.60	0.06	b.d.l.	100.34
	1 / 5 .		8.27	58.40	23.71	0.72	5.73	0.07	0.02	1.27	0.38	0.02	b.d.l.	98.61
	1 / 6 .		8.46	58.93	22.33	2.40	4.53	0.06	0.08	3.22	0.44	0.06	b.d.l.	100.49

Table A.6. EPMA analysis of plagioclase in Barwell Inclusion A

Site	Point	Mineral	Element										Total
			SiO_2	MgO	Al_2O_3	CaO	TiO_2	Cr_2O_3	MnO	FeO	V_2O3	NiO	
BAR_A_13	1 / 1 .	Chromite	b.d.l.	2.52	9.13	0.01	3.20	51.08	0.59	31.69	0.77	b.d.l.	98.98
	1 / 2 .		b.d.l.	2.54	9.16	0.02	3.22	51.30	0.58	31.65	0.76	b.d.l.	99.22
	1 / 3 .		0.04	2.56	9.18	0.00	3.10	51.18	0.56	31.71	0.76	0.03	99.12
BAR_A_14	1 / 1 .		0.03	2.63	9.53	0.02	3.26	51.25	0.59	31.50	0.75	b.d.l.	99.57
	1 / 2 .		b.d.l.	2.67	9.68	b.d.l.	3.19	51.11	0.57	31.43	0.78	b.d.l.	99.43
	1 / 3 .		0.02	2.71	9.71	b.d.l.	3.02	50.80	0.55	31.23	0.76	0.01	98.81
	1 / 4 .		0.07	2.68	9.87	0.02	3.15	51.28	0.58	31.29	0.77	0.01	99.70
	1 / 5 .		0.02	2.63	9.63	b.d.l.	3.12	51.20	0.55	31.56	0.78	0.02	99.51
BAR_A_15	1 / 1 .		0.06	2.50	9.03	0.01	4.02	49.98	0.57	32.73	0.75	b.d.l.	99.65
	1 / 2 .		0.03	2.62	8.89	0.01	4.05	50.33	0.57	32.40	0.75	b.d.l.	99.64
	1 / 3 .		b.d.l.	2.59	8.96	b.d.l.	3.93	50.25	0.58	32.54	0.77	b.d.l.	99.62
	1 / 4 .		0.02	2.59	8.88	b.d.l.	4.00	50.24	0.58	32.42	0.76	b.d.l.	99.50
	1 / 5 .		0.04	2.35	8.94	b.d.l.	3.50	50.21	0.54	32.26	0.74	b.d.l.	98.55
BAR_A_16	1 / 1 .		0.02	2.39	8.65	b.d.l.	2.88	52.49	0.59	31.75	0.71	b.d.l.	99.49
	1 / 2 .		0.03	2.36	8.65	b.d.l.	2.60	53.17	0.55	31.34	0.70	0.03	99.42
	1 / 3 .		b.d.l.	2.39	8.66	0.02	3.13	52.39	0.61	31.77	0.73	b.d.l.	99.68
	1 / 4 .		0.06	2.53	8.77	0.02	3.23	51.41	0.59	31.91	0.72	0.02	99.25
	1 / 5 .		0.05	2.46	8.72	0.02	3.12	52.11	0.59	31.51	0.71	0.01	99.29
BAR_A_17	1 / 1 .		0.02	2.51	9.28	b.d.l.	3.48	50.67	0.56	32.17	0.75	b.d.l.	99.44
	1 / 2 .		0.04	2.58	9.18	b.d.l.	3.69	50.26	0.55	32.31	0.75	b.d.l.	99.35
	1 / 3 .		0.01	2.62	9.18	b.d.l.	3.65	50.43	0.59	32.12	0.79	0.01	99.37
	1 / 4 .		0.04	2.68	9.31	b.d.l.	3.71	50.46	0.60	31.96	0.77	b.d.l.	99.52
	1 / 5 .		0.02	2.72	9.17	b.d.l.	3.67	50.64	0.60	32.06	0.77	b.d.l.	99.64
	1 / 6 .		0.04	2.56	9.23	b.d.l.	3.61	50.57	0.57	32.22	0.78	0.01	99.60
	1 / 7 .		0.03	2.58	9.32	b.d.l.	3.61	49.99	0.57	32.32	0.78	0.01	99.22
BAR_A_18	1 / 2 .		0.03	2.62	10.40	0.01	2.65	50.95	0.56	31.37	0.77	0.02	99.38
	1 / 5 .		0.07	2.64	10.37	0.01	2.59	50.70	0.59	31.44	0.75	b.d.l.	99.15
	1 / 6 .		0.04	2.64	10.51	0.01	2.64	50.83	0.59	31.41	0.77	b.d.l.	99.44
BAR_A_19	1 / 1 .		0.03	2.58	9.38	0.01	2.85	51.01	0.58	31.62	0.74	b.d.l.	98.78
	1 / 2 .		0.03	2.66	9.45	b.d.l.	2.64	52.11	0.60	30.96	0.76	b.d.l.	99.21
	1 / 3 .		0.03	2.64	9.48	0.01	2.55	52.42	0.58	30.91	0.74	b.d.l.	99.34
BAR_A_20	1 / 1 .		0.02	2.35	8.34	b.d.l.	3.54	50.86	0.60	32.52	0.73	b.d.l.	98.98
	1 / 2 .		0.04	2.33	8.30	b.d.l.	3.78	51.56	0.59	32.20	0.75	0.01	99.56
	1 / 3 .		0.03	2.35	8.23	b.d.l.	3.77	51.32	0.62	32.46	0.71	0.01	99.51
	1 / 4 .		0.05	2.48	8.22	b.d.l.	3.73	51.12	0.63	32.35	0.71	0.01	99.29
	1 / 5 .		0.07	2.37	8.20	0.03	3.64	50.75	0.61	32.42	0.72	b.d.l.	98.80

Table A.7. EPMA analysis of chromite in Barwell Inclusion A

Site	Point	Mineral	Element														Total
			Na_2O	MgO	Al_2O_3	SiO_2	K_2O	CaO	TiO_2	V_2O3	Cr_2O_3	MnO	FeO	CoO	NiO	Y_2O_3	
BAR_B_01	1 / 1 .	Olivine	b.d.l.	39.04	b.d.l.	38.51	b.d.l.	0.01	0.03	b.d.l.	0.02	0.48	23.16	0.04	b.d.l.	b.d.l.	101.27
	1 / 2 .		b.d.l.	39.07	b.d.l.	38.63	b.d.l.	0.01	0.04	b.d.l.	0.04	0.48	23.23	0.02	b.d.l.	b.d.l.	101.50
	1 / 3 .		b.d.l.	39.03	b.d.l.	38.41	b.d.l.	0.02	0.07	b.d.l.	0.02	0.52	23.26	0.03	b.d.l.	b.d.l.	101.34
	1 / 4 .		b.d.l.	38.78	b.d.l.	38.37	b.d.l.	0.02	0.12	b.d.l.	0.07	0.50	23.34	0.04	b.d.l.	b.d.l.	101.22
	1 / 5 .		b.d.l.	38.98	b.d.l.	38.60	b.d.l.	0.04	0.04	b.d.l.	b.d.l.	0.51	23.13	0.04	b.d.l.	b.d.l.	101.27
	1 / 6 .		b.d.l.	39.02	b.d.l.	38.49	b.d.l.	0.02	0.02	b.d.l.	0.05	0.48	23.26	0.02	b.d.l.	b.d.l.	101.32
BAR_B_02	1 / 1 .		b.d.l.	38.85	b.d.l.	38.47	b.d.l.	0.01	0.06	b.d.l.	0.01	0.47	23.19	0.03	b.d.l.	b.d.l.	101.05
	1 / 2 .		b.d.l.	38.91	b.d.l.	38.40	b.d.l.	0.04	0.04	b.d.l.	0.02	0.49	23.13	0.03	b.d.l.	b.d.l.	101.00
	1 / 3 .		b.d.l.	38.94	b.d.l.	38.47	b.d.l.	0.02	0.02	b.d.l.	b.d.l.	0.49	23.26	0.02	b.d.l.	b.d.l.	101.14
	1 / 4 .		b.d.l.	38.92	b.d.l.	38.41	b.d.l.	0.04	0.06	b.d.l.	b.d.l.	0.48	23.28	0.01	b.d.l.	b.d.l.	101.19
	1 / 5 .		b.d.l.	38.96	b.d.l.	38.38	b.d.l.	0.03	0.03	b.d.l.	b.d.l.	0.48	23.09	0.03	b.d.l.	b.d.l.	100.91
	1 / 6 .		b.d.l.	38.74	b.d.l.	38.49	b.d.l.	0.03	0.03	b.d.l.	b.d.l.	0.50	23.34	0.02	b.d.l.	b.d.l.	101.09
BAR_B_03	1 / 1 .		b.d.l.	38.85	b.d.l.	38.53	b.d.l.	0.03	0.08	b.d.l.	0.01	0.48	23.30	0.02	b.d.l.	b.d.l.	101.27
	1 / 2 .		b.d.l.	39.01	b.d.l.	38.46	b.d.l.	0.03	0.05	b.d.l.	0.01	0.48	23.03	0.03	b.d.l.	b.d.l.	101.10
	1 / 3 .		b.d.l.	38.99	b.d.l.	38.50	b.d.l.	0.04	b.d.l.	b.d.l.	b.d.l.	0.50	23.27	0.04	b.d.l.	b.d.l.	101.30
	1 / 4 .		b.d.l.	38.88	b.d.l.	38.44	b.d.l.	0.03	0.05	b.d.l.	b.d.l.	0.49	23.30	0.03	b.d.l.	b.d.l.	101.16
	1 / 5 .		b.d.l.	38.89	b.d.l.	38.43	b.d.l.	0.03	0.01	b.d.l.	0.02	0.49	23.13	0.04	b.d.l.	b.d.l.	101.02
	1 / 6 .		b.d.l.	38.88	b.d.l.	38.46	b.d.l.	0.03	0.04	b.d.l.	0.06	0.47	23.26	0.02	b.d.l.	b.d.l.	101.19
BAR_B_04	1 / 1 .		b.d.l.	38.86	b.d.l.	38.61	b.d.l.	0.02	0.03	b.d.l.	b.d.l.	0.51	23.20	0.03	b.d.l.	b.d.l.	101.23
	1 / 2 .		b.d.l.	38.79	b.d.l.	38.43	b.d.l.	0.03	0.04	b.d.l.	0.01	0.46	23.10	0.02	b.d.l.	b.d.l.	100.83
	1 / 3 .		b.d.l.	38.88	b.d.l.	38.39	b.d.l.	0.02	0.02	b.d.l.	b.d.l.	0.50	23.26	0.01	b.d.l.	b.d.l.	101.03
	1 / 4 .		b.d.l.	38.86	b.d.l.	38.47	b.d.l.	0.03	0.04	b.d.l.	b.d.l.	0.48	23.09	0.03	b.d.l.	b.d.l.	100.92
	1 / 5 .		b.d.l.	38.72	b.d.l.	38.40	b.d.l.	0.02	0.04	b.d.l.	0.01	0.51	23.10	0.03	b.d.l.	b.d.l.	100.81
BAR_B_05	1 / 1 .		b.d.l.	38.67	b.d.l.	38.28	b.d.l.	0.05	0.02	b.d.l.	0.01	0.47	23.15	0.01	b.d.l.	b.d.l.	100.62
	1 / 2 .		b.d.l.	38.67	b.d.l.	38.30	b.d.l.	0.03	0.05	b.d.l.	0.01	0.50	23.23	0.02	b.d.l.	b.d.l.	100.79
	1 / 3 .		b.d.l.	38.68	b.d.l.	38.22	b.d.l.	0.02	0.04	b.d.l.	0.01	0.50	23.31	0.03	b.d.l.	b.d.l.	100.79
	1 / 4 .		b.d.l.	38.58	b.d.l.	38.26	b.d.l.	0.01	0.05	b.d.l.	0.02	0.47	23.16	0.03	b.d.l.	b.d.l.	100.49
	1 / 5 .		b.d.l.	38.52	b.d.l.	38.21	b.d.l.	0.03	0.01	b.d.l.	0.01	0.51	23.16	0.02	b.d.l.	b.d.l.	100.44
	1 / 6 .		b.d.l.	38.61	b.d.l.	38.22	b.d.l.	0.01	b.d.l.	b.d.l.	0.03	0.48	23.18	0.02	b.d.l.	b.d.l.	100.49
BAR_B_06	1 / 1 .		b.d.l.	38.76	b.d.l.	38.29	b.d.l.	0.01	0.02	b.d.l.	b.d.l.	0.49	23.34	0.02	b.d.l.	b.d.l.	100.88
	1 / 2 .		b.d.l.	38.85	b.d.l.	38.47	b.d.l.	0.02	0.01	b.d.l.	b.d.l.	0.49	23.29	0.02	b.d.l.	b.d.l.	101.08
	1 / 3 .		b.d.l.	38.71	b.d.l.	38.34	b.d.l.	0.01	0.02	b.d.l.	0.02	0.48	23.19	0.03	b.d.l.	b.d.l.	100.76
	1 / 4 .		b.d.l.	38.72	b.d.l.	38.43	b.d.l.	0.01	0.03	b.d.l.	b.d.l.	0.48	23.09	0.02	b.d.l.	b.d.l.	100.68
	1 / 5 .		b.d.l.	38.84	b.d.l.	38.42	b.d.l.	0.01	0.01	b.d.l.	0.03	0.50	23.23	0.03	b.d.l.	b.d.l.	101.06
BAR_B_07	1 / 1 .		b.d.l.	39.17	b.d.l.	38.51	b.d.l.	0.00	0.01	b.d.l.	b.d.l.	0.49	22.91	0.04	b.d.l.	b.d.l.	101.03
	1 / 2 .		b.d.l.	39.01	b.d.l.	38.47	b.d.l.	0.01	b.d.l.	b.d.l.	b.d.l.	0.50	22.95	0.02	b.d.l.	b.d.l.	100.88
	1 / 3 .		b.d.l.	38.93	b.d.l.	38.52	b.d.l.	0.01	0.03	b.d.l.	b.d.l.	0.51	22.96	0.02	b.d.l.	b.d.l.	100.95
	1 / 4 .		b.d.l.	38.97	b.d.l.	38.54	b.d.l.	0.03	0.03	b.d.l.	b.d.l.	0.51	23.00	0.02	b.d.l.	b.d.l.	101.02
BAR_B_07a	1 / 1 .		b.d.l.	38.86	b.d.l.	39.10	b.d.l.	0.01	b.d.l.	b.d.l.	b.d.l.	0.53	23.11	0.01	b.d.l.	b.d.l.	101.59
	1 / 2 .		b.d.l.	38.81	b.d.l.	39.05	b.d.l.	b.d.l.	0.02	b.d.l.	b.d.l.	0.49	23.03	0.00	b.d.l.	b.d.l.	101.40
	1 / 3 .		b.d.l.	38.75	b.d.l.	39.05	b.d.l.	b.d.l.	0.01	b.d.l.	b.d.l.	0.48	23.12	0.00	b.d.l.	b.d.l.	101.43
	1 / 4 .		b.d.l.	38.65	b.d.l.	38.79	b.d.l.	0.02	0.01	b.d.l.	b.d.l.	0.48	23.26	-0.01	b.d.l.	b.d.l.	101.22
	1 / 5 .		b.d.l.	38.45	b.d.l.	38.76	b.d.l.	0.02	b.d.l.	b.d.l.	b.d.l.	0.48	22.99	-0.01	b.d.l.	b.d.l.	100.74
	1 / 6 .		b.d.l.	38.41	b.d.l.	38.84	b.d.l.	0.02	0.02	b.d.l.	0.01	0.49	23.09	-0.01	b.d.l.	b.d.l.	100.88

Table A.8. EPMA analysis of olivine in Barwell Inclusion B

Site	Point	Mineral	Element											Total
			Na_2O	SiO_2	Al_2O_3	MgO	CaO	TiO_2	MnO	FeO	K_2O	SrO	BaO	
BAR_B_23	1 / 1 .	Plagioclase	9.81	63.73	21.46	1.07	2.67	0.03	0.02	1.17	0.84	0.02	b.d.l.	100.81
	1 / 2 .		9.96	64.39	21.90	0.03	2.66	0.05	0.02	0.52	0.89	0.03	b.d.l.	100.41
	1 / 3 .		9.89	63.99	21.72	0.37	2.72	0.06	0.02	0.95	0.84	0.02	b.d.l.	100.55
	1 / 4 .		9.92	64.31	21.94	0.02	2.75	0.06	b.d.l.	0.56	1.01	0.02	0.01	100.61
	1 / 5 .		9.31	63.48	20.25	1.28	4.70	0.07	0.03	0.75	0.89	0.02	0.02	100.81
BAR_B_24	1 / 1 .		9.90	64.17	21.91	0.10	2.74	0.03	0.01	0.61	0.87	0.03	0.02	100.38
	1 / 2 .		9.99	63.79	21.35	0.40	3.66	0.06	0.01	0.62	0.65	0.04	b.d.l.	100.57
	1 / 3 .		9.41	63.51	20.01	1.30	4.88	0.09	0.02	0.91	0.76	0.01	b.d.l.	100.90
BAR_B_25	1 / 2 .		9.67	63.80	22.46	0.03	3.40	0.06	0.02	0.56	0.66	0.00	b.d.l.	100.65
	1 / 3 .		9.02	62.37	23.23	0.01	4.19	0.05	0.01	0.57	0.50	0.04	0.02	100.00
BAR_B_26	1 / 1 .		9.19	62.56	23.31	0.01	4.35	0.07	0.01	0.56	0.58	0.02	0.02	100.68
	1 / 2 .		9.09	62.37	23.73	b.d.l.	4.55	0.08	b.d.l.	0.50	0.48	0.02	b.d.l.	100.81
	1 / 3 .		9.61	63.63	22.23	0.04	3.12	0.06	0.01	0.61	0.69	0.02	b.d.l.	99.99
	1 / 5 .		9.72	64.21	21.83	0.14	2.64	0.03	0.01	0.73	0.88	0.01	b.d.l.	100.19
BAR_B_27	1 / 2 .		10.06	64.79	21.80	0.01	2.56	0.04	0.01	0.41	0.70	0.05	b.d.l.	100.41
	1 / 3 .		9.93	64.71	21.78	b.d.l.	2.63	0.04	0.01	0.40	0.99	0.05	b.d.l.	100.52
	1 / 4 .		10.10	65.00	21.59	0.02	2.40	0.05	0.02	0.44	0.86	0.02	b.d.l.	100.50
	1 / 5 .		9.93	64.86	21.55	0.05	2.48	0.03	0.01	0.57	0.94	0.03	0.01	100.46
	1 / 6 .		9.75	64.64	21.62	0.01	2.43	0.04	0.02	0.59	1.10	b.d.l.	0.01	100.22
	1 / 7 .		9.85	64.50	21.50	0.63	2.36	0.03	0.02	0.77	0.95	0.04	0.01	100.67

Table A.9. EPMA analysis of plagioclase in Barwell Inclusion B

Site	Point	Mineral	Element										Total
			Na_2O	SiO_2	MgO	Al_2O_3	CaO	TiO_2	Cr_2O_3	MnO	FeO	NiO	
BAR_B_012	1 / 1 .	High-Ca pyroxene	0.58	54.70	16.42	0.56	22.32	0.54	0.78	0.24	4.69	b.d.l.	100.81
	1 / 2 .		0.57	54.81	16.39	0.52	22.21	0.52	0.78	0.21	4.66	b.d.l.	100.67
	1 / 3 .		0.59	54.76	16.39	0.52	22.31	0.53	0.75	0.23	4.73	b.d.l.	100.78
	1 / 4 .		0.62	54.18	16.51	0.61	21.93	0.59	0.78	0.24	4.96	b.d.l.	100.42
	1 / 5 .		0.54	54.54	16.37	0.55	22.13	0.54	0.74	0.23	5.02	b.d.l.	100.66
	1 / 6 .		0.53	54.55	16.38	0.69	22.12	0.36	0.75	0.22	4.99	b.d.l.	100.59
	1 / 7 .		0.65	54.15	16.88	0.54	21.22	0.47	0.74	0.22	5.44	b.d.l.	100.31
BAR_B_013	1 / 1 .		0.60	54.74	16.48	0.60	21.98	0.66	0.82	0.21	5.01	b.d.l.	101.10
	1 / 2 .		0.62	55.02	16.48	0.67	22.02	0.67	0.81	0.26	5.07	b.d.l.	101.61
	1 / 3 .		0.59	54.79	16.37	0.66	21.97	0.68	0.79	0.21	5.07	b.d.l.	101.14
	1 / 4 .		0.60	54.72	16.37	0.61	21.87	0.65	0.84	0.26	5.01	b.d.l.	100.92
	1 / 5 .		0.61	54.88	16.30	0.56	21.80	0.67	0.84	0.24	5.18	b.d.l.	101.05
	1 / 6 .		0.59	54.86	16.47	0.56	21.90	0.63	0.81	0.21	5.18	b.d.l.	101.20
	1 / 7 .		0.52	55.19	16.52	0.54	22.74	0.53	0.77	0.21	4.33	b.d.l.	101.33
BAR_B_014	1 / 1 .		0.56	54.49	16.32	0.91	22.09	0.42	0.94	0.24	5.01	b.d.l.	100.97
	1 / 2 .		0.52	54.90	16.46	0.84	22.02	0.39	0.80	0.23	5.06	b.d.l.	101.21
	1 / 3 .		0.63	54.97	16.38	0.57	22.05	0.59	0.75	0.24	4.96	b.d.l.	101.13
	1 / 4 .		0.58	54.89	16.35	0.59	22.17	0.51	0.81	0.24	4.77	b.d.l.	100.90
	1 / 5 .		0.58	54.72	16.29	0.54	22.16	0.52	0.82	0.22	4.82	b.d.l.	100.67
	1 / 6 .		0.53	54.72	16.43	0.57	21.96	0.57	0.73	0.23	5.07	b.d.l.	100.81
	1 / 7 .		0.59	54.87	16.39	0.50	22.32	0.52	0.80	0.23	4.65	b.d.l.	100.85
	1 / 8 .		0.49	54.70	16.39	0.72	22.01	0.49	0.75	0.22	4.91	b.d.l.	100.69
BAR_B_015	1 / 4 .		0.59	54.34	16.37	0.55	21.89	0.54	0.82	0.22	5.10	b.d.l.	100.42
	1 / 5 .		0.55	54.65	16.39	0.50	22.73	0.49	0.75	0.22	4.35	b.d.l.	100.61
	1 / 6 .		0.52	54.60	16.51	0.59	22.18	0.41	0.72	0.24	5.01	b.d.l.	100.78
	1 / 7 .		0.55	54.64	16.60	0.67	22.24	0.29	0.84	0.24	4.98	b.d.l.	101.04
BAR_B_016	1 / 1 .		0.57	54.77	16.67	0.57	22.10	0.54	0.75	0.23	5.05	b.d.l.	101.23
	1 / 2 .		0.56	54.41	16.50	0.49	21.97	0.57	0.81	0.23	5.09	0.01	100.63
	1 / 3 .		0.53	54.82	16.56	0.54	22.20	0.54	0.75	0.23	5.02	0.02	101.20
	1 / 4 .		0.63	54.98	16.55	0.52	22.35	0.52	0.80	0.22	4.74	b.d.l.	101.27
	1 / 5 .		0.59	54.68	16.65	0.55	22.00	0.54	0.81	0.22	4.94	0.02	100.99
	1 / 6 .		0.56	54.71	16.53	0.53	22.05	0.52	0.83	0.24	5.01	b.d.l.	100.97
BAR_B_017	1 / 1 .		0.58	54.50	16.47	0.52	21.98	0.56	0.82	0.25	5.03	0.01	100.71
	1 / 2 .		0.53	54.83	16.62	0.55	21.97	0.47	0.82	0.24	5.14	b.d.l.	101.16
	1 / 3 .		0.56	54.94	16.61	0.52	22.47	0.50	0.81	0.22	4.59	b.d.l.	101.22
	1 / 4 .		0.57	54.86	16.37	0.53	21.93	0.53	0.86	0.25	4.95	b.d.l.	100.82
	1 / 5 .		0.53	54.09	18.13	0.47	19.40	0.45	0.72	0.27	5.72	b.d.l.	99.79
	1 / 6 .		0.60	54.50	16.60	0.57	22.06	0.37	0.83	0.23	5.05	0.01	100.82

Table A.10. EPMA analysis of high-Ca pyroxene in Barwell Inclusion B

Site	Point	Mineral	Element										Total
			Na_2O	SiO_2	MgO	Al_2O_3	CaO	TiO_2	Cr_2O_3	MnO	FeO	NiO	
BAR_B_015	1 / 1 .	Low-Ca pyroxene	b.d.l.	55.57	28.62	0.45	0.89	0.49	0.25	0.47	14.17	b.d.l.	100.92
	1 / 2 .		b.d.l.	55.55	28.30	0.41	0.98	0.45	0.24	0.50	14.10	b.d.l.	100.54
	1 / 3 .		0.03	55.62	28.61	0.37	0.89	0.43	0.21	0.50	14.00	b.d.l.	100.64
	1 / 7 .		0.03	56.38	28.84	0.32	0.81	0.34	0.22	0.48	13.93	b.d.l.	101.34
BAR_B_016	1 / 1 .		0.02	55.75	28.73	0.36	0.76	0.40	0.23	0.52	13.93	b.d.l.	100.71
	1 / 2 .		b.d.l.	55.63	28.46	0.37	0.86	0.43	0.21	0.50	14.20	b.d.l.	100.65
	1 / 3 .		b.d.l.	55.56	28.73	0.37	0.76	0.37	0.21	0.48	14.14	b.d.l.	100.61
	1 / 4 .		0.01	55.74	28.62	0.37	0.80	0.42	0.21	0.49	13.97	b.d.l.	100.62
	1 / 5 .		b.d.l.	55.57	28.63	0.28	0.76	0.32	0.20	0.50	14.04	b.d.l.	100.29
	1 / 6 .		0.01	55.43	28.53	0.37	0.79	0.43	0.22	0.46	13.96	b.d.l.	100.19
BAR_B_019	1 / 1 .		0.01	55.53	28.52	0.27	0.86	0.32	0.19	0.50	14.05	b.d.l.	100.26
	1 / 2 .		0.02	55.55	28.57	0.23	0.90	0.31	0.20	0.49	14.00	0.01	100.28
	1 / 3 .		0.02	55.62	28.74	0.15	0.71	0.21	0.14	0.50	14.03	0.01	100.13
	1 / 4 .		0.02	55.55	28.54	0.28	0.95	0.34	0.21	0.48	13.90	b.d.l.	100.24
	1 / 5 .		0.01	55.65	28.53	0.26	0.78	0.32	0.19	0.48	14.14	b.d.l.	100.35
	1 / 6 .		0.02	55.56	28.58	0.29	0.86	0.36	0.20	0.50	14.00	0.02	100.38
BAR_B_020	1 / 1 .		0.02	56.19	28.50	0.15	1.01	0.20	0.13	0.48	13.77	b.d.l.	100.46
	1 / 2 .		0.01	55.43	28.43	0.56	0.90	0.56	0.39	0.51	13.89	b.d.l.	100.67
	1 / 3 .		0.02	56.61	29.24	0.13	0.84	0.20	0.40	0.49	13.63	b.d.l.	101.56
	1 / 4 .		0.03	55.70	28.62	0.53	1.00	0.51	0.55	0.49	13.89	b.d.l.	101.31
	1 / 5 .		0.04	55.86	28.70	0.41	0.82	0.40	0.27	0.46	13.81	b.d.l.	100.74
	1 / 6 .		0.01	56.48	29.06	0.13	0.80	0.19	0.55	0.50	13.86	b.d.l.	101.55
BAR_B_021	1 / 1 .		0.03	55.90	28.64	0.30	0.83	0.33	0.22	0.48	13.95	0.01	100.66
	1 / 2 .		b.d.l.	55.85	28.39	0.40	0.96	0.40	0.27	0.50	13.93	b.d.l.	100.71
	1 / 3 .		0.03	55.81	28.55	0.46	0.95	0.45	0.29	0.50	13.99	0.02	101.05
	1 / 4 .		0.04	56.41	28.66	0.13	0.98	0.18	0.18	0.51	13.98	0.03	101.10
	1 / 5 .		0.03	56.51	28.80	0.14	1.05	0.19	0.16	0.49	13.84	0.05	101.25
	1 / 6 .		0.03	55.69	28.27	0.43	1.01	0.45	0.30	0.48	13.90	b.d.l.	100.57
BAR_B_022	1 / 1 .		b.d.l.	56.16	28.86	0.13	0.84	0.14	0.10	0.50	13.99	b.d.l.	100.69
	1 / 2 .		0.02	56.14	28.68	0.14	0.84	0.19	0.11	0.50	14.00	b.d.l.	100.63
	1 / 3 .		0.02	55.86	28.71	0.14	0.94	0.17	0.11	0.50	14.07	0.01	100.52
	1 / 4 .		0.01	56.14	28.72	0.15	0.93	0.19	0.10	0.53	14.01	0.01	100.78
	1 / 5 .		b.d.l.	56.26	28.77	0.17	1.00	0.17	0.14	0.48	13.96	b.d.l.	100.94

Table A.11. EPMA analysis of low-Ca pyroxene in Barwell Inclusion B

Site	Point	Mineral	Element										Total
			SiO_2	MgO	Al_2O_3	CaO	TiO_2	Cr_2O_3	MnO	FeO	V_2O3	NiO	
BAR_B_28	1 / 4 .	Chromite	0.78	3.79	9.01	0.11	1.88	54.01	0.57	28.77	0.57	0.02	99.52
	1 / 5 .		0.34	2.17	3.85	0.05	13.28	45.89	0.71	33.30	0.55	0.01	100.14
BAR_B_29	1 / 1 .		0.08	1.88	5.42	0.05	3.35	53.36	0.61	32.73	0.77	0.02	98.26
	1 / 4 .		0.65	2.35	5.43	0.04	3.25	52.58	0.63	32.50	0.73	b.d.l.	98.15
BAR_B_30	1 / 1 .		0.09	1.82	5.61	0.03	2.75	54.87	0.63	31.99	0.72	b.d.l.	98.50
	1 / 5 .		0.04	1.80	5.60	0.02	2.94	54.19	0.62	32.34	0.74	0.01	98.28
BAR_B_31	1 / 1 .		0.02	2.62	5.53	0.02	3.22	56.23	0.59	30.90	0.67	b.d.l.	99.78
	1 / 2 .		0.03	2.57	5.49	0.09	3.26	56.24	0.62	30.87	0.66	b.d.l.	99.82
	1 / 3 .		0.02	2.59	5.53	0.05	3.23	56.24	0.58	30.74	0.67	b.d.l.	99.64
	1 / 4 .		-0.01	2.59	5.56	0.04	3.25	56.17	0.59	30.72	0.67	0.01	99.59
	1 / 5 .		0.04	2.57	5.63	0.02	3.30	56.31	0.60	30.95	0.68	b.d.l.	100.10
	1 / 6 .		0.02	2.59	5.44	0.07	3.24	56.21	0.63	30.74	0.64	b.d.l.	99.56
	1 / 7 .		0.03	2.60	5.61	0.02	3.25	56.31	0.61	30.82	0.66	b.d.l.	99.88
BAR_B_32	1 / 1 .		0.01	2.72	5.54	b.d.l.	3.22	56.81	0.60	30.66	0.68	0.02	100.27
	1 / 2 .		0.01	2.69	5.51	0.01	3.17	56.66	0.59	30.60	0.68	0.02	99.93
	1 / 3 .		0.02	2.68	5.55	0.01	3.23	56.92	0.58	30.54	0.69	b.d.l.	100.21
	1 / 4 .		0.04	2.67	5.63	b.d.l.	3.10	56.75	0.57	30.38	0.69	0.01	99.85
	1 / 5 .		0.02	2.75	5.64	b.d.l.	3.11	56.74	0.58	30.49	0.68	b.d.l.	99.99
	1 / 6 .		0.02	2.82	5.60	b.d.l.	3.07	56.59	0.59	30.54	0.68	b.d.l.	99.90
BAR_B_33	1 / 1 .		0.03	2.05	5.66	0.03	3.28	55.63	0.61	31.83	0.74	b.d.l.	99.83
	1 / 2 .		0.06	2.12	5.80	0.01	3.26	55.61	0.61	31.75	0.75	0.02	99.99
	1 / 3 .		0.04	1.98	5.58	0.02	3.28	55.70	0.55	31.80	0.72	b.d.l.	99.64
	1 / 4 .		0.02	1.96	5.78	0.05	3.25	55.42	0.58	31.81	0.74	0.02	99.63
	1 / 5 .		0.02	2.03	5.64	0.01	3.33	55.71	0.62	31.70	0.71	0.01	99.78
	1 / 6 .		0.02	2.09	5.66	0.02	3.25	55.55	0.57	31.97	0.71	0.02	99.87
BAR_B_34	1 / 1 .		0.05	2.53	5.77	0.04	2.39	56.38	0.67	30.54	0.76	0.13	99.25
	1 / 2 .		0.09	2.44	5.76	0.04	2.59	55.74	0.66	30.54	0.71	0.10	98.67
	1 / 3 .		0.03	2.39	5.74	0.10	2.61	55.67	0.67	30.59	0.74	0.04	98.57
	1 / 4 .		0.01	2.32	5.79	0.04	2.47	56.38	0.71	30.48	0.75	0.01	98.96
	1 / 5 .		0.03	2.37	5.84	0.02	2.38	56.36	0.70	30.75	0.76	0.12	99.32
	1 / 6 .		0.04	2.29	5.84	0.02	2.14	56.61	0.67	30.60	0.77	0.21	99.18

Table A.12. EPMA analysis of chromite in Barwell Inclusion B

Site	Point	Mineral	Element													Total
			K_2O	CaO	TiO_2	V_2O3	Cr_2O_3	MnO	FeO	CoO	NiO	Na_2O	MgO	Al_2O_3	SiO_2	
BAR_C_01	1 / 1 .	Olivine	0.02	0.02	b.d.l.	b.d.l.	0.01	0.50	23.14	b.d.l.	b.d.l.	b.d.l.	38.54	0.01	38.47	100.70
	1 / 2 .		b.d.l.	0.03	b.d.l.	0.01	b.d.l.	0.50	23.01	b.d.l.	b.d.l.	0.02	38.58	0.00	38.51	100.63
	1 / 3 .		b.d.l.	0.01	0.02	0.00	0.01	0.50	22.90	b.d.l.	b.d.l.	b.d.l.	38.65	0.02	38.39	100.47
	1 / 4 .		b.d.l.	0.02	0.04	b.d.l.	0.02	0.47	22.93	b.d.l.	b.d.l.	b.d.l.	38.57	0.01	38.34	100.37
	1 / 5 .		b.d.l.	0.02	b.d.l.	0.01	0.02	0.48	22.95	b.d.l.	b.d.l.	b.d.l.	38.43	0.01	38.33	100.23
	1 / 6 .		b.d.l.	0.02	0.02	b.d.l.	0.01	0.49	23.00	b.d.l.	b.d.l.	b.d.l.	38.69	0.03	38.38	100.58
	1 / 7 .		b.d.l.	0.11	0.02	b.d.l.	0.01	0.49	23.05	b.d.l.	b.d.l.	b.d.l.	38.34	0.01	38.46	100.42
BAR_C_02	1 / 1 .		0.02	0.03	b.d.l.	0.01	0.02	0.49	23.14	b.d.l.	b.d.l.	b.d.l.	38.44	0.02	38.48	100.64
	1 / 2 .		0.01	0.06	b.d.l.	b.d.l.	0.01	0.49	22.81	b.d.l.	b.d.l.	b.d.l.	38.72	0.00	38.59	100.70
	1 / 3 .		b.d.l.	0.06	b.d.l.	0.01	0.05	0.47	22.82	b.d.l.	b.d.l.	b.d.l.	38.59	0.00	38.58	100.52
	1 / 4 .		b.d.l.	0.03	0.02	b.d.l.	0.08	0.48	23.12	b.d.l.	b.d.l.	b.d.l.	38.50	0.02	38.41	100.61
	1 / 5 .		0.01	0.02	0.01	b.d.l.	0.09	0.47	22.93	b.d.l.	b.d.l.	b.d.l.	38.54	0.02	38.44	100.53
	1 / 6 .		0.01	0.02	0.01	b.d.l.	0.03	0.50	22.96	b.d.l.	0.02	0.01	38.52	0.02	38.57	100.64
	1 / 7 .		0.01	0.02	0.01	b.d.l.	0.02	0.49	22.94	b.d.l.	b.d.l.	0.02	38.48	0.00	38.49	100.44
BAR_C_03	1 / 1 .		b.d.l.	0.02	b.d.l.	b.d.l.	b.d.l.	0.48	22.98	b.d.l.	b.d.l.	b.d.l.	38.43	0.03	38.58	100.47
	1 / 2 .		b.d.l.	0.02	0.01	0.01	0.02	0.47	22.89	b.d.l.	b.d.l.	b.d.l.	38.53	0.02	38.38	100.33
	1 / 3 .		b.d.l.	0.03	0.02	b.d.l.	0.03	0.46	22.93	b.d.l.	0.02	b.d.l.	38.48	0.02	38.50	100.43
	1 / 4 .		b.d.l.	0.03	0.01	0.01	0.02	0.50	22.94	b.d.l.	b.d.l.	b.d.l.	38.56	0.02	38.60	100.64
	1 / 5 .		b.d.l.	0.02	0.01	0.00	0.03	0.48	22.93	b.d.l.	b.d.l.	b.d.l.	38.45	0.01	38.33	100.25
	1 / 6 .		b.d.l.	0.02	0.01	0.00	0.18	0.46	23.16	b.d.l.	b.d.l.	b.d.l.	38.51	0.02	38.25	100.59
	1 / 7 .		b.d.l.	0.03	0.02	0.01	0.03	0.46	23.06	b.d.l.	0.02	b.d.l.	38.56	0.04	38.44	100.65
	1 / 8 .		0.01	0.03	b.d.l.	b.d.l.	0.03	0.48	22.97	b.d.l.	0.02	b.d.l.	38.39	0.01	38.51	100.45
BAR_C_04	1 / 1 .		b.d.l.	0.02	0.01	b.d.l.	0.01	0.47	23.00	b.d.l.	b.d.l.	b.d.l.	38.42	0.04	38.39	100.34
	1 / 2 .		b.d.l.	0.01	0.01	b.d.l.	0.00	0.49	23.04	b.d.l.	b.d.l.	b.d.l.	38.54	0.00	38.39	100.41
	1 / 3 .		b.d.l.	0.03	b.d.l.	0.01	b.d.l.	0.50	23.06	b.d.l.	b.d.l.	b.d.l.	38.50	0.01	38.37	100.46
	1 / 4 .		0.01	0.03	0.02	b.d.l.	0.02	0.49	23.12	b.d.l.	b.d.l.	b.d.l.	38.52	0.01	38.46	100.64
	1 / 5 .		0.01	0.02	b.d.l.	b.d.l.	0.02	0.51	22.92	b.d.l.	b.d.l.	b.d.l.	38.47	0.01	38.52	100.44
	1 / 6 .		b.d.l.	0.03	b.d.l.	0.01	0.02	0.53	23.03	b.d.l.	b.d.l.	0.04	38.54	0.04	38.57	100.76
	1 / 7 .		b.d.l.	0.03	0.02	b.d.l.	0.01	0.49	23.02	b.d.l.	0.02	b.d.l.	38.43	0.02	38.62	100.63
BAR_C_05	1 / 1 .		b.d.l.	0.02	0.02	0.02	0.04	0.48	23.03	b.d.l.	0.02	b.d.l.	38.55	0.02	38.31	100.48
	1 / 2 .		b.d.l.	0.03	0.01	b.d.l.	0.10	0.51	23.15	b.d.l.	b.d.l.	b.d.l.	38.40	0.02	38.18	100.35
	1 / 3 .		0.02	b.d.l.	0.02	b.d.l.	0.07	0.50	23.07	b.d.l.	b.d.l.	b.d.l.	38.69	0.02	38.19	100.57
	1 / 4 .		0.01	0.03	b.d.l.	b.d.l.	0.10	0.44	22.86	b.d.l.	b.d.l.	b.d.l.	38.44	0.02	38.17	100.03
	1 / 5 .		b.d.l.	0.01	b.d.l.	b.d.l.	0.08	0.46	23.12	b.d.l.	b.d.l.	b.d.l.	38.71	0.02	38.19	100.58
	1 / 6 .		b.d.l.	0.03	0.01	b.d.l.	0.04	0.47	23.11	b.d.l.	b.d.l.	b.d.l.	38.59	b.d.l.	38.13	100.30
	1 / 7 .		b.d.l.	0.01	0.02	b.d.l.	0.01	0.50	23.12	b.d.l.	b.d.l.	0.02	38.52	b.d.l.	38.14	100.30
BAR_C_06	1 / 1 .		0.01	0.03	b.d.l.	b.d.l.	b.d.l.	0.47	23.07	b.d.l.	b.d.l.	0.01	38.34	b.d.l.	38.14	100.07
	1 / 2 .		b.d.l.	0.01	0.02	0.01	b.d.l.	0.48	22.90	b.d.l.	b.d.l.	0.01	38.32	b.d.l.	38.36	100.08
	1 / 3 .		b.d.l.	0.01	b.d.l.	b.d.l.	0.01	0.48	22.91	b.d.l.	b.d.l.	0.01	38.18	0.02	38.07	99.69
	1 / 4 .		0.01	0.03	0.01	b.d.l.	0.01	0.50	22.98	b.d.l.	b.d.l.	b.d.l.	38.32	0.02	38.33	100.21
	1 / 5 .		0.02	0.03	0.02	b.d.l.	0.01	0.48	23.02	b.d.l.	b.d.l.	0.01	38.49	0.02	38.20	100.25
	1 / 6 .		0.02	0.01	0.03	b.d.l.	0.02	0.48	22.91	b.d.l.	b.d.l.	0.01	38.41	b.d.l.	38.33	100.19
	1 / 7 .		0.02	0.01	0.02	b.d.l.	0.01	0.51	23.03	b.d.l.	b.d.l.	b.d.l.	38.46	0.02	38.29	100.36
	1 / 8 .		0.01	0.03	b.d.l.	b.d.l.	0.01	0.48	22.98	b.d.l.	0.03	b.d.l.	38.34	b.d.l.	38.28	100.15

Table A.13. EPMA analysis of olivine in Barwell Inclusion C

Site	Point	Mineral	Element													Total
			Na_2O	SiO_2	P_2O_5	K_2O	CaO	TiO_2	V_2O3	Cr_2O_3	MnO	FeO	CoO	NiO	Al_2O_3	MgO	
B1_clastC_02	1 / 1 .	Plagioclase	9.62	64.22	b.d.l.	1.13	2.15	0.06	b.d.l.	0.03	0.06	1.45	b.d.l.	b.d.l.	20.43	1.11	100.24
B1_clastC_02	1 / 1 .		9.39	63.06	b.d.l.	1.04	3.98	0.08	b.d.l.	0.10	0.04	0.85	b.d.l.	b.d.l.	19.95	1.04	99.51
B1_clastC_03	1 / 1 .		10.02	65.40	b.d.l.	0.97	2.28	0.05	b.d.l.	0.01	0.04	1.09	b.d.l.	b.d.l.	20.26	0.76	100.85
B1_clastC_05	1 / 1 .		9.69	64.15	b.d.l.	0.85	2.23	0.08	b.d.l.	0.01	0.07	1.95	0.01	b.d.l.	20.25	1.82	101.11
B1_clastC_06	1 / 1 .		9.63	63.51	b.d.l.	1.03	2.28	0.03	b.d.l.	0.01	0.03	0.85	b.d.l.	b.d.l.	21.21	0.47	99.03
B1_clastC_07	1 / 1 .		9.76	64.58	b.d.l.	1.02	2.42	0.04	b.d.l.	0.01	0.02	0.57	0.01	b.d.l.	21.43	0.08	99.90
B1_clastC_08	1 / 1 .		9.77	64.25	b.d.l.	1.02	2.24	0.05	b.d.l.	0.02	0.01	0.63	0.01	b.d.l.	21.25	0.11	99.34
B1_clastC_09	1 / 1 .		9.77	64.62	b.d.l.	1.05	2.42	0.05	b.d.l.	0.00	0.01	0.53	b.d.l.	b.d.l.	21.48	0.06	99.95
B1_clastC_10	1 / 1 .		9.92	64.66	b.d.l.	0.89	2.15	0.03	b.d.l.	0.03	0.02	0.93	b.d.l.	0.01	21.26	0.27	100.19
B1_clastC_11	1 / 1 .		9.71	64.39	b.d.l.	1.04	2.20	0.04	b.d.l.	0.00	0.02	0.61	b.d.l.	b.d.l.	20.99	0.10	99.09
B1_clastC_12	1 / 1 .		9.58	63.35	0.03	0.74	2.07	0.08	b.d.l.	0.03	0.09	2.79	b.d.l.	b.d.l.	19.51	3.07	101.36
B1_clastC_14	1 / 1 .		9.69	64.27	b.d.l.	0.92	2.38	0.06	b.d.l.	0.01	0.02	0.64	0.02	b.d.l.	21.25	0.34	99.60
B1_clastC_15	1 / 1 .		9.94	64.98	b.d.l.	0.79	2.32	0.06	b.d.l.	0.02	0.03	0.55	0.01	b.d.l.	21.50	0.00	100.22
B1_clastC_16	1 / 1 .		9.74	63.86	b.d.l.	1.08	2.49	0.04	b.d.l.	0.02	0.01	0.50	b.d.l.	b.d.l.	21.74	0.02	99.50
B1_clastC_17	1 / 1 .		9.35	61.85	b.d.l.	0.88	2.35	0.05	b.d.l.	0.03	0.05	1.34	b.d.l.	b.d.l.	21.05	1.22	98.16
B1_clastC_18	1 / 1 .		9.99	64.99	b.d.l.	0.88	2.18	0.03	b.d.l.	0.01	0.03	0.55	b.d.l.	b.d.l.	21.42	0.01	100.07
B1_clastC_19	1 / 1 .		9.70	64.56	b.d.l.	0.89	2.14	0.06	b.d.l.	0.02	0.01	2.20	0.01	0.08	20.60	0.01	100.29
B1_clastC_20	1 / 1 .		9.72	64.75	b.d.l.	1.15	2.27	0.06	b.d.l.	0.01	0.02	0.62	b.d.l.	b.d.l.	21.27	0.06	99.91
B1_clastC_21	1 / 1 .		9.52	64.13	b.d.l.	1.19	2.44	0.05	b.d.l.	b.d.l.	0.02	0.61	b.d.l.	b.d.l.	21.50	0.13	99.56
B1_clastC_22	1 / 1 .		9.53	63.98	b.d.l.	0.99	2.42	0.05	b.d.l.	0.02	0.02	0.55	b.d.l.	b.d.l.	21.24	0.02	98.82
B1_clastC_23	1 / 1 .		9.43	62.47	b.d.l.	1.14	2.27	0.01	b.d.l.	0.02	0.04	1.83	b.d.l.	0.01	20.72	1.76	99.62
B1_clastC_24	1 / 1 .		9.82	64.35	b.d.l.	0.80	2.30	0.05	b.d.l.	b.d.l.	0.04	1.24	b.d.l.	b.d.l.	21.30	0.56	100.45
B1_clastC_25	1 / 1 .		9.71	64.47	b.d.l.	1.14	2.33	0.04	b.d.l.	0.01	0.00	0.62	b.d.l.	b.d.l.	21.34	0.04	99.70
B1_clastC_26	1 / 1 .		9.71	64.28	b.d.l.	0.94	2.48	0.05	b.d.l.	0.01	0.01	0.57	b.d.l.	b.d.l.	21.61	0.06	99.70

Table A.14. EPMA analysis of plagioclase in Barwell Inclusion C

Site	Point	Mineral	Element										Total
			Na_2O	SiO_2	MgO	Al_2O_3	CaO	TiO_2	Cr_2O_3	MnO	FeO	NiO	
BAR_C_07	1 / 1 .	Pyroxene	0.03	55.16	28.09	0.51	1.01	0.53	0.31	0.50	14.06	b.d.l.	100.19
	1 / 2 .		0.02	55.23	28.43	0.41	0.87	0.44	0.24	0.49	14.13	b.d.l.	100.26
	1 / 3 .		0.02	55.39	28.31	0.32	0.92	0.36	0.21	0.50	13.94	b.d.l.	99.96
	1 / 4 .		b.d.l.	55.43	28.09	0.36	0.96	0.36	0.21	0.51	14.08	b.d.l.	99.99
	1 / 5 .		0.01	55.15	28.16	0.46	0.91	0.47	0.26	0.51	14.05	b.d.l.	99.95
	1 / 6 .		b.d.l.	55.43	28.12	0.44	0.96	0.42	0.29	0.51	13.97	b.d.l.	100.13
	1 / 7 .		0.01	55.17	28.26	0.48	0.86	0.46	0.27	0.47	14.05	0.02	100.04
	1 / 8 .		b.d.l.	55.37	28.30	0.28	1.00	0.32	0.20	0.50	14.03	b.d.l.	99.99
BAR_C_08	1 / 1 .		b.d.l.	55.34	28.41	0.31	0.86	0.34	0.19	0.50	14.27	b.d.l.	100.20
	1 / 2 .		0.01	55.54	28.34	0.32	0.77	0.38	0.18	0.48	14.25	b.d.l.	100.27
	1 / 3 .		0.04	55.15	28.15	0.37	0.95	0.41	0.25	0.49	14.05	b.d.l.	99.85
	1 / 4 .		b.d.l.	55.35	28.29	0.35	0.88	0.39	0.20	0.47	14.17	b.d.l.	100.09
	1 / 5 .		b.d.l.	55.24	28.44	0.41	0.88	0.43	0.25	0.50	14.09	b.d.l.	100.22
	1 / 6 .		0.01	55.52	28.28	0.34	0.80	0.38	0.20	0.51	14.19	b.d.l.	100.23
	1 / 7 .		0.02	55.11	28.33	0.38	0.92	0.40	0.22	0.49	14.06	b.d.l.	99.92
	1 / 8 .		0.01	54.98	28.30	0.45	0.85	0.46	0.27	0.48	13.97	b.d.l.	99.76
	1 / 9 .		0.02	55.14	28.38	0.47	0.81	0.48	0.28	0.50	14.18	b.d.l.	100.25
BAR_C_09	1 / 1 .		0.02	55.38	28.22	0.51	0.89	0.52	0.27	0.48	14.07	b.d.l.	100.37
	1 / 2 .		0.01	54.88	28.16	0.50	0.89	0.52	0.30	0.48	13.97	b.d.l.	99.70
	1 / 3 .		b.d.l.	54.70	27.86	0.65	1.13	0.61	0.36	0.51	14.01	b.d.l.	99.79
	1 / 4 .		0.02	55.04	27.75	0.59	1.65	0.61	0.38	0.46	13.66	b.d.l.	100.14
	1 / 5 .		0.02	55.37	28.43	0.34	0.80	0.35	0.18	0.47	13.89	b.d.l.	99.83
	1 / 6 .		b.d.l.	55.15	28.14	0.45	0.88	0.51	0.30	0.47	13.95	b.d.l.	99.84
	1 / 7 .		b.d.l.	55.36	28.22	0.49	0.84	0.49	0.29	0.49	14.06	b.d.l.	100.23
BAR_C_10	1 / 1 .		0.02	55.35	28.54	0.17	0.67	0.23	0.12	0.51	14.03	b.d.l.	99.62
	1 / 2 .		0.01	55.26	28.40	0.27	0.92	0.28	0.18	0.47	13.90	0.01	99.69
	1 / 3 .		0.01	55.49	28.48	0.19	0.73	0.21	0.12	0.50	14.14	0.01	99.87
	1 / 4 .		b.d.l.	55.05	28.14	0.21	0.88	0.23	0.14	0.49	13.95	0.01	99.10
	1 / 5 .		b.d.l.	54.91	28.35	0.31	0.94	0.33	0.19	0.49	13.99	0.01	99.53
	1 / 6 .		b.d.l.	55.03	28.20	0.21	0.96	0.29	0.18	0.47	13.89	0.01	99.23
	1 / 7 .		b.d.l.	55.29	28.25	0.23	0.92	0.29	0.17	0.48	13.99	b.d.l.	99.60

Table A.15. EPMA analysis of pyroxene in Barwell Inclusion C

Site	Point	Mineral	Element														Total
			Na_2O	SiO_2	P_2O_5	K_2O	CaO	TiO_2	V_2O3	Cr_2O_3	MnO	FeO	CoO	NiO	Al_2O_3	MgO	
B1_clastC_44	1 / 1 .	Chromite	b.d.l.	0.13	b.d.l.	b.d.l.	0.03	2.66	0.89	54.46	0.65	31.68	b.d.l.	b.d.l.	5.54	1.63	97.65
B1_clastC_47	1 / 1 .		0.13	0.87	b.d.l.	b.d.l.	0.19	2.51	0.80	54.46	0.63	31.54	b.d.l.	b.d.l.	5.42	1.90	98.42
B1_clastC_49	1 / 1 .		0.01	0.07	b.d.l.	b.d.l.	0.03	2.50	0.82	55.74	0.64	31.40	0.01	0.02	5.27	1.70	98.21
B1_clastC_50	1 / 1 .		0.01	0.10	b.d.l.	b.d.l.	0.07	2.69	0.83	55.97	0.61	30.99	b.d.l.	0.01	5.34	1.96	98.54
B1_clastC_51	1 / 1 .		0.01	0.10	b.d.l.	0.02	0.04	2.53	0.83	55.89	0.58	30.77	0.02	b.d.l.	5.30	2.01	98.09
B1_clastC_52	1 / 1 .		0.06	0.17	b.d.l.	b.d.l.	0.07	1.97	0.89	57.05	0.61	30.51	0.01	b.d.l.	5.21	2.03	98.55
B1_clastC_53	1 / 1 .		b.d.l.	0.09	b.d.l.	0.01	0.06	2.24	0.92	55.81	0.64	31.32	0.01	b.d.l.	5.25	1.65	97.99
B1_clastC_54	1 / 1 .		0.03	0.12	b.d.l.	0.01	0.11	3.04	0.88	55.28	0.60	30.77	b.d.l.	0.03	5.39	2.18	98.40
B1_clastC_55	1 / 1 .		0.02	0.09	b.d.l.	b.d.l.	0.08	2.73	0.91	55.22	0.63	31.33	b.d.l.	b.d.l.	5.08	1.78	97.83
B1_clastC_56	1 / 1 .		b.d.l.	0.09	b.d.l.	0.02	0.14	2.42	0.88	55.95	0.59	30.71	0.01	0.01	5.16	1.99	97.97

Table A.16. EPMA analysis of chromite in Barwell Inclusion C

Site	Point	Mineral	Element													Total
			K_2O	CaO	TiO_2	V_2O3	Cr_2O_3	MnO	FeO	CoO	NiO	Na_2O	MgO	Al_2O_3	SiO_2	
BAR_D_01	1 / 1 .	Olivine	b.d.l.	0.02	0.02	b.d.l.	0.04	0.45	22.69	b.d.l.	b.d.l.	0.03	38.96	b.d.l.	39.39	101.56
	1 / 2 .		0.01	0.02	0.02	b.d.l.	0.06	0.48	23.17	b.d.l.	b.d.l.	b.d.l.	38.36	b.d.l.	38.93	101.01
	1 / 3 .		0.01	0.01	0.02	0.01	0.03	0.47	22.75	b.d.l.	b.d.l.	b.d.l.	38.72	b.d.l.	39.15	101.13
	1 / 5 .		0.03	0.02	0.01	0.02	0.05	0.51	23.28	b.d.l.	b.d.l.	b.d.l.	38.20	b.d.l.	39.07	101.17
	1 / 6 .		b.d.l.	0.01	0.03	b.d.l.	0.02	0.50	23.27	b.d.l.	b.d.l.	b.d.l.	38.43	b.d.l.	39.23	101.48
	1 / 7 .		0.02	0.02	b.d.l.	0.01	0.03	0.49	22.98	b.d.l.	b.d.l.	b.d.l.	38.82	b.d.l.	39.50	101.85
BAR_D_02	1 / 1 .		0.01	0.02	0.01	b.d.l.	0.10	0.49	23.01	b.d.l.	b.d.l.	b.d.l.	38.43	b.d.l.	38.97	100.96
	1 / 2 .		b.d.l.	0.11	0.01	b.d.l.	0.08	0.47	22.85	b.d.l.	b.d.l.	0.04	38.06	b.d.l.	39.13	100.87
	1 / 3 .		b.d.l.	0.05	b.d.l.	b.d.l.	0.02	0.46	23.02	b.d.l.	b.d.l.	0.01	38.41	b.d.l.	38.94	100.89
	1 / 4 .		b.d.l.	0.04	0.02	b.d.l.	0.02	0.50	23.06	b.d.l.	b.d.l.	0.01	38.36	b.d.l.	39.00	100.96
BAR_D_04	1 / 1 .		0.01	0.07	0.02	b.d.l.	0.03	0.50	23.07	b.d.l.	b.d.l.	0.01	38.35	b.d.l.	38.41	100.45
	1 / 2 .		0.01	0.06	b.d.l.	b.d.l.	0.01	0.48	22.98	b.d.l.	b.d.l.	b.d.l.	38.23	b.d.l.	38.50	100.31
	1 / 3 .		b.d.l.	0.04	0.02	b.d.l.	0.04	0.49	23.05	b.d.l.	b.d.l.	0.03	38.38	b.d.l.	38.52	100.56
	1 / 4 .		0.01	0.01	0.01	b.d.l.	0.02	0.51	23.19	b.d.l.	b.d.l.	0.02	38.36	b.d.l.	38.62	100.73
BAR_D_11	1 / 1 .		0.01	0.02	b.d.l.	b.d.l.	0.03	0.46	22.91	b.d.l.	b.d.l.	0.01	38.25	b.d.l.	38.56	100.23
	1 / 2 .		0.01	0.02	b.d.l.	b.d.l.	0.01	0.48	22.98	b.d.l.	b.d.l.	0.01	38.41	b.d.l.	38.55	100.40
	1 / 3 .		b.d.l.	0.03	0.01	b.d.l.	0.02	0.49	22.81	b.d.l.	b.d.l.	b.d.l.	38.28	b.d.l.	38.49	100.13
	1 / 4 .		0.01	0.04	0.01	b.d.l.	0.02	0.49	23.09	b.d.l.	b.d.l.	b.d.l.	38.31	b.d.l.	38.51	100.47
	1 / 5 .		0.01	0.06	0.01	b.d.l.	0.02	0.48	22.65	b.d.l.	b.d.l.	0.02	38.25	b.d.l.	38.55	99.99
	1 / 6 .		b.d.l.	0.08	0.03	b.d.l.	0.04	0.47	22.81	b.d.l.	b.d.l.	0.01	38.24	b.d.l.	38.46	100.16
BAR_D_12	1 / 1 .		0.01	0.03	0.03	b.d.l.	0.31	0.48	22.83	b.d.l.	b.d.l.	b.d.l.	38.28	b.d.l.	38.60	100.54
	1 / 2 .		b.d.l.	0.04	b.d.l.	b.d.l.	0.07	0.47	23.05	b.d.l.	b.d.l.	b.d.l.	38.14	b.d.l.	38.86	100.63
	1 / 3 .		b.d.l.	0.16	0.05	b.d.l.	0.60	0.48	23.28	b.d.l.	b.d.l.	0.02	38.30	b.d.l.	38.27	101.18
	1 / 4 .		b.d.l.	0.04	b.d.l.	b.d.l.	0.05	0.47	23.03	b.d.l.	b.d.l.	b.d.l.	38.05	b.d.l.	38.80	100.40
	1 / 5 .		b.d.l.	0.04	0.01	b.d.l.	0.05	0.44	22.86	b.d.l.	b.d.l.	0.01	38.37	b.d.l.	38.75	100.49
	1 / 6 .		b.d.l.	0.07	0.03	b.d.l.	0.02	0.46	22.94	b.d.l.	b.d.l.	0.01	38.07	b.d.l.	38.66	100.21
	1 / 7 .		b.d.l.	0.04	b.d.l.	b.d.l.	0.02	0.46	23.02	b.d.l.	b.d.l.	b.d.l.	38.29	b.d.l.	38.69	100.49
BAR_D_13	1 / 1 .		b.d.l.	0.04	b.d.l.	b.d.l.	0.05	0.50	22.90	b.d.l.	b.d.l.	b.d.l.	38.26	b.d.l.	38.91	100.60
	1 / 2 .		0.02	0.02	b.d.l.	b.d.l.	0.01	0.47	22.78	b.d.l.	b.d.l.	b.d.l.	38.77	b.d.l.	39.27	101.31
	1 / 3 .		b.d.l.	0.03	b.d.l.	b.d.l.	0.10	0.50	22.86	b.d.l.	b.d.l.	0.01	38.50	b.d.l.	39.13	101.09
	1 / 4 .		b.d.l.	0.49	0.01	b.d.l.	0.02	0.48	22.86	b.d.l.	b.d.l.	0.02	37.92	b.d.l.	39.76	101.54
	1 / 5 .		0.01	0.06	0.01	b.d.l.	b.d.l.	0.46	22.96	b.d.l.	b.d.l.	0.01	38.35	b.d.l.	38.97	100.82
	1 / 6 .		b.d.l.	0.03	0.02	b.d.l.	0.03	0.50	23.07	b.d.l.	b.d.l.	0.02	38.16	b.d.l.	38.94	100.77
	1 / 7 .		0.01	0.05	0.03	0.02	0.02	0.51	22.87	b.d.l.	b.d.l.	b.d.l.	37.97	b.d.l.	38.90	100.35
	1 / 8 .		b.d.l.	0.05	0.04	0.01	0.01	0.52	22.75	b.d.l.	b.d.l.	0.02	38.14	b.d.l.	38.90	100.42
	1 / 9 .		0.01	0.07	0.01	b.d.l.	0.01	0.45	22.87	b.d.l.	b.d.l.	0.01	38.13	b.d.l.	39.13	100.68
BAR_D_14	1 / 1 .		b.d.l.	0.03	0.01	0.01	0.04	0.47	23.04	b.d.l.	b.d.l.	b.d.l.	38.03	b.d.l.	39.09	100.70
	1 / 2 .		0.01	0.02	0.02	0.01	0.02	0.49	22.73	b.d.l.	b.d.l.	b.d.l.	38.28	b.d.l.	39.05	100.58
	1 / 3 .		b.d.l.	0.01	b.d.l.	0.01	0.08	0.48	23.06	b.d.l.	b.d.l.	b.d.l.	38.57	b.d.l.	39.08	101.31
	1 / 4 .		b.d.l.	0.03	0.01	b.d.l.	0.02	0.48	23.08	b.d.l.	b.d.l.	b.d.l.	38.25	b.d.l.	38.91	100.74
	1 / 5 .		b.d.l.	0.02	0.01	b.d.l.	0.02	0.49	22.98	b.d.l.	b.d.l.	b.d.l.	38.13	b.d.l.	38.94	100.58
	1 / 6 .		0.01	0.06	0.02	b.d.l.	0.01	0.50	22.91	b.d.l.	b.d.l.	b.d.l.	38.14	b.d.l.	39.02	100.68

BAR_D_15	1 / 1 .		b.d.l.	0.20	0.02	b.d.l.	0.01	0.48	22.61	b.d.l.	-0.01	0.02	37.97	0.01	38.81	100.10
	1 / 2 .		b.d.l.	0.04	0.02	b.d.l.	b.d.l.	0.49	22.86	b.d.l.	b.d.l.	b.d.l.	38.09	b.d.l.	38.77	100.26
	1 / 3 .		b.d.l.	0.01	0.01	b.d.l.	0.02	0.48	23.04	b.d.l.	0.02	b.d.l.	38.06	b.d.l.	38.69	100.30
	1 / 4 .		b.d.l.	0.02	0.01	0.01	0.02	0.49	22.99	b.d.l.	0.01	b.d.l.	38.21	b.d.l.	38.58	100.32
	1 / 5 .		0.02	0.03	0.01	0.01	0.03	0.50	23.22	b.d.l.	b.d.l.	0.01	38.18	b.d.l.	38.63	100.63
	1 / 6 .		0.01	0.05	0.02	b.d.l.	0.01	0.47	22.86	b.d.l.	b.d.l.	0.01	37.93	0.09	38.79	100.24
BAR_D_16	1 / 1 .		0.01	0.04	0.01	0.01	0.05	0.47	22.70	b.d.l.	0.01	b.d.l.	38.21	0.01	39.21	100.73
	1 / 2 .		b.d.l.	0.05	0.01	b.d.l.	0.09	0.49	23.16	b.d.l.	0.03	b.d.l.	38.11	b.d.l.	38.83	100.70
	1 / 4 .		b.d.l.	0.05	0.03	b.d.l.	0.06	0.50	22.94	b.d.l.	0.03	b.d.l.	38.07	b.d.l.	38.82	100.47
	1 / 5 .		b.d.l.	0.11	b.d.l.	0.01	0.06	0.49	22.53	b.d.l.	0.02	0.07	37.50	0.34	39.38	100.50
	1 / 6 .		b.d.l.	0.06	0.01	b.d.l.	0.03	0.49	23.03	b.d.l.	b.d.l.	0.01	38.08	b.d.l.	38.82	100.49
	1 / 7 .		0.01	0.04	0.01	b.d.l.	0.03	0.50	22.84	b.d.l.	b.d.l.	0.01	37.68	0.01	38.60	99.73

Table A.17. EPMA analysis of olivine in Barwell Inclusion D

Site	Point	Mineral	Element										Total
			Na_2O	SiO_2	MgO	Al_2O_3	CaO	TiO_2	Cr_2O_3	MnO	FeO	NiO	
BAR_D_05	1 / 1 .	High-Ca Pyroxene	0.61	54.29	16.84	0.50	22.08	0.50	0.85	0.26	5.16	0.01	101.09
	1 / 2 .		1.03	55.08	15.25	2.70	18.90	0.41	0.70	0.21	4.47	b.d.l.	98.74
	1 / 3 .		0.55	53.74	16.57	0.51	22.08	0.46	0.81	0.25	4.95	b.d.l.	99.91
	1 / 4 .		0.62	54.10	16.84	0.49	22.23	0.44	0.82	0.25	4.99	b.d.l.	100.78
	1 / 5 .		0.59	54.12	16.87	0.50	21.81	0.45	0.82	0.22	5.25	b.d.l.	100.62
	1 / 6 .		0.63	54.05	16.67	0.56	21.94	0.53	0.88	0.24	5.31	b.d.l.	100.79
	1 / 7 .		0.69	54.19	16.95	0.64	21.71	0.46	0.83	0.24	5.50	b.d.l.	101.19
BAR_D_06	1 / 2 .		0.57	54.04	16.72	0.48	21.84	0.53	0.86	0.25	5.24	0.02	100.53
	1 / 3 .		0.59	53.57	16.83	0.49	21.92	0.61	0.86	0.25	5.26	0.01	100.39
	1 / 4 .		0.58	53.86	16.60	0.48	21.93	0.47	0.89	0.26	5.24	0.01	100.30
	1 / 5 .		0.58	54.10	16.64	0.49	22.14	0.47	0.83	0.23	5.02	b.d.l.	100.50
BAR_D_07	1 / 1 .		0.61	53.90	16.64	0.49	21.95	0.48	0.87	0.25	5.26	0.01	100.45
	1 / 2 .		0.63	53.95	16.65	0.53	21.84	0.46	0.87	0.25	5.33	0.02	100.52
	1 / 3 .		0.48	54.02	17.15	0.47	21.70	0.50	0.81	0.25	5.16	0.03	100.57
	1 / 4 .		0.61	53.90	16.58	0.48	21.84	0.57	0.85	0.25	5.21	b.d.l.	100.27
	1 / 5 .		0.63	53.82	16.66	0.52	21.92	0.49	0.91	0.24	5.29	b.d.l.	100.48
	1 / 6 .		0.61	53.91	16.61	0.51	21.90	0.46	0.86	0.23	5.29	b.d.l.	100.39
	1 / 7 .		0.62	54.03	16.65	0.54	22.06	0.51	0.86	0.24	5.05	b.d.l.	100.55
BAR_D_08	1 / 1 .		0.64	54.07	16.61	0.52	21.90	0.52	0.85	0.22	5.14	0.01	100.47
	1 / 2 .		0.61	53.95	17.06	0.53	21.59	0.47	0.83	0.24	5.38	b.d.l.	100.66
	1 / 3 .		0.78	54.57	16.25	1.53	20.80	0.41	0.69	0.22	4.67	b.d.l.	99.92
	1 / 4 .		0.63	53.99	16.78	0.44	22.07	0.43	0.82	0.24	5.18	0.01	100.58
	1 / 5 .		0.56	53.98	16.96	0.52	21.99	0.49	0.82	0.25	5.18	0.01	100.76
	1 / 6 .		0.60	53.97	16.68	0.56	21.93	0.48	0.86	0.23	5.11	b.d.l.	100.41
	1 / 7 .		0.55	53.87	17.45	0.49	21.36	0.46	0.81	0.24	5.52	b.d.l.	100.75
BAR_D_09	1 / 1 .		0.59	53.96	16.58	0.50	22.33	0.45	0.81	0.24	4.93	b.d.l.	100.36
	1 / 2 .		0.71	54.10	16.49	0.76	21.87	0.48	0.83	0.22	5.14	b.d.l.	100.59
	1 / 3 .		0.50	50.98	18.67	0.44	19.56	0.42	0.73	0.26	7.11	b.d.l.	98.66
	1 / 4 .		0.57	54.02	16.62	0.47	22.13	0.44	0.85	0.23	5.14	b.d.l.	100.48
	1 / 6 .		0.59	53.91	16.64	0.51	21.91	0.48	0.85	0.23	5.19	b.d.l.	100.30
	1 / 7 .		1.10	54.72	15.92	1.75	21.24	0.45	0.80	0.22	5.12	0.01	101.34
	1 / 9 .		0.87	53.68	17.75	1.10	20.59	0.44	0.76	0.24	5.72	0.01	101.14
	1 / 10 .		0.98	55.17	15.19	2.45	20.15	0.42	0.68	0.21	4.27	b.d.l.	99.53
BAR_D_10	1 / 1 .		0.62	53.48	16.47	0.92	21.57	0.46	0.72	0.21	4.67	b.d.l.	99.12
	1 / 2 .		0.66	54.05	16.58	0.73	21.93	0.45	0.79	0.25	4.99	0.01	100.45
	1 / 3 .		0.53	54.04	17.32	0.49	21.76	0.45	0.80	0.24	5.19	b.d.l.	100.81
	1 / 4 .		0.57	54.05	16.68	0.50	21.96	0.50	0.83	0.27	5.18	b.d.l.	100.52
	1 / 5 .		0.60	53.97	16.75	0.47	22.00	0.45	0.84	0.24	5.21	b.d.l.	100.53
	1 / 7 .		0.60	54.01	16.69	0.50	22.14	0.45	0.82	0.22	5.09	b.d.l.	100.50
	1 / 11 .		0.58	53.86	16.68	b.d.l.	21.69	0.44	0.81	0.24	5.23	0.01	100.12

Table A.18. EPMA analysis of high-Ca pyroxene in Barwell Inclusion D

Site	Point	Mineral	Element										Total
			Na_2O	SiO_2	MgO	Al_2O_3	CaO	TiO_2	Cr_2O_3	MnO	FeO	NiO	
BAR_D_06	1 / 1 .	Low-Ca Pyroxene	0.02	55.56	29.04	0.18	0.85	0.21	0.13	0.49	13.97	b.d.l.	100.44
BAR_D_09	1 / 5 .		0.14	54.69	29.42	0.65	0.63	0.17	0.06	0.48	14.47	b.d.l.	100.71
BAR_D_10	1 / 6 .		0.03	55.52	29.40	0.14	0.64	0.19	0.10	0.48	14.33	0.01	100.83
	1 / 8 .		0.04	55.59	29.38	0.16	0.60	0.19	0.09	0.51	14.24	b.d.l.	100.81
	1 / 9 .		0.02	55.96	29.15	0.16	0.60	0.20	0.12	0.51	14.17	b.d.l.	100.86
	1 / 10 .		0.02	55.32	29.38	0.13	0.76	0.21	0.10	0.51	14.17	b.d.l.	100.59

Table A.19. EPMA analysis of low-Ca pyroxene in Barwell Inclusion D

Site	Point	Mineral	Element													Total
			Na_2O	SiO_2	P_2O_5	K_2O	CaO	TiO_2	V_2O3	Cr_2O_3	MnO	FeO	CoO	NiO	Al_2O_3	MgO	
B3_clastD_28	1 / 1 .	Plagioclase	10.38	65.60	-0.01	0.79	2.32	0.03	b.d.l.	0.02	0.02	0.53	b.d.l.	0.01	21.48	0.03	101.20
B3_clastD_29	1 / 1 .		10.27	65.71	0.01	1.01	2.25	0.04	0.01	0.01	b.d.l.	0.61	b.d.l.	0.01	21.35	0.08	101.38
B3_clastD_30	1 / 1 .		10.47	66.19	0.01	1.14	2.00	0.03	b.d.l.	0.01	0.01	0.48	b.d.l.	0.01	21.28	0.01	101.63
B3_clastD_31	1 / 1 .		10.13	65.73	0.02	1.01	2.27	0.06	b.d.l.	0.02	0.02	0.70	b.d.l.	b.d.l.	21.37	0.27	101.60
B3_clastD_32	1 / 1 .		9.97	64.97	0.01	1.15	2.32	0.01	b.d.l.	0.02	0.01	0.70	b.d.l.	0.02	21.31	0.21	100.69
B3_clastD_33	1 / 1 .		10.14	65.49	0.03	1.17	2.26	0.05	b.d.l.	0.11	0.01	0.49	b.d.l.	0.01	21.44	0.01	101.19
B3_clastD_34	1 / 1 .		9.94	65.12	0.03	1.21	2.34	0.03	0.01	b.d.l.	0.03	0.90	b.d.l.	b.d.l.	21.33	0.47	101.38
B3_clastD_35	1 / 1 .		10.32	66.09	0.03	1.26	1.75	0.01	0.01	0.02	0.02	0.57	b.d.l.	b.d.l.	21.08	0.03	101.16
B3_clastD_36	1 / 1 .		9.58	62.23	0.02	1.02	2.20	0.03	0.01	b.d.l.	0.05	1.48	b.d.l.	b.d.l.	20.70	1.50	98.80
B3_clastD_37	1 / 1 .		9.71	64.92	0.04	1.33	2.21	0.04	0.02	0.02	0.02	0.80	b.d.l.	0.02	20.97	0.32	100.39
B3_clastD_38	1 / 1 .		10.08	65.08	0.01	1.23	2.27	0.06	0.01	0.02	0.01	0.55	b.d.l.	b.d.l.	21.52	0.01	100.84
B3_clastD_39	1 / 1 .		9.93	65.16	0.01	1.27	2.28	0.05	b.d.l.	0.01	0.03	0.63	b.d.l.	b.d.l.	21.53	0.05	100.93
B3_clastD_40	1 / 1 .		9.87	64.05	0.03	1.00	2.24	0.02	b.d.l.	0.01	0.01	0.61	b.d.l.	0.02	21.55	0.24	99.65

Table A.20. EPMA analysis of plagioclase in Barwell Inclusion D

Site	Point	Mineral	Element													Total
			S	P	Ti	V	Cr	Mn	Fe	Co	Ni	Mg	Si	Cu	Zn	
BAR_D_21	1 / 1 .	Kamacite	b.d.l.	b.d.l.	b.d.l.	b.d.l.	0.06	0.02	93.65	0.90	4.61	b.d.l.	0.05	b.d.l.	b.d.l.	99.25
	1 / 2 .		b.d.l.	b.d.l.	0.01	b.d.l.	0.04	0.03	92.56	0.87	4.84	b.d.l.	0.01	b.d.l.	b.d.l.	98.33
	1 / 3 .		b.d.l.	b.d.l.	0.01	b.d.l.	0.04	0.02	92.60	0.89	4.81	b.d.l.	0.02	0.01	0.03	98.40
BAR_D_23a	1 / 3 .	Taenite	b.d.l.	b.d.l.	0.01	b.d.l.	0.07	0.02	82.26	0.74	14.94	0.09	0.16	0.06	b.d.l.	98.33
	1 / 5 .		0.01	b.d.l.	b.d.l.	0.01	0.09	0.01	83.46	0.70	14.03	0.08	0.23	0.05	b.d.l.	98.62
	1 / 6 .	Kamacite	b.d.l.	b.d.l.	0.01	b.d.l.	0.07	0.02	93.84	0.86	3.65	b.d.l.	0.12	b.d.l.	b.d.l.	98.53
BAR_D_25	1 / 1 .		b.d.l.	b.d.l.	b.d.l.	0.01	0.09	0.02	91.49	0.85	5.49	0.01	0.05	0.04	b.d.l.	98.03
	1 / 2 .		0.01	b.d.l.	0.01	b.d.l.	0.09	0.02	93.45	0.87	4.59	0.02	0.04	b.d.l.	0.02	99.09
	1 / 3 .		0.01	b.d.l.	0.01	b.d.l.	0.08	0.02	93.95	0.89	3.62	0.07	0.17	b.d.l.	0.01	98.79
	1 / 6 .	Taenite	0.01	b.d.l.	b.d.l.	b.d.l.	0.06	0.01	83.20	0.72	14.51	0.01	0.03	0.04	b.d.l.	98.57
BAR_D_25a	1 / 2 .	Kamacite	b.d.l.	b.d.l.	b.d.l.	0.02	0.08	0.02	93.64	0.87	4.49	0.01	0.08	0.02	b.d.l.	99.22
	1 / 3 .		0.01	b.d.l.	b.d.l.	0.01	0.09	0.03	93.89	0.89	3.71	0.10	0.27	0.01	b.d.l.	98.98
	1 / 4 .	Taenite	0.01	b.d.l.	0.01	b.d.l.	0.07	0.03	83.15	0.70	13.95	0.02	0.17	0.05	b.d.l.	98.10
	1 / 6 .		0.01	b.d.l.	0.01	b.d.l.	0.06	0.01	83.54	0.74	14.66	b.d.l.	0.06	0.07	0.01	99.16
	1 / 9 .		b.d.l.	b.d.l.	0.01	b.d.l.	0.09	0.03	80.91	0.70	16.29	0.02	0.05	0.06	b.d.l.	98.13
	1 / 10 .		0.01	b.d.l.	b.d.l.	b.d.l.	0.09	0.03	83.29	0.70	13.89	0.01	0.08	0.06	b.d.l.	98.12
	1 / 11 .		b.d.l.	b.d.l.	0.01	b.d.l.	0.09	0.03	83.44	0.72	14.08	0.03	0.09	0.07	b.d.l.	98.54
BAR_D_27	1 / 4 .	Kamacite	b.d.l.	b.d.l.	0.02	b.d.l.	0.07	0.02	94.78	0.91	3.40	0.05	0.07	b.d.l.	b.d.l.	99.33
	1 / 5 .	Taenite	b.d.l.	b.d.l.	b.d.l.	0.01	0.06	0.02	83.64	0.70	14.26	0.02	0.05	0.06	b.d.l.	98.77
BAR_D_30	1 / 1 .		0.01	b.d.l.	b.d.l.	b.d.l.	0.04	b.d.l.	83.67	0.73	14.60	0.01	0.05	0.05	0.02	99.17
	1 / 2 .		0.01	b.d.l.	b.d.l.	b.d.l.	0.04	0.02	83.08	0.73	14.46	0.02	0.05	0.05	0.01	98.46
	1 / 3 .		0.01	b.d.l.	b.d.l.	b.d.l.	0.05	0.01	83.97	0.76	13.48	0.02	0.04	0.07	b.d.l.	98.41
	1 / 4 .		0.02	b.d.l.	0.01	b.d.l.	0.04	0.02	84.43	0.69	13.54	0.01	0.04	0.04	0.01	98.84
	1 / 5 .		0.01	b.d.l.	b.d.l.	b.d.l.	0.05	0.03	82.65	0.68	15.05	b.d.l.	0.04	0.06	b.d.l.	98.52
BAR_D_32	1 / 2 .	Kamacite	b.d.l.	b.d.l.	b.d.l.	0.01	0.04	0.03	94.29	0.84	4.02	0.02	0.04	0.01	b.d.l.	99.27
	1 / 3 .		b.d.l.	b.d.l.	b.d.l.	0.01	0.07	0.01	93.55	0.87	3.85	0.01	0.21	b.d.l.	b.d.l.	98.58
	1 / 4 .		0.01	b.d.l.	b.d.l.	b.d.l.	0.05	b.d.l.	94.09	0.84	4.67	b.d.l.	0.04	0.02	b.d.l.	99.70
	1 / 5 .		0.01	b.d.l.	0.03	b.d.l.	0.05	0.01	92.66	0.83	4.76	0.02	0.17	0.01	b.d.l.	98.54
	1 / 6 .	Taenite	b.d.l.	b.d.l.	0.01	b.d.l.	0.05	0.01	73.74	0.53	25.12	0.01	0.04	0.10	b.d.l.	99.57
	1 / 7 .		0.01	b.d.l.	0.01	b.d.l.	0.06	0.01	84.26	0.69	13.70	0.01	0.07	0.05	0.02	98.87
	1 / 8 .		b.d.l.	b.d.l.	b.d.l.	b.d.l.	0.10	0.01	84.30	0.68	13.88	b.d.l.	0.06	0.05	0.02	99.08
	1 / 9 .		0.02	b.d.l.	0.01	b.d.l.	0.09	0.02	84.17	0.67	13.96	b.d.l.	0.07	0.07	b.d.l.	99.06
BAR_D_34	1 / 3 .		0.01	b.d.l.	b.d.l.	0.01	0.11	0.03	84.61	0.71	14.11	b.d.l.	0.04	0.05	b.d.l.	99.64
	1 / 4 .		b.d.l.	b.d.l.	0.01	b.d.l.	0.06	0.01	83.47	0.72	14.49	0.05	0.07	0.06	b.d.l.	98.90
	1 / 5 .	Kamacite	0.01	b.d.l.	b.d.l.	b.d.l.	0.04	0.02	93.21	0.84	4.72	0.02	0.04	0.02	b.d.l.	98.87
BAR_D_36	1 / 4 .		b.d.l.	b.d.l.	0.01	b.d.l.	0.05	0.01	83.64	0.69	13.98	b.d.l.	0.05	0.05	b.d.l.	98.48
	1 / 5 .		b.d.l.	b.d.l.	0.01	b.d.l.	0.05	b.d.l.	83.69	0.70	13.92	0.02	0.02	0.06	b.d.l.	98.43
	1 / 7 .		b.d.l.	b.d.l.	b.d.l.	b.d.l.	0.06	0.02	83.82	0.68	13.45	0.02	0.06	0.08	b.d.l.	98.17
	1 / 8 .		b.d.l.	b.d.l.	b.d.l.	b.d.l.	0.07	0.01	82.83	0.70	14.48	0.01	0.05	0.03	b.d.l.	98.15
BAR_D_36a	1 / 1 .		0.01	b.d.l.	0.01	0.01	0.05	0.01	84.01	0.69	14.05	0.01	0.07	0.05	b.d.l.	98.93
	1 / 2 .		0.01	b.d.l.	0.01	0.01	0.07	0.02	88.61	0.74	9.44	0.00	0.04	0.01	b.d.l.	98.95
	1 / 3 .		0.01	b.d.l.	0.01	0.01	0.07	0.03	83.90	0.70	13.96	0.01	0.06	0.04	0.01	98.79
	1 / 4 .		0.01	b.d.l.	0.01	b.d.l.	0.06	0.03	84.00	0.72	14.02	0.02	0.09	0.07	b.d.l.	98.97

	1 / 5 .	Taenite	b.d.l.	b.d.l.	0.01	b.d.l.	0.07	0.02	83.64	0.71	14.33	0.02	0.07	0.06	0.01	98.95
BAR_D_38	1 / 1 .		0.01	b.d.l.	b.d.l.	0.01	0.21	0.01	84.32	0.70	14.51	0.02	0.03	0.06	b.d.l.	99.82
	1 / 2 .		b.d.l.	b.d.l.	b.d.l.	b.d.l.	0.10	0.03	84.23	0.71	14.45	0.01	0.01	0.04	b.d.l.	99.55
	1 / 4 .		0.01	b.d.l.	0.02	b.d.l.	0.05	0.01	81.73	0.70	16.74	0.04	0.05	0.05	0.03	99.39
	1 / 5 .		b.d.l.	b.d.l.	0.03	b.d.l.	0.05	0.01	82.49	0.70	16.49	0.02	0.02	0.05	b.d.l.	99.85
BAR_D_40	1 / 1 .		0.01	b.d.l.	b.d.l.	b.d.l.	0.06	0.00	82.40	0.73	15.17	0.01	0.05	0.07	b.d.l.	98.45
	1 / 2 .		0.01	b.d.l.	0.01	b.d.l.	0.17	0.00	84.34	0.72	14.26	b.d.l.	0.05	0.04	b.d.l.	99.58
	1 / 3 .		0.01	b.d.l.	0.01	b.d.l.	0.05	0.04	83.25	0.74	14.78	0.02	0.06	0.06	b.d.l.	99.00
	1 / 4 .		b.d.l.	b.d.l.	b.d.l.	b.d.l.	0.04	0.01	86.58	0.73	11.98	0.01	0.05	0.04	b.d.l.	99.43
	1 / 5 .		b.d.l.	b.d.l.	b.d.l.	b.d.l.	0.04	0.01	91.18	0.81	7.50	b.d.l.	0.04	0.02	b.d.l.	99.58
BAR_D_43	1 / 1 .	Kamacite	b.d.l.	b.d.l.	0.09	b.d.l.	0.06	0.01	94.09	0.86	4.87	0.01	0.02	b.d.l.	b.d.l.	100.00
	1 / 2 .		b.d.l.	b.d.l.	0.03	b.d.l.	0.06	-0.01	94.10	0.88	4.74	0.01	0.03	b.d.l.	b.d.l.	99.82
	1 / 3 .	Taenite	b.d.l.	b.d.l.	0.01	b.d.l.	0.04	0.01	86.04	0.72	12.37	b.d.l.	0.05	0.04	0.01	99.27
	1 / 4 .		b.d.l.	b.d.l.	0.01	b.d.l.	0.07	0.03	51.81	0.15	47.32	0.02	0.03	0.30	b.d.l.	99.71

Table A.21. EPMA analysis of FeNi metal in Barwell Inclusion D

Site	Point	Mineral	Element													Total
			K_2O	CaO	TiO_2	V_2O3	Cr_2O_3	MnO	FeO	CoO	NiO	Na_2O	MgO	Al_2O_3	SiO_2	
BAR_B_bulk_01	1 / 1 .		b.d.l.	0.02	0.02	b.d.l.	b.d.l.	0.50	23.30	b.d.l.	b.d.l.	b.d.l.	38.98	b.d.l.	38.76	101.56
	1 / 2 .		b.d.l.	0.02	0.02	b.d.l.	b.d.l.	0.49	22.99	b.d.l.	b.d.l.	0.01	38.87	b.d.l.	38.83	101.16
	1 / 3 .		b.d.l.	0.02	0.02	b.d.l.	b.d.l.	0.49	23.07	b.d.l.	b.d.l.	0.01	38.85	0.03	38.67	101.14
	1 / 4 .		b.d.l.	0.02	b.d.l.	b.d.l.	b.d.l.	0.49	23.23	b.d.l.	0.03	b.d.l.	38.73	0.02	38.72	101.19
	1 / 5 .		b.d.l.	0.02	0.01	b.d.l.	b.d.l.	0.51	23.25	b.d.l.	b.d.l.	b.d.l.	38.93	0.03	38.64	101.32
	1 / 6 .		b.d.l.	0.02	0.02	b.d.l.	b.d.l.	0.49	23.07	b.d.l.	b.d.l.	b.d.l.	38.91	0.01	38.76	101.24
	1 / 7 .		b.d.l.	0.02	0.02	b.d.l.	b.d.l.	0.48	23.06	b.d.l.	b.d.l.	0.01	38.98	b.d.l.	38.86	101.43
BAR_B_bulk_02	1 / 1 .		b.d.l.	0.01	0.01	b.d.l.	b.d.l.	0.51	23.16	b.d.l.	b.d.l.	0.01	38.87	0.01	38.63	101.15
	1 / 2 .		b.d.l.	0.01	0.01	0.01	b.d.l.	0.50	23.29	b.d.l.	b.d.l.	b.d.l.	38.69	0.01	38.84	101.32
	1 / 3 .		b.d.l.	b.d.l.	0.01	b.d.l.	b.d.l.	0.51	23.03	b.d.l.	b.d.l.	b.d.l.	38.85	b.d.l.	38.67	101.01
	1 / 4 .		b.d.l.	0.01	b.d.l.	0.01	b.d.l.	0.49	23.00	b.d.l.	b.d.l.	b.d.l.	38.95	0.02	38.56	101.04
	1 / 5 .		b.d.l.	b.d.l.	b.d.l.	b.d.l.	b.d.l.	0.52	23.20	b.d.l.	b.d.l.	b.d.l.	38.73	0.01	38.82	101.25
	1 / 6 .		b.d.l.	0.01	0.03	b.d.l.	b.d.l.	0.49	23.27	b.d.l.	b.d.l.	b.d.l.	38.80	b.d.l.	38.90	101.45
BAR_B_bulk_03	1 / 1 .		0.02	0.03	b.d.l.	b.d.l.	b.d.l.	0.48	23.22	b.d.l.	b.d.l.	0.02	39.08	0.01	38.74	101.57
	1 / 2 .		b.d.l.	0.01	0.01	b.d.l.	0.02	0.50	23.19	b.d.l.	b.d.l.	b.d.l.	38.67	0.02	38.51	100.92
	1 / 3 .		b.d.l.	0.01	0.01	b.d.l.	0.04	0.51	23.36	b.d.l.	b.d.l.	0.01	38.85	b.d.l.	38.61	101.38
	1 / 4 .		b.d.l.	0.03	0.03	b.d.l.	0.02	0.49	23.15	b.d.l.	b.d.l.	b.d.l.	38.56	0.01	38.46	100.72
	1 / 5 .		0.02	0.02	b.d.l.	b.d.l.	b.d.l.	0.47	23.30	b.d.l.	b.d.l.	0.02	38.70	b.d.l.	38.84	101.34
	1 / 6 .		b.d.l.	0.01	0.01	b.d.l.	b.d.l.	0.51	23.18	b.d.l.	b.d.l.	0.01	38.67	0.02	38.66	101.09
	1 / 7 .		b.d.l.	0.01	0.02	b.d.l.	b.d.l.	0.47	23.14	b.d.l.	b.d.l.	0.01	38.70	b.d.l.	38.83	101.14
	1 / 8 .		b.d.l.	0.02	0.01	b.d.l.	b.d.l.	0.50	23.18	b.d.l.	b.d.l.	b.d.l.	38.65	0.02	38.49	100.83
BAR_B_bulk_04	1 / 1 .		b.d.l.	0.03	0.01	b.d.l.	b.d.l.	0.51	23.21	b.d.l.	b.d.l.	0.01	38.74	0.01	38.66	101.15
	1 / 2 .		b.d.l.	0.02	0.01	b.d.l.	b.d.l.	0.48	22.94	b.d.l.	b.d.l.	0.01	38.84	0.02	38.59	100.90
	1 / 3 .		b.d.l.	0.02	b.d.l.	0.01	b.d.l.	0.49	22.94	b.d.l.	b.d.l.	0.01	38.72	0.01	38.68	100.83
	1 / 4 .		b.d.l.	0.02	b.d.l.	b.d.l.	0.01	0.50	23.03	b.d.l.	b.d.l.	b.d.l.	38.88	b.d.l.	38.81	101.25
	1 / 5 .		b.d.l.	0.01	b.d.l.	0.01	b.d.l.	0.51	23.05	b.d.l.	b.d.l.	b.d.l.	38.74	0.03	38.69	100.98
	1 / 6 .		b.d.l.	0.01	b.d.l.	0.01	b.d.l.	0.51	22.80	b.d.l.	b.d.l.	b.d.l.	38.62	0.01	38.48	100.40
	1 / 7 .		0.01	0.03	b.d.l.	b.d.l.	b.d.l.	0.51	22.96	b.d.l.	b.d.l.	0.01	38.60	b.d.l.	38.77	100.87
BAR_B_bulk_05	1 / 1 .		b.d.l.	0.01	b.d.l.	b.d.l.	b.d.l.	0.52	23.20	b.d.l.	b.d.l.	0.01	38.92	0.02	38.68	101.31
	1 / 2 .		0.02	0.01	b.d.l.	b.d.l.	b.d.l.	0.49	23.10	b.d.l.	b.d.l.	b.d.l.	38.85	b.d.l.	38.91	101.35
	1 / 3 .		b.d.l.	0.04	0.02	b.d.l.	0.02	0.50	23.16	b.d.l.	b.d.l.	0.03	38.90	0.01	38.75	101.40
	1 / 4 .		0.01	0.02	0.00	b.d.l.	b.d.l.	0.49	23.16	b.d.l.	b.d.l.	0.01	38.85	0.02	38.58	101.11
	1 / 5 .		0.01	0.03	0.01	b.d.l.	b.d.l.	0.50	23.20	b.d.l.	b.d.l.	0.01	39.09	0.04	38.58	101.42
	1 / 6 .		b.d.l.	b.d.l.	b.d.l.	b.d.l.	b.d.l.	0.47	23.02	b.d.l.	b.d.l.	b.d.l.	38.92	0.01	38.65	101.04
	1 / 7 .		b.d.l.	0.02	0.01	b.d.l.	b.d.l.	0.50	22.98	b.d.l.	b.d.l.	b.d.l.	38.96	0.01	38.70	101.14
BAR_B_bulk_06	1 / 1 .		b.d.l.	0.02	0.04	b.d.l.	0.02	0.48	23.17	b.d.l.	b.d.l.	b.d.l.	38.51	0.03	38.76	101.01
	1 / 2 .		b.d.l.	0.02	0.03	0.01	0.02	0.52	23.32	b.d.l.	b.d.l.	b.d.l.	38.63	0.03	38.70	101.24
	1 / 3 .		0.01	0.03	0.02	b.d.l.	0.01	0.49	23.32	b.d.l.	b.d.l.	b.d.l.	38.65	b.d.l.	38.84	101.35
	1 / 4 .		b.d.l.	b.d.l.	0.04	0.01	0.02	0.47	23.18	b.d.l.	b.d.l.	0.01	38.57	0.01	38.73	101.05
	1 / 5 .		b.d.l.	0.04	0.03	b.d.l.	0.02	0.50	23.26	b.d.l.	b.d.l.	b.d.l.	38.73	b.d.l.	38.87	101.43
	1 / 6 .		0.01	0.03	0.02	b.d.l.	0.05	0.51	23.14	b.d.l.	b.d.l.	b.d.l.	38.67	0.01	38.85	101.26
	1 / 7 .		b.d.l.	0.02	0.08	b.d.l.	0.11	0.48	23.07	b.d.l.	b.d.l.	b.d.l.	38.75	0.03	38.66	101.14
	1 / 1 .		b.d.l.	0.02	0.02	b.d.l.	b.d.l.	0.47	23.08	b.d.l.	b.d.l.	b.d.l.	38.54	b.d.l.	38.56	100.65
	1 / 2 .	Olivine	b.d.l.	0.02	0.01	b.d.l.	b.d.l.	0.49	23.07	b.d.l.	b.d.l.	b.d.l.	38.63	0.01	38.47	100.66

BAR_C_BULK_01	1 / 3 .	b.d.l.	0.02	0.01	b.d.l.	b.d.l.	0.47	23.26	b.d.l.	0.01	0.01	38.76	0.01	38.38	100.88
	1 / 4 .	b.d.l.	0.02	0.01	b.d.l.	b.d.l.	0.48	22.99	b.d.l.	b.d.l.	b.d.l.	38.60	0.01	38.45	100.56
	1 / 5 .	b.d.l.	0.02	0.01	0.01	0.02	0.48	23.26	b.d.l.	0.01	b.d.l.	38.50	0.02	38.44	100.72
	1 / 6 .	b.d.l.	0.02	0.01	0.02	b.d.l.	0.51	23.29	b.d.l.	0.02	b.d.l.	38.37	0.04	38.37	100.56
	1 / 7 .	b.d.l.	0.00	0.01	0.01	b.d.l.	0.47	23.16	b.d.l.	0.02	b.d.l.	38.33	0.01	38.46	100.47
BAR_C_BULK_02	1 / 1 .	b.d.l.	0.03	b.d.l.	b.d.l.	b.d.l.	0.46	22.96	b.d.l.	b.d.l.	0.01	38.25	0.01	38.45	100.11
	1 / 2 .	b.d.l.	0.02	b.d.l.	b.d.l.	b.d.l.	0.49	23.03	b.d.l.	0.01	0.01	38.28	0.01	38.46	100.30
	1 / 3 .	b.d.l.	0.01	b.d.l.	b.d.l.	b.d.l.	0.49	22.89	b.d.l.	b.d.l.	0.01	38.04	b.d.l.	38.16	99.57
	1 / 4 .	b.d.l.	0.01	0.01	b.d.l.	b.d.l.	0.51	22.87	b.d.l.	b.d.l.	b.d.l.	38.28	0.03	38.14	99.84
	1 / 5 .	b.d.l.	0.00	0.01	b.d.l.	b.d.l.	0.50	22.95	b.d.l.	b.d.l.	0.02	38.41	0.01	38.28	100.14
	1 / 6 .	b.d.l.	0.00	0.01	b.d.l.	b.d.l.	0.52	23.00	b.d.l.	b.d.l.	0.01	38.39	b.d.l.	38.15	100.07
	1 / 7 .	b.d.l.	0.00	b.d.l.	b.d.l.	b.d.l.	0.49	22.93	b.d.l.	b.d.l.	b.d.l.	38.09	0.01	38.34	99.84
BAR_C_BULK_03	1 / 1 .	b.d.l.	0.01	b.d.l.	0.01	b.d.l.	0.47	23.03	b.d.l.	0.01	b.d.l.	38.53	0.01	38.14	100.16
	1 / 2 .	b.d.l.	0.03	0.02	0.01	b.d.l.	0.47	23.16	b.d.l.	0.01	0.02	38.25	b.d.l.	38.25	100.19
	1 / 3 .	0.02	0.02	0.03	b.d.l.	b.d.l.	0.49	23.23	b.d.l.	0.01	0.01	38.57	0.01	38.19	100.55
	1 / 4 .	0.01	0.02	0.02	0.01	b.d.l.	0.49	23.20	b.d.l.	b.d.l.	b.d.l.	38.44	0.02	38.38	100.55
	1 / 5 .	b.d.l.	0.02	b.d.l.	b.d.l.	b.d.l.	0.50	23.40	b.d.l.	b.d.l.	0.02	38.68	0.03	38.25	100.89
	1 / 6 .	b.d.l.	0.03	0.01	b.d.l.	b.d.l.	0.49	23.33	b.d.l.	0.01	0.02	38.35	0.03	38.20	100.42
	1 / 7 .	b.d.l.	0.02	0.01	b.d.l.	b.d.l.	0.47	23.18	b.d.l.	b.d.l.	0.01	38.39	0.03	38.24	100.34
	1 / 8 .	b.d.l.	0.01	0.01	b.d.l.	b.d.l.	0.51	23.06	b.d.l.	0.02	0.01	38.52	0.01	38.21	100.32
BAR_C_BULK_04	1 / 1 .	b.d.l.	0.02	b.d.l.	0.01	0.03	0.49	23.27	b.d.l.	b.d.l.	b.d.l.	38.83	0.01	38.48	101.10
	1 / 2 .	b.d.l.	0.02	0.01	b.d.l.	b.d.l.	0.47	23.01	b.d.l.	0.01	b.d.l.	38.58	0.02	38.53	100.63
	1 / 3 .	b.d.l.	0.03	0.01	0.01	b.d.l.	0.50	23.18	b.d.l.	b.d.l.	b.d.l.	38.70	0.02	38.52	100.96
	1 / 4 .	b.d.l.	0.02	0.01	0.01	b.d.l.	0.46	23.14	b.d.l.	b.d.l.	0.01	38.63	0.01	38.44	100.70
	1 / 5 .	b.d.l.	0.01	0.01	b.d.l.	b.d.l.	0.50	23.10	b.d.l.	b.d.l.	0.01	38.66	0.02	38.32	100.63
	1 / 6 .	b.d.l.	0.02	0.03	b.d.l.	b.d.l.	0.50	23.10	b.d.l.	b.d.l.	b.d.l.	38.72	0.02	38.44	100.78
	1 / 7 .	b.d.l.	b.d.l.	0.02	b.d.l.	0.03	0.44	23.08	b.d.l.	b.d.l.	b.d.l.	38.56	0.01	38.58	100.65
	1 / 8 .	b.d.l.	0.01	0.01	b.d.l.	0.03	0.49	23.28	b.d.l.	b.d.l.	0.02	38.58	0.02	38.36	100.79
BAR_C_BULK_05	1 / 1 .	0.01	0.02	0.02	0.01	0.01	0.50	22.92	b.d.l.	b.d.l.	b.d.l.	38.53	0.02	38.55	100.54
	1 / 2 .	0.01	0.01	0.01	0.01	0.01	0.52	23.13	b.d.l.	b.d.l.	b.d.l.	38.54	0.01	38.40	100.63
	1 / 3 .	b.d.l.	0.02	b.d.l.	b.d.l.	0.00	0.51	22.94	b.d.l.	b.d.l.	0.02	38.44	0.01	38.43	100.34
	1 / 4 .	b.d.l.	0.02	b.d.l.	0.01	0.06	0.52	23.15	b.d.l.	b.d.l.	b.d.l.	38.23	0.01	38.04	100.03
	1 / 5 .	0.01	0.01	0.01	0.01	0.01	0.51	23.18	b.d.l.	b.d.l.	b.d.l.	38.41	0.03	38.19	100.32
	1 / 6 .	b.d.l.	0.03	0.02	b.d.l.	b.d.l.	0.47	23.09	b.d.l.	b.d.l.	0.01	38.60	0.01	38.41	100.60
	1 / 7 .	0.01	0.03	b.d.l.	b.d.l.	b.d.l.	0.49	23.04	b.d.l.	b.d.l.	0.02	38.50	b.d.l.	38.39	100.49
B3_bulk_02	1 / 1 .	b.d.l.	0.01	0.02	b.d.l.	0.01	0.49	23.15	b.d.l.	b.d.l.	b.d.l.	38.11	b.d.l.	38.61	100.41
	1 / 2 .	0.01	0.01	b.d.l.	0.01	b.d.l.	0.44	23.14	b.d.l.	b.d.l.	b.d.l.	38.18	b.d.l.	38.68	100.47
	1 / 3 .	b.d.l.	0.03	0.01	b.d.l.	0.05	0.48	23.05	b.d.l.	0.02	b.d.l.	38.25	b.d.l.	38.87	100.73
	1 / 4 .	b.d.l.	0.02	0.03	0.02	b.d.l.	0.46	22.96	b.d.l.	0.01	b.d.l.	38.46	b.d.l.	38.87	100.79
B3_bulk_04	1 / 1 .	b.d.l.	0.01	0.03	b.d.l.	0.01	0.49	23.26	b.d.l.	b.d.l.	b.d.l.	38.11	b.d.l.	38.60	100.52
	1 / 2 .	b.d.l.	0.01	0.02	b.d.l.	b.d.l.	0.49	23.06	b.d.l.	b.d.l.	0.02	38.31	b.d.l.	38.64	100.49
	1 / 3 .	b.d.l.	b.d.l.	0.00	b.d.l.	0.04	0.46	23.10	b.d.l.	b.d.l.	b.d.l.	38.04	b.d.l.	38.56	100.21

Table A.22. EPMA analysis of olivine in host Barwell

Site	Point	Mineral	Element										Total
			Na_2O	SiO_2	MgO	Al_2O_3	CaO	TiO_2	Cr_2O_3	MnO	FeO	NiO	
BAR_B_bulk_07	1 / 1 .		0.03	56.17	28.54	0.15	0.84	0.20	0.17	0.49	13.99	b.d.l.	100.56
	1 / 2 .		0.02	56.37	28.84	0.11	0.87	0.17	0.11	0.49	14.09	b.d.l.	101.05
	1 / 3 .		b.d.l.	56.03	28.82	0.16	0.91	0.19	0.12	0.48	14.16	b.d.l.	100.85
	1 / 4 .		0.02	56.05	28.69	0.11	1.04	0.14	0.12	0.48	13.98	b.d.l.	100.61
	1 / 5 .		0.02	56.34	28.60	0.14	0.91	0.17	0.12	0.46	13.95	b.d.l.	100.73
	1 / 6 .		0.03	55.97	28.69	0.17	0.88	0.20	0.11	0.50	14.06	b.d.l.	100.60
	1 / 7 .		b.d.l.	56.06	28.78	0.17	0.70	0.18	0.10	0.50	14.08	b.d.l.	100.55
BAR_B_bulk_08	1 / 1 .		0.02	55.93	28.57	0.17	0.98	0.20	0.12	0.47	14.93	0.11	101.49
	1 / 2 .		0.01	56.57	28.80	0.01	1.02	0.04	0.05	0.50	13.99	0.08	101.06
	1 / 3 .		0.02	56.26	28.57	0.14	1.03	0.17	0.13	0.52	13.92	0.05	100.80
	1 / 4 .		0.04	56.26	28.79	0.15	0.99	0.19	0.13	0.47	14.04	0.03	101.07
	1 / 5 .		0.01	56.53	28.81	0.17	0.95	0.17	0.13	0.50	13.93	0.04	101.24
BAR_B_bulk_09	1 / 1 .		b.d.l.	56.10	28.87	0.10	0.76	0.15	0.31	0.49	14.14	0.01	100.92
	1 / 2 .		0.02	56.63	28.71	0.13	0.92	0.16	0.33	0.48	13.97	0.02	101.36
	1 / 3 .		0.02	56.54	28.87	0.11	0.86	0.15	0.30	0.47	14.03	0.02	101.36
	1 / 4 .		0.01	56.26	28.41	0.13	1.03	0.15	0.20	0.50	14.01	0.01	100.70
	1 / 5 .		0.03	56.25	28.52	0.10	1.08	0.15	0.18	0.52	13.82	b.d.l.	100.64
	1 / 6 .		0.03	56.31	28.81	0.13	1.07	0.16	0.21	0.46	13.94	0.01	101.13
	1 / 7 .		b.d.l.	56.46	28.76	0.16	0.88	0.20	0.35	0.50	13.99	b.d.l.	101.28
	1 / 8 .		b.d.l.	56.59	28.85	0.12	1.02	0.14	0.16	0.46	14.03	b.d.l.	101.35
BAR_B_bulk_10	1 / 1 .		0.02	56.24	28.91	0.06	0.97	0.08	0.06	0.49	13.95	b.d.l.	100.79
	1 / 2 .		0.02	56.24	28.78	0.08	0.95	0.05	0.07	0.48	13.90	b.d.l.	100.58
	1 / 3 .		0.01	55.94	28.77	0.14	0.97	0.17	0.11	0.50	13.97	0.03	100.61
	1 / 4 .		0.02	56.26	28.60	0.02	0.94	0.04	0.06	0.51	13.95	0.02	100.41
	1 / 5 .		0.02	56.15	28.88	0.08	1.06	0.12	0.11	0.49	14.03	0.02	100.96
	1 / 6 .		0.01	56.21	28.64	0.14	1.03	0.16	0.13	0.51	14.11	b.d.l.	100.94
	1 / 7 .		0.01	56.11	28.56	0.12	1.06	0.16	0.12	0.49	14.02	0.02	100.67
	1 / 8 .		0.01	56.10	28.74	0.17	1.00	0.18	0.14	0.47	14.18	0.02	101.00
	1 / 9 .		0.02	55.79	28.48	0.18	0.96	0.18	0.12	0.50	13.95	0.06	100.22
BAR_B_bulk_11	1 / 1 .		0.02	56.35	28.76	0.10	0.94	0.11	0.11	0.48	14.11	b.d.l.	100.96
	1 / 2 .		0.01	56.43	28.78	0.05	0.97	0.08	0.09	0.48	14.06	b.d.l.	100.96
	1 / 3 .		0.03	56.11	28.74	0.16	0.92	0.19	0.13	0.50	13.96	b.d.l.	100.72
	1 / 4 .		0.02	56.23	28.68	0.13	0.81	0.15	0.12	0.48	13.98	b.d.l.	100.60
	1 / 5 .		0.02	55.90	28.66	0.15	0.85	0.14	0.12	0.46	14.66	0.11	101.07
	1 / 6 .		b.d.l.	56.39	29.01	0.12	0.89	0.11	0.11	0.48	13.84	0.01	100.97
BAR_B_bulk_12	1 / 1 .		0.04	56.26	28.72	0.16	0.87	0.20	0.11	0.48	14.00	b.d.l.	100.82
	1 / 3 .		0.02	56.32	28.80	0.13	0.85	0.18	0.10	0.48	13.90	b.d.l.	100.77
	1 / 4 .		0.02	56.09	28.66	0.11	1.00	0.12	0.10	0.50	13.85	b.d.l.	100.44
	1 / 5 .		0.03	56.44	28.68	0.09	0.94	0.14	0.11	0.51	14.00	0.01	100.94
	1 / 6 .		0.03	56.27	28.64	0.13	1.04	0.14	0.12	0.47	13.89	0.01	100.73
	1 / 1 .	Pyroxene	0.02	55.83	28.74	0.14	0.57	0.21	0.07	0.49	13.98	0.01	100.04
	1 / 2 .		0.01	55.65	28.85	0.13	0.59	0.19	0.09	0.50	14.17	0.01	100.18
	1 / 3 .		b.d.l.	55.83	28.78	0.14	0.56	0.19	0.07	0.50	14.08	b.d.l.	100.15

BAR_C_bulk _06_	1 / 4 .	b.d.l.	55.59	28.62	0.14	0.56	0.15	0.08	0.48	13.93	b.d.l.	99.56
	1 / 5 .	0.01	55.58	28.60	0.14	0.53	0.18	0.07	0.48	14.10	b.d.l.	99.67
	1 / 6 .	0.02	55.44	28.64	0.16	0.52	0.18	0.07	0.50	14.04	b.d.l.	99.55
	1 / 7 .	b.d.l.	55.41	28.40	0.12	0.59	0.17	0.07	0.51	14.11	b.d.l.	99.37
	1 / 8 .	0.52	54.08	16.26	0.47	21.89	0.41	0.84	0.24	5.29	b.d.l.	99.99
BAR_C_bulk _07_	1 / 1 .	b.d.l.	55.72	28.68	0.15	0.57	0.19	0.11	0.50	13.85	b.d.l.	99.75
	1 / 2 .	0.01	55.79	28.37	0.15	0.72	0.18	0.12	0.48	14.07	b.d.l.	99.89
	1 / 3 .	b.d.l.	55.66	28.51	0.13	0.73	0.19	0.11	0.49	14.03	b.d.l.	99.84
	1 / 4 .	0.01	55.63	28.34	0.12	0.78	0.19	0.11	0.47	13.93	b.d.l.	99.56
	1 / 5 .	0.03	55.67	28.69	0.11	0.80	0.16	0.10	0.50	13.83	b.d.l.	99.87
	1 / 6 .	0.02	55.60	28.60	0.14	0.58	0.18	0.11	0.50	13.94	b.d.l.	99.66
	1 / 7 .	0.02	55.63	28.50	0.16	0.59	0.19	0.11	0.51	14.03	b.d.l.	99.74
	1 / 8 .	b.d.l.	55.62	28.41	0.11	0.79	0.19	0.10	0.51	14.00	b.d.l.	99.73
BAR_C_bulk _08_	1 / 1 .	b.d.l.	55.91	28.68	0.12	0.58	0.17	0.07	0.52	13.93	b.d.l.	99.98
	1 / 2 .	0.01	55.81	28.24	0.14	0.65	0.20	0.10	0.49	14.11	b.d.l.	99.74
	1 / 3 .	0.01	55.89	28.51	0.13	0.78	0.22	0.11	0.49	13.94	0.02	100.08
	1 / 4 .	0.55	54.36	16.06	0.47	22.06	0.49	0.86	0.23	4.99	b.d.l.	100.05
	1 / 5 .	0.03	55.67	28.42	0.15	0.80	0.20	0.11	0.49	14.08	b.d.l.	99.95
	1 / 6 .	0.01	55.85	28.57	0.11	0.83	0.16	0.08	0.49	13.99	b.d.l.	100.08
	1 / 7 .	0.03	55.60	28.36	0.14	0.91	0.19	0.12	0.51	13.87	b.d.l.	99.72
BAR_C_bulk _10_	1 / 1 .	b.d.l.	55.61	28.81	0.14	0.71	0.17	0.11	0.50	13.88	b.d.l.	99.91
	1 / 2 .	0.01	55.82	28.63	0.14	0.71	0.19	0.09	0.48	13.98	b.d.l.	100.05
	1 / 3 .	0.01	55.94	28.83	0.12	0.67	0.17	0.08	0.50	13.98	b.d.l.	100.28
	1 / 4 .	0.60	54.26	16.29	0.48	22.32	0.45	0.82	0.22	4.48	b.d.l.	99.93
	1 / 5 .	0.60	54.33	16.25	0.51	22.30	0.45	0.82	0.25	4.67	b.d.l.	100.19
BAR_C_bulk _11_	1 / 1 .	0.02	55.88	28.19	0.15	0.95	0.19	0.11	0.49	14.07	b.d.l.	100.04
	1 / 2 .	0.01	55.72	28.29	0.16	1.03	0.18	0.14	0.47	13.80	b.d.l.	99.82
	1 / 3 .	0.04	56.03	28.44	0.15	1.06	0.19	0.13	0.48	13.93	0.02	100.46
	1 / 4 .	0.01	55.84	28.27	0.16	1.07	0.17	0.13	0.48	13.73	0.02	99.86
	1 / 5 .	0.03	56.01	28.61	0.12	1.04	0.17	0.14	0.50	13.94	0.01	100.56
	1 / 6 .	0.04	55.77	28.43	0.13	1.02	0.18	0.12	0.46	13.91	0.01	100.06
B3_bulk_01_	1 / 1 .	0.02	56.86	29.10	0.14	0.95	0.21	0.12	0.50	13.99	0.01	101.89
	1 / 2 .	0.01	56.53	28.80	0.08	1.02	0.13	0.10	0.49	13.98	b.d.l.	101.16
	1 / 3 .	0.03	56.09	28.57	0.15	1.08	0.20	0.14	0.48	13.95	0.05	100.75
	1 / 4 .	0.01	56.07	28.53	0.13	1.07	0.16	0.14	0.48	13.82	0.02	100.46
B3_bulk_05_	1 / 1 .	0.55	54.47	16.74	0.45	22.12	0.42	0.77	0.25	5.04	b.d.l.	100.92
	1 / 2 .	0.62	53.79	16.52	0.48	22.82	0.46	0.79	0.24	4.47	0.01	100.93
	1 / 3 .	0.57	54.04	16.34	0.57	22.46	0.45	0.76	0.25	4.65	b.d.l.	100.61

Table A.23. EPMA analysis of pyroxene in host Barwell

Site	Point	Mineral	Element											Total
			Na_2O	SiO_2	Al_2O_3	MgO	CaO	TiO_2	MnO	FeO	K_2O	SrO	BaO	
BAR_B_bulk_28	1 / 1 .	Plagioclase	10.14	63.09	20.77	0.17	3.60	0.04	0.01	1.11	0.88	0.02	b.d.l.	99.82
	1 / 3 .		9.67	62.36	19.73	2.55	2.02	0.02	0.07	3.15	0.99	0.03	b.d.l.	100.57
	1 / 4 .		9.77	64.12	20.79	0.37	3.04	0.04	0.01	0.50	1.29	0.04	b.d.l.	99.96
	1 / 5 .		8.49	62.67	18.26	2.23	4.51	0.08	0.02	1.08	0.93	0.02	b.d.l.	98.31
BAR_B_bulk_29	1 / 2 .		8.80	62.34	18.39	1.79	4.56	0.09	0.04	1.79	1.05	0.03	0.01	98.89
	1 / 4 .		10.25	65.06	21.07	0.28	2.54	0.04	0.01	0.33	0.88	b.d.l.	0.02	100.47
BAR_B_bulk_30	1 / 2 .		9.68	64.38	21.08	0.24	2.51	0.03	0.02	0.63	1.31	0.03	0.03	99.95
	1 / 3 .		9.58	63.37	20.43	0.44	3.24	0.03	0.03	0.83	1.06	0.03	b.d.l.	99.04
	1 / 4 .		9.53	64.06	20.16	1.05	3.84	0.06	0.03	0.98	0.96	0.03	b.d.l.	100.71
	1 / 5 .		9.91	64.00	20.99	0.42	2.32	0.02	0.04	1.54	1.16	0.03	0.01	100.43
	1 / 6 .		9.41	62.32	19.85	0.75	3.42	0.05	0.01	1.28	0.96	0.01	b.d.l.	98.04
BAR_B_bulk_31	1 / 1 .		10.19	65.15	21.66	b.d.l.	2.25	0.05	b.d.l.	0.38	1.12	b.d.l.	b.d.l.	100.80
	1 / 2 .		9.94	65.22	21.71	b.d.l.	2.25	0.05	b.d.l.	0.35	1.17	0.04	0.02	100.74
	1 / 3 .		9.09	63.56	19.82	0.75	2.94	0.06	0.02	0.66	1.29	0.05	b.d.l.	98.25
B3_bulk_01	1 / 3 .		10.01	66.78	21.11	0.11	2.25	0.06	b.d.l.	0.49	0.93	n.a.	n.a.	101.74
B3_bulk_06	1 / 1 .		10.12	66.82	20.77	0.01	2.22	0.04	0.02	0.46	1.04	n.a.	n.a.	101.47
	1 / 2 .		9.85	66.29	20.78	0.01	2.26	0.05	b.d.l.	0.38	1.35	n.a.	n.a.	100.93
B3_bulk_07a	1 / 1 .		10.23	66.36	21.32	0.10	2.18	0.04	0.01	0.64	0.99	n.a.	n.a.	101.90
	1 / 2 .		9.95	65.65	20.91	0.18	2.57	0.05	0.02	0.55	1.20	n.a.	n.a.	101.11
	1 / 3 .		10.42	66.73	21.47	0.02	2.18	0.07	0.01	0.49	0.83	n.a.	n.a.	102.26
	1 / 5 .		9.99	66.18	21.25	b.d.l.	2.17	0.03	0.02	0.48	1.10	n.a.	n.a.	101.24
B3_bulk_08a	1 / 1 .		10.20	65.20	21.34	0.01	2.14	0.03	0.00	0.48	0.93	n.a.	n.a.	100.34
	1 / 2 .		10.24	65.42	21.46	0.02	2.12	0.05	0.02	0.46	0.97	n.a.	n.a.	100.75
	1 / 3 .		10.00	65.27	21.31	0.01	2.15	0.04	0.02	0.65	1.34	n.a.	n.a.	100.83
	1 / 4 .		10.12	65.09	21.46	0.04	2.26	0.04	0.02	0.96	1.11	n.a.	n.a.	101.22
	1 / 5 .		10.43	65.25	21.40	0.01	2.18	0.03	0.01	0.62	0.82	n.a.	n.a.	100.78
B3_bulk_09a	1 / 1 .		8.15	66.54	21.16	0.14	2.78	0.05	0.03	0.57	1.19	n.a.	n.a.	100.65
	1 / 2 .		9.07	66.90	21.38	0.02	2.22	0.05	b.d.l.	0.52	0.93	n.a.	n.a.	101.16
	1 / 3 .		10.15	66.11	21.25	0.04	2.20	0.05	0.02	0.47	0.90	n.a.	n.a.	101.22
	1 / 5 .		3.31	68.99	22.31	b.d.l.	2.20	0.05	0.01	0.47	0.93	n.a.	n.a.	98.34
	1 / 6 .		9.93	64.23	20.97	0.44	2.15	0.04	0.01	0.75	1.03	n.a.	n.a.	99.59
B3_bulk_10a	1 / 1 .		10.27	65.56	21.52	b.d.l.	2.22	0.05	0.02	0.38	0.99	n.a.	n.a.	100.97
	1 / 2 .		10.34	65.01	21.37	b.d.l.	2.15	0.05	0.02	0.35	0.89	n.a.	n.a.	100.19
B3_bulk_11a	1 / 1 .		10.35	65.46	21.37	0.05	2.22	0.04	0.01	0.43	0.78	n.a.	n.a.	100.75
	1 / 2 .		10.25	65.44	21.27	0.03	2.12	0.07	0.03	0.39	0.88	n.a.	n.a.	100.50
	1 / 3 .		10.34	65.47	21.18	0.01	2.15	0.05	0.02	0.38	0.91	n.a.	n.a.	100.58
	1 / 4 .		10.15	65.25	21.33	0.02	2.23	0.06	0.01	0.43	1.07	n.a.	n.a.	100.55
	1 / 5 .		10.13	63.61	21.33	b.d.l.	2.07	0.04	b.d.l.	0.40	1.07	n.a.	n.a.	98.70
	1 / 7 .		2.09	55.19	4.77	14.00	19.03	0.40	0.21	3.78	0.17	n.a.	n.a.	100.37
	1 / 8 .		9.21	64.32	21.55	0.31	2.28	0.05	0.01	0.56	1.08	n.a.	n.a.	99.37
B3_bulk_13a	1 / 1 .		9.40	64.86	20.25	0.54	2.18	0.05	0.02	0.61	1.11	n.a.	n.a.	99.07
	1 / 2 .		10.10	66.04	21.17	0.01	2.24	0.05	b.d.l.	0.28	0.94	n.a.	n.a.	100.83
	1 / 3 .		10.14	65.90	21.21	0.01	2.17	0.06	b.d.l.	0.32	0.82	n.a.	n.a.	100.67
	1 / 4 .		9.86	65.56	20.99	b.d.l.	2.09	0.04	0.01	0.21	1.54	n.a.	n.a.	100.29
	1 / 6 .		10.23	66.53	21.29	0.01	2.10	0.05	0.02	0.23	1.03	n.a.	n.a.	101.48

Table A.24. EPMA analysis of plagioclase in host Barwell

Site	Point	Mineral	Element										Total
			SiO_2	MgO	Al_2O_3	CaO	TiO_2	Cr_2O_3	MnO	FeO	V_2O3	NiO	
BAR_B_bulk_24	1 / 1 .	Chromite	0.03	2.41	5.70	0.01	2.92	56.85	0.69	30.44	0.75	0.02	99.81
	1 / 2 .		0.03	2.36	5.80	0.01	2.60	57.07	0.68	30.52	0.76	b.d.l.	99.82
	1 / 3 .		b.d.l.	2.44	5.61	b.d.l.	2.81	56.89	0.71	30.34	0.76	0.01	99.58
	1 / 4 .		0.03	2.46	5.64	0.01	2.95	56.72	0.69	30.66	0.76	b.d.l.	99.92
	1 / 5 .		0.02	2.47	5.61	b.d.l.	2.91	56.66	0.64	30.49	0.76	0.01	99.57
	1 / 6 .		0.04	2.41	5.64	0.01	2.87	56.73	0.67	30.44	0.75	b.d.l.	99.55
	1 / 7 .		0.04	2.41	5.71	b.d.l.	2.76	56.88	0.68	30.50	0.74	0.01	99.72
	1 / 8 .		0.04	2.45	5.67	0.01	2.65	57.05	0.69	30.31	0.79	b.d.l.	99.63
BAR_B_bulk_25	1 / 1 .		0.03	2.22	5.86	0.01	2.58	55.86	0.68	31.16	0.73	0.03	99.16
	1 / 2 .		0.01	2.36	6.02	0.01	2.58	56.45	0.65	30.94	0.74	b.d.l.	99.74
	1 / 3 .		0.05	2.09	6.00	0.02	2.41	56.37	0.64	30.97	0.73	0.03	99.30
	1 / 4 .		0.02	2.18	6.09	0.02	2.15	56.62	0.70	30.76	0.76	0.03	99.32
	1 / 5 .		0.07	2.27	6.05	0.01	2.40	56.08	0.65	31.00	0.72	0.02	99.27
	1 / 6 .		0.03	2.15	6.11	b.d.l.	2.49	56.63	0.67	30.82	0.74	b.d.l.	99.62
	1 / 7 .		0.06	2.26	6.22	0.01	2.39	56.24	0.71	31.00	0.74	0.01	99.66
BAR_B_bulk_26	1 / 1 .		0.02	2.12	5.65	0.01	2.83	55.94	0.64	31.91	0.71	b.d.l.	99.82
	1 / 2 .		0.01	2.12	5.71	0.01	2.93	56.35	0.60	31.29	0.71	0.02	99.74
	1 / 3 .		0.02	2.16	5.56	b.d.l.	2.84	56.26	0.66	31.37	0.70	b.d.l.	99.54
	1 / 4 .		0.01	2.22	5.79	0.01	2.95	56.46	0.63	31.16	0.70	b.d.l.	99.91
	1 / 5 .		0.07	2.29	5.90	0.01	2.81	55.42	0.62	30.81	0.71	0.03	98.68
	1 / 6 .		0.03	2.29	5.68	0.02	2.91	56.44	0.63	31.27	0.71	b.d.l.	99.97
BAR_B_bulk_27	1 / 1 .		0.03	1.95	5.68	0.01	2.88	56.36	0.56	31.81	0.74	b.d.l.	100.02
	1 / 2 .		0.03	2.02	6.03	b.d.l.	2.67	56.51	0.64	31.49	0.74	0.10	100.21
	1 / 3 .		0.03	2.02	5.81	b.d.l.	2.97	56.44	0.59	31.63	0.71	0.02	100.22
	1 / 4 .		0.02	1.88	5.66	b.d.l.	2.92	56.36	0.58	31.79	0.69	b.d.l.	99.91
	1 / 5 .		b.d.l.	2.02	5.83	b.d.l.	2.62	56.62	0.65	31.27	0.74	0.10	99.84
	1 / 6 .		0.02	1.99	5.77	b.d.l.	2.94	56.48	0.58	31.36	0.70	0.04	99.87
	1 / 7 .		0.04	1.95	5.72	b.d.l.	2.96	56.38	0.56	31.65	0.71	0.03	99.99
	1 / 8 .		0.03	1.96	5.77	b.d.l.	2.84	56.30	0.60	31.71	0.73	b.d.l.	99.95

Table A.25. EPMA analysis of chromite in host Barwell

Site	Point	Mineral	Element											Total
			S	P	Ti	V	Cr	Mn	Fe	Co	Ni	Mg	Si	
BAR_B_bulk_14	1 / 1 .	Kamacite	b.d.l.	b.d.l.	b.d.l.	b.d.l.	0.02	b.d.l.	94.11	0.89	5.13	b.d.l.	0.02	100.13
	1 / 2 .		b.d.l.	b.d.l.	b.d.l.	b.d.l.	0.02	b.d.l.	94.27	0.90	5.13	b.d.l.	b.d.l.	100.30
	1 / 3 .		b.d.l.	b.d.l.	b.d.l.	b.d.l.	0.01	b.d.l.	95.00	0.90	4.42	b.d.l.	0.03	100.36
	1 / 4 .	Taenite	b.d.l.	b.d.l.	b.d.l.	b.d.l.	b.d.l.	b.d.l.	48.18	0.11	52.54	b.d.l.	0.01	100.84
	1 / 5 .		b.d.l.	b.d.l.	b.d.l.	b.d.l.	0.14	b.d.l.	72.26	0.53	27.63	b.d.l.	0.03	100.59
BAR_B_bulk_16	1 / 1 .		b.d.l.	b.d.l.	b.d.l.	b.d.l.	0.01	b.d.l.	67.16	0.33	32.64	b.d.l.	0.02	100.15
	1 / 2 .		b.d.l.	b.d.l.	b.d.l.	b.d.l.	0.01	b.d.l.	65.70	0.27	34.00	b.d.l.	0.02	99.99
	1 / 3 .		b.d.l.	b.d.l.	b.d.l.	b.d.l.	0.01	b.d.l.	66.47	0.31	33.25	b.d.l.	0.01	100.03
	1 / 4 .		b.d.l.	b.d.l.	b.d.l.	b.d.l.	0.02	b.d.l.	66.09	0.28	33.54	b.d.l.	0.01	99.96
	1 / 5 .		b.d.l.	b.d.l.	b.d.l.	b.d.l.	b.d.l.	b.d.l.	62.13	0.17	37.43	b.d.l.	0.03	99.73
BAR_B_bulk_17	1 / 1 .		b.d.l.	b.d.l.	b.d.l.	b.d.l.	b.d.l.	b.d.l.	68.08	0.35	31.90	b.d.l.	0.01	100.27
	1 / 2 .		b.d.l.	b.d.l.	b.d.l.	b.d.l.	b.d.l.	b.d.l.	68.68	0.36	31.16	b.d.l.	b.d.l.	100.14
	1 / 3 .		b.d.l.	b.d.l.	b.d.l.	b.d.l.	0.01	b.d.l.	66.13	0.36	33.47	b.d.l.	0.02	99.96
	1 / 4 .		b.d.l.	b.d.l.	b.d.l.	b.d.l.	0.01	b.d.l.	69.97	0.36	29.93	b.d.l.	0.01	100.23
	1 / 5 .		b.d.l.	b.d.l.	b.d.l.	b.d.l.	0.01	b.d.l.	68.91	0.36	31.24	b.d.l.	0.01	100.51
	1 / 6 .		b.d.l.	b.d.l.	b.d.l.	b.d.l.	b.d.l.	b.d.l.	67.96	0.36	31.97	b.d.l.	b.d.l.	100.28
BAR_B_bulk_19	1 / 1 .		b.d.l.	b.d.l.	b.d.l.	b.d.l.	0.02	b.d.l.	66.34	0.29	33.95	b.d.l.	b.d.l.	100.57
	1 / 2 .		b.d.l.	b.d.l.	b.d.l.	b.d.l.	b.d.l.	b.d.l.	62.22	0.31	37.31	b.d.l.	0.03	99.84
	1 / 3 .		b.d.l.	b.d.l.	b.d.l.	b.d.l.	b.d.l.	b.d.l.	68.24	0.28	32.09	b.d.l.	0.02	100.60
	1 / 4 .		b.d.l.	b.d.l.	b.d.l.	b.d.l.	b.d.l.	b.d.l.	62.82	0.31	36.82	b.d.l.	0.01	99.92
	1 / 5 .		b.d.l.	b.d.l.	b.d.l.	b.d.l.	b.d.l.	b.d.l.	66.79	0.28	33.27	b.d.l.	0.01	100.33
	1 / 6 .		b.d.l.	b.d.l.	b.d.l.	b.d.l.	0.01	b.d.l.	67.03	0.31	32.89	b.d.l.	0.01	100.22
	1 / 7 .		b.d.l.	b.d.l.	b.d.l.	b.d.l.	0.01	b.d.l.	65.49	0.30	34.45	b.d.l.	0.01	100.21
BAR_B_bulk_20	1 / 1 .		b.d.l.	b.d.l.	b.d.l.	b.d.l.	0.04	b.d.l.	64.59	0.19	36.52	b.d.l.	0.02	101.35
	1 / 2 .		b.d.l.	b.d.l.	b.d.l.	b.d.l.	0.11	b.d.l.	60.77	0.16	39.45	b.d.l.	0.04	100.47
	1 / 3 .		b.d.l.	b.d.l.	b.d.l.	b.d.l.	0.05	b.d.l.	61.75	0.17	38.55	b.d.l.	0.03	100.52
	1 / 4 .		b.d.l.	b.d.l.	b.d.l.	b.d.l.	0.01	b.d.l.	62.97	0.15	37.71	b.d.l.	b.d.l.	100.82
	1 / 5 .		b.d.l.	b.d.l.	b.d.l.	b.d.l.	0.11	b.d.l.	56.66	0.16	43.99	b.d.l.	0.01	100.89
	1 / 6 .		b.d.l.	b.d.l.	b.d.l.	b.d.l.	0.06	b.d.l.	58.75	0.16	41.03	b.d.l.	0.01	99.95
	1 / 7 .		b.d.l.	b.d.l.	b.d.l.	b.d.l.	0.02	b.d.l.	58.84	0.15	41.19	b.d.l.	0.01	100.13
	1 / 8 .		b.d.l.	b.d.l.	b.d.l.	b.d.l.	0.05	b.d.l.	53.64	0.14	47.03	b.d.l.	0.01	100.85
BAR_B_bulk_22	1 / 1 .		b.d.l.	b.d.l.	b.d.l.	b.d.l.	0.01	b.d.l.	93.95	0.77	6.04	b.d.l.	0.03	100.80
	1 / 2 .		b.d.l.	b.d.l.	b.d.l.	b.d.l.	b.d.l.	b.d.l.	94.10	0.79	6.15	b.d.l.	0.02	101.04
	1 / 3 .		b.d.l.	b.d.l.	b.d.l.	b.d.l.	b.d.l.	b.d.l.	93.71	0.82	5.96	b.d.l.	0.02	100.49
	1 / 4 .		b.d.l.	b.d.l.	b.d.l.	b.d.l.	0.02	b.d.l.	94.20	0.79	5.75	b.d.l.	0.03	100.74
	1 / 5 .		b.d.l.	b.d.l.	b.d.l.	b.d.l.	0.03	b.d.l.	93.49	0.77	5.92	b.d.l.	0.01	100.21
	1 / 6 .		b.d.l.	b.d.l.	b.d.l.	b.d.l.	0.02	b.d.l.	93.61	0.79	5.86	b.d.l.	0.02	100.27
	1 / 7 .		b.d.l.	b.d.l.	b.d.l.	b.d.l.	0.06	b.d.l.	94.01	0.80	6.13	b.d.l.	0.01	100.99
	1 / 8 .		b.d.l.	b.d.l.	b.d.l.	b.d.l.	0.01	b.d.l.	93.93	0.82	5.90	b.d.l.	0.01	100.66

BAR_B_bulk_23	1 / 1 .	Kamacite	b.d.l.	b.d.l.	b.d.l.	b.d.l.	0.01	b.d.l.	93.75	0.79	6.15	b.d.l.	0.02	100.69
	1 / 2 .		b.d.l.	b.d.l.	b.d.l.	b.d.l.	0.02	b.d.l.	93.43	0.75	6.01	b.d.l.	0.01	100.22
	1 / 3 .		b.d.l.	b.d.l.	b.d.l.	b.d.l.	0.01	b.d.l.	94.00	0.80	5.88	b.d.l.	b.d.l.	100.66
	1 / 4 .		b.d.l.	b.d.l.	b.d.l.	b.d.l.	0.01	b.d.l.	93.88	0.75	6.20	b.d.l.	0.01	100.83
	1 / 5 .		b.d.l.	b.d.l.	b.d.l.	b.d.l.	0.01	b.d.l.	93.79	0.79	6.32	b.d.l.	0.01	100.94
	1 / 6 .		b.d.l.	b.d.l.	b.d.l.	b.d.l.	0.02	b.d.l.	93.65	0.80	6.19	b.d.l.	0.02	100.66
	1 / 7 .		b.d.l.	b.d.l.	b.d.l.	b.d.l.	0.02	b.d.l.	94.20	0.77	6.19	b.d.l.	b.d.l.	101.15
	1 / 8 .		b.d.l.	b.d.l.	b.d.l.	b.d.l.	0.01	b.d.l.	93.68	0.82	6.29	b.d.l.	b.d.l.	100.78
	1 / 9 .		b.d.l.	b.d.l.	b.d.l.	b.d.l.	0.02	b.d.l.	93.56	0.78	6.08	b.d.l.	0.01	100.43
BAR_C_bulk_12	1 / 1 .	Taenite	b.d.l.	b.d.l.	b.d.l.	b.d.l.	b.d.l.	b.d.l.	70.71	0.25	29.10	b.d.l.	0.01	100.01
	1 / 2 .		b.d.l.	b.d.l.	b.d.l.	b.d.l.	0.02	b.d.l.	71.79	0.24	27.81	b.d.l.	0.01	99.86
	1 / 3 .	Kamacite	b.d.l.	b.d.l.	b.d.l.	b.d.l.	0.01	b.d.l.	93.55	0.45	5.56	b.d.l.	b.d.l.	99.56
	1 / 4 .	Taenite	b.d.l.	b.d.l.	b.d.l.	b.d.l.	0.01	b.d.l.	70.19	0.22	29.60	b.d.l.	0.01	100.00
	1 / 5 .		b.d.l.	b.d.l.	b.d.l.	b.d.l.	0.01	b.d.l.	84.42	0.37	13.86	b.d.l.	b.d.l.	98.62
	1 / 7 .	Kamacite	b.d.l.	b.d.l.	b.d.l.	b.d.l.	0.01	b.d.l.	94.72	0.41	6.19	b.d.l.	0.01	101.32
	1 / 8 .	Taenite	b.d.l.	b.d.l.	b.d.l.	b.d.l.	0.01	b.d.l.	79.94	0.26	19.03	b.d.l.	b.d.l.	99.24
BAR_C_bulk_16	1 / 1 .	Kamacite	b.d.l.	b.d.l.	b.d.l.	b.d.l.	b.d.l.	b.d.l.	95.31	0.38	5.54	b.d.l.	b.d.l.	101.20
	1 / 2 .		b.d.l.	b.d.l.	b.d.l.	b.d.l.	b.d.l.	b.d.l.	94.98	0.40	5.81	b.d.l.	b.d.l.	101.14
	1 / 3 .	Taenite	b.d.l.	b.d.l.	b.d.l.	b.d.l.	0.01	b.d.l.	74.98	0.39	25.93	b.d.l.	0.02	101.29
	1 / 4 .		b.d.l.	b.d.l.	b.d.l.	b.d.l.	0.01	b.d.l.	57.52	0.20	42.12	b.d.l.	0.02	99.87
	1 / 5 .		b.d.l.	b.d.l.	b.d.l.	b.d.l.	0.01	b.d.l.	69.05	0.32	30.63	b.d.l.	0.02	100.00
	1 / 6 .		b.d.l.	b.d.l.	b.d.l.	b.d.l.	0.02	b.d.l.	72.27	0.34	27.20	b.d.l.	b.d.l.	99.81
	1 / 7 .	Kamacite	b.d.l.	b.d.l.	b.d.l.	b.d.l.	0.02	b.d.l.	95.63	0.40	5.66	b.d.l.	b.d.l.	101.66
	1 / 8 .		b.d.l.	b.d.l.	b.d.l.	b.d.l.	0.01	b.d.l.	94.21	0.38	5.45	b.d.l.	0.02	100.05
	1 / 9 .		b.d.l.	b.d.l.	b.d.l.	b.d.l.	0.01	b.d.l.	94.29	0.38	6.02	b.d.l.	b.d.l.	100.71

Table A.26. EPMA analysis of FeNi metal in host Barwell

Site	Point	Mineral	Element											Total
			S	P	Ti	V	Cr	Mn	Fe	Co	Ni	Mg	Si	
BAR_C_bulk_13	1 / 1 .	Sulphide	36.20	b.d.l.	b.d.l.	b.d.l.	0.02	b.d.l.	63.79	b.d.l.	b.d.l.	b.d.l.	0.02	100.01
	1 / 2 .		37.67	b.d.l.	b.d.l.	b.d.l.	0.01	0.01	62.74	b.d.l.	b.d.l.	0.06	0.04	100.52
	1 / 3 .		36.48	b.d.l.	b.d.l.	b.d.l.	0.02	b.d.l.	63.33	b.d.l.	b.d.l.	0.02	0.01	99.82
	1 / 4 .		36.43	b.d.l.	b.d.l.	b.d.l.	b.d.l.	b.d.l.	63.38	b.d.l.	b.d.l.	0.01	b.d.l.	99.80
	1 / 5 .		36.36	b.d.l.	b.d.l.	b.d.l.	0.02	0.01	63.42	b.d.l.	b.d.l.	b.d.l.	0.01	99.80
	1 / 6 .		36.00	b.d.l.	b.d.l.	0.01	0.01	b.d.l.	63.48	b.d.l.	b.d.l.	b.d.l.	b.d.l.	99.49
	1 / 7 .		36.10	b.d.l.	b.d.l.	b.d.l.	0.02	0.01	63.34	b.d.l.	b.d.l.	b.d.l.	b.d.l.	99.49
BAR_C_bulk_14	1 / 1 .		36.47	b.d.l.	b.d.l.	b.d.l.	b.d.l.	0.02	63.58	b.d.l.	b.d.l.	b.d.l.	0.02	100.07
	1 / 2 .		36.29	b.d.l.	b.d.l.	b.d.l.	0.01	b.d.l.	63.51	b.d.l.	b.d.l.	0.01	b.d.l.	99.81
	1 / 3 .		36.32	b.d.l.	b.d.l.	b.d.l.	0.02	0.02	63.56	b.d.l.	b.d.l.	b.d.l.	0.01	99.90
	1 / 4 .		36.11	b.d.l.	b.d.l.	0.01	0.03	0.01	63.67	b.d.l.	b.d.l.	b.d.l.	b.d.l.	99.81
	1 / 5 .		36.14	b.d.l.	b.d.l.	b.d.l.	b.d.l.	0.01	63.60	b.d.l.	b.d.l.	b.d.l.	0.02	99.76
	1 / 6 .		36.24	b.d.l.	b.d.l.	b.d.l.	0.02	0.01	63.80	b.d.l.	b.d.l.	b.d.l.	b.d.l.	100.04
	1 / 7 .		36.24	b.d.l.	b.d.l.	b.d.l.	0.01	b.d.l.	63.45	b.d.l.	b.d.l.	b.d.l.	0.01	99.69
	1 / 8 .		36.27	b.d.l.	b.d.l.	b.d.l.	0.02	b.d.l.	63.68	b.d.l.	b.d.l.	0.01	b.d.l.	99.98
	1 / 9 .		36.20	b.d.l.	b.d.l.	b.d.l.	0.01	b.d.l.	63.54	b.d.l.	b.d.l.	b.d.l.	0.01	99.72
BAR_C_bulk_15	1 / 1 .		36.61	0.02	b.d.l.	b.d.l.	0.01	b.d.l.	63.20	b.d.l.	b.d.l.	0.23	0.12	100.16
	1 / 2 .		36.53	b.d.l.	b.d.l.	b.d.l.	0.01	0.01	63.44	b.d.l.	b.d.l.	0.02	0.01	99.97
	1 / 3 .		36.48	b.d.l.	b.d.l.	0.01	0.02	0.01	63.35	b.d.l.	b.d.l.	b.d.l.	b.d.l.	99.88
	1 / 4 .		36.80	0.02	b.d.l.	0.02	b.d.l.	b.d.l.	63.55	b.d.l.	b.d.l.	b.d.l.	b.d.l.	100.38
	1 / 5 .		36.33	b.d.l.	b.d.l.	b.d.l.	b.d.l.	0.02	63.40	b.d.l.	b.d.l.	b.d.l.	0.01	99.69
	1 / 6 .		36.47	b.d.l.	b.d.l.	b.d.l.	0.02	b.d.l.	63.55	b.d.l.	b.d.l.	b.d.l.	b.d.l.	100.02
	1 / 7 .		36.72	b.d.l.	b.d.l.	0.01	0.03	0.02	62.48	b.d.l.	b.d.l.	0.01	0.01	99.27
	1 / 8 .		39.14	b.d.l.	b.d.l.	0.01	0.02	b.d.l.	59.72	b.d.l.	b.d.l.	0.33	0.29	99.60
BAR_C_bulk_16	1 / 10 .		36.28	b.d.l.	b.d.l.	b.d.l.	b.d.l.	0.01	63.17	b.d.l.	b.d.l.	b.d.l.	b.d.l.	99.44
	1 / 11 .		36.24	b.d.l.	0.01	b.d.l.	0.02	b.d.l.	63.57	b.d.l.	b.d.l.	b.d.l.	0.01	99.81
BAR_B_bulk_13	1 / 1 .		36.60	b.d.l.	0.02	0.01	b.d.l.	b.d.l.	61.66	b.d.l.	b.d.l.	0.01	0.08	99.67
	1 / 2 .		37.00	b.d.l.	0.01	0.01	b.d.l.	b.d.l.	63.70	b.d.l.	b.d.l.	b.d.l.	b.d.l.	100.70
	1 / 3 .		35.38	b.d.l.	0.01	b.d.l.	0.04	b.d.l.	62.74	b.d.l.	b.d.l.	0.08	0.04	98.52
	1 / 5 .		36.68	b.d.l.	b.d.l.	b.d.l.	0.02	0.01	63.74	b.d.l.	b.d.l.	0.01	0.01	100.44
BAR_B_bulk_15	1 / 1 .		36.84	b.d.l.	b.d.l.	b.d.l.	b.d.l.	0.01	63.73	b.d.l.	b.d.l.	0.01	b.d.l.	100.59
	1 / 2 .		36.68	b.d.l.	b.d.l.	b.d.l.	b.d.l.	0.01	63.55	b.d.l.	b.d.l.	b.d.l.	b.d.l.	100.18
	1 / 3 .		36.72	b.d.l.	b.d.l.	0.01	b.d.l.	b.d.l.	63.58	b.d.l.	b.d.l.	0.01	0.01	100.35
	1 / 4 .		36.75	b.d.l.	b.d.l.	b.d.l.	0.01	b.d.l.	63.73	b.d.l.	b.d.l.	b.d.l.	b.d.l.	100.50
	1 / 5 .		36.05	b.d.l.	b.d.l.	b.d.l.	0.01	b.d.l.	63.72	b.d.l.	b.d.l.	0.04	0.05	99.87
	1 / 6 .		36.68	b.d.l.	b.d.l.	b.d.l.	0.01	b.d.l.	63.54	b.d.l.	b.d.l.	b.d.l.	0.01	100.25
	1 / 1 .		36.64	b.d.l.	b.d.l.	b.d.l.	0.01	b.d.l.	63.96	b.d.l.	b.d.l.	b.d.l.	0.01	100.61
	1 / 2 .		36.60	b.d.l.	b.d.l.	0.01	0.01	b.d.l.	63.54	b.d.l.	b.d.l.	0.01	0.01	100.18
	1 / 3 .		36.68	b.d.l.	b.d.l.	b.d.l.	b.d.l.	b.d.l.	63.60	b.d.l.	b.d.l.	b.d.l.	0.01	100.28

BAR_B_bulk_18	1 / 4 .		36.79	b.d.l.	b.d.l.	b.d.l.	0.01	b.d.l.	63.66	b.d.l.	b.d.l.	0.01	0.01	100.47
	1 / 5 .		36.54	b.d.l.	b.d.l.	b.d.l.	b.d.l.	b.d.l.	63.81	b.d.l.	b.d.l.	0.01	0.01	100.35
	1 / 6 .		36.66	b.d.l.	b.d.l.	0.01	0.02	b.d.l.	63.66	b.d.l.	b.d.l.	b.d.l.	b.d.l.	100.34
	1 / 7 .		36.56	b.d.l.	b.d.l.	0.01	b.d.l.	0.01	63.70	b.d.l.	b.d.l.	0.01	0.01	100.31
BAR_B_bulk_21	1 / 1 .		36.81	0.01	b.d.l.	b.d.l.	0.00	b.d.l.	63.83	b.d.l.	b.d.l.	b.d.l.	0.01	100.67
	1 / 2 .		36.61	b.d.l.	b.d.l.	0.01	0.01	b.d.l.	63.58	b.d.l.	b.d.l.	b.d.l.	b.d.l.	100.21
	1 / 3 .		36.82	b.d.l.	0.01	b.d.l.	0.00	0.02	63.75	b.d.l.	b.d.l.	b.d.l.	0.02	100.58
	1 / 4 .		36.64	b.d.l.	0.01	b.d.l.	0.02	0.01	63.66	b.d.l.	b.d.l.	b.d.l.	0.02	100.35
	1 / 5 .		36.73	0.01	b.d.l.	b.d.l.	0.01	b.d.l.	63.54	b.d.l.	b.d.l.	b.d.l.	0.01	100.33
	1 / 6 .		36.66	b.d.l.	b.d.l.	0.01	0.01	b.d.l.	63.60	b.d.l.	b.d.l.	b.d.l.	b.d.l.	100.27
	1 / 7 .		36.73	0.01	0.01	b.d.l.	0.01	b.d.l.	63.80	b.d.l.	b.d.l.	b.d.l.	0.01	100.59

Table A.27. EPMA analysis of sulphide in host Barwell

11. Locations of LA-ICP-MS analyses of inclusions in Barwell meteorite

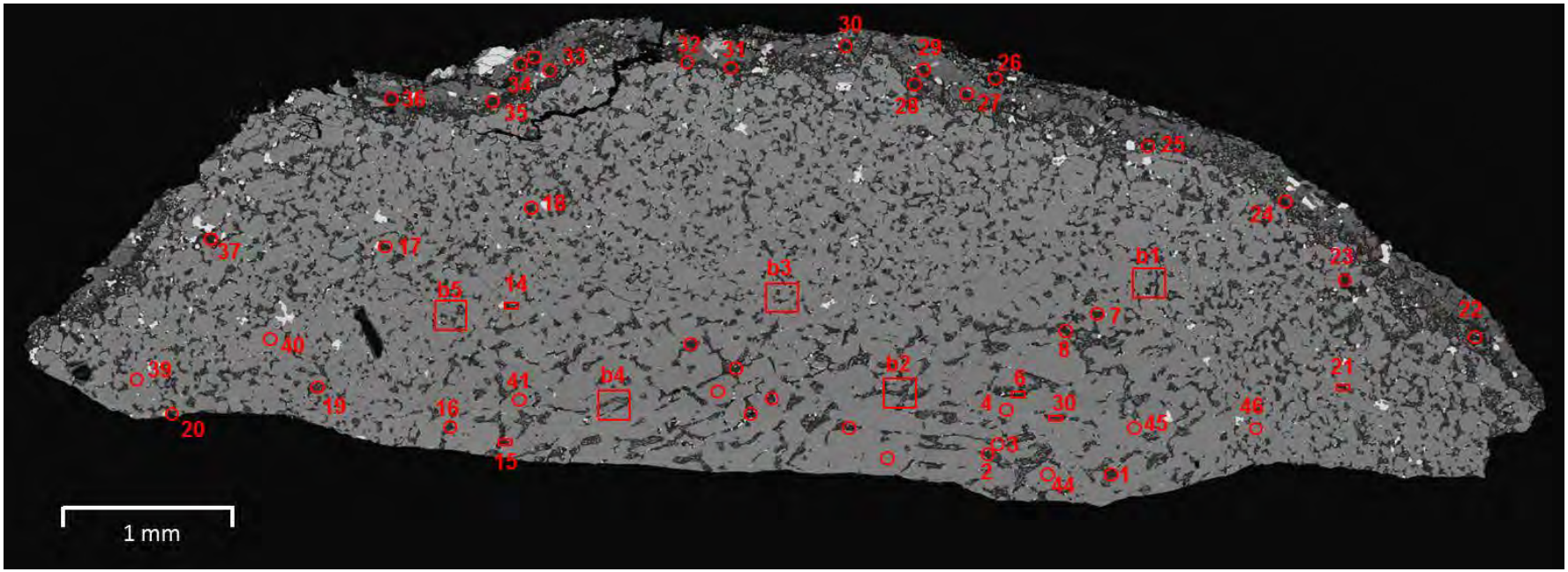

Figure A.10. Locations of LA-ICP-MS analyses in inclusion A.

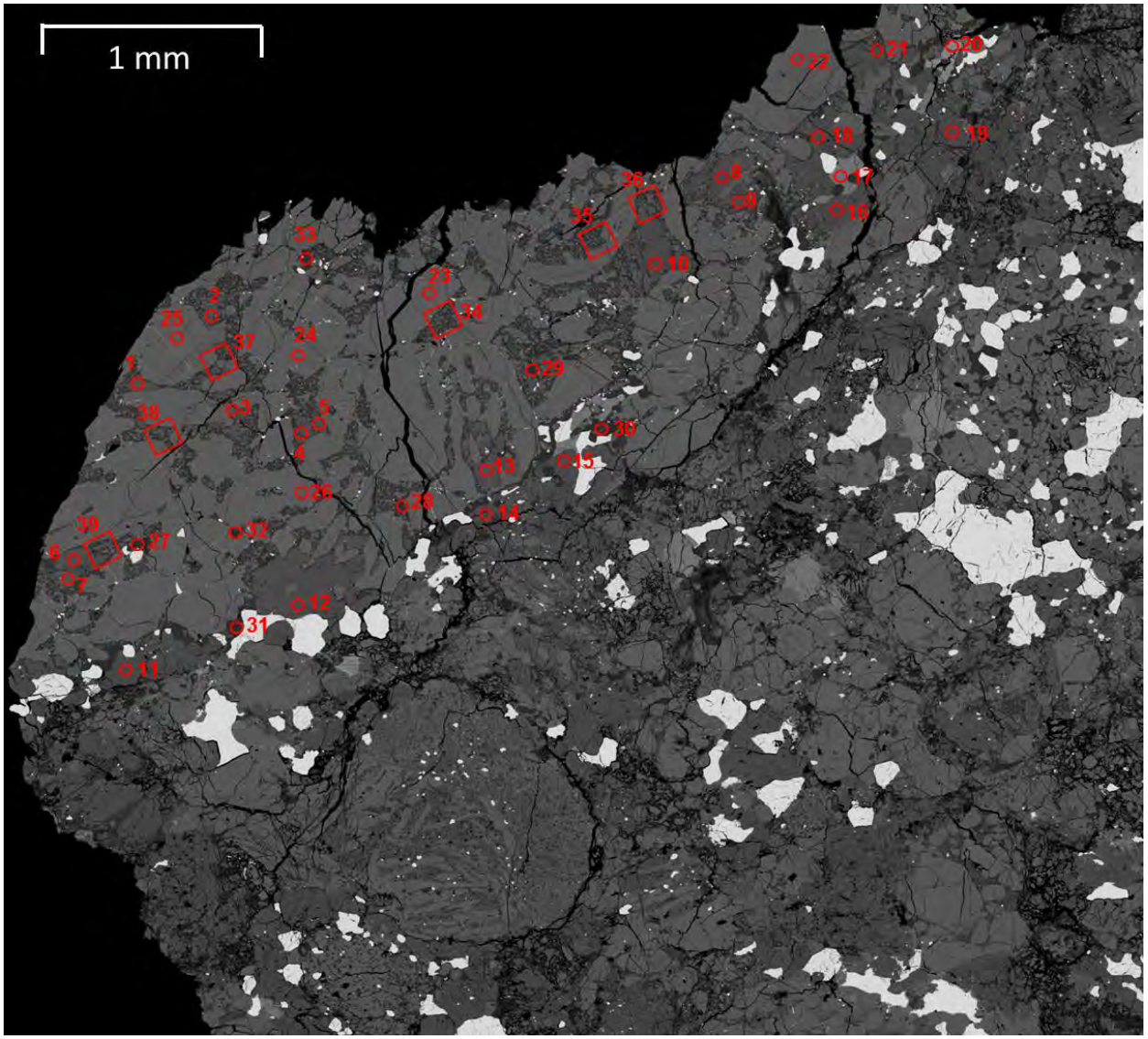

Figure A.11. Locations of LA-ICP-MS analyses in inclusion B.

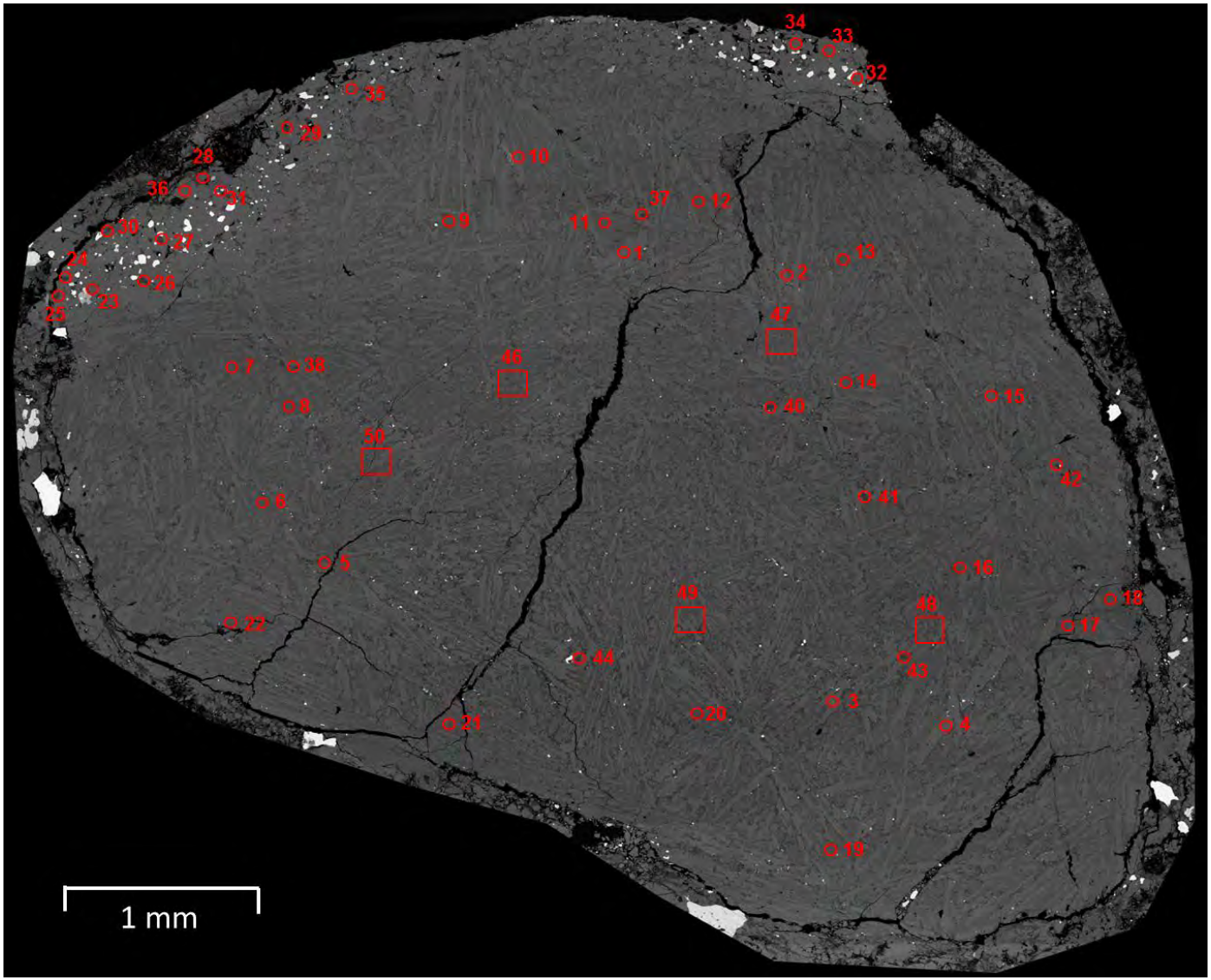

Figure A.12. Locations of LA-ICP-MS analyses in inclusion C.

12. Data tables for LA-ICP-MS analyses of inclusions in Barwell meteorite

Inclusion	Mineral	Run	Analysis No	Spot size	Ref.	Blank Start	Blank End	Mineral Start	Mineral End	Isotope internal standard	Internal std conc	29Si	31P	43Ca	45Sc	51V	53Cr	55Mn	59Co	60Ni	65Cu	66Zn	69Ga	72Ge	75As	85Rb	88Sr	95Mo	137Ba	139La	140Ce
A	Standard	MR10B16	MR10B18	40	BCR2G	3	63	75	150	29Si	252882	252882	1265	48225	32.4	412	15.1	1470	37.3	12.1	17.9	165	54.0	3.07	0.965	46.5	324	253	628	23.2	48.4
A	Standard	MR10C16	MR10C18	40	BCR2G	3	62	70	145	29Si	252882	252882	1205	49731	33.1	423	14.4	1509	38.0	11.7	17.2	167	49.1	3.08	1.01	46.3	330	252	654	24.1	50.6
A	Standard	MR15A16	MR15A18	40	BCR2G	3	66	75	156	29Si	252882	252882	1177	47984	31.0	411	14.1	1456	37.6	11.9	17.9	167	59.6	3.39	0.952	47.0	318	249	634	23.0	48.1
A	Standard	MR15B16	MR15B08	40	BCR2G	3	67	74	150	29Si	252882	252882	1209	50456	33.3	421	14.5	1510	38.1	12.2	17.5	168	51.9	3.22	0.919	46.5	338	248	673	24.6	51.3
A	Plag	MR10B16	MR10B03	28	2	3	57	62	67	29Si	283345	283345	<83.1	50584	6.96	34.2	2224	71.6	0.675	2.61	<2.08	36.8	16.7	<3.31	<2.71	18.2	169	<0.93	16.2	0.923	0.849
A	Plag	MR10B16	MR10B06	17x30	5	3	60	67	79	29Si	179802	179802	<40.9	<455	6.67	1.63	52.2	3376	12.6	12.2	3.73	73.8	<0.191	2.73	<1.08	<0.134	0.210	<0.49	<0.479	<0.0559	<0.0818
A	Plag	MR10B16	MR10B08	30	7	3	60	67	71	29Si	283345	283345	<88.4	41900	6.57	63.9	4112	68.2	0.489	<1.45	<1.89	30.6	17.4	<2.99	<2.29	23.6	150	<1.08	22.1	0.410	0.374
A	Plag	MR10B16	MR10B16	25x15	15	3	60	63	66	29Si	283345	283345	<223	52189	3.81	15.5	906	54.8	<0.617	<2.57	<5.4	10.4	12.7	<8.78	<4.09	18.3	164	<1.95	19.3	0.723	0.625
A	Plag	MR10C16	MR10C03	28	17	3	52	71	86	29Si	283345	283345	119	37632	4.68	49.2	3584	63.8	0.519	2.53	<2.19	27.9	17.8	<3.33	<2.28	6.38	139	<0.913	20.2	0.325	0.513
A	Plag	MR10C16	MR10C04	28	18	3	57	65	83	29Si	283345	283345	82.0	36135	5.39	<0.462	<13.6	106	<0.243	0.970	<1.64	<1.91	16.8	<2.4	<1.4	4.81	137	<0.71	22.3	0.214	0.292
A	Plag	MR10C16	MR10C05	25	19	3	53	74	89	29Si	283345	283345	<116	33775	4.40	4.14	195	711	2.65	2.51	<4.04	13.1	14.6	<5.13	<2.29	7.87	121	<1.31	21.0	0.388	0.391
A	Plag	MR10C16	MR10C06	25	20	3	54	70	87	29Si	283345	283345	164	38635	5.89	<1.19	<27.8	<2.22	6.51	57.6	<2.96	<4.75	20.0	<4.24	<3.26	4.72	145	<1.28	23.3	<0.282	1.21
A	Plag	MR10C16	MR10C07	25x15	21	3	61	76	97	29Si	283345	283345	<198	28100	7.47	6141	396387	6167	25.6	6.84	<5.47	4616	100	<8.15	<3.78	5.93	106	<2.59	17.8	<0.269	<0.365
A	Plag	MR10C16	MR10C08	30	22	3	64	72	88	29Si	283345	283345	63.3	17361	4.97	33.3	2583	143	0.279	<0.647	1.50	17.6	16.5	<2.2	<1.48	14.9	97.6	<0.687	31.5	0.0900	0.0948
A	Plag	MR10C16	MR10C09	30	23	3	59	69	131	29Si	283345	283345	33.6	27691	4.88	0.296	<7.25	<0.702	<0.128	<0.433	<0.8	<1.14	18.9	<1.46	<0.831	7.55	119	<0.341	26.7	0.199	0.262
A	Plag	MR10C16	MR10C10	30	24	3	65	74	81	29Si	283345	283345	84.4	22702	4.62	0.638	<16.3	67.6	3.21	13.9	4.22	<2.24	17.1	<2.89	<1.59	10.2	113	0.805	28.1	0.124	0.181
A	Plag	MR10C16	MR10C11	30	25	3	62	69	78	29Si	283345	283345	74.8	26680	5.04	0.727	<16.9	185	11.4	41.1	<2.11	<3.2	20.6	<2.86	<1.81	8.46	119	<0.735	27.8	0.128	0.172
A	Plag	MR10C16	MR10C12	30	26	3	62	75	94	29Si	283345	283345	119	11261	4.79	0.741	<12.6	829	0.835	26.4	3.43	10.0	27.8	<1.73	<1.15	18.0	79.0	<0.496	24.9	0.0812	0.108
A	Plag	MR10C16	MR10C13	30	27	3	55	66	107	29Si	283345	283345	46.2	12398	11.3	45.0	977	1869	2.62	5.35	3.17	32.0	11.5	2.24	<1.17	8.23	59.4	<0.5	16.4	0.115	<0.0676
A	Plag	MR10C16	MR10C14	30	28	3	64	83	100	29Si	283345	283345	<69.7	19366	3.92	1.53	<17.1	22.0	9.51	34.3	26.4	<2.6	18.5	6.48	<1.65	17.8	105	<0.799	32.2	0.127	0.143
A	Plag	MR10C16	MR10C15	30	29	3	55	82	103	29Si	283345	283345	89.8	13356	5.29	3.63	52.9	337	1.18	155	5.14	4.30	21.2	<3.17	<1.48	17.3	83.4	<0.897	29.8	0.113	<0.102
A	Plag	MR10C16	MR10C16	30	30	3	58	76	91	29Si	283345	283345	99.5	13045	6.28	21.9	1258	1605	3.24	1.75	1.66	35.6	12.4	<2.73	<1.35	11.5	72.7	<0.734	22.8	0.135	<0.119
A	Plag	MR10C16	MR10C17	30	31	3	56	65	75	29Si	283345	283345	<73.5	24628	4.36	<0.547	<15.5	10.2	0.723	13.5	5.51	<2.82	15.9	<3.09	<1.49	12.5	116	<0.833	30.1	0.131	0.176
A	Plag	MR15A16	MR15A06	30	35	3	56	90	153	29Si	283345	283345	54.6	15915	10.2	0.504	29.9	3.03	<0.159	<0.56	<0.839	<1.34	17.9	<1.85	<0.817	15.6	93.6	<0.447	28.6	0.117	0.0722
A	Plag	MR15A16	MR15A07	30	36	3	66	78	108	29Si	283345	283345	<41.5	12822	10.1	<0.431	8.50	<10.9	<0.18	<2.28	<2.82	<1.82	19.3	<1.91	<0.981	20.2	84.1	<0.443	33.2	<0.0726	0.0976
A	Plag	MR15A16	MR15A08	30	37	3	62	71	101	29Si	283345	283345	103	26197	9.33	<0.335	<9.27	<0.927	0.865	2.22	1.15	<1.69	19.6	<1.96	<1	10.6	129	<0.6	30.3	0.165	0.198
A	Ol	MR10B16	MR10B05	28	4	3	60	71	101	29Si	179802	179802	35.0	<245	8.34	2.45	38.6	3485	12.6	15.2	3.33	77.7	0.156	2.98	<0.678	<0.0628	0.0531	<0.282	<0.301	<0.0338	<0.0402
A	Ol	MR15A16	MR15A10	45	39	3	61	68	83	29Si	179802	179802	32.8	<138	8.04	4.37	174	3715	10.2	20.0	4.26	66.6	0.236	3.57	<0.232	<0.029	0.0269	0.469	<0.139	<0.0134	<0.0179
A	Ol	MR15A16	MR15A11	45	40	3	63	71	117	29Si	179802	179802	23.7	95.9	7.56	4.88	186	3609	10.6	14.0	3.87	74.9	0.175	3.57	<0.164	<0.019	<0.0123	0.423	<0.0889	<0.00916	<0.0123
A	Ol	MR15A16	MR15A12	45	41	3	61	69	99	29Si	179802	179802	15.4	116	8.94	3.24	52.0	3539	13.1	15.0	3.46	77.6	0.165	3.46	<0.203	<0.0223	0.0375	0.524	<0.0852	<0.0117	<0.0117
A	Ol	MR15A16	MR15A13	45	42	3	58	65	78	29Si	179802	179802	20.2	148	7.84	2.84	40.5	3641	11.9	14.4	4.29	70.6	0.151	3.76	<0.311	0.0378	0.0893	0.457	<0.139	<0.018	<0.0216
A	Ol	MR15A16	MR15A14	45	43	3	56	108	137	29Si	179802	179802	19.0	124	8.84	2.71	32.8	3414	12.8	16.9	3.71	73.7	0.163	3.51	<0.236	<0.0306	<0.0163	0.560	<0.125	<0.0157	<0.0113
A	Ol	MR15A16	MR15A16	45	45	3	66	76	87	29Si	179802	179802	14.8	<117	7.15	2.55	67.2	3587	11.7	13.6	3.98	68.8	0.165	3.83	<0.272	<0.0367	<0.0245	0.427	<0.147	<0.0175	<0.0154
A	Bulk	MR15B16	MR15B03	45	bulk 1	3	68	74	150	29Si	230000	230000	58.1	5258	7.30	59.3	3741	3709	19.3	360	12.4	106	3.76	3.72	<0.2	2.26	21.5	0.516	4.28	0.0509	0.0521
A	Bulk	MR15B16	MR15B04	45	bulk 2	3	65	71	150	29Si	230000	230000	66.7	8989	7.77	62.0	3567	3592	12.5	13.0	5.02	104	4.33	3.23	<0.233	1.95	31.8	0.490	4.28	0.110	0.144
A	Bulk	MR15B16	MR15B05	45	bulk 3	3	68	73	150	29Si	230000	230000	76.5	2501	7.94	44.1	2426	4358	17.4	75.6	6.39	109	1.91	4.00	<0.229	0.754	8.87	0.479	1.65	0.0315	0.0546
A	Bulk	MR15B16	MR15B06	45	bulk 4	3	68	73	150	29Si	230000	230000	46.6	3361	7.92	46.5	2475	4378	17.4	41.4	5.17	109	2.16	3.90	<0.202	0.483	11.3	0.660	1.56	0.0422	0.0591
A	Bulk	MR15B16	MR15B07	45	bulk 5	3	66	73	150	29Si	230000	230000	57.6	4754	7.59	40.9	2098	4067	15.2	97.9	7.78	102	2.55	3.42	<0.212	1.07	16.8	0.480	3.30	0.0456	0.0630

Inclusion	Mineral	Run	Analysis No	Spot size	Ref.	Blank Start	Blank End	Mineral Start	Mineral End	Isotope internal standard	Internal std conc	141Pr	145Nd	147Sm	151Eu	157Gd	159Tb	163Dy	165Ho	167Er	169Tm	173Yb	175Lu	177Hf	182W	195Pt	197Au	208Pb	209Bi	232Th	238U
A	Standard	MR10B16	MR10B18	40	BCR2G	3	63	75	150	29Si	252882	6.06	26.3	6.30	1.83	5.91	0.980	5.86	1.17	3.42	0.458	3.22	0.462	4.47	0.438	0.239	0.0332	10.1	0.0371	5.52	1.56
A	Standard	MR10C16	MR10C18	40	BCR2G	3	62	70	145	29Si	252882	6.33	26.8	6.43	1.86	6.48	1.01	5.99	1.25	3.51	0.462	3.38	0.477	4.76	0.481	0.144	<0.0429	10.1	0.0385	5.63	1.65
A	Standard	MR15A16	MR15A18	40	BCR2G	3	66	75	156	29Si	252882	6.04	26.1	6.30	1.76	6.08	0.943	5.74	1.15	3.29	0.456	2.99	0.453	4.46	0.462	0.173	<0.0414	10.2	0.0353	5.48	1.61
A	Standard	MR15B16	MR15B08	40	BCR2G	3	67	74	150	29Si	252882	6.35	28.1	6.52	1.91	6.34	0.987	6.21	1.27	3.59	0.493	3.42	0.489	4.68	0.458	0.204	<0.0464	10.3	0.0364	5.77	1.66
A	Plag	MR10B16	MR10B03	28	2	3	57	62	67	29Si	283345	<0.09	<0.976	<0.747	1.13	<0.686	<0.101	<0.352	<0.104	<0.423	<0.1	<0.553	<0.0929	<0.469	<0.51	<0.562	<0.321	<0.648	<0.111	<0.127	<0.108
A	Plag	MR10B16	MR10B06	17x30	5	3	60	67	79	29Si	179802	<0.0497	<0.647	<0.342	0.134	<0.363	<0.0487	<0.22	<0.0492	<0.196	<0.0473	<0.331	<0.0583	<0.338	<0.26	<0.356	<0.197	<0.281	<0.0646	<0.053	<0.0703
A	Plag	MR10B16	MR10B08	30	7	3	60	67	71	29Si	283345	<0.0895	<1.24	<0.511	0.921	<0.911	<0.133	<0.424	<0.0904	<0.46	<0.0953	<0.555	<0.106	<0.514	<0.516	<0.541	<0.419	<0.593	<0.163	<0.121	<0.124
A	Plag	MR10B16	MR10B16	25x15	15	3	60	63	66	29Si	283345	<0.2	<2.89	<1.66	1.18	<1.35	<0.194	<1.31	<0.239	<0.979	<0.203	<1.28	<0.228	<0.989	<1.23	<1.17	<0.656	<1.22	<0.292	<0.315	<0.25
A	Plag	MR10C16	MR10C03	28	17	3	52	71	86	29Si	283345	<0.119	<1.2	<0.713	1.16	<0.717	<0.126	<0.465	<0.086	<0.52	<0.11	<0.679	<0.0992	<0.399	<0.5	<0.543	<0.286	<0.526	<0.175	<0.122	<0.098
A	Plag	MR10C16	MR10C04	28	18	3	57	65	83	29Si	283345	<0.074	<0.798	<0.559	0.832	<0.461	<0.0723	<0.248	<0.054	<0.234	<0.0804	<0.484	<0.0845	<0.36	<0.324	<0.38	<0.267	<0.371	<0.104	<0.0851	<0.0598
A	Plag	MR10C16	MR10C05	25	19	3	53	74	89	29Si	283345	<0.144	<1.48	<1.07	0.846	<0.899	<0.145	<0.591	<0.178	0.499	<0.196	<0.908	<0.115	<0.87	<0.629	<1.03	<0.512	<0.611	<0.218	<0.177	<0.195
A	Plag	MR10C16	MR10C06	25	20	3	54	70	87	29Si	283345	<0.151	<1.78	<1.1	0.757	<0.935	<0.148	<0.49	<0.159	<0.521	<0.139	<1.25	<0.174	<0.881	<0.621	<0.943	<0.468	<0.71	<0.249	<0.177	<0.14
A	Plag	MR10C16	MR10C07	25x15	21	3	61	76	97	29Si	283345	<0.223	<2.8	<1.44	1.07	<1.93	<0.169	<0.875	<0.224	<1.25	<0.24	<1.34	<0.261	<1.44	<0.932	<1.48	<0.892	<1.05	<0.307	<0.239	<0.265
A	Plag	MR10C16	MR10C08	30	22	3	64	72	88	29Si	283345	<0.0836	<0.626	<0.388	0.533	<0.423	<0.0512	<0.21	<0.0475	<0.266	<0.0473	<0.396	<0.0624	<0.312	<0.342	<0.327	0.189	<0.309	<0.0827	<0.0521	<0.0688
A	Plag	MR10C16	MR10C09	30	23	3	59	69	131	29Si	283345	<0.0365	<0.411	<0.263	0.673	<0.277	<0.0411	<0.169	<0.0423	<0.18	<0.0468	<0.275	<0.0434	<0.226	<0.225	<0.156	<0.124	<0.232	<0.0497	<0.047	<0.0546
A	Plag	MR10C16	MR10C10	30	24	3	65	74	81	29Si	283345	<0.0776	<0.955	<0.611	0.645	<0.564	<0.0836	<0.349	<0.0895	<0.34	<0.0858	<0.6	<0.11	<0.565	<0.408	<0.575	<0.233	<0.335	<0.13	<0.104	<0.0823
A	Plag	MR10C16	MR10C11	30	25	3	62	69	78	29Si	283345	<0.0961	<1.22	<0.624	0.620	<0.707	<0.0859	<0.411	<0.118	<0.53	<0.0994	<0.613	<0.115	<0.636	<0.588	<0.601	<0.27	<0.453	<0.127	<0.107	<0.102
A	Plag	MR10C16	MR10C12	30	26	3	62	75	94	29Si	283345	<0.0669	<0.755	<0.414	0.495	<0.417	<0.0765	<0.272	<0.0616	<0.301	<0.056	<0.297	<0.0741	<0.288	<0.356	<0.397	<0.202	<0.321	<0.0859	<0.07	<0.0712
A	Plag	MR10C16	MR10C13	30	27	3	55	66	107	29Si	283345	<0.0516	<0.871	<0.301	0.351	<0.294	<0.0626	<0.211	<0.0561	<0.249	<0.0409	<0.374	<0.0648	<0.255	<0.223	<0.279	<0.133	<0.258	<0.0504	<0.089	<0.0477
A	Plag	MR10C16	MR10C14	30	28	3	64	83	100	29Si	283345	<0.109	<1.1	<0.721	0.630	<0.534	<0.07	<0.333	<0.083	<0.417	<0.0913	<0.467	<0.107	<0.427	<0.429	<0.439	<0.285	<0.43	<0.123	<0.116	<0.125
A	Plag	MR10C16	MR10C15	30	29	3	55	82	103	29Si	283345	<0.0756	<1.13	<0.635	0.731	<0.571	<0.09	<0.352	<0.0792	<0.409	<0.0824	<0.58	<0.0884	<0.404	<0.474	<0.616	<0.249	<0.421	<0.117	<0.0882	<0.108
A	Plag	MR10C16	MR10C16	30	30	3	58	76	91	29Si	283345	<0.0729	<1.03	<0.578	0.514	<0.453	<0.0818	<0.247	<0.0842	<0.327	<0.0805	<0.424	<0.0842	<0.347	<0.323	<0.515	<0.233	<0.353	<0.0869	<0.0844	<0.0873
A	Plag	MR10C16	MR10C17	30	31	3	56	65	75	29Si	283345	<0.108	<1.3	<0.647	0.864	<0.677	<0.0825	<0.39	<0.0864	<0.358	<0.0873	<0.404	<0.0975	<0.412	<0.508	<0.532	<0.307	<0.382	<0.128	<0.105	<0.084
A	Plag	MR15A16	MR15A06	30	35	3	56	90	153	29Si	283345	<0.0445	<0.743	<0.317	0.656	<0.229	<0.0412	<0.201	<0.05	<0.226	<0.0419	<0.213	<0.0419	<0.298	<0.225	<0.201	<0.136	<0.272	<0.0799	<0.0535	<0.0422
A	Plag	MR15A16	MR15A07	30	36	3	66	78	108	29Si	283345	<0.0508	<0.764	<0.483	0.464	<0.355	<0.0596	<0.223	<0.0552	<0.244	<0.0448	<0.376	<0.0523	<0.313	<0.271	<0.245	<0.168	<0.321	<0.0788	<0.0787	<0.0698
A	Plag	MR15A16	MR15A08	30	37	3	62	71	101	29Si	283345	<0.0495	<0.786	<0.348	0.876	<0.39	<0.0586	<0.234	<0.0505	<0.279	<0.0553	<0.319	<0.0492	<0.285	<0.309	<0.33	<0.196	<0.34	<0.0941	<0.0553	<0.0811
A	Ol	MR10B16	MR10B05	28	4	3	60	71	101	29Si	179802	<0.0321	<0.455	<0.194	<0.0558	<0.207	<0.0307	<0.114	<0.0251	<0.169	<0.032	<0.179	<0.0298	<0.169	<0.138	<0.155	<0.0812	<0.187	<0.046	<0.0325	<0.0289
A	Ol	MR15A16	MR15A10	45	39	3	61	68	83	29Si	179802	<0.0125	<0.168	<0.0847	<0.025	<0.0932	<0.0147	<0.0586	<0.014	<0.0536	<0.0168	<0.0807	<0.0172	<0.0811	<0.0756	<0.0641	<0.0473	<0.062	<0.0167	<0.0143	<0.0166
A	Ol	MR15A16	MR15A11	45	40	3	63	71	117	29Si	179802	<0.012	<0.151	<0.0908	<0.019	<0.0732	<0.00802	<0.0463	<0.00986	<0.0523	<0.00831	0.0573	<0.011	0.0976	<0.0555	<0.0493	<0.0375	<0.0595	<0.0159	<0.00996	<0.0119
A	Ol	MR15A16	MR15A12	45	41	3	61	69	99	29Si	179802	<0.012	<0.124	<0.0991	<0.0193	<0.0894	<0.00853	<0.0415	<0.00879	<0.0587	<0.00985	0.0576	<0.0111	0.0608	<0.056	<0.0544	<0.0258	<0.0652	<0.0148	<0.0138	<0.0145
A	Ol	MR15A16	MR15A13	45	42	3	58	65	78	29Si	179802	<0.0126	<0.122	<0.077	<0.0279	<0.0985	<0.0108	<0.048	<0.0134	<0.0663	<0.0142	<0.0975	<0.0175	0.137	<0.0642	<0.0727	<0.0346	<0.0893	<0.0191	<0.0199	<0.0171
A	Ol	MR15A16	MR15A14	45	43	3	56	108	137	29Si	179802	<0.0162	<0.121	<0.0827	<0.0245	<0.109	<0.0124	<0.0667	<0.0139	<0.0646	<0.0153	<0.125	<0.0134	<0.0869	<0.0655	<0.0838	<0.0377	<0.086	<0.0237	<0.0142	<0.0141
A	Ol	MR15A16	MR15A16	45	45	3	66	76	87	29Si	179802	<0.0128	<0.148	<0.106	<0.025	<0.0937	<0.0163	<0.0531	<0.0174	<0.0677	<0.0102	<0.088	<0.016	<0.0816	<0.0573	<0.0863	<0.0527	<0.0743	<0.0158	<0.0158	<0.0196
A	Bulk	MR15B16	MR15B03	45	bulk 1	3	68	74	150	29Si	230000	<0.0121	<0.19	<0.116	0.128	<0.0906	<0.0118	<0.048	<0.0107	<0.0549	<0.0141	<0.067	<0.0127	0.138	<0.0601	0.0949	<0.0297	0.396	<0.0153	<0.0131	<0.0158
A	Bulk	MR15B16	MR15B04	45	bulk 2	3	65	71	150	29Si	230000	<0.0141	<0.174	<0.125	0.191	<0.118	<0.0133	<0.0713	<0.0136	<0.0496	<0.0126	0.0930	0.0186	8.94	<0.0636	<0.0879	<0.0393	0.228	<0.022	0.0174	<0.0139
A	Bulk	MR15B16	MR15B05	45	bulk 3	3	68	73	150	29Si	230000	<0.015	<0.205	<0.103	0.0508	<0.102	<0.0142	<0.0581	<0.0109	<0.0778	<0.0145	<0.0771	<0.0124	<0.0736	<0.0502	<0.079	<0.0433	0.293	<0.0187	<0.0126	<0.0167
A	Bulk	MR15B16	MR15B06	45	bulk 4	3	68	73	150	29Si	230000	<0.0184	<0.168	<0.0849	0.0781	<0.0945	<0.0137	<0.0573	<0.0123	<0.0495	<0.0153	<0.0895	<0.0164	<0.0771	<0.0775	<0.0648	<0.042	0.208	<0.0202	<0.0133	<0.0109
A	Bulk	MR15B16	MR15B07	45	bulk 5	3	66	73	150	29Si	230000	<0.0171	<0.159	<0.0841	0.101	<0.112	<0.016	<0.0592	<0.0138	<0.0756	<0.014	0.105	<0.0156	<0.0856	<0.0713	<0.08	<0.0472	0.284	<0.0219	<0.0163	<0.0195

Table A.28. LA-ICP-MS data for Barwell Inclusion A. All concentrations in ppm.

Inclusion	Mineral	Run	Analysis No	Spot size	Ref.	Blank Start	Blank End	Mineral Start	Mineral End	Isotope internal standard	Internal std conc	29Si	31P	43Ca	45Sc	51V	53Cr	55Mn	59Co	60Ni	65Cu	66Zn	69Ga	72Ge	75As	85Rb	88Sr	95Mo	137Ba	139La	140Ce
B	Standard	MR15C16	MR15C18	40	BCR2G	3	60	65	150	29Si	252882	252882	1290	50428	33.4	427	16.0	1517	38.0	12.3	18.3	171	43.7	3.60	0.972	47.0	334	258	663	24.4	50.8
B	Standard	MR17A16	MR17A18	40	BCR2G	3	56	68	156	29Si	252882	252882	1176	50405	33.2	424	15.7	1517	37.8	12.1	17.1	168	53.5	3.03	1.05	46.4	332	255	666	23.9	50.9
B	Plag	MR17A16	MR17A14	30	27	3	56	69	87	29Si	179802	179802	95.2	3415	5.74	0.841	4.43	2274	10.2	61.7	2.52	36.7	5.78	2.23	<0.659	4.17	22.4	0.555	7.47	<0.042	<0.0497
B	Plag	MR17A16	MR17A15	27	28	3	56	64	72	29Si	283345	283345	<83.9	18985	5.45	1.79	73.0	377	1.57	6.79	<2.5	8.35	21.0	<3.82	<1.64	12.2	105	<0.864	27.1	<0.108	<0.164
B	Plag	MR17A16	MR17A17	30	30	3	56	65	69	29Si	283345	283345	<103	17066	4.22	20.8	1668	33.1	0.509	<1.89	<3.09	36.5	21.9	<4.83	<2.36	21.1	109	<1.32	34.0	<0.119	<0.172
B	Plag	MR17B16	MR17B03	30	31	3	60	76	93	29Si	283345	283345	98.6	14178	3.39	<0.585	<9.34	2.12	13.7	259	<1.9	<1.99	26.7	<3.69	<1.39	15.9	88.4	<1.32	30.2	<0.153	<0.107
B	Plag	MR17B16	MR17B04	27	32	3	56	70	83	29Si	283345	283345	106	13318	7.87	1.09	47.8	1191	4.61	29.2	<2.54	15.6	19.8	<3.62	<2.33	14.8	81.6	<1.03	25.6	<0.143	<0.14
B	Opx	MR15C16	MR15C10	40	8	3	62	76	102	29Si	255844	255844	16.4	22248	22.8	114	3316	3469	5.57	7.51	2.65	80.6	2.03	1.66	<0.297	<0.0462	0.440	0.396	<0.142	0.0351	0.133
B	Opx	MR15C16	MR15C12	40	10	3	50	70	107	29Si	255844	255844	15.5	5315	16.0	94.2	1962	3714	6.10	6.07	2.95	80.6	2.89	1.84	<0.266	0.0531	0.0336	0.370	<0.18	<0.023	<0.0265
B	Opx	MR15C16	MR15C13	40	11	3	58	67	146	29Si	255844	255844	26.4	6054	10.6	43.2	776	3538	6.06	5.61	2.70	79.8	1.24	1.57	<0.241	<0.0346	<0.0201	0.325	<0.181	0.0204	<0.0196
B	Opx	MR15C16	MR15C14	45	12	3	58	64	150	29Si	255844	255844	23.6	6826	17.2	95.8	1864	3553	11.7	229	3.31	79.3	2.74	1.81	<0.225	0.0307	0.0663	0.427	<0.125	<0.0147	<0.0172
B	Opx	MR15C16	MR15C16	40	14	3	50	68	126	29Si	255844	255844	14.4	6333	10.1	38.5	710	3644	6.41	12.4	3.20	79.5	1.08	1.77	<0.241	<0.0397	<0.025	0.391	<0.152	<0.0204	<0.0229
B	Opx	MR15C16	MR15C17	40	15	3	60	75	103	29Si	255844	255844	21.8	5737	13.9	79.7	2188	3636	5.87	5.49	3.08	84.6	2.29	1.95	<0.307	0.0615	0.0363	0.511	<0.16	<0.0244	<0.0242
B	Opx	MR17A16	MR17A05	40	18	3	56	86	120	29Si	255844	255844	23.4	5098	14.8	88.7	3104	3528	6.61	8.16	3.10	88.9	2.69	2.33	<0.24	<0.0354	<0.0232	0.515	<0.142	<0.0163	<0.0213
B	Opx	MR17A16	MR17A06	40	19	3	56	116	141	29Si	255844	255844	15.3	5547	14.9	73.4	1663	3410	6.37	8.04	3.14	81.5	2.32	1.99	<0.291	<0.0417	<0.0316	0.497	<0.163	<0.0202	<0.0179
B	Opx	MR17A16	MR17A08	40	21	3	56	69	87	29Si	255844	255844	24.5	5748	19.6	132	3874	3674	6.11	7.85	3.36	92.9	4.11	1.94	<0.33	0.132	0.537	0.515	<0.191	<0.0215	<0.021
B	Ol	MR17A16	MR17A09	40	22	3	56	68	156	29Si	179802	179802	24.3	189	4.78	7.46	297	3466	11.8	19.9	3.69	94.5	0.199	3.13	<0.192	0.422	0.0504	0.413	<0.108	<0.0131	<0.0134
B	Ol	MR17A16	MR17A10	40	23	3	56	68	156	29Si	179802	179802	24.0	135	4.64	10.2	436	3490	11.1	17.6	3.98	89.7	0.191	2.99	<0.178	0.0787	<0.0182	0.372	<0.0948	<0.0137	<0.015
B	Ol	MR17A16	MR17A11	40	24	3	62	71	156	29Si	179802	179802	29.0	120	5.58	1.77	18.7	3464	10.6	14.9	3.77	87.0	0.146	2.86	<0.182	<0.0198	<0.0169	0.382	<0.0874	<0.0102	<0.0139
B	Ol	MR17A16	MR17A12	40	25	3	56	68	113	29Si	179802	179802	16.3	153	5.83	2.43	32.8	3611	11.0	15.9	3.93	86.3	0.176	3.22	<0.185	<0.0294	<0.014	0.518	<0.111	<0.0127	<0.0148
B	Ol	MR17A16	MR17A13	40	26	3	56	71	103	29Si	179802	179802	29.6	108	5.26	2.76	50.6	3653	11.3	14.0	3.61	84.7	0.127	3.48	<0.188	0.0566	<0.0222	0.431	<0.13	<0.0122	<0.0164
B	Cpx	MR15C16	MR15C03	40	1	3	57	64	72	29Si	255844	255844	<18.9	159552	82.9	362	5620	1769	3.18	2.96	1.37	22.5	2.13	0.834	<0.578	<0.0744	4.58	<0.226	<0.278	1.36	5.94
B	Cpx	MR15C16	MR15C04	35	2	3	50	80	97	29Si	255844	255844	48.4	116105	71.6	256	3831	2579	9.14	14.9	2.91	44.7	2.15	2.21	0.593	0.310	4.62	0.279	0.431	1.17	4.86
B	Cpx	MR15C16	MR15C05	35	3	3	54	62	94	29Si	255844	255844	22.3	159639	96.0	370	5289	1803	3.68	6.66	2.08	21.0	2.83	<0.697	<0.337	0.623	7.16	<0.242	0.817	1.00	4.51
B	Cpx	MR15C16	MR15C06	35	4	3	50	64	79	29Si	255844	255844	25.3	164600	91.4	359	6194	1887	3.06	7.82	1.71	22.8	2.50	1.06	<0.513	0.370	5.46	<0.382	0.343	1.26	5.95
B	Cpx	MR15C16	MR15C07	35	5	3	50	66	76	29Si	255844	255844	<25.7	155748	82.9	315	4856	1717	2.64	5.13	2.11	20.9	3.97	<1.27	<0.697	1.95	14.2	<0.306	2.68	1.20	5.75
B	Cpx	MR15C16	MR15C08	35	6	3	61	67	94	29Si	255844	255844	24.9	156023	93.9	359	5455	2015	4.87	14.8	2.08	27.9	2.26	1.15	<0.434	0.0671	4.41	0.282	<0.183	0.586	2.54
B	Cpx	MR15C16	MR15C09	40	7	3	60	65	84	29Si	255844	255844	33.8	167098	96.8	386	5755	1920	3.97	15.2	1.88	22.1	2.12	1.02	<0.332	0.225	5.17	<0.277	<0.279	0.551	2.44
B	Bulk	MR17B16	MR17B07	174x137	35	3	70	77	152	29Si	230000	230000	49.6	14133	11.9	62.8	2821	3312	12.0	49.5	5.97	92.2	4.23	2.43	<0.239	3.68	20.2	0.592	5.54	0.0970	0.311
B	Bulk	MR17B16	MR17B08	174x137	36	3	70	76	149	29Si	230000	230000	75.1	32384	22.6	77.4	1396	2715	10.2	43.7	3.66	54.6	5.11	2.42	<0.219	4.72	24.1	0.643	6.94	0.143	0.560
B	Bulk	MR17B16	MR17B09	174x137	37	3	73	81	155	29Si	230000	230000	47.4	25600	19.1	61.4	1096	3239	11.6	16.6	4.29	74.8	3.78	2.72	0.364	3.58	19.2	0.449	4.70	0.165	0.515
B	Bulk	MR17B16	MR17B10	174x137	38	3	78	83	155	29Si	230000	230000	51.3	31251	21.2	74.0	1378	2914	10.7	17.8	7.96	60.5	4.37	2.11	<0.251	4.29	21.9	0.382	5.51	0.277	1.10
B	Bulk	MR17B16	MR17B11	174x137	39	3	74	81	155	29Si	230000	230000	48.6	44885	29.4	115	2220	2754	9.15	28.1	3.19	58.3	3.85	2.02	<0.237	3.35	16.9	0.418	4.83	0.225	0.952
B	Bulk	MR17B16	MR17B12	40	BCR2G	3	56	66	155	29Si	252882	252882	1294	50282	33.5	425	15.1	1499	38.1	12.2	17.2	161	45.2	3.44	1.11	46.7	336	254	659	24.6	50.8

Inclusion	Mineral	Run	Analysis No	Spot size	Ref.	Blank Start	Blank End	Mineral Start	Mineral End	Isotope internal standard	Internal std conc	141Pr	145Nd	147Sm	151Eu	157Gd	159Tb	163Dy	165Ho	167Er	169Tm	173Yb	175Lu	177Hf	182W	195Pt	197Au	208Pb	209Bi	232Th	238U
B	Standard	MR15C16	MR15C18	40	BCR2G	3	60	65	150	29Si	252882	6.35	27.6	6.38	1.90	6.26	0.996	6.17	1.29	3.60	0.496	3.51	0.492	4.77	0.512	0.230	<0.0432	10.3	0.0345	5.70	1.62
B	Standard	MR17A16	MR17A18	40	BCR2G	3	56	68	156	29Si	252882	6.24	26.8	5.93	1.85	6.23	0.981	5.97	1.25	3.35	0.480	3.26	0.466	4.55	0.476	0.362	<0.0345	10.2	0.0380	5.68	1.59
B	Plag	MR17A16	MR17A14	30	27	3	56	69	87	29Si	179802	<0.032	<0.415	<0.228	0.131	<0.211	<0.0342	<0.119	<0.0353	<0.169	<0.0389	<0.277	<0.034	<0.228	<0.175	<0.194	<0.0845	<0.168	<0.0466	<0.0419	<0.0362
B	Plag	MR17A16	MR17A15	27	28	3	56	64	72	29Si	283345	<0.118	<1.64	<0.825	0.504	<0.686	<0.136	<0.441	<0.109	<0.551	0.101	<0.824	<0.11	<0.659	<0.552	<0.69	<0.364	<0.518	<0.126	<0.125	<0.106
B	Plag	MR17A16	MR17A17	30	30	3	56	65	69	29Si	283345	<0.141	<2.21	<1.07	0.740	<0.836	<0.135	<0.729	<0.153	<0.602	<0.111	<0.814	<0.184	<0.808	<0.721	<0.793	<0.453	<0.639	<0.172	<0.197	<0.147
B	Plag	MR17B16	MR17B03	30	31	3	60	76	93	29Si	283345	<0.107	<1.22	<0.772	0.588	<0.622	<0.0911	<0.422	<0.114	0.508	<0.0922	<0.657	<0.112	<0.691	<0.465	<0.5	<0.251	<0.482	<0.146	<0.12	<0.114
B	Plag	MR17B16	MR17B04	27	32	3	56	70	83	29Si	283345	<0.118	<1.49	<0.843	0.450	<0.856	<0.138	<0.534	<0.118	<0.68	<0.128	<0.629	<0.104	<0.581	<0.578	<0.556	<0.263	<0.543	<0.14	<0.172	<0.138
B	Opx	MR15C16	MR15C10	40	8	3	62	76	102	29Si	255844	0.0283	<0.22	<0.138	<0.0292	<0.117	<0.0219	0.164	0.0421	0.133	0.0249	0.223	0.0394	0.480	0.114	<0.108	<0.0555	<0.0811	<0.027	0.0839	<0.017
B	Opx	MR15C16	MR15C12	40	10	3	50	70	107	29Si	255844	<0.0173	<0.17	<0.126	<0.0387	<0.125	<0.0185	<0.0767	0.0222	0.144	0.0183	0.227	0.0358	0.128	<0.0898	<0.104	<0.0543	<0.0839	<0.0247	0.0320	<0.0176
B	Opx	MR15C16	MR15C13	40	11	3	58	67	146	29Si	255844	<0.0159	<0.204	<0.125	<0.0328	<0.0769	<0.0122	<0.0692	<0.0144	<0.0579	<0.0186	0.120	<0.0207	<0.0668	<0.0747	<0.0758	<0.0482	<0.0608	<0.0262	<0.0177	<0.0137
B	Opx	MR15C16	MR15C14	45	12	3	58	64	150	29Si	255844	<0.0112	<0.158	<0.0839	<0.0239	<0.0796	<0.0127	0.106	0.0218	0.0938	0.0183	0.189	0.0367	<0.0635	<0.0598	<0.0642	<0.0436	<0.0549	<0.0164	<0.0142	<0.0139
B	Opx	MR15C16	MR15C16	40	14	3	50	68	126	29Si	255844	<0.0185	<0.25	<0.107	<0.0326	<0.092	<0.0156	<0.0567	<0.0205	<0.0907	<0.0128	<0.112	<0.0186	<0.111	<0.0862	<0.103	<0.0477	<0.0817	<0.0226	<0.0201	<0.0162
B	Opx	MR15C16	MR15C17	40	15	3	60	75	103	29Si	255844	<0.0207	<0.242	<0.152	<0.046	<0.113	<0.0189	0.100	<0.023	0.0891	0.0163	0.167	0.0257	<0.0913	<0.107	<0.101	<0.064	0.0868	<0.0333	<0.0243	<0.0191
B	Opx	MR17A16	MR17A05	40	18	3	56	86	120	29Si	255844	<0.0167	<0.164	<0.0905	<0.0357	<0.0952	<0.0134	0.0813	0.0190	<0.0746	0.0227	0.131	0.0328	<0.071	<0.0694	<0.0847	<0.0442	<0.071	<0.0201	<0.0145	<0.0125
B	Opx	MR17A16	MR17A06	40	19	3	56	116	141	29Si	255844	<0.0176	<0.226	<0.131	<0.0337	<0.116	<0.0153	0.101	<0.0167	0.0785	<0.0172	0.196	0.0417	<0.101	<0.11	<0.0903	<0.0572	<0.0941	<0.0233	<0.0228	<0.0146
B	Opx	MR17A16	MR17A08	40	21	3	56	69	87	29Si	255844	<0.0161	<0.232	<0.145	<0.0383	<0.118	<0.0208	0.0812	0.0226	<0.107	0.0172	0.135	0.0492	0.124	<0.0863	<0.0984	<0.0527	<0.0796	<0.0253	<0.0242	<0.0196
B	Ol	MR17A16	MR17A09	40	22	3	56	68	156	29Si	179802	<0.0119	<0.141	<0.0589	<0.0251	<0.0673	<0.0103	<0.0504	<0.0114	<0.0451	<0.0128	<0.0706	<0.0112	<0.0609	<0.0621	<0.0614	<0.036	<0.041	<0.0121	<0.0131	<0.0106
B	Ol	MR17A16	MR17A10	40	23	3	56	68	156	29Si	179802	<0.013	<0.111	<0.074	<0.0251	<0.0526	<0.011	<0.0452	<0.00946	<0.0488	<0.0129	<0.0648	<0.0115	<0.0694	<0.0484	<0.0505	<0.0319	<0.0529	<0.0152	<0.0121	<0.0129
B	Ol	MR17A16	MR17A11	40	24	3	62	71	156	29Si	179802	<0.0118	<0.126	<0.0894	<0.0278	<0.0728	<0.0113	<0.0463	<0.0103	<0.0504	<0.0135	<0.0754	<0.0128	<0.077	<0.0426	<0.0504	<0.0337	<0.0328	<0.0145	<0.0139	<0.0106
B	Ol	MR17A16	MR17A12	40	25	3	56	68	113	29Si	179802	<0.00923	<0.136	<0.0754	<0.0229	<0.0963	<0.0111	<0.0491	<0.0147	<0.0466	<0.0113	<0.089	<0.013	0.0624	<0.0666	<0.064	<0.0366	<0.053	<0.0186	<0.0126	<0.0115
B	Ol	MR17A16	MR17A13	40	26	3	56	71	103	29Si	179802	<0.0132	<0.166	<0.0725	<0.0299	<0.0791	<0.0121	<0.0487	<0.0145	<0.059	<0.0112	<0.093	<0.0148	<0.0662	<0.052	<0.0663	<0.0376	<0.0663	<0.0214	<0.0186	<0.0133
B	Cpx	MR15C16	MR15C03	40	1	3	57	64	72	29Si	255844	1.19	7.20	2.37	0.0744	3.75	0.622	3.63	0.855	1.79	0.233	1.50	0.233	3.47	<0.134	<0.131	<0.0754	<0.107	<0.0434	<0.033	<0.0264
B	Cpx	MR15C16	MR15C04	35	2	3	50	80	97	29Si	255844	0.921	6.24	1.83	<0.0742	2.55	0.476	2.49	0.485	1.28	0.128	1.10	0.168	2.35	<0.138	<0.14	<0.104	0.162	<0.0395	0.0664	<0.0359
B	Cpx	MR15C16	MR15C05	35	3	3	54	62	94	29Si	255844	0.889	5.59	1.81	0.115	2.98	0.483	2.94	0.571	1.37	0.210	1.27	0.184	2.81	<0.0839	<0.125	<0.0807	<0.0912	<0.0273	0.0387	<0.0207
B	Cpx	MR15C16	MR15C06	35	4	3	50	64	79	29Si	255844	1.15	5.85	2.52	0.0817	2.61	0.437	2.82	0.468	1.15	0.181	1.30	0.166	2.78	<0.126	<0.219	<0.09	<0.116	<0.0356	<0.0302	<0.0291
B	Cpx	MR15C16	MR15C07	35	5	3	50	66	76	29Si	255844	1.18	6.84	1.76	0.106	3.06	0.465	2.89	0.512	1.44	0.180	1.13	0.149	2.26	<0.148	<0.236	<0.105	<0.142	<0.0521	0.0393	<0.0339
B	Cpx	MR15C16	MR15C08	35	6	3	61	67	94	29Si	255844	0.489	3.06	1.42	<0.0368	2.04	0.331	2.31	0.421	1.30	0.172	1.15	0.174	3.07	<0.108	<0.124	<0.0502	<0.0745	<0.0287	<0.0254	<0.0205
B	Cpx	MR15C16	MR15C09	40	7	3	60	65	84	29Si	255844	0.557	2.66	1.11	0.0635	1.86	0.324	2.02	0.471	1.13	0.172	1.11	0.200	3.03	<0.12	<0.1	<0.0733	<0.0811	<0.0232	0.0343	<0.0265
B	Bulk	MR17B16	MR17B07	174x137	35	3	70	77	152	29Si	230000	0.0379	0.248	<0.119	0.155	<0.122	<0.0158	0.0898	0.0263	0.106	0.0243	<0.0966	<0.0178	0.324	<0.0773	<0.078	<0.047	0.120	<0.0208	<0.019	<0.0183
B	Bulk	MR17B16	MR17B08	174x137	36	3	70	76	149	29Si	230000	0.0893	0.532	0.232	0.156	0.376	0.0648	0.375	0.0837	0.216	0.0320	0.275	0.0389	0.604	<0.0547	<0.0752	<0.0489	0.0854	<0.0169	0.0206	<0.0158
B	Bulk	MR17B16	MR17B09	174x137	37	3	73	81	155	29Si	230000	0.108	0.544	0.224	0.112	0.289	0.0476	0.286	0.0603	0.198	0.0338	0.140	0.0312	0.465	<0.0764	<0.0847	<0.0432	0.0826	<0.0252	<0.0209	<0.0155
B	Bulk	MR17B16	MR17B10	174x137	38	3	78	83	155	29Si	230000	0.211	1.47	0.405	0.135	0.533	0.0799	0.472	0.0808	0.188	0.0324	0.276	0.0426	0.521	<0.0668	<0.0878	<0.0379	0.120	<0.0195	<0.0182	<0.0177
B	Bulk	MR17B16	MR17B11	174x137	39	3	74	81	155	29Si	230000	0.182	1.11	0.357	0.137	0.488	0.0859	0.518	0.113	0.319	0.0462	0.329	0.0722	0.789	<0.0622	<0.0766	<0.0433	0.124	<0.018	0.0355	<0.0126
B	Bulk	MR17B16	MR17B12	40	BCR2G	3	56	66	155	29Si	252882	6.36	26.9	6.36	1.94	6.53	0.994	6.25	1.29	3.55	0.503	3.32	0.500	4.90	0.462	0.231	<0.0505	10.2	<0.0244	5.76	1.66

Table A.29. LA-ICP-MS data for Barwell Inclusion B. All concentrations in ppm.

Inclusion	Mineral	Run	Analysis No	Spot size	Ref.	Blank Start	Blank End	Mineral Start	Mineral End	Isotope internal standard	Internal std conc	29Si	31P	43Ca	45Sc	51V	53Cr	55Mn	59Co	60Ni	65Cu	66Zn	69Ga	72Ge	75As	85Rb	88Sr	95Mo	137Ba	139La	140Ce
C	Standard	AP04A16	AP04A18	40	BCR2G	3	62	67	156	29Si	252882	252882	1200	49383	32.2	418	15.0	1472	37.5	11.7	17.7	164	54.6	3.28	1.13	45.8	324	249	648	23.6	49.3
C	Standard	AP04B16	AP04B18	40	BCR2G	3	62	68	155	29Si	252882	252882	1209	49196	32.8	422	14.1	1465	37.8	11.9	17.5	160	48.6	2.80	0.883	46.5	331	252	648	24.3	49.7
C	Standard	AP05A16	AP05A18	40	BCR2G	3	62	70	154	29Si	252882	252882	1179	48907	31.6	417	15.6	1457	37.5	12.0	17.9	170	60.3	3.10	1.02	47.0	325	256	640	23.4	49.2
C	Plag	AP04B16	AP04B12	20	25 plag	3	58	74	99	29Si	283345	283345	<84.3	15017	6.04	<0.699	<8.42	2.68	6.72	64.1	<2.26	<2.8	24.1	<3.39	<1.71	21.0	91.2	<1.26	30.9	<0.122	<0.114
C	Plag	AP04B16	AP04B13	20	26 plag	3	62	68	87	29Si	283345	283345	97.1	14698	5.90	<0.755	<10.1	<1.71	<0.295	<1.62	<2.57	<2.8	29.9	<3.23	<1.83	18.7	99.6	<0.858	30.5	<0.152	<0.165
C	Plag	AP04B16	AP04B15	20	28 plag	3	62	67	74	29Si	283345	283345	<126	12178	4.79	2.70	17.2	619	2.31	11.7	<2.87	12.2	22.0	<4.3	<2.21	18.5	79.7	<1.51	28.8	<0.174	<0.211
C	Plag	AP04B16	AP04B16	20	29 plag	3	59	68	100	29Si	283345	283345	<71.9	13153	6.00	0.847	9.37	4.49	0.414	5.71	<2.06	<2.13	25.6	<3.35	<1.32	22.3	91.1	<0.781	32.7	<0.094	<0.113
C	Plag	AP05A16	AP05A09	18	37 plag	3	63	69	79	29Si	179802	179802	<66.3	20007	12.7	50.8	1031	978	1.35	<1.1	<2.09	19.2	8.95	<2.76	<1.6	8.29	32.0	<0.965	14.2	0.174	0.227
C	Plag	AP05A16	AP05A10	18	38 plag	3	62	70	102	29Si	283345	283345	<78.5	28562	20.8	72.2	1105	2018	2.71	2.43	<2.09	35.8	10.00	<3.74	<1.48	9.81	42.0	<0.79	13.0	<0.122	0.158
C	Plag	AP05A16	AP05A12	18	40 plag	3	64	69	81	29Si	283345	283345	<180	14740	7.13	1493	114686	1510	8.80	<3.13	<4.71	1327	34.5	<8.27	<3.93	17.8	88.1	<1.6	27.2	<0.261	<0.322
C	Plag	AP05A16	AP05A13	18	41 plag	3	60	66	79	29Si	283345	283345	<104	44397	22.6	119	5077	559	1.17	3.06	<3.25	23.0	14.7	<4.83	<2.48	19.4	76.8	<1.23	26.7	0.181	0.386
C	Plag	AP05A16	AP05A16	18	44 plag	3	60	69	87	29Si	283345	283345	<112	8019	7.79	2.34	<14.7	2587	6.08	8.79	4.78	58.2	9.88	<4.72	<2.37	11.7	47.0	<1.3	16.2	<0.161	<0.173
C	Plag	AP05A16	AP05A17	18	45 plag	3	62	69	104	29Si	283345	283345	96.1	15673	6.24	18.3	1323	518	1.75	3.88	<2.13	36.1	18.5	<4.49	<1.84	17.6	87.7	<0.996	33.0	<0.145	<0.153
C	Opx	AP04A16	AP04A08	40	6 px	3	59	67	78	29Si	255844	255844	18.1	6178	18.6	94.6	1770	3724	5.84	3.62	2.30	80.1	2.54	1.61	<0.357	<0.0367	0.0296	0.415	<0.15	<0.0233	<0.0244
C	Opx	AP04A16	AP04A09	40	7 px	3	59	67	85	29Si	255844	255844	32.3	6014	14.7	60.8	1140	3555	6.36	8.12	3.24	79.1	1.59	2.37	<0.233	<0.0274	0.0682	0.360	<0.138	<0.0172	<0.0172
C	Opx	AP04A16	AP04A10	35	8 px	3	59	67	93	29Si	255844	255844	22.8	5641	17.3	86.2	1910	3763	7.03	6.28	2.77	85.4	2.50	2.06	<0.279	<0.0544	0.0330	0.457	<0.155	<0.0252	<0.0232
C	Opx	AP04A16	AP04A11	35	9 px	3	64	78	108	29Si	255844	255844	<16.6	6467	15.5	69.7	1391	3575	6.99	6.14	2.97	82.5	2.09	1.64	<0.291	<0.0415	<0.0262	0.416	<0.151	<0.02	<0.0222
C	Opx	AP04A16	AP04A13	40	11 px	3	59	66	86	29Si	255844	255844	25.1	8093	15.7	76.9	1896	3561	5.88	3.67	3.21	84.1	1.88	1.56	<0.219	0.177	0.730	0.521	0.198	<0.0189	0.0215
C	Opx	AP04A16	AP04A14	35	12 px	3	56	63	149	29Si	255844	255844	18.7	6566	15.3	74.5	1792	3404	6.30	4.37	2.72	82.3	2.21	1.74	<0.275	0.191	0.770	0.433	<0.222	<0.0234	<0.0209
C	Opx	AP04A16	AP04A15	35	13 px	3	59	67	153	29Si	255844	255844	25.8	5724	14.1	63.7	1409	3426	5.94	4.02	2.65	80.0	1.83	1.98	<0.282	<0.0334	0.0559	0.417	<0.186	<0.0191	<0.023
C	Opx	AP04A16	AP04A16	35	14 px	3	62	68	96	29Si	255844	255844	28.0	6451	18.5	106	2167	3672	5.66	3.48	2.96	79.4	2.99	1.81	<0.293	<0.0399	0.106	0.474	<0.188	<0.0222	<0.0273
C	Opx	AP04A16	AP04A17	35	15 px	3	64	70	108	29Si	255844	255844	36.3	5864	15.3	70.6	1286	3582	5.77	5.29	4.45	80.0	2.53	1.85	<0.332	0.446	1.92	0.300	0.712	<0.0247	0.0237
C	Opx	AP04B16	AP04B03	35	16 px	3	62	68	97	29Si	255844	255844	34.0	10206	18.7	91.5	2095	3629	6.06	3.98	3.23	81.0	2.24	1.46	<0.315	0.283	1.40	0.421	0.563	<0.0234	0.0301
C	Opx	AP04B16	AP04B04	45	17 px	3	62	68	135	29Si	255844	255844	20.3	5960	14.2	61.8	1093	3674	6.76	4.87	2.98	82.4	1.84	1.92	<0.172	<0.0234	0.0426	0.481	<0.108	<0.0154	<0.0138
C	Opx	AP04B16	AP04B05	45	18 px	3	62	71	103	29Si	255844	255844	20.8	6210	13.8	72.7	2264	3575	6.23	5.47	4.15	84.4	1.98	1.82	<0.154	<0.0248	0.0331	0.372	<0.138	<0.0148	<0.012
C	Opx	AP04B16	AP04B06	40	19 px	3	72	81	106	29Si	255844	255844	24.3	4703	15.2	83.5	1937	3879	7.88	6.20	2.85	87.6	2.31	1.88	<0.253	<0.033	0.0366	0.559	<0.17	0.0194	0.0198
C	Opx	AP04B16	AP04B07	35	20 px	3	62	65	77	29Si	255844	255844	25.4	6998	15.7	72.2	1169	3735	5.59	3.79	3.48	76.6	1.82	1.71	<0.465	0.156	0.123	0.510	<0.255	<0.0348	<0.0281
C	Opx	AP04B16	AP04B08	35	21 px	3	62	68	93	29Si	255844	255844	<18.9	5561	17.1	92.3	1762	3774	6.08	4.59	2.94	83.4	2.95	1.87	<0.317	0.167	0.510	0.526	<0.227	<0.0287	<0.0307
C	Opx	AP04B16	AP04B09	35	22 px	3	65	73	116	29Si	255844	255844	19.2	6730	17.3	106	3308	3654	7.47	15.1	4.31	87.5	2.59	1.27	<0.279	<0.041	0.0351	0.523	<0.221	<0.0151	<0.0187
C	Ol	AP04A16	AP04A05	35	3 olivine	3	59	82	100	29Si	179802	179802	20.3	<167	5.82	2.37	123	3417	11.7	13.7	3.90	73.8	0.124	2.63	<0.34	<0.0558	<0.0322	0.321	<0.263	<0.0276	<0.0247
C	Ol	AP04A16	AP04A07	35	5 olivine	3	63	70	79	29Si	179802	179802	59.1	<240	5.85	14.4	922	3475	11.0	12.0	4.19	89.3	0.239	2.69	<0.417	<0.0594	0.0955	0.455	<0.258	<0.0225	<0.0252
C	Ol	AP04B16	AP04B10	35	23 ol	3	62	70	120	29Si	179802	179802	32.9	215	4.70	1.33	17.7	3389	7.00	15.0	3.67	66.9	0.239	2.59	<0.26	<0.0364	<0.0238	0.425	<0.182	<0.0164	<0.025
C	Ol	AP05A16	AP05A05	40	33 ol	3	61	69	82	29Si	179802	179802	31.1	279	5.62	1.68	14.0	3632	6.70	11.9	4.37	74.5	0.196	4.01	<0.244	0.0577	<0.0246	0.576	<0.126	<0.0183	<0.0196
C	Ol	AP05A16	AP05A08	40	36 ol	3	55	74	94	29Si	179802	179802	25.4	132	5.24	2.13	15.1	3555	6.97	16.4	5.05	75.6	0.180	3.77	<0.227	<0.0312	<0.0231	0.401	<0.171	<0.0174	<0.0183
C	Cpx	AP05A16	AP05A04	25	32 px	3	55	67	88	29Si	255844	255844	43.6	147912	82.2	341	4769	1981	9.10	31.5	7.91	29.3	2.01	<1.25	<0.504	0.197	4.08	<0.352	0.346	0.145	0.674
C	Bulk	AP05B16	AP05B03	45	225sq bulk	3	78	85	152	29Si	230000	230000	37.7	6776	12.4	63.2	1651	3605	9.48	9.20	4.34	83.9	2.13	2.24	<0.149	1.25	4.72	0.449	1.74	0.0129	0.0358
C	Bulk	AP05B16	AP05B04	45	225sq bulk	3	70	77	150	29Si	230000	230000	38.6	8573	13.1	64.9	1651	3519	9.19	10.8	3.90	79.9	2.34	2.39	<0.137	1.42	5.33	0.485	1.89	0.0358	0.105
C	Bulk	AP05B16	AP05B05	45	225sq bulk	3	68	78	150	29Si	230000	230000	48.5	7601	11.7	55.3	1459	3505	9.30	12.9	5.59	81.4	2.44	2.35	<0.183	1.93	8.10	0.441	2.82	0.0213	0.0788
C	Bulk	AP05B16	AP05B06	45	225sq bulk	3	73	81	150	29Si	230000	230000	37.4	11274	13.5	51.6	828	3337	9.20	21.5	4.08	72.9	2.48	2.37	<0.177	2.22	9.08	0.361	3.14	0.0339	0.114
C	Bulk	AP05B16	AP05B07	45	225sq bulk	3	69	75	150	29Si	230000	230000	38.4	11481	15.5	73.6	1842	3429	8.57	12.7	6.94	77.9	2.34	2.00	<0.144	1.37	5.72	0.456	2.01	0.0433	0.212

Inclusion	Mineral	Run	Analysis No	Spot size	Ref.	Blank Start	Blank End	Mineral Start	Mineral End	Isotope internal standard	Internal std conc	141Pr	145Nd	147Sm	151Eu	157Gd	159Tb	163Dy	165Ho	167Er	169Tm	173Yb	175Lu	177Hf	182W	195Pt	197Au	208Pb	209Bi	232Th	238U
C	Standard	AP04A16	AP04A18	40	BCR2G	3	62	67	156	29Si	252882	6.25	26.3	6.15	1.88	6.38	0.994	6.04	1.23	3.52	0.507	3.11	0.488	4.91	0.436	0.187	<0.0378	10.2	<0.0306	5.69	1.62
C	Standard	AP04B16	AP04B18	40	BCR2G	3	62	68	155	29Si	252882	6.33	27.1	6.34	1.88	6.22	1.02	5.98	1.22	3.44	0.487	3.50	0.501	4.81	0.484	0.293	<0.048	10.1	0.0367	5.68	1.60
C	Standard	AP05A16	AP05A18	40	BCR2G	3	62	70	154	29Si	252882	6.21	26.8	6.12	1.82	6.26	0.963	5.81	1.23	3.39	0.523	3.10	0.444	4.76	0.475	0.280	<0.046	10.3	<0.0324	5.63	1.63
C	Plag	AP04B16	AP04B12	20	25 plag	3	58	74	99	29Si	283345	<0.0975	<1.27	<0.574	0.683	<0.665	<0.1	<0.415	<0.101	<0.392	<0.104	<0.524	<0.104	<0.646	<0.372	<0.432	<0.321	<0.489	<0.129	<0.103	<0.116
C	Plag	AP04B16	AP04B13	20	26 plag	3	62	68	87	29Si	283345	<0.0778	<1.31	<0.717	0.466	<0.684	<0.108	<0.506	<0.109	<0.514	<0.102	<0.674	<0.143	<0.863	<0.539	<0.605	<0.369	<0.44	<0.119	<0.145	<0.12
C	Plag	AP04B16	AP04B15	20	28 plag	3	62	67	74	29Si	283345	<0.113	<1.65	<1.2	0.418	<0.872	<0.139	<0.452	<0.119	<0.592	<0.137	<0.84	<0.127	<0.834	<0.751	<0.803	<0.361	<0.684	<0.158	<0.104	<0.14
C	Plag	AP04B16	AP04B16	20	29 plag	3	59	68	100	29Si	283345	<0.133	<1.1	<0.63	0.526	<0.726	<0.0733	<0.441	<0.0917	<0.383	<0.086	<0.507	<0.0653	<0.465	<0.45	<0.389	<0.258	<0.367	<0.12	<0.104	<0.0945
C	Plag	AP05A16	AP05A09	18	37 plag	3	63	69	79	29Si	179802	<0.081	<1.06	<0.78	0.284	<0.669	<0.0916	<0.335	<0.11	<0.476	<0.0968	<0.523	0.0759	<0.472	<0.48	<0.501	<0.234	<0.451	<0.133	<0.0959	<0.0909
C	Plag	AP05A16	AP05A10	18	38 plag	3	62	70	102	29Si	283345	<0.0777	<1.17	<0.63	<0.212	<0.722	<0.121	<0.449	<0.121	0.423	<0.0919	<0.582	<0.119	0.606	<0.626	<0.547	<0.316	<0.451	<0.145	<0.12	<0.124
C	Plag	AP05A16	AP05A12	18	40 plag	3	64	69	81	29Si	283345	<0.256	<2.91	<1.33	0.592	<1.42	<0.199	<0.865	<0.264	<1.01	<0.193	<1.29	<0.267	<1.11	<1.13	<1.14	<0.74	<1.27	<0.315	<0.303	<0.238
C	Plag	AP05A16	AP05A13	18	41 plag	3	60	66	79	29Si	283345	<0.18	<1.44	<1.02	0.459	<0.935	<0.172	<0.712	<0.142	<0.767	<0.16	<0.812	<0.175	<0.908	<0.643	<0.706	<0.429	<0.757	<0.166	<0.151	0.163
C	Plag	AP05A16	AP05A16	18	44 plag	3	60	69	87	29Si	283345	<0.133	<1.72	<0.834	0.328	<0.89	<0.132	<0.427	<0.184	<0.638	<0.16	<0.661	<0.132	<0.851	<0.649	<0.848	<0.399	<0.676	<0.204	<0.173	<0.148
C	Plag	AP05A16	AP05A17	18	45 plag	3	62	69	104	29Si	283345	<0.114	<1.44	<0.844	0.552	<0.923	<0.129	<0.608	<0.121	<0.453	<0.12	<0.763	<0.11	<0.573	<0.545	<0.784	<0.379	<0.685	<0.167	<0.122	<0.12
C	Opx	AP04A16	AP04A08	40	6 px	3	59	67	78	29Si	255844	<0.0165	<0.226	<0.109	<0.0323	<0.135	<0.0195	<0.066	0.0289	0.0996	<0.0145	0.273	0.0388	<0.0945	<0.104	<0.0854	<0.0462	<0.0891	<0.0229	<0.0201	<0.0142
C	Opx	AP04A16	AP04A09	40	7 px	3	59	67	85	29Si	255844	<0.0141	<0.173	<0.0983	<0.0283	<0.092	<0.0144	<0.0529	<0.0168	<0.0779	<0.0162	0.164	0.0213	<0.0631	<0.0678	<0.062	<0.0425	<0.0909	<0.0195	<0.0207	<0.0142
C	Opx	AP04A16	AP04A10	35	8 px	3	59	67	93	29Si	255844	<0.0157	<0.211	<0.122	<0.0415	<0.123	<0.0164	<0.0772	<0.0214	0.0882	<0.0156	0.192	0.0349	<0.0995	<0.0981	<0.0992	<0.0535	<0.107	<0.0228	<0.0223	<0.0202
C	Opx	AP04A16	AP04A11	35	9 px	3	64	78	108	29Si	255844	<0.0189	<0.186	<0.138	<0.0355	<0.129	<0.0133	<0.0819	<0.0178	<0.108	<0.0172	0.145	0.0331	<0.099	<0.096	<0.0859	<0.0417	<0.0749	<0.0217	<0.0198	<0.0205
C	Opx	AP04A16	AP04A13	40	11 px	3	59	66	86	29Si	255844	<0.018	<0.228	<0.125	<0.03	<0.106	<0.0165	<0.0643	<0.016	<0.0791	0.0317	0.258	0.0451	<0.0994	<0.0653	<0.0708	<0.0421	<0.0708	<0.0202	0.0551	<0.0177
C	Opx	AP04A16	AP04A14	35	12 px	3	56	63	149	29Si	255844	<0.0182	<0.194	<0.121	<0.0329	<0.0961	<0.0178	<0.0867	<0.0221	<0.0773	0.0205	0.236	0.0250	<0.0873	<0.0722	<0.0982	<0.052	<0.0782	<0.022	0.0565	<0.0178
C	Opx	AP04A16	AP04A15	35	13 px	3	59	67	153	29Si	255844	<0.0148	<0.193	<0.129	<0.0455	<0.109	<0.0173	<0.0817	<0.0204	0.0877	<0.0155	0.198	0.0336	<0.103	<0.0788	<0.0995	<0.0516	<0.0976	<0.0212	<0.0204	<0.0178
C	Opx	AP04A16	AP04A16	35	14 px	3	62	68	96	29Si	255844	<0.0159	<0.228	<0.129	<0.0351	<0.119	<0.0196	0.159	0.0309	0.0911	0.0169	0.370	0.0606	0.189	<0.0952	<0.113	<0.0506	<0.0808	<0.0216	<0.0185	<0.0228
C	Opx	AP04A16	AP04A17	35	15 px	3	64	70	108	29Si	255844	<0.0147	<0.264	<0.128	<0.0303	<0.126	<0.0167	<0.0725	<0.0172	<0.0928	0.0222	0.224	0.0207	<0.102	<0.101	<0.0844	<0.0581	<0.0836	<0.0206	<0.0223	<0.0206
C	Opx	AP04B16	AP04B03	35	16 px	3	62	68	97	29Si	255844	<0.0206	<0.238	<0.131	<0.0396	<0.152	<0.0206	0.0850	0.0207	<0.0981	<0.0241	0.217	0.0416	0.165	<0.0898	<0.131	<0.0735	<0.0816	<0.0336	0.0313	<0.0229
C	Opx	AP04B16	AP04B04	45	17 px	3	62	68	135	29Si	255844	<0.0115	<0.158	<0.079	<0.0225	<0.08	<0.0116	<0.0461	0.0157	0.0757	<0.0113	0.147	0.0279	<0.0562	<0.0439	<0.0524	<0.0353	<0.0487	<0.0141	<0.0101	<0.012
C	Opx	AP04B16	AP04B05	45	18 px	3	62	71	103	29Si	255844	<0.0104	<0.146	<0.083	<0.0256	0.0631	<0.0127	<0.0492	0.0134	0.0766	0.0134	0.157	0.0171	0.0734	<0.0649	<0.07	<0.034	<0.0586	<0.0122	<0.0165	<0.0107
C	Opx	AP04B16	AP04B06	40	19 px	3	72	81	106	29Si	255844	<0.0162	<0.188	<0.106	<0.0363	<0.0955	<0.0164	<0.0567	0.0191	<0.0964	<0.0125	0.173	0.0396	<0.0836	<0.0677	<0.0981	<0.0427	<0.0714	<0.0226	<0.0177	<0.0177
C	Opx	AP04B16	AP04B07	35	20 px	3	62	65	77	29Si	255844	<0.0216	<0.328	<0.183	<0.0469	<0.181	<0.0276	<0.0873	<0.0301	<0.122	0.0364	<0.197	0.0533	<0.184	<0.13	<0.159	<0.0752	<0.121	<0.0326	<0.0246	<0.0266
C	Opx	AP04B16	AP04B08	35	21 px	3	62	68	93	29Si	255844	<0.0211	<0.268	<0.165	<0.0528	<0.135	<0.021	<0.0915	<0.0206	0.123	<0.0229	0.220	0.0527	<0.135	<0.128	<0.0975	<0.064	<0.0967	<0.0283	<0.021	<0.0249
C	Opx	AP04B16	AP04B09	35	22 px	3	65	73	116	29Si	255844	<0.0189	<0.184	<0.119	<0.0331	<0.12	<0.0182	<0.0892	<0.0213	<0.0899	0.0212	0.250	0.0366	<0.129	<0.0792	<0.0962	<0.0678	<0.0895	<0.0223	<0.021	<0.0229
C	Ol	AP04A16	AP04A05	35	3 olivine	3	59	82	100	29Si	179802	<0.0237	<0.287	<0.126	<0.0454	<0.159	<0.0228	<0.0997	<0.02	<0.101	<0.0168	<0.134	<0.0236	<0.139	<0.0997	<0.138	<0.0642	<0.128	<0.0282	<0.0249	<0.0235
C	Ol	AP04A16	AP04A07	35	5 olivine	3	63	70	79	29Si	179802	<0.0243	<0.236	<0.172	<0.0437	<0.16	<0.0218	<0.0895	<0.0262	<0.101	<0.0209	<0.158	<0.0231	<0.133	<0.11	<0.123	<0.0783	<0.122	<0.0329	<0.0271	<0.0251
C	Ol	AP04B16	AP04B10	35	23 ol	3	62	70	120	29Si	179802	<0.0173	<0.207	<0.114	<0.039	<0.119	<0.017	<0.0657	<0.0198	<0.0632	<0.0148	<0.0889	<0.0192	<0.0916	<0.0765	<0.086	<0.0519	<0.079	<0.0216	<0.0208	<0.0169
C	Ol	AP05A16	AP05A05	40	33 ol	3	61	69	82	29Si	179802	<0.0177	<0.204	<0.118	<0.0277	<0.104	<0.0162	<0.0501	<0.015	<0.0663	<0.0149	<0.0967	<0.0176	<0.0819	<0.0802	<0.0791	<0.0444	<0.0856	<0.0215	<0.0177	0.0148
C	Ol	AP05A16	AP05A08	40	36 ol	3	55	74	94	29Si	179802	<0.013	<0.165	<0.0999	<0.0282	<0.0877	<0.0147	<0.058	<0.0186	<0.068	<0.0203	<0.113	<0.018	<0.0829	<0.0711	<0.0641	<0.0603	<0.0761	<0.0202	<0.0188	<0.0181
C	Cpx	AP05A16	AP05A04	25	32 px	3	55	67	88	29Si	255844	0.130	0.896	0.407	<0.0598	0.764	0.142	1.30	0.217	0.643	0.116	1.10	0.157	2.01	<0.158	<0.192	<0.103	<0.179	<0.0482	<0.0294	<0.04
C	Bulk	AP05B16	AP05B03	45	225sq bulk	3	78	85	152	29Si	230000	<0.0109	<0.102	<0.0742	0.0274	<0.0773	<0.0122	0.0640	0.0135	0.0615	0.0148	0.148	0.0221	0.0618	<0.0391	<0.0575	<0.0291	0.247	<0.0122	0.0315	<0.0135
C	Bulk	AP05B16	AP05B04	45	225sq bulk	3	70	77	150	29Si	230000	0.0163	<0.119	<0.0696	0.0268	<0.0579	<0.0123	0.0475	<0.0131	0.0801	0.0255	0.168	0.0264	0.0957	<0.0494	<0.0375	<0.028	0.191	<0.0108	0.0269	<0.0109
C	Bulk	AP05B16	AP05B05	45	225sq bulk	3	68	78	150	29Si	230000	<0.0129	0.120	<0.0774	0.0414	<0.0699	<0.0123	0.0634	0.0175	0.0670	0.0199	0.168	0.0181	0.125	<0.0505	<0.0589	<0.0323	0.167	<0.0141	0.0195	<0.0137
C	Bulk	AP05B16	AP05B06	45	225sq bulk	3	73	81	150	29Si	230000	0.0181	<0.125	<0.0957	0.0532	<0.0723	0.0146	0.100	0.0247	0.0655	<0.0138	<0.0779	0.0358	0.204	<0.0488	<0.0641	<0.0311	0.196	<0.0175	0.0271	0.0147
C	Bulk	AP05B16	AP05B07	45	225sq bulk	3	69	75	150	29Si	230000	0.0370	<0.135	<0.0761	0.0267	<0.0653	0.0130	0.0770	0.0286	0.105	0.0226	0.128	0.0388	0.124	<0.0427	<0.0537	<0.0344	0.240	<0.0172	0.0240	<0.00795

Table A.30. LA-ICP-MS data for Barwell Inclusion C. All concentrations in ppm.